

~~C. Matthews~~

~~AD~~

**NASA TECHNICAL  
MEMORANDUM**

NASA TM X-53782

October 15, 1968

*N69-15868*

**CASE FILE  
COPY**

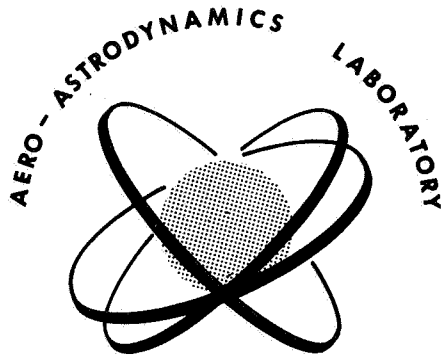
NASA TM X-53782

**AERO-ASTRODYNAMICS  
RESEARCH REVIEW NO. 7**

AERO-ASTRODYNAMICS LABORATORY  
RESEARCH AND DEVELOPMENT OPERATIONS  
GEORGE C. MARSHALL SPACE FLIGHT CENTER  
MARSHALL SPACE FLIGHT CENTER, ALABAMA

NASA - GEORGE C. MARSHALL SPACE FLIGHT CENTER

TECHNICAL MEMORANDUM X-53782



RESEARCH REVIEW NUMBER SEVEN

William D. Murphree - Editor

RESEARCH AND DEVELOPMENT OPERATIONS  
AERO-ASTRODYNAMICS LABORATORY

## PREFACE

The topics discussed in this seventh Aero-Astrodynamic Research Review cover a variety of subjects. Included are Acoustics, Atmospheric Physics, Celestial Mechanics, Flight Mechanics, Fluid Dynamics, Solar Physics, Statistical Analysis and Operations Analysis. Also included, under the heading "Publications and Presentations," are the titles and abstracts of the reports and papers which have been prepared during the period from July, 1967, through August, 1968. First, NASA reports are listed, followed by those papers which have been presented at symposia and those which were printed in the open literature.

The very nature of research precludes an even distribution of subject matter or the inclusion of all subject areas in one review. However, a study of reviews over a period of several years will give a fairly complete picture of the research being done by the laboratory. Furthermore, these reviews are not progress reports; rather it is attempted here to publish works of a research nature which have reached a milestone worthy of note. Other subjects will be discussed in forthcoming reviews.

It is hoped that this document will be interesting and helpful to other organizations engaged in space flight research and related efforts. Criticisms and discussions concerning individual papers with respective authors are invited.



E. D. Geissler  
Director, Aero-Astrodynamic Laboratory



**I. ACOUSTICS**

Acoustic Environments of Rocket Exhausts by G. A. Wilhold . . . . .	2
---	---

**II. ATMOSPHERIC PHYSICS**

A Study of Upper Atmospheric Models by James W. Johnson . . . . .	16
---	----

Interaction of Atmospheric Waves with the Ionosphere by Robert W. Porter . . . . .	22
--	----

The Theory for the Determination of Wind Velocity and the Associated Altitude by the Cross-Beam Method by M. Y. Su, J. B. Stephens and M. Phillips . . . . .	29
---	----

Remote Wind Detection With the Cross-Beam Method at Lower Heights by J. B. Stephens, Virgil A. Sanborn and A. J. Montgomery . . . . .	88
--	----

Optimum Averaging Times of Meteorological Data With Time Dependent Means by R. R. Jayroe, Jr. and M. Y. Su . . . . .	103
---	-----

**III. CELESTIAL MECHANICS**

The Binary Collision in the N-Body Problem by Hans J. Sperling . . . . .	116
--	-----

**IV. FLIGHT MECHANICS**

Optimization of "Ephemeridal" Parameters for Minimum Propellant Requirements on Multiplanet Roundtrip Swingby-Stopover Missions by Charles W. Mead and Archie C. Young..	126
---	-----

**V. FLUID DYNAMICS**

Rise Rate and Growth of Static Test Vehicle Engine Exhaust Clouds by Michael Susko, John W. Kaufman and Kelly Hill . . . . .	146
---	-----

**VI. SOLAR PHYSICS**

Frequency Distribution of Solar Radiation at Apalachicola, Florida, and Santa Maria, California by Glenn E. Daniels . . . . .	170
--	-----

Longitudinal Persistence of Major Solar Flares by T. E. Pratt . . . . .	184
---	-----

Solar Activity Indices by H. C. Euler . . . . .	188
---	-----

CONTENTS (Concluded) . . .	Page
<b>VII. OPERATIONS ANALYSIS</b>	
Automatic Experiment Scheduling and Optimization Program (AESOP) by R. F. Ball and W. D. McFadden . . . . .	198
<b>VIII. STATISTICAL ANALYSIS</b>	
Noise Elimination by Piecewise Cross Correlation of Photometer Outputs by Fritz R. Krause and Benjamin C. Hablutzel . . . . .	208
<b>IX. PUBLICATIONS AND PRESENTATIONS</b>	
A. Publications . . . . .	228
B. Presentations . . . . .	240

## I. ACOUSTICS

# ACOUSTIC ENVIRONMENTS OF ROCKET EXHAUSTS

By

G. A. Wilhold

## ABSTRACT

Importance of acoustic environment, environmental definitions, and acoustic environment prediction procedures for space vehicle engine static tests are discussed. Methods prescribed for predicting acoustic environments, when used correctly, provide fairly reliable estimates, but each method discussed has severe limitations requiring caution in their use.

## DEFINITION OF SYMBOLS

dB	$10 \log \overline{p^2}/p_{\text{ref}}^2$
p	acoustic pressure N/m <sup>2</sup>
$\overline{p^2}$	time average of the square of the acoustic pressure, i. e., mean squared pressure, N <sup>2</sup> /m <sup>4</sup>
N	Newtons, force
m	meters, distance
$p_{\text{ref}}$	reference pressure 0.00002 N/m <sup>2</sup>
f	frequency, Hz
$\Delta f$	bandwidth = $f_u - f_L$ Hz
$f_u$	upper frequency limit, Hz
$f_L$	lower frequency limit, Hz
$\text{SPL}_{\text{OA}}$	sound pressure level overall magnitude, dB
$\text{SPL}_{1/3}$	sound pressure level in a 1/3 octave frequency band, dB
$\text{SPL}_{\text{OB}}$	sound pressure level in an octave frequency band, dB

CPSD(f)	correlated acoustic pressure spectral density between two spatial points at a given frequency, N <sup>2</sup> /m <sup>4</sup> Hz
$\square^2$	d'Alembertian operator = $\nabla^2 - \frac{1}{C_o^2} \frac{\partial^2}{\partial t^2}$
$\nabla^2$	Laplacian operator = $\frac{\partial^2}{\partial X_1^2} + \frac{\partial^2}{\partial X_2^2} + \frac{\partial^2}{\partial X_3^2}$
t	time, seconds
X	spatial coordinate, m
$C_o$	isentropic speed of sound, m/sec
Q	mass flow rate, Kg(mass)/sec
$\nabla \cdot$	divergence = $\frac{\partial}{\partial X_1} + \frac{\partial}{\partial X_2} + \frac{\partial}{\partial X_3}$
F	body force, N
$\rho$	density, Kg(mass)/m <sup>3</sup>
q	fluid partical velocity, m/sec
i, k	subscripts, designating the i <sup>th</sup> and k <sup>th</sup> direction, respectively
$\tau_{i, k}$	viscous fluid stress, N/m <sup>2</sup>
R	distance from apparent source to point on the vehicle surface, m
$X_o$	distance from midpoint of vehicle in exhaust plane to apparent source, m
A(f)	is proportional to the apparent acoustic power density, for a given frequency, radiated back toward the vehicle from an apparent source, N <sup>2</sup> /m <sup>2</sup> Hz
T	thrust of one engine, N
D	exit diameter of one engine, m
V	exit velocity of rocket exhaust, m/sec

## DEFINITION OF SYMBOLS (Concluded)

n	number of rocket engines
$fD/V$	Strouhal number, nondimensional frequency
$\phi$	angle between ground and centerline of deflected exhaust stream, degrees
$\theta$	angle in ground plane measured from projection of centerline of deflected exhaust on ground plane, degrees
$\eta$	acoustic efficiency factor $\frac{A_{OA}}{W_M} = 0.005$ for large boosters nondimensional
$A_{OA}$	overall acoustic power, watts
$W_M$	mechanical power of rocket exhaust, watts
$A'(f)$	the apparent monopole acoustic power spectral density radiated in the ground plane for a given frequency f, watts/Hz

### I. INTRODUCTION

Perhaps the most disturbing and deleterious by-product of static tests and launch site space vehicle operations is the intense acoustic noise generated by the exhaust flow of the rocket motors. This adverse environment occurs during the hold-down period before launch release of a rocket and also during the static (restrained) firing tests of the rocket's booster and stages.

To provide some feel for the tremendous amount of acoustical energy generated during the firing of a rocket motor is very difficult. However, if the acoustic power of the Saturn V vehicle at launch (about  $2.0 \times 10^8$  watts) were converted to electrical power, it could supply enough electrical power to light about two hundred thousand average homes, assuming that about  $10^3$  watts would completely light up an average home. If the acoustic power were converted to mechanical power, it could lift an auto (one-ton of weight at the surface of the earth) at a rate of about 50 000 miles per hour. These crude analogies reveal the magnitude of the acoustic environments which must be considered in the development of space vehicles. Although much lower in total

magnitude, current and future jet aircraft are beginning to create similar significant acoustic environments which result in aircraft design and siting problems [1, 2].

The resultant acoustic environment is of such a magnitude that it dominates the structural and electronic design considerations of both rocket and ground support equipment (GSE). It also presents an operational hazard to astronauts, to static and launch site personnel, and to communities adjacent to launch sites. The psychological and physiological reactions to this intense noise field are extremely difficult to assess. Of course, as rockets have grown in size, the magnitude and the complexities of the problems associated with the acoustic environment have grown proportionately. It is not so difficult to see that the impact on the systems, and hence total cost, will be much greater if a "fix" instead of "cure" philosophy is adopted with respect to this important design consideration. Therefore, it is important that all aspects of the acoustic environment be defined at the earliest possible phase of the research, development, operational cycle of current and future space vehicle systems.

### II. IMPORTANCE AND ENVIRONMENTAL DEFINITION GOALS

The acoustic environment enters into most aspects of the design considerations for a proposed space vehicle system, influencing the static and launch site firing locations, orientation, operations, and the structural integrity of the space vehicle itself, as well as the design specifications for the space vehicle electronic systems. It also influences the structural and electronic integrity of the ground support equipment, and creates adverse vibration environments, which must be considered for the proper design and qualification of all the space vehicle structural and electronic components, as well as those of the ground support equipment. Therefore, it dictates indirectly the requirements for adequate acoustic and vibration test facilities necessary for qualification testing. It is well known that these tests involve astronomical expenditures of manpower and money. The extremely large space vehicles, such as the Saturn, have pushed current facility capabilities to the limit in size and achievable acoustic pressure levels. Since acoustic levels are expressed logarithmically (i. e., in dB Ref.  $0.00002 \text{ N/m}^2$ ), as the overall level becomes high, an error in the dB level represents a proportionately larger error in the absolute acoustic pressure value. An error at high

levels then results in increasing penalties from over-design and qualification testing. When the overall acoustic levels were much lower, these considerations were not so critical. However, the current levels are such that the fate (build or not-build decision) of new vehicle configurations is being decided by the anticipated acoustic environments. This trend is also indicated by the importance of the acoustic environment to the supersonic transport. These implications clearly point out the need for timely, accurate estimates of the acoustic environment associated with a given space vehicle or jet aircraft.

Basically, an estimate of the overall magnitude and the spectral and the spatial decomposition of the acoustic energy for an environmental definition is desirable. This estimate is provided by giving, at a point of observation, the overall sound pressure level ( $SPL_{OA}$ ), the spectral characteristics of the acoustic pressure (usually in one-third octave,  $SPL_{1/3}$ , or full octave band,  $SPL_{OB}$ , values versus frequency) and the cross power spectral characteristics (CPSD) of the acoustic pressure, usually 1/3 or full octave band levels reduced to spectrum values. These are the quantities used by the various structural and electronic system engineers for proper design and test criteria. For engineering purposes, the quantities provide an ideal environmental definition, and the efforts of the environmental dynamicist, i. e., the acousticist, should be oriented toward satisfying this ideal goal. However, because of difficulties which will be discussed later, the latter quantity (i. e., the CPSD) is usually missing in the first environmental estimates for a given configuration.

### III. ENVIRONMENTAL PREDICTION

The acoustic field around a rocket exhaust comprises three regions:

1. The farfield — Distances on the order of 50 to 100 nozzle diameters or so. The radiated noise field appears to be coming from a single point in a highly directional manner.

2. The midfield — Distances on the order of five wavelengths or so. The radiated field appears to be coming from a spatially extended source in a highly directional manner.

3. The nearfield — Distances within a wavelength or so. The fluctuating pressure field is not all radiated and is highly frequency dependent.

The ideal goal of the environmental dynamicist, as stated above, is to estimate the detailed characteristics of the noise field in each of these regions. This estimate would include an accurate definition of the overall energy and the spectral and spatial decomposition of the acoustic field. This is not currently possible. To overcome the deficiencies involved, the effort is broken into two parts. First, theoretical approaches are being advanced to gain better insight into the actual noise-generating mechanisms of hot rocket-exhaust flows, and second, analytical/empirical methods used for predicting the environments are being improved.

Theoretically, the wave equation for acoustic motions (assuming linear approximations) can be written most generally as [3] (see Fig. 1).

$$\square^2 P \equiv \nabla^2 P - \frac{1}{C_o^2} \frac{\partial^2 P}{\partial t^2} - \frac{\partial Q}{\partial t} \nabla \cdot F - \frac{\partial^2 (\rho q_i q_k - \tau_{ik})}{\partial x_i \partial x_k} - \frac{\partial^2}{\partial t^2} \frac{P}{C_o^2} - \rho$$

The right-hand terms will vanish in a source free, homogeneous, isentropic medium at rest, i. e., far from the source. In the confined region, where the violent exhaust flow exists, they become appreciable and may be regarded as sound sources. Such a representation provides some insight about the mechanism of sound generation; for example,

$\frac{\partial Q}{\partial t}$  represents an unsteady injection of fluid (i. e., pulsating mass flow through the nozzle exit area, etc.) — monopole type radiation.

$\nabla \cdot F$  spatial variation of body force (i. e., can represent pulsating thrust force across nozzle exit) — dipole radiation.

$\frac{\partial^2}{\partial x_i \partial x_k} (\rho q_i q_k)$  sound generation due to momentum fluctuations, including the Reynolds stress. This term is a major noise source in turbulent flow and turbulent jets — quadrupole radiation.

$\frac{\partial^2}{\partial x_i \partial x_k} \tau_{ik}$  sound generation from fluctuations of viscous stress; generally negligible.

$\frac{\partial^2}{\partial t^2} \left( \frac{P}{C_o^2} - \rho \right)$  may represent the effect of entropy fluctuation, temperature fluctuations. These can be monopole or quadrupole, depending on the influence of convection properties of flow.

provide only spectrums and overall sound pressure levels. Cross-correlation characteristics cannot be estimated from these prediction methods at this time. The analytical/empirical prediction techniques will be discussed next in the following order: mid-field, nearfield, and farfield.

The first such method is used to compute the midfield region of the static (restrained booster)

$$\square^2 p = \nabla^2 p - \frac{1}{c^2} \frac{\partial^2 \dot{Q}}{\partial t^2} = -\frac{\partial Q}{\partial t} + \nabla \cdot \bar{F} - \frac{\partial^2 (\rho \bar{q}_i \bar{q}_k - \tau_{ik})}{\partial x_i \partial x_k} - \frac{\partial^2}{\partial t^2} \left( \frac{p}{c^2} - \rho \right)$$

$\frac{\partial Q}{\partial t}$  Represents an unsteady injection of fluid (i.e. pulsating mass flow thru the nozzle of exit plane, etc.)—monopole type radiation.

$\nabla \bar{F}$  Spatial or unsteady variation of body force, (i.e. pulsating thrust force across nozzle exit plane, etc.)—dipole type radiation.

$\frac{\partial^2 \rho \bar{q}_i \bar{q}_k}{\partial x_i \partial x_k}$  Sound generation due to momentum fluctuations including the Reynolds stress. This term is a major noise source in a turbulent flow field—quadrupole type radiation.

$\frac{\partial^2}{\partial x_i \partial x_k} \tau_{ik}$  Sound generation due to fluctuations of the viscous stress of the fluid; usually negligible—quadrupole type radiation.

$\frac{\partial^2}{\partial t^2} \left( \frac{p}{c_o^2} - \rho \right)$  May represent the effect of entropy fluctuations, temperature fluctuation—type of radiation depends on assumption of region in which these fluctuations are being studied high speed convection region quadrupole nature; low speed after-burning combustion monopole nature.

FIGURE 1. THEORETICAL ASPECTS OF NOISE GENERATED BY FLOW FIELDS

The relative importance of the above terms to the noise field generated by hot rocket-exhaust flow fields is the subject of much debate, and a great deal of effort is being expended to determine their relative importance. Detailed knowledge of these quantities does not exist, and therefore the radiated acoustic field of a free (undeflected), hot, rocket exhaust by the theoretical approach cannot yet be estimated [4].

Deflecting the flow, as done in the practical situation, further complicates the theoretical approach, and hence the principles of dynamic similarity and model and full-scale test data must be used to generate prediction techniques. Although these methods are computerized at MSFC, they will

and launch pad acoustic environments for the vehicle surface itself. It was generated by considering the flow stream to consist of apparent sources of a single frequency (Fig. 2) distributed at apparent locations in the stream with respect to the nozzle exit plane. Since these apparent sources are considered to be statistically independent of one another, their effect at the vehicle surface can be combined (i.e., their mean square pressure values can be added directly) to calculate the overall values. The apparent source strength and location are evaluated from measured spectra taken from full scale and model data and normalized for dynamically similar conditions. Their apparent characteristics (i.e., strength and location) are purely arbitrary; that is, they can be adjusted simultaneously to give results

which are the same. If the source is arbitrarily moved farther away, its strength is increased to maintain the measured value being used to generate the model. In this respect, not being unique, they are called apparent.

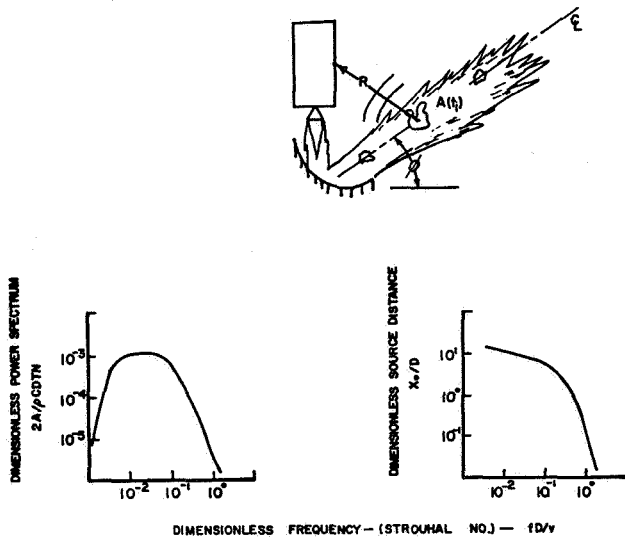


FIGURE 2. VEHICLE APPARENT SOURCE MODEL

From sets of dynamically similar experimental data, apparent source strengths and locations are solved for simultaneously and then nondimensionalized by dividing the acoustic power by the mechanical power of the system to give nondimensional source strength and dividing the apparent source distance by the exit nozzle diameter to give nondimensional location. These empirically derived quantities are then plotted versus nondimensional frequency. The nondimensional curves can then be used to estimate environments for future vehicles with similar characteristics. To model the condition of launch, for example, the flow field is split by the deflector into two streams. Each of these streams is then assumed or replaced by the apparent acoustic source characteristics. The contribution from a source in each stream representing a given frequency is calculated at an observation point and then combined in the conventional manner, i. e., the mean square radiated pressure values added directly. See Figure 3 for predicted versus measured results.

The curves generated above for bell-nozzle deflected flow cannot arbitrarily be applied to nozzles of different configuration; i. e., the slotted ring

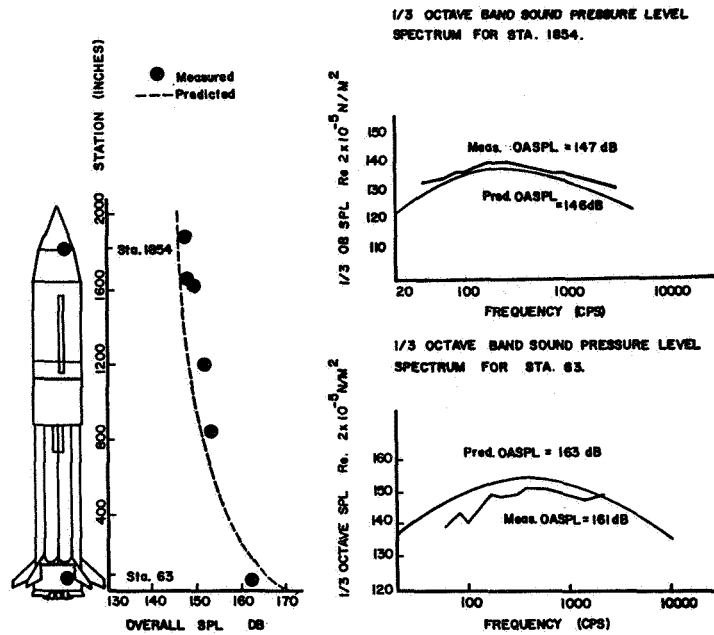


FIGURE 3. ON-PAD ACOUSTIC ENVIRONMENTS FOR APOLLO-SATURN IB FLIGHT VEHICLE AS-203

engine. Also caution must be used when applying such curves to very high speed flows (i. e., 10 to 20 000 ft/sec). New curves must be generated from model experiments for new conditions. Clustering effects, exit-plane-to-deflector distance, and in general all of the important scaling factors influence the limitations of such a prediction model as described above. Additionally, these methods do not provide correlation characteristics.

New prediction models are being developed. The limitations of these models are being defined and noise generation mechanisms of hot rocket exhausts are being studied at Marshall Space Flight Center's new and unique "Acoustic Model Test Facility" (AMTF) (Fig. 4 and Table I) and the "Thermo-Acoustic Simulation Facility (Table I). The Acoustic Model Test Facility is a self-contained highly flexible facility with its own blockhouse control center, data acquisition system, thrust reaction structure, and propellant storage system. This system includes conventional and exotic propellant capabilities. The engines tested at AMTF exhaust over a hard surface which encompasses a very acoustically clean area, including minimum interference by thrust reaction structure. Designed specifically for acoustic testing and experimentation, the AMTF even includes capabilities for acquiring detailed meteorological conditions during a test.

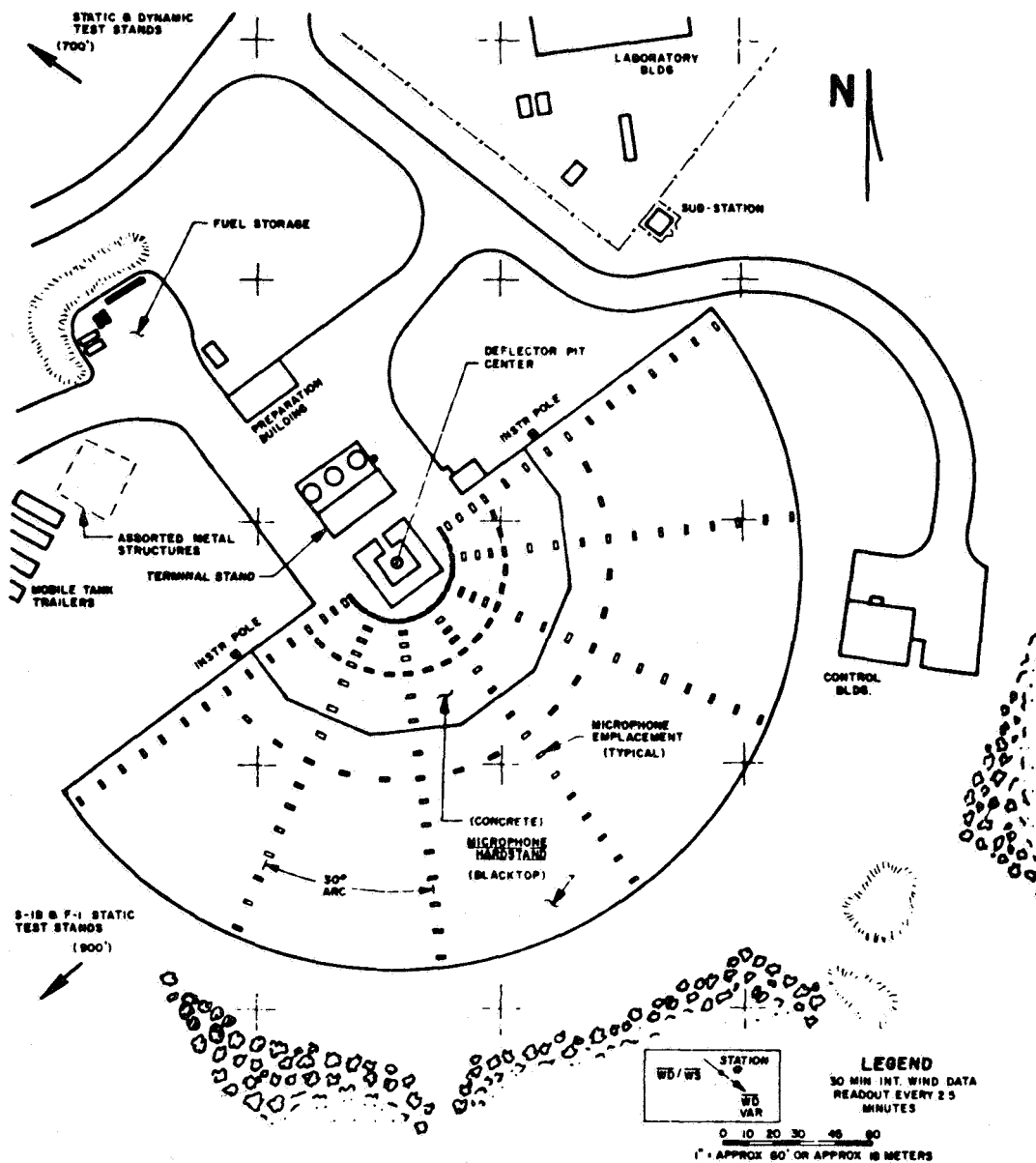


FIGURE 4. ACOUSTIC MODEL TEST FACILITY CTL 116 — MSFC/NASA

TABLE I. ROCKET ENGINE EXHAUST NOISE

A. ACOUSTIC MODEL FACILITY: (thrust, up to 70 000 lb, exhaust field can be oriented anywhere from 25 degrees above horizontal to vertical downward)			
<u>Type of Measurement</u>	<u>Location</u>	<u>Frequency Range</u>	<u>Number</u>
a. Meteorological (Ane.)	External	Static	12
b. Acoustic			
Amplitude	External	20 - 200 KC	100
Phase	External	20 - 20 KC	60
c. Temperature	External	Static	100
d. Pressure	External	Static	100
e. Humidity Sensor	External	Static	1
<u>Current Experiments:</u>			
1. Study of the effects of cone or bell shaped nozzles upon the radiated pressure field.			
2. Evaluation of meteorological characteristics on acoustic data.			
<u>Planned Experiments:</u>			
1. Saturn V launch configuration to define the S-IC on-pad acoustic environment specifically the cross correlation characteristics.			
2. Sound source location study utilizing phase correlation techniques.			
3. Definition of source characteristics for various types of expanding flows with a given nozzle configuration.			
4. Evaluation of engine cluster geometry upon external acoustic field.			
B. THERMO ACOUSTIC SIMULATION FACILITY: (pressure, 1500 psi; temperature, 1500° F)			
<u>Type of Measurement</u>	<u>Location</u>	<u>Frequency Range</u>	<u>Number</u>
a. Temperature	Internal	Static	Traversing
b. Pressure	Internal	Static	Traversing
c. Gas Composition (alphatron)	Internal	Static	Traversing
<u>Current Experiments:</u>			
1. Studies of eddy Mach wave radiation utilizing shadowgraphs in free and deflected cold flow, $M = 2.5$ .			
<u>Planned Experiments:</u>			
1. Simulation of a hot rocket velocity and density profiles with He as a substitute gas for three nozzle configurations.			
2. Measurement of turbulent flow properties of rocket exhausts.			

Correlation characteristics of the radiated acoustic field of the rocket or jet exhaust can be scaled [5]. However, it is important to have the reflecting surfaces of the vehicle or structure of interest present if proper correlation characteristics are to be obtained. These surfaces influence the correlation characteristics appreciably in certain frequency ranges. An experiment to measure correlation characteristics will be performed at MSFC's AMTF on a scaled model of the Saturn V vehicle for launch conditions. It is hoped that the results of this test can be nondimensionalized and applied to dynamically similar configurations of other vehicles.

The midfield environments in the ground plane are much more difficult to compute because for every radius there exists a different apparent source distribution and set of power characteristics. Here, the source appears as a spatially extended source, and thus this geometric effect (which seems to be different for each radius) must be taken into account. By using a 180 degree sector in the ground plane, a series of apparent source models is generated for chosen radii at various angular orientations around the deflected exhaust system; these models are stored on the computer for extrapolation to dynamically similar conditions.

The spatial distribution of the noise source is not only important to the midfield region, its spatial characteristics become even more significant with respect to the nearfield region. In addition to the geometric effect of a spatially distributed source, the primary mechanisms of noise generation in the flow field become significant factors in determining the fluctuating pressure field in the nearfield, and as already mentioned, detailed knowledge of these mechanisms does not exist at this time. Currently, there is not enough experimental data available to attempt to generate an adequate analytical/empirical prediction model for the nearfield region [6].

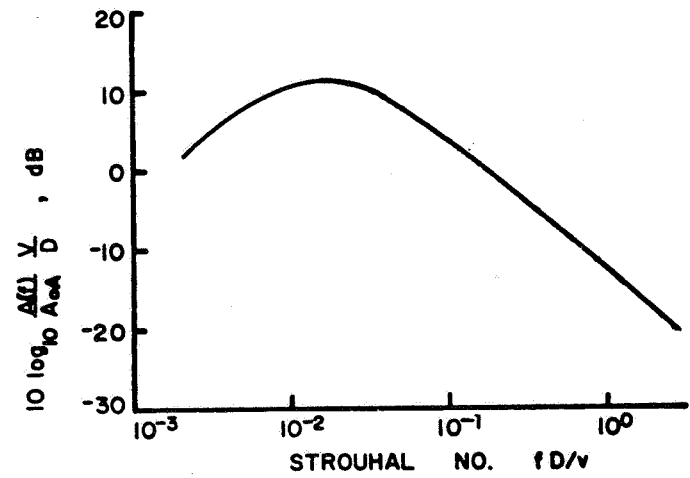
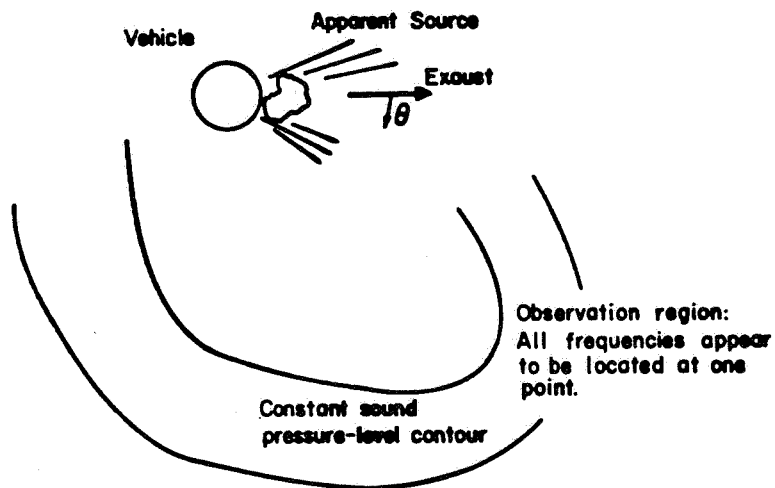
In the farfield region (Fig. 5), all the sources (i. e., for the different frequencies) appear to be located at a single point. Again experimental data and similarity principles are used to generate apparent source characteristics. These apparent characteristics are monopole source strength and directivity effects (i. e., the deviation from the perfect symmetrical radiation of the assumed monopole). The apparent source strength for each frequency is normalized to the overall acoustic power, which is calculated by multiplying an acoustic

efficiency factor  $\eta$  (0.005 for high thrust systems) by the total mechanical power of the rocket exhaust system. Again, this efficiency factor is derived from many sets of experimental data [7].

The acoustic sound pressure level (SPL) at an observation point is then computed for the monopole source in the conventional manner for a homogenous, isotropic medium. This is done for 1/3-octave or octave center band frequencies and since all the monopole sources seem to be at a single point, this is a relatively straightforward and easy calculation. Corrections are then applied to account for the directional properties of the source by using directivity curves such as those shown in Figure 5 which account for the deviation of the source from a monopole as a function of angular position around the vehicle. Such directivity curves are generated for each center frequency. After the directivity corrections are applied, the resultant sound pressure spectrum (1/3-octave or octave) represents the best estimate of the acoustic environment at that point. It can then be summed in the usual way to obtain an overall sound pressure level. This approach is applicable to all dynamically similar configurations. Where distances become appreciable, absorption and attenuation effects must be taken into account. Typical results for the Saturn V vehicle static firing conditions for Huntsville, Athens, and Decatur, Alabama are shown in Figure 6.

The above technique was modified for use in computing the farfield ground environments as the space vehicle flies through its boost phase [8]. The effects of vehicle velocity and exhaust plume changes on the apparent source characteristics were evaluated, and a new set of apparent source characteristics derived. This information allows the estimation of the farfield ground environment for the period from holddown to the end of boost phase flight. These environments are calculated (by computer) as a function of time at any desired observation point on the ground plane. Typical results of these estimates are presented in Figures 7 and 8 and in Reference 9.

One of the major restrictions on the estimation of farfield environments by the farfield techniques is the assumption of a homogeneous, isotropic propagational medium. For this medium, it is sufficient to derive the apparent source characteristics for the ground plane only. However, if the propagational medium is inhomogeneous, the acoustic energy arriving at an observation point on the ground plane may be due to refraction. The three-dimensional radiation characteristics of the source then become



NORMALIZED ACOUSTIC POWER SPECTRA

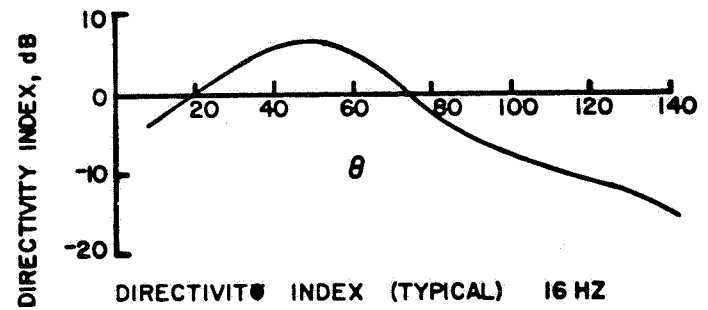


FIGURE 5. FARFIELD GROUND PLANE APPARENT SOURCE MODEL

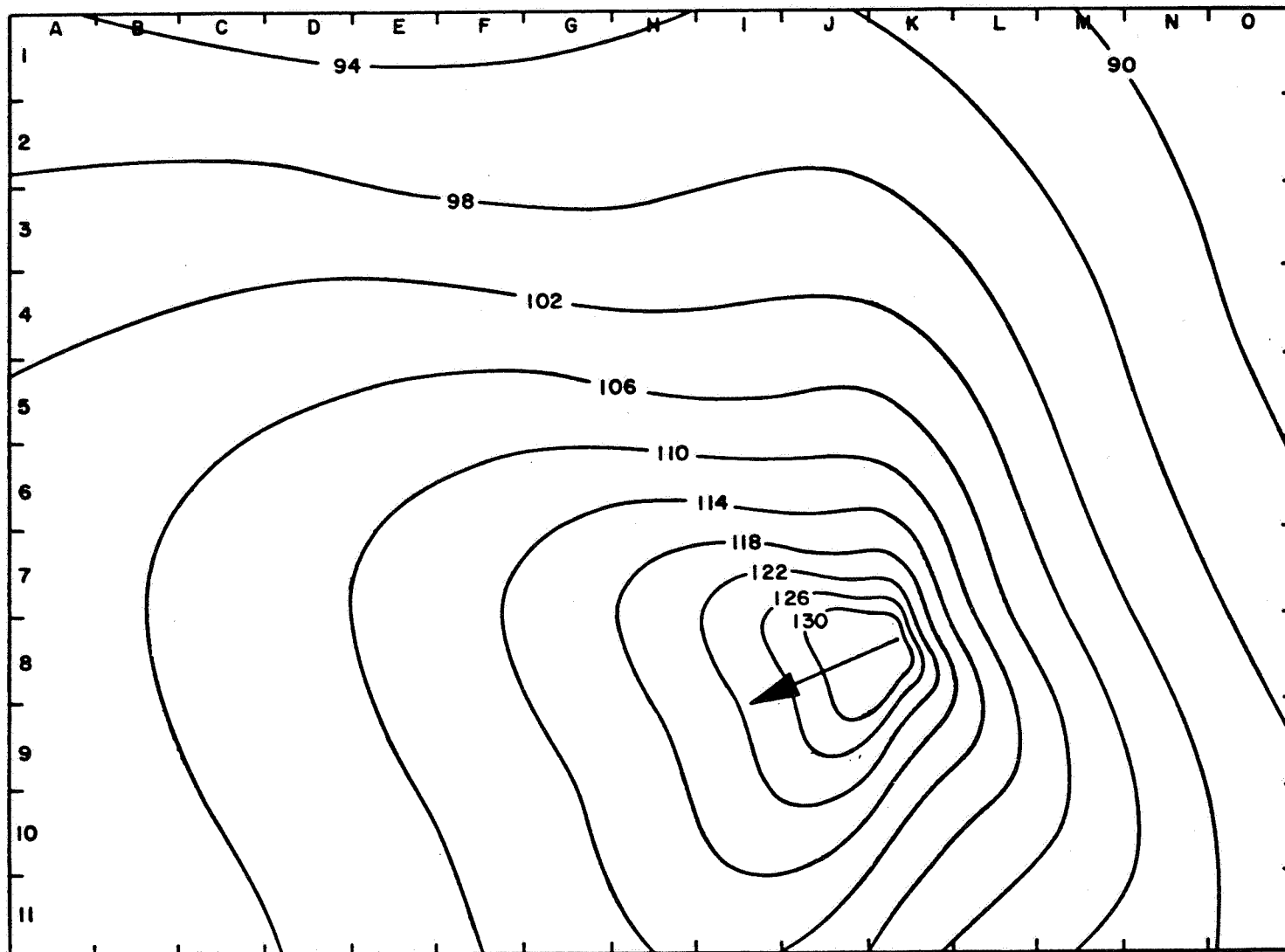


FIGURE 6. CONSTANT OVERALL SOUND PRESSURE LEVEL CONTOURS S-IC STATIC FIRING

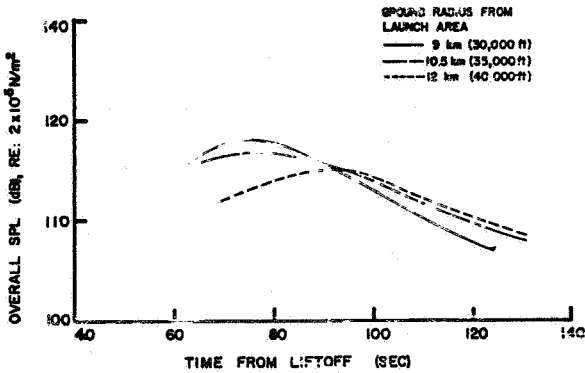


FIGURE 7. PREDICTED MAXIMUM OVERALL SOUND PRESSURE LEVEL TIME HISTORY FOR VARIOUS GROUND STATIONS FOR SATURN V LAUNCH

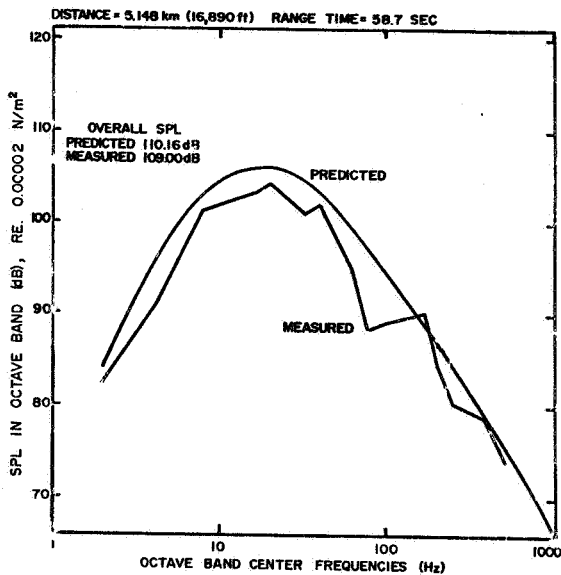


FIGURE 8. MEASURED ACOUSTIC DATA FROM SA-5 FLIGHT (SATURN I VEHICLE) WITH PREDICTED ENVIRONMENTS AT 5.148 km

important. To generate a prediction model for these conditions, three-dimensional apparent source characteristics are derived from experimental data and coupled with a modified ray acoustic approach using a linear layer model for the inhomogeneous atmosphere [10]. This model estimates the sound field

spectrum due to the refracted energy, but is still limited by the restrictions on ray acoustics. For instance, one of the major restrictions is that the sound pressure level at a focal point becomes infinite. The atmospheric inhomogeneities, therefore, play a prominent role in restrictions on the operational procedures of the static test firing of boosters. High acoustic energy levels may be refracted into surrounding highly populated communities. If meteorological conditions indicate this probability, the firing must be postponed until the conditions change.

#### IV. CONCLUSIONS

From the foregoing discussion, the following conclusions are drawn:

1. There is extremely limited knowledge of the basic noise generating mechanisms of a free (undeflected) hot rocket-exhaust flow field. Even less basic knowledge exists for the deflected condition.

2. Analytical/empirical techniques are in existence and are computerized for estimation of the overall and spectral characteristics of the acoustic field at the vehicle surface due to the rocket exhaust flow for static firing and launch conditions. Cross correlation characteristics, hence, realistic structural response values, cannot be calculated at this time. Experimental efforts are underway to overcome this problem.

3. Techniques are available and computerized for estimating the ground plane midfield acoustic environment in terms of both spectral and overall environment.

4. The nearfield fluctuating pressure environment for a hot rocket exhaust cannot be estimated. There is an acute lack of experimental data for this region. Also, the details of noise generation mechanisms are not yet defined.

5. Methods are available and programmed to estimate the ground plane farfield environments for: (1) a homogeneous, isotropic medium for both restrained (static and launch) firing and inflight conditions (the inflight conditions are given as a function of time), and (2) an inhomogeneous medium (restrained firing only).

6. Although the above described methods, when used correctly, provide fairly reliable estimates of

the acoustic environments, each has severe restrictions and limitations, and therefore extreme caution must be used when applying them to new situations.

7. New, unique, and extremely flexible experimental facilities for studying the acoustic environments and noise generation mechanisms for any type of rocket or jet propulsion systems are available at MSFC.

8. At the extremely high sound pressure levels generated by current space vehicles, small errors in dB values result in large errors in structural response analyses. This results in costly over-design and qualification penalties. Continued effort must therefore be expended to improve the existing analytical/empirical prediction techniques.

9. The importance of obtaining accurate estimates of the acoustic environments at the earliest possible time during the R&D phase of space vehicle or large jet aircraft is of vital importance and cannot be overemphasized. A "cure" instead of "fix" philosophy will save large amounts of monetary and manpower resources with respect to design and qualification problems. Also dynamic test facility capabilities, for qualifying vehicle and ground support structures and equipment, are dictated directly by the magnitude and characteristics of the acoustic environment.

## REFERENCES

1. Golovin, Nicholas: Alleviation of Aircraft Noise. *Astronautics and Aeronautics Magazine*, January 1967, p. 71.
2. Richards, E. J.: Aircraft Noise — Mitigating the Nuisance. *Astronautics and Aeronautics Magazine*, January 1967, p. 34.
3. Wu, T. Yao-tsu: Introductory Lectures on Hydro-Acoustics. *Schiffstechnik, Forschungshefte Fur Schiffbau Und Schiffsmaschinenbau*, September 1966, p. 93.
4. Williams, J. E. Ffowcs: Possible Effects in Rocket Exhaust Noise. *Wyle Laboratories Technical Memorandum 67-8*, October 1967.
5. Clarkson, B. L.: Scaling of the Near Field Pressure Correlation Patterns Around a Jet Exhaust. *Acoustical Fatigue in Aerospace Structures: Trapp and Forney*, Syracuse University Press, p. 19.
6. Ollerhead, J. B.: On the Prediction of the Near Field Noise of Supersonic Jets. *NASA CR-857*, August 1967.
7. Guest, S. H.: Acoustic Efficiency Trends for High Thrust Boosters. *NASA TN D-1999*, July 1964.
8. Wilhold, G., Guest, S., and Jones, J.: A Technique for Predicting Far Field Acoustic Environments due to a Moving Rocket Sound Source. *NASA TN D-1832*, August 1963.
9. Guest, S. and Jones, J.: Far Field Acoustic Environmental Predictions for Launch of Saturn V and a Saturn V MLV (Modified Launch Vehicle) Configuration. *NASA TN D-4117*, September 1967.
10. Jones, J.: Sound Pressure Estimations from a Point Directional Acoustic Source Radiating in an Inhomogeneous Medium. *Aero-Astrodynamic Research Review No. 3*, *NASA TM X-53389*, October 1965, p. 2.



## II. ATMOSPHERIC PHYSICS

# A STUDY OF THE UPPER ATMOSPHERIC MODELS

By

James W. Johnson

## ABSTRACT

This paper contains information related to the upper atmospheric models used in determining the various parameters, the assumptions used to develop them, and the particular advantages of each. Theoretical aspects of upper atmospheric models as well as empirical models are discussed.

## I. INTRODUCTION

The motion of a satellite in the gravitational force field of the earth is well known, but the drag effects of the earth's atmosphere on the satellite's motion have not been determined precisely enough to predict the dynamics and lifetime of the satellite with the desired precision. To make such predictions, values of the various parameters of the earth's upper atmosphere (120-800 km) are needed. The desire to determine precisely the drag effects (plus the development during recent years of improved techniques for collecting data related to the upper atmosphere) has greatly stimulated research in this area. Of greatest significance in determining atmospheric parameters are probably those experiments performed by studying the orbital decay of satellites and various rocket probes such as those developed by Marshall Space Flight Center and the University of Michigan.

The process of radiation absorption and reradiation by the earth's atmosphere are very complicated and, although the microscopic details of such processes are well understood, the macroscopic quantities needed to correlate orbital parameters with radiation energy have not been determined in an entirely satisfactory manner. Before very refined models of the earth's upper atmosphere can be developed, more measurements of the solar radiation impinging upon the outer expanses of the atmosphere must be made.

The present study investigates some of the models used in determining the various parameters, the

assumptions used to develop them, and the particular advantages of each. It is hoped that this paper will provide an introduction to present upper atmospheric research and indicate areas in which further investigation may lead to improvements in the present models.

## II. THEORETICAL ASPECTS OF UPPER ATMOSPHERIC MODELS

Models of the upper atmosphere have been constructed basically by two means: an empirical-theoretical model (derived from satellite drag data) and a theoretical model based on conservation equations of mass, momentum, and energy in conjunction with the ideal gas law or the diffusion equation. The empirical model has the advantages of flexibility and direct correlation with satellite data. This approach is concerned only with providing an operational technique and not with the detailed physical processes involved. However, any satisfactory empirical model must be in agreement with the general physical laws describing the system.

For providing an overall picture of the structure of the upper atmosphere pertinent to the design and maintenance of a vehicle in an earth-based orbit such a model is extremely valuable, but it does require accurate and detailed data in order to determine orbital parameters with the necessary precision. Unfortunately, upper atmospheric data are still subject to controversy. Problems in both measurement and data reduction must still be solved, although considerable advancement has been made in this field.

The empirical models of Jacchia [1] and Harris and Priester [2] have proved to be especially valuable in providing orbital parameters of satellites. Jacchia has developed a quasi-static, multi-component model by assuming a fixed set of boundary conditions (given below) for temperature and partial number densities at 120 km.

$$\begin{aligned}
T &= 355^\circ\text{K} \\
N(\text{N}_2) &= 4.0 \times 10^{11} \text{ C}^{-3} \\
N(\text{O}_2) &= 7.5 \times 10^{10} \text{ C}^{-3} \\
N(\text{O}) &= 7.6 \times 10^{10} \text{ C}^{-3} \\
N(\text{He}) &= 3.4 \times 10^7 \text{ C}^{-3}
\end{aligned}$$

Also, as in the other models investigated, hydrostatic equilibrium is assumed. Thomas [3] has shown that errors in the hydrostatic assumption is small even for major temperature changes over tens of minutes. A temperature profile is constructed empirically of the form

$$T = T_\infty - (T_\infty - T_{120}) \exp[-s(z - 120)] \quad (1)$$

where  $s$  is a constant different for each profile and  $T_\infty$  is the exospheric temperature. A reasonable fit can be made for

$$s = 0.0291 \exp\left(\frac{-x^2}{2}\right) \quad (2)$$

where

$$x = \frac{T_\infty - 800}{750 + 1.722 \times 10^{-4} (T_\infty - 800)^2} \quad (3)$$

From the temperature profile given by equation (1), the number densities,  $n_i$ , are computed by assuming diffusive equilibrium. Assuming that the diffusion velocity is zero, we may write the diffusion equation in the form

$$\frac{dn_i}{n_i} = -\frac{dz}{H_i} - \frac{dT}{T} (1 + K_T) \quad (4)$$

where

$$H_i = \frac{KT}{m_i g} \quad (5)$$

and  $K_T$  is the thermal diffusion ratio. For He,  $K_T$  is approximately -0.4 and, for  $\text{O}_2$  and  $\text{N}_2$ ,  $K_T$

is approximately zero. The negative value for  $K_T$  indicates that the He component moves into a "hot" region.

Variations of the exospheric temperature,  $T_\infty$ , are given by Harris and Priester [2] and Jacchia [1]. Empirical equations are given for variations of  $T_\infty$  with solar cycle by correlations with  $F_{10.7}$  solar flux, the variation of  $T_\infty$  within one solar rotation, the semi-annual variation, the diurnal variation (which takes into account latitude and declination of the sun), and variations with geomagnetic activity. A consequence of the fixed boundary conditions of the Jacchia model is a nearly isopycnic layer at 200 km. A result is that, as the exospheric temperature varies, the density at 200 km should remain constant. The effect of the diurnal variation does not affect the density at 200 km noticeably, but contrary to this prediction at times of high solar activity, the erratic "27-day" component of the  $F_{10.7}$  flux does produce an observable variation.

The Harris and Priester [2] model assumes the number density to be in hydrostatic equilibrium, and the temperature is then computed from an energy equation. After each new profile has been determined, the densities are recomputed. This process is continued until an equilibrium configuration is attained. Consider the general equation of motion of a dilute gas in a gravitational field in the absence of chemical reactions.

$$\frac{\partial \vec{v}}{\partial t} + (\vec{v} \cdot \nabla) \vec{v} + \frac{1}{\rho} \nabla P = -\vec{g}(\vec{r}) \quad (6)$$

where  $\vec{v}$  is the macroscopic motion of the gas,  $\rho$  is the mass density,  $P$  is the total pressure, and  $\vec{g}(\vec{r})$  the gravitational acceleration of the earth. For hydrostatic equilibrium,  $\vec{v} = 0$ , and equation (6) reduces to

$$\nabla P = -\rho \vec{g} \quad (7)$$

or, in one-dimension,

$$\frac{dP}{dz} = -\rho g(z) \quad (8)$$

If we assume that the atmosphere behaves as an ideal gas, the equation of state

$$P = nKT \quad (9)$$

where  $n$  is the total number density,  $n = \sum_i n_i$ ,  $T$  is the temperature, and  $K$  is Boltzmann's constant, may be used with equation (8) to compute  $P_i$ ,  $n_i$ , and  $\rho_i$  for each constituent. From the general energy-conservation equation derived by Hirschfelder, Curtiss, and Bird [4], neglecting chemical reactions, we have

$$\begin{aligned} \rho C_v \left[ \frac{\partial T}{\partial t} + (\vec{v} \cdot \nabla) T \right] = & -\nabla \cdot \vec{q} - P \nabla \cdot \vec{v} \\ & + \sum_i n_i (\vec{v}_i \cdot \vec{x}_i) \\ & + \sum_i U_i \nabla \cdot \rho_i \vec{v}_i + Q \end{aligned} \quad (10)$$

where

$C_v$  = specific heat at constant volume

$T$  = temperature

$\vec{q}$  = energy flux vector

$\vec{x}_i$  = gravitation force on species  $i$

$$= -\frac{m_i \mu r}{r^3}$$

$\mu$  = earth's gravitational constant

$$= 3.99 \times 10^{-5} \text{ km}^3 \text{ sec}^{-2}$$

$U_i$  = internal energy of species  $i$

$Q$  = external energy source.

By considering only vertical energy transport due to heat conduction, energy transport due to the diurnal expansion or contraction when the density bulge builds up in the morning and shrinks after 14:00 hours local time, and the various physical processes which provide the heat sources  $Q$  by absorption of solar energy and reradiation at longer wavelengths, equation (10) reduces to

$$\begin{aligned} \frac{\partial}{\partial z} \left[ K(T) \frac{\partial T}{\partial z} \right] - \rho C_p \frac{\partial T}{\partial z} \int_{z_0}^z \frac{1}{T^2} \frac{\partial T}{\partial z} dz' + Q \\ = \rho C_p \frac{\partial T}{\partial t} \end{aligned} \quad (11)$$

where  $K(T)$  is the thermal conductivity and  $C_p$  is the heat capacity at constant pressure. The term

$$v = T \int_{z_0}^z \frac{1}{T^2} \frac{\partial T}{\partial t} dz' \quad (12)$$

which is the vertical flow velocity may be shown to satisfy the continuity equation for  $\rho_i$ , the density of the  $i^{\text{th}}$  constituent, provided  $z_0 \neq z_0(t)$ . However,

the expression does not conserve total mass.

Equation (11) and an expression for  $n_i$  solved

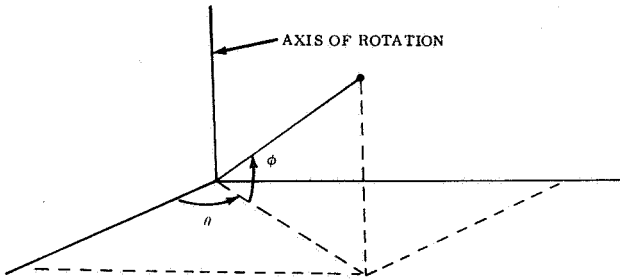
simultaneously, taking into consideration heat sources due to absorption of solar extreme ultraviolet radiation by molecular nitrogen and reradiation (negative heat source) by atomic oxygen in the infrared (from the  $3_{P_1}$  to the  $3_{P_2}$  level), do not give a diurnal

variation in agreement with the observed variation.

To correct for this difficulty, Harris and Priester introduced a "virtual heat source" in such a way that agreement between the observed and the calculated densities and their diurnal variations was obtained. This heat is now thought to be due to horizontal motion in the atmosphere. Both of the above described models are designed to fit the available experimental data.

Different approaches in describing the upper atmosphere have been taken by Friedman [5] and Thomas [3]. In both treatments, the conservation equations are solved using a simplified expression for radiation heating. Friedman develops a three-dimensional model by assuming that the atmosphere rotates as a rigid body with the earth — i.e., winds are not considered — but a diffusion velocity of each of the chemical species relative to the others is allowed. Solar extreme ultraviolet radiation is considered as the main external energy source, reradiation by atomic oxygen in the infrared region being neglected. Collision between hot ambient

electrons and the neutral atmospheric constituents provide about 10-20 percent of the EUV heating from the F<sub>2</sub> peak downward on the sunny side of the earth. (On the nighttime side, electrons provide the only source of energy.) Energy transmitted by hot ambient electrons affects only the magnitude of the temperature and density and has no effect on the time locations of their maxima and minima. Also, the assumption is made that energy is transported internally by conduction and diffusion. With these assumptions, the conservation equations are solved after being transformed to a three-dimensional spherical coordinate system shown in Figure 1.



$\theta = 0^\circ$  at 6h;  $\phi = 0^\circ$  at equinox

FIGURE 1. COORDINATE SYSTEM FOR THE THREE-DIMENSIONAL MODEL

Equation (6) then becomes

$$\begin{aligned} \frac{1}{\rho} \frac{\partial P}{\partial r} &= r\omega^2 \cos^2 \phi - g(r) \\ \frac{1}{\rho r} \frac{\partial P}{\partial \phi} &= -r\omega^2 \cos \phi \sin \phi \\ \frac{\partial P}{\partial \theta} &= 0 \end{aligned} \quad (13)$$

and equation (10) becomes

$$\rho C_p \omega \frac{\partial T}{\partial \theta} = \nabla \cdot K(T) \nabla T - \sum \rho_i C_{p_i} \vec{v}_i \cdot \nabla T + Q \quad (14)$$

where  $\omega = \frac{d\theta}{dt}$ .

Simplified expressions for the diffusion velocity and thermal conductivity in equation (14) are obtained from theory [6, 7, 8]. The processes of absorption of photon energy flux by atmospheric constituents are quite complicated. To provide a simple

means of calculating the radiation absorbed, it is assumed that the energy transfer at a point P is proportional to the total cross section of all the species times the flux at that point:

$$Q_\Lambda = I_\Lambda(P) \left[ \sum_i \epsilon_i \sigma_i(P) n_i \right] \quad (15)$$

where

$$I_\Lambda(P) = I_\Lambda(0) \exp \left[ -T_\Lambda(P) \right] \quad (16)$$

$I_\Lambda(P)$  = radiation intensity at P for energy of wavelength  $\Lambda$

$I_\Lambda(0)$  = radiation intensity at the top of the atmosphere

$\epsilon_i$  = efficiency of energy conversion

$\sigma_i(\Lambda)$  = radiation cross section of species i to wavelength  $\Lambda$

$T_\Lambda(P)$  = optical thickness at point P for wavelength  $\Lambda$ .

An expression for the energy transmitted by electrons is given by Dalgarno, McElroy, and Moffett [9]:

$$\begin{aligned} Q_{EL} &= 2.06 \times 10^{-30} N(e) (T_e - T_n) [N(0) T_e^{1/2} \\ &\quad + N(N_2) (0.076 T_e + 1200 - 0.56 T_n) \\ &\quad + N(O_2) (4T_e - 800)] \text{ erg cm}^{-3} \text{ sec}^{-1} \end{aligned} \quad (17)$$

where

$N$  = number densities

$T_e$  = electron temperature

$T_n$  = neutral temperature.

The equation of continuity as derived by Chapman and Crowling [10] for the  $i^{\text{th}}$  neutral constituent of a dilute gas in the absence of chemical reactions

$$\frac{\partial n_i}{\partial t} + \nabla \cdot [n_i (\vec{v} + \vec{v}_i)] = 0 \quad (18)$$

becomes

$$\omega \frac{\partial n_i}{\partial \theta} + \nabla \cdot n_i \vec{v}_i = 0 \quad (19)$$

Equations (13), (14), and (19) are solved simultaneously subject to the conditions

$$\frac{\partial T}{\partial r} = 0$$

$$\frac{\partial n_i}{\partial r} = -\beta n_i$$

Boundary conditions are allowed to vary until a set is obtained that agrees with measured data. Initial conditions and exospheric temperatures used are similar to those given by Jacchia. The advantage of a three-dimensional model is that it is physically realistic, it accounts for horizontal heat conduction and mass diffusion, it is designed to give the diurnal variation, it removes the necessity of patching together a set of one-dimensional atmospheres to simulate global distribution, and horizontal winds can be introduced.

Thomas [3] develops a new analytical method for the solution of the one-dimensional, time-dependent heat equation. The only heat transfer process considered is heat conduction and the solar EUV,  $Q_h$ , and the radiative cooling,  $Q_{1R}$ , are taken to be external energy sources. The one-dimensional conservation equations are transformed to an isobaric frame by means of the transformation

$$\xi = \exp \left( - \int_{z_0}^z \frac{dz}{2H} \right) = \left( \frac{P}{P_0} \right)^{1/2} \quad (20)$$

and are shown to have simple analytic Green's function solutions. Favorable comparison with more precise numerical method demonstrates the usefulness of the simple analytic approach.

### III. ANALYSIS AND CONCLUSION

Although there is a need for more refined data, sufficient data have been taken to construct several types of working models of the upper atmosphere. The models based on empirical results provide a simple and readily usable technique for developing values of atmospheric parameters, but as better measurements become available, models based on energy relations should provide the more accurate calculations. There should be attempts made to justify purely empirical calculations by considering actual physical processes. Also, it seems desirable to investigate, both theoretically and experimentally, the effect of neglecting minor processes in developing an atmospheric model. The development of larger computers has made feasible the implementation of more refined models and consideration of the detailed processes involved.

### REFERENCES

1. Jacchia, L. G.: Static Diffusion Models of the Upper Atmosphere with Empirical Temperature Profiles, Smithsonian Astrophys. Obs. Special Report No. 170, 1964.
2. Harris, I. and Priester, W.: The Upper Atmosphere in the Range From 120 to 800 km, Proposal for CIRA, 1964.
3. Thomas, G. E.: Analytic Solutions of the Heat Conduction Equation in the Thermosphere, Air Force Report No. SAMSO-TR-67-118, 1963.
4. Hirschfelder, J. O.; Curtiss, C. F.; and Bird, R. B.: Molecular Theory of Gases and Liquids, John Wiley and Sons, 1963.
5. Friedman, M. P.: A Three-Dimensional Model of the Upper Atmosphere, Smithsonian Astrophys. Obs. Special Report No. 250, 1967.
6. Buddenberg, J. W. and Wilke, C. R.: Calculation of Gas Mixture Viscosities, Industrial and Eng. Chem., Vol. 41, 1949.

## REFERENCES (Concluded)

7. Brokaw, R. S.: Approximate Formulas for the Viscosity and Thermal Conductivity of Gas Mixtures, *J. Chem. Phys.*, Vol. 29, 1958.
8. Brokaw, R. S.: Energy Transport in High Temperatures and Reacting Gases, *Planet. Space Sci.*, Vol. 3, 1961.
9. Dalgarno, A.; McElroy, M. B.; and Moffett, R. J.: Electron Temperature in the Ionosphere, *Planet. Space Sci.*, Vol. 11, 1963.
10. Chapman, S. and Cowling, T. G.: *The Mathematical Theory of Nonuniform Gases*, Cambridge Univ. Press, 1960.

# INTERACTION OF ATMOSPHERIC WAVES WITH THE IONOSPHERE

By

Robert W. Porter<sup>1</sup>

## ABSTRACT

A study of the interaction of atmospheric waves with the ionosphere was made using a linearized three fluid hydrodynamic model. A system of six linear algebraic equations is presented for the solution of the orthogonal components of electron and ion velocity in terms of the incident wave and local ionospheric properties.

## I. INTRODUCTION

Radio observations indicate that wave propagation upward from the lower atmosphere is a source of ionospheric motion. The waves, attributed to large scale air motion, thunderstorms, explosions, rocket firings, etc., have a tendency to grow in relative amplitude with altitude because of atmospheric density stratification. The purpose of this investigation was to develop theory for the induced motion of charged particles due to the incidence of a wave defined by the neutral particle motion.

For this study a linearized three fluid hydrodynamic model was used. The various property frequencies have been retained for uniform validity through the lower (100 km) to upper (500 km) regions. The induced electric charge density and electric field intensity are shown to be directly coupled to differential ion and electron motion. A system of six linear algebraic equations is presented for the solution of the orthogonal components of electron and ion velocity in terms of the incident wave and local ionospheric properties.

The research is associated with the experimental and theoretical efforts of the Space Environment Branch, Aerospace Environment Division, Aero-Astrodynamic Laboratory, for determination of the effect of acoustic waves of ground origin on the ionosphere.

## II. ATMOSPHERIC WAVES

High frequency acoustic waves propagate essentially upward and involve motion in that direction. While there is a tendency for growth in relative amplitude due to density stratification with altitude, viscous effects result in increasing attenuation with altitude and frequency [1]. For example, waves of frequency of 1 Hz propagate only to about 100 km while those of frequency of 0.01 Hz may reach 500 km. Density stratification also results in an acoustic cut-off at about  $10^{-3}$  Hz. The corresponding range of angular frequency  $\omega$  for 100 to 500 km is of order  $10^{-2}$  to 10 rad/sec.

At the lower frequencies, acoustic waves are strongly influenced by gravity and acquire transverse motion. Data from radio sounding correlate waves of this type with thunderstorms [1], sonic booms [2], explosions [3], and static rocket firings [4]. The experimental work at MSFC with the latter is discussed by Roberts [5].

The flight of Explorer 32 of 25 May, 1966, with perigee of 286 km and initial apogee of 2700 km provided detailed measurement of neutral particle number density using three cold cathode magnetron gauges [6]. Amplitudes of neutral particle fluctuations were commonly 10-20 percent but were frequently as large as 50 percent. The apparent fundamental angular frequency was about 0.2 rad/sec. The phenomenon was interpreted as an acoustic-gravity wave.

The linear theory of wave propagation in the neutral atmosphere is well developed [7]. Viscous and thermal effects can be included for a realistic atmosphere by means of numerical computation. The objective is to relate this neutral particle motion to charged particle motion which is observed by electromagnetic means of probing the ionosphere. The usual approach is to consider the neutral motion as an extension of the motion of the lower atmosphere,

---

1. Participant in ASEE/NASA Summer Faculty Fellowship Program Aero-Astrodynamic Laboratory, 1968. Assistant Professor of Mechanical and Aerospace Engineering, Illinois Institute of Technology, Chicago, Illinois 60616.

the ionosphere being weakly ionized at the altitudes of interest. Whether or not the neutral particle wave is altered by the charged particles, we regard the neutral motion as known. For the neutral species  $n$ ,

$$\tilde{V}_n = \tilde{V}_n \exp [i (\omega t - \tilde{k} \cdot \tilde{r})], \quad (1)$$

where  $\tilde{V}$  is velocity,  $\tilde{k}$  is propagation vector,  $t$  is time, and  $\tilde{r}$  the radius vector. (We consider a layer wherein the amplitude vector  $\tilde{V}$  is constant.)

For the case of small disturbances, linear theory is applicable and the Fourier components are analyzed separately. A typical component is considered here. It should be pointed out that there is reason to doubt the validity of linear theory. Einaudi [8] argues that singular rather than regular expansions should be used. Solutions including second order terms break down at great distances. Also, it is well known that compression waves steepen into shock discontinuities and expansion waves spread. The approximate theory of shock propagation in the atmosphere is discussed by Hayes [9].

### III. PLASMA OSCILLATIONS

A three-fluid model of electrons, ions, and neutrals is employed. We seek the average dynamical state of the charged particles in terms of the neutral particle velocity wave defined by Equation (1). Viscosity, ambient particle motion and perturbation of the chemical rates, composition and transport properties are neglected. The region of interest is considered uniform except for the wave and the motions are assumed adiabatic. While all of these effects are important for a detailed description, the dynamical coupling is retained and considerable simplicity is obtained. Since the ambient atmosphere appears electrically neutral, this condition is applied. However, the wave is shown to induce charge separation accompanied by an excess charge density and electric field intensity.

The dynamical equations for ions and electrons are linearized in the usual way and the zeroth order terms are subtracted leaving the perturbation equations

$$\begin{aligned} \frac{\partial \tilde{V}_e}{\partial t} + \frac{\tilde{\nabla} p_e}{n_e m_e} + \frac{e}{m_e} (\tilde{E} + \tilde{V}_e \times \tilde{B}_0) \\ - \nu'_{en} (\tilde{V}_n - \tilde{V}_e) - \nu'_{ei} (\tilde{V}_i - \tilde{V}_e) = 0 \end{aligned} \quad (2)$$

$$\begin{aligned} \frac{\partial \tilde{V}_i}{\partial t} + \frac{\tilde{\nabla} p_i}{n_e m_i} - \frac{e}{m_i} (\tilde{E} + \tilde{V}_i \times \tilde{B}_0) \\ - \nu'_{in} (\tilde{V}_n - \tilde{V}_i) - \nu'_{ie} (\tilde{V}_e - \tilde{V}_i) = 0 \end{aligned} \quad (3)$$

where  $p$  is partial pressure,  $m$  is particle mass,  $e$  is absolute electron charge,  $\tilde{E}$  is electric field intensity,  $\tilde{B}$  is magnetic field intensity,  $\nu'$  is effective collision frequency, subscripts  $e$  and  $i$  denote electron and ion species, respectively, and  $o$  denotes the unperturbed state. All other variables are first order perturbation quantities.

For the adiabatic frictionless process assumed here,

$$\frac{\tilde{\nabla} p_e}{n_e m_e} = \frac{m_i}{m_e} \frac{a_o^2}{n_e} \tilde{\nabla} n_e \quad (4)$$

$$\frac{\tilde{\nabla} p_i}{n_e m_i} = \frac{a_o^2}{n_e} \tilde{\nabla} n_i, \quad (5)$$

where  $a$  is speed of sound. It is tacitly assumed that the specific heat ratio for electrons, ions, and neutrals is the same and that they are in thermal equilibrium.

The perturbation continuity equations are

$$\frac{\partial n_e}{\partial t} + n_e \tilde{\nabla} \cdot \tilde{V}_e = 0 \quad (6)$$

$$\frac{\partial n_i}{\partial t} + n_e \tilde{\nabla} \cdot \tilde{V}_i = 0. \quad (7)$$

The perturbation Maxwell equations are

$$\tilde{\nabla} \cdot \tilde{E} = e(n_i - n_e)/\epsilon_0 \quad (8)$$

$$\tilde{\nabla} \times \tilde{E} = - \frac{\partial \tilde{B}}{\partial t} \quad (9)$$

$$\tilde{\nabla} \times \tilde{B} = \frac{en_e}{\epsilon_0 c^2} (\tilde{V}_i - \tilde{V}_e) + \frac{1}{c^2} \frac{\partial \tilde{E}}{\partial t} \quad (10)$$

where  $\epsilon_0$  is electric permittivity and  $c$  is speed of light. The numerator of the RHS of equation (8) is the electric excess charge density and the first term of the RHS of equation (10) is the product of magnetic permeability and electric current density.

Variations of the above system have been studied by a number of investigators from the point of view of induced ionospheric plasma motion. Georges [1], Bugnolo [10], and Hook [11] have neglected the electric field term which is of possible importance. Kantor and Pierce [12] considered only longitudinal neutral waves. Poverlein [13] considered the low frequency limit. The terms are retained here for a wide range of uniform validity. However, it is assumed that the phase velocity is nonrelativistic.

The single Fourier component of a wave in a uniform medium is given by

$$\vec{F} = \vec{F} \exp[i(\omega t - \vec{k} \cdot \vec{r})]. \quad (11)$$

The angular frequency  $\omega$  and propagation vector  $\vec{k}$  are those of the neutral wave as given by equation (1).

The continuity equations (6) and (7) result in specification of the number densities in terms of velocities

$$n_e = n_{e0} \frac{\vec{k}}{\omega} \cdot \hat{k} \cdot \vec{V}_e \quad (12)$$

$$n_i = n_{i0} \frac{\vec{k}}{\omega} \cdot \hat{k} \cdot \vec{V}_i, \quad (13)$$

where  $k$  is the wave number and  $\hat{k}$  the unit propagation vector ( $\vec{k} = k\hat{k}$ ). It is apparent that the charge density is

$$\rho_e = e(n_i - n_e) = en_{e0} \frac{\vec{k}}{\omega} \cdot \hat{k} \cdot (\vec{V}_i - \vec{V}_e) \quad (14)$$

and is proportional to the differential charged particle velocity in the direction of propagation of the wave.

Using the form (11) and equations (12) and (13) in the Maxwell Equations (8)-(10), we find the electric field intensity to be

$$\vec{E} = - \frac{en_{e0}\omega}{\epsilon_0 (ck)^2} \frac{1}{1 - \left(\frac{\omega}{ck}\right)^2} \left[ \left(\frac{ck}{\omega}\right)^2 \hat{k}\hat{k} + i \frac{I}{\omega} \right] \cdot (\vec{V}_i - \vec{V}_e).$$

For nonrelativistic phase velocities

$$\left(\frac{\omega}{ck}\right)^2 \ll 1. \quad (15)$$

Introducing the plasma frequency

$$\omega_p = e \left( \frac{n_{e0}}{\epsilon_0 m_e} \right)^{1/2}, \quad (16)$$

the electric field intensity becomes

$$\vec{E} = - \frac{m_e \omega}{e} \left(\frac{\omega_p}{ck}\right)^2 \left[ \left(\frac{ck}{\omega}\right)^2 \hat{k}\hat{k} + i \frac{I}{\omega} \right] \cdot (\vec{V}_i - \vec{V}_e). \quad (17)$$

Equation (2) shows that the electric field term is comparable with or greater than the electron-ion collision term when

$$\omega \lesssim \frac{\omega_p^2}{\nu_{ei}} = \frac{\omega_p^2}{\nu_{ei}}, \quad (18)$$

unless the component of differential charged particle velocity vanishes for the direction of propagation. For elastic collisions, the quantity usually tabulated is

$$\nu_{AB} = \frac{m_A + m_B}{m_B} \nu'_{AB}, \quad (19)$$

where  $\nu$  is the average collision cross section. For the case  $m_e \ll m_i$ ,  $\nu_{ei} = \nu'_{ei}$ . For ions,  $\nu'_{ei} = \nu'_{ei} m_e/m_i$ . Property frequencies are estimated in Table I (data from Georges [1]). Using  $\omega_p^2 = 10^{15} \text{ (rad/sec)}^2$  and  $\nu_{ei} = 10^3 \text{ rad/sec}$ , we find the electric field to be of importance when  $\omega \lesssim 10^{12} \text{ rad/sec}$  or, for all practical cases for the

TABLE I. ORDER OF MAGNITUDE OF PROPERTY FREQUENCIES

Z (km)	$\omega_c$ (sec <sup>-1</sup> )	$\omega_p^2$ (sec <sup>-2</sup> )	$\nu_{in}$ (sec <sup>-1</sup> )	$\nu_{en}$ (sec <sup>-1</sup> )	$\nu_{ei}$ (sec <sup>-1</sup> )
100	10 <sup>7</sup>	10 <sup>14</sup>	10 <sup>4</sup>	10 <sup>5</sup>	10 <sup>3</sup>
200	10 <sup>7</sup>	10 <sup>15</sup>	1	10 <sup>2</sup>	10 <sup>2</sup>
300	10 <sup>7</sup>	10 <sup>15</sup>	1	10	10 <sup>3</sup>
500	10 <sup>7</sup>	10 <sup>15</sup>	-	-	-

higher altitude range of interest, when electron-ion collisions are important.

It remains to develop expressions for the charged particle velocities. Introducing the electron cyclotron frequency,

$$\omega_c = \frac{eB_o}{m_e}, \quad (20)$$

and the unit magnetic intensity vector,

$$\hat{b} = \frac{B_o}{B_o} \quad (21)$$

and using equations (4), (5), (12), (13), and (17) and the functional form (1) in equations (2) and (3), we obtain vector equations for  $\tilde{V}_e$  and  $\tilde{V}_i$ . Using the identity

$$\hat{k} = \hat{b} \times (\hat{k} \times \hat{b}) + (\hat{k} \cdot \hat{b}) \hat{b} \quad (22)$$

and forming the scalar product of these equations with an arbitrary unit vector  $\hat{n}$ , we find

$$\begin{aligned} & \left\{ \frac{\nu_{ei} + \nu_{en}}{\omega} + i \left[ 1 + \left( \frac{\omega_p}{ck} \right)^2 \right] \right\} \hat{n} \\ & + \left\{ (\hat{n} \cdot \hat{k})(\hat{k} \cdot \hat{b}) \left[ \left( \frac{\omega_p}{\omega} \right)^2 + i \frac{m_i}{m_e} \left( \frac{a_o k}{\omega} \right)^2 \right] \right\} \hat{b} \\ & + \left\{ (\hat{n} \cdot \hat{k}) \left[ \left( \frac{\omega_p}{\omega} \right)^2 + i \frac{m_i}{m_e} \left( \frac{a_o k}{\omega} \right)^2 \right] \right\} \hat{b} \times (\hat{k} \times \hat{b}) \\ & - \frac{\omega_c}{\omega} (\hat{n} \times \hat{b}) \cdot \tilde{V}_e \end{aligned}$$

$$\begin{aligned} & + \left\{ \left[ -\frac{\nu_{ei}}{\omega} + i \left( \frac{\omega_p}{ck} \right)^2 \right] \hat{n} \right. \\ & - \left[ (\hat{n} \cdot \hat{k})(\hat{k} \cdot \hat{b}) \left( \frac{\omega_p}{\omega} \right)^2 \right] \hat{b} \\ & - \left. \left[ (\hat{n} \cdot \hat{k}) \left( \frac{\omega_p}{\omega} \right)^2 \right] \hat{b} \times (\hat{k} \times \hat{b}) \right\} \cdot \tilde{V}_i \\ & - \frac{\nu_{en}}{\omega} \hat{n} \cdot \tilde{V}_n = 0 \quad (23) \end{aligned}$$

and

$$\begin{aligned} & \left\{ \left( \frac{m_e}{m_i} \frac{\nu_{ei}}{\omega} + \frac{\nu_{in}}{\omega} + i \right) \hat{n} \right. \\ & + (\hat{n} \cdot \hat{k})(\hat{k} \cdot \hat{b}) \left[ -\frac{m_e}{m_i} \left( \frac{\omega_p}{\omega} \right)^2 + i \left( \frac{a_o k}{\omega} \right)^2 \right] \hat{b} \\ & + (\hat{n} \cdot \hat{k}) \left[ \frac{m_e}{m_i} \left( \frac{\omega_p}{\omega} \right)^2 - i \left( \frac{a_o k}{\omega} \right)^2 \right] \hat{b} \times (\hat{k} \times \hat{b}) \\ & + \left. \frac{m_e}{m_i} \frac{\omega_c}{\omega} \hat{n} \times \hat{b} \right\} \cdot \tilde{V}_i \\ & + \left\{ \frac{m_e}{m_i} \left[ -\frac{\nu_{ei}}{\omega} + i \left( \frac{\omega_p}{ck} \right)^2 \right] \hat{n} \right. \\ & + \left[ \frac{m_e}{m_i} (\hat{n} \cdot \hat{k})(\hat{k} \cdot \hat{b}) \left( \frac{\omega_p}{\omega} \right)^2 \right] \hat{b} \\ & - \left. \left[ \frac{m_e}{m_i} (\hat{n} \cdot \hat{k}) \left( \frac{\omega_p}{\omega} \right)^2 \right] \hat{b} \times (\hat{k} \times \hat{b}) \right\} \cdot \tilde{V}_e \\ & - \frac{\nu_{in}}{\omega} \hat{n} \cdot \tilde{V}_n = 0. \quad (24) \end{aligned}$$

The natural choice of orthogonal coordinates appears to be

$$\hat{n} = \hat{b}, \hat{k} \times \hat{b}, \hat{b} \times (\hat{k} \times \hat{b}) \quad (25)$$

which is illustrated in Figure 1. This choice gives

velocities along and perpendicular to the magnetic field lines which are of particular interest. A well known approximation that is often employed in the upper atmosphere is that the charged particles are locked on to the component of neutral motion along the magnetic field lines.

The system of equations (23) and (24) is most conveniently handled in terms of a single  $6 \times 6$  matrix. By using the identity

$$[\hat{b} \times (\hat{k} \times \hat{b})] \times \hat{b} = \hat{k} \times \hat{b} \quad (26)$$

and the following angles defined in Figure 1

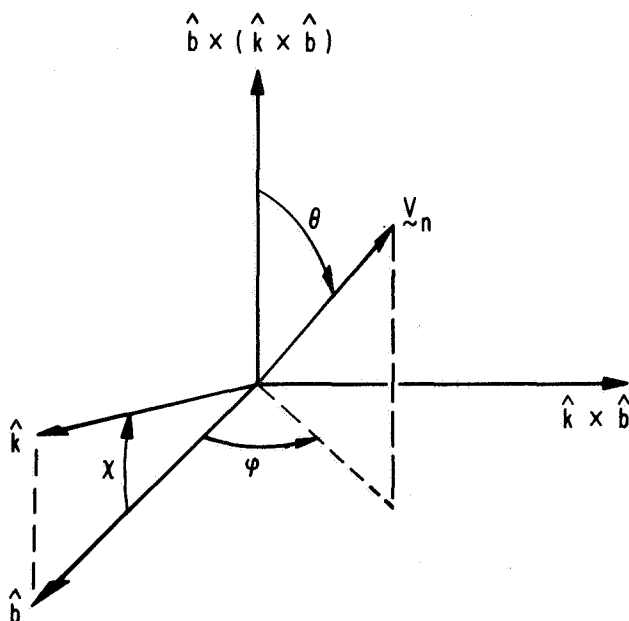


FIGURE 1. COORDINATE SYSTEM BASED ON WAVE PROPAGATION VECTOR AND UNIT MAGNETIC INTENSITY VECTOR

$$\hat{k} \cdot \hat{b} = \cos \psi \quad (27)$$

$$\frac{\tilde{V}_n}{V_n} \cdot [\hat{b} \times (\hat{k} \times \hat{b})] = \cos \theta \quad (28)$$

$$\frac{\tilde{V}_n}{V_n} \cdot \hat{b} = \sin \theta \cos \varphi, \quad (29)$$

the system can be written

$$\sum_{i=1}^6 A_{ji} W_i = B_j, \quad (30)$$

where  $W$  is a six vector which gives the desired velocities as a fraction of the neutral particle velocity

$$\begin{aligned} W_1 &= V_{e_b} / V_n \\ W_2 &= V_{e_{k \times b}} / V_n \\ W_3 &= V_{e_{b \times (k \times b)}} / V_n \\ W_4 &= V_{i_b} / V_n \\ W_5 &= V_{i_{k \times b}} / V_n \\ W_6 &= V_{i_{b \times (k \times b)}} / V_n \end{aligned} \quad (31)$$

with the coefficient matrix given by

$$\begin{aligned} A_{11} &= \frac{\nu_{ei} + \nu_{en}}{\omega} + \left(\frac{\omega_p}{\omega}\right)^2 \cos^2 \psi \\ &+ i \left[ 1 + \left(\frac{\omega_p}{\omega}\right)^2 + \frac{m_i}{m_e} \left(\frac{a_k}{\omega}\right)^2 \cos^2 \psi \right] \end{aligned}$$

$$\begin{aligned} A_{12} &= A_{15} = A_{21} = A_{24} = A_{26} = A_{35} = A_{42} \\ &= A_{45} = A_{51} = A_{53} = A_{54} = A_{62} = 0 \end{aligned}$$

$$A_{13} = \left(\frac{\omega_p}{\omega}\right)^2 \cos \psi + i \frac{m_i}{m_e} \left(\frac{a_k}{\omega}\right)^2 \cos \psi$$

$$A_{14} = -\frac{\nu_{ei}}{\omega} - \left(\frac{\omega_p}{\omega}\right)^2 \cos^2 \psi + i \left(\frac{\omega_p}{ck}\right)^2$$

$$A_{16} = -A_{43} = -\left(\frac{\omega_p}{\omega}\right)^2 \cos \psi$$

$$A_{22} = \frac{\nu_{ei} + \nu_{en}}{\omega} + i \left[ 1 + \left(\frac{\omega_p}{ck}\right)^2 \right]$$

$$A_{23} = -A_{32} = -A_{56} = A_{65} = \frac{\omega_c}{\omega}$$

$$A_{25} = A_{52} = -\frac{\nu_{ei}}{\omega} + i \left(\frac{\omega_p}{ck}\right)^2 \quad (32)$$

$$A_{31} = \sin^2 \psi \cos \psi \left[ \left( \frac{\omega_p}{\omega} \right)^2 + i \left( \frac{a k}{\omega} \right)^2 \frac{m_i}{m_e} \right]$$

$$A_{33} = \frac{\nu_{ei} + \nu_{en}}{\omega} + \left( \frac{\omega_p}{\omega} \right)^2 \sin^2 \psi + i \left[ 1 + \left( \frac{\omega_p}{ck} \right)^2 + \frac{m_i}{m_e} \left( \frac{a k}{\omega} \right)^2 \sin^2 \psi \right]$$

$$A_{34} = -A_{61} = -\left( \frac{\omega_p}{\omega} \right)^2 \sin^2 \psi \cos \psi$$

$$A_{36} = A_{63} = -\frac{\nu_{ei}}{\omega} + \left( \frac{\omega_p}{\omega} \right)^2 \sin^2 \psi + i \left( \frac{\omega_p}{ck} \right)^2$$

$$A_{41} = -\frac{\nu_{ei}}{\omega} + \left( \frac{\omega_p}{\omega} \right)^2 \cos^2 \psi + i \left( \frac{\omega_p}{ck} \right)^2$$

$$A_{44} = \frac{\nu_{ei}}{\omega} + \frac{m_i}{m_e} \frac{\nu_{in}}{\omega} - \left( \frac{\omega_p}{\omega} \right)^2 \cos^2 \psi$$

$$+ i \frac{m_i}{m_e} \left[ 1 + \left( \frac{a k}{\omega} \right)^2 \cos^2 \psi \right]$$

$$A_{46} = -\left( \frac{\omega_p}{\omega} \right)^2 \cos \psi + i \frac{m_i}{m_e} \left( \frac{a k}{\omega} \right)^2 \cos \psi$$

$$A_{55} = \frac{\nu_{ei}}{\omega} + \frac{m_i}{m_e} \frac{\nu_{in}}{\omega} + i \frac{m_i}{m_e}$$

$$A_{64} = -\sin^2 \psi \cos \psi \left[ \left( \frac{\omega_p}{\omega} \right)^2 - i \frac{m_i}{m_e} \left( \frac{a k}{\omega} \right)^2 \right]$$

$$A_{66} = \frac{\nu_{ei}}{\omega} + \frac{m_i}{m_e} \frac{\nu_{in}}{\omega} + \left( \frac{\omega_p}{\omega} \right)^2 \sin^2 \psi + i \frac{m_i}{m_e} \left[ 1 + \left( \frac{a k}{\omega} \right)^2 \sin^2 \psi \right]$$

and the vector  $\underline{B}$  is given by

$$B_1 = \frac{\nu_{en}}{\omega} \sin \theta \cos \varphi$$

$$B_2 = \frac{\nu_{en}}{\omega} \sin \theta \sin \varphi$$

$$B_3 = \frac{\nu_{en}}{\omega} \cos \theta \quad (33)$$

$$B_4 = \frac{m_i}{m_e} \frac{\nu_{in}}{\omega} \sin \theta \cos \varphi$$

$$B_5 = \frac{m_i}{m_e} \frac{\nu_{in}}{\omega} \sin \theta \sin \varphi$$

$$B_6 = \frac{m_i}{m_e} \frac{\nu_{in}}{\omega} \cos \theta$$

Considering individual equations of the system (30) and the orders of magnitude of Table I, very few terms can be dropped with retention of uniform validity at all altitudes. Any approximations must be made equation by equation and by considering real and complex parts.

The inverted system will yield a solution such as

$$\frac{v_{eb}}{V_n} = a_1 + i a_2,$$

where  $a_1$  and  $a_2$  are real numbers. The amplitude ratio in this case is  $(a_1^2 + a_2^2)^{1/2}$  and the phase lead is  $\tan^{-1} a_2/a_1$ .

#### IV. CONCLUSIONS

The dynamics of charged particles in a weakly ionized plasma subjected to a neutral particle wave have been analyzed using linear theory. A system of six algebraic equations allows determination of electron and ion velocities parallel and perpendicular to the unperturbed magnetic field lines for arbitrary propagation and velocity vector of the neutral particle wave. The plasma excess charge and induced electric field intensity are shown to be dependent on the difference between ion and electron velocities. The equations are valid over a wide range of state and wave properties since all frequency terms have been retained except those which are important for relativistic phase velocities.

The principle limitation to the theory is the assumption of uniform unperturbed state and small perturbations about it. With respect to the former, application to the ionosphere would infer neglect of ambient diffusion and indirect gravity effects. For large amplitudes, the full nonlinear equations are necessary. Alteration of chemical reaction and transport rates and a detailed thermal balance have not been included.

In conclusion, we ascertain the type of correlations that may be obtained from the theory. First, specification of the neutral wave velocity vector, propagation vector and frequency determines the charged particle dynamics at altitude. Secondly, the system associated with equation (30) is such that the neutral and ion motions are determined if the electron velocity vector, propagation vector and frequency are specified along with altitude. This would be the approach using electromagnetic probes.

## REFERENCES

1. Georges, T. M.: Ionospheric Effects of Atmospheric Waves, ESSA Technical Report No. IER 57-ITSA 54, October 1967.
2. Marcos, F. A.: Aircraft-Induced Ionospheric Disturbances, AFCRL-66-229, Air Force Cambridge Research Laboratories, April 1966.
3. Barry, G. H.; Griffiths, L. T.; and Taenzer, J. C.: HF Radio Measurements of High-altitude Acoustic Waves from a Ground-level Explosion, *Journal of Geophysical Research*, Vol. 71, 1966, p. 4173.
4. Detert, D. G.: Acoustic-Gravity Wave Study, Technical Report No. RADC-TR-68-53, Rome Air Development Center, April 1968.
5. Roberts, W. T.: Ionospheric Disturbances Caused by Ground Based Acoustic Energy Sources, *Research Achievements Review*, Vol. II, Report No. 10, NASA TM X-53706, 1967, 57-62.
6. Newton, G. P.; Plez, D. T.; and Volland, H.: Direct In Situ Measurements of Wave Propagation in the Neutral Thermosphere, NASA X-621-68-44, Aeronomy Branch, Goddard Space Flight Center.
7. Midgley, J. E. and Liehmohn, H. B.: Gravity Waves in a Realistic Atmosphere, *Journal of Geophysical Research*, Vol. 71, August 1966, 3729-3748.
8. Einaudi, F.: Higher Order Approximations in the Theory of Acoustic-Gravity Waves, ESSA/ARPA Symposium on Acoustic-Gravity Waves, Boulder, July 1968.
9. Hayes, W. D.: The Propagation Upward of the Shock Wave from a Strong Explosion in the Atmosphere, *Journal of Fluid Mechanics*, Vol. 32, May 1968, 317-331.
10. Bugnolo, D. S.: The Interaction of Internal Gravity Waves with the Ionosphere at the F<sub>1</sub> and F<sub>2</sub> Levels, Technical Report No. 140, Hudson Laboratories of Columbia University, Dobbs Ferry, July 1967.
11. Hook, W. H.: Ionosphere Irregularities Produced by Internal Atmospheric Waves, *Journal of Atmospheric and Terrestrial Physics*, Vol. 30, May 1968, 795-823.
12. Kantor, G. and Pierce, A. D.: Acoustic Waves in the Lower Ionosphere, Avco Scientific Report AVSSD 0308-67-CR, September 1967.
13. Poeverlien, H.: Ion-Acoustic Waves Modified by Gravity, *Annales de Geophysique*, Vol. 24, January-March 1968, 325-332.

# THEORY FOR THE DETERMINATION OF WIND VELOCITY AND THE ASSOCIATED ALTITUDE BY THE CROSS-BEAM METHOD

By

M. Y. Su<sup>1</sup>, J. B. Stephens<sup>2</sup>, and M. Phillips<sup>3</sup>

## ABSTRACT

Methods for determining the wind velocity (speed and direction) and the altitude for the wind measurement from transit times obtained by employing the cross-beam technique are discussed in this report. To obtain a turbulent speed for a region in space using the cross-beam technique, it is necessary to know the beam geometry and the flow direction from which the turbulent transit path and turbulent velocity can be determined.

All cross-beam measurements made to date have been restricted to a turbulence flow normal to the plane of the two beams. This analysis, both analytically and numerically, presents three formulations to obtain the direction of flow. These formulations differ in the assumed types of wind profile used. Once the flow direction is determined, the transit height, the transit distances and the turbulence speed can then be obtained.

The merits of the formulations for wind direction have been explored with and without the influences of possible error due to resolution in the cross-beam transit times.

## DEFINITION OF SYMBOLS

<u>Symbol</u>	<u>Definition</u>
b	Length of baseline between two photometers
$D_i$	Transit distance for the $i^{\text{th}}$ beam

$H_i$	Transit height for $i^{\text{th}}$ beam
$H_o$	Reference height for wind speed profile as defined in equation (10)
$P_{1c}, P_{2c}$	Geometrical constants as defined in equation (12a)
$P_{1\ell}, P_{2\ell}, P_{3\ell}$	Geometrical constants as defined in equation (14a)
$Q_{1c}, Q_{2c}$	Geometrical constants as defined in equation (12a)
$Q_{1\ell}, Q_{2\ell}, Q_{3\ell}$	Geometrical constants as defined in equation (14a)
$V_o$	Reference speed for wind speed profile as defined in equation (10)
$V_i$	Wind speed at transit height $H_i$
$\alpha_{10}$	Elevation angle of the optical axis of the multiple-beam photometer
$\alpha_2$	Elevation angle of the single-beam photometer
$\alpha_{1i}$	Elevation angle of $i^{\text{th}}$ beam of the multiple-beam photometer ( $i = 1, 2, 3$ )
$\beta_{10}$	Azimuth angle of the optical axis of the multiple-beam photometer
$\beta_{1i}$	Azimuth angle of $i^{\text{th}}$ beam of the multiple-beam photometer

1. Nortronics-Huntsville

2. Aero-Astrodynamic Laboratory, George C. Marshall Space Flight Center

3. IIT Research Institute

## DEFINITION OF SYMBOLS (Concluded)

$\Delta\beta_{i0}$	Angle between the $i^{\text{th}}$ beam and the optical axis of the multiple-beam photometer
$\epsilon$	Percentage error of transit times
$\rho$	Exponent of power-law for wind profile
$\tau_i$	Transit time of $i^{\text{th}}$ beam of the multiple-beam photometer ( $i = 1, 2, 3$ )
$\phi$	Wind direction with respect to the baseline

<u>Subscripts</u>	<u>Definition</u>
$i$	Denotes $i^{\text{th}}$ beam of the fan detector
$\epsilon$	Denotes percentage error $\epsilon$ in transit time included

## I. INTRODUCTION

Three formulations for obtaining the wind direction, and a formulation for obtaining the transit height and transit distance from the transit times obtained from atmospheric multiple cross-beam measurements are presented in this report. The current atmospheric cross-beam experiments have assumed a wind normal to the plane of two single beams<sup>1</sup> [1, 2] as shown in Figure 1. It is then possible to determine the wind speed from the transit time obtained from the associated covariance curve [3, 4], since for a given beam geometry the transit distance was defined. Further, the transit height was also known.

In atmospheric wind measurements, as well as other cross-beam applications, it is most desirable to be able to obtain directly from the determined cross-beam transit times the wind speed, wind direction, and the associated altitude. It will be shown when a multiple detection system (a single-beam

unit and a fan, Fig. 2) is employed for cross-beam measurements, the above three parameters can be found.

The formula for transit distances and heights are derived in Section II, while Section III contains the formulation for obtaining the wind direction. Three different formulations were presented for the wind direction based on three different assumptions for the profile of horizontal wind. They are a constant wind profile, a linear wind profile, and a power-law wind profile for the region between the transit paths.

A quantitative comparison between the formulations of these profiles is made (Section IV) by examining the effect that a small error in transit time would introduce in the calculations for the wind direction. The computer program used in obtaining these results has been included in the appendix.

## II. TRANSIT HEIGHT AND TRANSIT DISTANCE

The formula for the transit distance and transit height of two crossed beams will be derived in terms of beam geometry and wind direction. This derivation assumes a horizontal wind and a constant wind direction over the region of interest. Each wind direction (for a given beam geometry) uniquely determines a transit height and transit distance for the cross-beam configuration. The transit height and transit distance are the altitude and distance of the path traversed by turbulent eddies moving from beam A to beam B.

Two detectors located at points A and B (Fig. 3) with beams along  $AA_1$  and  $BB_1$  have elevation angles of  $\alpha_{1i}$  and  $\alpha_2$ , respectively. The azimuth angles of beams  $AA_1$  and  $BB_1$ ,  $\beta_{1i}$  and  $\beta_2$ , are measured counterclockwise from the baseline,  $b$ , of the two detectors A and B. The wind direction  $\phi$  is measured from the wind vector counterclockwise to the baseline.

The transit height  $H_i$  can be obtained from triangle A'B'C' which is in the plane normal to the wind direction (side view I) in terms of the projected elevation angles as

1 Heybey, W. H. On the Wind Component Measurable by Crossed-Beam Arrangement. IN-AERO-7-67, MSFC, October 1967

$$H_i = \frac{b \sin \phi}{\cot \alpha'_{1i} + \cot \alpha'_2} \quad (1)^1$$

where  $\alpha'_{1i}$  and  $\alpha'_2$  are the projections in the plane of A'B'C' of the actual elevation angles,  $\alpha_{1i}$  and  $\alpha_2$ . The projected angles are related to the actual elevation angles by

$$\cot \alpha'_{1i} = \cot \alpha_{1i} \sin(\phi + \beta_{1i}) \quad (2)^1$$

and

$$\cot \alpha'_2 = \cot \alpha_2 \sin(\phi + \beta_2) \quad (3)^1$$

from triangles BEK and ACH, respectively. Thus, the transit height (Eq. 1) can now be written in terms of the actual elevation angles as

$$H_i = \frac{b \sin \phi}{\cot \alpha_{1i} \sin(\phi + \beta_{1i}) + \cot \alpha_2 \sin(\phi + \beta_2)} \quad (4)^1$$

The transit distance,  $D_i$ , for the  $i^{\text{th}}$  beam of detector A, which is by definition at the transit height  $H_i$ , can be obtained in the following manner.

By the law of sines the triangle ACG gives

$$\frac{\overline{CG}}{\sin \beta_{1i}} = \frac{H_i \cot \alpha_{1i}}{\sin \phi} \quad (5)^1$$

and from triangle BEG,

$$\frac{\overline{GE}}{\sin \beta_2} = \frac{H_i \cot \alpha_2}{\sin \phi} \quad (6)$$

Since

$$D_i = \overline{CG} + \overline{GE} \quad (7)$$

the transit distance can be written as

$$D_i = \frac{H_i}{\sin \phi} [\cot \alpha_{1i} \sin \beta_{1i} + \cot \alpha_2 \sin \beta_2] \quad (8)$$

It follows then that the turbulence speed  $V_i$  at the transit height  $H_i$  can be written in terms of the transit time  $\tau_i$ , which is the time required by turbulent eddies to traverse the transit distance  $D_i$ , as

$$V_i = \frac{D_i}{\tau_i} \quad (9)$$

Thus, to obtain the transit height, distance, and speed [Eq. (4), (8), and (9)] requires a knowledge of the cross-beam geometry, transit time, and wind direction. The beam geometry can be obtained readily since only a knowledge of the detectors' elevation angles and azimuth angles, along with the distance between the detectors, is needed. The transit time can be obtained from the cross-beam technique [2]. This means that the wind direction still must be determined. The next section will consider the formulation for the wind direction.

### III. DETERMINATION OF WIND DIRECTION AND SPEED

Since the cross-beam method is a method for performing remote measurements of winds, it is desirable that the entire measurement be self-contained within the cross-beam system. With a pair of single beams, such as the one discussed in Section II (Fig. 1), we must know the wind direction in order to obtain the wind speed and height. To retrieve information about direction, speed, and height of the wind using the cross-beam technique, we must use some form of a multiple cross-beam system along with an assumption concerning the wind profile. The

1. See Appendix B for derivation

fan system in Figure 2 affords a simple multiple-beam system which will provide the transit times from which the wind direction can be obtained when an assumption for the wind profile is used. Since the cross-beam technique requires about an hour of data [4] to retrieve a transit time with sufficient statistical accuracy, there is a limited resolution in these times that could induce an error in the wind direction calculations.

Presumably, the most realistic assumption for the wind profile will yield the best results for the wind velocity and height. For the average surface winds, (up to 150 m) the power-law profile is generally considered the best profile [5]:

$$V_i = V_o \left( \frac{H_i}{H_o} \right)^\rho, \quad (10)$$

where  $V_o$  is the wind speed at the reference height  $H_o$ , while  $\rho$  is some constant depending on wind speed and ground roughness. The constant will increase as the wind speed decreases. For the purpose of this analysis,  $\rho = 0.2$  is adopted. The wind profile thus provided by the power law is shown in Figure 4.

Suppose that the height ranges from 50 m to 150 m; then, an assumption of a linear wind profile, as indicated by AC, is a reasonable approximation. The simplest approximation is the constant wind profile for the region of interest. With the latter approximation, the largest error in wind speed would be

$$\frac{V_i(150 \text{ m}) - V_i(50 \text{ m})}{\frac{1}{2} [V_i(150 \text{ m}) + V_i(50 \text{ m})]} = 22\%.$$

Based on the fan system and the wind profiles discussed, the wind direction will be formulated in three ways:

1. A constant wind profile for mathematical simplicity
2. A linear wind profile for a compromise between mathematical simplicity and physical realism

---

1. See Appendix B for derivation

3. A power-law wind profile for physical realism.

## A. Formulation with Constant Wind Profile

By assuming the wind speed and direction to be constant over the height of interest, the system of equations (4), (8), and (9) is closed for the determination of the wind speed, direction, and height when two independent transit times and the beam geometry are known. The term  $\tau_i$  denotes the transit time between the single beam and the  $i^{\text{th}}$  beam in the fan.

By this assumption

$$V_1 = V_2;$$

i. e.,

$$\frac{D_1}{\tau_1} - \frac{D_2}{\tau_2} = 0. \quad (11)$$

Substituting equations (4) and (8) into (11), the equation for the wind direction is obtained:

$$\phi = \text{arc cot} \left[ \begin{array}{c} P_{2c} - \left( \frac{\tau_2}{\tau_1} \right) P_{1c} \\ (-) \frac{P_{2c} - \left( \frac{\tau_2}{\tau_1} \right) P_{1c}}{Q_{2c} - \left( \frac{\tau_2}{\tau_1} \right) Q_{1c}} \end{array} \right]. \quad (12)$$

The geometric constants are

$$P_{1c} = E_1 [\cot \alpha_{12} \cos \beta_{12} + \cot \alpha_2 \cos \beta_2]$$

$$P_{2c} = E_2 [\cot \alpha_{11} \cos \beta_{11} + \cot \alpha_2 \cos \beta_2]$$

$$Q_{1c} = E_1 [\cot \alpha_{12} \sin \beta_{12} + \cot \alpha_2 \sin \beta_2]$$

$$Q_{2c} = E_2 [\cot \alpha_{11} \sin \beta_{11} + \cot \alpha_2 \sin \beta_2]$$

and

$$E_i = \cot \alpha_{1i} \sin \beta_{1i} + \cot \alpha_2 \sin \beta_2, \quad (12a)$$

where  $\alpha_{1i}$  and  $\beta_{1i}$  ( $i = 1, 2$ ) are the elevation and azimuth angles of the  $i^{\text{th}}$  beam of the fan, while  $\alpha_2$  and  $\beta_2$  are the elevation and azimuth angles of the single-beam detector.

Thus, the wind direction  $\phi$  can be calculated from the two transit times  $\tau_1$  and  $\tau_2$ , which are obtained by the cross-beam method. Hence, wind speed equations (8) and (9) and height equation (4) can be obtained. If these two transit heights do not differ very much, then the constant wind speed profile is a valid approximation (Fig. 4).

## B. Formulation with Linear Wind Profile

By assuming that the wind speed varies linearly over the height of interest, the system of equations (4), (8), and (9) can be closed to determine wind direction, speed, and height, when three independent transit times  $\tau_i$  ( $i = 1, 2, 3$ ) are given.

Using the assumption of a linear wind profile, we obtain

$$\frac{V_3 - V_1}{V_2 - V_1} = \frac{H_3 - H_1}{H_2 - H_1} \quad (13)$$

Substituting equations (8) and (9) into the above equation, one obtains the following relationship for the wind direction

$$\phi = \text{arc cot} \left( - \frac{\sum_{i=1}^3 \frac{P_{i\ell}}{\tau_i}}{\sum_{i=1}^3 \frac{Q_{i\ell}}{\tau_i}} \right), \quad (14)^1$$

where  $P_{i\ell}$  and  $Q_{i\ell}$  ( $i = 1, 2, 3$ ) are functions of the beam geometry.

$$P_{1\ell} = E_1 (\cot \alpha_{13} \cos \beta_{13} - \cot \alpha_{12} \cos \beta_{12})$$

$$P_{2\ell} = E_2 (\cot \alpha_{11} \cos \beta_{11} - \cot \alpha_{13} \cos \beta_{13})$$

$$P_{3\ell} = E_3 (\cot \alpha_{12} \cos \beta_{12} - \cot \alpha_{11} \cos \beta_{11})$$

$$Q_{1\ell} = E_1 (\cot \alpha_{13} \sin \beta_{13} - \cot \alpha_{12} \sin \beta_{12})$$

$$Q_{2\ell} = E_2 (\cot \alpha_{11} \sin \beta_{12} - \cot \alpha_{11} \sin \beta_{11})$$

$$Q_{3\ell} = E_3 (\cot \alpha_{12} \sin \beta_{12} - \cot \alpha_{11} \sin \beta_{11})$$

and

$$E_i = \cot \alpha_{1i} \sin \beta_{1i} + \cot \alpha_2 \sin \beta_2. \quad (14a)$$

$\alpha_{1i}$  and  $\beta_{1i}$  are true elevation and azimuth angles of each of the multiple beams. These multiple beams are coplanar and the inclination angle of the plane spanned by these beams is equal to the elevation angle  $\alpha_{10}$  of the optical axis of the detector. It is much easier to refer the elevation and azimuth angles of these multiple beams on their coplanar plane rather than with respect to the baseline and the ground. The orientation of the  $i^{\text{th}}$  beam is simply specified with respect to that of the optical axis of the detector (whose azimuth angle will be denoted by  $\beta_{10}$ ) by the angle between them,  $\Delta\beta_{10}$ . The sign of  $\Delta\beta_{10}$  is the same as the difference  $(\beta_i - \beta_o)$ . The true elevation and azimuth angles can then be obtained by

$$\beta_{1i} = \beta_{10} + \text{arc tan} \left[ \frac{\tan \Delta\beta_{10}}{\cos \alpha_{10}} \right] \quad (14b)^1$$

and

$$\alpha_{1i} = \text{arc tan} [\tan \alpha_{10} \cos (\beta_{10} - \beta_{1i})] \quad (14c)^1$$

1. See Appendix B for derivation

Given the three transit times,  $\tau_i$ , a wind direction can be calculated (Eq. 14). This permits us to obtain three velocities at the three transit heights. The linear wind profile permits the transit heights to differ more than the constant wind profile did, without invalidating the approximation.

### C. Formulation with Power-Law Wind Profile

By assuming that the wind profile follows the power-law (Eq. 10), and has a constant wind direction, the system of equations (4), (8), and (9) can again be closed when two independent transit times  $\tau_i$  ( $i = 1, 2$ ) are given.

From the power-law profile (Eq. 10), we obtain

$$\frac{V_1}{V_2} = \left( \frac{H_1}{H_2} \right)^\rho \quad (15)$$

where  $\rho = 0.2$ . Using equations (4), (8), and (9), we obtain

$$\frac{\tau_2}{\tau_1} \cdot \frac{H_1}{H_2} \cdot \frac{(\cot \alpha_{11} \sin \beta_{11} + \cot \alpha_2 \sin \beta_2)}{(\cot \alpha_{12} \sin \beta_{12} + \cot \alpha_2 \sin \beta_2)} - \left( \frac{H_1}{H_2} \right)^\rho = 0 \quad (16)$$

where

$$\frac{H_1}{H_2} = \frac{\cot \alpha_{11} \sin(\phi + \beta_{12}) + \cot \alpha_2 \sin(\phi + \beta_2)}{\cot \alpha_{11} \sin(\phi + \beta_{11}) + \cot \alpha_2 \sin(\phi + \beta_2)} \quad (17)$$

Different from the two previous formulations, the governing relationship (Eq. 16) for the wind direction is an implicit function of  $\phi$ ; and thus, the iterative method is used to solve for  $\phi$ . Once the value of  $\phi$  is obtained, the wind speeds at the transit heights  $H_1$  and  $H_2$  can be evaluated again by equation (9).

## IV. NUMERICAL EXPERIMENTS AND COMPARISONS

This section will demonstrate quantitatively the capability of the three formulations for different wind profiles discussed in the last section to retrieve the wind direction, wind speed, and the transit height using a hypothetical power-law wind profile (Eq. 10), under the following conditions:

1. varying beam geometries,
2. with and without errors induced in the transit times.

The purpose of these experiments is to establish the best beam geometry and formulation for the wind direction calculation from atmospheric cross-beam experiments. The first set of numerical experiments will examine the effects of beam geometry as well as the wind profile assumptions.

The second set of numerical experiments is designed to examine the effects of the resolution in transit times on the effectiveness of the three formulations for the wind direction. The transit times obtained from the covariance curve [2] are never a result of a sharp peak in the curve. This is an inherent quality of atmospheric cross-beam measurements, because of the flow noise in the cross-beam data and the unsteady wind velocity over the period of measurement. The minimum period of atmospheric cross-beam measurement is shown to be about one hour for sufficient statistical accuracy [4]. Thus, the transit time obtained is a most probable value rather than a unique value.

Furthermore, because the cross-beam data is reduced digitally, the covariance curve as a function of transit time has a digital resolution. This resolution can result in a slight error in transit time. Based on results obtained from the initial cross-beam tests [2] and the theoretical prediction [4] it is reasonable to assume that a 5 percent error due to resolution could exist in the transit times.

In both groups of experiments the same general procedure was used. A wind direction  $\phi_{act}$  was

assumed, and then utilized to obtain the transit height (Eq. 4) and the transit distance (Eq. 8). This transit height along with the power-law wind profile, equation (10) (with  $V_0 = 10$  m/sec,  $H_0 = 3$  meters,  $\rho = 0.2$ ) gives the assumed actual wind speed. This speed, along with the transit distance, provides the transit time. Using these transit times in the wind direction formula, as if they were obtained from cross-beam measurements, a wind direction,  $\phi_{cal}'$  was calculated. Using this calculated wind direction, a calculated transit height and distance were obtained. With this calculated transit height and the transit times, the calculated wind speed can be obtained. An expression for the percentage of the absolute difference between the actual speed and the calculated speed divided by the actual wind speed,  $\left| \frac{\Delta V_i}{V_i} \right|$ ,

was then obtained as a function of the actual wind direction. This is graphically shown along with a plot of  $\phi_{cal}$  versus  $\phi_{act}$ . Each graph also contains a region showing the 10 percent error in  $\left| \frac{\Delta V_i}{V_i} \right|$  and 10 degrees error in  $\phi_{cal}$ . In these comparisons, the following are held fixed: the single beam elevation angle  $\alpha_2$  and the optical axis of elevation  $\alpha_{10} = 45$  degrees; and the baseline,  $b = 244$  meters. An average transit height of approximately 100 meters was maintained. The following were varied: single beam azimuth angles,  $\beta_2$  of 0 degrees or 20 degrees; optical axis azimuth angles  $\beta_{10}$  of 30 degrees, 50 degrees, or 70 degrees; and  $\Delta\beta_{11}$  of  $\pm 6.25$  degrees,  $\pm 12.5$  degrees, or  $\pm 25.0$  degrees.

For convenience, a term called "the acceptable wind direction,"  $\Delta\phi_{acp}$ , is used, which is defined as the acceptable actual range in wind direction such that less than a 10-percent error exists in the calculated wind speed and less than 10-degree error in the calculated wind direction from the actual values.

### A. Performance of the Three Wind Direction Formulations with Error Free Transit Times

Based on the geometries previously given, an attempt to estimate the performance of the three wind direction formulations will be made.

1. Constant Wind Assumption. The obvious region where this assumption is poor is where the wind speed changes violently with a small change in height, i. e., near the ground. A height of about 100 meters is considered in Figures 5 through 10. This change of wind speed with height is small. These figures contain graphs for the relative calculated errors in both wind direction and wind speed as a function of the actual wind direction. A comparison of the various beam geometries represented by these figures suggests the following:

a. The smaller the angle between the two beams in the fan, the more reliable the results obtained.

b. When the vertical planes of the single beam and the optical axis of the fan are parallel, the best results are obtained.

c. The combination of the above two characteristics yields the best results (Fig. 6). The acceptable range of wind direction,  $\Delta\phi_{acp}$ , is about 80 degrees for the constant wind profile assumption.

2. Linear Wind Assumption. The validity of the linear wind profile for the wind direction formulation (Eq. 13) is doubtful whenever the transit heights are all approximately equal, i. e., when  $H_1 \approx H_2 \approx H_3$ . The transit height used is about 100 meters for the center beam of the fan. The results for the linear wind profile assumption are shown in Figures 11 through 17.

$$\left| \frac{\Delta V_2}{V_2} \right|$$

was found to be the average error for the three velocities; therefore, for simplicity this is the only one plotted.

A comparison of the results obtained for the linear profile is the same as for the constant wind profile; i. e., the single beam and the optical axis of the fan should be parallel, and the fan angle should be as small as possible for best results, (Fig. 12). It was noted that the errors are less for the linear assumption than for the constant profile assumption.

3. Power-Law Assumption. The test profile (Eq. 10) is exactly the same wind profile as used

in this formulation for wind direction, so there is no error.

4. Comparisons Among Three Formulations for Wind Direction. Three conclusions can be inferred for the results just obtained:

a. The better the comparison between the assumed wind profile and the actual wind profile, the better the results.

b. Better results seem to be obtained when the vertical planes of the beam and the optical axis of the fan are parallel.

c. Better results also seem to be obtained for a smaller azimuth angle between the beams of the fan.

The next question is whether these conclusions are valid when the transit time resolution problem is introduced.

## B. The Effects of Transit Time Resolution on the Performance of These Formulations

The analysis in the last subsection will be repeated with the problem of transit time resolution added. The resolution limits in transit times obtained from cross-beam results could introduce an error in the transit times used in these calculations. Thus, the analysis will introduce a fixed percentage of error into the transit time such that the most drastic effects of the errors on the results can be seen. The most severe error patterns with respect to the test wind profile (Eq. 10) are:

$$\begin{aligned} \tau_{1, \epsilon} &= (1 + \epsilon) \tau_1 \\ \tau_{2, \epsilon} &= (1 - \epsilon) \tau_2 \end{aligned} \quad (18)$$

for the formulations with constant or power-law profile; and

$$\begin{aligned} \tau_{1, \epsilon} &= (1 + \epsilon) \tau_1 \\ \tau_{2, \epsilon} &= (1 - \epsilon) \tau_2 \\ \tau_{3, \epsilon} &= (1 + \epsilon) \tau_3, \end{aligned} \quad (19)$$

for the formulation with linear wind profile. The wind direction angle  $\phi$  in equations (12) and (17) depends on the ratio of two transit times,  $\tau_1/\tau_2$ . In equation (14), the wind direction angle  $\phi$  depends on two ratios of transit times,  $\tau_1/\tau_2$  and  $\tau_3/\tau_2$ , instead of individual transit times. Thus, the error patterns in equations (18) and (19) can be rewritten as

$$\frac{\tau_{1, \epsilon}}{\tau_{2, \epsilon}} = \frac{(1 + \epsilon) \tau_1}{(1 - \epsilon) \tau_2} \approx (1 + 2\epsilon) \frac{\tau_1}{\tau_2} \quad (20)$$

for formulations with constant or power-law profile, and

$$\frac{\tau_{1, \epsilon}}{\tau_{2, \epsilon}} \approx (1 + 2\epsilon) \frac{\tau_1}{\tau_2},$$

and

$$\frac{\tau_{3, \epsilon}}{\tau_{2, \epsilon}} \approx (1 + 2\epsilon) \frac{\tau_3}{\tau_2} \quad (\text{for } \epsilon \ll 1), \quad (21)$$

for the formulation with linear wind profile.

Equations (20) and (21) indicate that the most severe error patterns in transit times are essentially those which cause the largest deviation in the ratios of two (or three) transit times with a given percentage error  $\epsilon$ . In this numerical analysis, the value of  $\epsilon$  is set at 5 percent, which is about the best that can be obtained from the present atmospheric cross-beam measurements.

1. Constant Wind Profile. The same beam geometries examined in the previous subsection have been re-examined with the introduction of error in transit times. The effect of this error in the results (Figs. 17 through 24) is to reverse the requirement for fan angle from the no error case (Figs. 17 and 18); i.e., the best results are obtained:

a. for large azimuth fan angles, and

b. for the vertical planes of the single beam unit and the optical axis of the fan being parallel.

2. Linear Wind Profile. The calculated wind speeds and direction with errors in transit times using the assumption of linear wind profile were plotted in Figures 25 through 30. The

$$\left| \frac{\Delta V_2}{\Delta_2} \right|$$

plotted is for the center beam of the three beams in the fan detector since this is again the average result. These plots show the drastic effects of errors in transit times on the performance of this formulation. For every beam geometry calculated, the acceptable wind direction range,  $\Delta\phi_{acp}$ , is less than 20 degrees. The magnitude of the error in the input, transit time, is generally directly proportional to the correct transit times; therefore, even if the input errors are small, the same errors will be magnified when compared with the differences in wind speeds. This may explain the poor performance of this formulation under the influence of the errors involved in given transit times.

3. Power-Law Profile. The calculated wind speeds and directions using the assumption of the power-law profile with errors in transit times were plotted in Figures 31 through 36. The general observation of these figures is that the larger the azimuth angle between two beams in the fan  $\Delta\beta_{11}$ , the smaller the effects of errors in transit times, and that the azimuth angle of the single beam  $\beta_2$  seems to have little effect on the wind speeds and direction calculations (Figs. 34 through 36). To determine the best among these three beam geometries we need now to consider the transit heights and distances (Figs. 40 through 42). Figure 40 shows that the transit height  $H_i$  is almost constant over the whole range of  $\phi_{act}$  from 10 to 90 degrees for  $\beta_{10} = 30$  degrees but that the corresponding transit distance  $D_i$  is too small (about 15 m versus  $b = 244$  m) for the suitable cross-beam measurements. The best configuration from the viewpoint of transit heights and distances is that with  $\beta_2 = 30$  degrees,  $\beta_{10} = 30$  degrees,  $\Delta\beta_{10} = 25$  degrees, and  $\Delta\beta_{20} = 25$  degrees, as shown in Figure 41.

4. Comparisons Among Three Formulations. Comparisons among the above three formulations with the influences of errors in transit times indicate that the power-law wind profile gives the greatest range of acceptable wind directions  $\Delta\phi_{acp}$ .

The constant wind profile gives the second widest range of  $\Delta\phi_{acp}$ , while the linear wind profile gives only a  $\Delta\phi_{acp} = 20$  degrees. A large fan azimuth angle,  $\Delta\beta_{11}$ , gives better results when errors in transit time exist.

Each wind profile has its own advantages and disadvantages. This paper has perhaps clouded the disadvantages of the power-law profile because the power-law profile was used both as the standard in calculations and used as an assumption for formulating the wind direction.

## V. CONCLUSIONS

The transit height, transit distance, and wind direction have been formulated for multiple cross-beam systems and are summarized in this section. To calculate the wind direction, it was necessary to assume a wind profile. Three such profiles were employed to obtain three formulations for wind direction (constant, linear, and power-law wind profiles). The performance of these three wind direction formulations was examined by assuming that the atmospheric wind profile follows the power-law (Eq. 10). The effect of the transit time resolution on the performance was also taken into consideration. The results suggest that the vertical plane of the single beam and the optical axis of the fan should be parallel, and that the azimuth angle between the beams of the fan should not be made too small (about 25 degrees). The order of choice for assumptions on wind profile is:

1. Power-law profile
2. Constant wind profile
3. Linear wind profile.

A combination of these methods with a comparison of those results and employing a fan with more than 3 beams could be used to obtain better results. A field test program is needed to establish which wind direction assumption or assumptions are best for the wind direction measurements.

### A. Listing of Basic Formulation

The geometry for the following formulas is shown in Figure 3.

1. Transit Height

$$H_i = \frac{b \sin \phi}{\cot \alpha_{1i} \sin(\phi + \beta_{1i}) + \cot \alpha_2 \sin(\phi + \beta_2)} \quad (4)$$

2. Transit Distance

$$D_i = \frac{H_i}{\sin \phi} [\cot \alpha_{1i} \sin \beta_{1i} + \cot \alpha_2 \sin \beta_2] \quad (8)$$

3. Wind Speed

$$V_i = \frac{D_i}{\tau_i} \quad (9)$$

4. Wind Direction

a. Constant wind profile

$$\phi = \text{arc cot} \left[ (-) \frac{P_{2c} - \left(\frac{\tau_2}{\tau_1}\right) P_{1c}}{Q_{2c} - \left(\frac{\tau_2}{\tau_1}\right) Q_{1c}} \right] \quad (12)$$

where  $P_{ic}$  and  $Q_{ic}$  are geometric constants, see (12a)

b. Linear wind profile

$$\phi = \text{arc cot} \left[ (-) \frac{\sum_{i=1}^3 \frac{P_{i\ell}}{\tau_i}}{\sum_{i=1}^3 \frac{Q_{i\ell}}{\tau_i}} \right] \quad (14)$$

where  $P_{i\ell}$  and  $Q_{i\ell}$  are geometric constants, see (14a).

c. Power-law profile

$$\frac{\tau_2}{\tau_1} \cdot \frac{H_1}{H_2} \cdot \frac{(\cot \alpha_{11} \sin \beta_{11} + \cot \alpha_2 \sin \beta_2)}{(\cot \alpha_{12} \sin \beta_{12} + \cot \alpha_2 \sin \beta_2)} - \left(\frac{H_1}{H_2}\right)^\rho = 0,$$

where

$$\frac{H_1}{H_2} = \frac{\cot \alpha_{12} \sin(\phi + \beta_{12}) + \cot \alpha_2 \sin(\phi + \beta_2)}{\cot \alpha_{11} \sin(\phi + \beta_{11}) + \cot \alpha_2 \sin(\phi + \beta_2)} \quad (17)$$

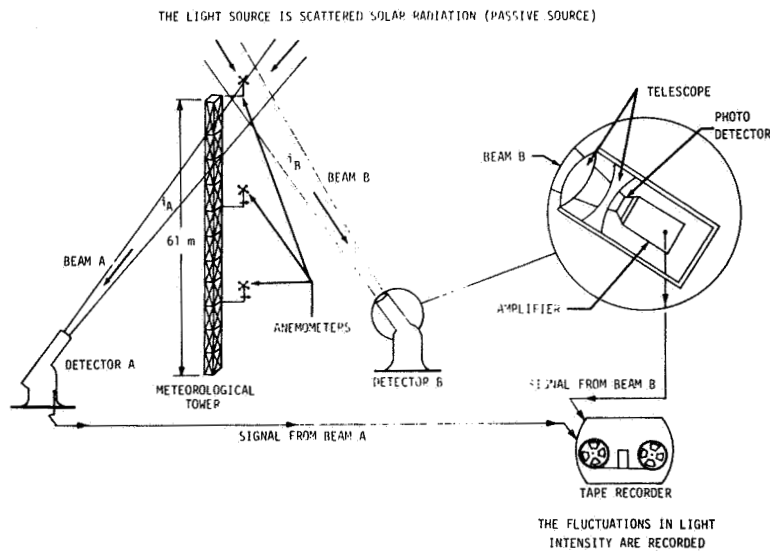


FIGURE 1. CROSS-BEAM DETECTION SYSTEM

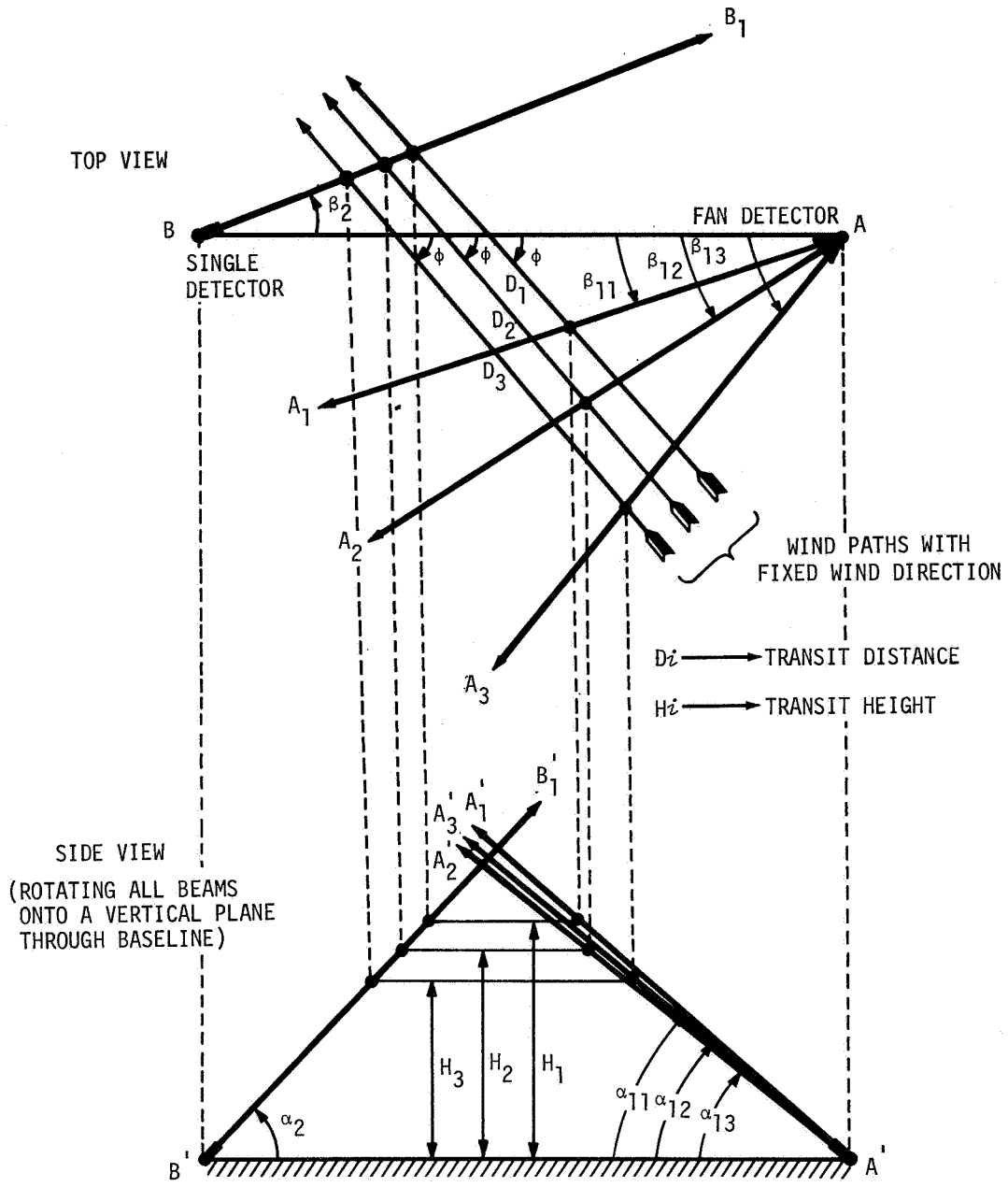


FIGURE 2. THE MULTIPLE-BEAM CROSS-BEAM SETUP CONFIGURATION

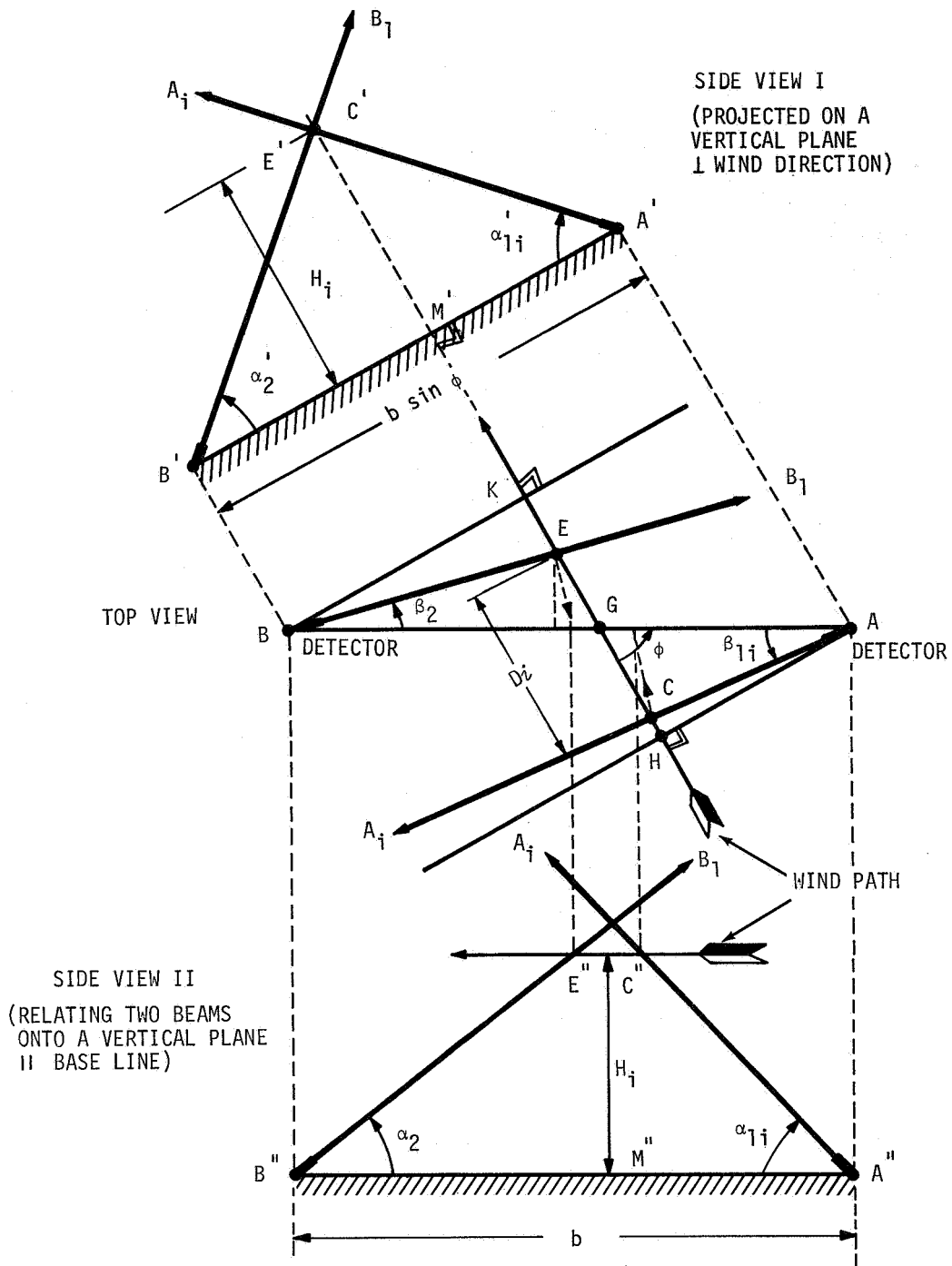


FIGURE 3. CROSS-BEAM GEOMETRY

$$V_i = V_0 \left( \frac{H_i}{H_0} \right)^\rho$$

$$\left\{ \begin{array}{l} \rho = 0.2 \\ V_0 = 10 \text{ m/sec} \\ H_0 = 3 \text{ m} \end{array} \right.$$

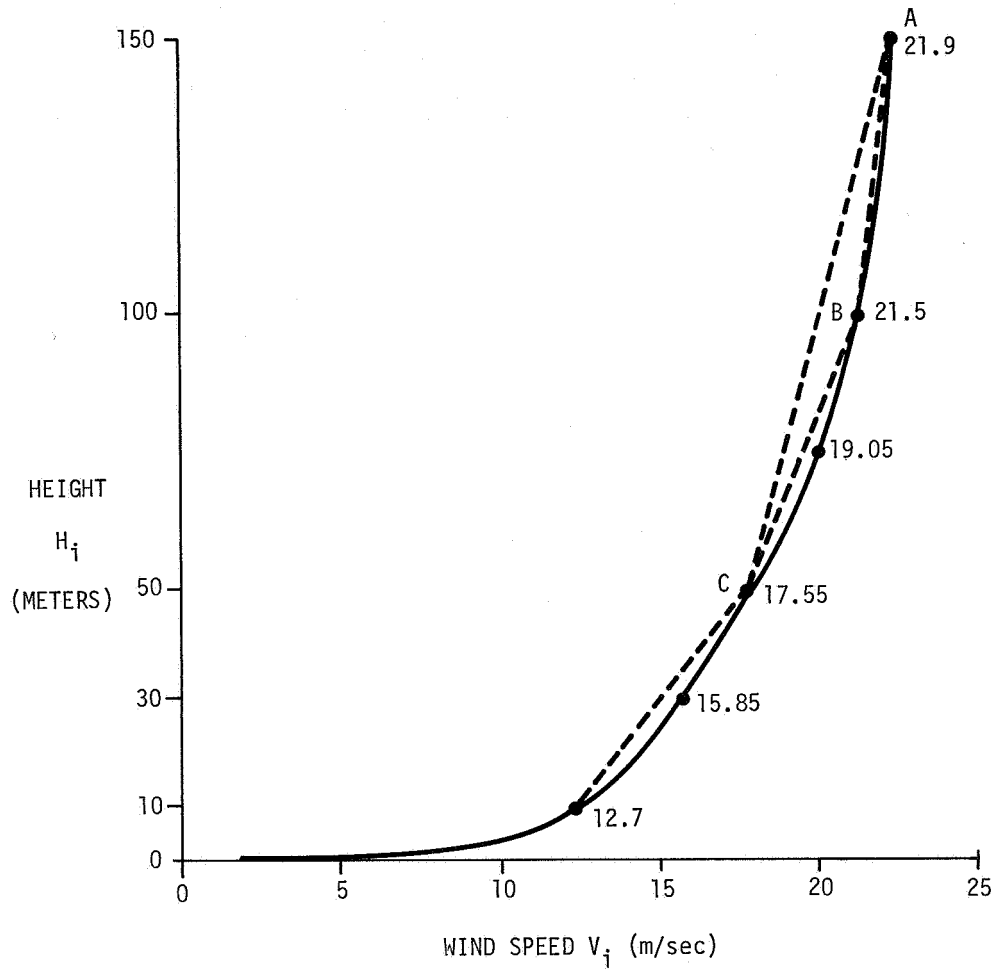


FIGURE 4. SURFACE WIND PROFILE

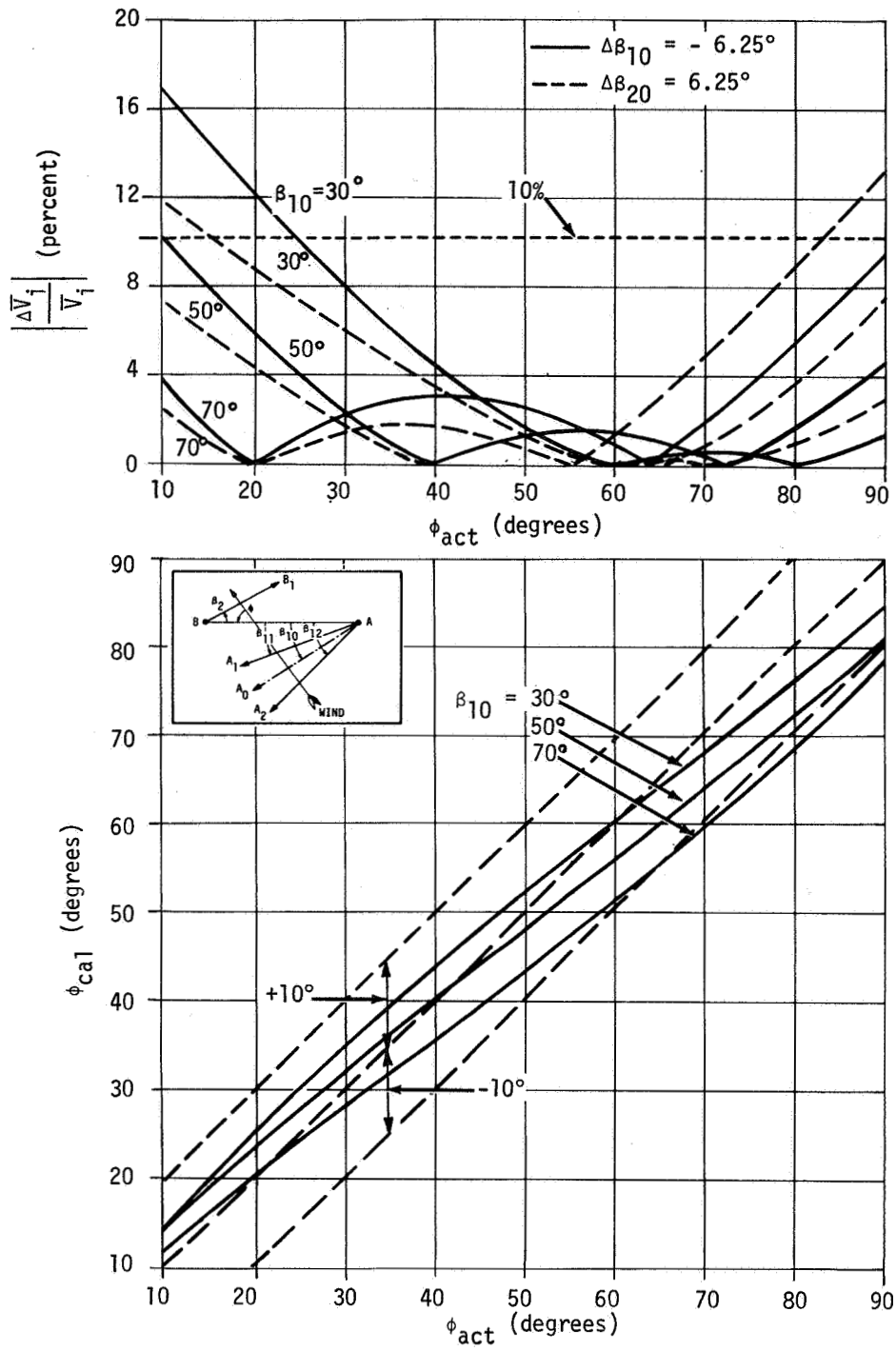


FIGURE 5. CONSTANT WIND PROFILE ( $\Delta\beta_{10} = -6.25^\circ$ ,  $\Delta\beta_{20} = 6.25^\circ$ ,  $\beta_2 = 0^\circ$  and  $\epsilon = 0$ )

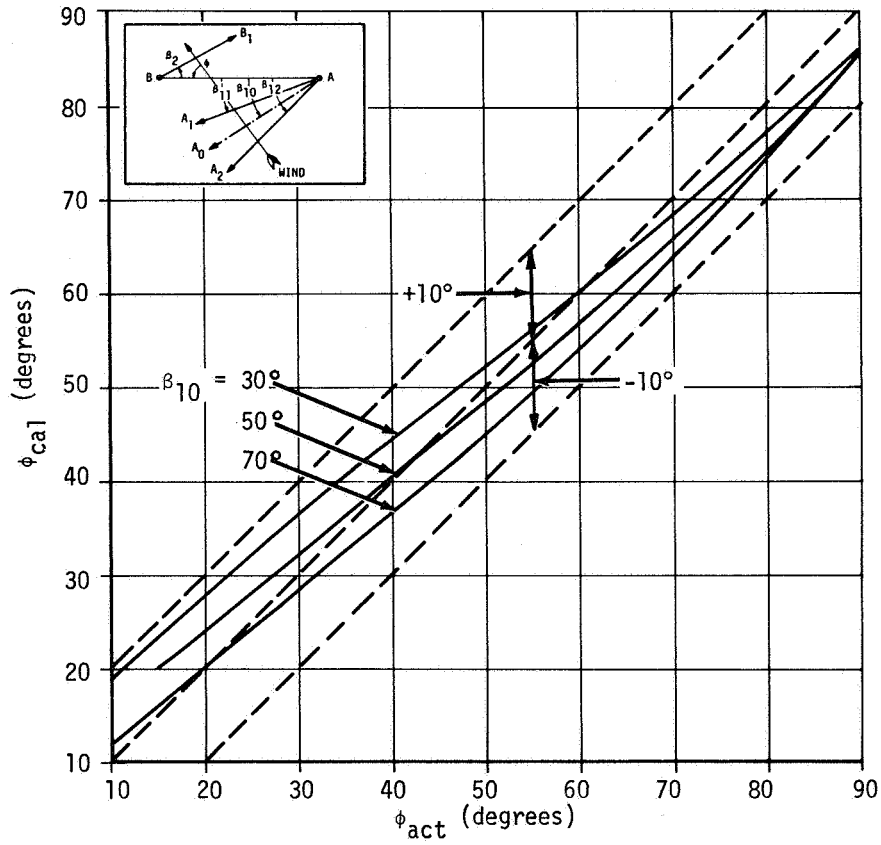
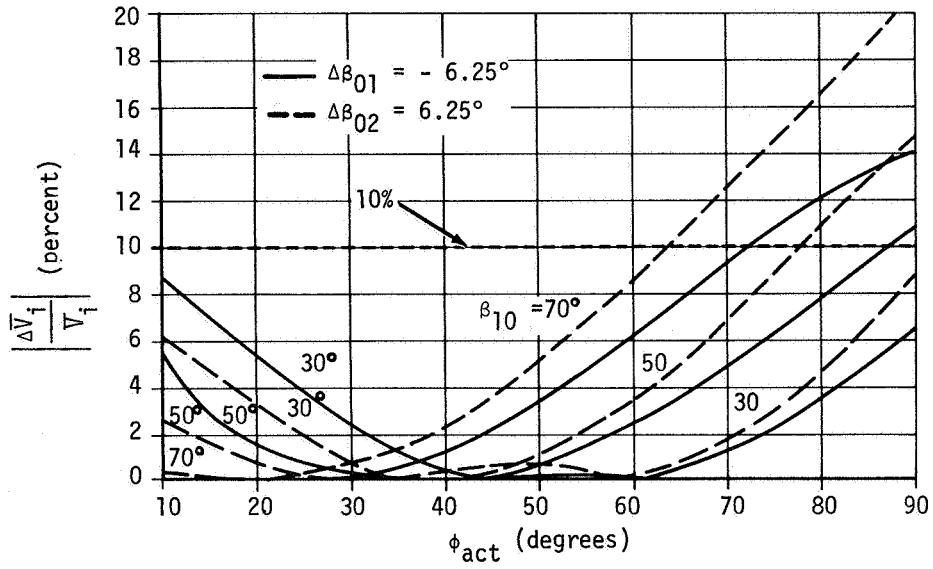


FIGURE 6. CONSTANT WIND PROFILE ( $\Delta\beta_{10} = -6.25^\circ$ ,  $\Delta\beta_{20} = 6.25^\circ$ ,  $\beta_2 = 20^\circ$  and  $\epsilon = 0$ )

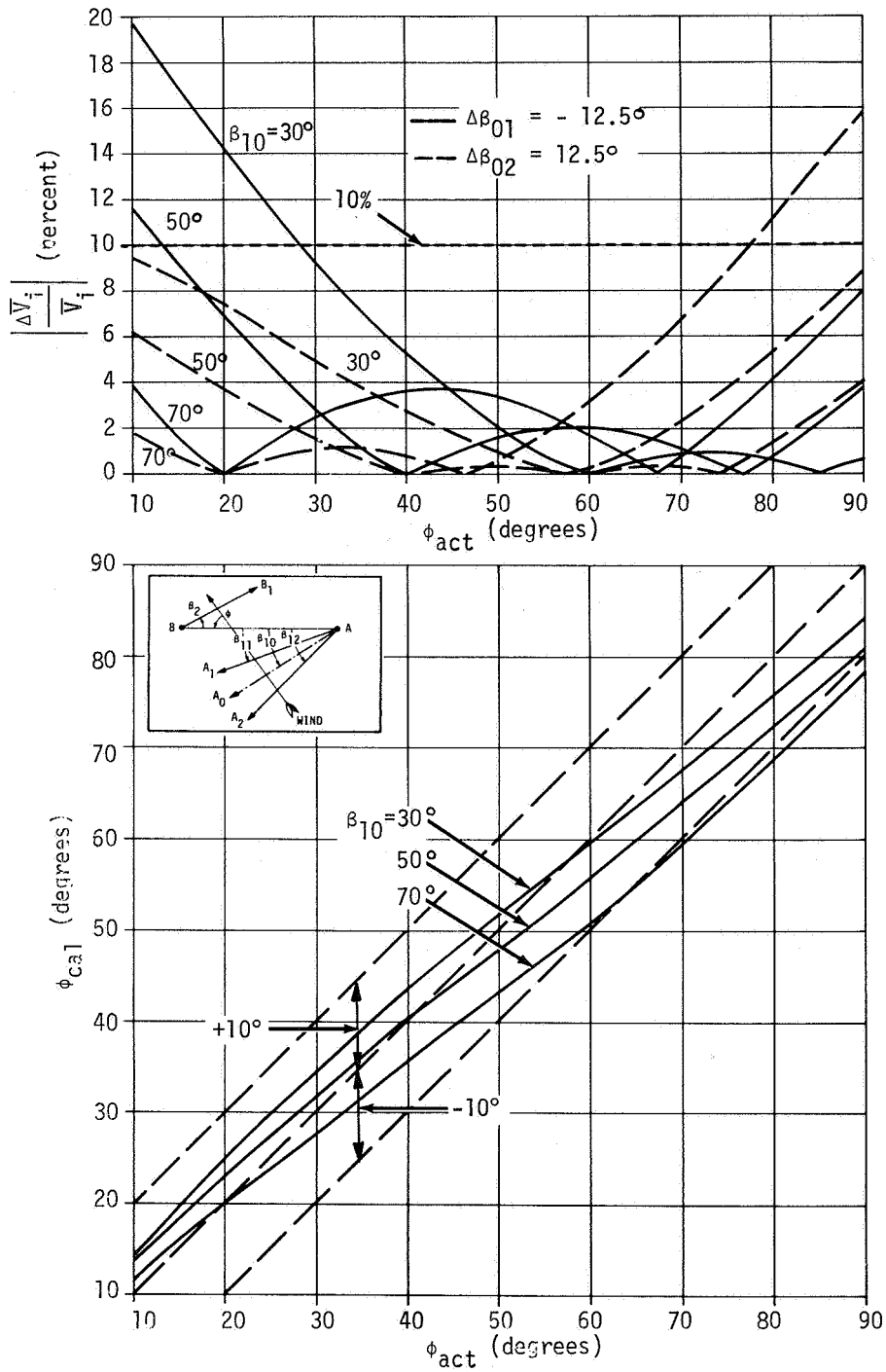


FIGURE 7. CONSTANT WIND PROFILE ( $\Delta\beta_{10} = -12.5^\circ$ ,  $\Delta\beta_{20} = 12.5^\circ$ ,  $\beta_2 = 0^\circ$  and  $\epsilon = 0$ )

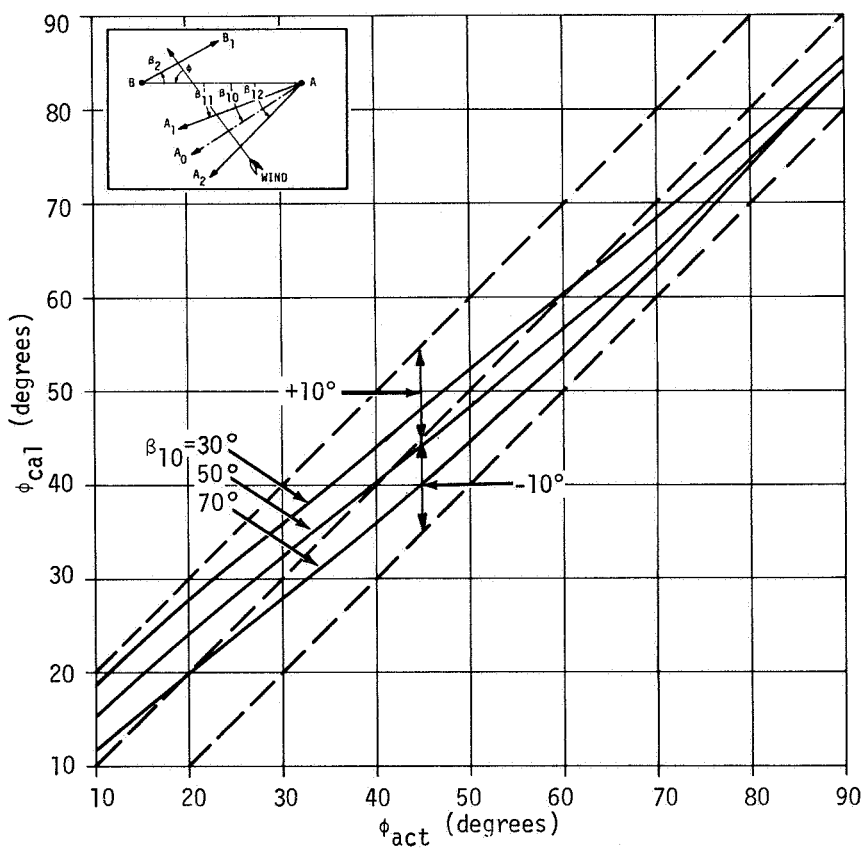
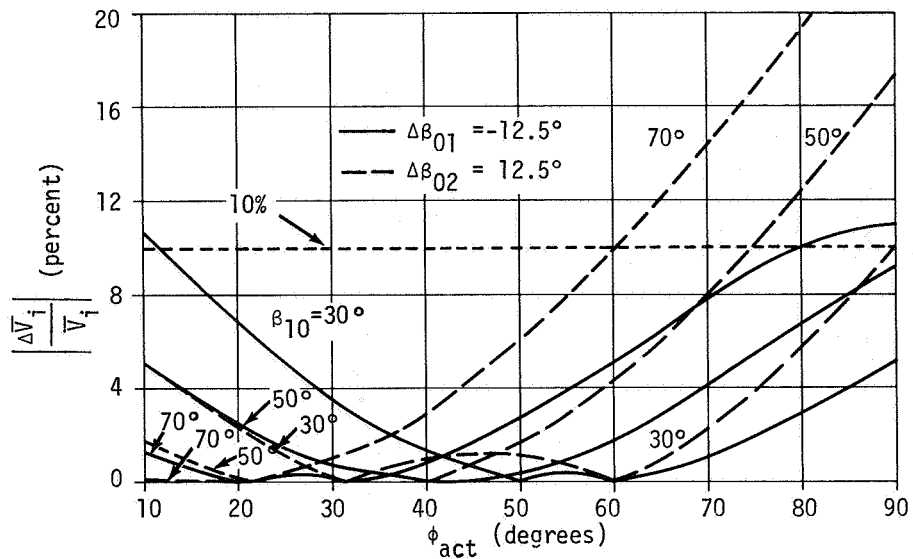


FIGURE 8. CONSTANT WIND PROFILE ( $\Delta\beta_{10} = -12.5^\circ$ ,  $\Delta\beta_{20} = 12.5^\circ$ ,  $\beta_2 = 20^\circ$  and  $\epsilon = 0$ )

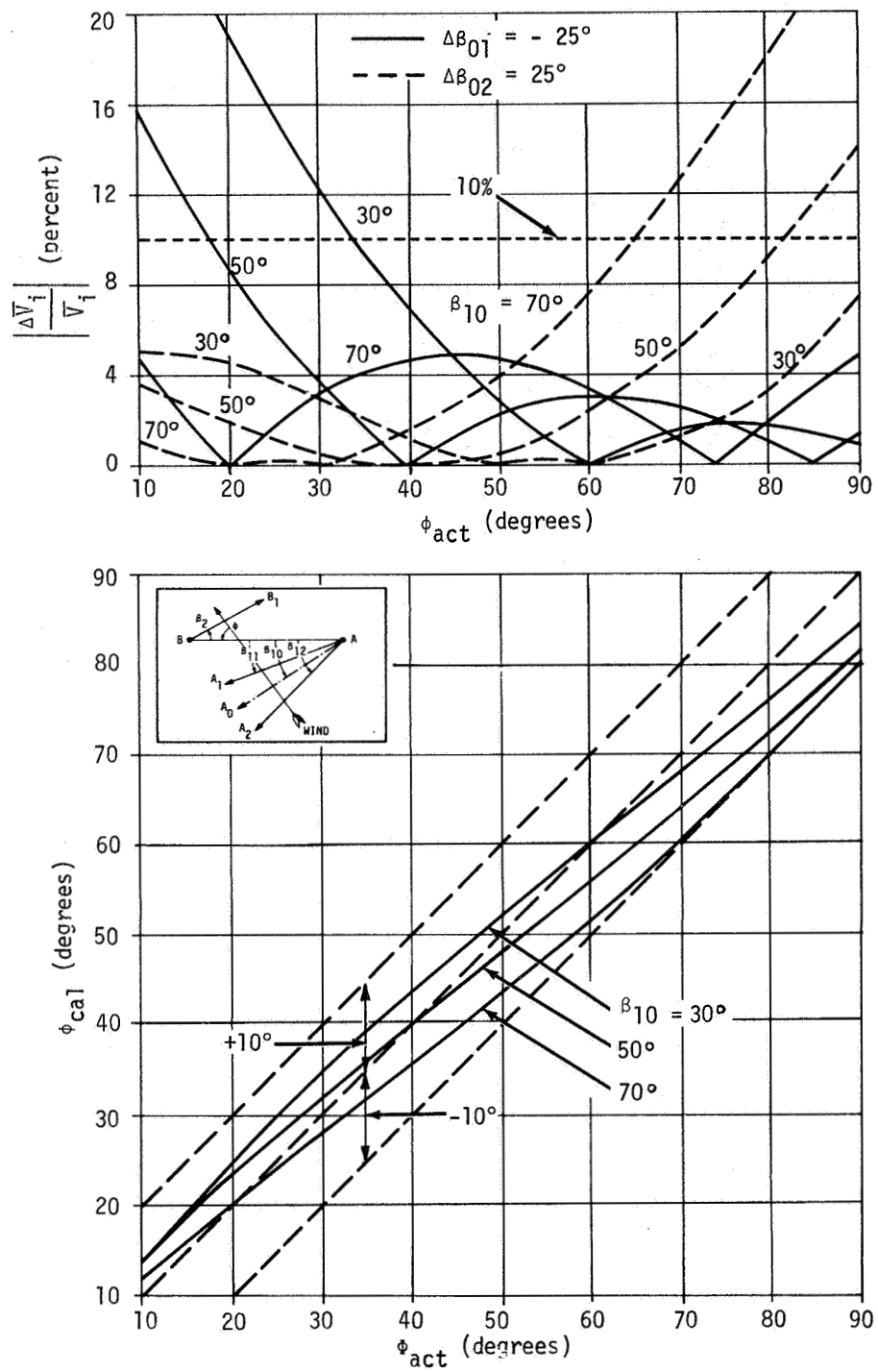


FIGURE 9. CONSTANT WIND PROFILE ( $\Delta\beta_{10} = -25^\circ$ ,  $\Delta\beta_{20} = 25^\circ$ ,  $\beta_2 = 0^\circ$  and  $\epsilon = 0$ )

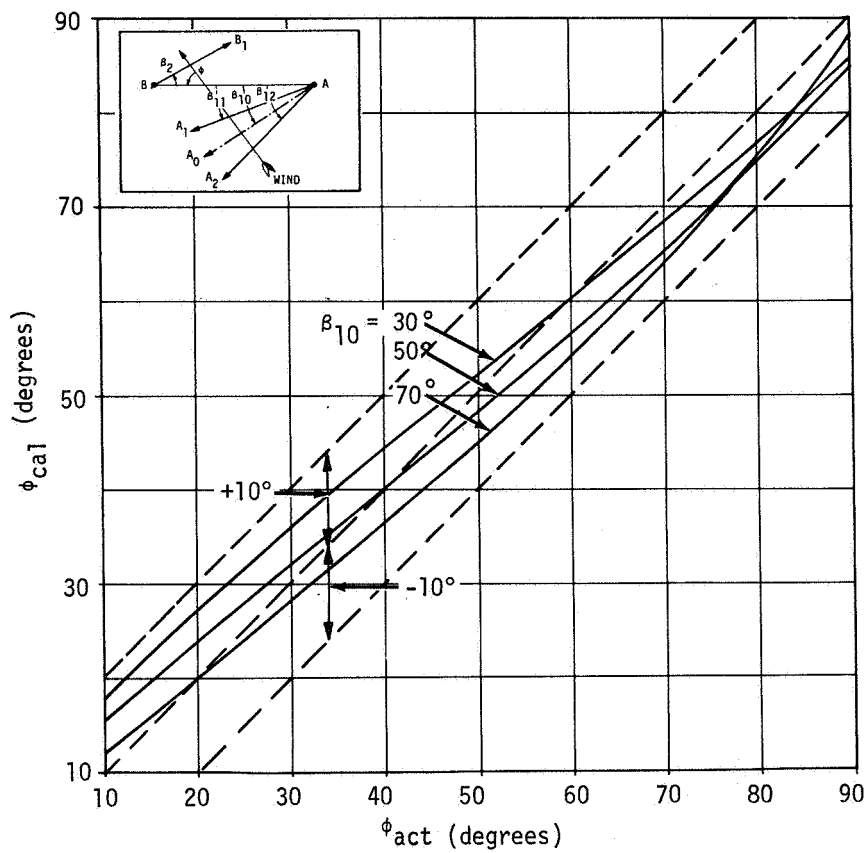
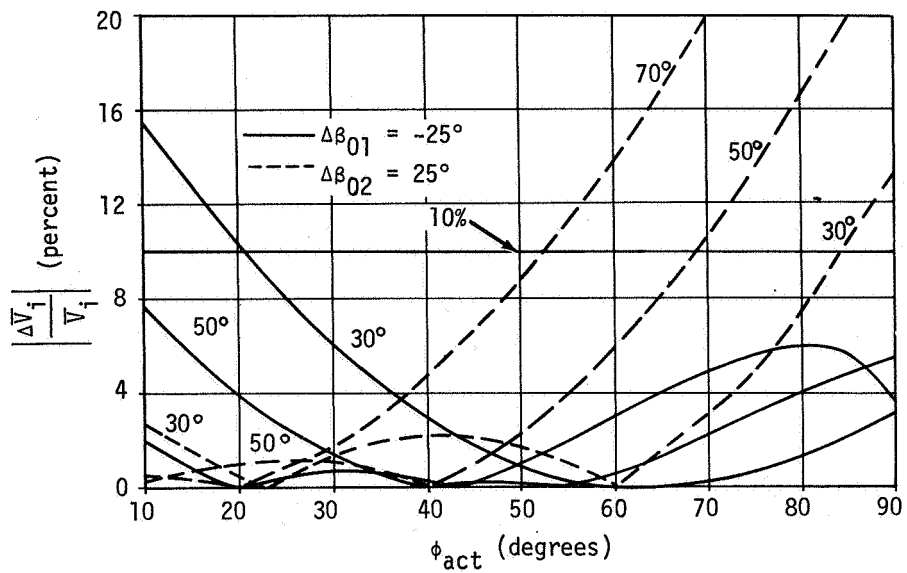


FIGURE 10. CONSTANT WIND PROFILE ( $\Delta\beta_{10} = -25^\circ$ ,  $\Delta\beta_{20} = 25^\circ$ ,  $\beta_2 = 20^\circ$  and  $\epsilon = 0$ )

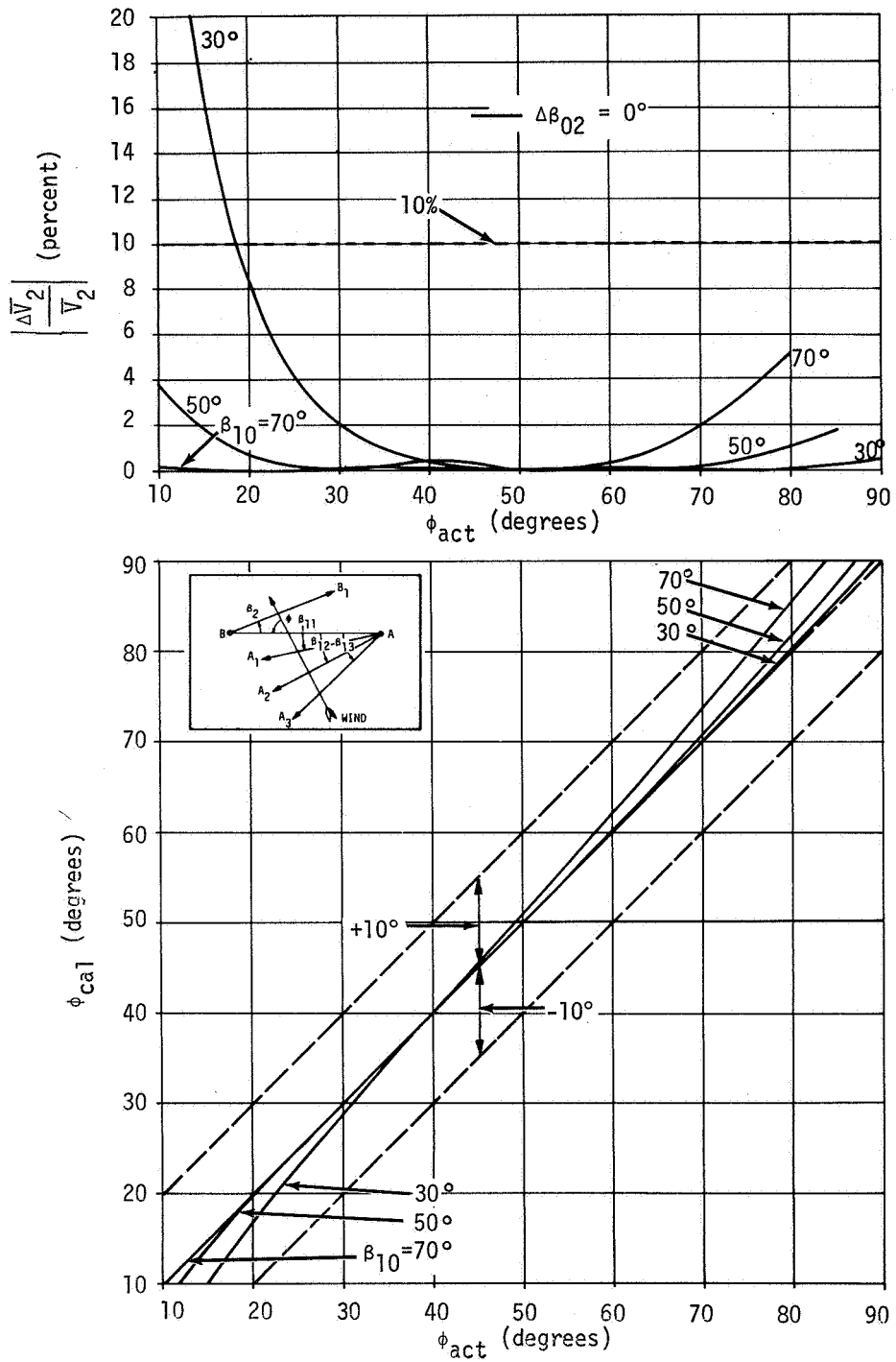


FIGURE 11. LINEAR WIND PROFILE ( $\Delta\beta_{10} = -6.25^\circ$ ,  $\Delta\beta_{20} = 0^\circ$ ,  $\Delta\beta_{30} = 6.25^\circ$ ,  $\beta_2 = 0^\circ$  and  $\epsilon = 0$ )

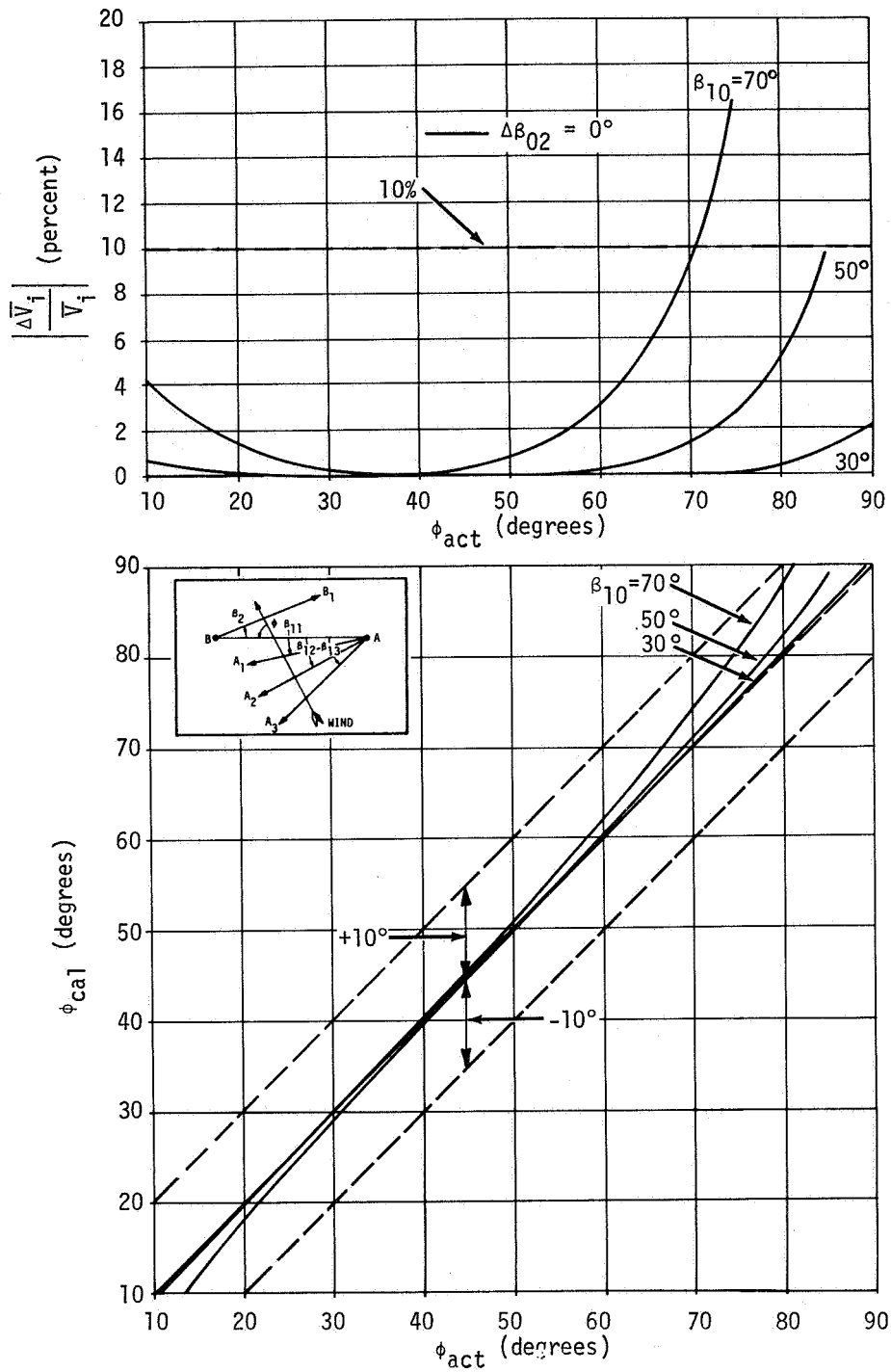


FIGURE 12. LINEAR WIND PROFILE ( $\Delta\beta_{10} = -6.25^\circ$ ,  $\Delta\beta_{20} = 0^\circ$ ,  $\Delta\beta_{30} = 6.25^\circ$ ,  $\beta_2 = 20^\circ$  and  $\epsilon = 0$ )

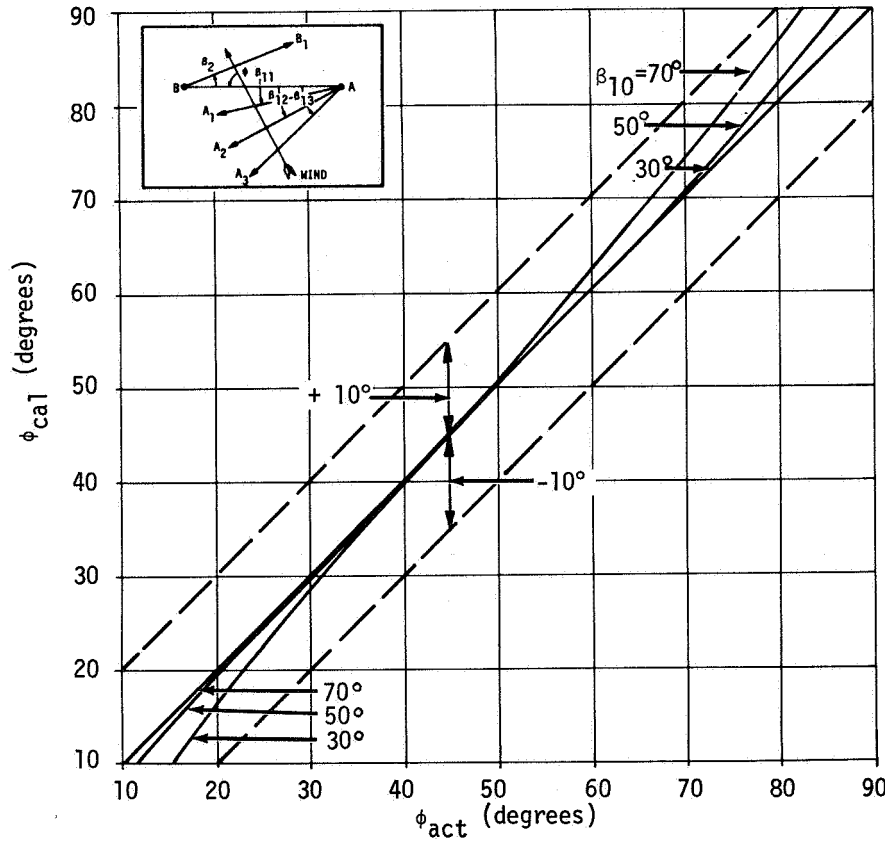
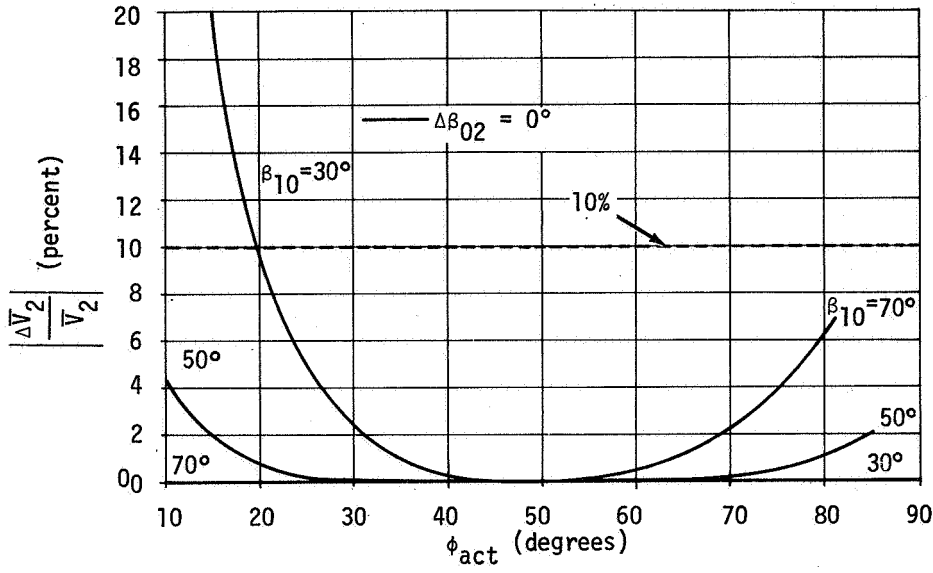


FIGURE 13. LINEAR WIND PROFILE ( $\Delta\beta_{10} = -12.5^\circ$ ,  $\Delta\beta_{20} = 0^\circ$ ,  $\Delta\beta_{30} = 12.5^\circ$ ,  $\beta_2 = 0^\circ$  and  $\epsilon = 0$ )

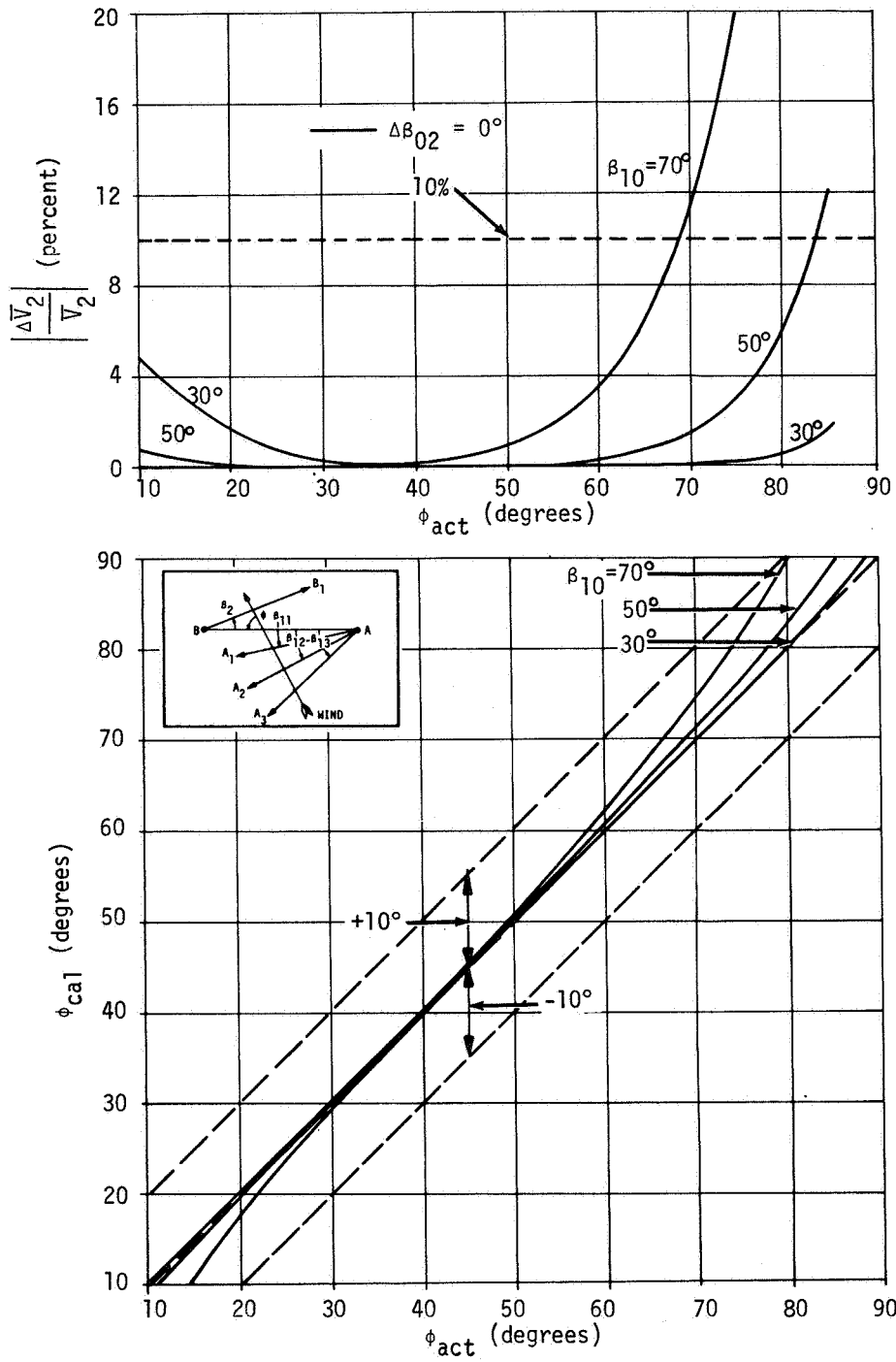


FIGURE 14. LINEAR WIND PROFILE ( $\Delta\beta_{10} = -12.5^\circ$ ,  $\Delta\beta_{20} = 0^\circ$ ,  $\Delta\beta_{30} = 12.5^\circ$ ,  $\beta_2 = 20^\circ$  and  $\epsilon = 0$ )

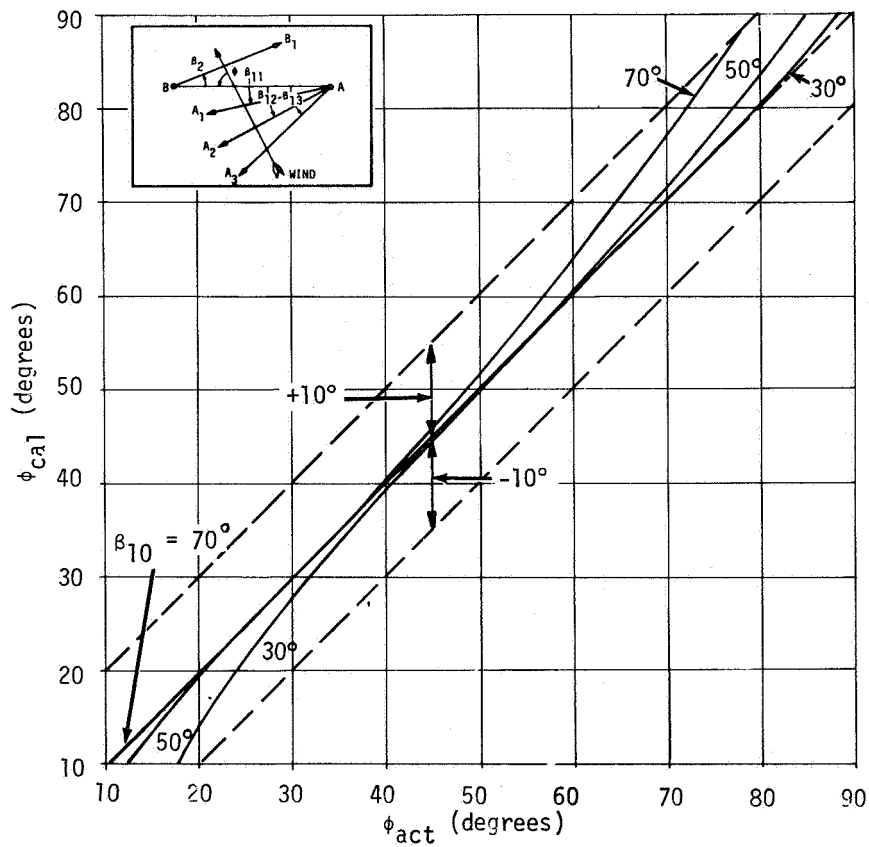
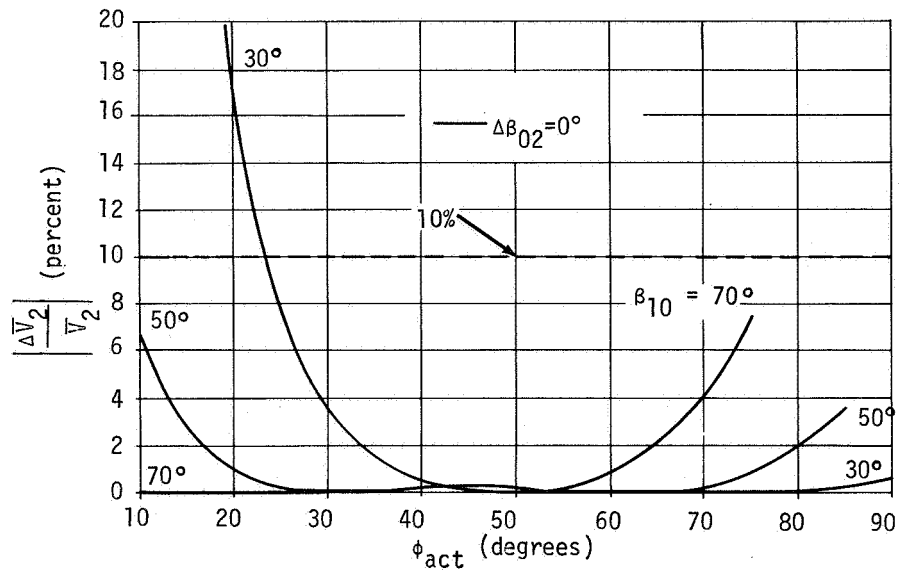


FIGURE 15. LINEAR WIND PROFILE ( $\Delta\beta_{10} = -25^\circ, \Delta\beta_{20} = 0^\circ, \Delta\beta_{30} = 25^\circ, \beta_2 = 0^\circ$  and  $\epsilon = 0$ )

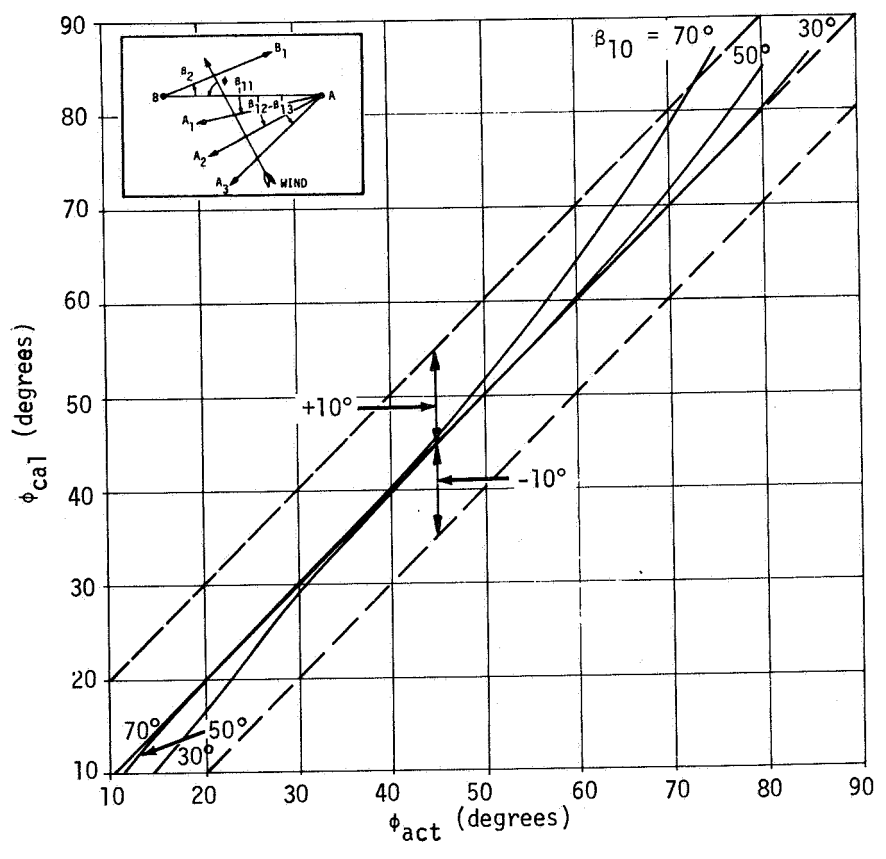
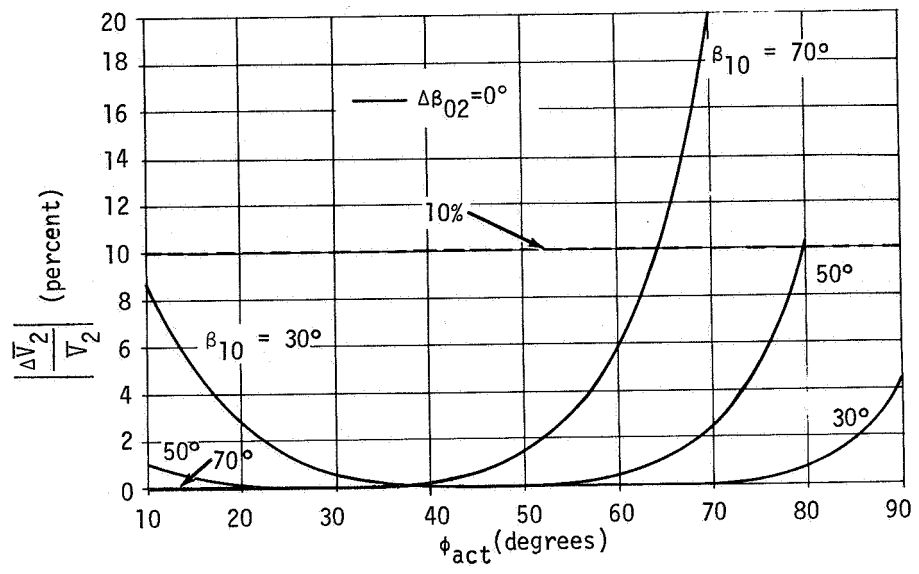


FIGURE 16. LINEAR WIND PROFILE ( $\Delta\beta_{10} = -25^\circ$ ,  $\Delta\beta_{20} = 0^\circ$ ,  $\Delta\beta_{30} = 25^\circ$ ,  $\beta_2 = 20^\circ$  and  $\epsilon = 0$ )

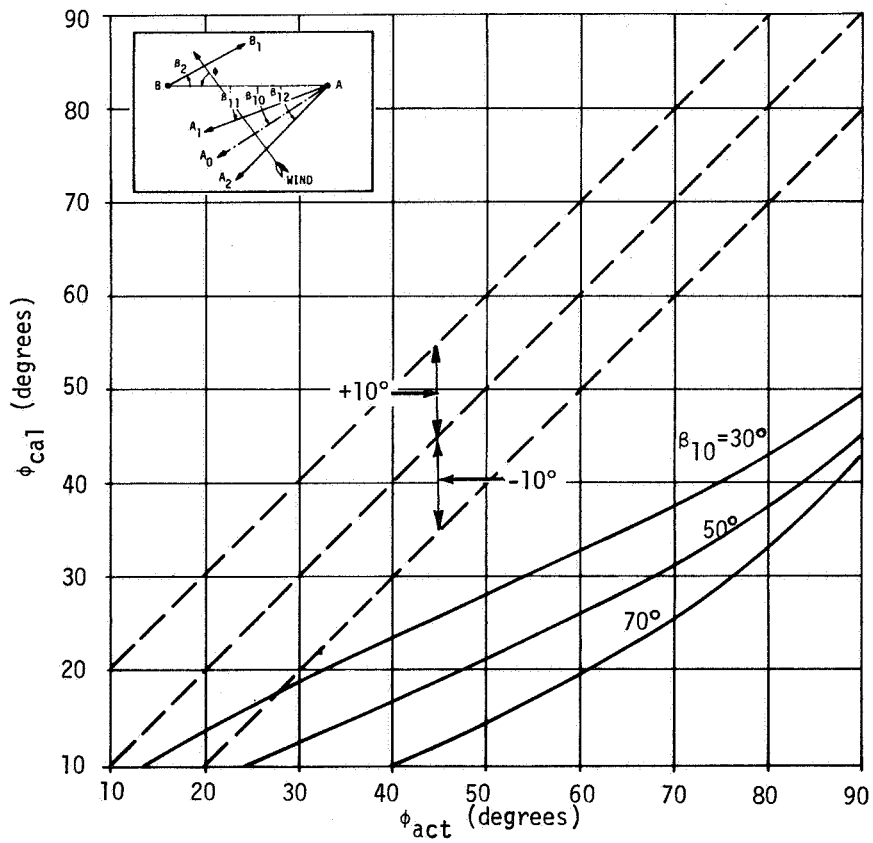
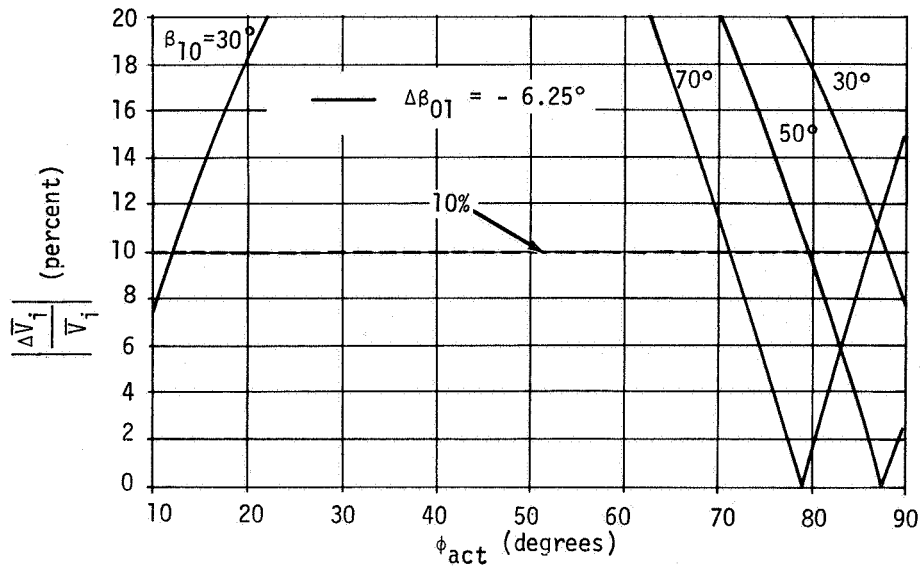


FIGURE 17. CONSTANT WIND PROFILE ( $\Delta\beta_{10} = -6.25^\circ$ ,  $\Delta\beta_{20} = 6.25^\circ$ ,  $\beta_2 = 0^\circ$ , and  $\epsilon = 5\%$ )

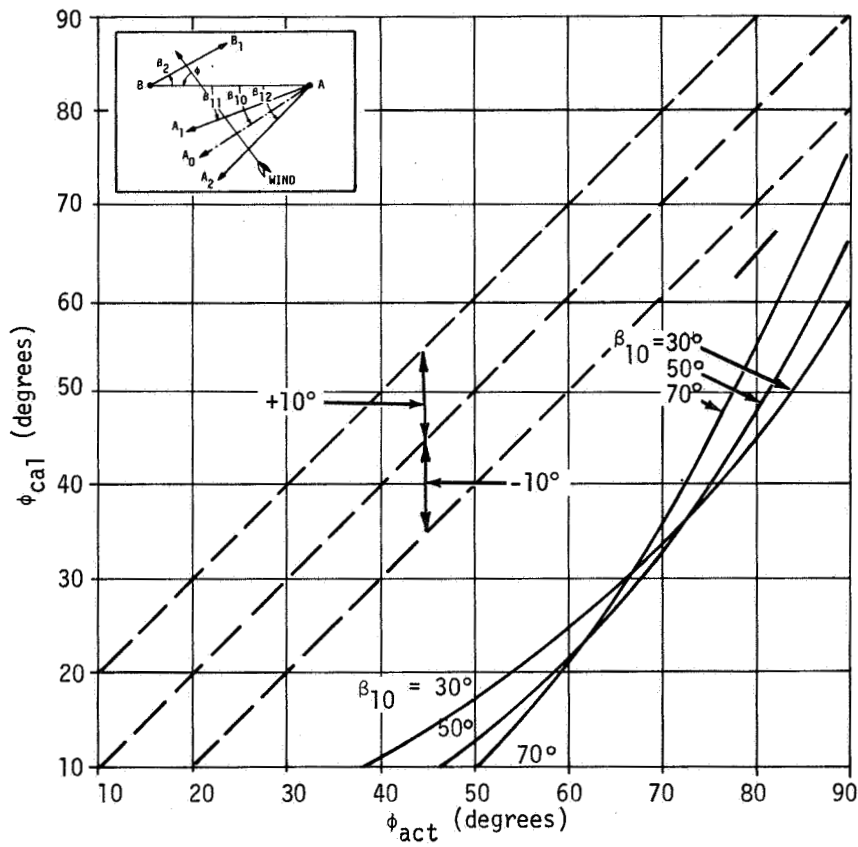
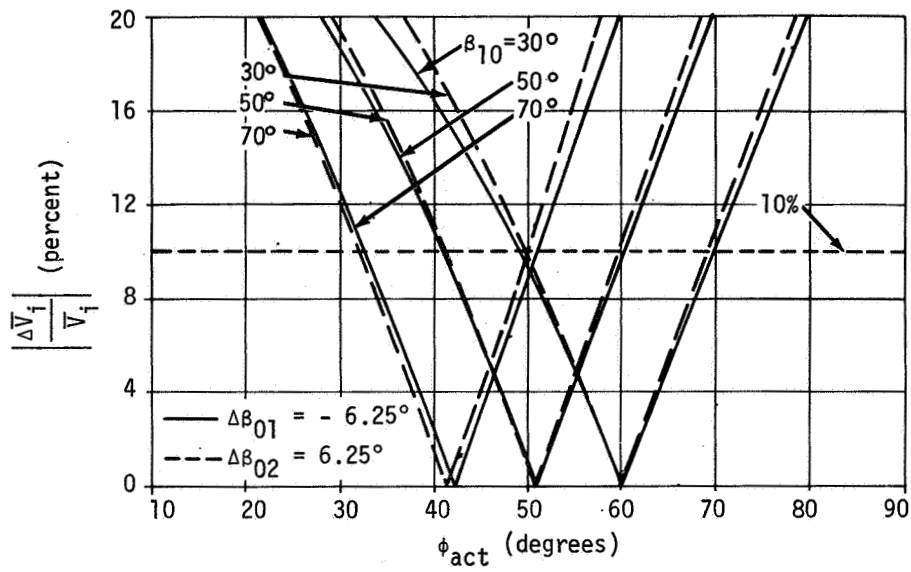


FIGURE 18. CONSTANT WIND PROFILE ( $\Delta\beta_{10} = -6.25$ ,  $\Delta\beta_{20} = 6.25$ ,  $\beta_2 = 20^\circ$ , and  $\epsilon = 5\%$ )

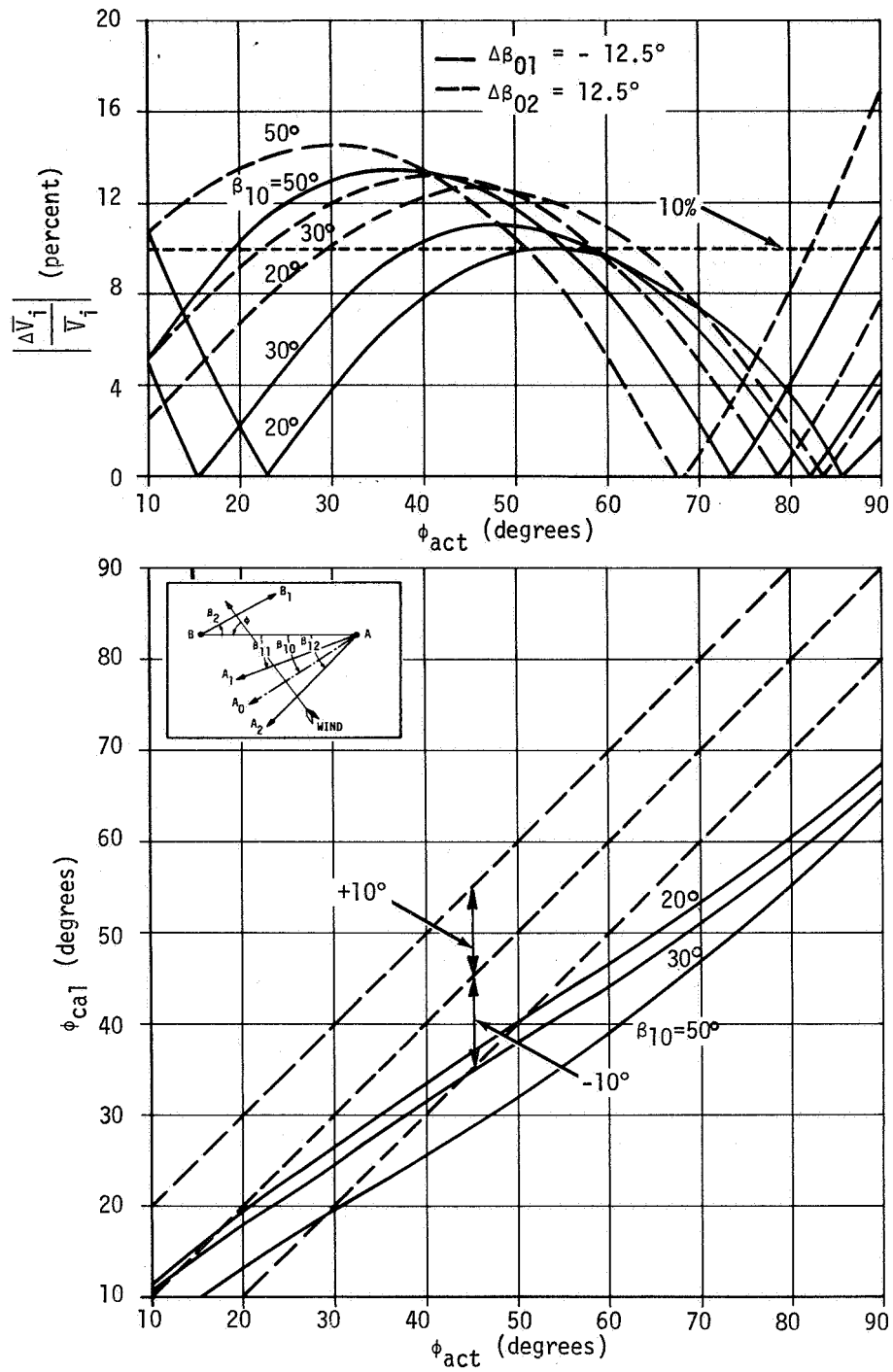


FIGURE 19. CONSTANT WIND PROFILE ( $\Delta\beta_{10} = -12.5^\circ$ ,  $\Delta\beta_{20} = 12.5^\circ$ ,  $\beta_2 = 10^\circ$ , and  $\epsilon = 5\%$ )

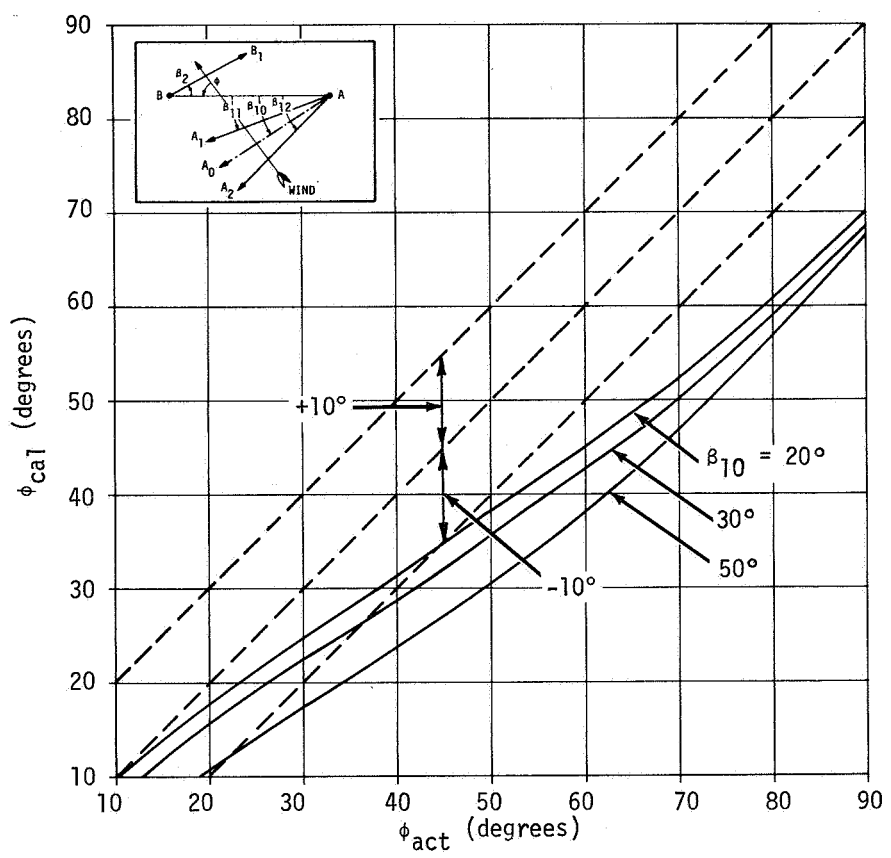
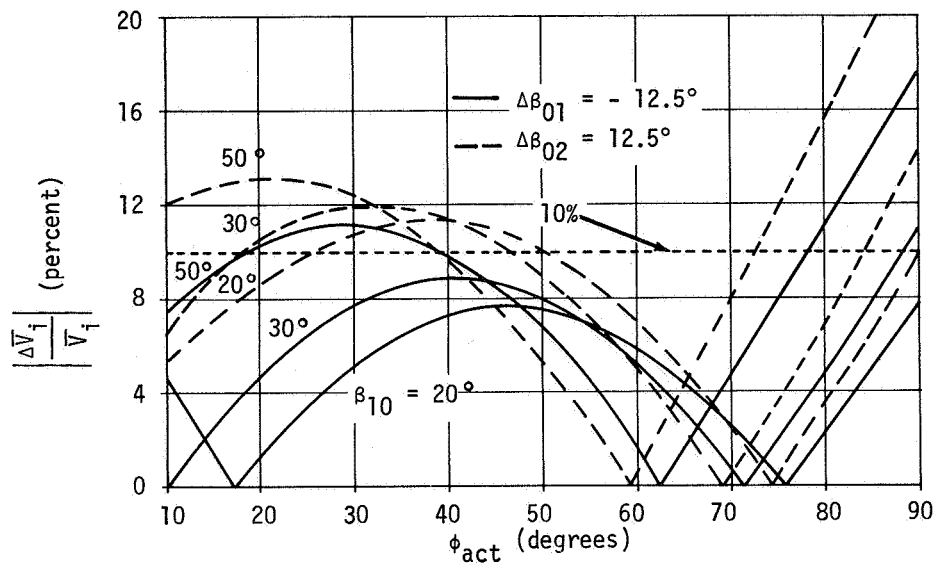


FIGURE 20. CONSTANT WIND PROFILE ( $\Delta\beta_{10} = -12.5^\circ$ ,  $\Delta\beta_{20} = 12.5^\circ$ ,  $\beta_2 = 30^\circ$ , and  $\epsilon = 5\%$ )

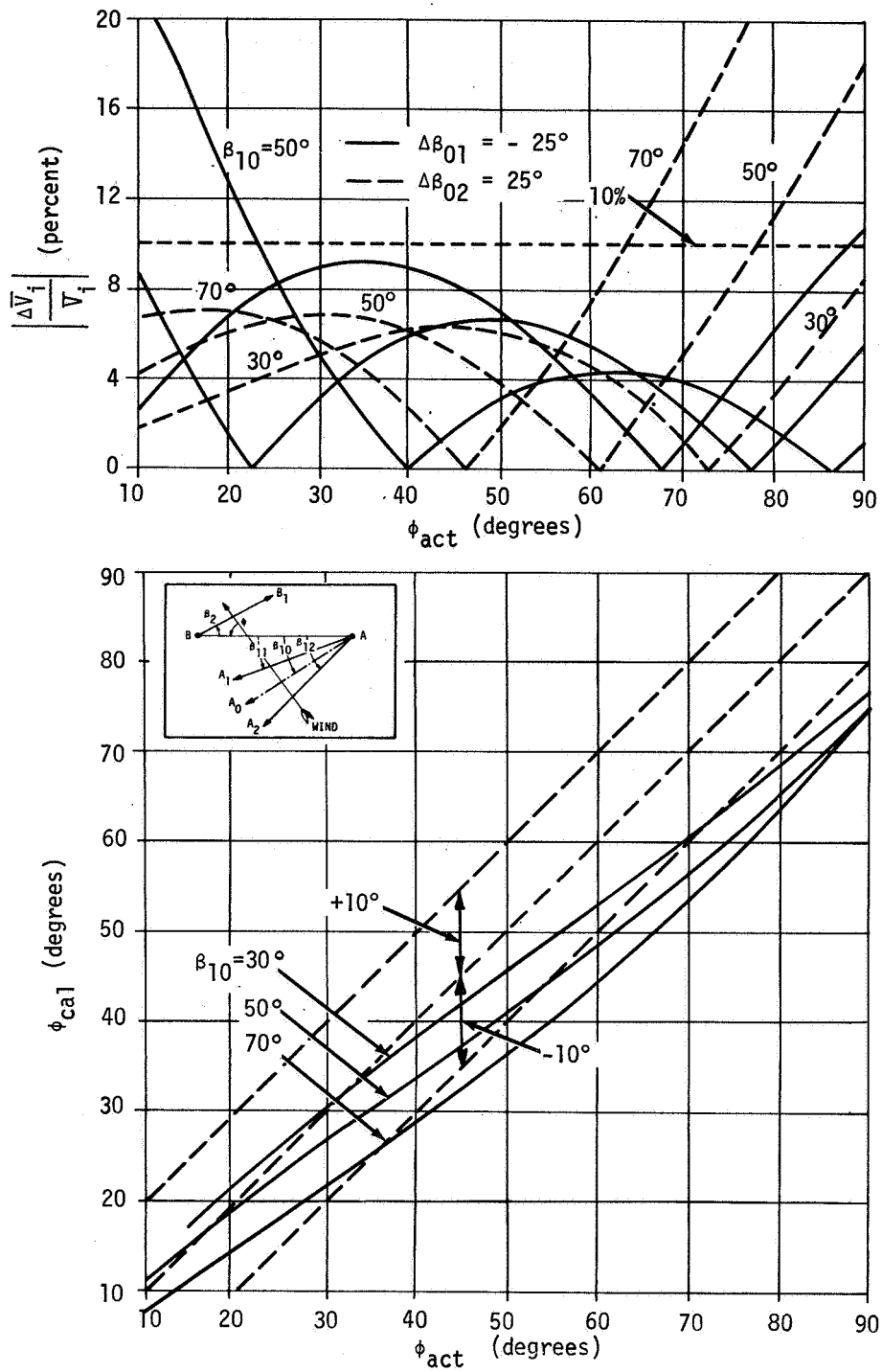


FIGURE 21. CONSTANT WIND PROFILE ( $\Delta\beta_{10} = -25^\circ$ ,  $\Delta\beta_{20} = 25^\circ$ ,  $\beta_2 = 0^\circ$ , and  $\epsilon = 5\%$ )

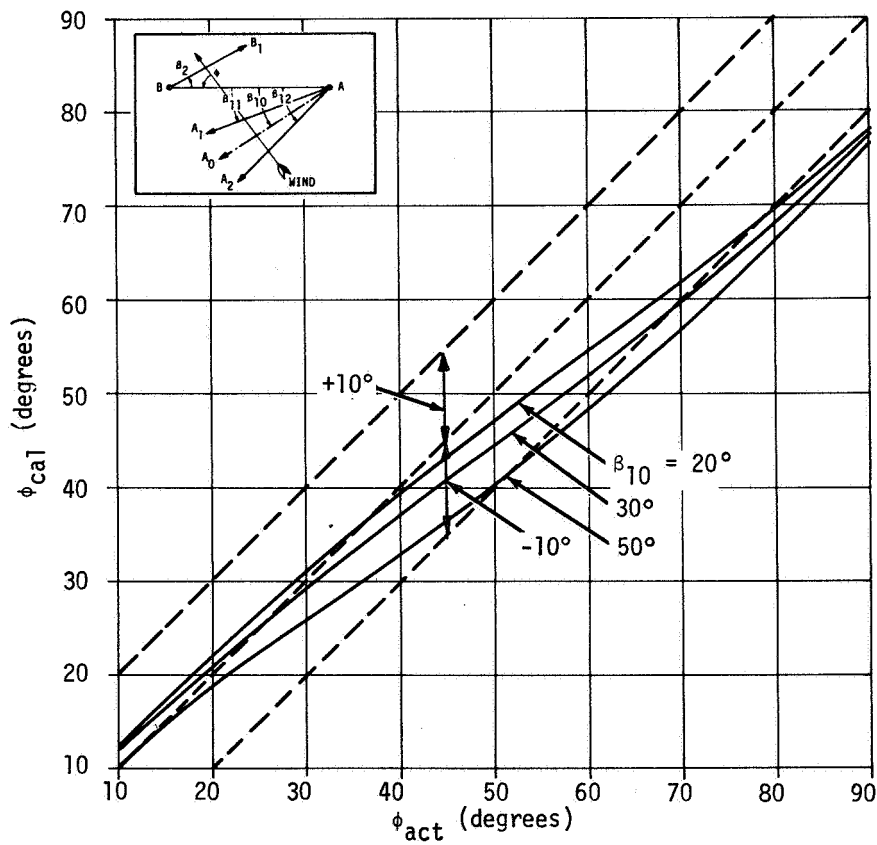
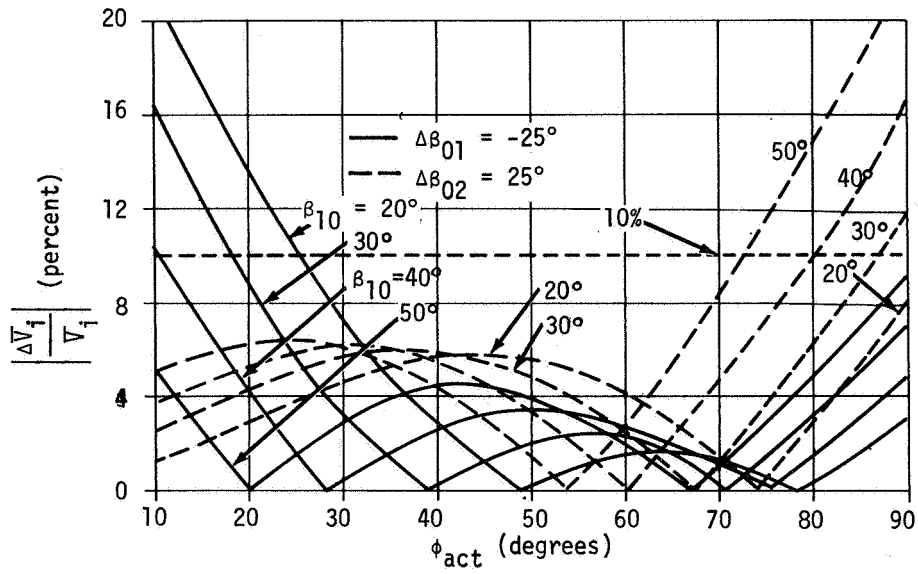


FIGURE 22. CONSTANT WIND PROFILE ( $\Delta\beta_{10} = -25^\circ$ ,  $\Delta\beta_{20} = 25^\circ$ ,  $\beta_2 = 20^\circ$ , and  $\epsilon = 5\%$ )

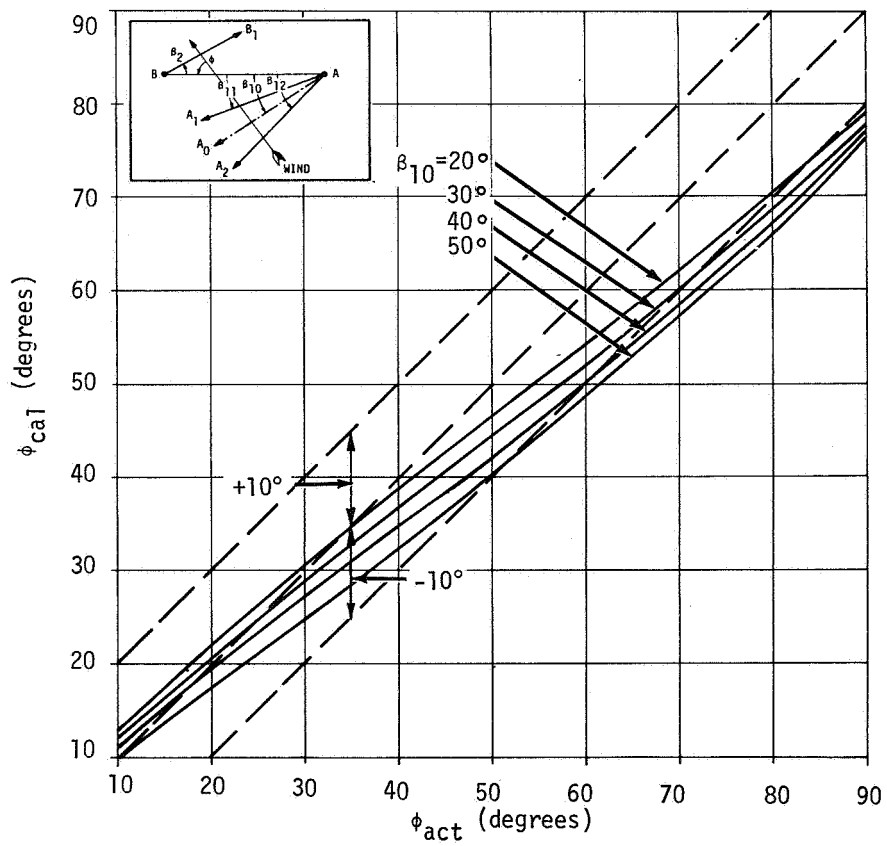
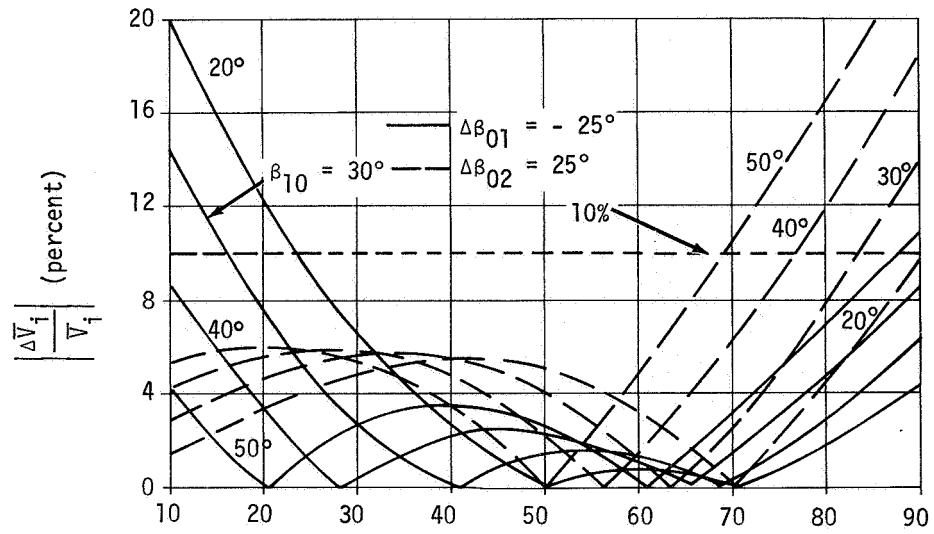


FIGURE 23. CONSTANT WIND PROFILE ( $\Delta\beta_{10} = -25^\circ$ ,  $\Delta\beta_{20} = 25^\circ$ ,  $\beta_2 = 30^\circ$ , and  $\epsilon = 5\%$ )

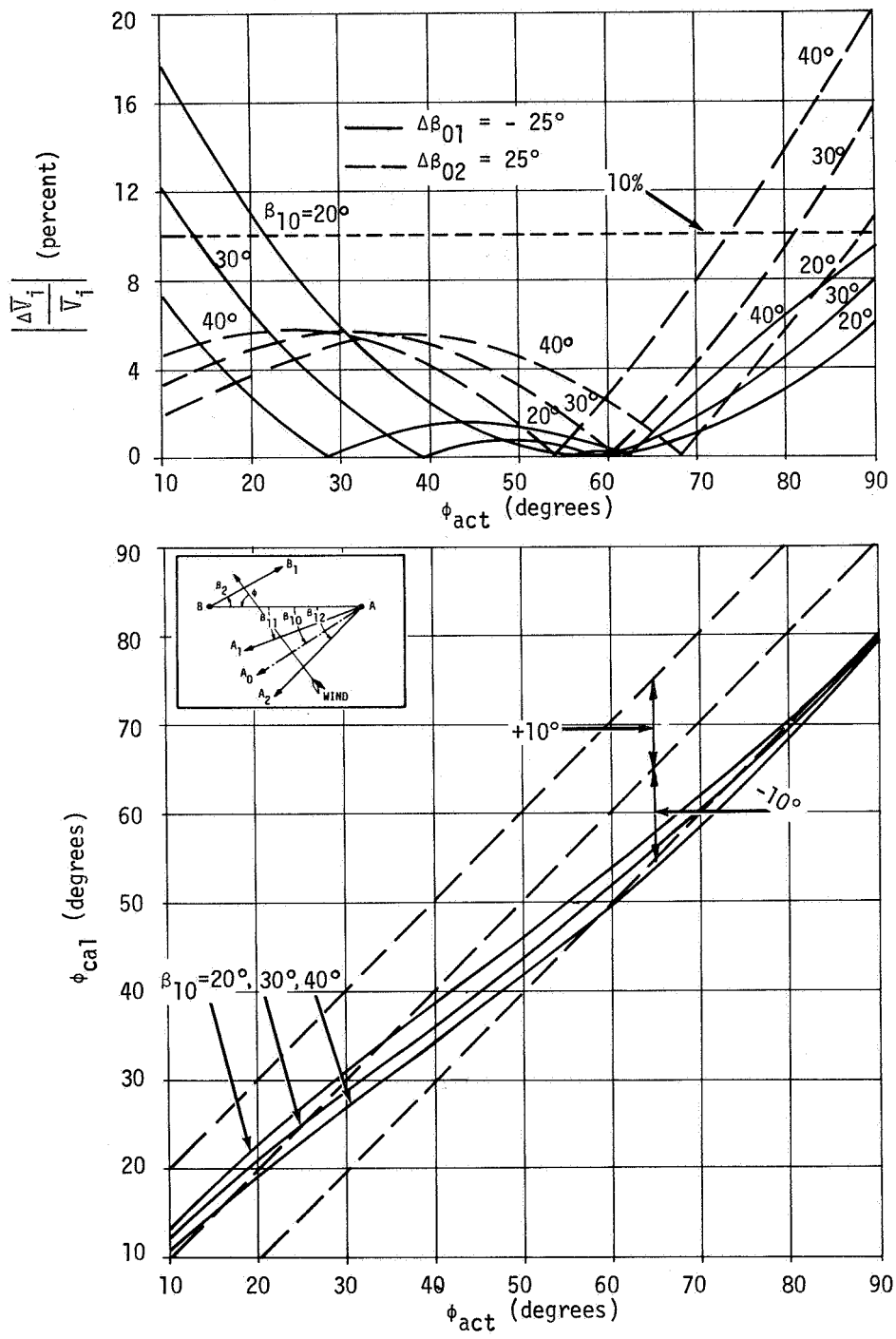


FIGURE 24. CONSTANT WIND PROFILE ( $\Delta\beta_{10} = -25^\circ$ ,  $\Delta\beta_{20} = 25^\circ$ ,  $\beta_2 = 40^\circ$ , and  $\epsilon = 5\%$ )

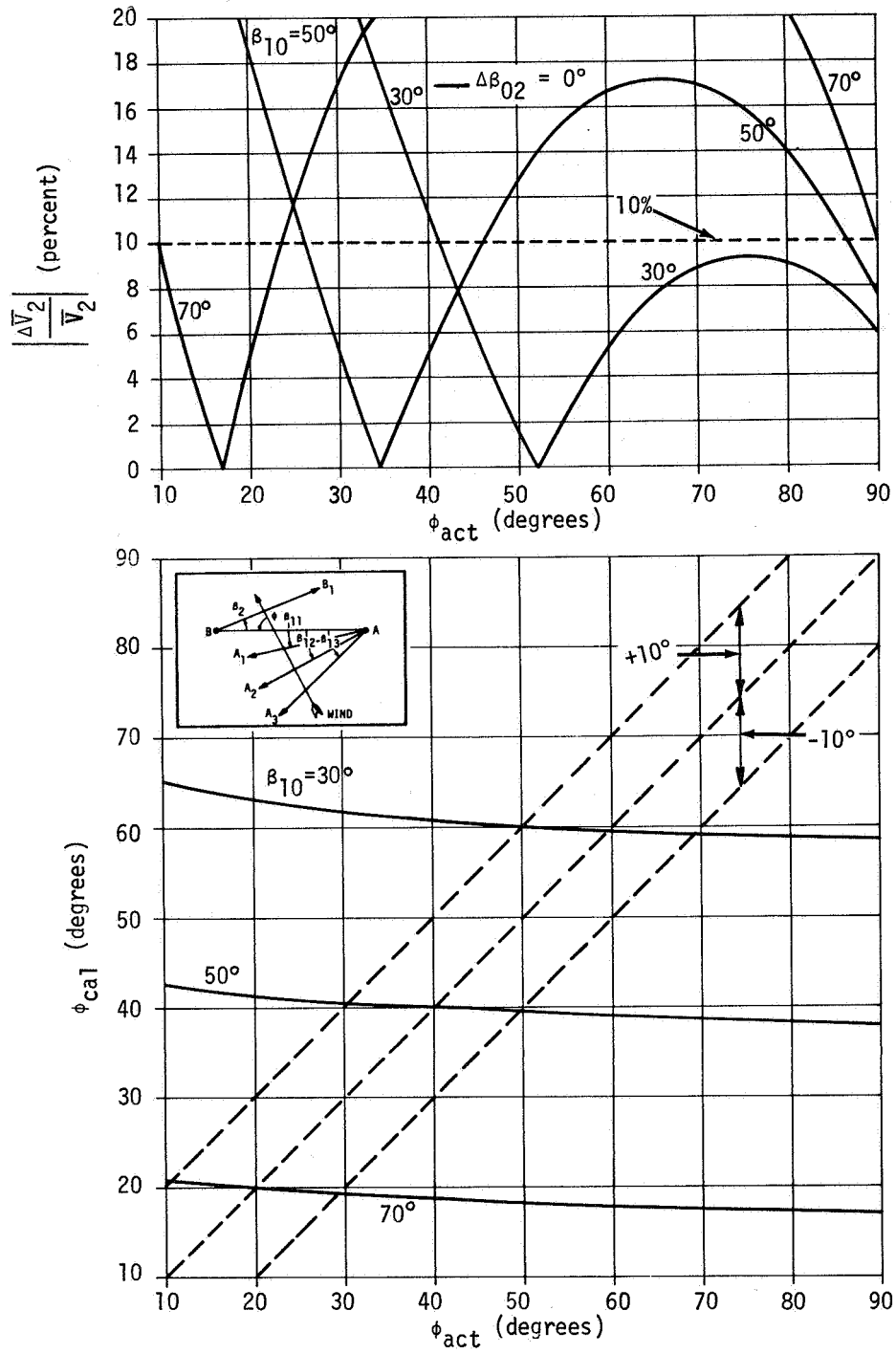


FIGURE 25. LINEAR WIND PROFILE ( $\Delta\beta_{10} = -6.25^\circ$ ,  $\Delta\beta_{20} = 0^\circ$ ,  $\Delta\beta_{30} = 6.25^\circ$ ,  $\beta_2 = 0^\circ$  and  $\epsilon = 5\%$ )

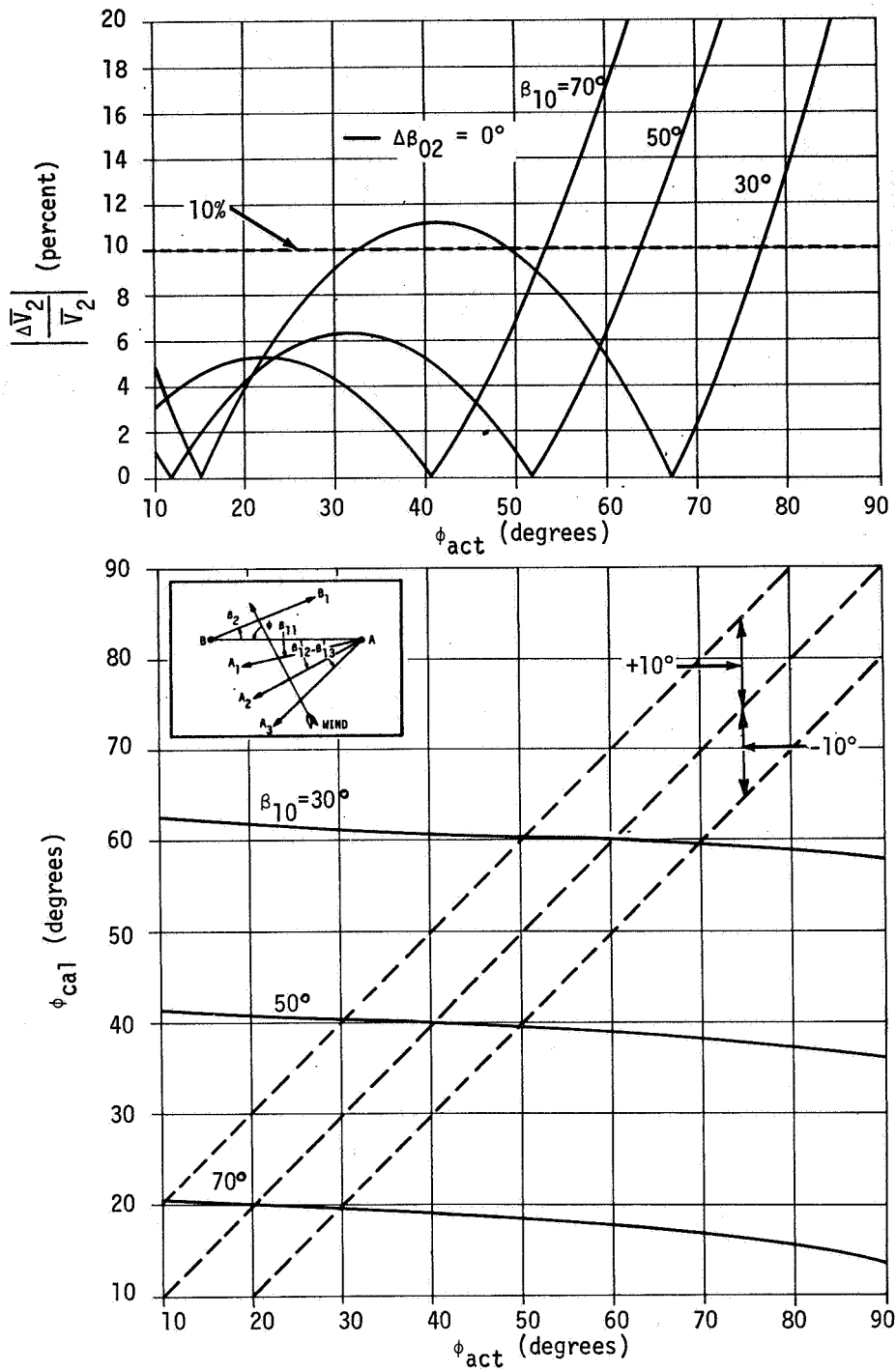


FIGURE 26. LINEAR WIND PROFILE ( $\Delta\beta_{10} = -6.25^\circ$ ,  $\Delta\beta_{20} = 0^\circ$ ,  $\Delta\beta_{30} = 6.25^\circ$ ,  $\beta_2 = 20^\circ$  and  $\epsilon = 5\%$ )

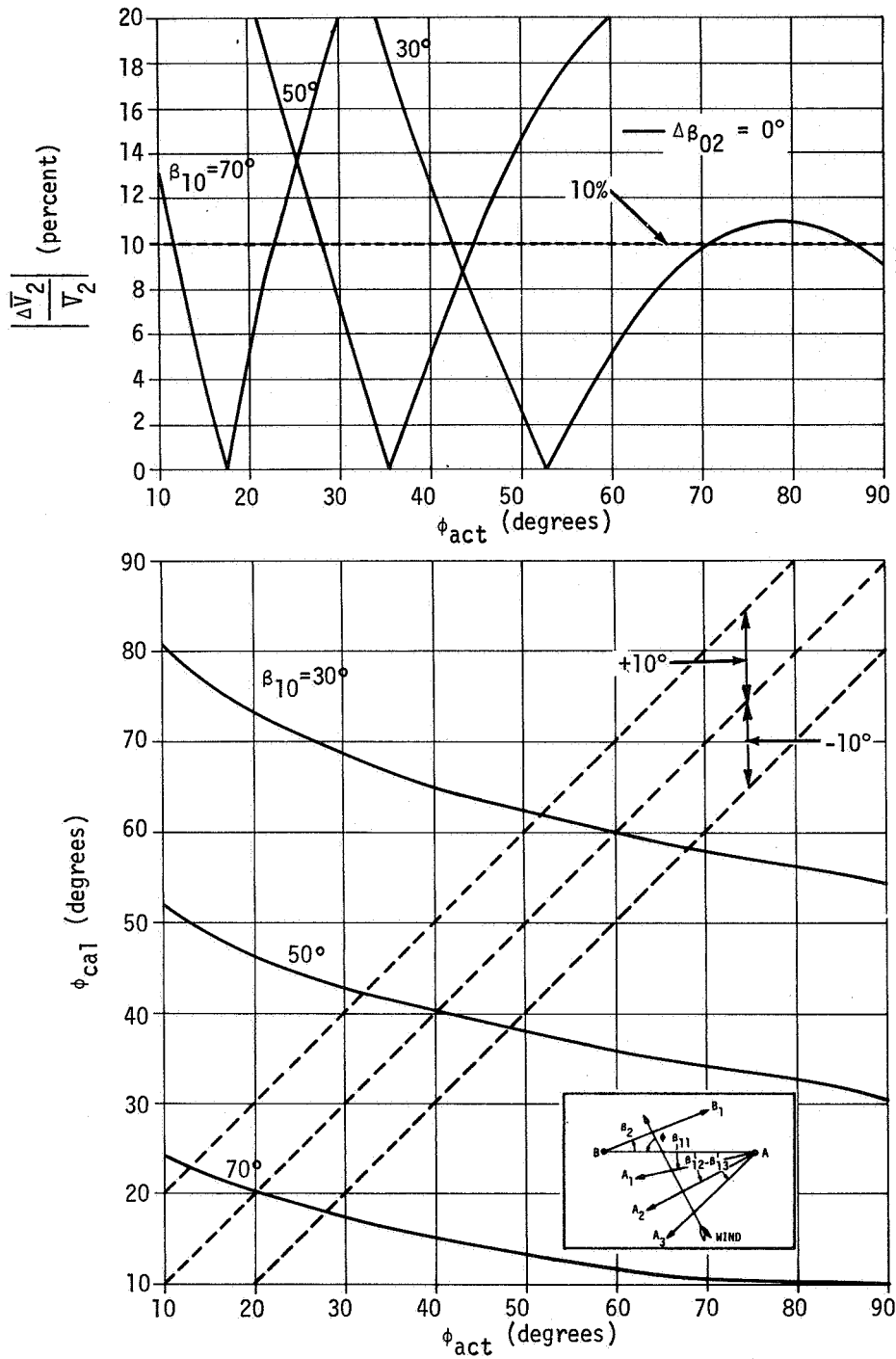


FIGURE 27. LINEAR WIND PROFILE ( $\Delta\beta_{10} = -12.5^\circ$ ,  $\Delta\beta_{20} = 0^\circ$ ,  $\Delta\beta_{30} = 12.5^\circ$ ,  $\beta_2 = 0^\circ$  and  $\epsilon = 5\%$ )

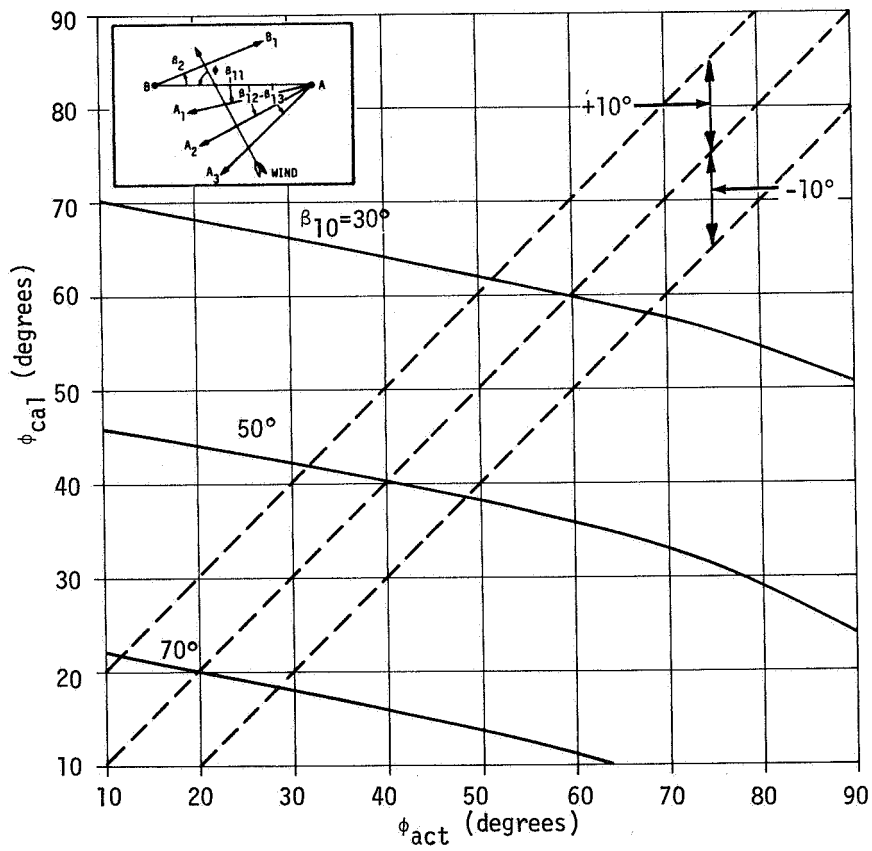
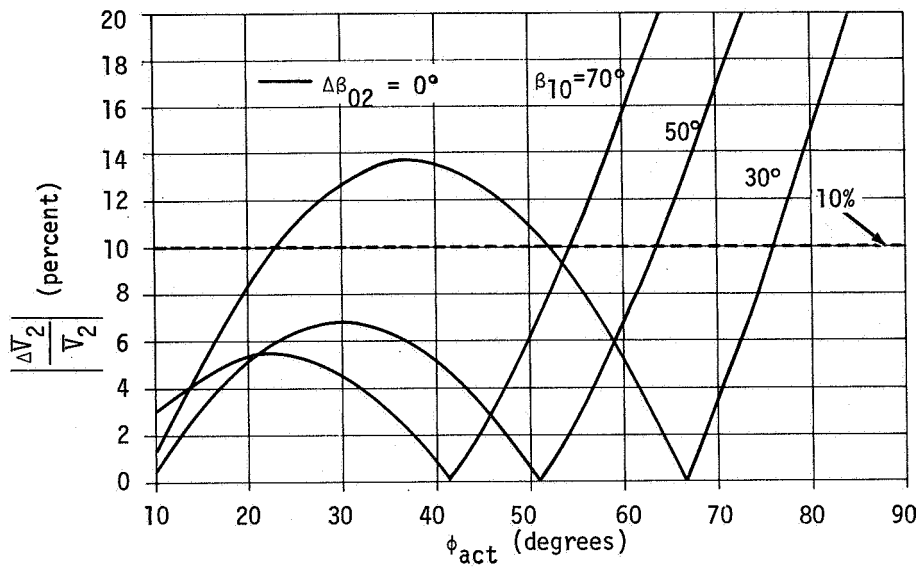


FIGURE 28. LINEAR WIND PROFILE ( $\Delta\beta_{10} = -12.5^\circ$ ,  $\Delta\beta_{20} = 0^\circ$ ,  $\Delta\beta_{30} = 12.5^\circ$ ,  $\beta_2 = 20^\circ$  and  $\epsilon = 5\%$ )

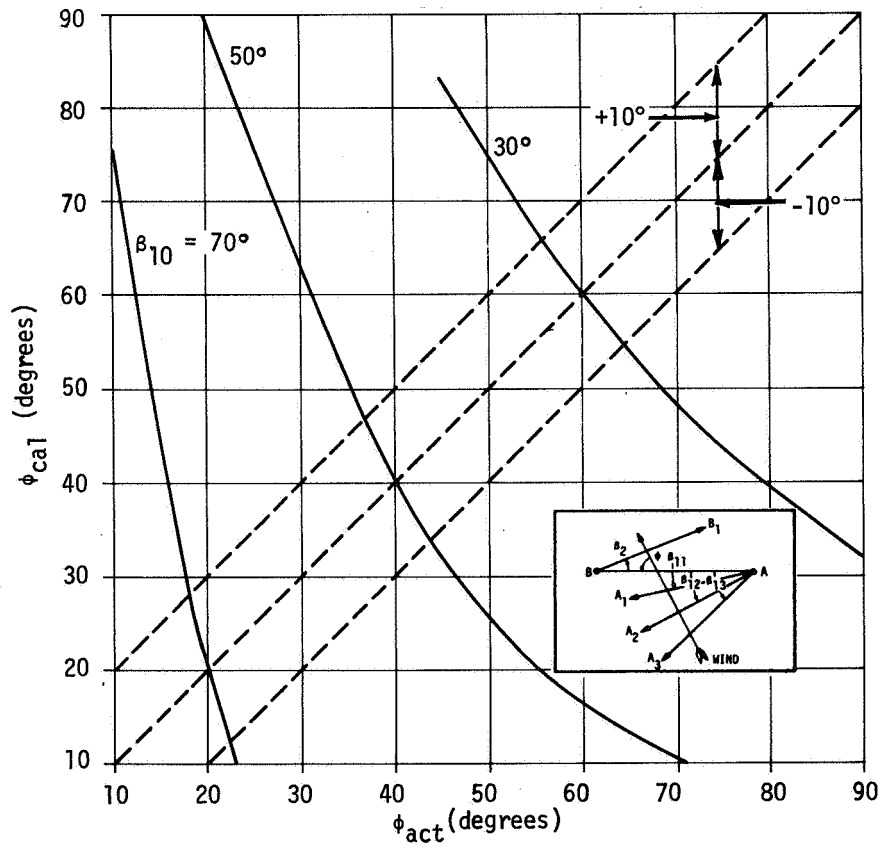
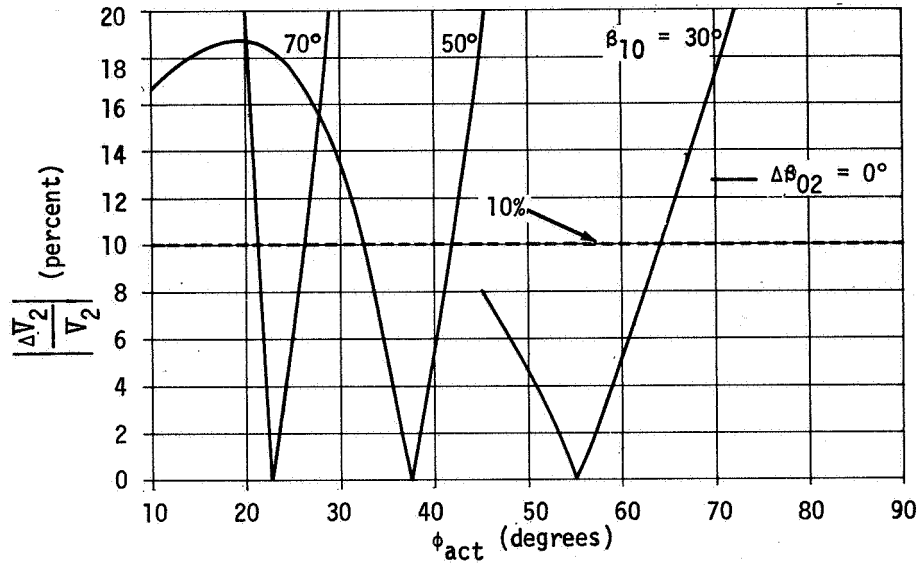


FIGURE 29. LINEAR WIND PROFILE ( $\Delta\beta_{10} = -25^\circ$ ,  $\Delta\beta_{20} = 0^\circ$ ,  $\Delta\beta_{30} = 25^\circ$ ,  $\beta_2 = 0^\circ$  and  $\epsilon = 5\%$ )

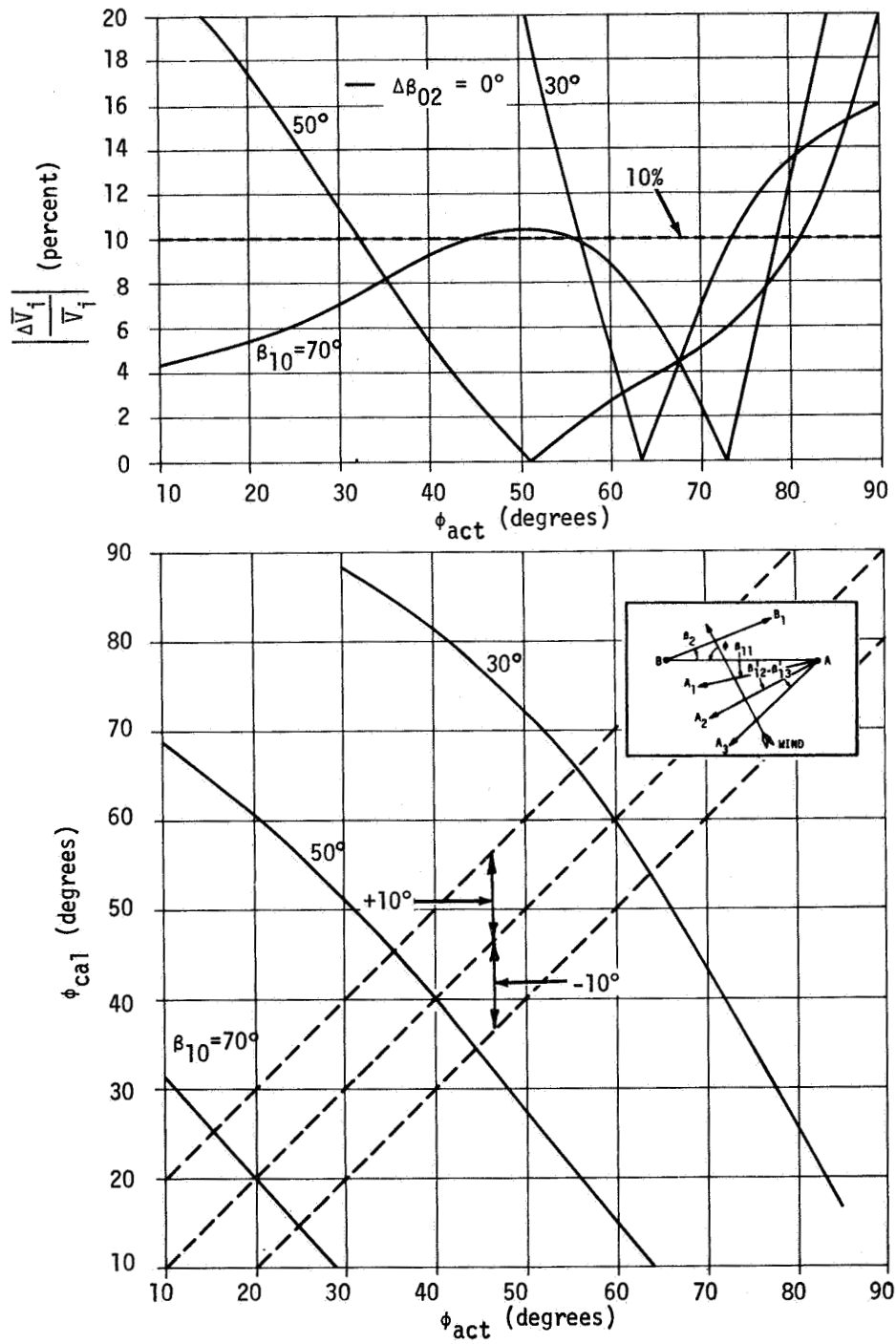


FIGURE 30. LINEAR WIND PROFILE ( $\Delta\beta_{10} = -25^\circ$ ,  $\Delta\beta_{20} = 0^\circ$ ,  $\Delta\beta_{30} = 25^\circ$ ,  $\beta_2 = 20^\circ$  and  $\epsilon = 5\%$ )

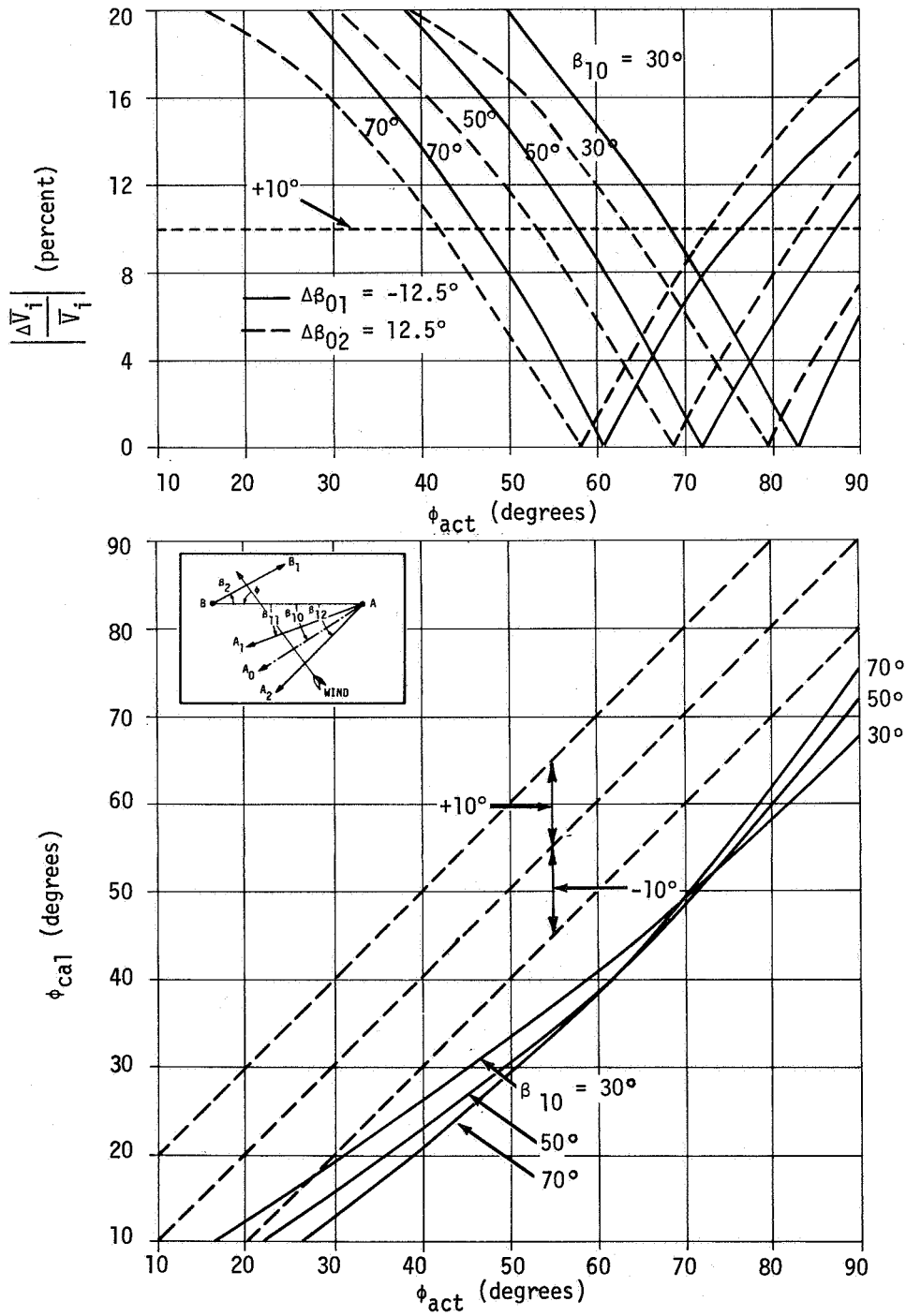


FIGURE 31. POWER-LAW PROFILE ( $\Delta\beta_{10} = -12.5^\circ$ ,  $\Delta\beta_{20} = 12.5^\circ$ ,  $\beta_2 = 10^\circ$ , and  $\epsilon = 5\%$ )

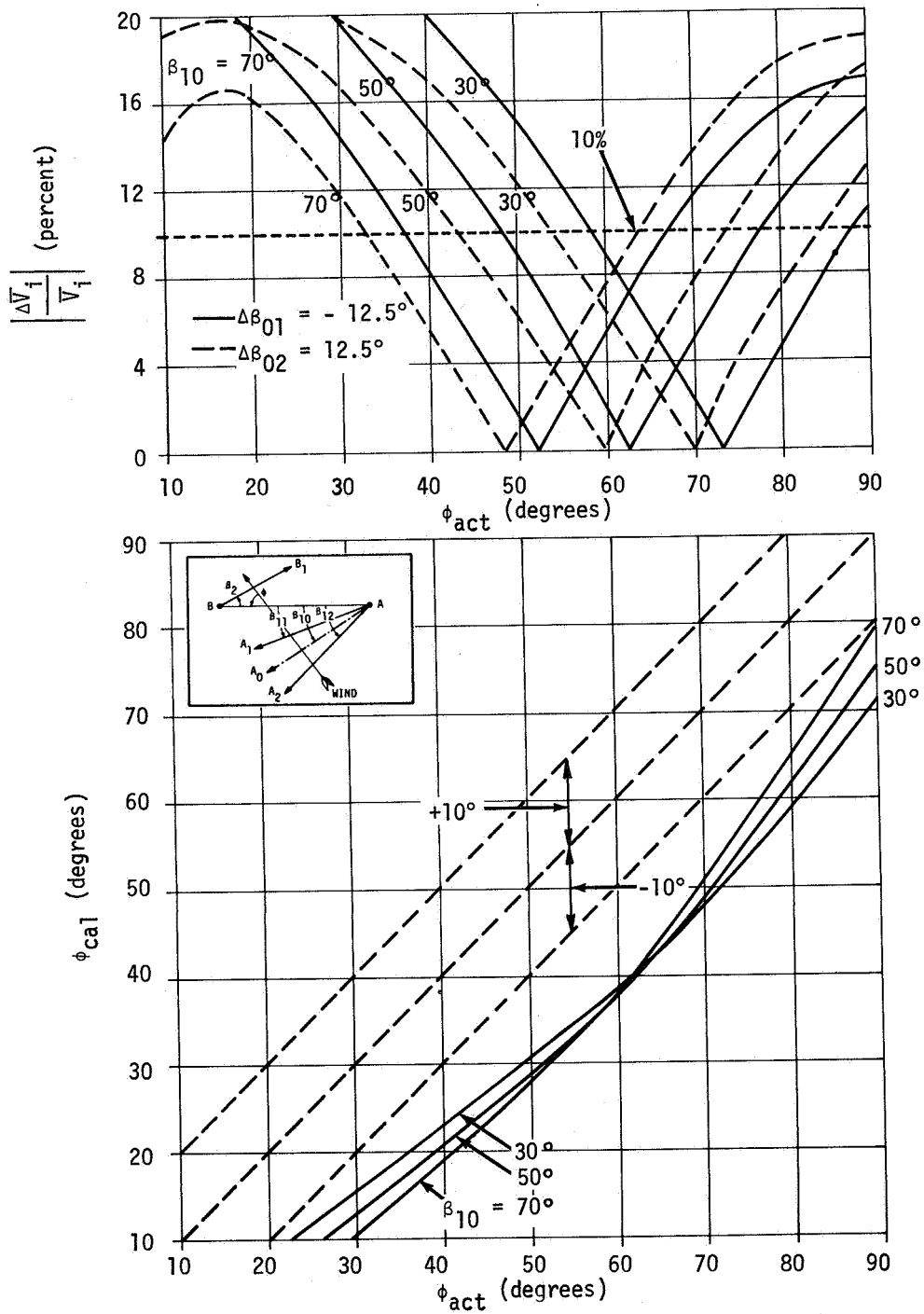


FIGURE 32. POWER-LAW WIND PROFILE ( $\Delta\beta_{10} = -12.5^\circ$ ,  $\Delta\beta_{20} = 12.5^\circ$ ,  $\beta_2 = 30^\circ$ , and  $\epsilon = 5\%$ )

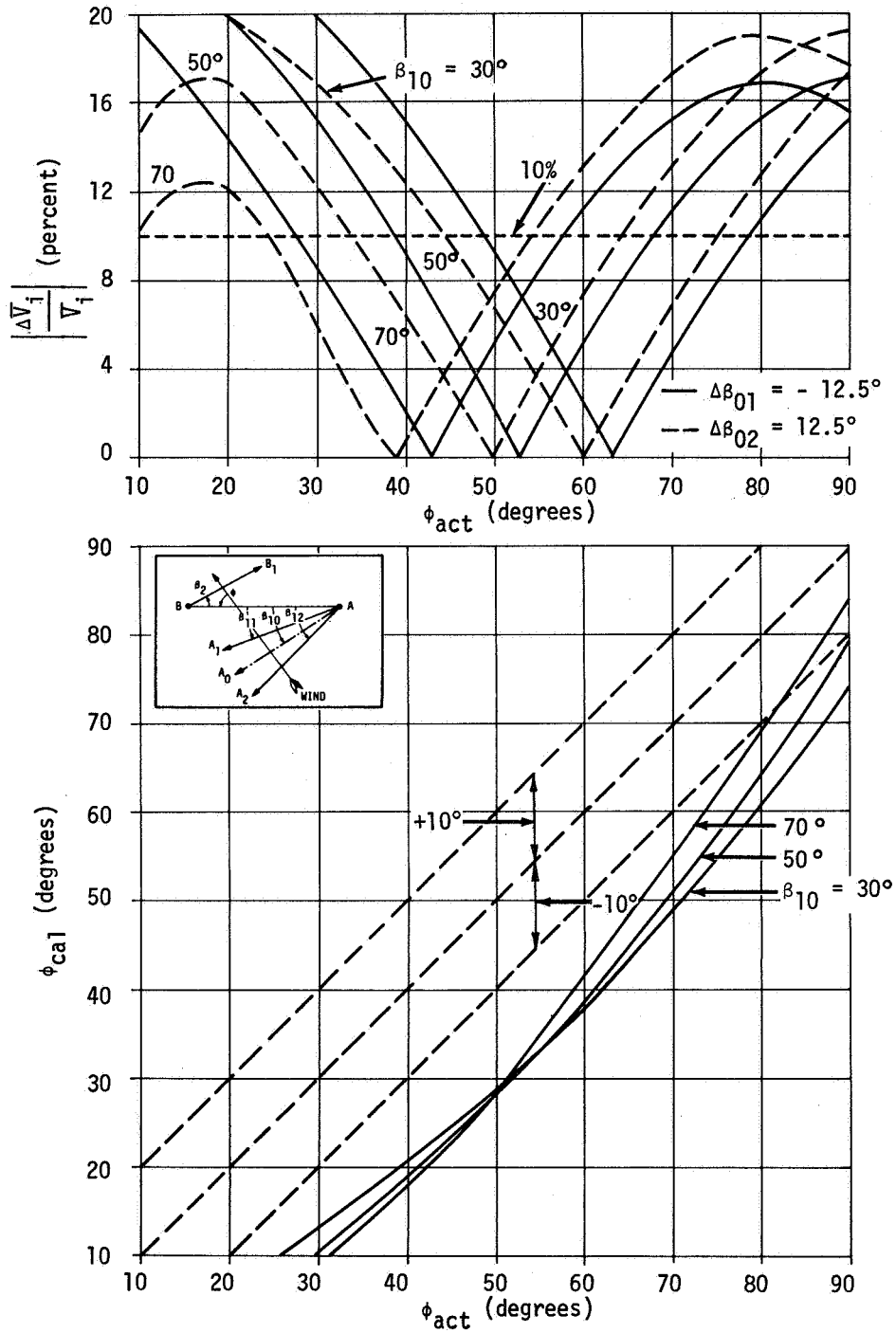


FIGURE 33. POWER-LAW WIND PROFILE ( $\Delta\beta_{10} = -12.5^\circ$ ,  $\Delta\beta_{20} = 12.5^\circ$ ,  $\beta_2 = 50^\circ$ , and  $\epsilon = 5\%$ )

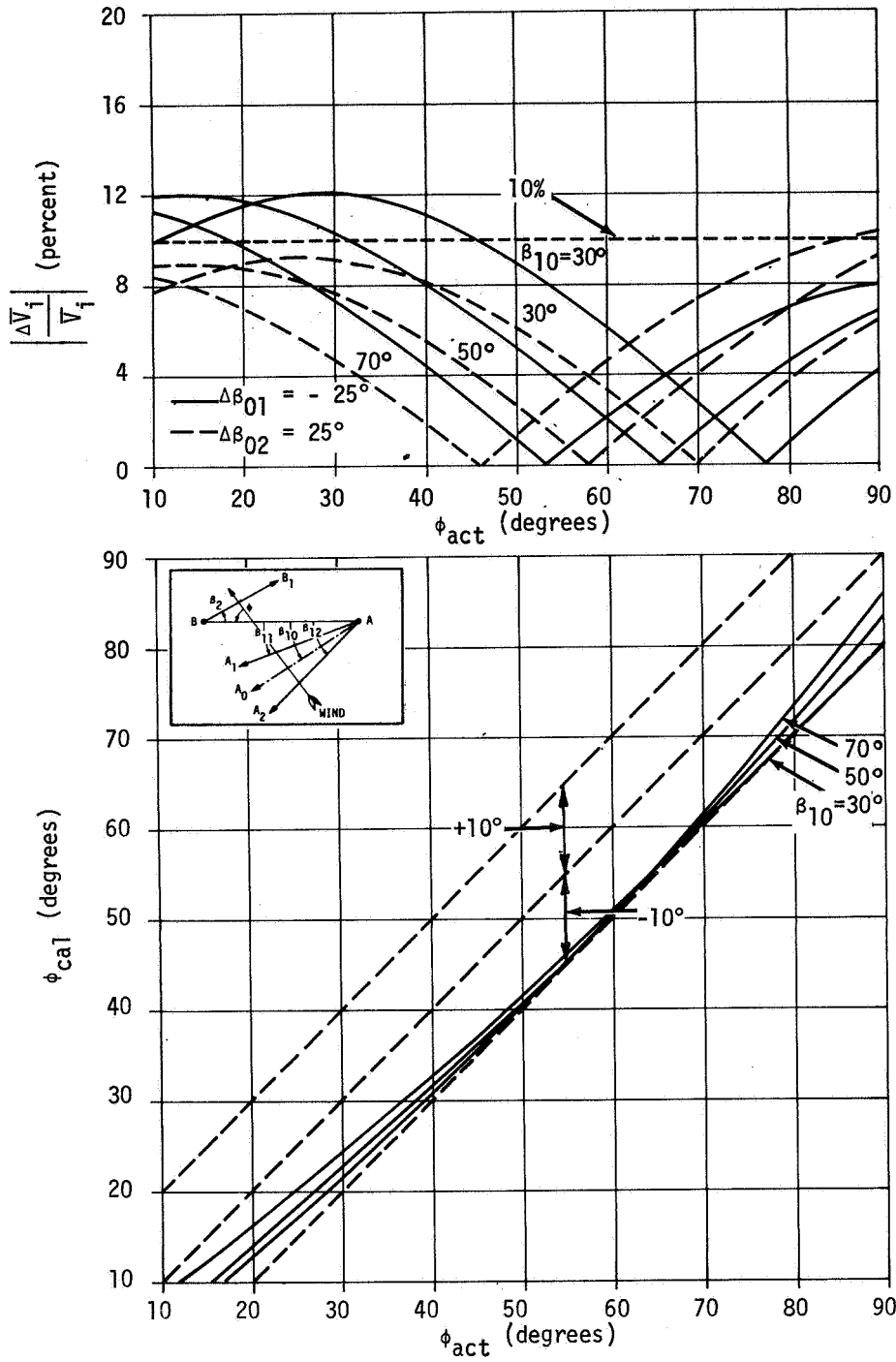


FIGURE 34. POWER-LAW WIND PROFILE ( $\Delta\beta_{10} = -25^\circ$ ,  $\Delta\beta_{20} = 25^\circ$ ,  $\beta_2 = 10^\circ$ , and  $\epsilon = 5\%$ )

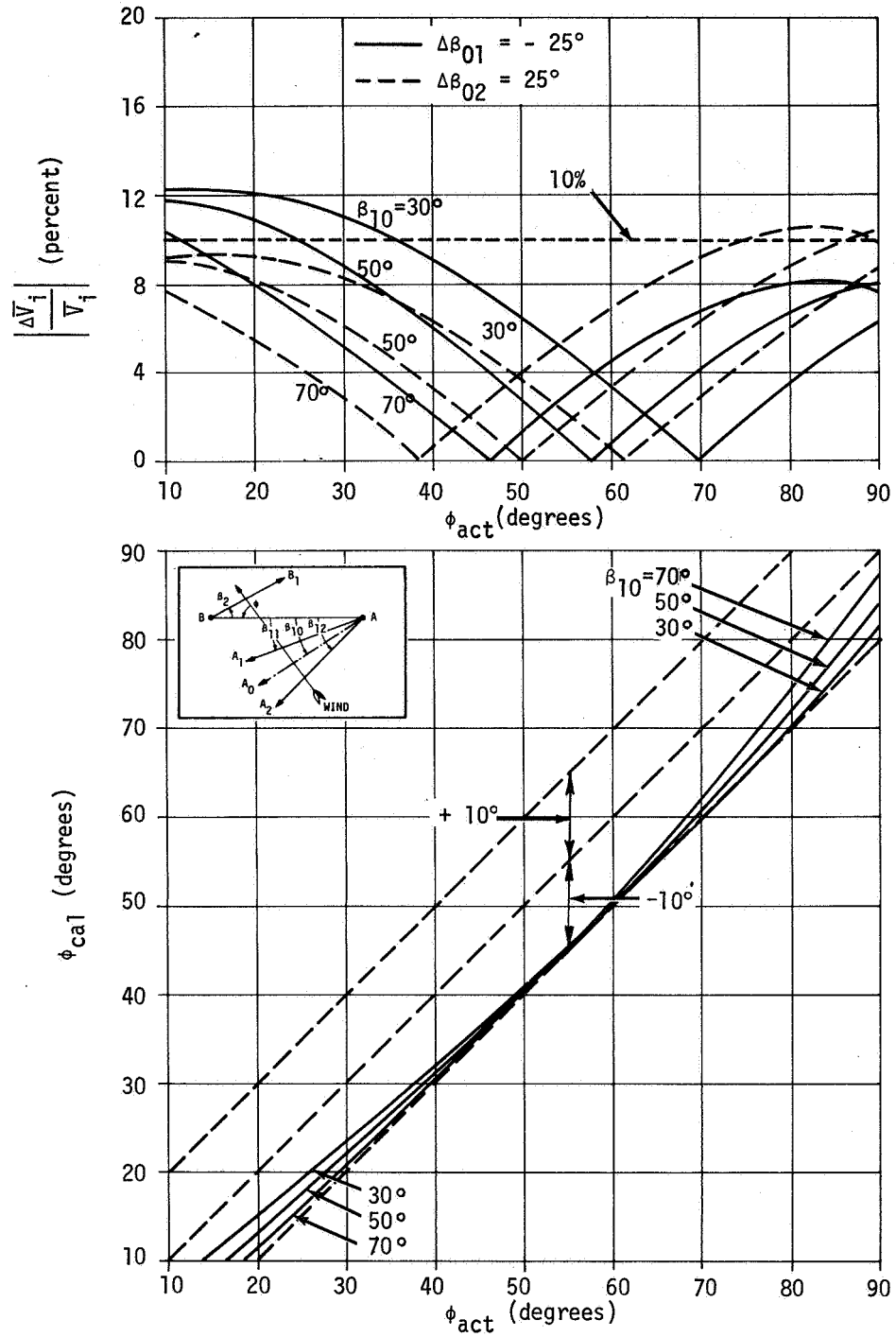


FIGURE 35. POWER-LAW WIND PROFILE ( $\Delta\beta_{10} = -25^\circ$ ,  $\Delta\beta_{20} = 25^\circ$ ,  $\beta_2 = 30^\circ$ , and  $\epsilon = 5\%$ )

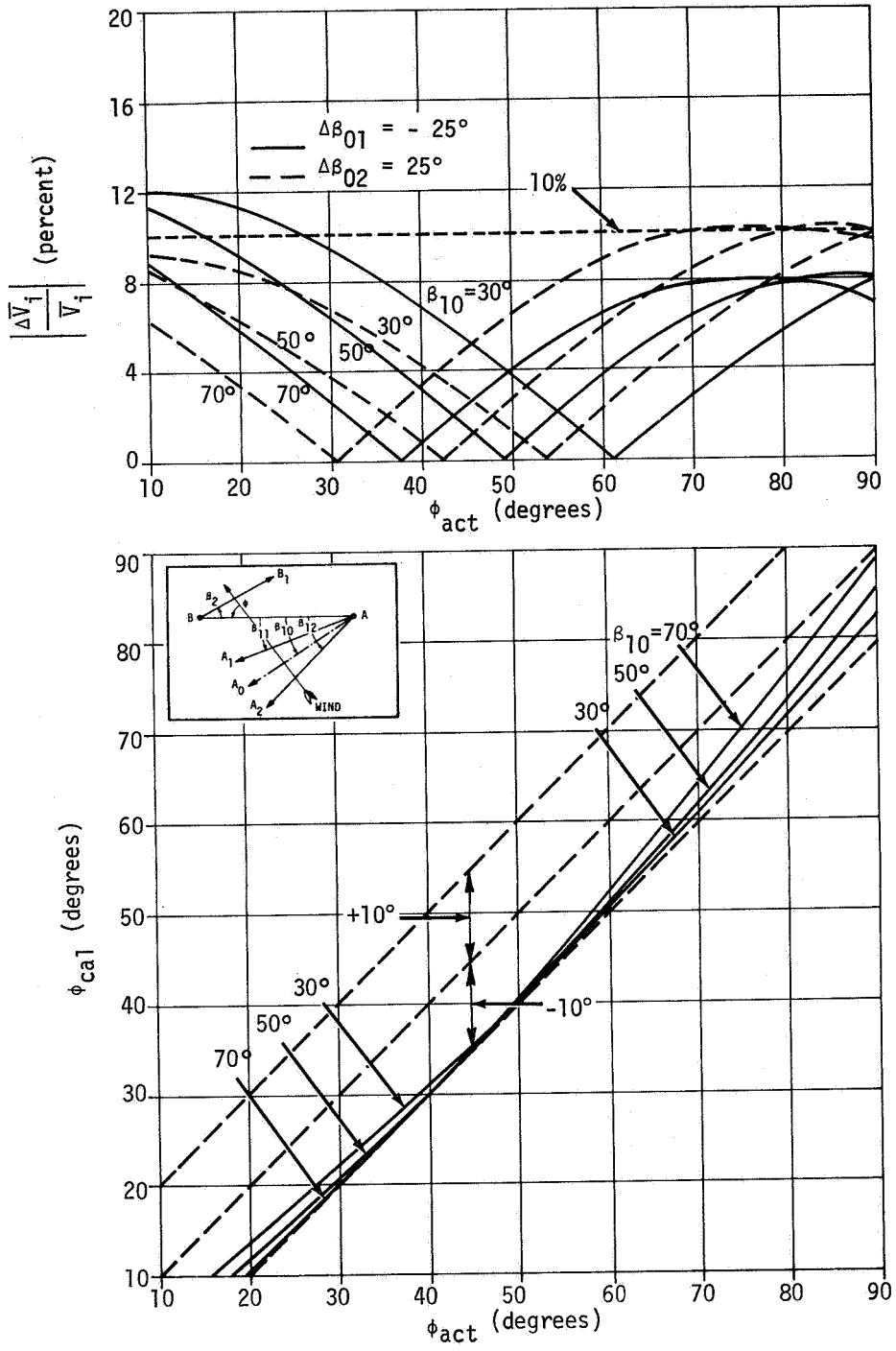


FIGURE 36. POWER-LAW WIND PROFILE ( $\Delta\beta_{10} = -25^\circ$ ,  $\Delta\beta_{20} = 25^\circ$ ,  $\beta_2 = 50^\circ$ , and  $\epsilon = 5\%$ )

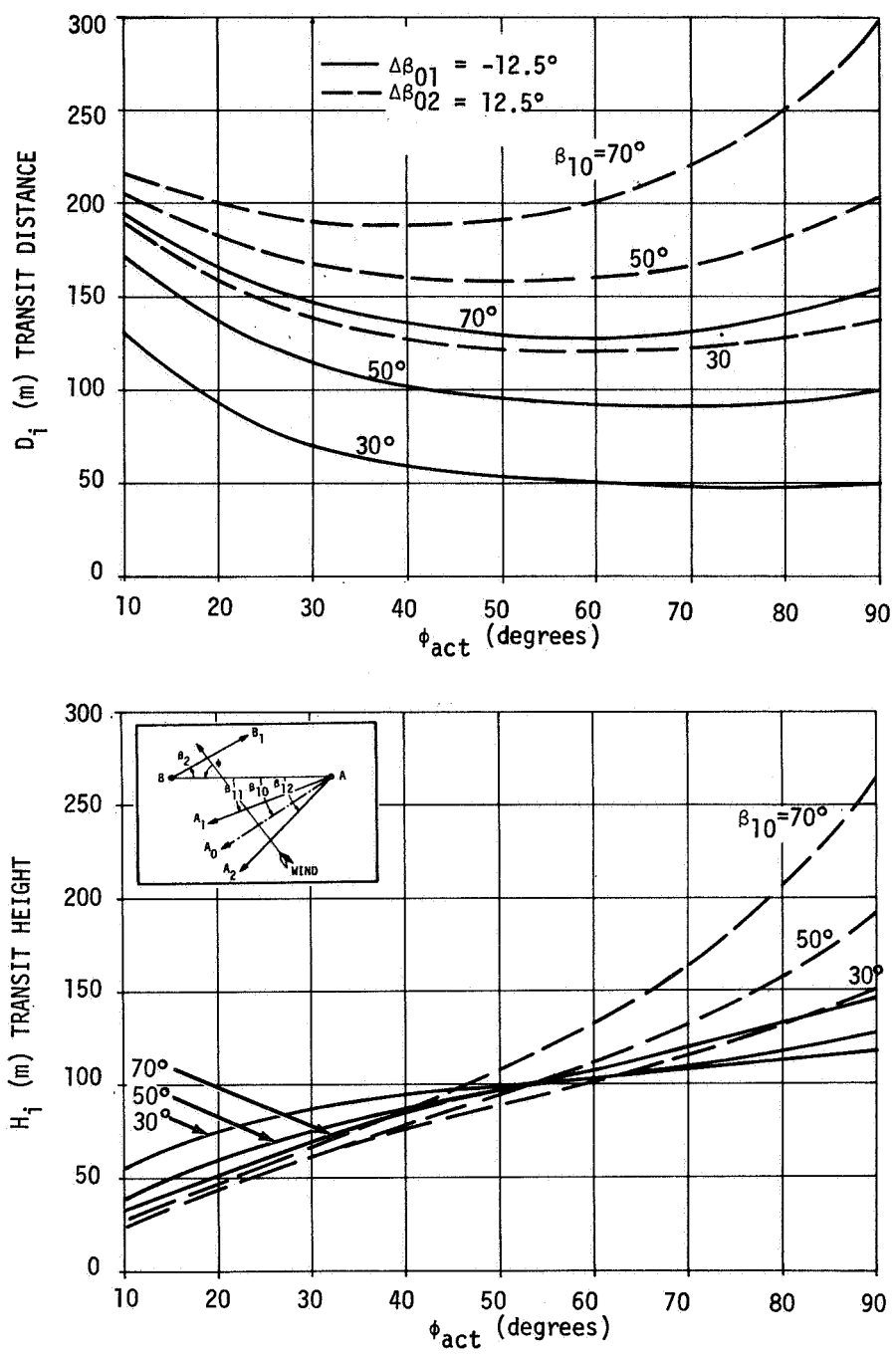


FIGURE 37. TRANSIT HEIGHTS AND TRANSIT DISTANCES VERSUS WIND DIRECTION  
 ( $\Delta\beta_{10} = -12.5^\circ$ ,  $\Delta\beta_{20} = 12.5^\circ$ ,  $\beta_2 = 10^\circ$ , and  $b = 244$  m)

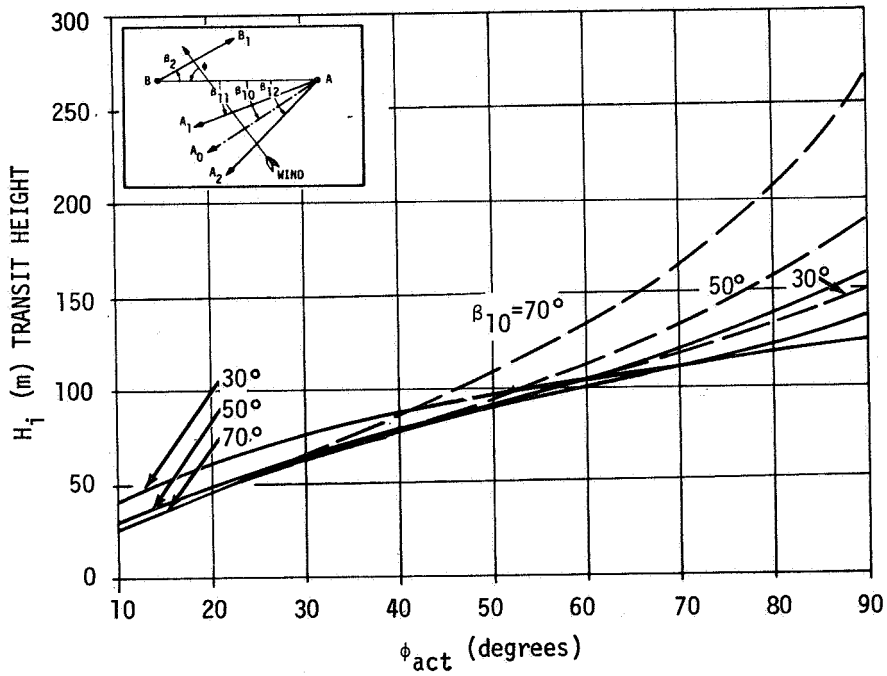
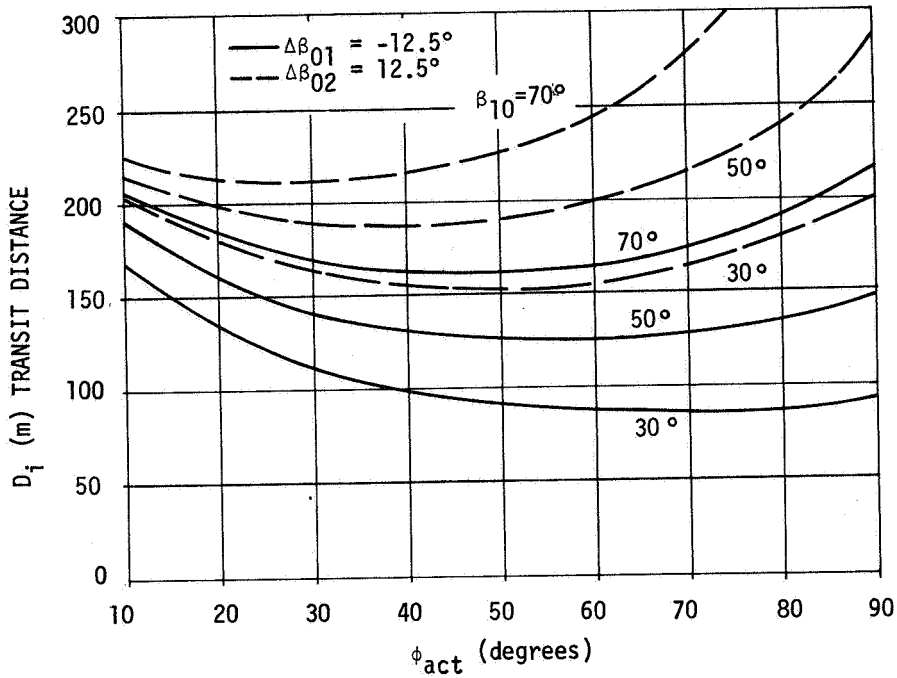


FIGURE 38. TRANSIT HEIGHTS AND TRANSIT DISTANCES VERSUS WIND DIRECTION  
 ( $\Delta\beta_{10} = -12.5^\circ$ ,  $\Delta\beta_{20} = 12.5^\circ$ ,  $\beta_2 = 30^\circ$ , and  $b = 244$  m)

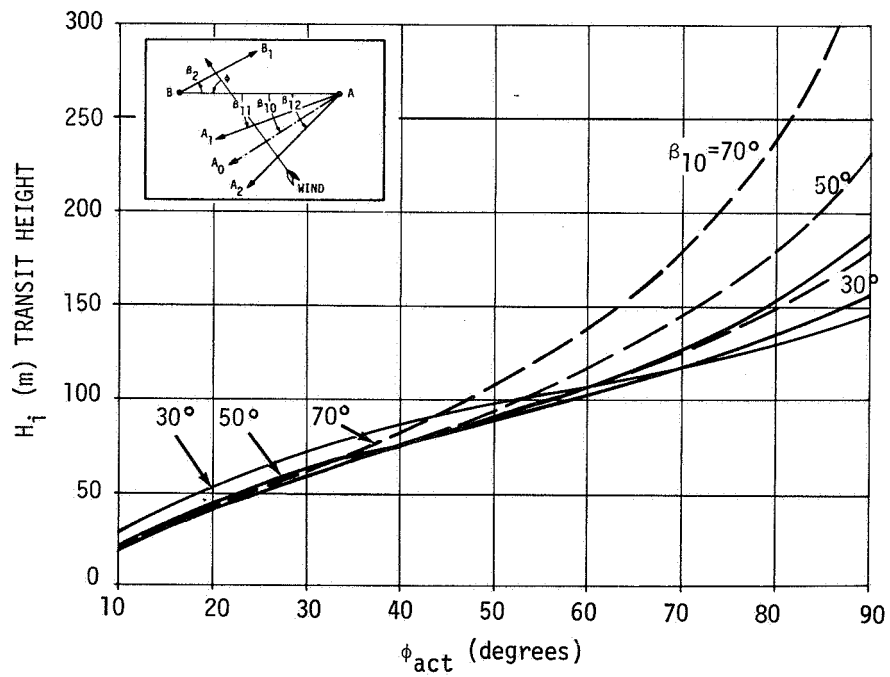
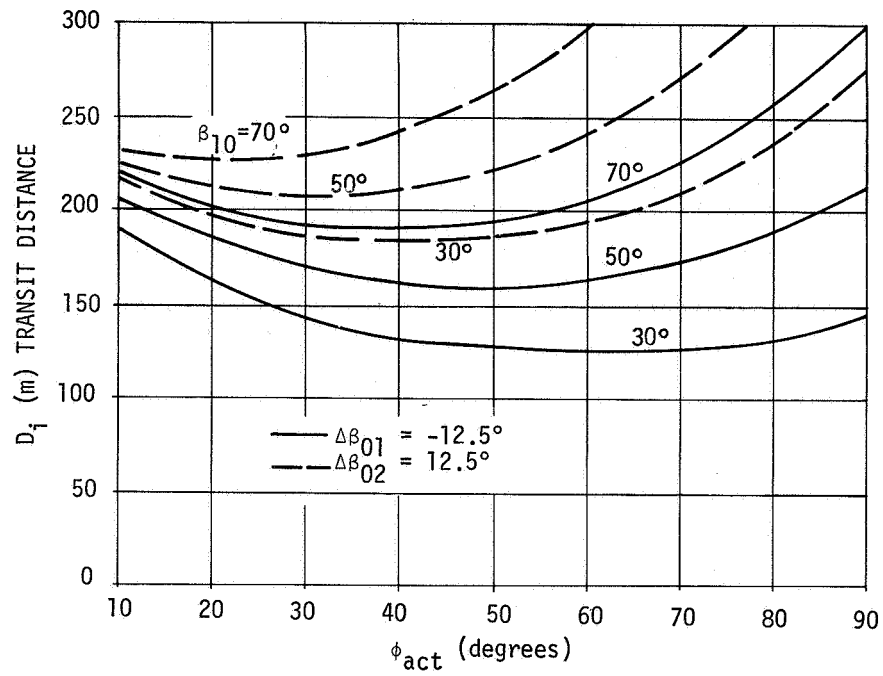


FIGURE 39. TRANSIT HEIGHTS AND TRANSIT DISTANCES VERSUS WIND DIRECTION  
 $(\Delta\beta_{10} = -12.5^\circ, \Delta\beta_{20} = 12.5^\circ, \beta_2 = 50^\circ, \text{ and } b = 244 \text{ m})$

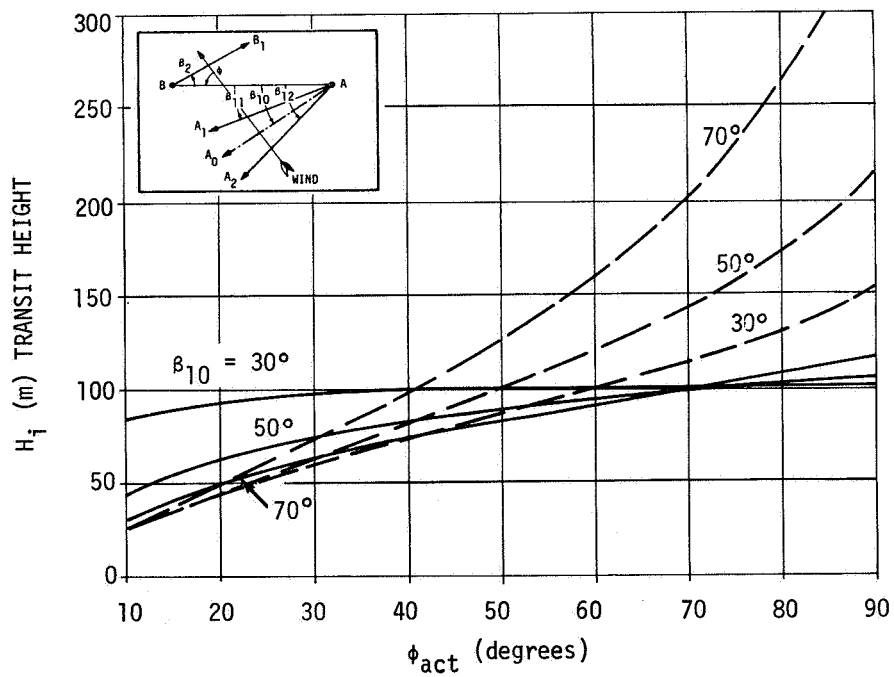
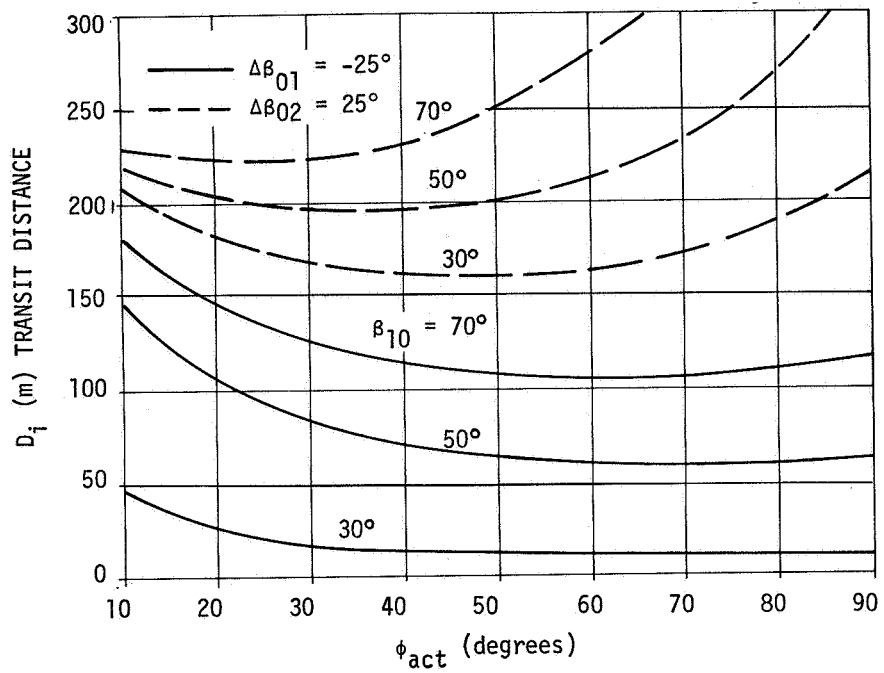


FIGURE 40. TRANSIT HEIGHTS AND TRANSIT DISTANCES VERSUS WIND DIRECTION  
 ( $\Delta\beta_{10} = -25^\circ$ ,  $\Delta\beta_{20} = 25^\circ$ ,  $\beta_2 = 10^\circ$ , and  $b = 244$  m)

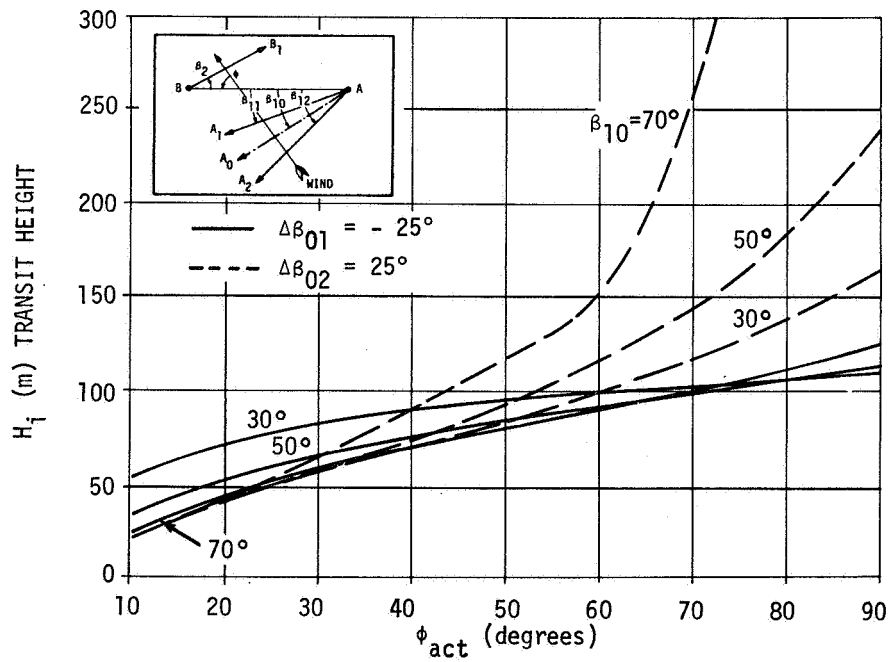
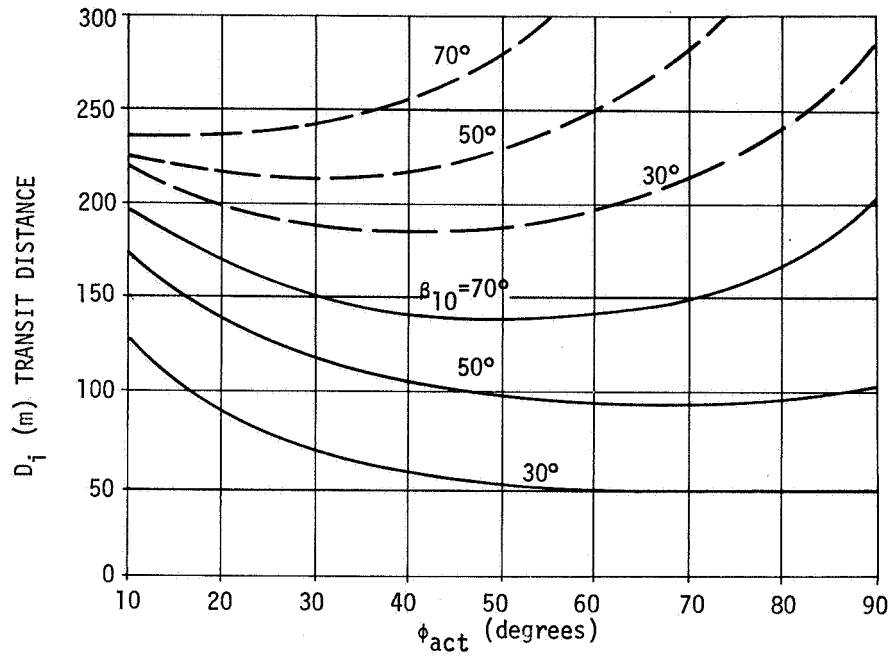


FIGURE 41. TRANSIT HEIGHTS AND TRANSIT DISTANCES VERSUS WIND DIRECTION  
 $(\Delta\beta_{10} = -25^\circ, \Delta\beta_{20} = 25^\circ, \beta_2 = 30^\circ, \text{ and } b = 244 \text{ m})$

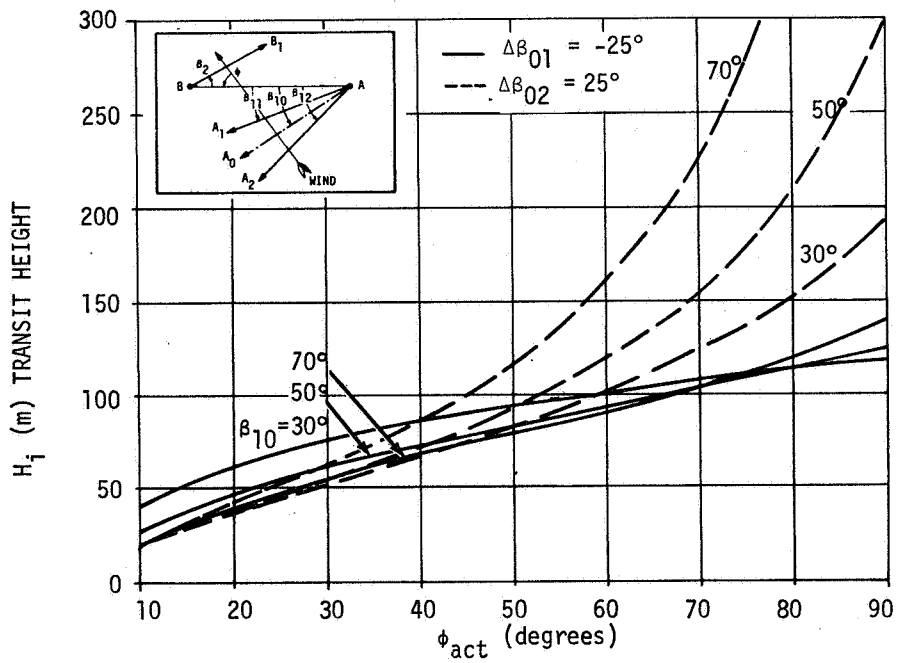
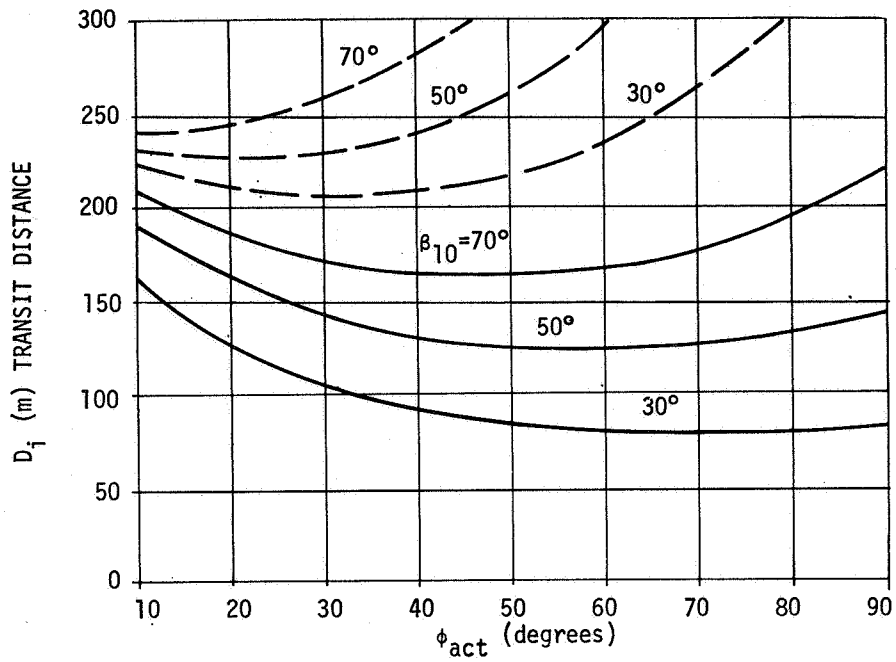


FIGURE 42. TRANSIT HEIGHTS AND TRANSIT DISTANCES VERSUS WIND DIRECTION  
 ( $\Delta\beta_{10} = -25^\circ$ ,  $\Delta\beta_{20} = 25^\circ$ ,  $\beta_2 = 50^\circ$ , and  $b = 244$  m)

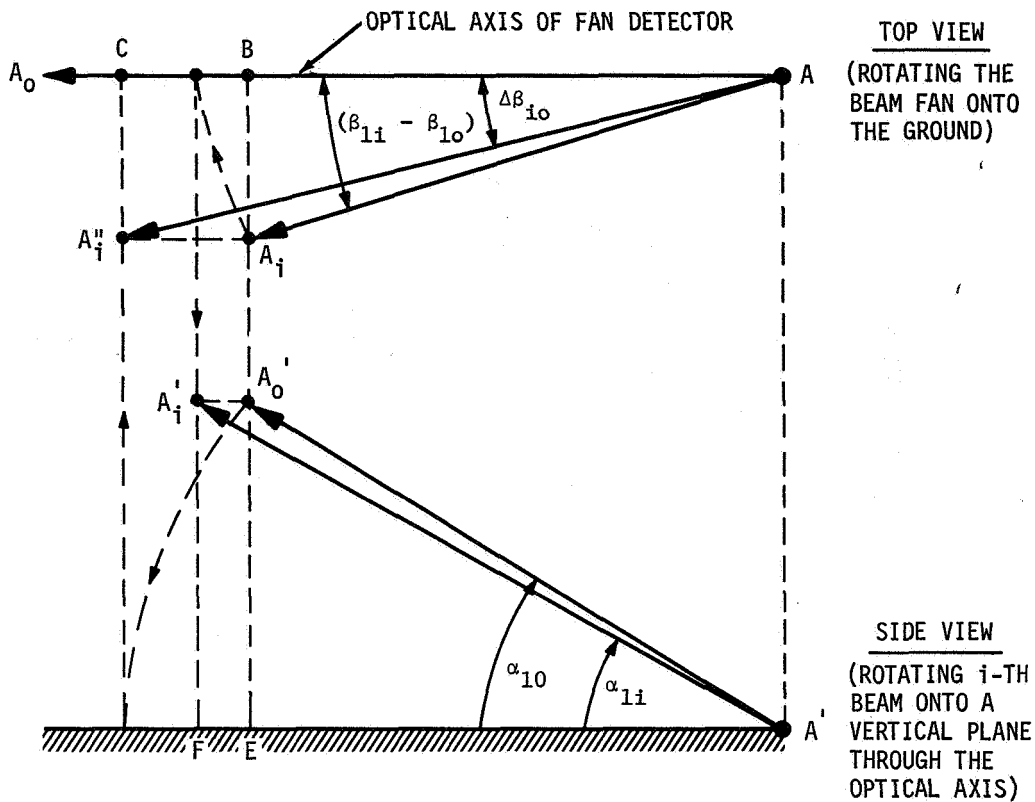


FIGURE 43. BEAM-FAN GEOMETRY

## APPENDIX A

### COMPUTER PROGRAMS

Two computer programs for determining the wind speed and direction are included. The first one, denoted by Program I, is used for the hypothetical numerical tests discussed in Section IV. The second one, denoted by Program II, is to be used for actual tests where the transit times will be given as inputs by actual cross-beam tests. In these two computer programs, several parameters concerning beam geometry are given specific numbers, which may be subject to changes, if desired. The pertinent variable names used in the programs are given below their counterparts used in the text, and their definitions are explained in the definition of symbols.

Variable Names	Equivalent
ALPH1	$\alpha_1$
ALPH2	$\alpha_{10}$

Variable Names	Equivalent
B	b
BETA2	$\beta_2$
BETAC(I)	$\beta_{10}$
BI(I)	$\beta_{1i}$
D(I)	$D_i$
DE(I, J)	$D_i, \epsilon^{*1}$
DELB(I)	$\Delta\beta_{10}$
DELV(I, J)	$\left  \frac{\Delta\bar{V}_i}{\bar{V}_i} \right ^{*1}$
ERROR	$\epsilon$
H(I)	$H_i$
HE(I, J)	$H_i, \epsilon^{*1}$

1. Superscript \* indicates that the argument J stands for J<sup>th</sup> pattern of errors in transit times.

Program I.

```

ASSIGN S=MTD,SI=CR,BQ=MT1,LO=LP.
REWIND MT1.
FORTRAN BQ,LO.
    DIMENSION DELB(3),BETAC(9),PHI(24),B1(3),A1(3),H(3),D(3),V(
13),T(3),F(3),TF(3,2),DUMA(3),P(3),Q(3),PHIE(2),HE(3,2),VE(3,2),DE(
13,2),DELV(3,2)
1  FORMAT(92H INDEX      HI      DI      VI      VI,A      VI,B D
1ELVI,A  DELVI,B      PHI,A      PHI,B/)
2  FORMAT(1H I3,9F10.2)
3  FORMAT(1H //)
8  FORMAT (17H FAN CENTER BEAM=F6.2/)
4  FORMAT(9H ALPHA1= F5.1,8HALPHA2= F5.1/)
6  FORMAT (20H1BASE LINE DISTANCE=F6.2/)
7  FORMAT (17H TRUE WIND ANGLE=F6.2)
9  FORMAT (33H ANGLES MEASURED FROM CENTER BEAM)
10  FORMAT (18H BETA2 BEAM ANGLE=F6.3)
11  FORMAT (3(1H F9.3//))
12  FORMAT (23H ERROR IN TRANSIT TIME=F6.3//)
13  FORMAT (3F10.5)
15  FORMAT (2I2)
16  FORMAT (1H I3,8F10.5)
17  FORMAT (9F8.3)
    READ 15, NBEAM,ITER
700  READ 13, BETA2
    READ 13, (DELB(I),I=1,NBEAM)
    B=244.0
    ALPHA1=45.0
    ALPHA2=45.0
    ERROR=0.05
    PRINT 6,B
    PRINT 4,ALPHA1,ALPHA2
    PRINT 10, BETA2
    PRINT 9
    PRINT 11,(DELB(I),I=1,NBEAM)
    PRINT 12, ERROR
    ALPHA1=ALPHA1*.01745
    ALPHA2=ALPHA2*.01745
    BETA2=BETA2*.01745
    DELB(1)=DELB(1)*.01745
    DELB(2)=DELB(2)*.01745
    DELB(3)=DELB(3)*.01745
    ZO=3.0
    UO=5.0
    RHO=.2
    BETAC(1)=20.0
    BETAC(2)=30.0
    BETAC(3)=40.0
    BETAC(4)=50.0
    BETAC(5)=60.0
    BETAC(6)=70.0
    BETAC(7)=80.0
    BETAC(8)=90.0
    DO 500 K=1,8
    PRINT 8, BETAC(K)
    BETAC(K)=BETAC(K)*.01745
    PHI(1)=10.0
    DO 21 J=2,9
    PHI(J)=PHI(J-1)+10.0
21  CONTINUE

```

Program I.

```

DO 600 J=1,9
PRINT 7, PHI(J)
PHI(J)=PHI(J)*.01745
DO 100 I=1,NBEAM
B1(I)=BETAC(K)+ATANF((SINF(DEL B(I))/COSF(DEL B(I)))/COSF(ALPH1))
A1(I)=ATANF(TANF(ALPH1)*COSF(BETAC(K)-B1(I)))
DUMA(I)=COSF(A1(I))/SINF(A1(I))
DUMB=COSF(ALPH2)/SINF(ALPH2)
H(I)=B*SINF(PHI(J))/(DUMA(I)*SINF(PHI(J)+B1(I))+DUMB*SINF(PHI(J)+B
ETA2))
E(I)=DUMA(I)*SINF(B1(I))+DUMB*SINF(BETA2)
D(I)=(H(I)/SINF(PHI(J)))*E(I)
V(I)=UO*(H(I)/ZO)**RHO
T(I)=D(I)/V(I)
100 CONTINUE
TE(1,1)=T(1)*(1.0+ERROR)
TE(2,1)=T(2)*(1.0-ERROR)
TE(3,1)=T(3)*(1.0+ERROR)
TE(1,2)=T(1)*(1.0-ERROR)
TE(2,2)=T(2)*(1.0+ERROR)
TE(3,2)=T(3)*(1.0-ERROR)
IF (NBEAM-3) 800,900,900
800 P(1)=E(1)*(DUMA(2)*COSF(B1(2))+DUMB*COSF(BETA2))
P(2)=E(2)*(DUMA(1)*COSF(B1(1))+DUMB*COSF(BETA2))
Q(1)=E(1)*(DUMA(2)*SINF(B1(2))+DUMB*SINF(BETA2))
Q(2)=E(2)*(DUMA(1)*SINF(B1(1))+DUMB*SINF(BETA2))
GO TO 801
900 P(1)=E(1)*(DUMA(3)*COSF(B1(3))-DUMA(2)*COSF(B1(2)))
P(2)=E(2)*(DUMA(1)*COSF(B1(1))-DUMA(3)*COSF(B1(3)))
P(3)=E(3)*(DUMA(2)*COSF(B1(2))-DUMA(1)*COSF(B1(1)))
Q(1)=E(1)*(DUMA(3)*SINF(B1(3))-DUMA(2)*SINF(B1(2)))
Q(2)=E(2)*(DUMA(1)*SINF(B1(1))-DUMA(3)*SINF(B1(3)))
Q(3)=E(3)*(DUMA(2)*SINF(B1(2))-DUMA(1)*SINF(B1(1)))
801 CONTINUE
DO 200 L=1,2
IF (ITER) 802,802,971
802 CONTINUE
IF (NBEAM-3) 950,960,960
950 SUMNU=P(1)/TE(1,L)-P(2)/TE(2,L)
SUMDE=Q(1)/TE(1,L)-Q(2)/TE(2,L)
GO TO 970
960 SUMNU=0.0
SUMDE=0.0
DO 201 I=1,3
SUMNU=SUMNU+P(I)/TE(I,L)
SUMDE=SUMDE+Q(I)/TE(I,L)
201 CONTINUE
970 CONTINUE
PHI(L)=-ATANF(SUMDE/SUMNU)
GO TO 803
971 CONTINUE
C INITIALIZE PHI EQUALS 0 DEGREES REFERENCED TO THE BASE LINE B.
PHIMIN=0.0
PHIMAX=180.0
PHIMIN=PHIMIN*.01745
PHIMAX=PHIMAX*.01745
PHIMID=(PHIMIN+PHIMAX)/2.0
C SET UP COUNTER
II=0
1040 II=II+1

```

Program I.

```
IF (II-20)1011,1011,1000
1011 H1MID=DUMA(2)*SINF(PHIMID+B1(2))+DUMB*SINF(PHIMID+BETA2)
      H2MID=DUMA(1)*SINF(PHIMID+B1(1))+DUMB*SINF(PHIMID+BETA2)
      DELTA2=(TE(2,L)/TE(1,L))*(H1MID/H2MID)*(E(1)/E(2))-(H1MID/H2MID)
      1**RHO
      IF (DELTA2) 1030,1000,1050
1030 PHIMAX=PHIMID
      PHIMID=(PHIMID+PHIMIN)/2.0
      IF (ABSF(PHIMAX-PHIMID)-.001745) 1000,1000,1040
1050 PHIMIN=PHIMID
      PHIMID=(PHIMID+PHIMAX)/2.0
      IF (ABSF(PHIMIN-PHIMID)-.001745) 1000,1000,1040
1000 CONTINUE
      PHIE(L)=PHIMID
803 CONTINUE
200 CONTINUE
      PHIE(1)=PHIE(1)/.01745
      PHIE(2)=PHIE(2)/.01745
      PRINT 18, PHIE(1),PHIE(2)
      GO TO 700
      END
-EOF.
-ASSIGN BI=MT1.
-REWIND MT1.
-FORTLOAD BIU.
2.1
10.0
30.0
-12.5 12.5
2.5 3.8 6.7
```

Program II.

```

ASSIGN S=MTO,SI=CR,BO=MT1,LO=LP.
REWIND MT1.
FORTRAN BC,LO.
    DIMENSION DELB(3),BETAC(9),PHI(24),B1(3),A1(3),H(3),D(3),V(
    13),1(3),E(3),TE(3,2),DUMA(3),P(3),Q(3),PHIE(2),HE(3,2),VE(3,2)DE(
    13,2),DELV(3,2)
    1 FORMAT(92H INDEX          HI          DI          VI          VI,A          VI,B F
    IELVI,A  DELVI,B          PHI,A          PHI,B/)
    2 FORMAT(1H 13,9F10.2)
    3 FORMAT(1H //)
    8   FORMAT (17H FAN CENTER BEAM=F6.2/)
    4   FORMAT(9H ALPHA1= F5.1,8HALPHA2= F5.1/)
    6   FORMAT (20H1BASE LINE DISTANCE=F6.2/)
    7   FORMAT (17H TRUE WIND ANGLE=F6.2)
    9   FORMAT (33H ANGLES MEASURED FROM CENTER BEAM)
    10  FORMAT (18H BETA2 BEAM ANGLE=F6.3)
    11  FORMAT (3(1H F9.3/))
    12  FORMAT (23H ERROR IN TRANSIT TIME=F6.3//)
    13  FORMAT (3F10.5)
    15  FORMAT (2I2)
    16  FORMAT (1H 13,8F10.5)
    17  FORMAT (9F8.3)
    18  FORMAT (25HLOWER BOUND  UPPER BOUND/1H 2F12.6)
    READ 15, NBEAM,ITER
700   READ 13, BETA2
    READ 13, BETAC
    READ 13, (DELB(I),I=1,NBEAM)
    READ 13, (T(I),I=1,NBEAM)
    B=244.0
    ALPH1=45.0
    ALPH2=45.0
    ERROR=0.05
    PRINT 6,B
    PRINT 4,ALPH1,ALPH2
    PRINT 10, BETA2
    PRINT 9
    PRINT 11,(DELB(I),I=1,NBEAM)
    PRINT 12, ERROR
    ALPH1=ALPH1*.01745
    ALPH2=ALPH2*.01745
    BETA2=BETA2*.01745
    DELB(1)=DELB(1)*.01745
    DELB(2)=DELB(2)*.01745
    DELB(3)=DELB(3)*.01745
    BETAC=BETAC*.01745
    DO 100 I=1,NBEAM
    B1(I)=BETAC+ATANF((SINF(DELB(I))/CCSF(DELB(I)))/COSF(ALPH1))
    A1(I)=ATANF(TANF(ALPH1)*COSF(BETAC-B1(I)))
    DUMA(I)=COSF(A1(I))/SINF(A1(I))
    DUMB=COSF(ALPH2)/SINF(ALPH2)
    E(I)=DUMA(I)*SINF(B1(I))+DUMB*SINF(BETA2)
100  CONTINUE
    TE(1,1)=T(1)*(1.0+ERROR)
    TE(2,1)=T(2)*(1.0-ERROR)
    TE(3,1)=T(3)*(1.0+ERROR)
    TE(1,2)=T(1)*(1.0-ERROR)
    TE(2,2)=T(2)*(1.0+ERROR)
    TE(3,2)=T(3)*(1.0-ERROR)

```

Program II.

```

      IF (NBEAM-3) 800,900,900
800  P(1)=E(1)*(DUMA(2)*COSF(B1(2))+DUMB*COSF(BETA2))
      P(2)=E(2)*(DUMA(1)*COSF(B1(1))+DUMB*COSF(BETA2))
      Q(1)=E(1)*(DUMA(2)*SINF(B1(2))+DUMB*SINF(BETA2))
      Q(2)=E(2)*(DUMA(1)*SINF(B1(1))+DUMB*SINF(BETA2))
      GO TO 801
900  P(1)=E(1)*(DUMA(3)*COSF(B1(3))-DUMA(2)*COSF(B1(2)))
      P(2)=E(2)*(DUMA(1)*COSF(B1(1))-DUMA(3)*COSF(B1(3)))
      P(3)=E(3)*(DUMA(2)*COSF(B1(2))-DUMA(1)*COSF(B1(1)))
      Q(1)=E(1)*(DUMA(3)*SINF(B1(3))-DUMA(2)*SINF(B1(2)))
      Q(2)=E(2)*(DUMA(1)*SINF(B1(1))-DUMA(3)*SINF(B1(3)))
      Q(3)=E(3)*(DUMA(2)*SINF(B1(2))-DUMA(1)*SINF(B1(1)))
801  CONTINUE
      DO 200 L=1,2
      IF (ITER) 802,802,971
802  CONTINUE
      IF (NBEAM-3) 950,960,960
950  SUMNU=P(1)/TE(1,L)-P(2)/TE(2,L)
      SUMDE=Q(1)/TE(1,L)-Q(2)/TE(2,L)
      GO TO 970
960  SUMNU=0.0
      SUMDE=0.0
      DO 201 I=1,3
      SUMNU=SUMNU+P(I)/TE(I,L)
      SUMDE=SUMDE+Q(I)/TE(I,L)
201  CONTINUE
970  CONTINUE
      PHIF(L)=-ATANF(SUMDE/SUMNU)
      GO TO 803
971  CONTINUE
C    INITIALIZE PHI EQUALS 0 DEGREES REFERENCED TO THE BASE LINE B.
      PHIMIN=0.0
      PHIMAX=180.0
      PHIMIN=PHIMIN*.01745
      PHIMAX=PHIMAX*.01745
      PHIMID=(PHIMIN+PHIMAX)/2.0
C    SET UP COUNTER
      II=C
1040 II=II+1
      IF (II-20)1011,1011,1000
1011 H1MID=DUMA(2)*SINF(PHIMID+B1(2))+DUMB*SINF(PHIMID+BETA2)
      H2MID=DUMA(1)*SINF(PHIMID+B1(1))+DUMB*SINF(PHIMID+BETA2)
      DELTA2=(TE(2,L)/TE(1,L))*(H1MID/H2MID)*(E(1)/E(2))-(H1MID/H2MID)
      I**RHC
      IF (DELTA2) 1030,1000,1050
1030 PHIMAX=PHIMID
      PHIMID=(PHIMID+PHIMIN)/2.0
      IF (ABSF(PHIMAX-PHIMID)-.001745) 1000,1000,1040
1050 PHIMIN=PHIMID
      PHIMID=(PHIMID+PHIMAX)/2.0
      IF (ABSF(PHIMIN-PHIMID)-.001745) 1000,1000,1040
1000 CONTINUE
      PHIE(L)=PHIMID
803  CONTINUE
200  CONTINUE
      PHIE(1)=PHIE(1)/.01745
      PHIE(2)=PHIE(2)/.01745
      PRINT 18, PHIE(1),PHIE(2)
      GO TO 700
      END

```

<u>Variable Names</u>	<u>Equivalent</u>
ITER	Control flag for iteration; 1 → Yes and 0 → No: should be 0 for NBEAM = 3.
NBEAM	No. of beams used in multiple- beam detector
P(I)	$P_{ic}$ of $P_{i\ell}$ (Eq. 12a and 14a)
PHI(I)	$\phi$
PHIE(I, J)	$\phi, \epsilon^{*1}$
Q(I)	$Q_{ic}$ or $Q_{i\ell}$ (Eq. 12a and 14a)
T(I)	$\tau_i$
TE(I, J)	$\tau_i, \epsilon$
V(I)	$V_i$
VE(I, J)	$V_i, \epsilon^{*1}$

## APPENDIX B

### DETAILED DERIVATIONS OF EQUATIONS

From Sideview I in Figure 3, one obtains

$$H_i = \overline{B'C'} \sin \alpha'_2 = \overline{A'C'} \sin \alpha'_{1i} \quad (B-1)$$

and

$$\overline{A'B'} = b \sin \phi = \overline{B'C'} \cos \alpha'_2 + \overline{A'C'} \cos \alpha'_{1i} \quad (B-2)$$

Substituting (B-1) in (B-2) and solving for  $H_i$ , one obtains equation (1).

$$H_i = \frac{b \sin \phi}{\cot \alpha'_{1i} + \cot \alpha'_2} \quad (1)$$

1. Superscript \* indicates that the argument J stands for  $J^{\text{th}}$  pattern of errors in transit times.

From triangles  $A'C'M'$  and  $A''C''M''$ , respectively, one obtains

$$\cot \alpha'_{1i} = \frac{\overline{A'M'}}{H_i}$$

and

$$\cot \alpha_{1i} = \frac{\overline{A''M''}}{H_i}$$

Hence,

$$\cot \alpha'_{1i} = \cot \alpha_{1i} \frac{\overline{A'M'}}{\overline{A''M''}} \quad (B-3)$$

One further notices that

$$\overline{A'M'} = \overline{AH}, \quad \overline{A''M''} = \overline{AC} \quad (B-4)$$

and

$$\frac{\overline{AH}}{\overline{AC}} = \sin(\text{angle } ACH) = \sin(\phi + \beta_{1i}) \quad (B-5)$$

Substituting (B-4) and (B-5) in (B-3) yields the equation (2).

$$\cot \alpha'_{1i} = \cot \alpha_{1i} \sin(\phi + \beta_{1i}) \quad (2)$$

Similarly, equation (3) can be derived.

We now turn to the derivation of equation (12). Substituting equations (4) and (8) into (11), one obtains

$$\begin{aligned} & \frac{E_1}{\tau_1} [\cot \alpha_{12} \sin(\phi + \beta_{12}) + \cot \alpha_2 \sin(\phi + \beta_2)] \\ & - \frac{E_2}{\tau_2} [\cot \alpha_{11} \sin(\phi + \beta_{11}) \\ & + \cot \alpha_2 \sin(\phi + \beta_2)] = 0, \end{aligned} \quad (B-6)$$

where

$$E_i = \cot \alpha_{1i} \sin \beta_{1i} + \cot \alpha_2 \sin \beta_2. \quad (B-7)$$

Expanding out the sines of multiple angles in (B-6) and then dividing the resulting expression by  $\sin \phi$  yields

$$\begin{aligned} & \frac{E_1}{\tau_1} [\cot \alpha_{12} (\cos \beta_{12} + \sin \beta_{12} \cot \phi) \\ & + \cot \alpha_2 (\cos \beta_2 + \sin \beta_2 \cot \phi)] \\ & - \frac{E_2}{\tau_2} [\cot \alpha_{11} (\cos \beta_{11} + \sin \beta_{11} \cot \phi) \\ & + \cot \alpha_2 (\cos \beta_2 + \sin \beta_2 \cot \phi)] = 0. \end{aligned}$$

Factoring out  $\cot \phi$  in the above equation will then yield equation (12). The derivation of equation (14) from (13) follows exactly the same procedure as for equation (12) except that one might first rewrite equation (13) as

$$V_1(H_2 - H_3) + V_2(H_3 - H_1) + V_3(H_1 - H_2) = 0$$

before substitution of equations (4), (8), and (9).

We now derive equations (14b) and (14c). Referring to Figure 43, the difference in azimuth angles of  $i^{\text{th}}$  beam  $\overline{AA_i}$  and the optical axis of fan detector  $\overline{AA_o}$  is given by the angle  $\angle A_i A A_o = \beta_{1i} - \beta_{10}$ .

On the other hand, the angle between  $i^{\text{th}}$  beam and the optical axis measured on the beam fan is given by the angle  $\angle A_i' A A_o = \Delta \beta_{10}$ . Furthermore, the angles  $\angle A_i A A_o$  and  $\angle A_i' A A_o$  are related by

$$\frac{\tan(\beta_{1i} - \beta_{10})}{\tan \Delta \beta_{10}} = \frac{\overline{AC}}{\overline{AB}} = \frac{\overline{A'A_i}}{\overline{A'F}} = \cos \alpha_{10}. \quad (B-8)$$

Solving the above equation for  $\beta_{1i}$  gives equation (14b). The elevation angles for the  $i^{\text{th}}$  beam and the optical axis,  $\alpha_{1i}$  and  $\alpha_{10}$ , are related by

$$\frac{\tan \alpha_{1i}}{\tan \alpha_{10}} = \frac{\overline{A'E}}{\overline{A'F}} = \frac{\overline{AB}}{\overline{AG}} = \cos(\beta_{1i} - \beta_{10}) \quad (B-9)$$

Solving the above equation for  $\alpha_{1i}$  gives equation (14c).

## REFERENCES

1. Fisher, M. J., and Krause, F. R.: The Crossed Beam Correlation Technique. J. Fluid Mechanics, No. 28, 1967.
2. Stephens, J. B., Sandborn, V. A., and Montgomery, A. J.: Remote Wind Detection With the Cross-Beam Method at Tower Heights. Paper presented at 3rd Nat. Conf. on Aerospace Meteorology. (New Orleans, La.), May 1968.
3. Jayroe, R. R., Jr., and Su, M. Y.: Optimum Averaging Times of Meteorological Data with Time Dependent Means. Paper presented at 3rd Nat. Conf. on Aerospace Meteorology. (New Orleans, La.), May 1968.
4. Su, M. Y.: Statistical Error and Required Averaging Time for Evaluating Cross-Correlation of Crossed-Beam Data. Nortronics-Huntsville, Tech. Memo. M-794-8-362, May 24, 1968.
5. Daniels, G. E., Scoggins, J. R., and Smith, O. E.: Terrestrial Environment (Climatic) Criteria Guidelines for Use in Space Vehicle Development, 1966 Revision. NASA TM X-53328, May 1, 1966.

# REMOTE WIND DETECTION WITH THE CROSS-BEAM METHOD AT TOWER HEIGHTS

By

J. Briscoe Stephens,<sup>1</sup>  
Virgil A. Sandborn,<sup>2</sup> and A. J. Montgomery<sup>3</sup>

## ABSTRACT

A technique for the remote detection of atmospheric winds from fluctuations in scattered sunlight has been developed using a ground-based cross-beam detection system. Winds measured with anemometers on a meteorological tower were compared with these optical measurements of the tower.

The validity of the cross-beam concept has previously been established in subsonic and supersonic jets by comparing velocity components, turbulence scales, and temporal correlation functions that had been measured with both cross beam and hot wires. Experimental results presented here were obtained in the atmosphere. The atmospheric experiments differ from wind tunnel experiments in that: (1) A passive optical detection is employed using locally scattered sunlight instead of man-made light sources. (2) Contrary to the wind tunnel experiments, the convective velocity may vary during the period of observation. (3) The smallest local beam modulation that can be retrieved by digital cross correlation is set by temporal trends in the statistics of wind fluctuations (the non-stationarity of the data) and not by the maximum observation time.

## I. INTRODUCTION

The need for more refined and flexible methods of obtaining an atmospheric wind profile has prompted the development of a remote-sensing technique, optical in nature, known as the cross-beam method. Successfully used by Fisher and Krause [1] in their

wind tunnel measurements of turbulence, the method is now being adapted to the more variable and valuable task of measuring turbulence in the uncontrolled environment of the atmosphere.

Although the theory of the atmospheric cross-beam method, its problems, procedures and results, are also discussed, much of this paper is concerned with adjusting this technique so that it will yield valid measurements in the atmosphere. Thus far, the results are most encouraging for future development.

## II. CROSS-BEAM TECHNIQUE

The cross-beam optical measurement of turbulence is based on the concept that when turbulence eddies pass through a beam of light, they produce fluctuations in the intensity of the beam. These fluctuations are probably ascribable largely to absorption or scattering of the light occasioned by the presence of tracer like water vapor, dust, and air pollutants in the atmosphere. The movement of the tracer is assumed to be directly related to the mass motion of the atmosphere. The fluctuations of light intensity are detected, and related to the turbulence motion by statistical correlation. Fisher and Krause [1] have demonstrated that the cross-beam technique can measure convective speeds, turbulence scales, and turbulence correlation in an air flow.

The measurement of intensity fluctuation along two small-diameter optical paths (which are called beams) can be used to determine the speed of a turbulence disturbance. The evaluation of the convective wind speed is of specific importance in the

---

<sup>1</sup>Aero-Astroynamics Laboratory, Marshall Space Flight Center, Alabama.

<sup>2</sup>Colorado State University, Ft. Collins, Colorado.

<sup>3</sup>IIT Research Institute, Chicago, Illinois.

atmosphere, because the turbulence convective speed is nearly equal to the mean wind speed. The simplified sketch shown in Figure 1 demonstrates the concept of the cross-beam method. As the test object passes through each beam, the light intensity of each varies in an identical manner. The velocity of the test object can be determined by measuring the elapsed time of light intensity traces and knowing the distance between the two beams. Space resolution of the cross-beam system is obtained by placing the plane of the two beams such that they intersect only at one common stream line between the two beams. For example, one could place the B beam (Fig. 1) at a right angle to the direction of the A beam. With beam B normal to beam A, there is only one path that a test subject traveling normal to the beams could take and pass through both beams. In general, it is impossible to visually identify corresponding fluctuations from two detector traces when the fluctuations are due to turbulence. Thus, it is necessary to use a time-delay correlation technique [2] to determine the transit time between the two beams. The signal from detector B (Fig. 1) would be delayed in time and compared to the signal from detector A. The best match between signals A and B occurs when the delay time just equals the transit time for the disturbance to move from beam A to beam B. This comparison can be obtained mathematically by computing the correlation coefficient  $R(\tau)$ , which is given by

$$R(\tau) = \frac{1}{T} \int_0^T i_A(t) \cdot i_B(t - \tau) dt \quad (1)$$

where  $i_A$  and  $i_B$  are the instantaneous, fluctuating intensity,  $T$  is the total integration time (length of the record used),  $t$  is the time from the start of the record, and  $\tau$  is the delay time. The correlation  $R(\tau)$  will be a maximum for the value of the delay time,  $\tau$ , that corresponds to the convective speed. The normalized magnitude of  $R(\tau)$  gives the degree of match between the two signals. The details of the evaluation of the correlation curves are given by Jayroe and Su [3].

For the measurement of convective speeds in the atmosphere, two ground-based detectors (Fig. 2) are employed. The two beams are parallel to the plane of the figure, although detector A would be set out of the plane and detector B would be set back of the plane of the figure. The light source for the detectors was scattered sunlight. The wind speed normal to the plane of the figure is measured in the area of common intersection of the two beams.

Details of the detectors used are shown in Figure 3. The radiation input to the telescope was chopped to prevent the 1/f noise from being the dominant noise source at low frequencies. While the output signals can have a bandpass between 0.01 to 300.0 cycles per second, the data were filtered to a bandpass from 0.01 to 3.0 cycles per second.

### III. APPLICATION TO ATMOSPHERIC MEASUREMENTS

The measurement of atmospheric winds, as opposed to wind tunnel measurements, is formidable because additional variables are encountered in the atmosphere. To apply the cross-beam technique to atmospheric measurements, the detectors must be capable of retrieving the signatures of the turbulence eddies in terms of intensity fluctuations, and the statistical techniques must be capable of isolating the desired fluctuations for varying atmospheric conditions. Thus, the requirements of detection are:

1. The cross-beam detection system must provide a dynamic range compatible with atmospheric intensity fluctuations.
2. The cross-beam detection system must have a detector noise level less than the signal from atmospheric fluctuations.
3. The cross-beam detection system must have a frequency response that includes the primary frequencies from the turbulence power spectrum.

The requirements for the statistics are:

1. The variability in wind velocity must be taken into account.
2. The effect of nonstationarity trends (varying of means and variance) in the data must be kept to a minimum.
3. The validity of the resultant correlation curve must be established.

The current cross-beam detectors were not capable of providing intelligence over the entire range of atmospheric intensity fluctuations. A passive source (scattered sunlight) was used in these experiments; this means that the level of intensity of the source of the radiation will vary as the meteorological conditions change. If clouds enter the field of view

**MODEL  
CORRELATION  
EXPERIMENT**

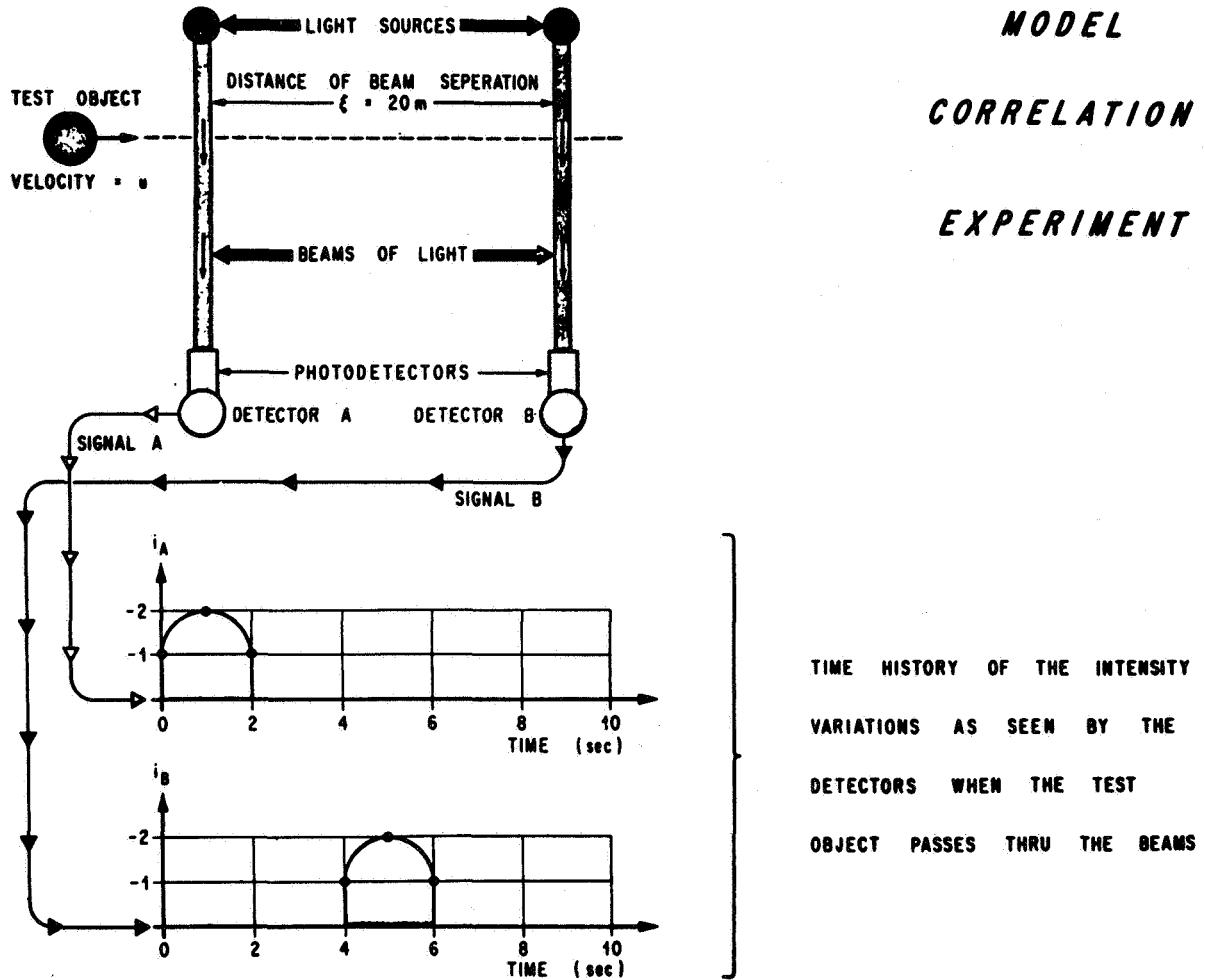


FIGURE 1. CROSS BEAM METHOD CONCEPT

of the detectors, they produce a large fluctuation in the atmospheric intensity level which drives the detector amplifiers into saturation. When the gain of the amplifiers was reduced, the small fluctuations in intensity caused by the turbulence eddies could not be retrieved efficiently. To circumvent this obstacle, data were collected only under clear skies.

To ascertain whether the signal obtained from the detection system reflected actual fluctuations in the atmospheric radiation rather than detector noise, a light calibration cell was placed in front of the telescope of the detector, and calibration data were recorded. From the collected calibration data and the collected atmospheric data, the power spectrum in Figure 4 was obtained. From this power spectrum, it may be inferred that the power from the atmospheric fluctuations is about 20 dB higher than the noise over the frequency range from 0.01 to 2 cps.

The power spectrum shown in Figure 5 illustrates that the frequency range from 0.01 to 1 cps contains the major portions of the power reflecting fluctuations in the atmospheric radiation. Since the cross-beam detection system permits data collection over the range of 0.01 to 3 cps, it can be concluded that the signal reflects both the atmospheric fluctuation in radiation and the primary power due to these fluctuations.

To reduce the complexity of analysis introduced by varying wind velocity, the components — varying speed and varying direction — were isolated and treated separately. The correlation curve obtained from cross-beam measurements was found to be effectively a first order probability curve. The analysis of varying wind speed can thus be reduced to a comparison of the cross-beam results with the first order probability curve obtained from the

THE LIGHT SOURCE IS SCATTERED SOLAR RADIATION (PASSIVE SOURCE)

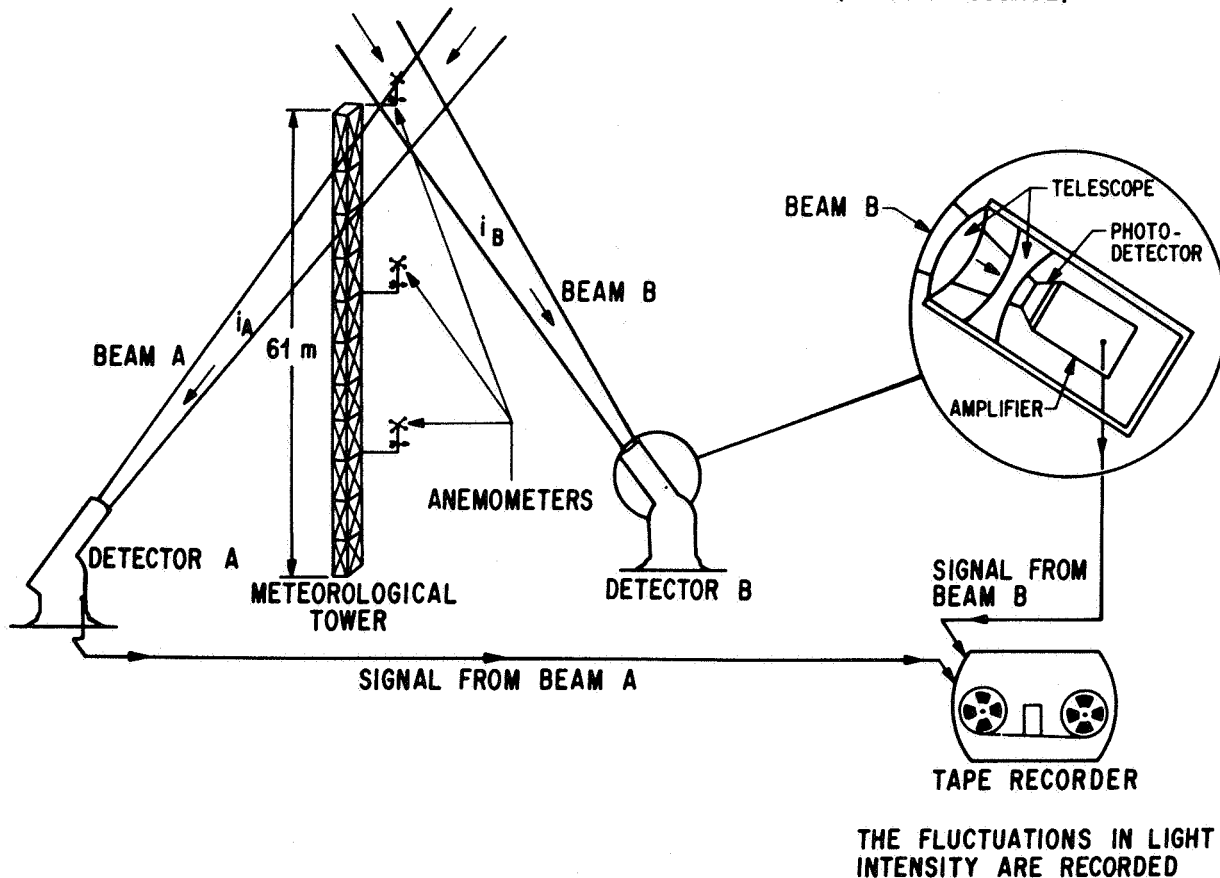


FIGURE 2. CROSS-BEAM DETECTION SYSTEM

anemometer measurements of wind speed. A more subtle error is introduced by a change in wind direction, in that the change produces a change in transit height (the altitude, measured from the ground, at which the turbulence eddies are passing through the two beams). To alleviate this problem and achieve reliable results with less than ten percent error, data are collected only when the wind direction remains within  $\pm 20$  degrees of the normal to the plane of the beams.

To evaluate the non-stationary characteristics of the atmospheric winds, an error criterion, accompanied by a weighting procedure, was established by Jayroe and Su [3]. This error criterion permits a choice of the data segment and the data reduction method, which makes the segment of data behave as if it were stationary, thus permitting the data's evaluation.

Intensity fluctuations can always produce a correlation curve, but not all correlation curves thus obtained have significance. To establish a standard of validity, the statistical error is used. Only where the correlation curve is greater than the statistical error was it said to have a statistical significance [3]. This criterion results in a greater than ninety percent probability that the correlation results are due to intensity fluctuations common to both beams.

#### IV. FIELD TEST PROCEDURES

Preliminary field tests of the ground-based cross-beam system, at a 61-meter meteorological tower, were conducted at the Colorado State University meteorological field site in the North Platte River Valley. This site in northeastern Colorado is about

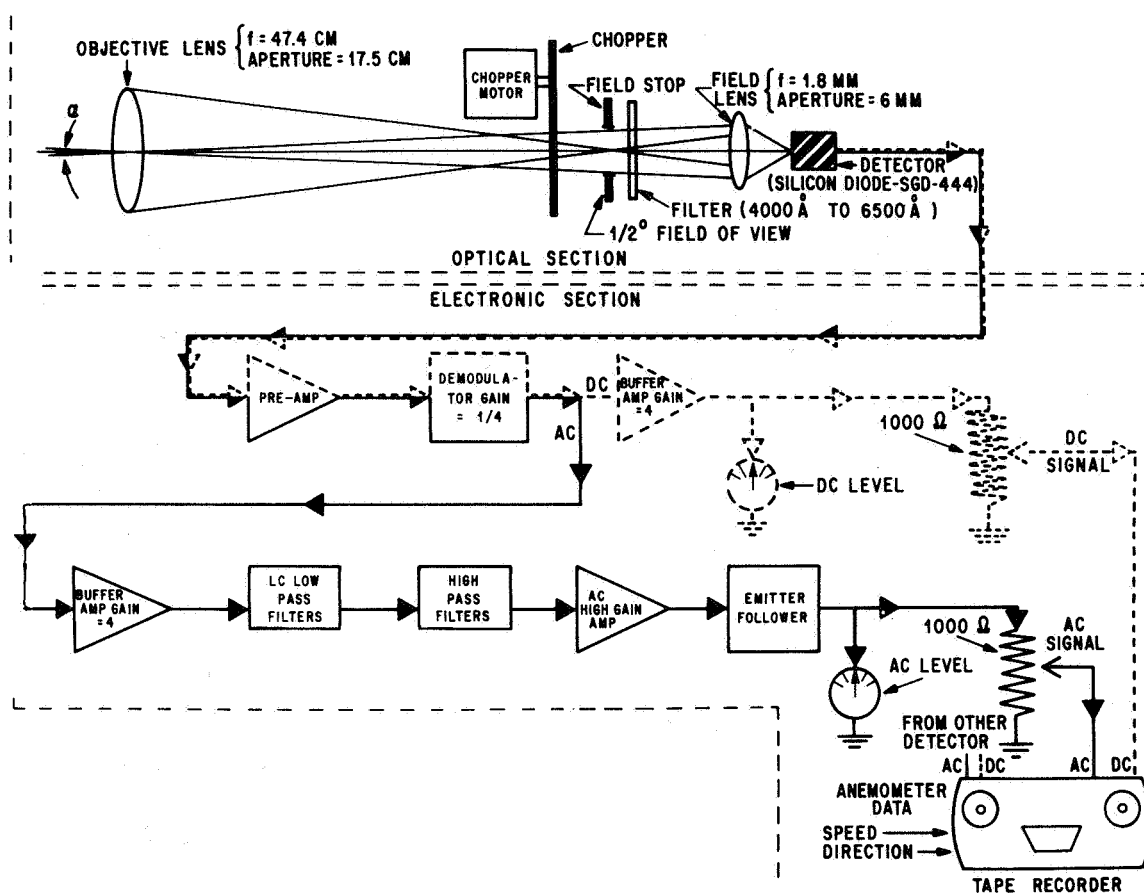


FIGURE 3. BLOCK DIAGRAM OF THE DETECTION STAGE

fifteen miles east of the first major pressure rise of the Rocky Mountains (Fig. 6). This semi-arid locale was selected because it combines clear skies with winds which cover a wide range of speeds (1 m/sec to 25 m/sec) and remain in a semi-constant direction.

An absence of the intensity fluctuations was never observed during these experiments, but the magnitude and frequency of these fluctuations did vary both as a function of the time of day and from day to day. Figure 7 shows a typical trace of the fluctuations of intensity for a wind speed of approximately 15 m/sec. The major problem experienced during these experiments, even under clear skies, was the variation in the level of intensity fluctuations. The limits of the levels of acceptable intensity fluctuation as set by the amplifier gain are as follows:

1. When the level of fluctuation is very small, then the signal is not well enough defined to be retrievable when it is correlated.

2. When the level of fluctuation is large, then any increase in the signal will drive the system into saturation.

Over a 15 to 30-minute interval, the level of fluctuations will generally vary by an order of magnitude; and unless great care is taken in setting the gain, the signal will exceed the limits of the system.

Before the data were digitally reduced at MSFC, they were subjected to two field analog tests. An oscillograph (time history of the signal) of the data

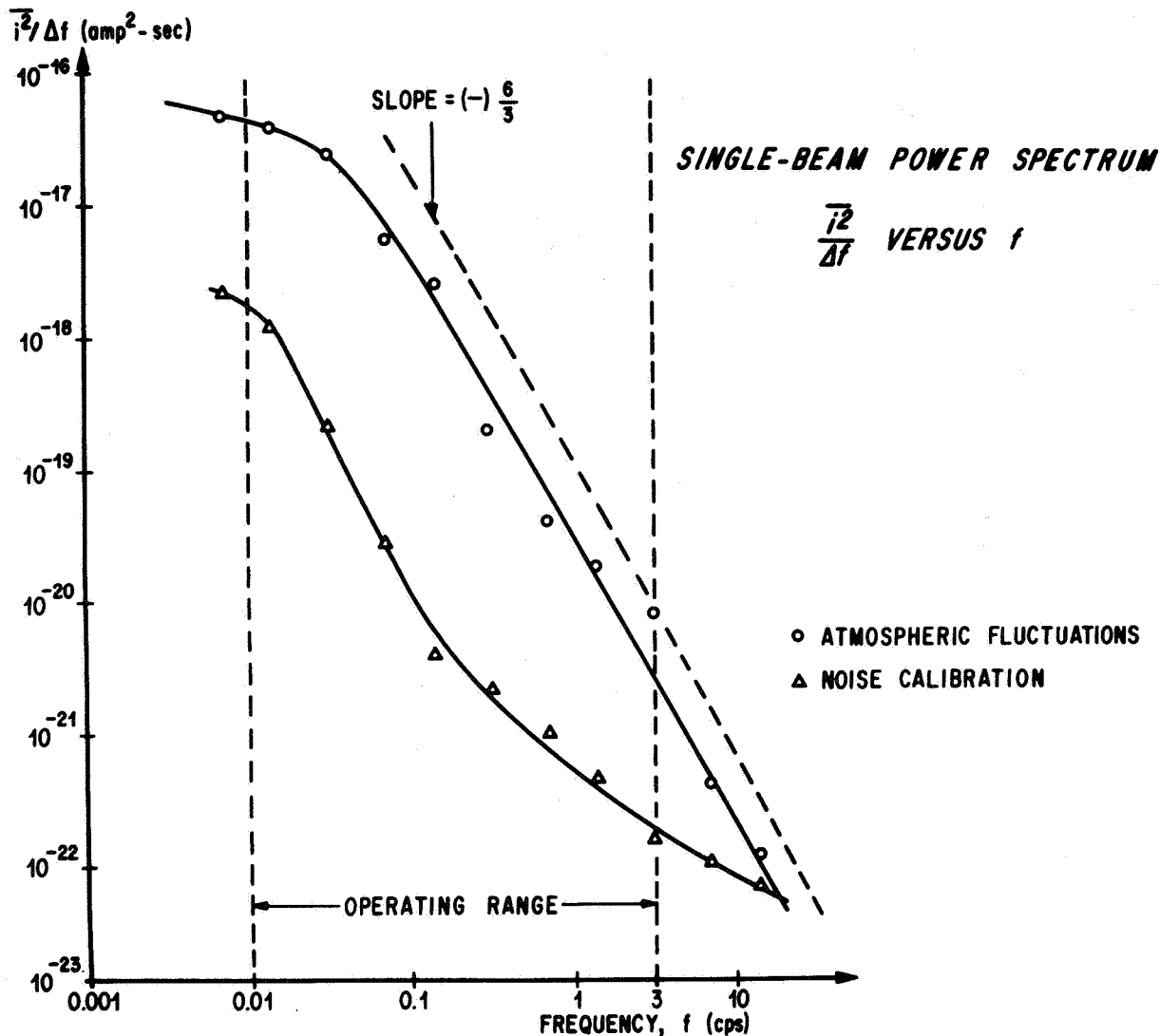


FIGURE 4. POWER SPECTRUM CALIBRATION AND ATMOSPHERIC DATA

was made in the field to determine whether the data remained within the system's limits. If the data were acceptable, the Princeton analog correlator was then used to obtain an estimate of the results.

## V. RESULTS

In analyzing the results of these experiments, the first consideration was the validity of the cross-

beam concept in the atmosphere. The second consideration was to corroborate the capabilities of the cross-beam technique to measure atmospheric wind with the anemometer data.

The cross-beam model required that when the two beams intersect in space the maximum correlation between the two signals must occur at a zero time lag. That is, when an intensity fluctuation occurs in the common volume formed by the intersection of the two beams, both detectors will basically sight this fluctuation simultaneously.

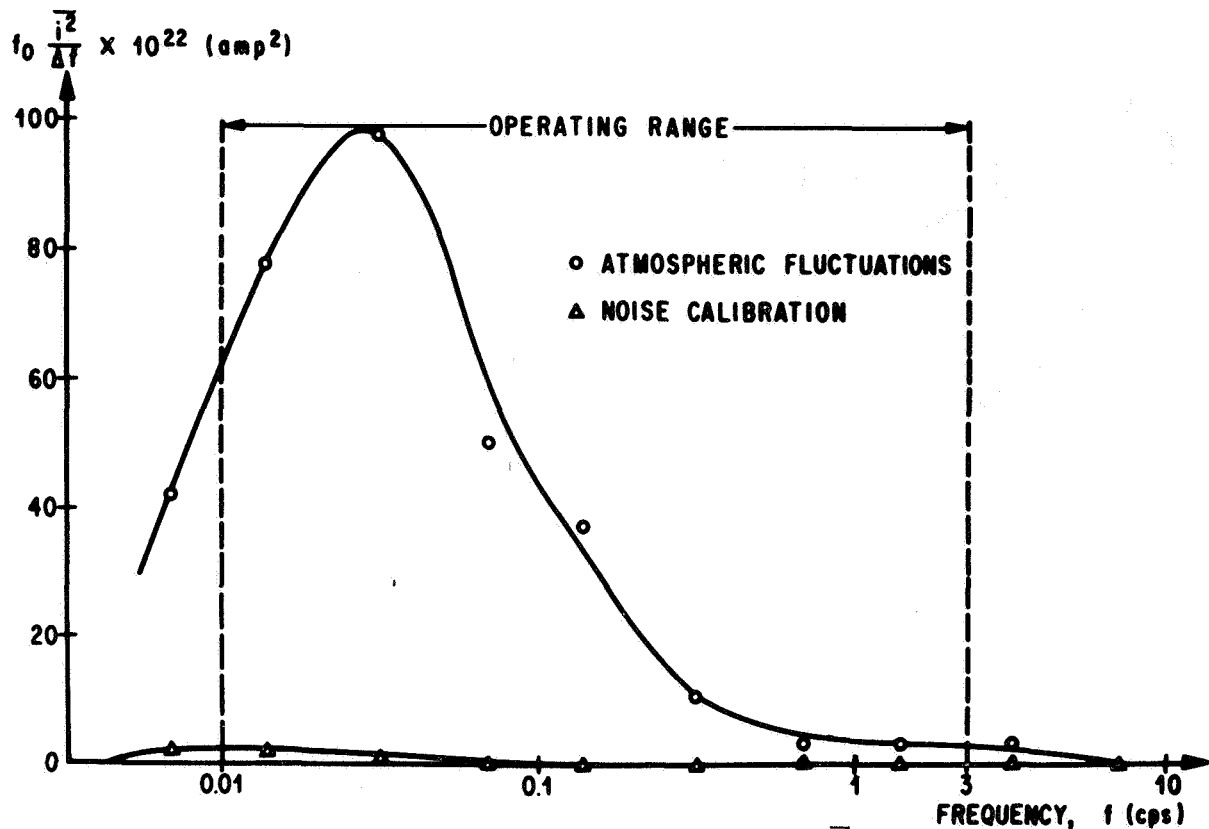


FIGURE 5. SINGLE-BEAM POWER SPECTRUM  $f_0 \frac{\bar{i}^2}{\Delta f}$  VERSUS  $f$

Data obtained from a zero beam separation experiment were reduced with an analog correlator (Fig. 8). The initial reaction to this result is to accept it as a verification of the model. When the data used to obtain the above result were reduced on the computer where the confidence limits could be readily obtained, Figure 9 resulted. One observes that the peak at zero time delay is less than the statistical error. This means that there is less than a ninety percent probability that the result is significant; therefore, this result is rejected. This is an implication that the result might be erroneous. Thus, a peak in the correlation curve at zero time lag does not in itself fulfill the qualification demands of the cross-beam model; for this peak must also be greater than the statistical error. The correlation curve for a second example of a zero beam separation is shown in Figure 10. The peak of the correlation at zero time delay in this example is greater than the statistical error, and is thus an acceptable verification of the cross-beam model.

The cross-beam model further requires that no significant correlation be found outside of the common volume due to the intersection of the two beams. When the two beams are pointing in the opposite directions, for instance, there should be no significant correlation between the two signals. Results of such a test showed that the peaks in the correlation curve were always less than the statistical error, thereby eliminating their statistical significance. It may be concluded, therefore, that the cross-beam model is applicable to the atmosphere.

Comparisons of cross-beam measurements with those of the anemometer have given positive results. The cross-beam technique, when applied to wind speed measurements over the range of 1 m/sec to 20 m/sec, produces significant correlation peaks at about the same wind speed as the most probable velocity measured by the anemometer. Figures 11 through 14 show four examples of this relationship. The histograms in the curves represent the

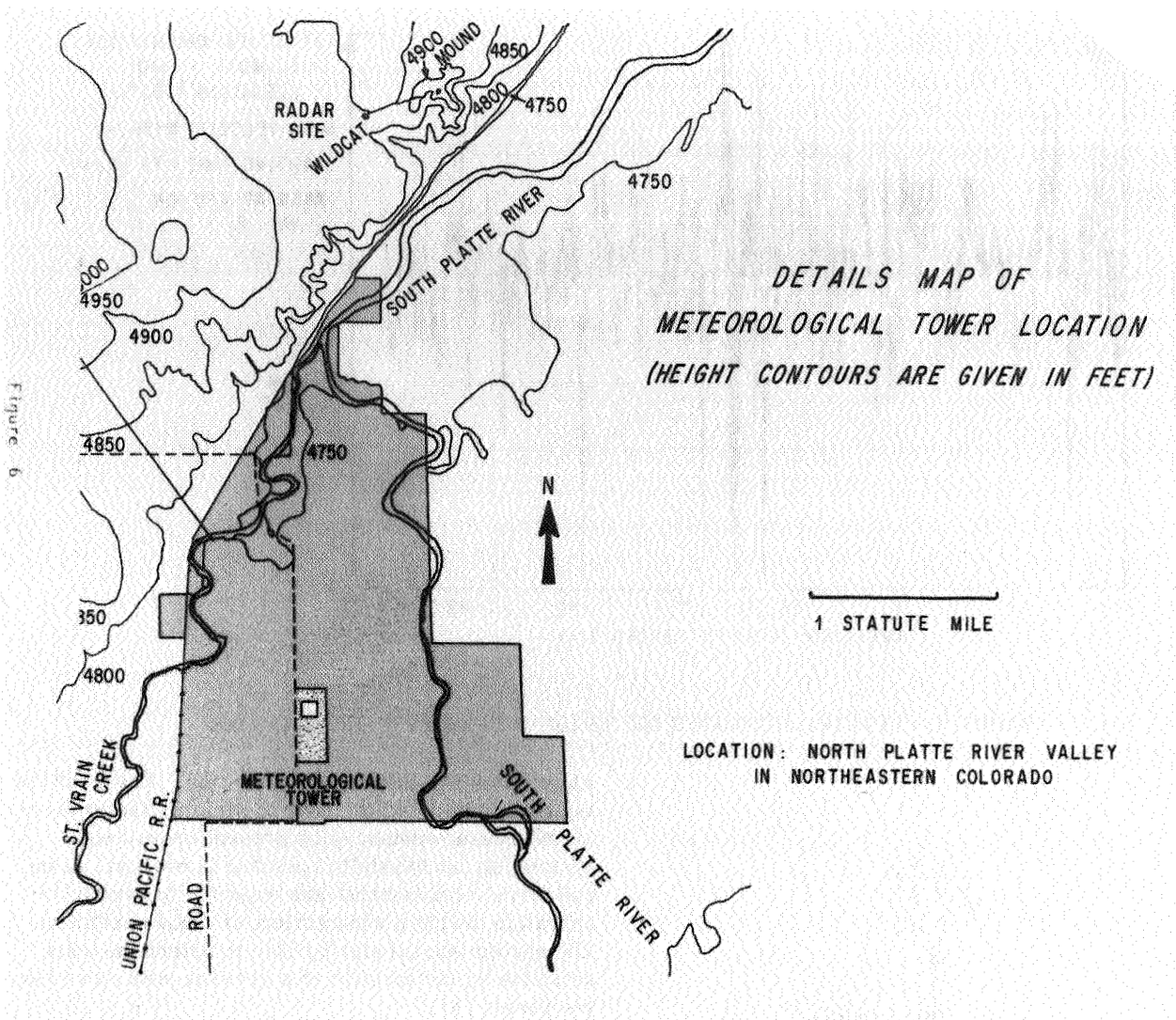


FIGURE 6. COLORADO STATE UNIVERSITY METEOROLOGICAL FIELD SITE

first order probability density of the wind speeds measured by the anemometer during the period of cross-beam observation. These four examples indicate that the cross-beam method can measure wind speeds normally experienced in the lower atmosphere. In cases where the winds were within  $\pm 25$  degrees of the normal to the plane of the beams, and when at least 45 minutes of the data was collected under clear skies, the cross-beam results were both statistically significant and in agreement with anemometer results.

## VI. CONCLUDING REMARKS

The present feasibility studies demonstrate that the cross-beam system can remotely measure convective speeds in the atmosphere. Wind speeds in the range from 1 m/sec to 20 m/sec have been evaluated. The results from Figure 11 through 14 have been summarized in Table I. Winds at altitudes up to 122 meters have been remotely measured with the system. The present studies were limited to

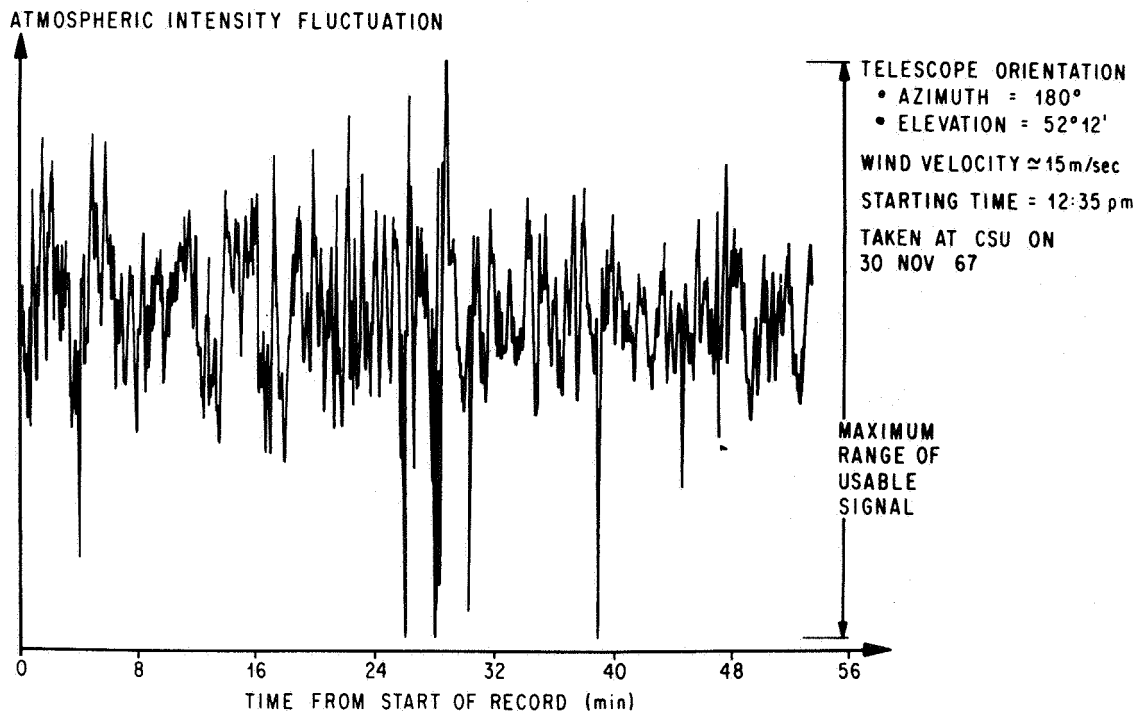


FIGURE 7. TYPICAL ATMOSPHERIC LIGHT INTENSITY FLUCTUATIONS

clear skies and known wind direction. These limitations were imposed in order to simplify the evaluation of the measurements. The present cross-beam system has successfully operated in overcast skies, and further refinements are expected to permit its operation during a wide variety of cloud conditions. The system should also be able to determine wind direction by the addition of a detector with more than two beams [4].

During the course of the feasibility studies, several beam intersection angles and separation distances were used. No clear evidence of a preferred separation distance or intersection angle was found. The optical bandpass is also a variable, which may increase the flexibility of atmospheric cross-beam operation.

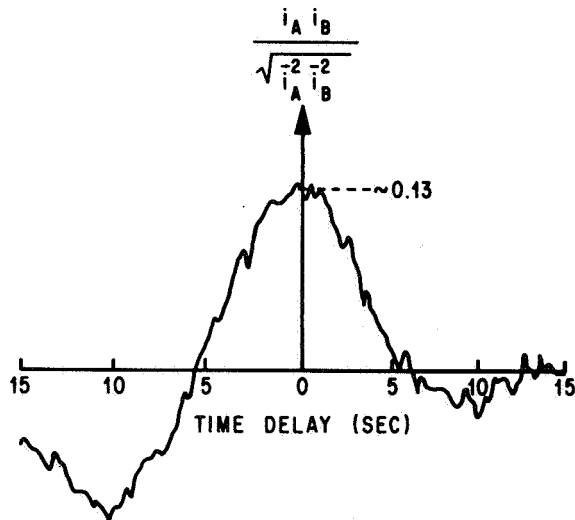


FIGURE 8. ZERO BEAM SEPARATION REDUCED WITH ANALOG CORRELATOR

## REFERENCES

1. Fisher, M. J., and Krause, F. R.: The Crossed Beam Correlation Technique. *J. Fluid Mech.*, No. 28, 1967, pp. 705-717.

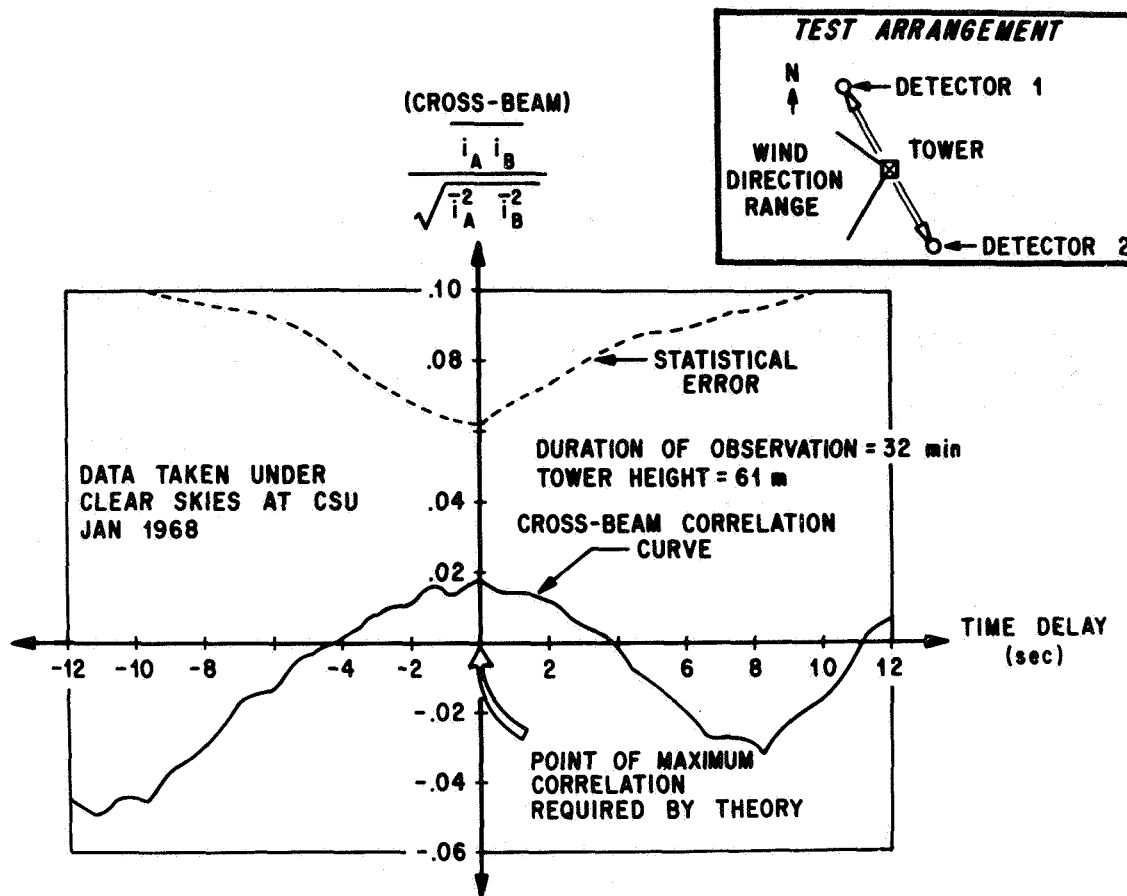


FIGURE 9. ZERO BEAM SEPARATION — UNACCEPTABLE RESULT

2. Bendat, J. S., and Piersol, A. G. P.: Measurements and Analysis of Random Data. John Wiley and Sons, Inc., 1966.
3. Jayroe, R. R., and Su, M. Y.: Optimum Averaging Time of Meteorological Data with Time-Dependent Means. Presented at 3rd National Conference on Aerospace Meteorology, May 1968.
4. Su, M. Y., Stephens, J. B., and Phillips, M.: The Theory for the Determination of Wind Velocity and the Associated Altitude by the Cross-Beam Technique. NASA TM X-53782, 1968.

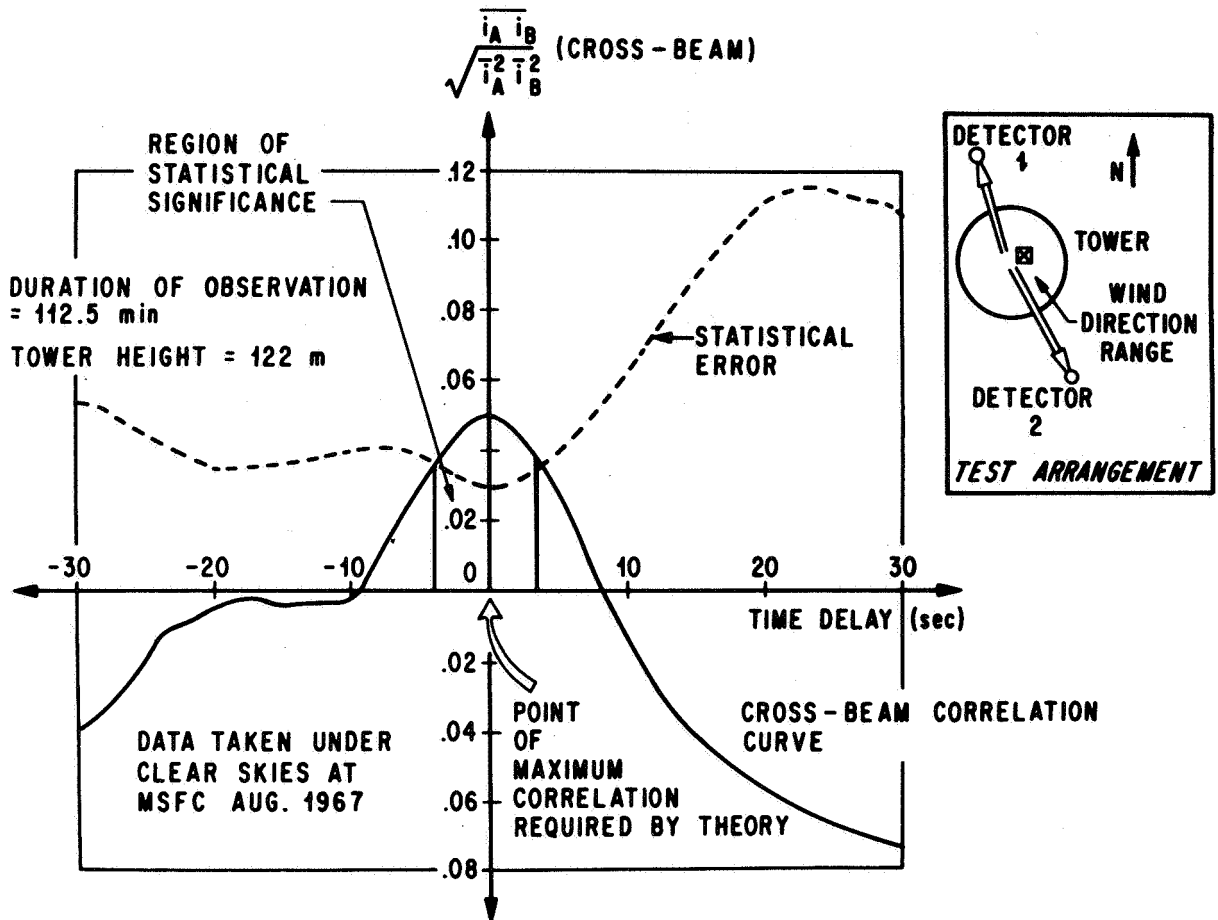
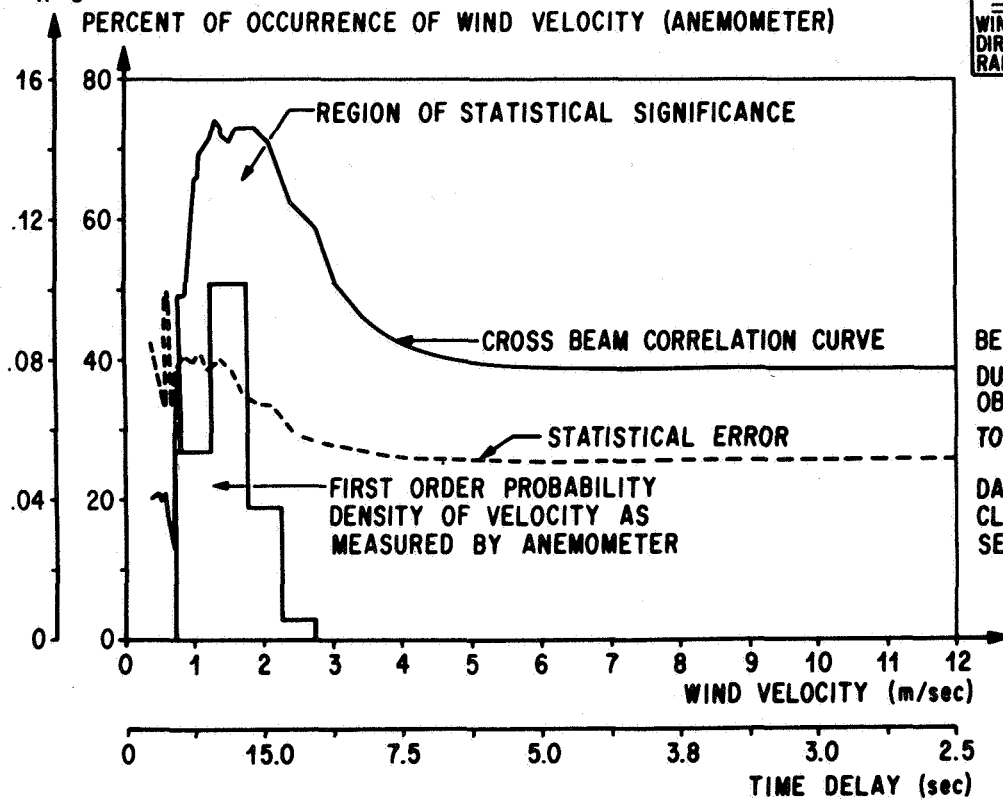
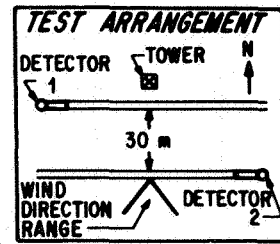


FIGURE 10. ZERO BEAM SEPARATION — ACCEPTABLE RESULT

(CROSS-BEAM)

$$\frac{\overline{i_A i_B}}{\sqrt{i_A^2 i_B^2}}$$



BEAM SEPARATION = 30m  
DURATION OF OBSERVATION = 1 hr 11min  
TOWER HEIGHT = 61 m  
DATA TAKEN UNDER CLEAR SKIES AT CSU SEPT 67

FIGURE 11. LIGHT WIND VELOCITY (3 mph)

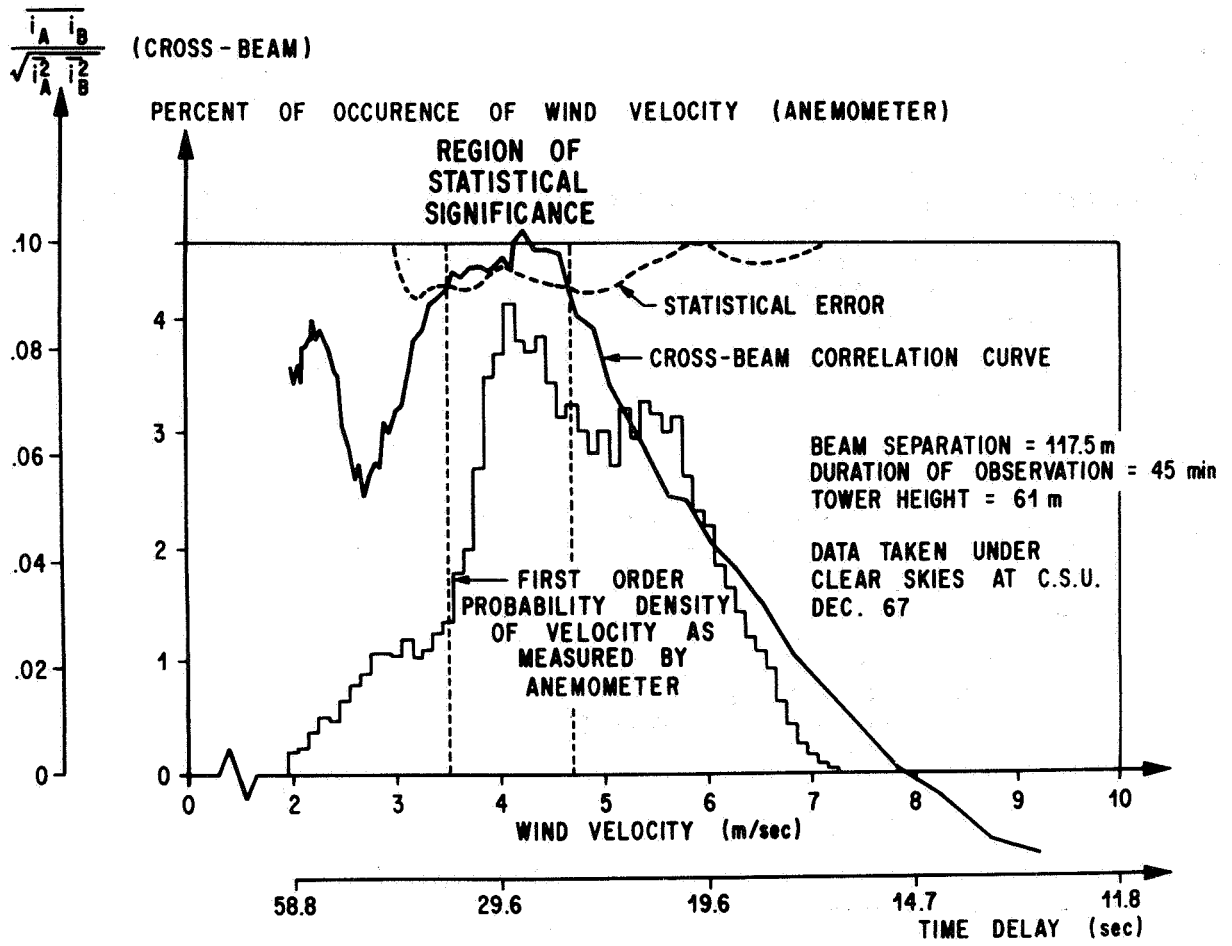


FIGURE 12. CROSS-BEAM AND ANEMOMETER COMPARISONS

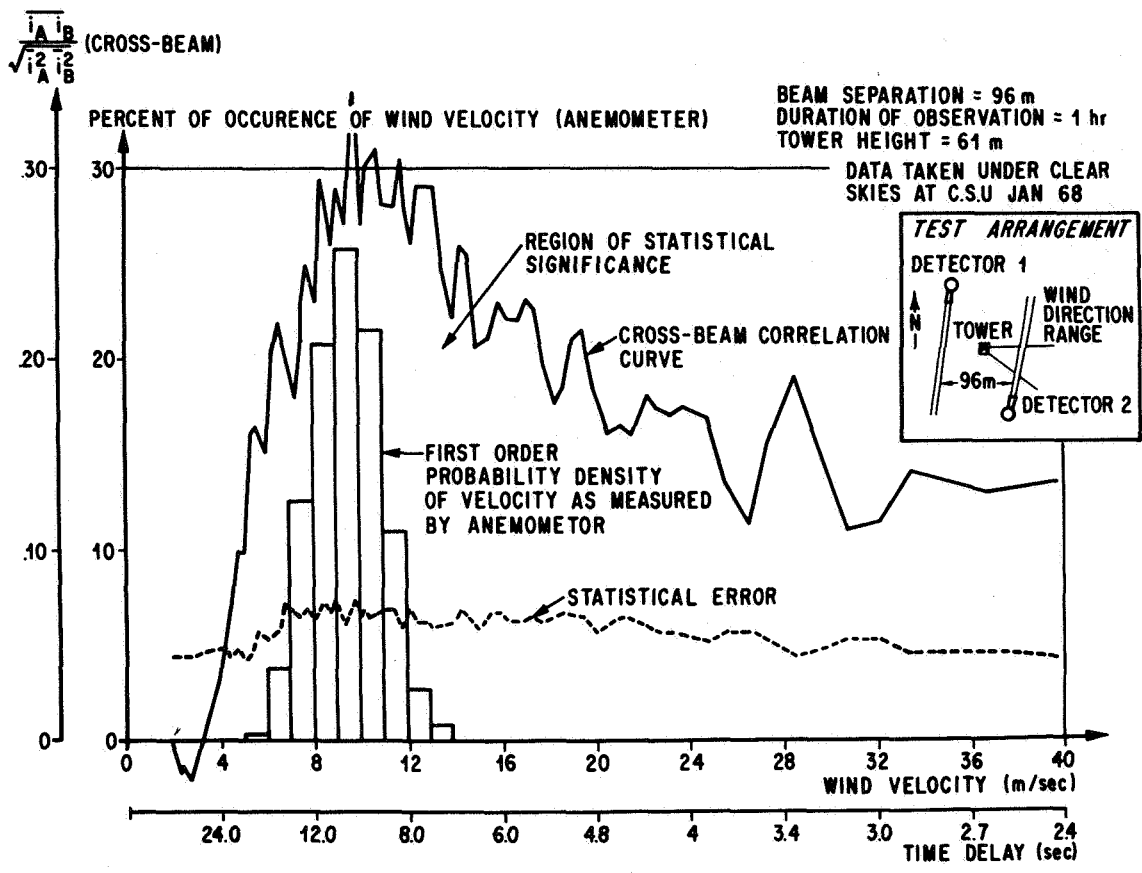


FIGURE 13. MEDIUM WIND SPEED (20 mph)

$$\frac{i_A i_B}{\sqrt{i_A^2 + i_B^2}}$$

(CROSS-BEAM)

DATA TAKEN UNDER  
CLEAR SKIES AT  
C.S.U. NOV 67

BEAM SEPARATION  
= 71.7 m

DURATION OF  
OBSERVATION  
= 2 hr 54 min

TOWER HEIGHT  
= 61 m

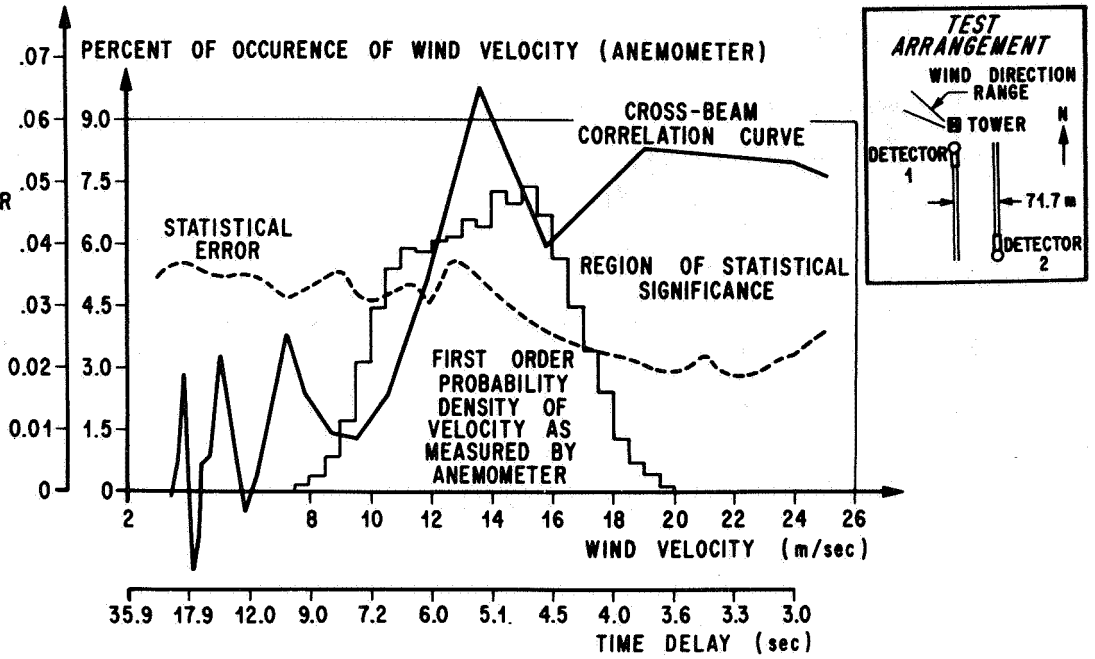


FIGURE 14. HIGH WIND SPEED (30 mph)

TABLE I. X-BEAM AND ANEMOMETER COMPARISON

TEST CONDITIONS*							ANEMOMETER RESULTS			X-BEAM RESULTS		
RUN	DATE	T <sub>START</sub> (hr)	T <sub>STOP</sub> (hr)	WIND CONDITIONS	DIR. FLUCT. (deg)	BEAM SEP. (m)	(U <sub>N</sub> ) MIN. (m/s)	(U <sub>N</sub> ) MAX. (m/s)	(U <sub>N</sub> ) (m/s)	(U <sub>N</sub> ) (m/s)	B (cps)	$\frac{(U_N)_{XB} - (U_N)_{AN}}{(U_N)_{AN}}$ (%)
I	9/29/67	0905	1038	LIGHT WIND FROM SOUTH	±23	30	0.7	2.5	1.6	1.3	.45	17.65
II	1/03/68	1101	1203	LIGHT TO MODERATE WIND FROM EAST	±38	116	2.0	7.0	4.1	4.4	.50	6.82
III	1/03/68	1343	1445	MODERATE TO STRONG WIND FROM SE	±25	96	6.0	13.0	9.5	9.7	.63	2.11
IV	11/30/67	1235	1535	STRONG NW WIND	±30	71	8.0	20.0	14.6	13.6	.73	6.84

\* ALL DATA TAKEN UNDER CLEAR SKIES IN NORTH PLATTE RIVER VALLEY, COLORADO

# OPTIMUM AVERAGING TIMES OF METEOROLOGICAL DATA WITH TIME DEPENDENT MEANS

By

R. R. Jayroe, Jr.<sup>1</sup>, and M. Y. Su<sup>2</sup>

## ABSTRACT

A set of accumulation procedures is introduced to classify the temporal trends in time series. In addition to straight time integration, two new accumulation procedures are proposed: the piecewise detrending method and the statistical weighting method. These two methods are useful for suppressing certain types of nonstationarities. A new concept of accumulative statistical error for covariance function is introduced which, in case of stationary process, can be directly related to the variance of the accumulative covariance. From the plot of statistical error versus the averaging time, optimum starting time and optimum stopping time can be chosen for time series with varying means. This in turn, determines the optimum averaging period. Optimum averaging periods and the statistical error depend strongly on the accumulation procedure used. The use of the optimum averaging period permits signals to be retrieved out of a record with a statistical accuracy higher than that commonly attained.

## DEFINITION OF SYMBOLS

### Symbol

$C(\tau)$	Covariance function, [xy]
f	frequency, cycles/sec
$r_m(\tau, T)$	accumulative statistical error for delay time $\tau$ , [xy]
$S(f)$	power spectral density, [xyt]
t	time, seconds
$\Delta T$	piece length, seconds

T	averaging time (variable), seconds
$x(t), y(t)$	time histories of physical variables x, y, [x], [y]
$\rho(\tau)$	covariance coefficient, [1]
$\sigma$	root mean square value of x, y, [x], [y]
$\tau$	delay time, seconds

### Subscripts

i	denotes i <sup>th</sup> piece
m	total number of pieces used
d	denotes use of piecewise detrending method
a	denotes straight time integration method
w	denotes statistical weighting method

### Superscripts

k	denotes k <sup>th</sup> sample from an ensemble
-	denotes time average over a piece of length $\Delta T$
=	denotes an accumulation over m pieces
$E[ ]$	denotes expected value from an ensemble

- 
1. Aero-Astrodynamic Laboratory, George C. Marshall Space Flight Center
  2. Nortronics-Huntsville, Huntsville, Alabama 35805

## I. INTRODUCTION

The concept of an "accumulative" mean originated by attempting to describe the time dependence of statistical parameters. This concept consists of breaking a time history of a physical variable into pieces of equal length,  $\Delta T$ , and treating each piece as if it were a statistically independent experiment. For each piece, a mean value is calculated by a time integration over that piece. The accumulative mean is constructed by averaging over the  $m$  available piecewise means.

Temporal trends become obvious if the piecewise means are plotted as a function of piece number. However, these trends are obscured by the statistical variation or error associated with the individual piece, and therefore cannot be put into a quantitative form. This paper proposes to classify these trends by using different accumulation procedures. A multitude of accumulative means could be conceived depending on the statistical weights and detrending procedures that are applied to each piece in the accumulation process. These different accumulative procedures will give different statistical errors, and the temporal trends could be classified indirectly by that accumulation procedure which gives the smallest statistical error. Such accumulation procedures might provide new insight into the time dependence of meteorological averages, which cannot be retrieved with straight time averages in present use. This approach will be demonstrated by applying three different accumulative means to the same set of anemometer outputs.

The second section contains the mathematical formulation of the three different accumulation procedures applied to the piecewise time averaged covariance of the anemometer data.

The third section is concerned with the statistical error for the accumulated covariance. Also the statistical error is interpreted for stationary processes.

The fourth section contains a discussion of the anemometer results with respect to accumulation procedures, piece lengths and averaging times, and a summary of conclusions.

## II. ACCUMULATION PROCEDURES

Three different methods for taking accumulative means will be presented. The first method, a straight time integration as it is commonly used, provides a basis for comparison with other accumulation procedures. The second is a statistical weighting method, which employs the piecewise mean square value as a weight, and the third is a piecewise detrending method. All three accumulation procedures will be applied to temporal covariance functions, which are piecewise time averages of the lagged product of  $x(t)$  and  $y(t)$ . The temporal covariance function is given by

$$\bar{C}_i(\tau) = \frac{1}{\Delta T} \int_{(i-1)\Delta T}^{i\Delta T} [x(t) - \bar{x}_m] [y(t + \tau) - \bar{y}_m] dt \quad (1)$$

where  $\bar{x}_m$  and  $\bar{y}_m$  are accumulative means of  $x$  and  $y$ :

$$\bar{x}_m = \frac{1}{T} \int_0^T x(t) dt = \frac{1}{m} \sum_{i=1}^m \bar{x}_i$$

and

$$\bar{x}_i = \frac{1}{\Delta T} \int_{(i-1)\Delta T}^{i\Delta T} x(t) dt \quad (2)$$

Similar definitions are used for  $y(t)$ .

### A. Straight Time Integration

The simple addition of these piecewise estimates will provide an accumulative covariance given by

$$\begin{aligned} \bar{C}_{m,a}(\tau) &= \frac{1}{m} \sum_{i=1}^m \bar{C}_i(\tau) \\ &= \frac{1}{T} \int_0^T \left[ x(t) - \bar{x}_m \right] \left[ y(t + \tau) - \bar{y}_m \right] dt, \end{aligned} \quad (3)$$

which is equivalent to the straight time integration of duration  $T$ .

For later comparisons of different accumulation procedures, the covariance functions are converted into accumulative covariance coefficients as in equation (4)

$$\rho_{m,a}(\tau) = \frac{\bar{C}_{m,a}(\tau)}{\bar{\sigma}_{xm} \bar{\sigma}_{ym}} \quad (4)$$

where  $\bar{\sigma}_{xm}$  and  $\bar{\sigma}_{ym}$  are the accumulative root mean square values. These accumulated values are time averages of the piecewise root mean square values  $\bar{\sigma}_{xi}$  and  $\bar{\sigma}_{yi}$  as defined below.

$$\bar{\sigma}_{xi}^2 = \frac{1}{\Delta T} \int_{(i-1)\Delta T}^{i\Delta T} \left[ x(t) - \bar{x}_m \right]^2 dt \quad (5)$$

and

$$\bar{\sigma}_{xm}^2 = \frac{1}{m-1} \sum_{i=1}^m \bar{\sigma}_{xi}^2 \quad (6)$$

Similar definitions are used for  $y(t)$ .

## B. Statistical Weighting

Each piece of data may be regarded as an independent sample function from an ensemble of size  $m$ . Dividing the piecewise covariance by the corresponding piecewise root mean square values gives the piecewise covariance coefficient. Adding these coefficients provides another type of accumulative covariance coefficient:

$$\rho_{m,w}(\tau) = \frac{1}{m} \sum_{i=1}^m \frac{\bar{C}_i(\tau)}{\bar{\sigma}_{xi} \bar{\sigma}_{yi}} \quad (7)$$

The advantage of the statistical weighting method is its ability to suppress a common type of non-stationarity in time series, which is characterized by the following features:

1. The mean value over each piece is approximately constant, but mean values over different pieces may vary. That is, plots of  $x(t)$  and  $y(t)$  versus  $t$  will resemble step functions.

2. The piecewise root mean square value is linearly proportional to the corresponding piecewise mean value.

This type of nonstationarity approximates the turbulent fluctuation of moderate wind speeds near the ground.

Statistically, piecewise covariance coefficients for this type of time series are more equally weighted than the corresponding piecewise covariances. Hence, the statistical weighting method tends to make the whole record stationary. Experience indicates that the straight time integration and the statistical weighting methods produce the same results if the time series  $x(t)$  and  $y(t)$  are stationary. At present, a mathematical proof directly relating these two accumulation means for stationary data has not been accomplished.

## C. Piecewise Detrending

Piecewise linear trends in time series are also a common type of nonstationarity. A method for removing these trends will now be derived. This method requires that the ordinate of each piecewise covariance curve be shifted such that the integral of the shifted piecewise covariance over the time lag range vanishes. The amount of ordinate shift  $\Delta C_i$  is obtained from equation (8).

$$\int_{-\tau}^{\tau} \left[ \bar{C}_i(\tau) - \Delta C_i \right] d\tau = 0. \quad (8)$$

Thus,

$$\Delta \bar{C}_i = \frac{1}{2\tau_m} \int_{-\tau_m}^{\tau_m} \bar{C}_i(\tau) d\tau \quad (9)$$

Equation (8) can also be written as

$$\begin{aligned} \int_{-\tau_m}^{\tau_m} \Delta \bar{C}_i d\tau &= \int_{-\tau_m}^{\tau_m} \bar{C}_i(\tau) d\tau \approx \int_{-\infty}^{\infty} \bar{C}_i(\tau) d\tau \quad (10) \\ &= \bar{S}_i(f=0), \end{aligned}$$

where  $\bar{S}_i(f)$  is the cross-spectrum function of  $x(t)$  and  $y(t)$  at frequency  $f$ . Hence, the ordinate shifting of the piecewise covariance is equivalent to removing the "power" or "energy" at zero frequency. Using this detrending procedure for each piece, we obtain the third kind of accumulative covariance:

$$\bar{C}_{m,d}(\tau) = \frac{1}{m} \sum_{i=1}^m \left[ \bar{C}_i(\tau) - \frac{1}{2\tau_m} \int_{-\tau_m}^{\tau_m} \bar{C}_i(\tau) d\tau \right] \quad (11)$$

The corresponding accumulative covariance coefficient is given by

$$\bar{\rho}_{m,d}(\tau) = \frac{\bar{C}_{m,d}(\tau)}{\bar{\sigma}_x \bar{\sigma}_y} \quad (12)$$

It remains to be shown that piecewise linear trends result in adding a constant value to the covariance obtained without the presence of trends. Time series with piecewise linear trends can be expressed as

$$\begin{aligned} x(t) &= x_s(t) + a_{x_i} \left( t - \frac{1}{2} \Delta T \right) + \bar{x}_i \\ y(t) &= y_s(t) + a_{y_i} \left( t - \frac{1}{2} \Delta T \right) + \bar{y}_i \end{aligned} \quad (13)$$

where  $x_s(t)$  and  $y_s(t)$  stand for true stationary signals, and  $a_{x_i}$  and  $a_{y_i}$  are the slopes of linear

trends. When we substitute the above expressions in equation (1), the piecewise covariance becomes

$$\begin{aligned} \bar{C}_i(\tau) &= \frac{1}{\Delta T} \int_{(i-1)\Delta T}^{i\Delta T} x_s(t) y_s(t+\tau) dt \\ &+ \frac{1}{12} a_{x_i} a_{y_i} \Delta T^2 \left\{ 1 - \frac{1}{3} \frac{\tau}{\Delta T} + 0 \left[ \frac{\tau}{\Delta T} \right]^2 \right\} \\ &\approx \frac{1}{\Delta T} \int_{(i-1)\Delta T}^{i\Delta T} x_s(t) y_s(t+\tau) dt \\ &+ \frac{1}{12} a_{x_i} a_{y_i} \Delta T^2 \end{aligned} \quad (14)$$

for  $\Delta T \gg \tau$ . Here, the first term is the covariance of true signals. The second term, which is due to piecewise linear trends, weakly depends on the time lag and is approximately a constant.

### III. STATISTICAL ERRORS OF ACCUMULATIVE MEANS

The calculation of a statistical error as a function of averaging time is needed for

1. the choice of piece length,
2. the comparison of accumulative procedures,
3. and the determination of an "optimum averaging time."

The statistical error, which meets the above criteria, is calculated by taking the mean square variation of the piecewise means about the chosen accumulative mean. For the autocovariance, the accumulative statistical error is written as

$$\bar{r}_m^2(\tau, T) = \frac{1}{m(m-1)} \sum_{i=1}^m \left[ \bar{C}_i(\tau) - \bar{C}_m(\tau) \right]^2 \quad (15)$$

Even though the discussion of the statistical error is limited here to the autocovariance, the limitation is by no means necessary.

In principle, the use of the statistical error can be interpreted only for data which are stationary over every piece of length  $\Delta T$ . The weak stationarity assumption suffices, since only the second order probability density function need be stationary. In practice, the use of the statistical error still provides insight on statistical processes, even if they are not stationary at all. This will be explained in Section IV.

The accumulative statistical error,  $\bar{r}_m(\tau, T)$ , is introduced to classify temporal trends indirectly by isolating that particular accumulation procedure which gives the smallest accumulative statistical error. Examination of the statistical error is, therefore, the key to the proper choice of piecewise statistical weighting and detrending methods. The method used here is based on relating the accumulative statistical error to the time-averaged variance for an ensemble of sample means.

Assume that  $k = 1, 2, \dots, N$  realizations of the atmospheric flow field have been observed. The ensemble average or expected mean of these independent realizations is denoted by the operation

$$E \left[ (\cdot)^{(k)} \right] = \frac{1}{N} \sum_{k=1}^N (\cdot)^{(k)}. \quad (16)$$

This operation is applied to the piecewise sample means of the time-averaged autocovariance function of a meteorological variable  $x$ . The expected value of the time-averaged autocovariance for the  $i^{\text{th}}$  piece is given by

$$E \left[ \bar{C}_i^{(k)}(\tau) \right] = \frac{1}{N} \sum_{k=1}^N \frac{1}{\Delta T} \int_{(i-1)\Delta T}^{i\Delta T} \left[ x^{(k)}(t) - \bar{x}_m^{(k)} \right] \left[ x^{(k)}(t + \tau) - \bar{x}_m^{(k)} \right] dt \\ \equiv \bar{C}_i(\tau). \quad (17)$$

The mean square error associated with these time-averaged sample means is given by

$$\text{Var} \left[ \bar{C}_i^{(k)}(\tau) \right] = \frac{1}{N} \sum_{k=1}^N \left[ \bar{C}_i^{(k)}(\tau) - \bar{C}_i(\tau) \right]^2. \quad (18)$$

Unfortunately, the variance cannot be calculated directly from experimental data since we can never obtain more than a few realizations of the same meteorological conditions. In most cases, only one function is available. However, the preceding ensemble averages, equations (19), (20) and (24), can still be used if it is assumed that each piece of a long record can be treated as if it were a statistically independent realization. This assumption is expressed by the operation

$$\frac{1}{N} \sum_{k=1}^N (\cdot)^{(k)} = \frac{1}{m} \sum_{i=1}^m (\cdot)_i \equiv (\cdot)_m. \quad (19)$$

The above assumption is valid if the following three conditions hold:

1. the time history is a self-stationary process,
2. the autocovariance function fulfills certain integrability conditions, and
3. the individual piece lengths,  $\Delta T$ , exceed the time lag range within which the autocovariance has become exceedingly small.

Using this assumption, the expected value of the time-averaged sample means can be expressed in terms of the experimentally accessible accumulative mean. This result follows by substituting equation (19) into equations (16) through (18).

The substitution into equation (16) shows that the ensemble average and accumulative mean are identical:

$$E \left[ (\cdot)^{(k)} \right] = (\cdot)_m. \quad (20)$$

The substitution into equation (17) shows that the expected value of all piecewise means are identical, and that the expected value can be calculated from the accumulative mean

$$E \left[ \overline{C}_i^{(k)}(\tau) \right] = \overline{C}_m(\tau) = \overline{C}(\tau). \quad (21)$$

The substitution into equation (18) gives the desired relation between the variance of the time-averaged sample means and the accumulative statistical error.

$$\begin{aligned} \text{Var} \left[ \overline{C}_i^{(k)}(\tau) \right] &= \frac{1}{N} \sum_{i=1}^N \left( \overline{C}_i^{(k)}(\tau) - \overline{C}_i(\tau) \right)^2 \\ &= \frac{1}{m} \sum_{i=1}^m \left( \overline{C}_i(\tau) - \overline{C}_m(\tau) \right)^2 \end{aligned}$$

$$\text{Var} \left[ \overline{C}_i^{(k)}(\tau) \right] = (m-1) \overline{r}_m^2(\tau, T). \quad (22)$$

Equation (22) gives an estimate of the variance of the sample means, which are averaged over their respective piece of length  $\Delta T$ . This estimate can be calculated directly by the accumulation of mean square fluctuations between the piecewise means and their accumulative mean. Because each piece has been assumed to be a statistically independent stationary realization, the variance of the accumulation over  $m$  realizations is  $1/m$  times the variance of the individual parts

$$\text{Var} \left[ \overline{C}_m^{(k)}(\tau) \right] = \frac{1}{m} \overline{C}_i^{(k)}(\tau). \quad (23)$$

Combining equations (22) and (23) relates the variance of the accumulative mean to the experimentally accessible accumulative statistical error:

$$\overline{r}_m^2(\tau, T) = \frac{m}{m-1} \text{Var} \left[ \overline{C}_m^{(k)}(\tau) \right]. \quad (24)$$

The factor  $m/m-1$  is introduced in the definition of  $\overline{r}_m^2(\tau, T)$  so that an unbiased estimate of the variance is obtained.

By virtue of the assumption previously made, an identity can be established for the accumulative statistical error given by

$$\begin{aligned} \overline{r}_m^2(\tau, T) &\approx \frac{1}{T} \int_{-\infty}^{\infty} C^2(\xi) d\xi \\ &+ \frac{1}{T} \int_{-\infty}^{\infty} C(\eta) C(2\tau - \eta) d\eta \end{aligned} \quad (25)$$

where  $\xi$  and  $\eta$  are time-delay parameters [1]. The accumulative statistical error can then be related to the special data characteristics, which are expressed in terms of the power spectrum,  $S(f)$ , by use of the Faltung theorem [2].

$$\int_{-\infty}^{\infty} C(\eta) C(2\tau - \eta) d\eta = \int_{-\infty}^{\infty} S^2(f) e^{-j2\tau f} df \quad (26)$$

$$\int_{-\infty}^{\infty} C^2(\xi) d\xi = \int_{-\infty}^{\infty} S^2(f) df. \quad (27)$$

This substitution leads to

$$\begin{aligned} \overline{r}_m^2(\tau, T) &\approx \frac{1}{T} \int_{-\infty}^{\infty} S^2(f) df \\ &+ \frac{1}{T} \int_{-\infty}^{\infty} S^2(f) e^{-j2\tau f} df. \end{aligned} \quad (28)$$

If the statistical error is integrated over the time lag range, with  $\tau_m$  being the maximum time lag, we obtain

$$\begin{aligned} \frac{1}{2\tau_m} \int_{-\tau_m}^{\tau_m} \overline{r}_m^2(\tau, T) d\tau &\approx \frac{1}{T} \int_{-\infty}^{\infty} S^2(f) dt \\ &+ \frac{1}{2\tau_m T} \int_{-\infty}^{\infty} S^2(f) \frac{\sin 2\tau_m f}{2\tau_m f} d(2\tau_m f). \end{aligned} \quad (29)$$

The second integral on the right-hand side is negligible if there is no power at the low frequency end. On the

other hand, if there is a considerable amount of power at low frequencies and  $\tau_m \gg 1/2f_{\text{lower}}$ ,

then  $\sin 2\tau_m f/2\tau_m f$  is practically a delta function. Thus,

$$\frac{1}{2\tau_m} \int_{-\tau_m}^{\tau_m} \bar{r}_m^2(\tau, T) d\tau = \frac{1}{T} \left[ \int_{-\infty}^{\infty} S^2(f) df + \frac{S^2(0)}{2\tau_m} \right] = \bar{r}_m^2(T). \quad (30)$$

If one defines

$$\left[ \int_{-\infty}^{\infty} S^2(f) df + \frac{S^2(0)}{2\tau_m} \right]^{1/2} \equiv \frac{\sigma_x^2(T)}{\sqrt{B_{\text{eff}} T}}, \quad (31)$$

B is an effective bandwidth of the data, then the classic result that the error decreases as  $1/\sqrt{B_{\text{eff}} T}$  is obtained

$$\frac{\bar{r}_m(T)}{\sigma_x^2(T)} = \frac{1}{\sqrt{B_{\text{eff}} T}} \quad (32)$$

When the statistical error is plotted versus reciprocal square root of averaging time for stationary data, we obtain a straight line which passes through the origin. The slope of this line is proportional to the integral of the square of the power spectral density. In the previous section, it was shown that the power at zero frequency could be eliminated by shifting the ordinate of the covariance curve such that the total area under the covariance curve is zero.

Based upon the above results for stationary data, the statistical error decreases in inverse proportion to the square root of the averaging time, and infinitely accurate results are obtained for infinitely long averaging times.<sup>1</sup>

## IV. DISCUSSIONS OF ANEMOMETER RESULTS AND CONCLUSIONS

The ideas of the previous sections were tried out on anemometer data which were recorded under a cloudless sky. The anemometer was located at a height of 122 meters on the U.S. Army meteorological tower at MSFC, Huntsville, Alabama. The recording time was between 10:04 a.m. and 11:52 a.m. on 14 August 1967.

The horizontal wind speed and direction measured by the anemometer were recorded on an analog tape, which was then converted into a digital tape with a sampling rate of 8 samples per second. From these data, a time history of the wind speed component in the direction of 78 degrees clockwise from North was calculated. Piecewise mean wind components, root mean square wind components, and turbulent intensity were evaluated and plotted in Figure 1. Since the piecewise mean wind speeds were quite low, the turbulent intensity varies quite randomly. This indicates that a low wind speed is less stable than a high wind speed. We have purposely chosen the less stable data as a critical test for the three different accumulation procedures.

Figure 2A shows the accumulative autocovariance coefficients for three different piece lengths: 270, 360, and 450 seconds. Inspection of these curves shows that the zero-crossing time lags are linearly proportional to the piece lengths used. Figure 2B shows the power spectrum functions. The peaks of these spectra shift to a higher frequency as the piece length becomes shorter. The spectral density functions were also plotted in log-log scale in Figure 2C, and the slopes follow very closely the (-5/3) power law in the frequency range from 0.01 cps to 0.4 cps. It therefore appears that the piecewise detrending method operates much like a high-pass filter with a low frequency cut-off, which is inversely proportional to the piece lengths. For stationary time series, the statistical error of the accumulative autocovariance will follow a straight line passing through the origin when plotted against the inverse square root of the averaging time. However, because of nonstationarity, the statistical error curve may deviate from this straight line. Actually, this statistical error will reach a minimum, when the error due to the nonstationarity starts to overpower the gain in

1. If one wishes to consider that the time history is signal plus noise then equation (30) still has the same form except that the spectrum,  $S^2(f)$ , is replaced by  $S_s^2(f) + S_n^2(f)$  and the power at zero frequency,  $S^2(0)$ , is replaced by  $S_s^2(0) + S_n^2(0)$  where the subscript s refers to the signal and the subscript n refers to the noise.

statistical accuracy because of increasing the averaging time. The averaging time corresponding to this minimum statistical error will be called the "optimum stopping time."

Figures 3A, B and C compare the statistical error curves for the accumulative autocovariance coefficients by three different accumulation procedures. Figure 3A shows that the statistical error curve resulting from the straight time-integration method leveled off because of the presence of non-stationarity in the data. Figure 3B shows the statistical error curves resulting from the use of the piecewise detrending method. These curves clearly indicate that the time series after detrending become approximately stationary for two parts of the record, and that the errors are about 50 percent less than those by the straight time integration. Notice that there is a steep jump in the error curves, which must be due to a sudden change in statistical characteristics of these two different parts of the record. Figure 3C shows the corresponding error curves obtained from the statistical weighting method. The error is about the same as that obtained by the detrending method, but the jump in the error has been smoothed out. Hence, the statistical weighting method has made the record stationary as a whole. These figures also show that the optimum stopping time, for the same set of data, obtained by the straight time-integration method, by piecewise detrending, and by the statistical weighting method increases in respect to the order of the methods listed. The longer the optimum stopping time, the smaller will be the statistical error.

Because of the randomness of the data, the statistical error for the first few pieces is usually not dependable. However, if the statistical error keeps increasing from the very first piece, then the data must be highly nonstationarity for this part of the record. When more pieces of data are accumulated, the statistical error often starts to decrease

and to follow the pattern for stationary processes. The averaging time corresponding to this maximum statistical error will be called the "optimum starting time" as shown in Figure 4. The duration from the optimum starting time to the optimum stopping time is then called the "optimum averaging period" of the time series. It is expected that the optimum averaging period of the time series will produce the accumulative covariance with the least statistical error.

The above analytical and experimental results can be summarized as follows:

1. A set of accumulation procedures is introduced to classify the temporal trends in time series. In addition to the commonly used straight time integration, two new accumulation procedures are proposed: the piecewise detrending method and the statistical weighting method. These two methods are useful for suppressing certain common types of nonstationarities.
2. A new concept of accumulative statistical error for covariance functions is introduced which, in case of stationary processes, can be directly related to the variance of the accumulative covariance.
3. From the plot of the statistical error versus the averaging time, the optimum starting time and the optimum stopping time can be chosen for time series with varying means. This, in turn, determines the optimum averaging period.
4. Optimum averaging periods and the statistical error depend strongly on the accumulation procedures used.
5. The use of the optimum averaging period permits signals to be retrieved out of a record with a statistical accuracy higher than that commonly obtained from straight time integration.

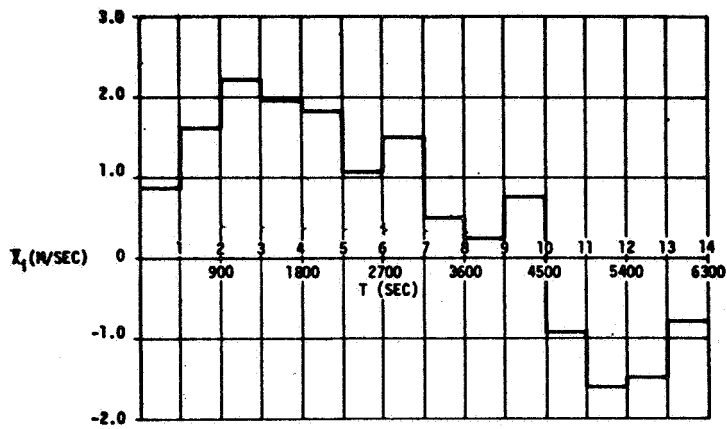


FIGURE 1A. PIECEWISE MEAN WIND COMPONENT

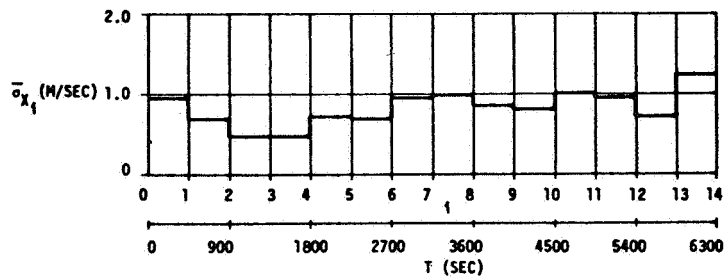


FIGURE 1B. PIECEWISE RMS VALUE OF WIND COMPONENT

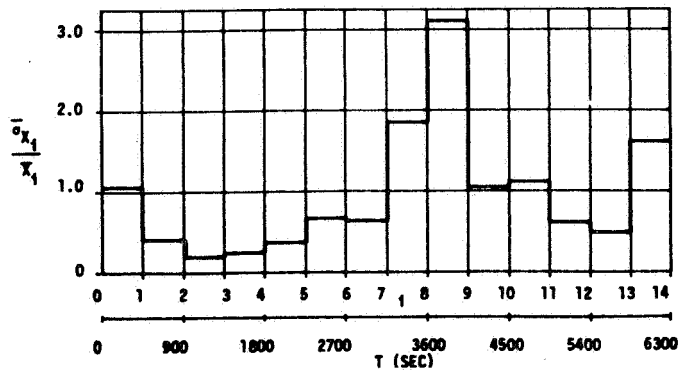


FIGURE 1C. PIECEWISE TURBULENT WIND COMPONENT INTENSITY

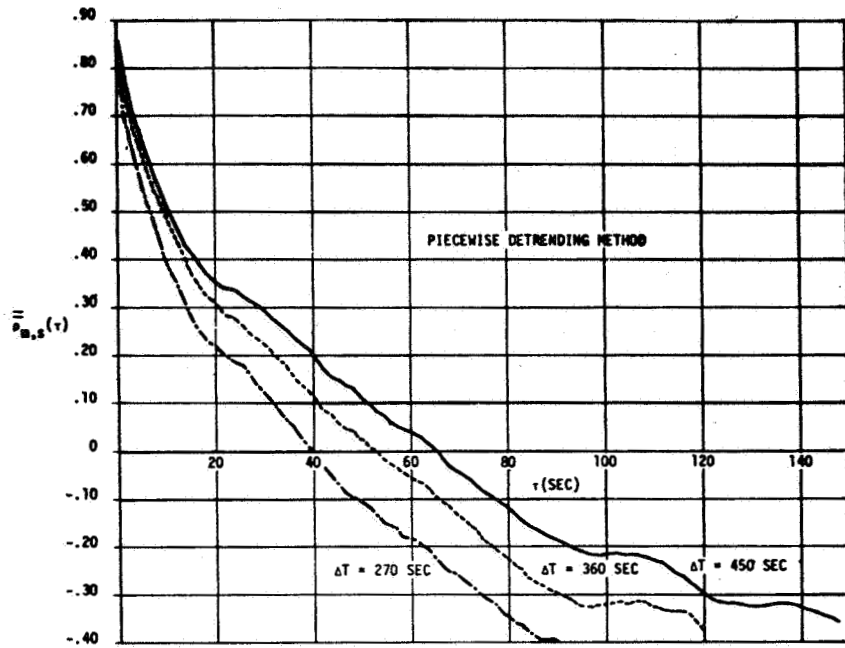


FIGURE 2A. ACCUMULATIVE AUTOCOVARANCE COEFFICIENTS OF WIND COMPONENT

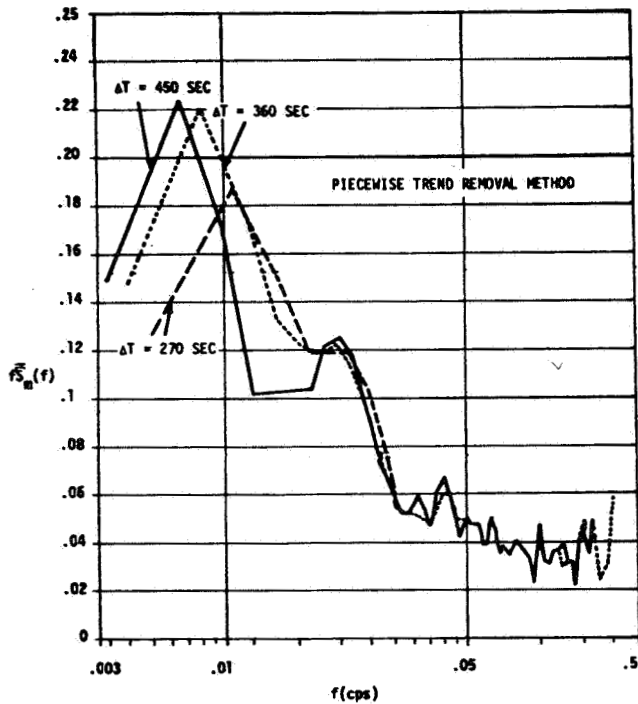


FIGURE 2B. ACCUMULATIVE POWER SPECTRA

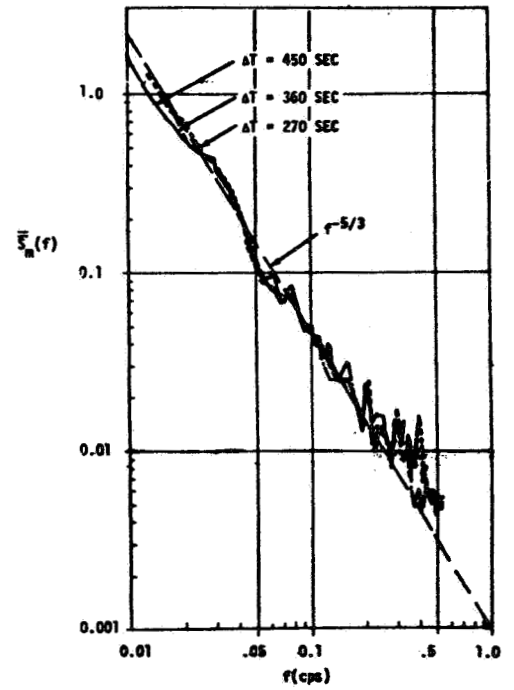


FIGURE 2C. ACCUMULATIVE POWER DENSITY SPECTRA

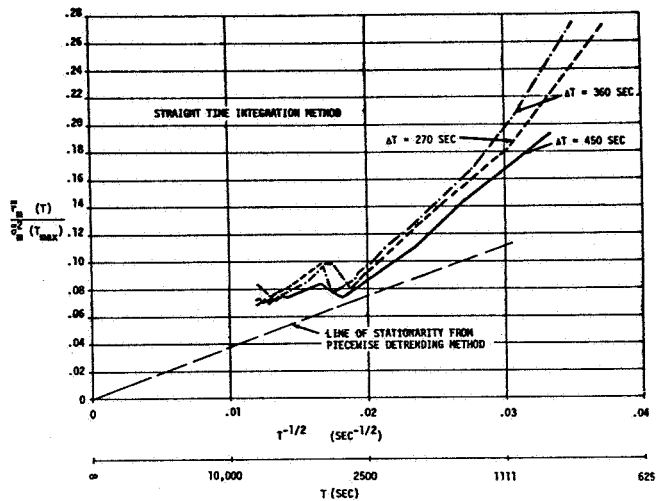


FIGURE 3A. STATISTICAL ERROR CURVES FOR AUTOCOVARANCE COEFFICIENTS

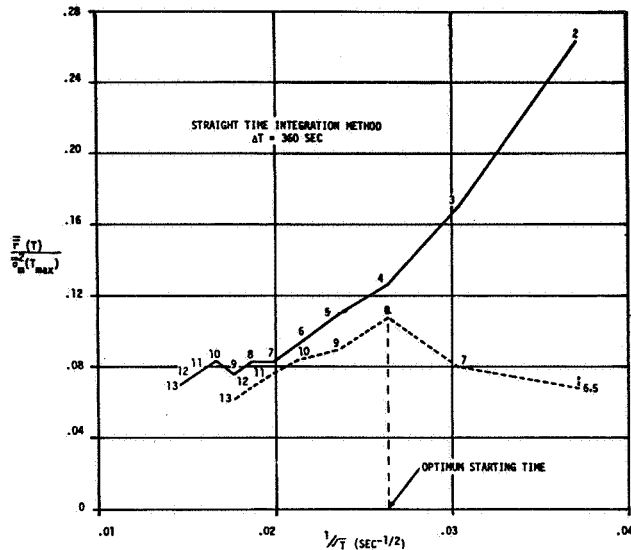


FIGURE 4. EFFECT OF STARTING TIME ON STATISTICAL ERROR CURVES

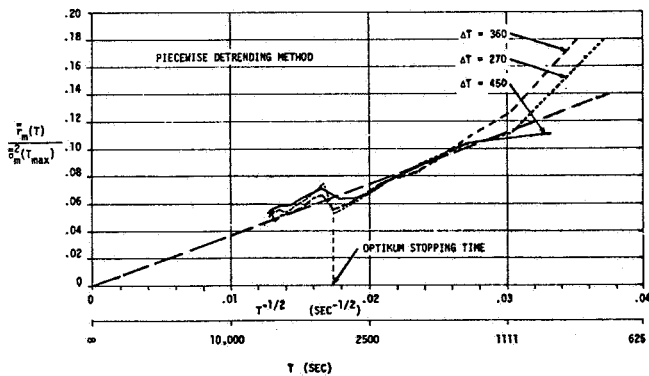


FIGURE 3B. STATISTICAL ERROR CURVES FOR AUTOCOVARANCE COEFFICIENTS

## REFERENCES

1. Bendat, J. S. and Piersol, A. G.: Measurement and Analysis of Random Data, John Wiley, New York, 1966.
2. Sneddon, I. N.: Fourier Transforms, McGraw-Hill, 1951, New York.

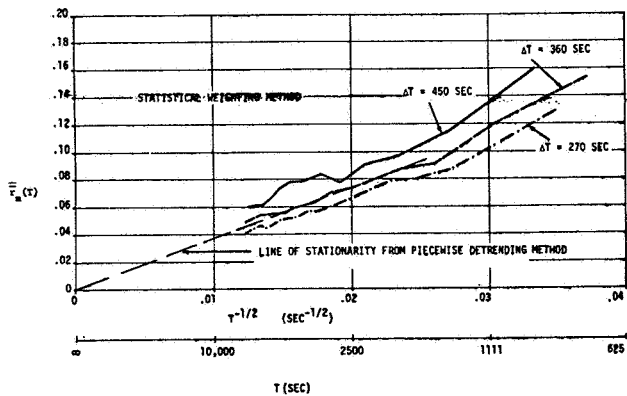


FIGURE 3C. STATISTICAL ERROR CURVES FOR AUTOCOVARANCE COEFFICIENTS



### III. CELESTIAL MECHANICS

# THE BINARY COLLISION IN THE N-BODY PROBLEM

By

Hans J. Sperling

## ABSTRACT

The binary collision in the N-Body problem of celestial mechanics and its regularization are studied from the point of view of analytic differential equations, i. e., for complex values of the time and of the coordinates as independent and dependent variables. Based on a suitable definition of a binary collision, a proof is given for the classical result that a binary collision corresponds to an algebraic branch point of the first or second order. The convergence of Sundman's integral and the regularization of the binary collision are briefly discussed also for more general problems not necessarily possessing an energy integral; this situation is present, e. g., in the Reduced Three-Body problem.

## I. INTRODUCTION

The equations of motion of the N-Body problem of celestial mechanics, written in inertial Cartesian coordinates, form a system of analytic differential equations (7). This suggests that all variables be allowed to take complex values and complex analysis be applied to the study of the solution. The basic existence and uniqueness theorem establishes the solution as a system of holomorphic functions of the independent variable and the initial values locally only, and for a deeper insight into their properties, it seems natural to try to explore the nature of their singularities. Painlevé was the first to suggest this point of view and the first results are due to him; he also derived a general result about the points at which singularities are possible.

From the form of the equations of motion, we infer the following by applying Painlevé's result about the singularities of the solution of a system of analytic differential equations: There is a sequence of points in the plane of the independent variable (time) converging towards the (finite) singularity such that at least one dependent variable grows unboundedly, or that at least one distance becomes arbitrarily

small, or both. Exclude the case that a variable grows unboundedly. Apparently, the simplest case then is that exactly one distance decreases without bound to zero, while all others remain sufficiently far from zero. If all variables are real, this corresponds to an arbitrarily close approach of exactly two bodies, and this case is called, also for complex variables, the "binary collision." Sundman did the first systematic study of the binary collision in the real case, and a considerable number of papers have been published on this subject. The only other case that has been dealt with successfully is the real triple collision in the Three-Body problem (i. e., all three bodies collide simultaneously).

In this paper two problems are considered: the binary collision (1) in the N-Body problem, and (2) more generally, in certain "perturbed Two-Body problems," both cases allowing for complex variables.

1. Inertial Cartesian coordinates have disadvantages for a discussion of the binary collision, since the "critical distance" (the distance tending towards zero as the instant of collision is approached) occurs in more than one equation. Because the so-called "Jacobian" coordinates avoid this difficulty, they are used here. For the definition of a binary collision, it should be observed that there must also be specified a continuous rectifiable curve on which the independent variable time approaches the instant of collision. The method of proof used here puts further restrictions on this curve. The basic fact permitting the regularization of the binary collision is the convergence of Sundman's integral for the instant of collision: This integral ("Sundman's variable") is introduced into the equations of motion as the new independent variable, and the new equations of motion, after some modification, remain holomorphic at the point corresponding to the instant of collision. The type of the singularity can then be determined easily: The dependent variables possess algebraic branch points or algebraic poles at the time of collision.

2. The results of (1) can be extended to more general "perturbed Two-Body problems" [equation (34)], for which an energy integral — or a similar

integral, as Jacobi's integral in the Restricted Three-Body problem — does not necessarily exist. Under certain conditions for the perturbing forces it can be shown that Sundman's integral converges, and the process of regularization can be carried out as before. An example for this second kind of problem is the Reduced Three-Body problem — or more generally, a Three-Body problem with one zero mass and the two heavy masses moving on Keplerian conic sections. An energy or Jacobian type of integral does not exist, but it is possible to regularize the binary collisions by the usual procedure.

## II. AUXILIARY LEMMAS

Vectors, denoted by bars, have three complex components; the scalar and vector product are defined as usual by

$$\begin{aligned}\bar{a}\bar{b} &= (a_1, a_2, a_3) (b_1, b_2, b_3) \\ &= a_1b_1 + a_2b_2 + a_3b_3\end{aligned}$$

$$\begin{aligned}\bar{a} \times \bar{b} &= (a_2b_3 - a_3b_2, a_3b_1 - a_1b_3, \\ & a_1b_2 - a_2b_1).\end{aligned}$$

Throughout the following, let  $C = C[t_0, t^*]$  be a nondegenerate ( $t_0 \neq t^*$ ) continuous rectifiable curve in the complex  $t$ -plane with initial point  $t_0$  and terminal point  $t^*$ , and let  $C[t_0, t^*]$  be this curve without its terminal point  $t^*$ . We can assume  $t$  is represented by a continuous function of bounded variation  $t = t(u)$  of the real parameter  $u$ ,  $0 \leq u \leq 1$ . Denote the length of  $C[t_1, t_2]$  by  $LC[t_1, t_2]$ . All integrations and limits are performed on  $C$ , unless otherwise stated; the existence of a limit shall always imply its finiteness.

The situation discussed in the following and expressed in lemma 1 occurs in the present treatment of the binary collision in the  $N$ -Body problem in this manner: The equations of motion (7)

$$\ddot{\bar{\rho}}_k = - \sum_{\substack{\nu=1 \\ \nu \neq k}}^N \gamma m_\nu \frac{\bar{\rho}_k - \bar{\rho}_\nu}{\rho_{\nu k}^3} \quad k = 1 \text{ -- } N$$

show that the coordinates  $\bar{\rho}_k$  satisfy linear differential equations, provided that the  $\rho_{\nu k}$  are known functions of time. Of course, this fact is of no help to

solve the equations, but under certain conditions, it will allow us to put bounds on the change of the  $\bar{\rho}_\nu$ .

If we assume, as we shall do in the definition of a binary collision, that a solution exists on  $C[t_0, t^*]$ , and that the  $\bar{\rho}_\nu$  remain bounded and satisfy for a  $k$  the condition  $|\rho_{\nu k}| \geq c > 0$ , i. e.,  $|\rho_{\nu k}^{-3}| \leq c^{-3}$ , for some constant  $c$ , then  $\bar{\rho}_k$  satisfies a linear differential equation of the form (7) or (3), from which desired limit properties of  $\bar{\rho}_k$  as  $t \rightarrow t^*$  on  $C$  can be inferred. In fact, this process will be applied to the equations of motion (13b), having the same form as (7), rather than to (7) itself. We will now formulate this in a general and more precise manner.

Let  $x_1(t), \dots, x_n(t)$  be holomorphic and solutions of the equations

$$\begin{aligned}\dot{x}_k &= \sum_{\nu=1}^n g_{k\nu}(x_1, \dots, x_n, t) x_\nu + h_k(x_1, \dots, x_n, t) \\ & \quad k = 1 \text{ -- } n\end{aligned}\quad (1)$$

on  $C[t_0, t^*]$ . Assume that the  $g_{k\nu}$  and  $h_k$  are holomorphic for all values of  $x_1, \dots, x_n, t$  involved, i. e., on the set

$$\begin{aligned}\{x_1, \dots, x_n, t/x_k = x_k(t(u)), t = t(u), \\ u \in [0, 1]\},\end{aligned}$$

and that they remain bounded on  $C[t_0, t^*]$ . Then it is easily seen that the functions  $x_k(t)$  remain bounded on  $C[t_0, t^*]$  and possess a limit as  $t \rightarrow t^*$  on  $C$ . Substitute the functions  $x_1(t), \dots, x_n(t)$  into  $g_{k\nu}$  and  $h_k$ ,

$$\begin{aligned}g_{k\nu}(x_1(t), \dots, x_n(t), t) &= g_{k\nu}^*(t), \\ h_k(x_1(t), \dots, x_n(t), t) &= h_k^*(t).\end{aligned}\quad (2)$$

Then the  $x_k$  satisfy, in the neighborhood of  $C[t_0, t^*]$ , the linear system

$$\dot{x}_k = \sum_{\nu=1}^n g_{k\nu}^*(t) x_\nu + h_k^*(t) \quad (3)$$

with holomorphic and bounded coefficients. The solutions of this system exist and are unique by the existence theorem for analytic differential equations (therefore, equal to the original  $x_k(t)$  we started from) and they can be constructed and estimated by Picard's iteration process, yielding,

$$|x_k(t) - x_k(t_0)| < \frac{nX+1}{n} (\exp(n\text{GLC}[t_0, t])), \quad (4)$$

where

$$|g_{k\nu}| < G \text{ and } |h_k| < G \text{ on } C[t_0, t], \text{ and} \\ |x_k(t_0)| < X \quad (5)$$

are assumed to hold.

The Picard iteration is standard, except that it is performed on  $C[t_0, t]$  instead of a straight line as usual. The estimates require the easily proved formula

$$\int_{t_0}^t (\text{LC}[t_0, \tau])^q d\text{LC}[t_0, \tau] = \frac{1}{q+1} (\text{LC}[t_0, t])^{q+1}, \\ \text{valid for } q > -1. \quad (6)$$

The estimate of  $x_k(t)$ , given by relation (4) implies the existence of  $x_k(t)$  as  $t \rightarrow t^*$  on  $C$ . We formulate the foregoing as follows:

Lemma 1: Let  $C[t_0, t^*]$  be a rectifiable curve and let  $x_1(t), \dots, x_n(t)$  be holomorphic on  $C[t_0, t^*]$  and satisfy

$$\dot{x}_k = \sum_{\nu=1}^n g_{k\nu}(x_1, \dots, x_n, t) x_\nu + h_k(x_1, \dots, x_n, t), \\ k = 1 \dots n$$

the  $g_{k\nu}$  and  $h_k$  being holomorphic for all values of  $x_1, \dots, x_n, t$  involved and  $|g_{k\nu}| < G, |h_k| < G, |x_k(t_0)| < X$  there. Then the  $x_k(t)$  are bounded on  $C[t_0, t^*]$  and  $\lim x_k(t)$  as  $t \rightarrow t^*$  on  $C$  exists and is finite.

In the following we will also use Painlevé's theorem stating, roughly speaking, that the solution of a system of differential equations cannot possess a singularity at a point where the right sides of the equations are holomorphic.

### III. EQUATIONS OF MOTION

For reference we list the equations of motion referred to an inertial coordinate system. Let  $\gamma$  be the gravitational constant and  $\bar{\rho}_k$  the position vector of the particle with mass  $m_k$ . The equations of motion of the N-Body problem read

$$\ddot{\rho}_k = - \sum_{\substack{\nu=1 \\ \nu \neq k}}^N \gamma m_\nu \frac{\bar{\rho}_k - \bar{\rho}_\nu}{\rho_{\nu k}^3} = - \text{grad}_{\rho_k} U^+, \\ k = 1 \dots N, \quad (7)$$

where

$$\rho_{\nu k} = \sqrt{(\bar{\rho}_k - \bar{\rho}_\nu) \cdot (\bar{\rho}_k - \bar{\rho}_\nu)}, \quad (8)$$

and

$$U^+ = - \sum_{\substack{j, l=1 \\ j < l}}^N \gamma m_j m_l \frac{1}{\rho_{jl}} \quad (9)$$

is the potential energy of the system. We also have the following two equations: The conservation of energy ( $h = \text{constant of energy}$ ),

$$\frac{1}{2} \sum_{\nu=1}^N m_\nu \dot{\bar{\rho}}_\nu \cdot \dot{\bar{\rho}}_\nu + U^+ = T^+ + U^+ = h, \quad (10)$$

and the Lagrange-Jacobi equation,

$$\frac{d^2}{dt^2} \sum_{\nu=1}^N m_\nu \bar{\rho}_\nu \cdot \bar{\rho}_\nu = 4h - 2U^+. \quad (11)$$

The following discussions will be based on the equations of motion expressed in Jacobian coordinates. The Jacobian coordinates  $\bar{r}_k = (x_k, y_k, z_k)$  of the particle  $m_k, k = 2 \dots N$ , are defined as follows:

(a) the coordinate systems  $\bar{\rho}$  and  $r_k$  are parallel, and

(b) the origin of the  $\bar{r}_k$ -coordinate system is located at the center of mass of the particles  $m_1, \dots, m_{k-1}$ .

Hence,  $m_2$  is referred to  $m_1$ . Let  $r_{j\ell}^*$  be the  $\rho_{j\ell}$ , expressed in Jacobian coordinates (without restriction of generality, we may assume that  $j < \ell$ ); the  $\bar{\rho}_k$  are linear combinations of the  $r_k$ , and  $r_{j\ell}^*$  depends only on the  $r_\nu$  with  $j \leq \nu \leq \ell$ :

$$r_{j\ell}^{*2} = \left( \sum_{\nu=j}^{\ell} d_{j\ell\nu} \bar{r}_\nu \right)^2, \quad d_{j\ell\nu} \text{ constants.} \quad (12)$$

For simplicity of notation we will (from now on) frequently drop the subscript "2"; i.e., write  $\bar{r}$  for  $\bar{r}_2$ , and also write  $\bar{r}$  for  $r_{12}^*$ .

The equations (7) - (11), referred to Jacobian coordinates, read as follows:

Equations of motion:

$$\ddot{\bar{r}} = -\Gamma \frac{\bar{r}}{r^3} + P \quad k = 2 \quad (13a)$$

where

$$\begin{aligned} \bar{P} &= \bar{P}_2, \quad \Gamma = \gamma(m_1 + m_2) \\ \ddot{\bar{r}}_k &= \bar{P}_k \quad K = 3 \text{ -- } N. \end{aligned} \quad (13b)$$

The  $\bar{P}_j$ ,  $j = 2 \text{ -- } N$ , are linear combinations of terms  $\bar{r}_\nu / r_{j\ell}^{*3}$ ,  $j\ell \neq 12$ ; i.e.,  $1/r^3$  does not occur in these expressions.

Conservation of energy:

$$\frac{1}{2} \sum_{\nu=2}^N \mu_\nu \dot{\bar{r}}_\nu \dot{\bar{r}}_\nu - \sum_{\substack{j, \ell \\ j < \ell}} \gamma m_j m_\ell \frac{1}{r_{j\ell}^*} = T + U = h,$$

where

1. Sperling, Hans J.: The Binary Collision In The N-Body Problem. ICARUS, Sept. 1968, pp. 305-314

$$\mu_\nu = m_\nu \frac{\sum_{k=1}^{\nu-1} m_k}{\sum_{k=1}^{\nu} m_k}, \quad \nu = 2 \text{ -- } N. \quad (14)$$

Lagrange-Jacobi equation:

$$\frac{d^2}{dt^2} \sum_{\nu=2}^N \mu_\nu \bar{r}_\nu \bar{r}_\nu = 4h - 2U. \quad (15)$$

## IV. DEFINITION OF BINARY COLLISION

It is no restriction of generality to assume that the binary collision takes place between the particles  $m_1$  and  $m_2$ . We shall use the following:

Definition of a binary collision: There is a binary collision of the particles  $m_1$  and  $m_2$  at  $t = t^*$  along  $C[t_0, t^*]$  if:

(1)  $\bar{r}$  and  $\bar{r}_k$ ,  $k = 3 \text{ -- } N$ , are holomorphic and bounded on  $C[t_0, t^*]$ ;

(2)  $|r_{j\ell}^*| \geq c > 0$  on  $C[t_0, t^*]$ ,  $j\ell \neq 12$ , for some positive constant  $c$ ;

(3)  $r \neq 0$  on  $C[t_0, t^*]$  and  $\liminf r = 0$  as  $t \rightarrow t^*$  on  $C$ ;

(4)  $LC[t, t^*] \leq M |t - t^*|^\alpha$ ,  $M > 0$ ,  $\alpha > \frac{2}{3}$ , for all  $t$  sufficiently close to  $t^*$ .

Remark: Condition (3) implies that  $r$  is not a constant, i.e., that  $\dot{r}$  does not vanish identically. Condition (4) is required only in part of this paper and is necessitated by our method of proof.

## V. CONVERGENCE OF SUNDMAN'S INTEGRAL

In this part we discuss briefly the steps leading to the convergence proof for Sundman's integral. The method used for this proof in the real case cannot be applied, since it is based on considerations that cannot be carried over to the complex case; thus, a different approach had to be devised. The detailed proof is contained in the literature.<sup>1</sup>

Theorem 1:

(a) All  $r_{j\ell}^*$  are bounded on  $C[t_0, t^* [$  ;

(b) the  $\bar{r}_k$ ,  $k = 3 \dots N$ , are bounded on  $C[t_0, t^* [$ ;

(c)  $\bar{r}_k$  and  $\frac{d}{dt}\bar{r}_k$ ,  $k = 3 \dots N$ , are bounded on  $C[t_0, t^* [$  and  $\lim_{t \rightarrow t^*} \bar{r}_k$  and  $\lim_{t \rightarrow t^*} \frac{d}{dt}\bar{r}_k$  as  $t \rightarrow t^*$  on  $C$  exist.

The key for the proof of the convergence of Sundman's integral

$$\int_{t_0}^t \frac{dt}{r}$$

as  $t \rightarrow t^*$  is the Lagrange-Jacobi equation (15), put into a suitable form. To simplify the notation, we set

$$R = r^2; \quad (16)$$

since  $r \neq 0$  on  $C[t_0, t^* [$ ,  $r$  can be recovered uniquely from  $R$ . Split the potential  $U$  [compare with equation (14)] into the sum

$$U = -\gamma m_1 m_2 \frac{1}{r} + U^*, \quad (17)$$

where  $U^*$  does not contain a term proportional to  $\frac{1}{r}$ ; i.e.,  $U^*$  is holomorphic and bounded on  $C[t_0, t^* [$ . Solving for  $\ddot{R}$ , we write the Lagrange-Jacobi equation as

$$\mu_2 \ddot{R} = 2\gamma m_1 m_2 \frac{1}{\sqrt{R}} + 4h - 2U^* - \frac{d^2}{dt^2} \sum_{\nu=3}^N \mu_\nu \bar{r}_\nu \bar{r}_\nu \quad (18a)$$

or, combining the bounded terms on the right into one term  $b = b(t)$  — the last term is bounded by theorem 1:

$$\ddot{R} = \frac{2\Gamma}{\sqrt{R}} + b, \quad b = b(t) \text{ holomorphic and bounded on } C[t_0, t^* [ \quad (18b)$$

Theorem 2:

(a)  $\lim R = \lim r = 0$  as  $t \rightarrow t^*$  ;

(b)  $\dot{R}$  is bounded on  $C[t_0, t^* [$  and  $\lim_{t \rightarrow t^*} \dot{R}$  exists.

Theorem 3: The limit of Sundman's integral:

$$s = s_0 + \int_{t_0}^t \frac{d\tau}{r}$$

as  $t \rightarrow t^*$  on  $C$  exists and is finite.

Proof: Integrating the Lagrange-Jacobi equation (18b) from  $t_0$  to  $t \neq t^*$ , we get

$$2\Gamma \int_{t_0}^t \frac{d\tau}{r} = \dot{R}(t) - R(t_0) - \int_{t_0}^t R b d\tau, \quad (19)$$

and, by Theorem 2 and the fact that integrals over bounded functions (compare with lemma 1) exist, the limit on the right exists as  $t \rightarrow t^*$  on  $C$ .

## VI. REGULARIZATION OF THE EQUATIONS OF MOTION

We shall now introduce Sundman's variable  $s$  instead of time  $t$  as the independent variable into the equations of motion. The rectifiable curve  $C[t_0, t^* [$  is transformed by

$$s = s_0 + \int_{t_0}^t \frac{d\tau}{r}$$

into a bounded curve  $C^* = C^*[s_0, s^* [$  in the  $s$ -plane, where  $s^* = s(t^*)$  (existing by theorem 3). Under the assumption that  $C^*$  is rectifiable, we will show that all dependent variables occurring in the transformed equations of motion possess limits as  $s \rightarrow s^*$  on  $C^*$  and that these equations, after slight modification, remain holomorphic at the point (limits of the dependent variables,  $s^*$ ) in the space of the dependent variables and  $s$ . Consequently, by Painlevé's theorem, they possess a unique holomorphic continuation of the given solution into this point.

Denote differentiation with respect to  $s$  by a prime; then the transformation equations are

$$\frac{d}{dt} = \frac{1}{r} \frac{d}{ds}; \quad \frac{d^2}{dt^2} = \frac{1}{r^2} \frac{d^2}{ds^2} - \frac{r'}{r^3} \frac{d}{ds} \quad (20)$$

The equations of motion are easily transformed as follows: Equation (13b) yields

$$\bar{r}_k'' = \frac{r' \bar{r}'_k}{r} + r^2 \bar{p}_k \quad k = 3 \dots N ; \quad (21)$$

the quantity

$$\bar{S}_k = \frac{\bar{r}'_k}{r} = \dot{\bar{r}}_k \quad k = 3 \dots N \quad (22)$$

is holomorphic and bounded on  $C[t_0, t^*[$  and by theorem 1 has a limit as  $t \rightarrow t^*$  on  $C$ ; therefore, the limit as  $s \rightarrow s^*$  on  $C^*$  exists. Differentiating (22), we find

$$\bar{S}'_k = r \bar{p}_k \quad k = 3 \dots N, \quad (23)$$

and we can replace equation (13b) by the system (22) and (23):

$$\bar{r}'_k = r \bar{S}_k \quad k = 3 \dots N. \quad (24)$$

$$\bar{S}'_k = r \bar{p}_k$$

The Lagrange-Jacobi equation (18a) can be written, substituting for  $\bar{r}'_k$  and  $\bar{S}'_k$  from (13b) and (22), as

$$\frac{d^2}{dt^2} r^2 = \frac{2\Gamma}{r} + 2W, \quad (25)$$

$$W = \frac{2h - U^*}{\mu} \sum_{k=3}^N \frac{\mu_k}{\mu} (\bar{r}_k \bar{p}_k + \bar{S}_k \bar{S}_k);$$

with

$$\frac{d^2}{dt^2} r^2 = 2 \frac{r''}{r},$$

we get

$$r'' = \Gamma + rW. \quad (26)$$

Equation (13a) is transformed into

$$r \bar{r}'' = r' \bar{r}' - \Gamma \bar{r} + r^3 \bar{p}. \quad (27)$$

We differentiate and substitute from equation (26); then,

$$\bar{r}''' = W \bar{r}' + 3 r r' \bar{p} + r^2 \bar{p}'. \quad (28)$$

Recall from equation (13) that  $\bar{p}$  is a sum of terms  $\bar{r}'_{j\ell} / r^{*3}$ ,  $j\ell \neq 12$ . It follows that  $\bar{p}'$  is a linear function of the  $s'_\nu, y'_\nu, z'_\nu$ , and since by theorem 1 for  $\nu \geq 3$ , these variables have limits (zero, because  $\bar{r}'_k = r \dot{\bar{r}}_k$ ) as  $s \rightarrow s^*$  on  $C^*$ , we can consider  $\bar{p}'$  as a linear function of  $x'_\nu, y'_\nu, z'_\nu$ , with coefficients that are holomorphic and bounded on  $C^*[s_0, s^*[$ . Setting

$$\bar{p}' = \bar{L}_1(\bar{r}') + \bar{L}_2 \quad (29)$$

we write, for (28),

$$\bar{r}''' = W \bar{r}' + r^2 \bar{L}_1(\bar{r}') + 3 r r' \bar{p} + r^2 \bar{L}_2. \quad (30)$$

For the following, we must assume that  $C^*[s_0, s^*]$  is rectifiable. Since  $W$  is holomorphic and bounded on  $C^*[s_0, s^*[$  we infer (compare with lemma 1) from equation (26) that  $\lim r'$  as  $s \rightarrow s^*$  on  $C^*$  exists and is finite (we know this already of  $r$ ). Write equation (30) as a system of differential equations of the first order (the variables  $\bar{p}^+$  occurring in the following are not related to the  $\bar{p}$ 's in Sections I and II):

$$\begin{aligned} \bar{r}' &= \bar{\rho}_1^+ \\ \bar{\rho}_1^+ &= \bar{\rho}_2^+ \\ \bar{\rho}_2^+ &= W \bar{\rho}_1^+ + r^2 \bar{L}_1(\bar{\rho}_1^+) + 3 r r' \bar{p} \\ &\quad + r^2 \bar{L}_2. \end{aligned} \quad (31)$$

The coefficients 1,  $W$ , etc., are holomorphic and bounded on  $C^*[s_0, s^*[$ , and (compare with lemma 1) we infer that the limits of  $\bar{r}, \bar{r}' = \bar{\rho}_1^+$ , and  $\bar{r}'' = \bar{\rho}_2^+$  as  $s \rightarrow s^*$  on  $C^*$  exist and are finite. Thus, we have that all dependent variables have finite limits  $\bar{r}_k^*, \dots, \bar{\rho}_2^{*+}$  as  $s \rightarrow s^*$  on  $C^*$ , and the right sides of the full system of the equation of motion (24), (26), and (31)

$$\begin{aligned} \bar{r}'_k &= r \bar{S}_k \\ \bar{S}'_k &= r \bar{p}_k \end{aligned} \quad k = 3 \dots N$$

$$\begin{aligned}
r' &= \rho^+ \\
\rho^+ &= \Gamma + rW \\
\bar{r}' &= \bar{\rho}_1^+ \\
\bar{\rho}_1^+ &= \bar{\rho}_2^+ \\
\bar{\rho}_2^+ &= W \bar{\rho}_1^+ + r^2 \bar{L}_1(\bar{\rho}_1^+) + 3r \rho^+ \bar{P} \\
&\quad + r^2 \bar{L}_2
\end{aligned} \tag{32}$$

remain holomorphic at the point  $(\bar{r}_3^*, \dots, \bar{\rho}_2^+, s^*)$ . Therefore, by Painlevé's theorem, the system (32) possesses a unique holomorphic solution  $\bar{r}_k(s), \dots, \bar{\rho}_2^+$  at this point, being the holomorphic continuation of the given solution.

We had to assume in the foregoing that  $C^*[s_0, s^*]$  is rectifiable, i.e., that

$$\int_{t_0}^t \left| \frac{dt}{r} \right|$$

converges as  $t \rightarrow t^*$ . It appears to be difficult to find general conditions for  $C$  such that  $C^*$  is also rectifiable, because not enough is known about  $r(t)$  for general  $C$ : the estimates cannot be made sharp enough. It can be shown that the condition

$$\begin{aligned}
LC[t, t^*] &\leq M |t - t^*|^\alpha, \quad M > 0, \quad \alpha > \frac{2}{3}, \\
&t \text{ sufficiently close to } t^*
\end{aligned}$$

is sufficient for the rectifiability of  $C^*[s_0, s^*]$ .

Observe that the case of  $C$  being (eventually) a line segment is included for  $M = \alpha = 1$ .

## VII. THE NATURE OF THE SINGULARITY AT A BINARY COLLISION

Denote by  $Q_j = Q_j(s - s^*)$  a power series in  $s - s^*$  that converges on some neighborhood of  $s^*$ ; since  $r(s^*) = 0$ , we have  $r = r'(s^*)(s - s^*) + \dots$ . Set  $rW = (s - s^*) Q_1$  and integrate equation (26) twice from  $s^*$  to  $s$ :

$$r'' = \Gamma + (s - s^*) Q_1$$

$$\begin{aligned}
r' &= r'(s^*) + \Gamma(s - s^*) + (s - s^*)^2 Q_2 \tag{33} \\
r &= r'(s^*)(s - s^*) + \frac{1}{2} \Gamma(s - s^*)^2 + (s - s^*)^3 Q_3.
\end{aligned}$$

From

$$t - t^* = \int_{s^*}^s r \, ds,$$

we find then

$$\begin{aligned}
t - t^* &= \frac{1}{2} r'(s^*)(s - s^*)^2 + \frac{1}{6} \Gamma(s - s^*)^3 \\
&\quad + (s - s^*)^4 Q_4,
\end{aligned}$$

and by inversion

$$\begin{aligned}
s - s^* &= \text{power series in } (t - t^*)^{1/2} \\
&\quad \text{if } r'(s^*) \neq 0, \\
s - s^* &= \text{power series in } (t - t^*)^{1/3} \\
&\quad \text{if } r'(s^*) = 0.
\end{aligned}$$

The condition for  $\bar{r}(s^*) = 0$  can be determined easily (observe that  $r(s^*) = 0$  does not imply  $\bar{r}(s^*) = 0$  in the complex): Substitute (33) and  $\bar{r} = \bar{r}(s^*) + \bar{r}'(s^*)(s - s^*) + \dots$ , into the equation of motion (27)

$$r \bar{r}'' = r' \bar{r}' - \Gamma \bar{r} + r^3 \bar{P}.$$

Comparison of coefficients yields

$$r'(s^*) \bar{r}'(s^*) - \Gamma \bar{r}(s^*) = 0.$$

Therefore,  $r'(s^*) = 0$  implies  $\bar{r}(s^*) = 0$ ; let  $r'(s^*) \neq 0$ ; then  $\bar{r}(s^*) = \bar{r}'(s^*) = 0$ , or  $\bar{r}(s^*) \neq 0$ . Comparing the power series for  $r^2 = \bar{r} \bar{r}$  at  $s^*$  from (33) and from

$$\begin{aligned}
\bar{r}(s) &= \bar{r}(s^*) + \bar{r}'(s^*)(s - s^*) \\
&\quad + \frac{1}{2} \bar{r}''(s^*)(s - s^*)^2 + \dots
\end{aligned}$$

and observing that  $\bar{r}'(s^*) \bar{r}'(s^*) = 0$ , we find the relation

$$r'(s^*)^2 = \bar{r}(s^*) \bar{r}(s^*).$$

Hence,  $r'(s^*) \neq 0$  implies  $\bar{r}(s^*) \neq 0$  and  $\bar{r}(s^*) \neq 0$ .

We can now formulate the following:

**Theorem 4:** A binary collision takes place at an algebraic branch point  $t^*$  in the  $t$ -plane. If  $r(s^*) \neq 0$ , then the branch point is of the first order, and the coordinates  $\bar{r}$ , etc., are in a neighborhood of  $t^*$

meromorphic functions of  $(t - t^*)^{1/2}$  with finite principal parts at  $t^*$ . If  $\bar{r}(s^*) = 0$ , then the branch point is of the second order, and the coordinates  $\bar{r}$ , etc., are in a neighborhood of  $t^*$  meromorphic functions of  $(t - t^*)^{1/3}$  with finite principal parts at  $t^*$ .

**Remark:** Since  $\dot{R}(t^*) = 2r'(s^*)$ ,  $r'(s^*) = 0$  if and only if  $\dot{R}(t^*) = 0$ . From the previously used formula,

$$\frac{1}{4} \dot{R}(t)^2 = r(t)^2 \dot{\bar{r}}(t) \ddot{\bar{r}}(t) - \bar{K}(t)^2,$$

we see that  $\lim_{t \rightarrow t^*} K(t) = 0$  if and only if  $\dot{R}(t^*) = 0$ .

### VIII. AN ENERGY INTEGRAL DOES NOT NECESSARILY EXIST

The foregoing discussion of the regularization of a binary collision is based on the Lagrange-Jacobi equation (15) (or (18b)), which in turn is derived using the energy integral. There are important cases, however, where an energy integral -- or a similar integral, as the Jacobi integral in the Restricted Three-Body problem -- does not exist; the Reduced Three-Body problem and certain "perturbed Two-Body problems" are examples.

With suitable restrictions on the "perturbative force," the regularization of the binary collision can be carried out in these cases similarly to the N-Body problem. We shall briefly discuss the procedure leading to an analogon of the Lagrange-Jacobi equation, the convergence of Sundman's integral, and the regularization of the equations of motion at a binary collision by a modification of the process used before.

Write the equation of motion as a perturbed Two-Body problem:

$$\ddot{\bar{r}} = -\Gamma \frac{\bar{r}}{r^3} + \bar{P}. \quad (34)$$

The notation is as before: the particle  $m = m_2$  at  $\bar{r}$  is to collide with the particle  $m_1$  resting at the origin,

and we assume that the perturbative force  $\bar{P} = \bar{P}(\bar{r}, t)$  is bounded on  $C[t_0, t^*]$  and that it can be derived

from a potential  $U = U(\bar{r}, t)$  such that  $U$  and  $\partial U / \partial t$  remain bounded on  $C[t_0, t^*]$ . This is the case, e.g.,

for the Reduced Three-Body problem.

Define an "energy"  $h$  by

$$h = \frac{1}{2} \dot{\bar{r}} \dot{\bar{r}} - \frac{\Gamma}{r}. \quad (35)$$

Then we derive from (34)

$$\dot{h} = \dot{\bar{r}} \bar{P}. \quad (36)$$

By assumption

$$\bar{P} = -\text{grad}_{\bar{r}} U; \quad (37)$$

therefore,

$$\frac{dU}{dt} = -\dot{\bar{r}} \bar{P} + \frac{\partial U}{\partial t}, \quad \dot{h} = -\frac{dU}{dt} + \frac{\partial U}{\partial t}$$

and by integration

$$h = -U + \int \frac{\partial U}{\partial t} dt + \text{const}. \quad (38)$$

Since  $U$  and  $\partial U / \partial t$  are bounded on  $C[t_0, t^*]$ ,  $h$  is so. The analogon of the Lagrange-Jacobi equation is derived as follows:

$$r^2 = \bar{r} \bar{r}$$

$$\frac{d^2}{dt^2} r^2 = 2 \bar{r} \ddot{\bar{r}} + 2 \dot{\bar{r}} \dot{\bar{r}}.$$

Substituting from (34) and (35), we find

$$\frac{d^2}{dt^2} r^2 = \frac{2\Gamma}{r} + 4h + 2 \bar{r} \bar{P} \quad (39)$$

(where  $h$  generally is not constant). We observe that this equation is of the form (18b), and the convergence of Sundman's integral follows as before.

If we make suitable assumptions about the differentiability of  $\bar{P}$ , we can regularize the equations of motion by the method we have used before; otherwise, a modification of the method first used by Sundman leads to the regularization.

Introducing into equation (34) Sundman's variable  $s$ , we get

$$\bar{r}'' = \frac{r' \bar{r}' - \Gamma \bar{r}}{r} + r^2 \bar{P}; \quad (40)$$

(compare with equation (27)).

Setting

$$\bar{S} = \frac{r' \bar{r}' - \Gamma \bar{r}}{r}, \quad (41)$$

we easily find, by means of the transformed Lagrange-Jacobi equation

$$r'' = \Gamma + r(2h + \bar{r} \bar{P}), \quad (42)$$

that

$$\bar{S}' = (2h + \bar{r} \bar{P}) \bar{r}' + r r' \bar{P}. \quad (43)$$

From (42) it follows that  $r'$  remains bounded on  $C^*[s_0, s^*[$  and that  $\lim r'$  as  $s \rightarrow s^*$  on  $C^*$  exists. Assume now, as before, that  $C^* = C^*[s_0, s^*]$  is rectifiable. Writing (40), (41), (43) as a system of differential equations of the first order for  $\bar{r}$ ,  $\bar{\rho}_1^+ = \bar{r}'$ , and  $\bar{S}$ :

$$\bar{r}' = \bar{\rho}_1^+$$

$$\bar{\rho}_1^{+'} = \bar{S} + r^2 \bar{P} \quad (44)$$

$$\bar{S}' = (2h + \bar{r} \bar{P}) \bar{\rho}_1^+ + r r' \bar{P},$$

we see that lemma 1 is applicable and conclude that  $\bar{r}$ ,  $\bar{r}'$ , and  $\bar{S}$  remain bounded on  $C^*[s_0, s^*[$  and that their limits as  $s \rightarrow s^*$  exist.

Therefore, as before, all dependent variables have limits  $\bar{r}^*, \dots, \rho^{+*}$  as  $s \rightarrow s^*$  on  $C^*$ , the right sides of the system of equations of motion

$$\bar{r}' = \bar{\rho}_1^+$$

$$\bar{\rho}_1^{+'} = \bar{S} + r^2 \bar{P}$$

$$\bar{S}' = (2h + \bar{r} \bar{P}) \bar{\rho}_1^+ + r \rho^+ \bar{P} \quad (45)$$

$$h' = \bar{\rho}_1^+ \bar{P}$$

$$r' = \rho^+$$

$$\rho^{+'} = \Gamma + r(2h + \bar{r} \bar{P})$$

remain holomorphic at  $s^*$ , and we conclude as previously that the system (45) possesses a unique holomorphic solution  $\bar{r}(s), \dots, \rho^+(s)$  at the point  $(\bar{r}^*, \dots, \rho^{+*}, s^*)$ , being the holomorphic continuation of the given solution.

#### IV. FLIGHT MECHANICS

# OPTIMIZATION OF "EPHEMERIDAL" PARAMETERS FOR MINIMUM PROPELLANT REQUIREMENTS ON MULTIPLANET ROUNDTRIP SWINGBY-STOPOVER MISSIONS

By

Charles W. Mead<sup>1</sup> and Archie C. Young<sup>2</sup>

## ABSTRACT

A completely automatic computerized method for determining the ephemeridal parameters (launch and arrival dates, trip times, heliocentric transfer angle, etc) for roundtrip swingby-stopover missions, for one-way planetary capture missions which result in minimum mission propellant requirements is discussed. The computer program in its present form is designed to optimize missions requiring up to four major propulsive maneuvers. The interplay of the magnitudes of these velocity changing maneuvers ( $\Delta V$ 's) as they are related to the total initial weight of the vehicle is described as a "snowballing" effect. The magnitudes of the velocity impulses themselves are governed primarily by the trajectory ephemeridal conditions. However, the propellant required for each maneuver is a function of the total mass of the vehicle at the time of the impulse application; i.e., when the first  $\Delta V$  is applied, the total mass of the vehicle includes the propellants necessary to perform the second, third and fourth maneuvers, as well as the inert structure and engine weight for each stage. The vehicle is configured by the program by means of parameter options and payload specifications. All variable weights are sized using general scaling laws which are dependent upon propellant loading and whose coefficients are input. The program uses unique numerical and analytical mathematic techniques for computing, storing and sorting of trajectory and performance data to minimize the ratio of initial vehicle weight just before boost out of Earth parking orbit to the final weight returned to Earth, or in the case of one-way capture missions, the weight delivered to a planetary parking orbit. The program is coded in FORTRAN IV and the run time, on the IBM 7094 computer, is typically 2000 trajectories per minute for roundtrip Mars stopover-Venus swingby missions.

## DEFINITION OF SYMBOLS

A	Constant defining planetary parking orbit shape $A = \frac{2n}{n+1}$
a	Semi-major axis
C	Constant used in rocket equation accounting for gravity losses
G	Constant used in vehicle propellant tank weight calculation
g	Gravitational acceleration at surface of Earth
$I_{sp}$	Propulsion system specific impulse
n	Ratio of apoapsis to periapsis radius of planetary parking orbit
r	Radius vector from center of planet to spacecraft
$r_a$	Apoapsis radius
$r_p$	Periapsis radius
U	Ratio of stage drop weight, that is independent of the propellant loading, to terminal payload weight
V	Velocity
$\Delta V$	Impulsive velocity change
$V_{ep}$	Velocity at periapsis of elliptic planetary parking orbit

- 
1. Lockheed Missiles & Space Company, Huntsville Research & Engineering Center
  2. Aero-Astroynamics Laboratory, George C. Marshall Space Flight Center.

$V_h$	Hyperbolic path speed	4	Braking maneuver at Earth return
$V_{hp}$	Periapsis velocity of planetocentric hyperbolic trajectory	f	Conditions just after a $\Delta V$ maneuver
$W_D$	Stage drop weight that is not dependent upon propellant loading	i	Refers to the $i^{\text{th}}$ $\Delta V$ maneuver ( $i = 1$ to 4, above)
$W_f$	Vehicle gross weight immediately following a $\Delta V$ maneuver		
$W_o$	Vehicle gross weight immediately preceding a $\Delta V$ maneuver.		
$W_p$	Propellant weight		
$W_{PL}$	Terminal payload weight		
$\alpha$	Right ascension of hyperbolic excess velocity vector referenced to planet's vernal equinox.		
$\beta$	Bend angle increment for corrected pericenter passages		
$\gamma$	Vehicle weight ratio		
$\delta$	Declination of hyperbolic excess velocity vector referenced to planet's equatorial plane		
$\eta$	Payload ratio		
$\kappa$	Bend angle		
$\mu$	Planetary gravitational constant		
$\psi$	Complement of half-angle of passage hyperbola		
<b>Subscripts</b>			
$\infty$	Infinity relative to planet		
0	Conditions just prior to a $\Delta V$ maneuver		
1	Injection maneuvers at Earth departure; also refers to hyperbolic excess velocity vector at swingby planet arrival.		
2	Capture maneuver at target planet arrival; also refers to hyperbolic excess velocity vector at swingby planet departure		
3	Injection maneuver at stopover planet departure		

## I. INTRODUCTION

All studies of present and future interplanetary missions require a broad analysis of various aspects of interplanetary trajectory design. Since all interplanetary missions in the foreseeable future will be limited by the propulsive capabilities of the launch vehicle and spacecraft, the most important criteria used in interplanetary trajectory design and selection will be based on minimizing the mission energy requirements which leads directly to a minimization of vehicle mass and propellant requirements. This paper presents a discussion of a completely automatic computerized method for determining the ephemerical parameters (launch date, trip time, heliocentric transfer angle, etc) for roundtrip swingby-stopover missions or for one-way planetary capture missions which result in minimum mission propellant requirements.

The motivation for developing this computerized optimization scheme was provided when attempts to perform mission optimization studies by hand methods using cross-plots of various trajectory parameters proved to be prohibitive because of the large amount of data involved. The computer program in its present form is designed to handle missions requiring up to four major propulsive maneuvers. The interplay of the magnitudes of these velocity changing maneuvers ( $\Delta V$ 's) as they are related to the total initial weight of the vehicle is described as a "snowballing" effect. The magnitudes of the velocity impulses themselves are governed primarily by the trajectory ephemerical conditions. However, the propellant required for each maneuver is a function of the total mass of the vehicle at the time of the impulse application; i.e., when the first  $\Delta V$  is applied, the total mass of the vehicle includes the propellants necessary to perform the second, third, and fourth maneuvers, as well as inert structure and engine weight for each stage. Thus, the sum of the  $\Delta V$ 's does not give an adequate indication of the amount of propellant required; instead, the total propellant requirements are arrived at by working backward through the mission

to determine the propellant for each maneuver based on the requirements of all subsequent maneuvers.

This program uses, in a unique manner, numerical and analytical mathematic techniques for computing, storing and sorting of trajectory and performance data to minimize the ratio of initial vehicle weight just before boost out of Earth parking orbit to the final weight returned to Earth, or in the case of one-way capture missions, the weight delivered to a planetary parking orbit. Parameters specified are Earth launch window duration, stopover time, parking orbit altitudes, maximum declination of the departure hyperbolic asymptote, minimum passage distance at the swingby planet, and Earth reentry speed limit (for round-trip missions). When the program is used for optimizing direct one-way capture missions, the type of interplanetary trajectory (Type I or Type II, depending upon whether the heliocentric transfer angle is less than  $180^\circ$  or greater than  $180^\circ$ ) can be specified as an input. The vehicle configuration is determined by parameter options and payload specifications. All variable weights are sized using general scaling laws which are dependent upon propellant loading and whose coefficients are input.

The program has the capability of optimizing a mission for one or more constrained trajectory parameters. These include launch or arrival date at Earth and arrival or departure date at the target planet, as well as a specified Earth departure window duration. When one of these independent parameters is constrained, the program optimizes those that are nonconstrained; if all are constrained, the vehicle is sized for a fixed trajectory.

## II. MISSION MODE CAPABILITIES OF THE SWISTO PROGRAM

The SWISTO program (SWingby-STopover Optimization) is capable of performing optimization analyses of interplanetary missions which involve one, two, or three interplanetary transfer trajectories. Flexibility of the program allows six interplanetary mission modes to be analyzed. These six types of missions are outlined by the schematic mission profiles of Figures 1 through 3-b and are grouped according to the number of individual interplanetary trajectory "legs" required by the missions. As indicated in the diagrams of Figures 1 through 3-b, all missions

involving roundtrip stopovers require four  $\Delta V$ 's while the roundtrip flybys and one-way capture missions require only two  $\Delta V$ 's.

For the missions which are of most interest currently, the departure planet is Earth, while the swingby and stopover planets are Venus and Mars, respectively. However, the program is designed so that any of the nine planets or the asteroid Ceres can be designated to fulfill any of the roles indicated, so long as the same planet is not designated for two successive roles.

The direct roundtrip Mars missions have been studied by many investigators, and the time intervals which are favorable for such missions during the next thirty years are fairly well known. Recently, the notion of using a Venus swingby for the Mars mission has been introduced and studied in some detail [1, 2, 3, 4, 5, 6]. These studies showed that by using the Venus swingby to shape the Mars mission trajectory, the energy (therefore propellant) requirements can in most cases be reduced significantly. The opportunities for this type of mission occur less frequently than those for the direct missions, yet the advantages make this mode of transfer particularly attractive. Deerwester [1] has shown that usually each opportunity for an opposition class Mars stopover mission, using an outbound Venus swingby, is separated by two opportunities for opposition class missions using an inbound Venus swingby. However, of these two inbound swingby opportunities only one is clearly attractive for trajectory shaping purposes, and the other represents a marginal situation in which either an outbound or inbound swingby is possible, with most cases favoring the inbound swingby. Thus, the opportunities for attractive outbound Venus swingbys to Mars occur only about every six years, corresponding to one out of each three Earth-Mars opposition periods. Even though the opportunities for using the outbound swingby mode for Mars missions are somewhat restricted, this mode is very attractive when Jupiter is used as the swingby planet to the outer regions of the solar system [7, 8, 9, 10].

### A. Direct One-Way Capture Mission Mode

The direct one-way planetary capture mission is the simplest of all the SWISTO mission modes, since only one interplanetary trajectory leg is involved and the mission requires only two major propulsive maneuvers, as depicted schematically by Figure 1. The primary purpose of a mission of this type would

be to place an unmanned scientific payload into orbit about the target planet so as to gather the maximum amount of scientific data compatible with the design of the spacecraft and the constraints placed on the mission definition. To accomplish such a mission, it is necessary to examine the interrelationships between the flight mechanical parameters of the injection, heliocentric transfer, and capture maneuvers, consistent with the launch vehicle capabilities, spacecraft orbit insertion limitations, communications, and scientific experiment requirements [11].

With these considerations in mind, this version of the SWISTO program was designed to calculate the launch and arrival dates which satisfy the various mission and vehicle performance constraints and result in minimum mission propellant requirements.

A general discussion of the vehicle weight, performance calculation and optimization, and the launch window analysis, for all mission modes of the SWISTO program, will be presented later.

## B. One-Way Swingby Capture Mission Mode

The mission profile for this mode is represented schematically by Figure 2-a. The basic objectives of a mission of this type are the same as those of the direct capture missions. The only reason for using the swingby of the intermediate planet is to use the planet's gravitational field to shape the interplanetary trajectory and reduce the total mission energy requirements. However, as previously stated, this mode of transfer provides a "savings" in mission energy, over the direct mission only if the planets' relative positions are such that the swingby planet can be used effectively. Hollister's analysis [2] presents the geometric criteria necessary to assure the availability of Venus for a swingby to Mars.

Figure 2-a shows that this mode of transfer has an added degree of complexity when compared to the direct transfer. The main reason for the added complexity of the swingby is the requirement that the two separate heliocentric legs properly match at the swingby planet. The technique used for matching successive single leg trajectories at the swingby planet will be discussed later.

## C. Direct Roundtrip Flyby Mission Mode

The mission profile for this mode is shown in Figure 2-b. As can be seen by comparing Figures 2-a and 2-b, the profiles for the direct roundtrip flyby mission is very similar to the one-way swingby capture mission except the departure and target planets are the same for the roundtrip flyby mission. Both missions usually require two major  $\Delta V$  maneuvers. Thus, the trajectory calculation and optimization schemes are identical between these two mission modes.

## D. Direct Roundtrip Stopover Mission Mode

In general, roundtrip stopover missions are composed simply of two single-leg trajectories. The first is the single-leg trajectory connecting the departure planet on the departure date with the target planet on the arrival date. The spacecraft is then captured (goes into orbit or lands) at the target planet and after a specified stopover time is injected onto a return trajectory back to Earth (Figure 2-c). At first glance, a roundtrip seems to produce no new problems, since its return leg simply repeats the problems of the outbound leg in reverse order. However, since all the basic astrodynamics problems of interplanetary travel are time-dependent, what is easy at one time may be impractical at some subsequent time. Therefore, since the return leg must follow the outbound leg in time, it does introduce new problems, which in fact make it just about impossible to use the optimum trajectory for either leg. An optimum roundtrip trajectory usually can be achieved only if both legs are compromised to some extent (assuming that the stopover time is short, i. e., <60 days).

The direct roundtrip stopover missions that this version of the SWISTO program is designed to optimize can be further divided into two subcases, commonly referred to as the "direct mode" and the "direct inverted mode," described as follows. (The Mars stopover mission will be used to discuss the two modes; however, the mechanics of these modes of transfer are applicable for missions to other planets as well.) In the direct mode, the outbound trajectory approximates a Hohmann transfer with the Earth-Mars opposition occurring about half way enroute to Mars (see Figure 4). This results in low propulsion

requirements at Earth departure. Assuming a reasonable short stay on Mars of perhaps one month, the return leg, however, will deviate considerably from the Hohmann transfer, for the angular relationship of Earth and Mars will have changed drastically since the time of Earth launch. Returning to Earth, it will be necessary to cover an angular distance considerably exceeding 180 degrees. This will increase the  $\Delta V$  requirement for launch from Mars and, more important, lead to a high arrival velocity at Earth. Since Mars will lag the Earth by a large angle at the time of return launch, the spacecraft will have to move inside the Earth's orbit if it is to catch up with the Earth. As a result it will acquire a high angular velocity which will result in a high  $\Delta V$  at Earth return in order to reduce the spacecraft's velocity to within acceptable reentry limits.

The direct inverted mode is simply the mirror image of the direct mode — now it is the outbound leg that deviates from the near Hohmann transfer and the return leg approximates one, with the Earth-Mars opposition occurring about half way on the return leg (see Figure 5). Earth arrival velocity therefore will be low, but the  $\Delta V$  for Earth launch will be extremely high.

Both the initial propulsion requirement and the Earth arrival velocity, as well as the problem of timing the launch, can be reduced if an extended stopover at Mars is assumed. The insertion of a separating period of time in effect divides the overall journey into two missions that, to a large extent, can be optimized independently of each other through the choice of favorable launch date for each (see Figure 6). Unfortunately, the separation time must be considerable. In fact, one cannot take full advantage of this mission mode without a stopover on Mars lasting one to two years, which appears impractical for missions in the near future.

The optimization scheme used in this version functions basically the same way as for the versions previously described, except an allowance is made for two additional  $\Delta V$  maneuvers, namely, for departing the stopover planet and arriving back at Earth.

### E. Roundtrip Outbound Swingby-Stopover Mission Mode

The outbound swingby-stopover mission design is based on using a combination of the best features

of one-way outbound swingby capture missions and the direct roundtrip stopover capture missions previously described. For example, starting with the "direct inverted mode" profile for the roundtrip Mars mission, shown in Figure 5, it is seen that the outbound leg passes within the vicinity of Venus' orbit, thus giving rise to a possible use of Venus' gravity field to "shape" this portion of the trajectory in such a manner that the energy requirements will be reduced. It is also observed that if the swingby is used to reduce the outbound energy requirements, and since the inbound leg approximates a Hohmann transfer, thus reducing the Earth return  $\Delta V$  requirements, then the total mission energy can be reduced considerably by using this mode of transfer. As previously discussed, such mission opportunities exist about every six years. Thus, this version of the SWISTO program was designed to determine the ephemeridal parameters (launch date, swingby date, arrival date, restart date, return date, etc.) that minimizes the ratio of initial weight in Earth orbit at departure to the weight returned to Earth, for a specified Earth departure window duration and stopover planet staytime.

### F. Roundtrip Inbound Swingby-Stopover Mission Mode

The inbound swingby-stopover mission design is very similar to that of the outbound swingby-stopover mission. The basic difference in the mission chronology and interplanetary trajectory design, between the inbound and outbound swingbys, is the timing of the swingby planet encounter, which, as previously discussed, occurs on the outbound leg of the mission for an outbound swingby and on the inbound leg of the mission for an inbound swingby. Thus, an inbound swingby-stopover mission is designed using the "direct mission mode" profile of Figure 4 as the basic "building block." Here, it is observed that, since the inbound leg passes within the vicinity of Venus' orbit, a judicious choice of planetary encounter dates will result in a swingby of Venus that can be used to reduce the Earth return velocity. It is shown in Reference 1 that opportunities for such missions occur during two of each three Earth-Mars opposition periods, with an outbound swingby opportunity occurring during the third opposition period.

The launch window selection and mission optimization for the inbound swingby-stopover missions is accomplished in the same manner as that for the outbound swingby-stopover mission mode.

### III. INTERPLANETARY TRAJECTORY CALCULATION

An initial step in planning any interplanetary mission is the selection of a suitable transfer trajectory connecting two given planets on two prescribed dates. Although the advent of practical, continuous, low-thrust propulsion devices may significantly alter the situation, interplanetary missions now under consideration, using impulsive high thrust propulsion systems, must be designed for essentially free-fall ballistic heliocentric transfers under the influence of solar and planetary gravity fields.

The method of calculating the heliocentric segment of all single-leg trajectories in the SWISTO program is based on a purely Keplerian transfer. A frame of reference located at the sun is chosen, and the planets are assumed to be massless points. The resulting trajectories are the usual conic sections associated with an inverse square force field, subject to the timing restrictions concerning the departure and arrival dates. The transfer trajectories are determined by an iterative solution of the Kepler relations. Lambert's Theorem is convenient for this purpose: "The transfer time between any two points on an ellipse is a function of the sum of the distances of each point from the focus, the distance between the points, and the semimajor axis of the ellipse." Lambert's Theorem can be represented by the following equation:

$$\Delta t = \Delta t(a, r_1 + r_2, c) . \quad (1)$$

These parameters are presented in Figure 7. A detailed discussion of the mathematical approach used in the SWISTO program for calculating all conic single leg interplanetary trajectories is presented in Reference 12.

In determining the trajectory characteristics during the planetocentric phases of the mission, it is of interest to transform the velocity vectors at departure and arrival from heliocentric coordinates into planetocentric coordinates, yielding values for hyperbolic velocities with respect to the planets. In this way, the speed and direction of escape and arrival at the departure and target planets, respectively, are found. If we look at the conditions at departure, the vehicle is imagined to have just escaped the planet's gravitational field, and the departure velocity vector is imagined to be located at "infinity" as seen from the planet. Any arbitrary escape maneuver may now be matched to the central, heliocentric

segment of the trajectory by causing the escaping vehicle to meet the prescribed conditions for velocity and direction at a great distance from the planet. The departure velocity at planetary infinity is usually referred to as the hyperbolic excess velocity, since it represents the excess velocity still possessed by the vehicle after escaping the planet's gravitational field.

To convert hyperbolic excess speed,  $V_\infty$ , to the speed near the planet,  $V$ , the law of conservation of energy is applied. The planetocentric hyperbolic path speed is given by the vis viva equation for hyperbolic motion as

$$V_h^2 = \left( \frac{2\mu}{r} + \frac{\mu}{a} \right) . \quad (2)$$

If this equation is evaluated at the planet's sphere of influence ( $r = \infty$ ), we obtain

$$V_\infty^2 = \frac{\mu}{a} . \quad (3)$$

By combining equations (2) and (3), the planetocentric hyperbolic path speed, in terms of the hyperbolic excess speed, is given by

$$V_h^2 = \left( \frac{2\mu}{r} + V_\infty^2 \right) . \quad (4)$$

### IV. IMPULSIVE INJECTION OR ORBIT INSERTION VELOCITY CALCULATION

The impulsive  $\Delta V$  required to transfer a space vehicle from a parking orbit about the departure planet onto the desired departure hyperbolic trajectory is determined as follows.

If the parking orbit is elliptic, the injection maneuver is accomplished most efficiently by applying the  $\Delta V$  impulse at the distance of closest approach to the planet, and is given by

$$\Delta V = V_{hp} - V_{ep} \quad (5)$$

where

$V_{hp}$  = velocity on hyperbolic departure trajectory at periapsis

$V_{ep}$  = velocity on elliptic parking orbit at periapsis.

The equations for  $V_{hp}$  and  $V_{ep}$  are obtained from the vis viva equations for hyperbolic and elliptic motion, respectively.

$$V_{hp} = \sqrt{\frac{2\mu}{r_p} + V_\infty^2} \quad (6)$$

$$V_{ep} = \sqrt{\frac{2\mu}{r_p} + \frac{\mu}{a}} \quad (7)$$

The semimajor axis of the elliptic parking orbit is given by

$$a = \frac{r_a + r_p}{2} \quad (8)$$

Thus, the equation for  $V_{ep}$  becomes

$$V_{ep} = \sqrt{\frac{2\mu}{r_p} \left( \frac{r_a}{r_a + r_p} \right)} \quad (9)$$

By combining equations (6), (7) and (9), the equation for the required injection  $\Delta V$  becomes

$$\Delta V = \sqrt{\frac{2\mu}{r_p} + V_\infty^2} - \sqrt{\frac{2\mu}{r_p} \left( \frac{r_a}{r_a + r_p} \right)} \quad (10)$$

Define

$$A = \frac{2n}{n+1},$$

where

$$n = \frac{r_a}{r_p}.$$

Equation (10) can now be written as

$$\Delta V = \sqrt{\frac{2\mu}{r_p} + V_\infty^2} - \sqrt{\frac{\mu A}{r_p}} \quad (11)$$

The spacecraft can be captured by the target planet if its velocity with respect to the planet is reduced to escape speed or less. Thus, the capture maneuver is essentially the reverse of the injection maneuver and the  $\Delta V$  equations for the injection maneuver apply equally as well for the capture maneuver, with the  $\Delta V$  being applied in the direction opposite to the motion.

## V. SWINGBY TRAJECTORY DESIGN

At a sufficiently great distance, the motion of the spacecraft with respect to the swingby planet is essentially along the asymptote of a hyperbola as shown in Figure 8. During the planetary encounter, the planet would do work on the spacecraft and, conversely, by conservation of energy, the spacecraft would do work on the planet. However, by conservation of momentum, the relative velocity changes of the planet and the spacecraft would be in inverse proportion to their masses. The spacecraft may, in general, increase or decrease its heliocentric speed depending on whether the pericenter of the passage hyperbola lies behind or in front of the planet. The amount by which the vehicle's heliocentric velocity is changed depends also on its hyperbolic excess velocity relative to the planet and the bend angle about the planet.

As shown in Figure 8, the effect on the velocity of the vehicle, after its encounter with the planet, is to rotate the incoming relative velocity vector,  $V_{\infty 1}$ , through the angle  $2\psi$  to form the outgoing relative velocity vector  $V_{\infty 2}$ . The magnitude of the relative velocity vector, however, remains unchanged. Thus, the criteria that must be satisfied for the trajectories of two consecutive legs of a swingby mission to match at the swingby planet are as follows: (1) The magnitude of the relative velocity vector after encounter must equal to the magnitude of the relative velocity vector prior to encounter, and (2) the radius of closest approach to the swingby planet must be such that the required bend angle can be produced without causing the spacecraft to impact the planet's surface or encounter its atmosphere.

### A. Swingby Date Selection

The calculational procedure used in the SWISTO program for determining swingby (or roundtrip flyby) trajectories is formulated as follows. The dates at

the departure and target planets are specified along with an initial estimated range of passage dates at the swingby planet.<sup>1</sup> The problem of establishing the exact date, at the swingby planet, that results in a suitable swingby trajectory is solved as an iteration. Each leg of the trajectory is determined using the same calculational procedure outlined in Reference 12. The iteration on swingby data is accomplished as follows: the trajectories for each successive leg of the mission are calculated using the first date of the range of swingby planet dates in conjunction with the specified departure and arrival dates. This procedure is then repeated, using the last date of the initial range of swingby dates and the same departure and arrival dates as before. This procedure yields trajectories "bracketing" the end points of the estimated swingby data range. The relative velocity ( $V_{\infty}$ ) magnitudes on approach and departure at the swingby planet are then compared for each of the "candidate" swingby trajectories calculated. Upon comparing the arrival and departure  $V_{\infty}$  magnitudes for each trajectory, two conditions are possible — either the approach and departure relative velocity magnitudes are equal or they are not. If the velocity magnitudes of either of these trajectories do not match, then the program has a built-in iteration scheme which searches the initial estimated range of swingby dates until a swingby date which produces a velocity match between the two successive legs of the trajectory is isolated. It is, of course, possible that no date, within the estimated passage date range, exists producing a velocity match for the combination of departure and arrival date chosen. If this situation occurs, the program will automatically adjust the initial estimated swingby date range and repeat the iteration outlined above to isolate the exact swingby date.

When a matching pair of trajectories, for two successive legs, has been found, one final step remains. It is necessary to determine if the hyperbolic bend requirements at the passage point can be effected during the planetary encounter solely by the planet's gravitational field. The required bend angle is readily computed in terms of the right ascensions and declinations of the inbound and outbound hyperbolic excess velocity vectors as

$$\cos \kappa = \cos \delta_1 \cos \delta_2 \cos (\alpha_2 - \alpha_1) + \sin \delta_1 \sin \delta_2. \quad (12)$$

The radius of closest approach ( $r_p$ ) required to produce the required bend angle is given by

$$r_p = \frac{\mu}{V_{\infty}^2} \left( \csc \frac{\kappa}{2} - 1 \right). \quad (13)$$

The computed pericenter distance of each matched trajectory is compared with the specified maximum and minimum pericenter distance which is an input to the program. If the computer pericenter distance is outside the specified range, pericenter is held at the appropriate value (i. e., either maximum or minimum) and the velocity increment necessary to rotate the departure asymptote by the proper amount is computed. The velocity increment is applied at the sphere of influence of the swingby planet. The procedure used for calculating the  $\Delta V$  required for correct pericenter passages is outlined below.

## B. Corrected Pericenter Passage

The required bend angle,  $\kappa$ , based on the requirements of the inbound and outbound hyperbolic trajectories, is given by equation (12). The bend angle that can be produced solely by the planet's gravity field for a given pericenter radius is equal to  $2\psi$ , as shown in Figure 9. Suppose  $\kappa$  is greater than  $2\psi$  by an amount  $\beta$ . In other words, the following condition must be satisfied:

$$\beta = \kappa - 2\psi. \quad (14)$$

The  $\Delta V$  required to rotate the outgoing hyperbolic excess velocity vector through an angle  $\beta$  is given by

$$\Delta V = \sqrt{V_{\infty 2}^2 + V_{\infty 2}'^2 - 2V_{\infty 2} V_{\infty 2}' \cos \beta}. \quad (15)$$

However, since  $V_{\infty 2} = V_{\infty 2}'$  equation (15) reduces to

<sup>1</sup>The criteria for obtaining an initial estimate of the passage data range that results in a suitable swingby trajectory are presented in References 1 and 2.

$$\Delta V = V_{\infty 2} | \sin \frac{1}{2} \beta | . \quad (16)$$

## VI. VEHICLE PERFORMANCE AND WEIGHT ANALYSIS

In the interest of keeping the vehicle weight at Earth departure as low as possible, consistent with the type and objectives of the mission, it is important to understand how the mission velocity distribution affects the Earth departure weight of a planetary spacecraft of given terminal payload weight (i.e., payload weight left after the Earth capture maneuver, or in the case of one-way missions, after the planetary capture maneuver). Knowledge of favorable and unfavorable mission velocity distribution is an important factor in the comparative evaluation of interplanetary mission profiles.

### A. Maneuver $\Delta V$ Requirements

The  $\Delta V$ 's at various points in the mission (i.e., for injection or orbit insertion maneuvers) are determined, using the patched conic approach outlined in Reference 12 with the "surface" of each planet's sphere of influence separating the planetocentric conic from the heliocentric conic.

The incremental velocity for all injection or orbit insertion maneuvers (assuming all such maneuvers are impulsive, coplanar, tangential, periapsis to periapsis transfers) is calculated using the following equation:

$$\Delta V_i = \sqrt{V_{\infty i}^2 + \frac{2\mu_i}{r_i}} - \sqrt{\frac{A_i \mu_i}{r_i}} , \quad (17)$$

where  $i = 1$  to 4.

### B. Vehicle Weight Ratio Definition

The vehicle weight ratio is defined as the gross vehicle weight before a  $\Delta V$  maneuver divided by the gross vehicle weight after the completion of the maneuver, and is represented by  $\gamma$ . Thus,

$$\gamma_i = \frac{W_{oi}}{W_{fi}} . \quad (18)$$

Using the rocket equation, the weight ratio for each  $\Delta V$  impulse can be determined.

$$\gamma_i = \exp \left[ \frac{\Delta V_i}{g I_{sp_i}} C_i \right] . \quad (19)$$

The propellant used during the maneuver is given by

$$W_{pi} = W_{oi} - W_{fi} . \quad (20)$$

### C. Vehicle Weight Calculations

The gross vehicle weight before the first  $\Delta V$  maneuver is determined by starting with the last propulsive maneuver and working backward through the mission as follows.

The final weight of the vehicle after the braking maneuver at Earth return is given by

$$W_{f4} = W_{PL} / [1 - G_4 (\gamma_4 - 1)] . \quad (21)$$

The burnout weight of the vehicle after performing the Earth return injection maneuver at the stopover planet is given by

$$W_{f3} = (\gamma_4 W_{f4} + W_{D3}) / [1 - G_3 (\gamma_3 - 1)] . \quad (22)$$

The gross vehicle weight inserted into a parking orbit at the stopover planet is given by

$$W_{f2} = (\gamma_3 W_{f3} + W_{D2}) / [1 - G_2 (\gamma_2 - 1)] . \quad (23)$$

The vehicle weight after the Earth departure injection maneuver is given by

$$W_{f1} = (\gamma_2 W_{f2} + W_{D1}) / [1 - G_1(\gamma_1 - 1)]. \quad (24)$$

Finally, the gross vehicle weight just before the Earth departure injection maneuver is given by

$$W_{01} = W_{f1} + W_{p1} \quad (25)$$

where

$$W_{p1} = F_{f1}(\gamma_1 - 1) \quad (26)$$

Thus, it is seen that the vehicle weight at Earth departure is strongly dependent upon the mission velocity distribution, through the  $\gamma_i$ 's.

It is of interest to express the vehicle weights at the various points along the mission in terms of the terminal payload weight  $W_{PL}$ . In doing this, expressions for payload ratio,  $\frac{W_{fi}}{W_{PL}}$ , will be

presented, and an expression for the ratio of initial weight at Earth departure to terminal payload weight,  $\frac{W_{01}}{W_{PL}}$ , will be derived. Minimizing this ratio is equivalent to minimizing the mission propellant requirements.

#### D. Payload Ratio Definitions

The payload ratio at Earth return is defined by the following equation:

$$\eta_{f4} = \frac{W_{f4}}{W_{PL}} = 1 / [1 - G_4(\gamma_4 - 1)]. \quad (27)$$

The payload ratio at departure from the stopover planet is given by

$$\eta_{f3} = \frac{W_{f3}}{W_{PL}} (\gamma_4 \eta_{f4} + U_3) / [1 - G_3(\gamma_3 - 1)]. \quad (28)$$

The payload ratio at the stopover planet arrival is defined by

$$\eta_{f2} = \frac{W_{f2}}{W_{PL}} (\gamma_3 \eta_{f3} + U_2) / [1 - G_2(\gamma_2 - 1)]. \quad (29)$$

The payload ratio at Earth departure is given by

$$\eta_{f1} + \frac{W_{f1}}{W_{PL}} = (\gamma_2 \eta_{f2} + U_1) / [1 - G_1(\gamma_1 - 1)]. \quad (30)$$

And finally, the expression for the ratio of initial weight in Earth orbit to terminal payload weight is given by

$$\eta_{01} = \gamma_1 \cdot \eta_{f1} \quad (31)$$

The optimization scheme employed by the SWISTO program is designed to determine the ephemeridal parameters (planetary encounter dates, trip times, etc.) that minimizes  $\eta_{01}$ .

#### E. Maximum Vehicle Performance Capability

The maximum  $\Delta V$  that can be obtained for a given spacecraft configuration and payload is limited by the propulsion system specific impulse and maximum propellant capacity of the fuel tanks. The rocket equation, given by equation (19), in conjunction with the payload ratio expressions, given by equations (27) through (31), can be used to determine the maximum  $\Delta V$  capability of a given vehicle configuration and payload.

If we look at the payload ratio expressions, we see that each contains denominators of the form

$$[1 - G_i(\gamma_i - 1)].$$

Thus, each of these equations are undefined when

$$G_i(\gamma_i - 1) = 1 \quad (32)$$

Therefore, any  $\gamma_i$  satisfying the expression,

$$\gamma_1 \geq \frac{1 + G_i}{G_i}, \quad (33)$$

is impossible to achieve. The maximum  $\Delta V$  that can be produced during a given maneuver is limited by the value of  $\gamma_1$  satisfying the equality of equation (33).

The SWISTO program continuously monitors the values of  $\Delta V_i$  and  $\gamma_i$ , and when a combination of dates are encountered, resulting in a  $\Delta V_i$ , thus  $\gamma_i$ , which satisfies equation (33), the program prints a value of "1000" in the column listed as ETAO ( $\eta_{01}$ ) on the printout (see Table I). This indicates that the trajectory  $\Delta V$  requirements exceed the capability of the vehicle propulsion system for that particular combination of dates.

## VII. EARTH LAUNCH WINDOW ANALYSIS

The practical design of any interplanetary mission will involve the establishment of a launch window, which is a period of consecutive days on which launch is possible. On each day during this launch window, the trajectories will have to satisfy numerous constraints, such as those placed on energy, hyperbolic asymptote declination, communication distance, etc.

The basis for launch window selection in the SWISTO program is the selection of mission dates which produces the minimum value of  $\eta_{01}$ , previously discussed, while satisfying the geometric launch window constraints. This permits a round-trip or planetary capture mission to be flown using a minimum amount of propellant while providing a specified launch window duration at Earth departure.

The example printouts presented in Tables I through III display the mission dates, impulse requirements, launch window selection and summary trajectory data for missions requiring one, two, and three interplanetary trajectory legs, respectively. Table I presents these data for a typical 1980 direct Mars capture mission using the Type I transfer (heliocentric transfer angle  $< 180$  degrees). Table II presents the mission data for a typical 1980 round-trip Mars stopover mission with a 20-day staytime at Mars. The data of Table III represent a typical

1984 Mars stopover mission using an inbound Venus swingby on the Earth return leg. The ETAO ( $\eta_{01}$ )

data presented in these tables are for illustrative purposes only. In an actual case ETAO is dependent upon the vehicle/payload configuration, as well as the planetary parking orbit shape and altitude. The data presented in the tables are based on a hypothetical vehicle/spacecraft configuration and upon circular parking orbits at the departure and target planets. The Earth return velocity increment (DELV4) is computed based upon a maximum Earth reentry speed limit of 15 km/sec. Comparison of the Earth-return velocity increments in Tables II and III clearly illustrates the advantages of the inbound Venus swingby over the direct Mars stopover missions.

### A. Earth Launch Window Selection

The 1980 direct Mars stopover mission data of Table II will be utilized for a general discussion of the approach used in the SWISTO program for launch window selection. For convenience of discussion, the data of Figure 2 are divided into three parts. The "block" of data at the top of the table presents the planet encounter dates and corresponding  $\Delta V$  and  $\eta_{01}$  data for the mission. The Earth departure dates are divided into three possible 20-day launch windows (numbered 1, 2, and 3) during a 30-day span of Earth departure dates. The Earth return date for each combination of Earth departure and Mars arrival (or Mars departure) dates is chosen so as to minimize ETAO ( $\eta_{01}$ ). For each Earth launch data considered, the minimum ETAO is indicated by the symbol ( $\star$ ) on the printout. Each 20-day Earth launch window is divided into 5-day increments as indicated by the launch dates on the printout. During each 20-day launch window considered, the maximum  $\Delta V$ 's for each maneuver, corresponding to the minimum ETAO's are selected. The  $\Delta V$ 's underlined by the brackets indicate the method of selecting the maximum  $\Delta V$ 's corresponding to the minimum ETAO's for each 20-day launch window. The numbers beside each of the maximum  $\Delta V$ 's (i.e., numbers 1, 2, or 3) refer to the launch window that the  $\Delta V$  corresponds to (again, #1, #2, or #3). This method of selecting the  $\Delta V_1$ 's,  $\Delta V_2$ 's,  $\Delta V_3$ 's and  $\Delta V_4$ 's ensures the capability of performing any of the required maneuvers for any launch data during the 20-day launch window, provided the optimum trajectory (minimum ETAO) is flown for the particular launch date chosen. These

$\Delta V$ 's and corresponding ETAO's are summarized in the middle portion of the printout (also numbered #1, #2 and #3) for each of the 20-day launch windows. The first of the three possible 20-day launch windows results in the lowest ETAO, also indicated by the symbol (★), during the 30-day span of dates chosen. The  $\Delta V$  and ETAO requirements for a 30-day launch window are also presented. The bottom portion of the table presents the summary trajectory data for each launch date corresponding to the minimum ETAO's designated by the symbol (★) in the top portion of the table.

The approach used in the launch window selection of the other five mission modes of the SWISTO program, previously discussed, functions basically the same way as that outlined above for the direct stop-over mission mode.

## REFERENCES

1. Deerwester, J. M.: Initial Mass Savings Associated with the Venus Swingby Mode of Mars Round Trips. AIAA Paper No. 65-89, January 1965.
2. Holister, W. M., and Prussing, J. E.: Optimum Transfer to Mars via Venus. AIAA Paper No. 65-700, September 1965.
3. Battin, R. H.: Astronautical Guidance, McGraw-Hill Book Co. Inc., 1964.
4. Gillespie, R. W., and Ross, S.: The Venus Swingby Mission Mode and Its Role in the Manned Exploration of Mars. AIAA Paper No. 66-37, January 1966.
5. Young, A. C.: Multiple Planet Flyby Missions to Venus and Mars in 1975 to 1980 Time Period. NASA TM X-53511, 1966.
6. Mead, C. W. and Noblitt, B. G.: Impulsive Velocity Requirements for Aborting Mars Stopover Mission while in the Martian Sphere of Influence during the 1978-1986 Time Period. AAS Paper No. MAM-10, Presented at American Astronautical Society 1967 National Symposium: Saturn V/Apollo and Beyond, June 1967.
7. Niehoff, J. C.: An Analysis of Gravity Assisted Trajectories to Solar System Targets. AIAA Paper No. 66-10, January 1966
8. Silver, B. W.: Grand Tours of the Jovian Planets. AIAA Paper No. 67-613, August 1967.
9. Jones, M. F.: Trajectories to the Outer Planets via Jupiter Swingby. NASA CR-61186, January 1968.
10. Smith, J. N. and Mead, C. W.: Mission Profiles for the Exploration of the Outer Solar System with Nuclear Pulse Rockets, Presented at the New York Academy of Sciences, "Second Conference on Planetology and Space Mission Planning," New York, N. Y., October 26-27, 1967.
11. Mead, C. W.: Parametric Analysis of Mars Mission Requirements for Missions Occurring during the 1973-1979 Time Period. LMSC/HREC A784862, Lockheed Missiles & Space Company, Huntsville Research & Engineering Center, October 1967.
12. Breakwell, J. V., Gillespie, R. W. and Ross S.: Researches in Interplanetary Transfer, ARS J., Vol. 31, No. 2, February 1961.

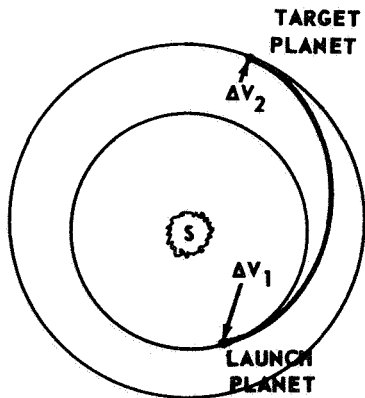


FIGURE 1. DIRECT ONE-WAY CAPTURE MISSION (Requiring one interplanetary transfer trajectory)

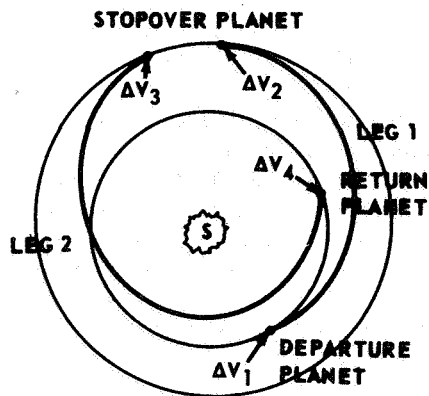


FIGURE 2c. DIRECT ROUNDTRIP STOPOVER MISSION

FIGURE 2. (Concluded)

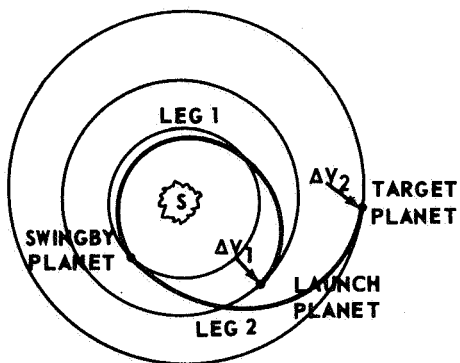


FIGURE 2a. ONE-WAY SWINGBY CAPTURE MISSION

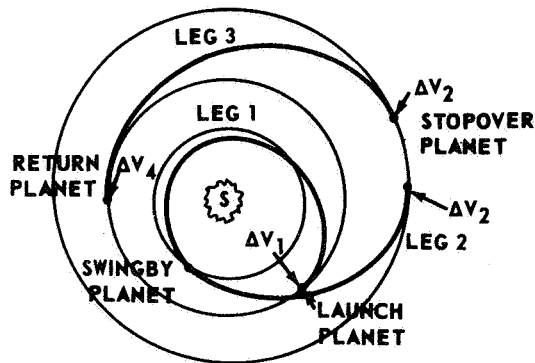


FIGURE 3a. ROUNDTRIP OUTBOUND SWINGBY STOPOVER MISSION

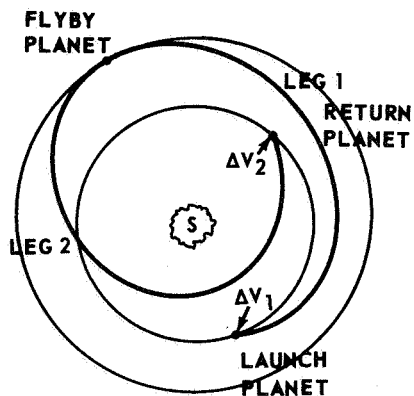


FIGURE 2b. ROUNDTRIP FLYBY MISSION

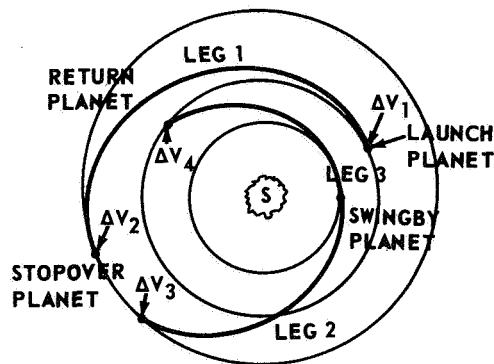


FIGURE 3b. ROUNDTRIP INBOUND SWINGBY STOPOVER MISSION

FIGURE 2. MISSIONS REQUIRING TWO INTERPLANETARY TRANSFER TRAJECTORIES

FIGURE 3. MISSIONS REQUIRING THREE INTERPLANETARY TRANSFER TRAJECTORIES

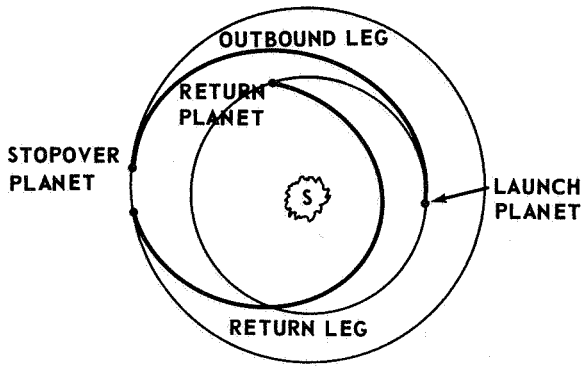


FIGURE 4. DIRECT STOPOVER MISSION MODE

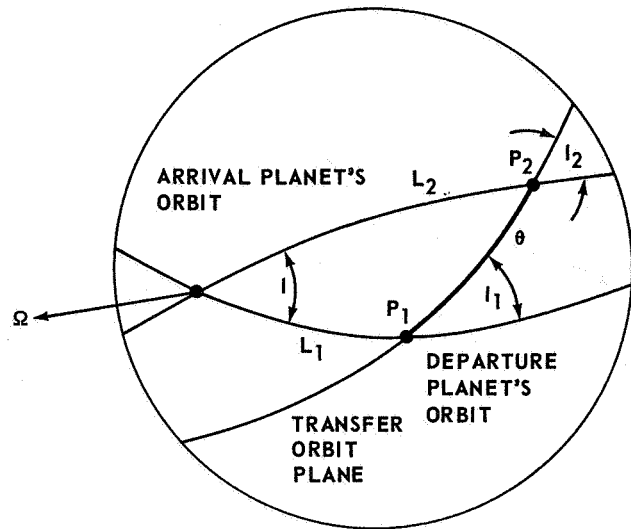


FIGURE 7a. SINGLE PLANE TRANSFER GEOMETRY

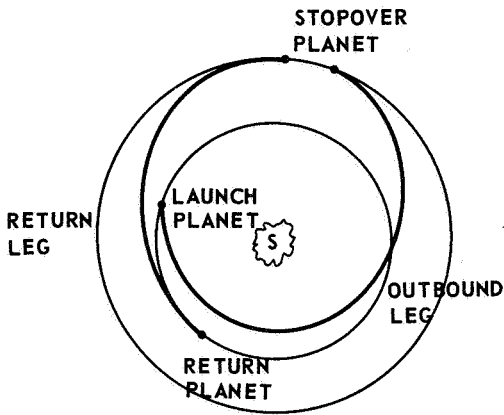


FIGURE 5. DIRECT INVERTED STOPOVER MISSION MODE

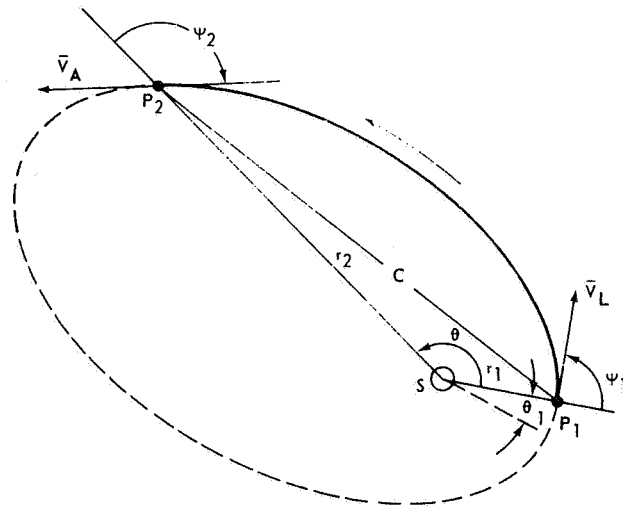


FIGURE 7b. RELATIONSHIPS IN THE TRANSFER PLANE

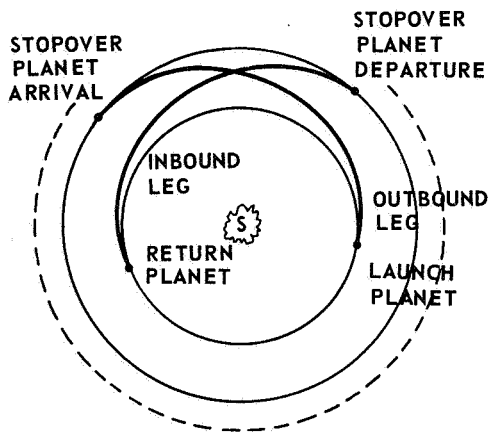


FIGURE 6. CONJUNCTION STOPOVER MISSION MODE

FIGURE 7. SINGLE PLANE INTERPLANETARY TRANSFER GEOMETRY

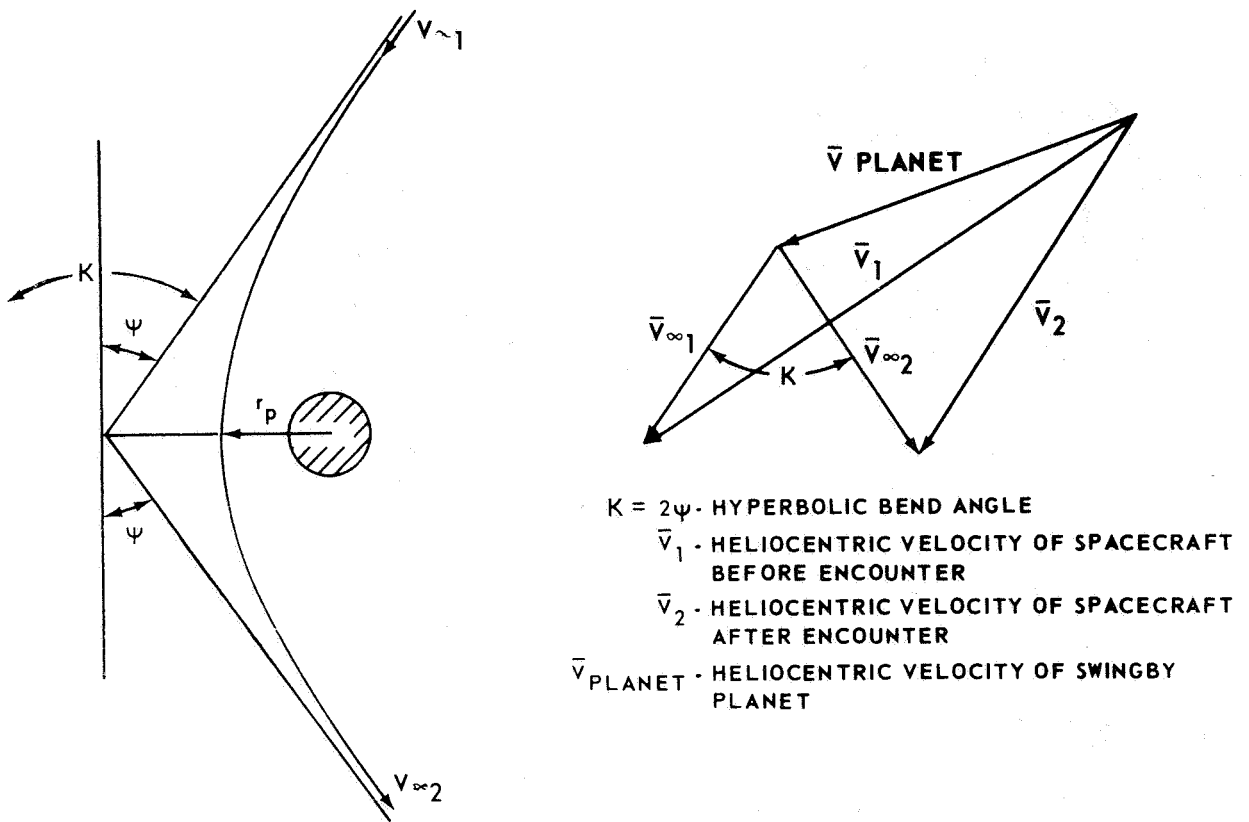


FIGURE 8. GEOMETRY OF SPACECRAFT MOTION AT SWINGBY PLANET

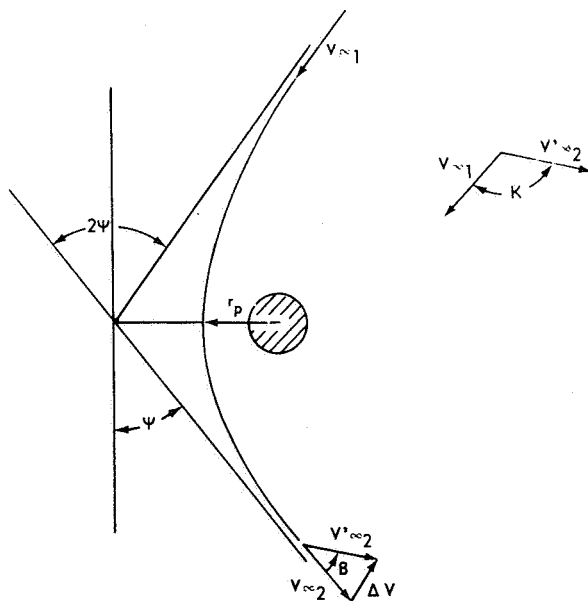


FIGURE 9. GEOMETRY OF CORRECTED PERICENTER MANEUVER

TABLE I. 1980 DIRECT MARS CAPTURE MISSION

\*\*\* DATE DISPLAY \*\*\* \*\* IMPULSE REQUIREMENTS \*\*\*

LAUNCH	STOP	DELV1	DELV2	ETA#
2444200.0	2444450.0	3.74437	2.44221	4.62303
2444200.0	2444460.0	3.73876	2.34152	4.57092
2444200.0	2444470.0	4.06980	2.80965	5.12229
2444205.0	2444450.0	3.32042	2.45418	4.69797
2444205.0	2444460.0	3.81269	2.33718	4.63534
2444205.0	2444470.0	3.84307	2.35102	4.66995
2444205.0	2444480.0	4.83861	3.63330	6.58199
2444210.0	2444450.0	3.92114	2.46430	4.79716
2444210.0	2444460.0	3.91202	2.34170	4.72886
2444210.0	2444470.0	3.91467	2.30053	4.71173
2444210.0	2444480.0	4.00538	2.45745	4.87419
2444210.0	2444490.0	6.17848	4.96451	10.62660
2444215.0	2444450.0	4.04874	2.47548	4.92554
2444215.0	2444460.0	4.03692	2.35132	4.85213
2444215.0	2444470.0	4.02865	2.29399	4.81620
2444215.0	2444480.0	4.04536	2.33395	4.85177
2444215.0	2444490.0	4.22850	2.66582	5.20850
2444220.0	2444450.0	4.20502	2.48858	5.08929
2444220.0	2444460.0	4.18961	2.36565	5.01020
2444220.0	2444470.0	4.17371	2.30324	4.96276
2444220.0	2444480.0	4.16642	2.31039	4.95905
2444220.0	2444490.0	4.20213	2.43506	5.05891
2444225.0	2444450.0	4.39252	2.50574	5.29658
2444225.0	2444460.0	4.37167	2.38626	5.20989
2444225.0	2444470.0	4.34818	2.32377	5.15221
2444225.0	2444480.0	4.32681	2.31951	5.12757
2444225.0	2444490.0	4.31969	2.38907	5.15634
2444230.0	2444450.0	4.61399	2.52895	5.55844
2444230.0	2444460.0	4.59576	2.41458	5.46128
2444230.0	2444470.0	4.55305	2.35516	5.39154
2444230.0	2444480.0	4.51883	2.34788	5.34942
2444230.0	2444490.0	4.49004	2.39702	5.34421

20 - DAY	LAUNCH	OPPORTUNITY	ETA#	ETA#		
DV1	GAM1	GAM2	ETA1	ETA#		
4.16642	2.34152	1.66848	1.32435	3.04772	1.09450	4.97467
DV1	DV2	GAM1	GAM2	ETA1	ETA2	ETA#
4.32681	2.33718	1.68031	1.32366	3.05665	1.09428	5.13673
DV1	DV2	GAM1	GAM2	ETA1	ETA2	ETA#
4.49004	2.39702	1.71375	1.33319	3.11844	1.09733	5.34421

**SUMMARY TRAJECTORY DATA**

DEPARTURE PLANET = EARTH  
ARRIVAL PLANET = MARS

DEPARTURE PLANET = EARTH  
ARRIVAL PLANET = MARS

DEPART	ARRIVE	C3	R A	DECL	I 1	V 1	PSI 1	ECCEN	SMA	THET1	THET2	PERIH	APHEL	I 2	V 2	PSI 2	R A	DECL	VHP
DV1	DV2	GAM1	GAM2	GAM2	ETA1	ETA2	ETA#	ETA#	ETA#										
44200.0	44460.0	11.54	119.6	15.2	-0.55	1.111	87.6	0.223	1.265	13.3	185.5	---	1.547	2.40	0.710	88.4	265.6	-7.7	3.17
3.73876	2.34152	1.56604		1.32435	2.91878		1.09450	4.57092											
44205.0	44460.0	13.26	117.6	17.9	-0.34	1.111	86.6	0.226	1.262	18.5	185.6	---	1.547	2.18	0.709	88.4	264.8	-9.2	3.16
3.81269	2.33718	1.57999		1.32366	2.93378		1.09428	4.63534											
44210.0	44470.0	15.64	114.6	12.3	-1.08	1.110	85.7	0.227	1.255	23.8	191.0	---	1.540	2.89	0.713	86.8	260.2	-3.4	3.09
3.91467	2.30053	1.59944		1.31785	2.94586		1.09243	4.71173											
44215.0	44470.0	18.32	114.2	15.5	-0.76	1.110	34.6	0.231	1.251	29.1	191.3	---	1.541	2.58	0.712	86.6	258.3	-5.5	3.08
4.02865	2.29399	1.62146		1.31682	2.97028		1.09210	4.81620											
44220.0	44480.0	21.61	113.7	12.1	-1.33	1.108	83.7	0.235	1.245	34.1	196.3	---	1.538	3.07	0.717	85.1	253.6	-1.5	3.11
4.16642	2.31039	1.64848		1.31941	3.00825		1.09293	4.95905											
44225.0	44480.0	25.43	114.5	14.7	-1.04	1.107	82.6	0.241	1.240	39.5	196.6	---	1.539	2.77	0.714	84.9	251.5	-3.6	3.13
4.32681	2.31951	1.68051		1.32085	3.05119		1.09339	5.12757											
44230.0	44490.0	29.47	115.6	12.3	-1.48	1.106	81.7	0.247	1.234	43.8	201.2	---	1.539	3.13	0.720	83.4	246.7	-1.1	3.27
4.49004	2.39702	1.71375		1.33319	3.11844		1.09733	5.34421											

TABLE II. 1980 DIRECT ROUNDTRIP MARS STOPOVER MISSION

DATE DISPLAY				IMPULSE REQUIREMENTS					
LAUNCH	ARRIVE	RESTART	RETURN	DELV1	DELV2	DELV3	DELV4	ETA8	
2444150.0	2444400.0	44420.0	44635.0	4.36415	3.73902	5.26616	5.06405	154.01126	
2444150.0	2444410.0	44430.0	44645.0	1 4.17516	1 3.28240	5.37511	5.28364	148.38584	
2444150.0	2444420.0	44440.0	44650.0	4.06914	2.94038	5.61359	5.43151	149.67216	
2444150.0	2444430.0	44450.0	44660.0	4.02266	2.67540	5.76494	5.61902	154.91914	
2444150.0	2444440.0	44460.0	44660.0	5.95945	2.46978	6.16894	5.74135	167.78049	
2444155.0	2444400.0	44420.0	44635.0	4.54011	4.09705	5.26616	5.06405	170.23988	
2444155.0	2444410.0	44430.0	44645.0	4.15083	3.43096	5.37511	5.28364	151.49962	
2444155.0	2444420.0	44440.0	44650.0	4.00446	3.02642	5.61359	5.43151	149.92550	
2444155.0	2444430.0	44450.0	44660.0	3.92688	2.72974	5.76494	5.61902	154.00303	
2444155.0	2444440.0	44460.0	44660.0	3.88071	2.50503	6.16894	5.74135	166.15930	
2444160.0	2444400.0	44420.0	44635.0	6.53893	5.96280	5.26616	5.06405	387.17772	
2444160.0	2444410.0	44430.0	44645.0	4.27809	3.72889	5.37511	5.28364	163.76657	
2444160.0	2444420.0	44440.0	44650.0	3.97154	3.14027	5.61359	5.43151	151.86551	
2444160.0	2444430.0	44450.0	44660.0	3.86573	2.79087	5.76494	5.61902	153.72584	
2444160.0	2444440.0	44460.0	44660.0	3.81364	2.54165	6.16894	5.74135	164.98513	
2444165.0	2444400.0	44420.0	44635.0	10.15759	7.83772	5.26616	5.06405	249.365182	
2444165.0	2444410.0	44430.0	44645.0	6.05313	5.46647	5.37511	5.28364	335.87693	
2444165.0	2444420.0	44440.0	44650.0	4.04826	3.36984	5.61359	5.43151	160.07868	
2444165.0	2444430.0	44450.0	44660.0	3.82840	2.87184	5.76494	5.61902	154.69618	
2444165.0	2444440.0	44460.0	44660.0	3.75969	2.58135	6.16894	5.74135	164.33557	
2444170.0	2444400.0	44420.0	44635.0	4.52554	4.04326	5.26616	5.06405	168.08832	
2444170.0	2444410.0	44430.0	44645.0	7.60890	5.87125	5.37511	5.28364	556.86276	
2444170.0	2444420.0	44440.0	44650.0	5.44853	4.84174	5.61359	5.43151	281.90211	
2444170.0	2444430.0	44450.0	44660.0	3.85947	3.02867 1 2 3	5.76494 1 2 3	5.61902	158.82977	
2444170.0	2444440.0	44460.0	44660.0	3.72284	2.63043	6.16894	5.74135	164.50000	
2444175.0	2444400.0	44420.0	44635.0	2 3 4.06722	2 3.88394	5.26616	5.06405	148.81525	
2444175.0	2444410.0	44430.0	44645.0	4.19405	3.57488	5.37511	5.28364	156.70420	
2444175.0	2444420.0	44440.0	44650.0	5.86633	4.43380	5.61359	5.43151	287.72194	
2444175.0	2444430.0	44450.0	44660.0	4.76406	4.09297	5.76494	5.61902	231.61872	
2444175.0	2444440.0	44460.0	44660.0	5.72174	2.71816	6.16894	5.74135	166.89334	
2444180.0	2444400.0	44420.0	44635.0	3.92290	3.90120	5.26616	5.06405	145.05681	
2444180.0	2444410.0	44430.0	44645.0	3.89859	3.48849	5.37511	5.28364	145.52946	
2444180.0	2444420.0	44440.0	44650.0	3.95361	3.17572	5.61359	5.43151	152.24749	
2444180.0	2444430.0	44450.0	44660.0	4.71627	3.40695	5.76494	5.61902	203.04197	
2444180.0	2444440.0	44460.0	44660.0	4.11692	3.28898	6.16894	5.74135	198.82328	

#1	20 - DAY				LAUNCH OPPORTUNITY				ETA1	ETA2	ETA3	ETA4	ETA8
	DV1	DV2	DV3	DV4	GAMA1	GAMA2	GAMA3	GAMA4					
1	4.17516	3.28240	5.76494	5.61903	1.65021	1.48260	1.99698	5.67684	107.70898	56.68619	22.17541	1.86726	177.74278 *
#2	4.06722	3.86394	5.76494	5.61903	1.62898	1.59355	1.99698	5.67684	118.66088	58.67464	22.17541	1.86726	193.29639
#3	4.06722	3.90120	5.76494	5.61903	1.62898	1.59686	1.99698	5.67684	119.02751	58.73598	22.17541	1.86726	193.89362

#1	30 - DAY				LAUNCH OPPORTUNITY				ETA1	ETA2	ETA3	ETA4	ETA8
	DV1	DV2	DV3	DV4	GAMA1	GAMA2	GAMA3	GAMA4					
1	4.17516	3.90120	5.76494	5.61903	1.65021	1.59686	1.99698	5.67684	120.06727	58.73598	22.17541	1.86726	198.13660

### SUMMARY TRAJECTORY DATA

DEPART	ARRIVE	C3	R A	DECL	I L	V I	PSI 1	ECCEN	SHA	THET1	THET2	PERI	APHEL	I 2	V 2	PSI 2	R A	DECL	VHP
RESTART	RETURN	C3	R A	DECL	I L	V I	PSI 1	ECCEN	SHA	THET1	THET2	PERI	APHEL	I 2	V 2	PSI 2	R A	DECL	C3
DV1	DV2	DV3	DV3	CV4	GAM1	GAM2	GAM3	GAM4	GAM3	GAM4	GAM4	ETA1	ETA2	ETA3	ETA4	ETA4	ETA4	ETA8	ETA8
44150.0	44410.0	21.77	144.4	-3.1	-2.29	1.108	96.7	0.254	1.295	326.0	523.8	0.966	---	3.89	0.690	95.4	265.7	-6.5	4.64
44430.0	44645.0	53.54	199.8	-4.0	1.90	0.564	104.9	0.544	1.056	193.3	476.9	0.481	---	0.41	1.039	122.8	128.8	15.3	288.03
4.17516	3.28240	5.37511	5.28364	1.65021	1.48260	1.90573	5.11794	89.91919	47.21966	18.90792	1.65191	148.38584							
44155.0	44420.0	17.72	144.5	-1.1	-1.83	1.107	95.7	0.244	1.289	330.4	527.9	0.974	---	3.51	0.693	93.8	267.0	-6.8	4.27
44440.0	44650.0	57.75	202.5	-5.3	1.89	0.568	106.2	0.551	1.050	194.2	478.1	0.472	---	0.25	1.036	123.3	133.3	17.9	294.04
4.00446	3.02642	5.61359	5.43151	1.61676	1.43776	1.96104	5.35723	92.73196	50.93605	20.33629	1.76279	149.92550							
44160.0	44420.0	16.94	142.5	-7.1	-2.53	1.109	95.0	0.243	1.292	334.1	526.7	0.978	---	4.24	0.694	94.2	268.2	-3.9	4.44
44440.0	44650.0	57.75	202.5	-5.3	1.89	0.568	106.2	0.551	1.050	194.2	478.1	0.472	---	0.25	1.036	123.3	133.3	17.9	294.04
3.97154	3.14027	5.61359	5.43151	1.61039	1.45753	1.96104	5.35723	94.30361	51.24133	20.33629	1.76279	151.86551							
44165.0	44430.0	13.59	141.6	-2.8	-1.87	1.109	94.0	0.235	1.285	338.9	531.3	0.984	---	3.63	0.698	92.6	268.8	-5.0	4.04
44450.0	44660.0	60.47	211.9	-9.1	1.88	0.556	104.7	0.561	1.026	192.1	481.1	0.450	---	0.09	1.023	124.1	141.7	15.2	301.73
3.82840	2.87184	5.76494	5.61903	1.58297	1.41134	1.99698	5.67684	97.72525	55.47870	22.17541	1.86726	154.69618							
44170.0	44430.0	14.32	136.6	-12.9	-3.09	1.111	93.2	0.233	1.287	343.0	530.5	0.987	---	4.87	0.699	92.9	269.5	0.4	4.27
44450.0	44660.0	60.47	211.9	-9.1	1.88	0.556	104.7	0.561	1.026	192.1	481.1	0.450	---	0.09	1.023	124.1	141.7	15.2	301.73
3.85947	3.02867	5.76494	5.61903	1.58888	1.43815	1.99698	5.67684	100.59261	55.92687	22.17541	1.86726	159.82977							
44175.0	44400.0	19.20	165.5	42.3	4.09	1.124	93.4	0.261	1.333	343.5	511.7	0.985	---	-2.35	0.700	99.1	271.1	-32.9	5.46
44420.0	44635.0	51.66	190.4	0.0	1.85	0.575	106.3	0.534	1.081	195.4	473.8	0.504	---	0.56	1.051	121.9	119.9	21.5	279.17
4.06722	3.88394	5.26616	5.60405	1.62898	1.59355	1.88098	4.78216	91.35478	45.63777	17.43855	1.60155	148.81525							
44180.0	44400.0	15.80	158.8	36.2	2.89	1.126	92.6	0.261	1.336	347.6	510.8	0.987	---	-1.12	0.701	99.4	271.9	-28.2	5.49
44420.0	44635.0	51.66	190.4	0.0	1.85	0.575	106.3	0.534	1.081	195.4	473.8	0.504	---	0.56	1.051	121.9	119.9	21.5	279.17
3.92290	3.90120	5.26616	5.06405	1.60102	1.59686	1.88098	4.78216	90.60283	45.08485	17.43855	1.60155	145.05681							

TABLE III. 1984 ROUNDTRIP MARS STOPOVER - INBOUND VENUS SWINGBY MISSION

LAUNCH		ARRIVE	RESTART	PASS	RETURN	DELVL	DELV2	DELV3	DELV4	ETAB
2445725.0	2445900.0	45920.0	46082.8	46210.0	3.74255	5.24578	3.82413	0.00000		84.70540
2445725.0	2445905.0	45925.0	46082.7	46210.0	3.76907	4.88590	3.95005	0.00000		79.81341
2445725.0	2445910.0	45930.0	46082.6	46210.0	3.60883	4.55549	4.11700	0.00000		76.30446
2445725.0	2445915.0	45935.0	46082.5	46210.0	3.68156	4.28404	4.33151	0.00000		74.63628
2445725.0	2445920.0	45940.0	46082.4	46210.0	3.69008	4.04543	4.66172	0.00000		74.27306
2445725.0	2445925.0	45945.0	46082.3	46210.0	3.71852	3.85559	4.92648	0.00000		75.52456
2445725.0	2445930.0	45950.0	46082.2	46210.0	3.77606	3.71990	5.31373	0.00000		78.92200
2445730.0	2445900.0	45920.0	46082.8	46210.0	3.71835	5.30001	3.82413	0.00000		85.20087
2445730.0	2445905.0	45925.0	46082.7	46210.0	3.68392	4.92528	3.95005	0.00000		80.01755
2445730.0	2445910.0	45930.0	46082.6	46210.0	3.60939	4.58865	4.11700	0.00000		76.41520
2445730.0	2445915.0	45935.0	46082.5	46210.0	3.64793	4.29035	4.33151	0.00000		74.23653
2445730.0	2445920.0	45940.0	46082.4	46210.0	3.64616	4.02958	4.66172	0.00000		73.43671
2445730.0	2445925.0	45945.0	46082.3	46210.0	3.69682	3.85682	4.92648	0.00000		74.04688
2445730.0	2445930.0	45950.0	46082.2	46210.0	3.68204	3.63161	5.31373	0.00000		76.32424
2445735.0	2445900.0	45920.0	46082.8	46210.0	3.70741	5.35236	3.82413	0.00000		85.89334
2445735.0	2445905.0	45925.0	46082.7	46210.0	3.67352	4.90555	3.95005	0.00000		80.46786
2445735.0	2445910.0	45930.0	46082.6	46210.0	3.64949	4.61605	4.11700	0.00000		76.63820
2445735.0	2445915.0	45935.0	46082.5	46210.0	3.63448	4.30452	4.33151	0.00000		74.23368
2445735.0	2445920.0	45940.0	46082.4	46210.0	3.62796	4.02889	4.66172	0.00000		73.17902
2445735.0	2445925.0	45945.0	46082.3	46210.0	3.63019	3.79070	4.92648	0.00000		73.48286
2445735.0	2445930.0	45950.0	46082.2	46210.0	3.64220	3.58954	5.31373	0.00000		75.12720
2445740.0	2445900.0	45920.0	46082.8	46210.0	3.71125	5.40370	3.82413	0.00000		86.82709
2445740.0	2445905.0	45925.0	46082.7	46210.0	3.67841	5.00422	3.95005	0.00000		81.13798
2445740.0	2445910.0	45930.0	46082.6	46210.0	3.65477	4.64438	4.11700	0.00000		77.11967
2445740.0	2445915.0	45935.0	46082.5	46210.0	3.63991	4.32129	4.33151	0.00000		74.52448
2445740.0	2445920.0	45940.0	46082.4	46210.0	3.63032	4.03523	4.66172	0.00000		73.28580
2445740.0	2445925.0	45945.0	46082.3	46210.0	3.63019	3.78416	4.92648	0.00000		73.31767
2445740.0	2445930.0	45950.0	46082.2	46210.0	3.63310	3.56902	5.31373	0.00000		74.77466
2445745.0	2445900.0	45920.0	46082.8	46210.0	3.73184	5.45281	3.82413	0.00000		88.02263
2445745.0	2445905.0	45925.0	46082.7	46210.0	3.70032	5.04219	3.95005	0.00000		82.07532
2445745.0	2445910.0	45930.0	46082.6	46210.0	3.67740	4.67240	4.11700	0.00000		77.86181
2445745.0	2445915.0	45935.0	46082.5	46210.0	3.66165	4.33998	4.33151	0.00000		75.10555
2445745.0	2445920.0	45940.0	46082.4	46210.0	3.65194	4.04505	4.66172	0.00000		73.72140
2445745.0	2445925.0	45945.0	46082.3	46210.0	3.64767	3.78486	4.92648	0.00000		73.60136
2445745.0	2445930.0	45950.0	46082.2	46210.0	3.64845	3.59931	5.31373	0.00000		74.87111
2445750.0	2445900.0	45920.0	46082.8	46210.0	3.71911	5.49991	3.82413	0.00000		89.54276
2445750.0	2445905.0	45925.0	46082.7	46210.0	3.74155	5.07869	3.95005	0.00000		83.31506
2445750.0	2445910.0	45930.0	46082.6	46210.0	3.71937	4.69891	4.11700	0.00000		78.88633
2445750.0	2445915.0	45935.0	46082.5	46210.0	3.70372	4.33912	4.33151	0.00000		75.98406
2445750.0	2445920.0	45940.0	46082.4	46210.0	3.69324	4.05608	4.66172	0.00000		74.43320
2445750.0	2445925.0	45945.0	46082.3	46210.0	3.68766	3.78955	4.92648	0.00000		74.23458
2445750.0	2445930.0	45950.0	46082.2	46210.0	3.68584	3.55688	5.31373	0.00000		75.38353
2445755.0	2445900.0	45920.0	46082.8	46210.0	3.83487	5.54459	3.82413	0.00000		91.46034
2445755.0	2445905.0	45925.0	46082.7	46210.0	3.80508	5.11417	3.95005	0.00000		84.93016
2445755.0	2445910.0	45930.0	46082.6	46210.0	3.78231	4.72575	4.11700	0.00000		80.27381
2445755.0	2445915.0	45935.0	46082.5	46210.0	3.76738	4.37668	4.33151	0.00000		77.25528
2445755.0	2445920.0	45940.0	46082.4	46210.0	3.75449	4.06928	4.66172	0.00000		75.55854
2445755.0	2445925.0	45945.0	46082.3	46210.0	3.74928	3.79719	4.92648	0.00000		75.22958
2445755.0	2445930.0	45950.0	46082.2	46210.0	3.74532	3.55927	5.31373	0.00000		76.29152

DVI		DV2		DV3		DV4		20 - DAY LAUNCH OPPORTUNITY		ETA1		ETA2		ETA3		ETA4		ETA8	
3.69006	4.04543	4.92648	0.00000	1.55692	1.62473	1.80587	1.00000	49.90748	24.59021	8.51711	1.00000								
3.68766	4.03523	4.92648	0.00000	1.55647	1.62274	1.80587	1.00000	49.80804	24.57462	8.51711	1.00000								
3.74928	4.03523	4.92648	0.00000	1.56801	1.62274	1.80587	1.00000	50.03695	24.57462	8.51711	1.00000								

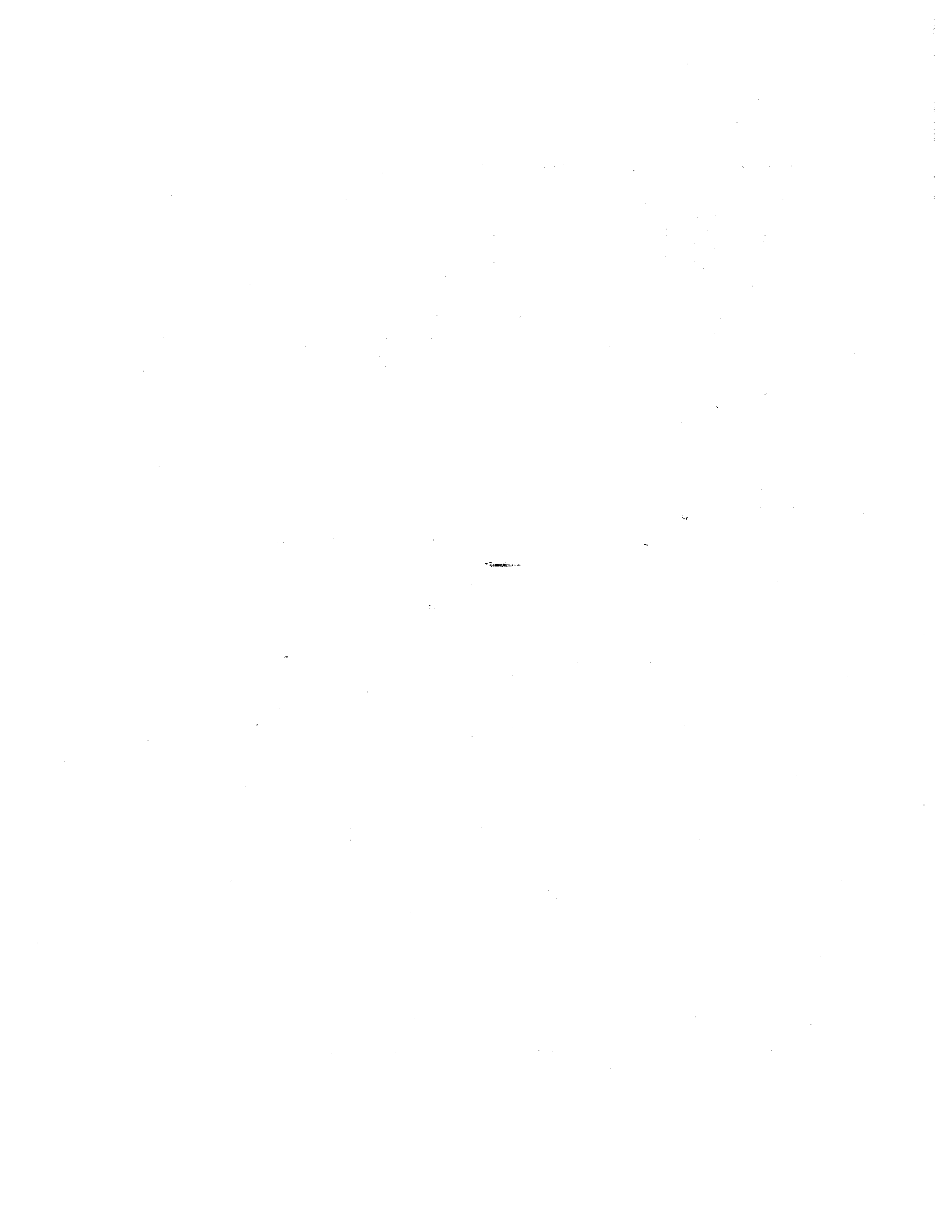
  

DVI		DV2		DV3		DV4		30 - DAY LAUNCH OPPORTUNITY		ETA1		ETA2		ETA3		ETA4		ETA8	
3.74928	4.04543	4.92648	0.00000	1.56801	1.62473	1.80587	1.00000	50.12787	24.59021	8.51711	1.00000								

### SUMMARY TRAJECTORY DATA

DEPARTURE PLANET = MARS		PASSAGE PLANET = VENUS		ARRIVAL PLANET = EARTH		DEPARTURE PLANET = MARS		PASSAGE PLANET = VENUS		ARRIVAL PLANET = EARTH										
LAUNCH	STBP	C3-00	R A	DECL	I L	V I	PSI	ECCEN	SMA	THET1	THET2	PERI	APHEL	I 2	V 2	PSI 2	R A	DECL	C3-00	VHP
DEPART	PASS	C3-00	R A	DECL	I L	V I	PSI	ECCEN	SMA	THET1	THET2	PERI	APHEL	I 2	V 2	PSI 2	R A	DECL	C3-00	VHP
PASS	ARRIVE	C3-00	R A	DECL	I L	V I	PSI	ECCEN	SMA	THET1	THET2	PERI	APHEL	I 2	V 2	PSI 2	R A	DECL	C3-00	VHP
RPC	KAPPA	VP	AH	EH	ANMAX	IAH	KAP	CECP	RAS	DECS	ETA	PASS	CONDITION	COR01	COR02	COR03				
45725.0	45920.0	10.40	207.1	-49.0	-3.22	1.105	90.5	0.202	1.233	357.1	511.3	0.984	---	4.10	0.762	96.7	332.5	6.2	5.67	
45940.0	46082.4	40.68	253.5	-28.3	-1.60	0.720	104.6	0.359	1.120	209.9	348.3	---	---	-0.43	1.371	86.9	47.4	-2.9	36.01	
46082.4	46210.0	36.77	71.8	-54.3	-7.45	1.279	94.0	0.192	0.879	334.7	508.6	0.710	---	4.10	0.915	96.8	211.7	16.0	18.14	
1.687	55.1	0.3324	1.452	2.162	117.6	72.93	279.03-55.36	117.95	0.00	122.53										
3.69008	4.04543	4.60070	0.00000	1.55692	1.62473	1.73665	1.00000	47.69552	23.47640	8.32189	1.00000									
45730.0	45920.0	9.39	206.2	-44.0	-2.73	1.105	89.8	0.202	1.234	1.5	150.6	---	---	3.55	0.763	96.9	333.9	4.3	5.65	
45940.0	46082.4	40.68	253.5	-28.3	-1.60	0.720	104.6	0.359	1.120	209.9	348.3	---	---	-0.43	1.371	86.9	47.4	-2.9	36.01	
46082.4	46210.0	36.77	71.8	-54.3	-7.45	1.279	94.0	0.192	0.879	334.7	508.6	0.710	---	4.10	0.915	96.8	211.7	16.0	18.14	
1.687	55.1	0.3324	1.452	2.162	117.6	72.93	279.03-55.36	117.95	0.00	122.53										
3.64616	4.02958	4.60070	0.00000	1.54874	1.62164	1.73665	1.00000	47.41060	23.45329	8.32189	1.00000									
45735.0	45920.0	8.97	204.3	-39.5	-2.39	1.104	89.0	0.203	1.235	6.0	150.0	---	---	3.14	0.763	97.0	334.9	2.9	5.65	
45940.0	46082.4	40.68	253.5	-28.3	-1.60	0.720	104.6	0.359	1.120	209.9	348.3	---	---	-0.43	1.371	86.9	47.4	-2.9	36.01	
46082.4	46210.0	36.77	71.8	-54.3	-7.45	1.279	94.0	0.192	0.879	334.7	508.6	0.710	---	4.10	0.915	96.8	211.7	16.0	18.14	
1.687	55.1	0.3324	1.452	2.162	117.6	72.93	279.03-55.36	117.95	0.00	122.53										
3.62796	4.02889	4.60070	0.00000	1.54536	1.62151	1.73665	1.00000	47.34166												



## V. FLUID DYNAMICS

# RISE RATE AND GROWTH OF STATIC TEST VEHICLE ENGINE EXHAUST CLOUDS

By

Michael Susko,  
John W. Kaufman and Kelly Hill

## ABSTRACT

The rise rates and growth of exhaust clouds produced from static vehicle engine tests conducted at the Marshall Space Flight Center, Huntsville, Alabama, are discussed. The data for this study were obtained from 20 static engine firings from June 1964 through May 1965. Time sequential photographs were used to extract original data on the growth and rise rates of exhaust clouds. These data, along with the existing atmospheric phenomena, were analyzed to generate the information presented. Existing equations were used to calculate the height of rise of buoyant clouds, and the results were compared to measured test values.

## I. INTRODUCTION

The physical processes that take place when buoyant gases are released into the lower atmosphere are indeed complex, as complex as the problem of estimating the downwind concentrations of such substances. The problem of atmospheric diffusion has had extensive investigation; however, the initial behavior of a buoyant gas is not sufficiently understood [1, 2, 3, 4]. Therefore this discussion will treat specifically the growth and rise rates of space vehicle engine exhausts.

During static tests of the engines of a space vehicle, voluminous amounts of gaseous by-products are generated. Since thousands of gallons of water are sprayed into the exhaust deflector during engine firings, much of the gas ejected into the lower atmosphere is made up of water vapor. The question then arises: "Does cooling the exhaust gases by water injection cause the exhaust cloud to reach its environmental equilibrium point at a higher or lower altitude?" A guess would be that the water vapor would

cause the cloud to reach a higher altitude. From cloud physics, we know that cumulo-nimbus clouds (warm and moist) ascend to thousands of meters in altitude before stabilizing. Such clouds have been observed, particularly over mountainous regions, to penetrate the tropopause. It is therefore reasonable to assume that the principles of the relatively moist buoyant source under consideration would apply to such latent heat processes of water vapor, which are applicable to cloud rise behavior. Also, the density of the exhaust gas mixture, including the water vapor, would be less than the ambient air.

To determine the maximum height attained and the growth and rise rates of these exhaust gases, time-sequenced frames of 16 mm movie film were extracted and enlarged. Because the meteorological conditions play an important role in the physical behavior of the gas rise rate, cloud growth, etc., these conditions were evaluated for each of the 20 static tests analyzed and the results are discussed in detail.

The engine exhaust data primarily studied were: (1) height and rate of cloud rise, (2) horizontal cloud growth at top of plume, and (3) the height at which the cloud became stable. The observed maximum height of cloud rise could not be studied in detail because the top of the clouds usually ascended to an altitude above the field of view of the camera.

Some information on the initial heat,  $Q_H$ , generated by the static engine has been included. Most of the  $Q_H$  values used were obtained from existing documentation or were made available by personnel of the Thermal Environment Branch of the Aero-Astrodynamic Laboratory, MSFC/NASA. The  $Q_H$  data were used in the height of the rise equations, which were taken from the technical literature.

## II. EXHAUST CLOUD PHOTOGRAPHIC, METEOROLOGICAL, AND ENGINE TEST DATA

### A. Cloud Growth and Rise Rates

To obtain movies of several static firings of engines, a camera was fixed in position on top of Building 4200, located about 4116 and 3475 meters from the S-I and S-IC static stands, respectively. The position of the building (including camera position) is shown in Figure 1 in reference to the MSFC static test stands, the S-I (modified S-I) and S-IC. The camera used to photograph the exhaust clouds was a 16 mm Mitchell which has a film advance rate of 24 frames per second. The photographers began shooting film a few seconds before engine ignition and continued until the exhaust clouds disappeared, dissipated, or was displaced by winds until they were out of the field of view of the camera.

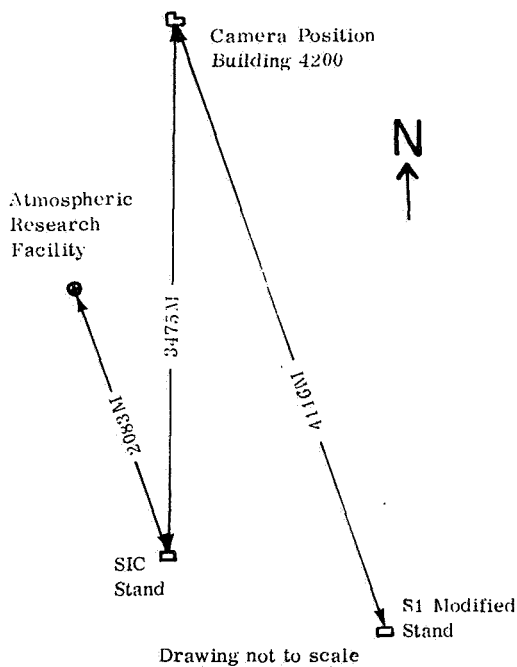


FIGURE 1. LOCATION OF S1 MODIFIED AND SIC STATIC ENGINE TEST STANDS, ATMOSPHERIC RESEARCH FACILITY AND CAMERA POSITION

The time-sequencing procedure for selecting the movie film frames used to extract data is as follows:

I + 0	Engine Ignition Time
I + 2, 4, 6, ..., 20	Seconds

then,

I + 20, 30, 40, ..., 100 Seconds until the exhaust cloud disappeared from view.

A selected sequence of the frames taken from static firing No. TWF 034 on October 9, 1964, is shown in Figure 2 (a through u).<sup>1</sup> Once the frames were time-sequenced, enlargements were printed. These photographs were then used with proper scaling magnification lenses, etc., to obtain the cloud growth measurements. (Figure 3 illustrates how the data were extracted from the prints.)

The height of rise and cloud growth (i.e., cloud diameter) data, extracted from the time-sequenced photographs for each of the 20 static engine tests, are presented in Tables 1 through 20, where pertinent comments about the behavior of the exhaust clouds for some engine tests have been added.

One important comment must be made at this point. Only one movie camera was available to photograph the exhaust cloud for each of the 20 static engine firings analyzed. Although the cloud growth rate data may be somewhat questionable because of wind direction/wind shear effects, the rate of rise data should be fairly accurate. It is realized that a camera triangulation procedure would have been the optimum approach to acquire data for such a study.

### B. Meteorological Data

Surface and upper level atmospheric data are measured for all static engine firings at the Marshall Space Flight Center, by the Atmospheric Research Facility of the Aerospace Environment Division (see Figure 1). Wind speed, wind direction, ambient temperature, and relative humidity profile data, measured during the 20 static engine tests studied for this report are listed in Tables 21 through 24 for the surface, 500, 1000, 1500, and 2000 meter heights only. The Rawin Set AN/GMD-IB was used

1. For reference the height of large structure in Figure 2 (a through u) is 111 meters.

ATMOSPHERIC DATA

HEIGHT (M)	WIND SPEED (M/SEC)	WIND DIR. (DEG)	TEMP. (°C)	HUM. (%)
SFC	3.1	310	15.9	43
500	6.6	350	11.2	46
1000	6.6	353	6.7	59
1500	6.5	329	5.1	12
2000	8.1	312	3.7	10

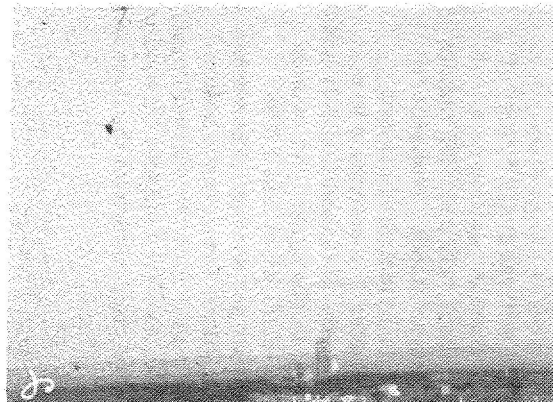
a

TEST: STATIC TEST FIRING NO. TWF 034  
 DATE: 9 OCTOBER 1964  
 FIRING TIME: 1621 CST  
 DURATION: 24 SECONDS  
 ENGINE: F-1 F 1002  
 FUEL: 8,186 GALLONS LOX  
 4,952 GALLONS RP-1  
 STAND: MODIFIED S-1  
 DEFLECTOR ANGLE: 30° FROM HORIZONTAL  
 DEFLECTOR AZIMUTH: 228° FROM TRUE NORTH

b

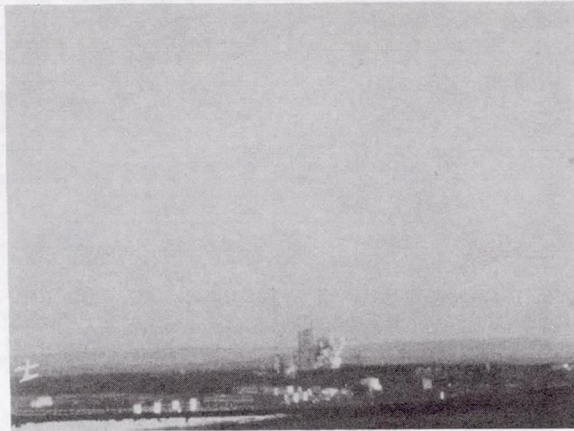


c

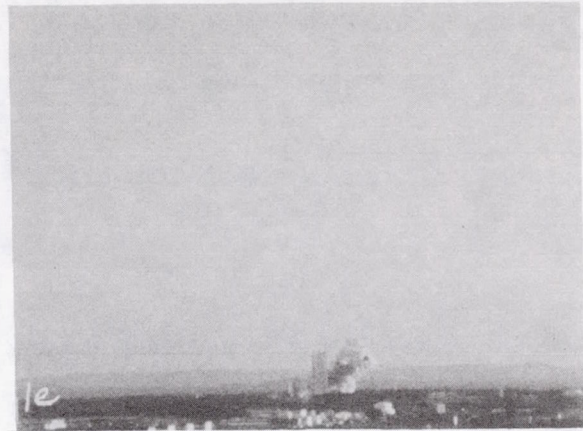


d

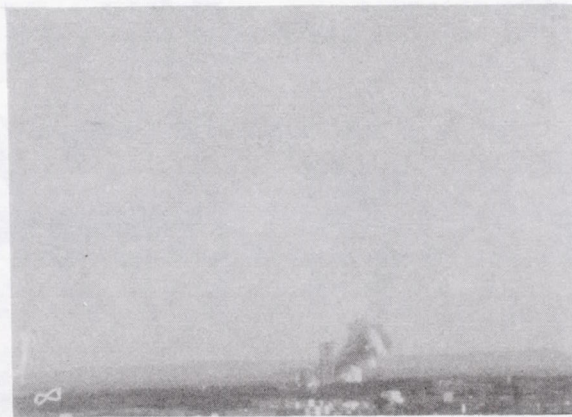
FIGURE 2 (a through d). ATMOSPHERIC DATA, TWF NO. 034 ENGINE TEST CONDITIONS AND EXHAUST CLOUD PICTURE AT IGNITION (I + 0) AND I + 2 SECONDS



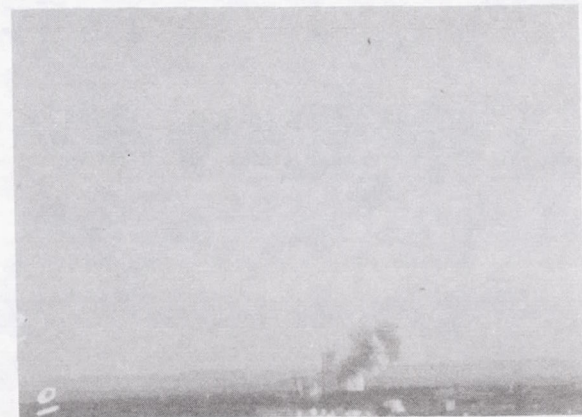
e



f



g



h

FIGURE 2 (e through h). EXHAUST CLOUD PICTURES AT I + 4, I + 6, I + 8, AND I + 10 SECONDS



i



j



k

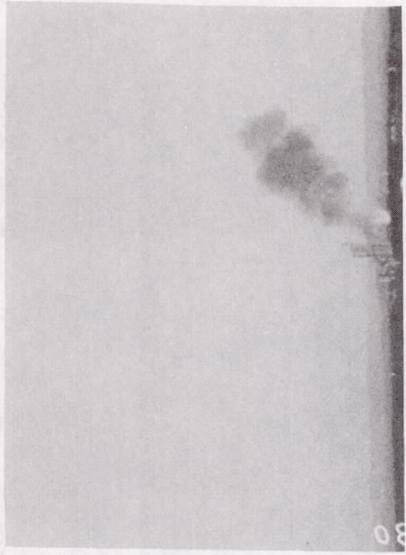


l

FIGURE 2 (i through l). EXHAUST CLOUD PICTURES AT I + 12, I + 14, I + 16, AND I + 18 SECONDS



m



n



o



p

FIGURE 2 (m through p). EXHAUST CLOUD PICTURES AT I + 20, I + 30, I + 40, AND I + 50 SECONDS



q



r



s



t

FIGURE 2 (q through t). EXHAUST CLOUD PICTURES AT I + 60, I + 70, I + 80, AND I + 90 SECONDS

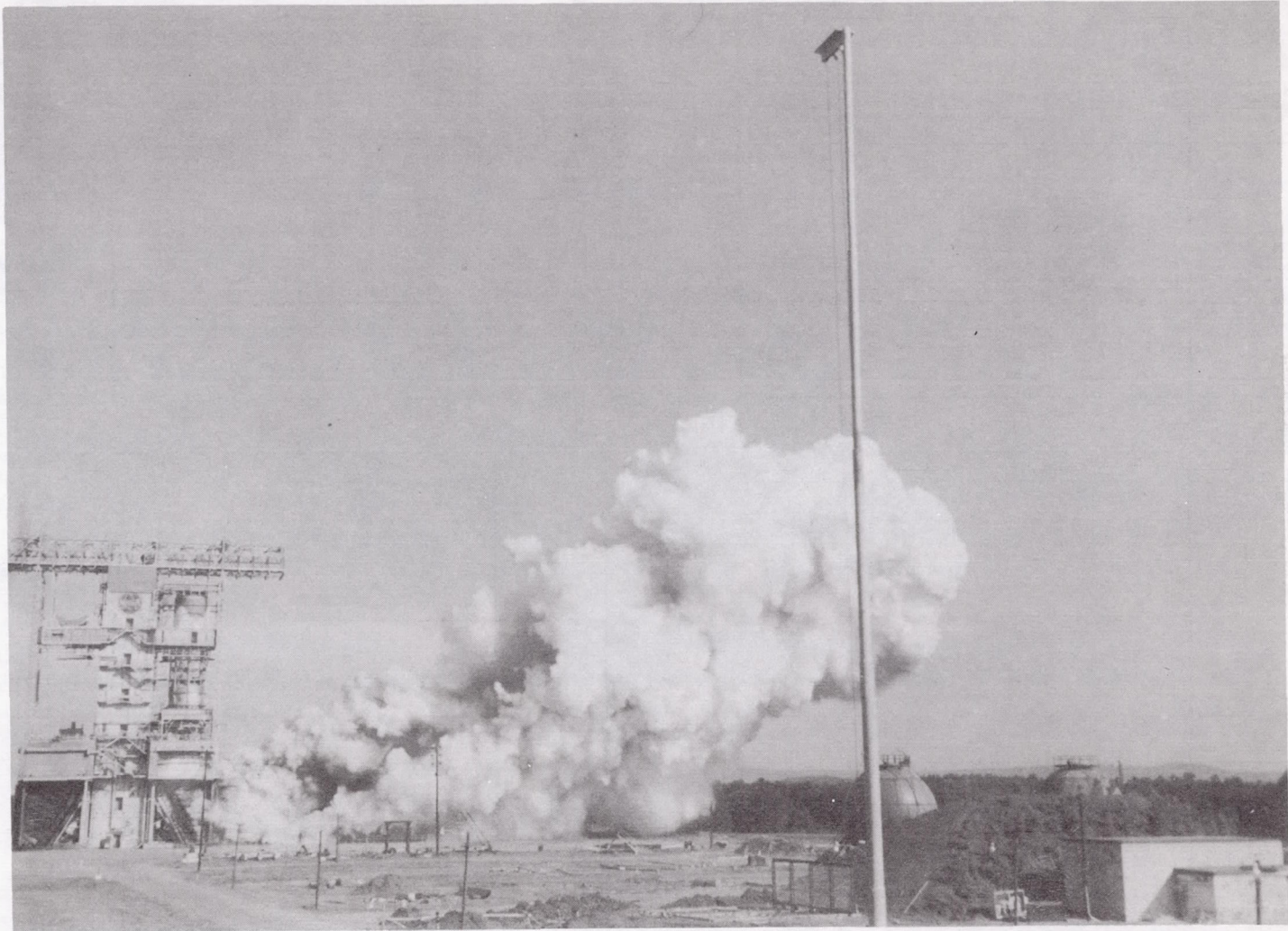


FIGURE 2(u). CLOSEUP VIEW OF ENGINE EXHAUST CLOUD SHORTLY AFTER IGNITION

TABLE I. STATIC ENGINE EXHAUST CLOUD  
DATA (TEST NO. 1)<sup>a, b</sup>

Time (sec)	Height of Rise <sup>c</sup> (H) (m)	Rate of Rise ( $\Delta H$ ) (m/sec)	Cloud Diameter (D) (m)
2	56	28	56
4	129	37	64
6	145	8	81
8	162	9	88
10	178	8	96
12	185	4	113
14	202	9	129
16	210	4	137
18	218	4	145
20	226	4	153

- a. Engine firing duration less than 5.0 seconds
- b. Top of exhaust cloud out of view of camera
- c. All heights are above ground level

TABLE II. STATIC ENGINE EXHAUST CLOUD  
DATA (TEST NO. 2)

Time (sec)	Height of Rise (H) (m)	Rate of Rise ( $\Delta H$ ) (m/sec)	Cloud Diameter (D) (m)
2	65	33	40
4	113	24	81
6	138	13	121
8	186	24	138
10	218	16	145
12	259	21	154
14	292	17	162
16	323	16	178
18	364	21	202
20	388	12	210
30	518	13	242
40	630	11	325
50	776	14	356
60	850	7	404

TABLE III. STATIC ENGINE EXHAUST CLOUD  
DATA (TEST NO. 3)

Time (sec)	Height of Rise (H) (m)	Rate of Rise ( $\Delta H$ ) (m/sec)	Cloud Diameter (D) (m)
2	97	49	64
4	135	19	97
6	150	8	122
8	185	18	137
10	226	21	145
12	264	19	154
14	300	18	162
16	324	12	170
18	354	15	186
20	360	3	202
30	490	13	226
40	710	22	250
50	870	16	290
60	930	6	324

TABLE IV. STATIC ENGINE EXHAUST CLOUD  
DATA (TEST NO. 4)<sup>a</sup>

Time (sec)	Height of Rise (H) (m)	Rate of Rise ( $\Delta H$ ) (m/sec)	Cloud Diameter (D) (m)
2	CAMERA STARTED LATE		
4	144	72	89
6	153	5	113
8	186	17	121
10	202	8	146
12	226	12	178
14	242	8	186
16	275	17	210

- a. Data limited due to lack of film coverage

TABLE V. STATIC ENGINE EXHAUST CLOUD DATA (TEST NO. 5)

Time (sec)	Height of Rise (H) (m)	Rate of Rise ( $\Delta H$ ) (m/sec)	Cloud Diameter (D) (m)
2	89	45	64
4	130	21	80
6	178	24	97
8	226	24	122
10	258	16	129
12	290	16	137
14	298	4	162
16	324	13	178
18	340	8	196
20	404	32	210
30	485	8	242

TABLE VII. STATIC ENGINE EXHAUST CLOUD DATA (TEST NO. 7)

Time (sec)	Height of Rise (H) (m)	Rate of Rise ( $\Delta H$ ) (m/sec)	Cloud Diameter (D) (m)
2	105	53	64
4	145	20	80
6	194	25	121
8	210	8	162
10	226	8	202
12	290	32	227
14	323	17	227
16	370	24	227
18	420	25	227
20	460	20	227
30	613	15	292
40	740	12	308
50	821	8	325
60	935	11	340
70	1050	11	365
80	1170	12	405

TABLE VI. STATIC ENGINE EXHAUST CLOUD DATA (TEST NO. 6)

Time (sec)	Height of Rise (H) (m)	Rate of Rise ( $\Delta H$ ) (m/sec)	Cloud Diameter (D) (m)
2	CLOUD BEHIND TOWER		
4	114	57	64
6	164	25	96
8	180	8	128
10	222	21	162
12	254	16	178
14	284	15	210
16	344	30	218
18	368	12	234
20	384	8	242
30	532	14	250
40	720	18	258
50	850	13	284

TABLE VIII. STATIC ENGINE EXHAUST CLOUD DATA (TEST NO. 8)

Time (sec)	Height of Rise <sup>a</sup> (H) (m)	Rate of Rise ( $\Delta H$ ) (m/sec)	Cloud Diameter (D) (m)
2	113	57	64
4	129	8	97
6	162	17	107
8	226	32	116
10	258	16	124
12	308	25	148
14	356	24	165
16	388	16	165
18	420	16	165
20	470	25	174
30	600	13	198
40	760	16	232
50	875	11	290
60	900	2	290
70	910	1	290

a. Cloud ascended beyond top of frame

TABLE IX. STATIC ENGINE EXHAUST CLOUD DATA (TEST NO. 9)

Time (sec)	Height of Rise (H) (m)	Rate of Rise ( $\Delta H$ ) (m/sec)	Cloud Diameter (D) (m)
2	64	32	40
4	121	29	80
6	178	29	113
8	186	4	122
10	202	8	146
17	226	12	171
14	258	16	210
16	290	16	210
18	324	17	210
20	346	11	218
30	452	10	242
40	516	6	325
50	665	14	405
60	710	4	453
70	750	4	470
80	809	5	470
90	850	4	470
100	890	4	470

TABLE XI. STATIC ENGINE EXHAUST CLOUD DATA (TEST NO. 11)

Time (sec)	Height of Rise (H) (m)	Rate of Rise ( $\Delta H$ ) (m/sec)	Cloud Diameter (D) (m)
2	65	33	49
4	105	20	81
6	129	12	97
8	154	13	129
10	178	12	153
12	200	11	153
14	230	15	162
16	258	14	162
18	290	16	162
20	324	17	162
30	428	10	202
40	525	9	242
50	590	6	283
60	605	1	324
70	645	4	386
80	725	8	420
90	780	5	485
100	809	2	565

TABLE X. STATIC ENGINE EXHAUST CLOUD DATA (TEST NO. 10)

Time (sec)	Height of Rise (H) (m)	Rate of Rise ( $\Delta H$ ) (m/sec)	Cloud Diameter (D) (m)
2	121	61	80
4	145	12	105
6	170	13	113
8	210	20	121
10	226	8	129
12	242	8	162
14	258	8	194
16	283	13	202
18	306	12	210
20	340	17	240
30	485	14	282
40	565	8	307
50	760	19	405
60	875	11	485
70	950	7	525
80	1010	6	565

TABLE XII. STATIC ENGINE EXHAUST CLOUD DATA (TEST NO. 12)

Time (sec)	Height of Rise (H) (m)	Rate of Rise ( $\Delta H$ ) (m/sec)	Cloud Diameter (D) (m)
2	113	57	64
4	153	20	97
6	202	25	113
8	243	21	119
10	258	8	145
12	282	12	162
14	324	21	178
16	364	20	186
18	404	20	186
20	420	8	194
30	525	10	242
40	661	13	284
50	809	14	324
60	880	7	388
70	1050	17	444

TABLE XIII. STATIC ENGINE EXHAUST CLOUD DATA (TEST NO. 13)

Time (sec)	Height of Rise (H) (m)	Rate of Rise ( $\Delta H$ ) (m/sec)	Cloud Diameter (D) (m)
2	40	20	40
4	121	41	56
6	154	17	121
8	194	20	145
10	226	16	154
12	258	16	161
14	275	9	170
16	281	3	178
18	324	22	194
20	354	15	210
30	500	14	226
40	630	13	242
50	780	15	276
60	878	9	276
70	1040	16	283
80	1160	12	283

TABLE XIV. STATIC ENGINE EXHAUST CLOUD DATA (TEST NO. 14)

Time (sec)	Height of Rise (H) (m)	Rate of Rise ( $\Delta H$ ) (m/sec)	Cloud Diameter (D) (m)
2	81	41	65
4	146	33	121
6	170	12	162
8	194	12	178
10	234	20	178
12	275	21	178
14	308	17	178
16	324	8	178
18	372	24	186
20	405	17	202
30	600	19	202
40	790	19	228

TABLE XV. STATIC ENGINE EXHAUST CLOUD DATA (TEST NO. 15)

Time (sec)	Height of Rise (H) (m)	Rate of Rise ( $\Delta H$ ) (m/sec)	Cloud Diameter (D) (m)
2	113	57	48
4	145	16	96
6	153	4	105
8	185	16	129
10	234	25	162
12	290	28	170
14	338	24	178
16	404	33	178
18	426	11	178
20	468	21	178
30	630	16	242
40	848	21	290
50	1000	15	324

TABLE XVI. STATIC ENGINE EXHAUST CLOUD DATA (TEST NO. 16)<sup>a</sup>

Time (sec)	Height of Rise (H) (m)	Rate of Rise ( $\Delta H$ ) (m/sec)	Cloud Diameter (D) (m)
2	25	13	31
4	113	44	93
6	176	32	126
8	220	2	132
10	252	16	157
12	283	16	164
14	333	25	170
16	364	16	189
18	377	7	220
20	408	16	226
30	502	9	226

a. Engine firing duration of 11.0 seconds

TABLE XVII. STATIC ENGINE EXHAUST CLOUD DATA (TEST NO. 17)

Time (sec)	Height of Rise (H) (m)	Rate of Rise ( $\Delta H$ ) (m/sec)	Cloud Diameter (D) (m)
2	24	12	18
4	97	36	91
6	133	18	103
8	194	31	121
10	230	18	151
12	291	31	181
14	315	12	181
16	351	18	193
18	412	31	230
20	448	18	242
30	665	11	266
40	775	11	302

TABLE XIX. STATIC ENGINE EXHAUST CLOUD DATA (TEST NO. 19)

Time (sec)	Height of Rise (H) (m)	Rate of Rise ( $\Delta H$ ) (m/sec)	Cloud Diameter (D) (m)
2	97	49	64
4	129	16	81
6	186	29	97
8	194	4	105
10	210	8	113
12	258	24	129
14	318	30	145
16	380	31	161
18	420	20	170
20	452	16	186
30	660	20	202
40	850	19	242
50	970	12	324
60	1050	8	485

TABLE XVIII. STATIC ENGINE EXHAUST CLOUD DATA (TEST NO. 18)

Time (sec)	Height of Rise (H) (m)	Rate of Rise ( $\Delta H$ ) (m/sec)	Cloud Diameter (D) (m)
2	31	16	31
4	75	22	62
6	113	19	125
8	198	43	156
10	262	32	174
12	300	19	219
14	344	22	250
16	362	9	282
18	386	12	294
20	437	26	300
30	625	18	354
40	825	20	362

TABLE XX. STATIC ENGINE EXHAUST CLOUD DATA (TEST NO. 20)

Time (sec)	Height of Rise (H) (m)	Rate of Rise ( $\Delta H$ ) (m/sec)	Cloud Diameter (D) (m)
2	105	53	48
4	121	8	105
6	178	29	121
8	202	12	125
10	226	12	129
12	283	29	138
14	298	8	148
16	356	29	154
18	364	4	178
20	380	8	186
30	525	14	243
40	630	10	283
50	809	17	323

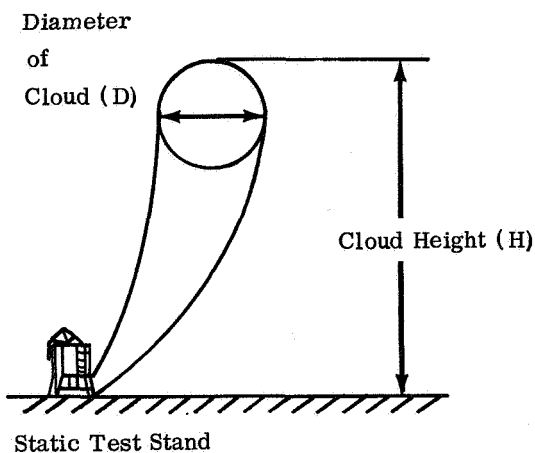


FIGURE 3. METHOD USED TO OBTAIN HEIGHT AND DIAMETER OF TOP OF CLOUD

to obtain the upper atmospheric profile data (i.e., 500 meter height data and above). Other atmospheric data observed and measured at the static test stands, remote meteorological towers, etc., during these static engine tests were not available in this study.

TABLE XXI. ATMOSPHERIC DATA -- WIND SPEED (m sec<sup>-1</sup>)

Test No.	SFC	500 (m) <sup>a</sup>	1000 (m)	1500 (m)	2000 (m)
1	2.1	2.5	5.5	8.2	10.6
2	2.1	8.3	5.4	4.8	5.4
3	5.7	5.0	5.1	6.5	9.3
4	3.1	5.5	7.6	8.8	10.1
5	3.1	4.8	7.7	9.9	9.9
6	2.1	3.7	5.8	6.2	7.0
7	2.1	8.0	7.7	7.6	13.1
8	3.1	9.3	8.3	9.2	10.1
9	3.1	6.6	6.6	6.5	8.1
10	2.6	7.7	8.5	8.7	7.2
11	3.1	9.0	0.7	10.9	11.0
12	3.6	4.4	5.6	6.4	8.1
13	4.1	6.5	9.1	14.9	20.4
14	3.1	6.2	9.3	9.6	11.9
15	3.1	4.8	7.7	11.5	16.7
16	4.1	6.6	5.8	7.4	9.5
17	1.5	3.4	5.3	6.8	7.6
18	1.8	2.4	2.7	3.0	3.3
19	4.6	7.6	8.0	8.9	11.2
20	2.6	6.7	10.7	13.0	10.3

a. All heights are above ground level

TABLE XXII. ATMOSPHERIC DATA -- WIND DIRECTION (DEGREES)

Test No.	SFC	500 (m)	1000 (m)	1500 (m)	2000 (m)
1	080	126	149	175	197
2	250	274	291	327	324
3	020	025	327	316	314
4	100	352	316	314	311
5	250	275	329	340	348
6	130	169	269	281	292
7	300	322	304	292	317
8	340	356	360	003	360
9	310	350	353	329	312
10	340	011	031	027	012
11	330	360	359	343	328
12	250	311	329	322	316
13	290	294	302	313	314
14	130	203	263	287	299
15	350	349	359	343	328
16	340	331	336	339	338
17	210	173	189	186	195
18	360	026	097	162	190
19	210	205	198	206	219
20	270	250	246	243	242

TABLE XXIII. ATMOSPHERIC DATA -- TEMPERATURE (°C)

Test No.	SFC	500 (m)	1000 (m)	1500 (m)	2000 (m)
1	26.5	22.2	17.8	16.0	12.2
2	28.1	25.2	21.6	17.6	14.2
3	29.0	24.3	20.4	16.4	12.6
4	24.9	24.6	20.5	16.4	14.0
5	33.1	27.4	25.2	22.8	18.5
6	22.5	22.0	20.1	18.0	15.3
7	21.8	18.6	13.8	8.7	7.0
8	14.6	10.7	5.5	0.5	-2.5
9	15.9	11.2	6.7	5.1	3.7
10	16.8	10.0	6.8	8.2	9.7
11	15.2	12.0	7.7	7.8	5.3
12	15.2	10.5	8.6	5.9	2.9
13	9.7	4.6	-0.3	-2.2	-2.2
14	14.4	9.4	10.6	10.1	7.2
15	20.3	15.5	11.8	12.9	11.3
16	19.2	11.9	6.9	4.6	4.4
17	28.5	22.7	18.1	13.1	10.8
18	28.0	22.2	18.6	15.8	11.0
19	31.3	25.1	20.2	15.8	11.6
20	24.2	19.4	15.8	13.5	10.1

TABLE XXIV. ATMOSPHERIC DATA —  
HUMIDITY (%)

Test No.	SFC	500 (m)	1000 (m)	1500 (m)	2000 (m)
1	63	25	31	62	83
2	50	67	66	74	67
3	54	51	58	65	64
4	90	64	73	75	63
5	60	57	52	42	58
6	94	65	75	65	55
7	35	25	28	31	21
8	38	30	41	58	47
9	43	46	59	12	10
10	34	18	15	10	10
11	43	24	23	26	23
12	32	24	8	4	4
13	35	31	39	36	27
14	68	64	38	4	12
15	32	29	22	*	4
16	34	29	4	8	2
17	36	59	67	72	50
18	55	72	68	57	72
19	48	41	58	65	73
20	79	76	82	81	72

\* No Data

### C. Static Engine Test Data

Data on the static engine tests used for this evaluation are listed in Table XXV. Such information as duration of each engine firing in seconds, type of fuel and amount expended, exhaust deflector angle in degrees above the horizon, etc., is of interest and is pertinent criteria for completing the study. Of interest, and which will be discussed in detail later, is the characteristic behavior of the exhaust cloud phenomena for tests 1 and 16. These engine tests were of the shortest duration; test 1 was less than 5 seconds and test 16 was an 11 second engine test.

## III. CLOUD RISE AND GROWTH PHENOMENA

Figure 4 shows the height the exhaust clouds obtain with respect to time (See Tables I through

XX). The cloud diameter data have also been plotted in Figure 5, and are listed in Tables I through XX. Most of the results shown in Figures 4 and 5 are as expected. Some cloud rise and growth data terminate in the 20 to 30 second time range (refer to data for tests 1, 4, and 16). Data for tests 1 and 16 are very limited because of the briefness of these static engine tests (See Table XXV) and data for test 4 was terminated early because of the lack of film coverage after ignition plus 16 seconds (I + 16 seconds).

The rate of rise of the exhaust clouds varies appreciably. This variation can be seen in Figure 6, a plot of rise rate ( $\Delta H \Delta T^{-1}$ ) versus time. The reason for the large variation in the rise rates, at least for the initial time period, is twofold: (1) the rise rate is greater for warmer sources, and (2) the rise rate varies according to the thermal properties of the ambient air. In general, the more unstable the ambient temperature profile conditions, the greater the height and rise rate of hot clouds. More will be said about the synoptic weather conditions associated with these 20 static tests in Section III B. An interesting factor noticed during the examination of the height and rise rate data is that wind direction and speed do not appear to affect the height and rise rates of exhaust clouds.<sup>1</sup> However, there is a direct correlation of cloud diameter and wind velocity conditions. If the winds are blowing with the direction of the deflected exhaust gases, the exhaust cloud tends to "lean over;" whereas, if the winds are blowing against the deflected exhaust gases, the plume tends to be more vertical. Naturally, the angle the exhaust plumes create depends on the wind speed and shear conditions, and not totally on wind azimuth angles.

Figure 7 shows the mean, maximum, and minimum cloud height curves as a function of time. These results were computed by fitting polynomials to the height of exhaust cloud data in Tables I through XX. Subsequently, the curves were plotted on log-linear paper to bring out a special point, this is, that the height of cloud stabilization is shown to be in the neighborhood of 1000 meters. This is the average height obtained from exhaust clouds generated from one engine. The maximum height of rise versus number of engines is discussed further in Section III-C.

1. On the contrary, Holland [2] found plume height to decrease with increasing wind speed; however, this behavior was not too discernible because of the wide scatter in his height versus wind speed data.

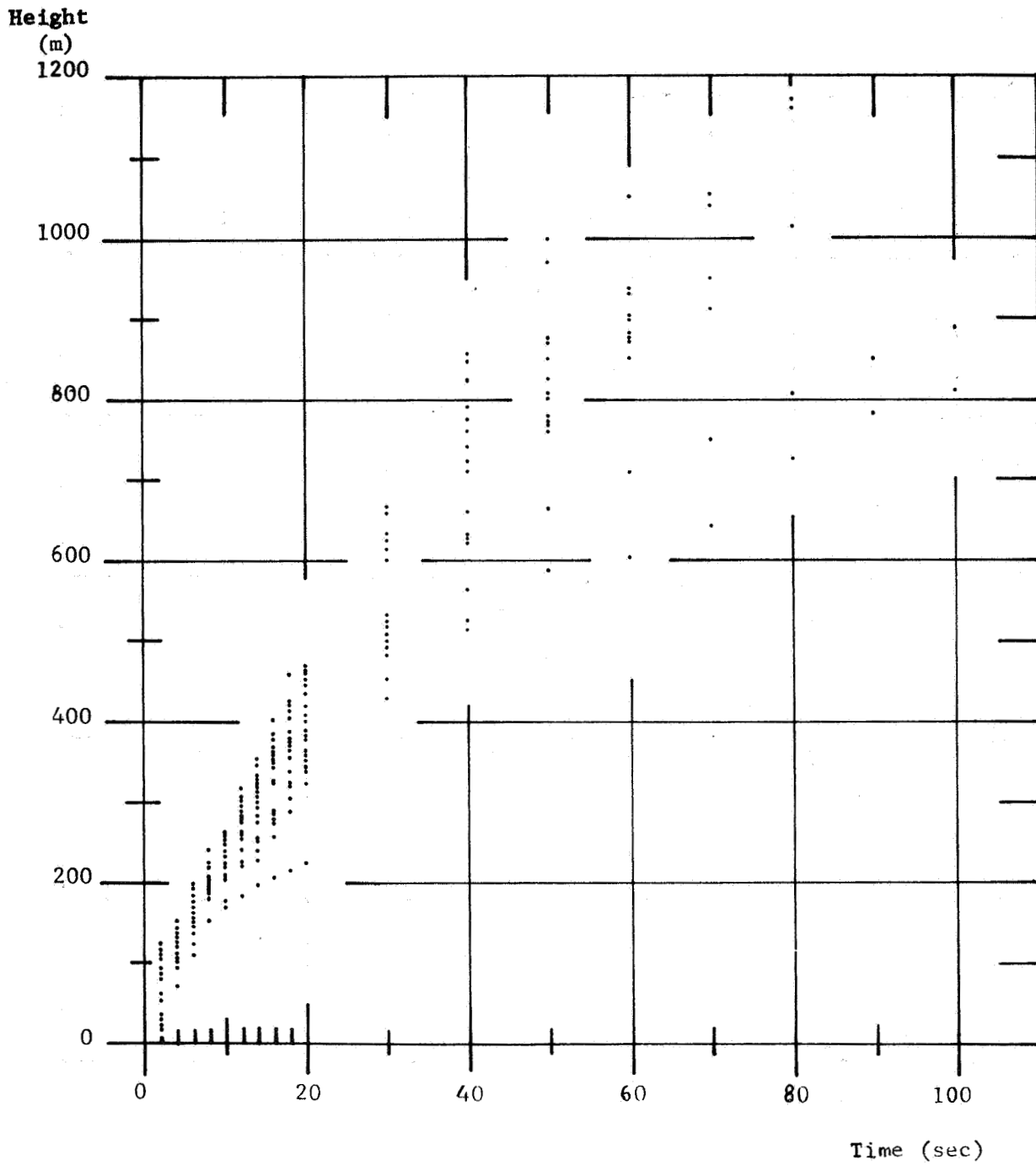


FIGURE 4. HEIGHT OF EXHAUST CLOUD AS A FUNCTION OF TIME FOR ALL TESTS

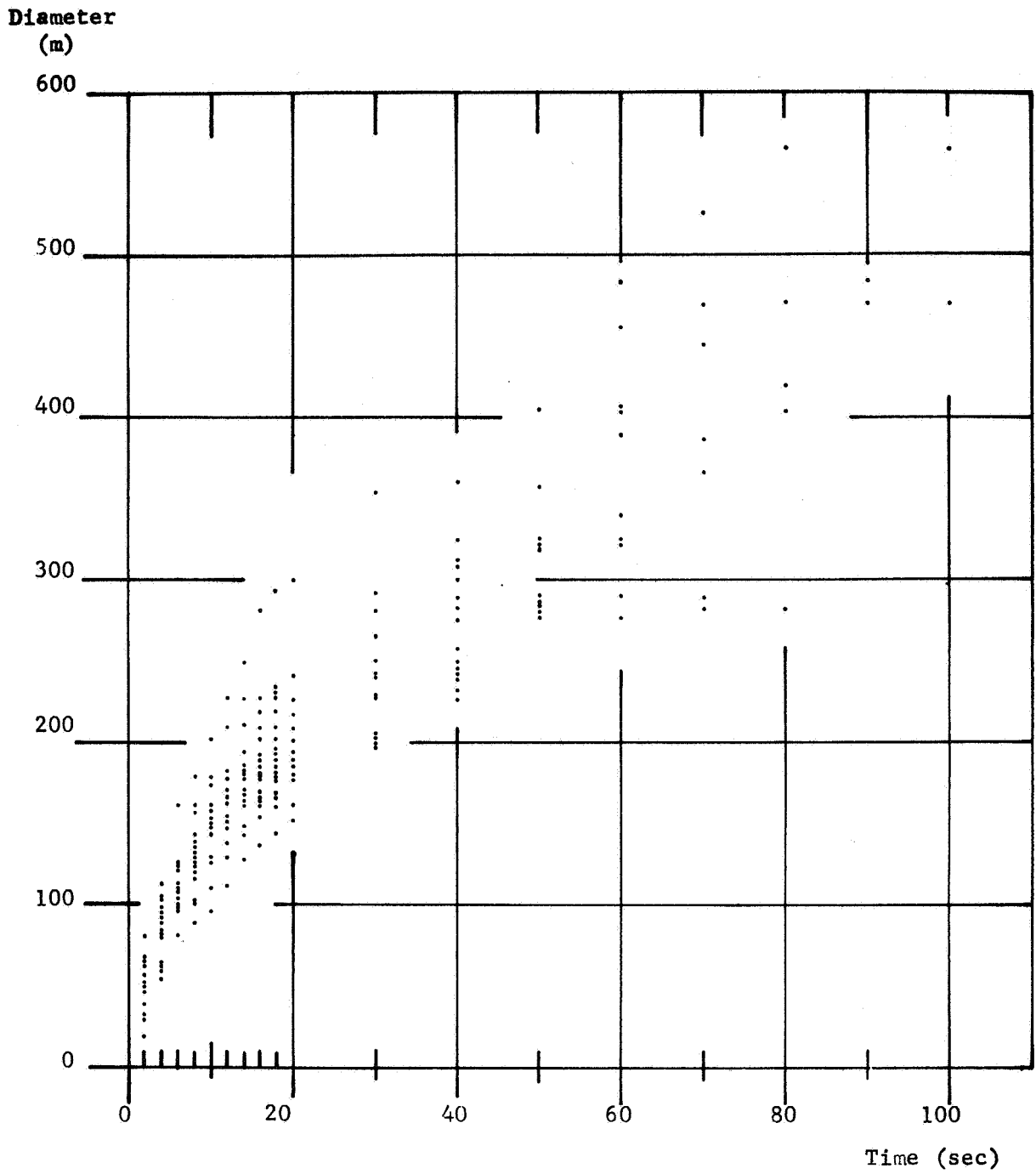


FIGURE 5. DIAMETER OF TOP OF CLOUD AS A FUNCTION OF TIME FOR ALL TESTS

TABLE XXV. DATA FROM TWENTY STATIC VEHICLE FIRING TESTS AT MARSHALL SPACE FLIGHT CENTER (MSFC), HUNTSVILLE, ALABAMA

	Test	Date	Firing Time (CST)	Duration (sec)	Engine	Fuel (gal)	Stand	Deflector Angle <sup>a</sup>	Deflector Azimuth <sup>b</sup>
1.	TWF023	6/30/64	1642	<5	F-1 F-1002	2000 LOX 900 RP-1	Modified S-I	30°	228°
2.	TWF026	7/9/64	1619	23	F-1 F-1002	20 000 LOX 14 000 RP-1	Modified S-I	30°	228°
3.	TWF027	7/10/64	1654	50	F-1 F-1002	55 000 LOX 35 000 RP-1	Modified S-I	30°	228°
4.	TWF028	7/20/64	1638	125	F-1 F-1002	55 000 LOX 6000 RP-1	Modified S-I	30°	228°
5.	TWF031	8/4/64	1124	20	F-1 F-1002	15 000 LOX 10 000 RP-1	Modified S-I	30°	228°
6.	NO 033	8/25/64	1706	66	F-1 F-1002	25 000 LOX 17 000 RP-1	Modified S-I	30°	228°
7.	NO 23	9/24/64	1637	35	S-I	17 500 LOX 1000 RP-1	Modified S-I	30°	48°
8.	NO 24	10/6/64	1638	154	S-I	64 560 LOX 40 224 RP-1	Modified S-I	30°	48°
9.	TWF034	10/9/64	1621	24	F-1 F-1002	8186 LOX 4952 RP-1	Modified S-I	30°	228°
10.	TWF035	10/10/64	1429	132	F-1 F-1002	55 150 LOX 33 660 RP-1	Modified S-I	30°	228°
11.	TWF037	10/23/64	1640	119	F-1 F-1002	48 000 LOX 34 000 RP-1	Modified S-I	30°	228°
12.	TWF050	2/18/65	1639	48	F-1 F-1002	21 000 LOX 15 000 RP-1	Modified S-I	30°	228°
13.	TWF052	3/1/65	1414	60	F-1 F-1002	30 000 LOX 17 000 RP-1	Modified S-I	30°	228°
14.	SA-25	4/1/65	1703	60.4	S-IB-I	25 000 LOX 16 000 RP-1	Modified S-I	30°	48°
15.	SA-26	4/13/65	1639	145	S-IB-I	62 000 LOX 41 000 RP-1	S-I	30°	48°
16.	S-IC-04	4/16/65	1459	11	S-IC	N/A LOX N/A RP-1	S-IC	10°	247.5°
17.	S-IC-05	5/6/65	1510	15.6	S-IC	36 000 LOX 19 000 RP-1	S-IC	10°	247.5°
18.	S-IC-05	5/20/65	1200	40.6	S-IC	18 000 LOX 13 000 RP-1	S-IC	10°	247.5°
19.	TWF056	5/26/65	1400	40	F-1	17 000 LOX 7000 RP-1	Modified S-I	30°	228°
20.	TWF050	5/27/65	1400	100	F-1	45 000 LOX 20 000 RP-1	Modified S-I	30°	228°

a. Measured from horizontal.

b. Measured from true North.

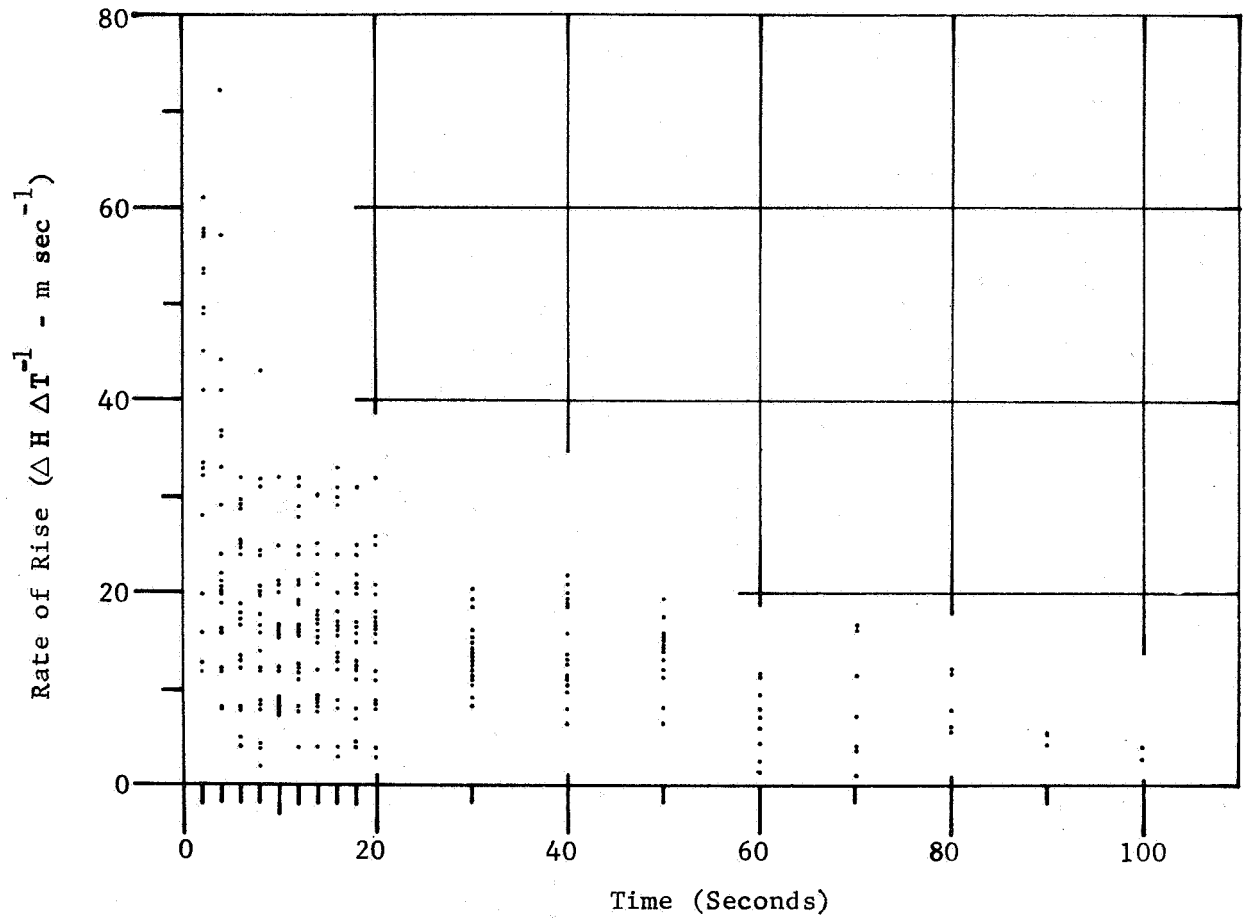


FIGURE 6. VEHICLE EXHAUST CLOUD RISE RATE ( $\Delta H \Delta T^{-1}$ ) VERSUS TIME FOR ALL TESTS

The equation and coefficients for the curves shown in Figure 7 are as follows:

$$Y = a_0 + a_1 t + a_2 t^2, \quad (1)$$

where Y is height in meters and time (t) in seconds.

The minimum curve constants are:

$$a_0 = 2.51 \times 10^1$$

$$a_1 = 1.52 \times 10^1$$

$$a_2 = -8.15 \times 10^{-2}$$

The average curve constants are:

$$a_0 = 1.98 \times 10^1$$

$$a_1 = 2.00 \times 10^1$$

$$a_2 = -1.06 \times 10^{-1}$$

The maximum curve constants are:

$$a_0 = 1.66 \times 10^1$$

$$a_1 = 2.65 \times 10^1$$

$$a_2 = -1.44 \times 10^{-1}$$



## C. Meteorological Analysis and Results

1. Temperature/Humidity Profiles. All of the firings occurred between 11:24 a. m. and 5:06 p. m. local time (Table XXV). This time period generally ensures that isothermal or unstable temperature lapse rates will persist in the lower troposphere at the time of firing. This is the optimum time of day from an operational standpoint and it is also the most meteorologically useful period for modeling exhaust clouds because there is little likelihood of having strong temperature inversions near the ground during the afternoon hours. The surface temperature profiles given in Table XXIII show values ranging between 9.7°C and 31.3°C for the 20 firings. This range is indicative of the seasonal differences under which the measurements were made. The relative humidity (Table XXIV) varied between 32 and 90 percent at the surface, thereby reflecting the influence at difference times of both frontal weather, as well as dry air associated with the high pressure or anti-cyclonic systems.

2. Synoptic Weather Patterns and Local Winds. The surface synoptic weather patterns associated with these static firings have been analyzed. The cold high pressure system or anticyclone was the dominant feature in seven cases, while persistent wind from the northwest or north was evident. Two other cases were closely associated with rather strong and warmer high pressure systems centered off the east coast of the United States. Five other firings occurred when synoptic weather patterns showed weak horizontal pressure gradients associated with weak anticyclonic systems. Although cyclonic wind flow was evident in the six remaining cases, in only two cases of these was the surface pressure gradient of any measurable importance.

The synoptic weather systems have been compared with the locally measured wind speed and direction profiles for each individual firing using data listed in Tables XXI and XXII. Some relationships which are interesting and, more importantly, meteorologically consistent with theory are discussed. There were eleven cases which reflect strong synoptic pressure systems, including both cyclonic and anticyclonic, and in all these, the total wind directional change over the surface to 2000m layer never exceeded 24 degrees. The other nine cases, where the surface pressure systems were relatively weak, showed wind direction change magnitudes over this same 2000m layer ranging from

66 to 190 degrees. Such cases as these made the photographic analysis difficult and open to greater chance of errors. Furthermore, only seven of the 20 wind profiles analyzed indicated a counterclockwise directional turning in the 2000m layer irrespective of intermediate variations. Five of these seven were associated with the strong pressure systems already discussed above. It is known that well-developed synoptic-scale pressure systems almost always slope with altitude, the amount being dependent upon the particular situation. Therefore, for analysis purposes the location of the center of the local pressure system with reference to the point of measurement of a particular data point will determine to a great extent the directional variability in the near surface layers of the atmosphere. The wind is known to frequently spiral or turn clockwise with height near the ground unless there are synoptic or local influences which are more dominant.

The wind speeds occurring during the firings ranged between 1.5 and 5.7 m sec<sup>-1</sup> at the surface and between 3.3 and 20.4 m sec<sup>-1</sup> at the 2000m level. Individual profiles showed minimum scalar wind speed changes over 2000m of 1.5 m sec<sup>-1</sup> and maximum values of 16.3 m sec<sup>-1</sup>. It is important to point out here that the maximum wind directional change already noted (190 degrees) over the referenced 2000m layer occurred with the minimum wind speed change (1.5 m sec<sup>-1</sup>). Further, the maximum wind speed change (16.3 m sec<sup>-1</sup>) occurred with a relatively small directional change of 24 degrees.

These meteorological analyses have provided a close look at important relationships which exist between the synoptic-scale weather patterns and the locally measured profiles of wind, temperature, and humidity. All of the factors discussed influence the measured values for rise rate and growth of exhaust clouds. This influence may be primarily meteorological, because the atmosphere governs the real rise rate and growth values, or it may be analytical. The latter possibility means that the atmosphere also governs the effectiveness of the photographic reduction techniques employed in this study.

3. Comparison of Theoretical to Observed Results. A large amount of theoretical work has been done on the rate of rise and maximum height that hot buoyant clouds obtain [1, 2, 3, 4]. Morton, Taylor and Turner [1] found that

$$H = 0.410 \alpha^{-1/2} \left( \frac{g Q_H}{T_1 \rho_1 C_p} \right)^{1/4} \left[ \frac{g \Gamma}{T_1} (1 + n) \right]^{-3/8} x_1,$$

where

$\alpha$  = a proportionality constant which is a measure of the rate of the entrainment ( $\alpha = 0.093$  from laboratory experiments).

$Q_H$  = rate of emitted heat on continuous basis

$T_1$  = ambient air temperature

$\rho_1$  = ambient air density

$C_P$  = specific heat at constant pressure

$\Gamma$  = adiabatic lapse rate of temperature

$n$  = ratio of actual lapse rate to  $\Gamma$

$X_1$  = 2.8 at level where the vertical velocity first vanishes

Using this equation to determine the height to which buoyant cloud will ascend before becoming thermally stable and estimates of heat generated from 1, 2, 3, 4 and 5 engines, we calculated height of rise ( $H$ ) for selected source strengths ( $Q_H$ ) using standard day atmospheric conditions (F-1 type engine):

No. of Engine	$Q_H$ (cal/sec) Source Strength	Height (m)
1	$2.68 \times 10^9$	1450
2	$5.36 \times 10^9$	1650
3	$8.04 \times 10^9$	1850
4	$1.07 \times 10^{10}$	2050
5	$1.34 \times 10^{10}$	2250

It is interesting that, for one engine, which emits  $2.68 \times 10^9$  cal  $\text{sec}^{-1}$ , the height to which the cloud will rise was calculated to be 1450 meters. This value compares quite well with the observed maximum heights which such clouds obtained (Fig. 7). The standard atmospheric conditions (standard day) used for these calculations were taken from Reference 5.

Sutton [2] indicates that a favorable coefficient to work with is the coefficient of plume, which is simply the ratio of the radius of the cloud top to the cloud height:

$$p_c = r/H.$$

These coefficient were determined for the data presented here. Figure 8, which only shows the maximum and minimum envelopes of the data values, was then developed. No rigorous treatment is given the coefficient of plume ( $p_c$ ); however, the results

shown in Figure 8 may be of real interest to subjectively analyze the behavior of cloud growth to cloud rise.

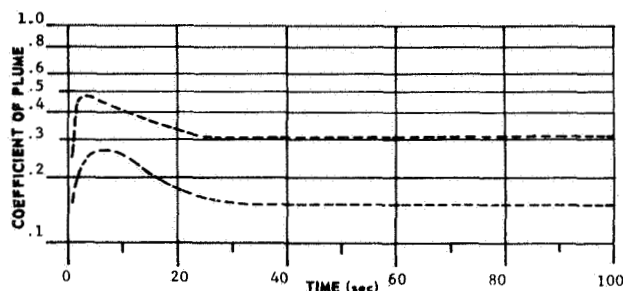


FIGURE 8. COEFFICIENT OF PLUME (Radius of Cloud Top to Cloud Height)

## V. CONCLUDING REMARKS

The rise and growth characteristics of static engine exhaust clouds is an interesting phenomenon to observe. This presentation relates some of the factors on rise, rise rates, and cloud growth to show the orderly behavior of the hot buoyant effluents generated by static fired vehicle engines. Significantly, these data compare with theoretical findings established by authorities on this subject.

These findings should provide vehicle aerodynamicists, aerospace engineers, meteorologists, and others with some general insight as to the behavior of engine exhaust clouds. It is obvious that these findings pertain not only to static fired engines, but may also be used to estimate cloud rise related to actual launchings of space vehicles. Having such information available for vehicle launches would be most valuable if toxic propellants or other potentially hazardous atmospheric pollutants were on board.

Although much information has been gained from this study, additional studies of this type should be made to give greater statistical confidence to the results obtained. A more sophisticated camera arrangement would be necessary to capture cloud rise and growth data for better results in future studies.

It has been shown that the behavioral rise and growth characteristics of hot effluents are particularly governed by the initial heat generated by the source emitter and the thermodynamic properties of the atmosphere into which the effluents are ejected.

## REFERENCES

1. Hage, Keith D. and Bowne, Norman E.: Preliminary Estimates of Environmental Exposure for Fuel and Exhaust Products. NASA Report CR-61056, January 1965.
2. Pasquill, F.: Atmospheric Diffusion. D. Van Nostrand Company, New York, 1962.
3. Sutton, O. G.: Micrometeorology. McGraw-Hill Company, Inc., 1963.
4. Slade, David H., ed.: Meteorology and Atomic Energy, 1968. United States Atomic Energy Commission, July 1968.
5. U.S. Standard Atmosphere, 1962. U.S. Government Printing Office, Washington, D.C., December 1962.

## VI. SOLAR PHYSICS

# FREQUENCY DISTRIBUTION OF SOLAR RADIATION AT APALACHICOLA, FLORIDA AND SANTA MARIA, CALIFORNIA

By

Glenn E. Daniels

## ABSTRACT

Hourly solar radiation data have been analysed to provide frequency distributions useful for heat load computations of objects exposed to the sun on or near the earth's surface. The method used to analyse the data and compute diffuse radiation is described. Tables of the frequency distributions of hourly values for each month for total horizontal and normal incident solar radiation for Apalachicola, Florida are included, as well as tables of June and December values of solar radiation data extremes for Apalachicola, Florida, and Santa Maria, California.

## I. INTRODUCTION

To provide information on heat loads for on-pad design and operation of large space vehicles, a study was made of solar radiation data from Apalachicola, Florida and Santa Maria, California. Extremes and frequency distributions were computed from the data, a part of which was used for criteria in the Terrestrial Environment Criteria Guideline document [ 1 ].

Since there are only 28 stations in the United States where solar radiation intensities have been continuously recorded on strip charts, to permit a statistical analysis of the data on an hourly basis, two stations were selected as representative of areas of greatest interest to NASA. One of these stations, Apalachicola, Florida, was selected as representative of the eastern United States and also the White Sands Proving Ground area. Santa Maria, California, represented the western United States. The last ten years of data at each station was used for the study.

Hourly totals of total horizontal solar radiation measured near the earth's surface were available from each station. The data for Santa Maria, California, also included hourly weather observations. These total horizontal solar radiation data are a measure of the direct solar radiation from the sun on

a horizontal surface plus the diffuse (sky) radiation from the total sky hemisphere. Since the altitude of the sun changes with time of day, it was desirable to also express the solar radiation from the sun as that received on a surface normal to the sun. To obtain these data, a method was developed to estimate diffuse radiation from the total horizontal solar radiation data. The estimated diffuse radiation was subtracted from the total horizontal radiation before the normal incident radiation was computed.

Frequency distributions were computed, for each hour of the day for monthly periods of the diffuse (sky) radiation and of the solar radiation on a horizontal surface, a surface normal to the sun, a surface facing south at 45 degrees to the horizon and of the diffuse (sky) radiation.

## II. ANALYSIS

### A. Solar Electromagnetic Spectrum

The most important source of radiation is the sun which is emitting in the electromagnetic spectrum between 0.0001 angstroms and 1,000,000 angstroms. This radiation ranges from cosmic rays through the very long radio waves.

Of the total electromagnetic spectrum of the sun, only the radiant energy from that portion of the spectrum between 2200 angstroms and 70,000 angstroms (the light spectrum) is important in design. This portion contains 99.8 percent of the total electromagnetic energy. The spectral distribution of this region closely resembles the emission of a gray body radiating at 6000°C. This is the spectral region which results in heating or cooling of an object.

The distribution of the solar radiation outside the atmosphere is a continuous spectrum with many narrow absorption bands caused by the elements and

molecules in the colder solar atmosphere. These absorption bands are the Fraunhofer lines, whose widths are very small (usually less than 1 angstrom). The earth's atmosphere also absorbs a part of the solar radiation such that the major portion of the solar radiation reaching the earth is between about 3500 angstroms and 40,000 angstroms.

## B. Instrumentation for Solar Radiation Measurements

The previous discussion of solar radiation emphasized the distribution of intensity with wavelength. Such data are required when selective absorption is considered in design. Only a limited number of measurements have been made of this type, and each of these cover only a portion of the total spectrum. In contrast, we find that there have been a number of stations (actually 47) in the continental United States which have measured hourly solar radiation (measurement of intensity of white light). At present, 28 stations are collecting hourly data on a regular basis. There are 85 stations (including the 28 hourly) which regularly report daily totals of solar radiation. This is a small number of stations compared to the many which measure air temperature, but it is sufficient to provide a representative knowledge of the total solar radiation distribution within the United States.

The pyranometer (manufactured by the Eppley Laboratories as the Eppley 180 degree Pyrheliometer) has been used in the United States almost exclusively for all long-term solar radiation measurements. (The Moll-Gorczyński solarimeter is frequently used as the pyranometer in other countries.) The pyranometer used in the United States has two thermally insulated silver rings, mounted near the center of a sealed soda-glass bulb. One ring is coated with magnesium oxide to make it white, and the other with Parsons Optical Black Lacquer to make it black. When radiation of the proper wavelengths fall on these rings, the black rings get hot in relation to the white ring. To determine the differences in temperature between the two rings either 10 or 50 thermocouple junctions are mounted in the rings with alternate junctions in the black and white rings. The pyranometer is sensitive to solar radiation in the spectral region between 3,500 and 40,000 angstroms, and thus gives a good measurement of the shorter wavelength thermal radiation. The 50-junction pyranometer has an output of about 7 to 8 millivolts per gram

calorie per square centimeter per minute. The instrument is installed with the face of the two rings horizontal. A single pen potentiometer recorder is usually used to record the measurements.

To obtain the data from the chart records, the area under the curve and between two time lines (such as two lines one hour apart) is found. Methods have been developed, using transparent scales which make reading the data relatively simple, even for records during periods of scattered clouds when the record is very irregular.

The probable error of the tabulated data is about 0.02 gram calories per square centimeter per minute, or about 1.5 percent for the higher values on clear days. This is one of the most accurate meteorological measuring instruments in use.

Most of the solar radiation stations reporting hourly data have been in operation since 1952. The horizontal hourly solar radiation data are available in punched cards at the National Weather Records Processing Center (NWRC). Also included in the cards are the solar altitude and the amount of cloudiness for a number of stations.

## C. Recent Analysis of Solar Radiation Data

The solar radiation from two selected stations was analyzed by the National Weather Records Center, ESSA, under NASA contract. This was the first detailed analysis of the hourly solar radiation in the files of the National Weather Records Center.

The standard solar radiation sensors measure the intensity of direct solar radiation falling on a horizontal surface plus the diffuse (sky) radiation from the total sky hemisphere. Diffuse radiation is lowest with dry clear air; it increases with increasing dust and moisture in the air; with extremely dense clouds or fog, the measured horizontal solar radiation will be nearly all diffuse radiation. The higher values of measured horizontal solar radiation (extremes, 95 percentile) will occur during clear skies. Because part of the plan of analysis of the data was to determine the solar radiation on surfaces normal to the sun and a surface facing south at 45 degrees to the horizon, it was desirable to use only the direct solar radiation, i. e., take out the diffuse (sky) radiation from the measured data, in the computations of the normal values. When solar radiation data are used in

design studies, the direct solar radiation should be applied from one direction as parallel rays and, at the same time, the diffuse radiation should be applied as rays from all directions of a hemisphere to the object as shown in Figure 1.

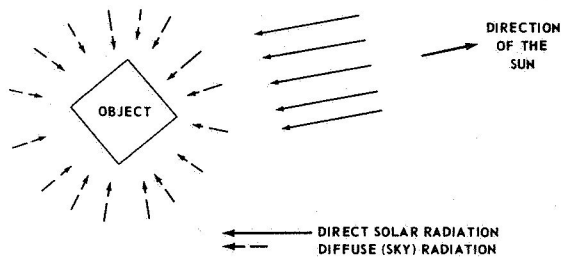


FIGURE 1. METHOD OF APPLYING DIFFUSE RADIATION FOR DESIGN

A search of the literature on diffuse radiation was made. It was decided, based mostly on a paper by Parmalee [2] that the amount of diffuse radiation could be estimated quite well from the hourly total horizontally measured solar and sky radiation and the altitude of the sun above the horizon. A nomograph was prepared as shown in Figure 2.

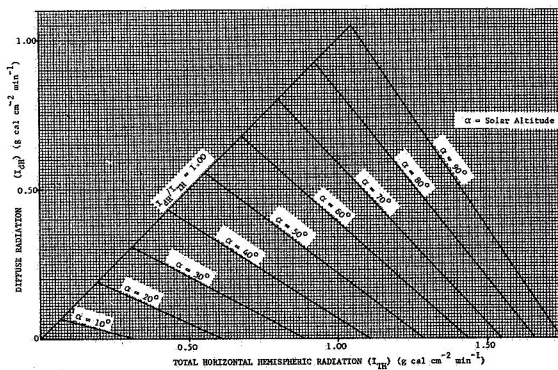


FIGURE 2. RELATIONSHIP OF DIFFUSE SOLAR RADIATION TO TOTAL HORIZONTAL HEMISPHERIC RADIATION AND SOLAR ALTITUDE

For computer operation, equation (1) was derived from the nomograph:

$$I_{dH} = \frac{0.012334 b - 0.06102 - (0.004200b + 0.2224)(I_{TH})}{0.7776 - 0.004200b}, \quad (1)$$

where

$I_{dH}$  = diffuse radiation

$I_{TH}$  = measured horizontal solar radiation

$b$  = altitude of the sun.

Values of diffuse radiation were computed for each hourly observation using equation (1). To simplify computations and eliminate impossible results, the following restrictions were placed on the derived values of diffuse radiation:

1. If the derived diffuse radiation was negative, then zero was used for diffuse radiation.
2. If the derived diffuse radiation was greater than the total horizontal measured radiation, the value of the total horizontal measured radiation was used for the diffuse radiation.

The basic data used were total horizontal solar and sky radiation ( $I_{TH}$ ) for each hour of the day for ten-year periods at two stations: Apalachicola, Florida and Santa Maria, California. Average intensity values were computed by dividing each hourly value by 60. The diffuse sky radiation intensities ( $I_{dH}$ ) were empirically estimated for each value, based on the amount of total horizontal solar and sky radiation and solar altitude using equation (1). After subtracting the diffuse sky radiation from the total horizontal solar and sky radiation, the resultant horizontal solar radiation ( $I$ ) can be used to compute the direct normal incident solar radiation ( $I_{DN}$ ) using equation (2) [3, 4]:

$$I_{DN} = \frac{I}{\sin b} \quad (2)$$

where

$I_{DN}$  = direct normal incident solar radiation

$I$  = horizontal solar radiation =  $I_{TH} - I_{dH}$

$b$  = sun's altitude [5].

The total normal incident solar radiation ( $I_{TN}$ ) values were found by adding the direct normal incident solar radiation ( $I_{DN}$ ) and the diffuse sky radiation ( $I_{dH}$ ) previously estimated. This method of

finding the total normal incident solar radiation may result in a slight overestimation of the value at low solar altitudes because the sky hemisphere is intercepted by the ground surface, but this error will be small enough to be ignored when working with extreme values, or any values on the high end of the frequency distribution (i. e., means plus one standard deviation or greater).

Total solar radiation intensities on a south-facing surface, with the normal to the surface at 45 degrees to the horizontal, were found as follows:

$$I_{D45} = I(\sin 45^\circ + \cot b \cos a \cos 45^\circ), \quad (3)$$

where

$I_{D45}$  = intensity of direct solar radiation on a south-facing surface, with normal 45 degrees to the horizontal.

$I$  = horizontal solar radiation =  $I_{TH} - I_{dH}$

$a$  = sun's azimuth measured from the south direction

$b$  = sun's altitude

The values of total intensity ( $I_{T45^\circ}$ ) on a south-facing surface, with normal 45 degrees to the horizontal were found by adding the direct solar radiation on the south-facing surface, with normal 45 degrees to horizontal ( $I_{D45^\circ}$ ) and the diffuse sky radiation ( $I_{DF}$ ) previously estimated.

## D. Statistical Analysis

Frequency distributions were computed for each hourly value of solar radiation for each month for the following:

1. Total horizontal solar radiation ( $I_{TH}$ ).
2. Diffuse solar radiation ( $I_{dH}$ )
3. Total normal incident radiation ( $I_{TN}$ ).
4. Total radiation on a 45 degree surface ( $I_{T45^\circ}$ ).

For each hourly value, the following were tabulated:

1. Total horizontal radiation ( $I_{TH}$ ).
2. Derived diffuse radiation ( $I_{dH}$ )
3. Direct normal incident solar radiation ( $I_{DN}$ ).
4. Total radiation on a plane normal to the sun ( $I_{TN}$ )
5. Direct solar radiation on a south facing surface, 45 degrees to the horizon ( $I_{D45^\circ}$ ).
6. Total solar radiation on a south-facing surface, 45 degrees to the horizon ( $I_{T45^\circ}$ ).

On examining the tabulations, it was found that negative values of the diffuse radiation resulted from equation (3), when the sun's altitude was low (less than 15 degrees) or the measured horizontal radiation values were high and the solar altitude exceeded 60 degrees. This indicates that the nomograph underestimates the diffuse radiation for high solar altitudes, but the errors of the estimates are small, less than 0.2 gram calorie per square centimeter per minute.

When the computed diffuse radiation exceeded the measured horizontal solar radiation for Santa Maria, California, the sky was completely overcast for all cases. The total radiation measured was small during these cases. (Cloudiness data were not available for Apalachicola, Florida.) Since the data of Parmalee [2] and other data used to prepare the nomograph to estimate the diffuse radiation was based on data from cloudless skies, it was not surprising that the diffuse radiation value for completely overcast skies was overestimated.

Since the present study was concerned only with the extreme values of solar radiation, the data in the frequency distribution being studied will be from cloudless days, and values of diffuse radiation will be small or conform reasonably well to the method used to estimate values of diffuse radiation. Those values in which the diffuse radiation estimates are out of line will not occur in the portion of the frequency distribution being used.

A future study of solar radiation data using stations where both total horizontal radiation and normal incident solar radiation have been measured is being

considered. Diffuse radiation may then be calculated accurately, and a new empirical equation can be derived to estimate diffuse radiation using total horizontal radiation, solar altitude, and cloudiness as the variables.

The results of the statistical analysis in this report (Tables 1 and 2) give the June and December extreme values and 95 percentile values of total horizontal, diffuse, and total normal incident, and total 45 degree surface solar radiation for Santa Maria, California, and Apalachicola, Florida, respectively. The month of June was selected to represent the extremes during the summer and the longest days, and December was selected to represent the extremes during the winter and the shortest days. The values of the June extreme normal incident solar radiation data for Santa Maria, California, were increased for the period from 1100 to 1900 hours to reflect the higher solar radiation values which occur in the first week of July during the afternoon. (See Tables 1 and 2 for the solar radiation extreme data for time of day.) The values given for diffuse radiation are the highest values associated with the other extremes of solar radiation given and not the extremes of diffuse radiation that occurred during the period of record. Since the diffuse radiation is low with high values of total measured solar radiation, the values given are considerably lower than the highest values of diffuse radiation which occurred during the period, and the values for association with the extremes are less than those for the 95 percentile.

Table 3 gives the hourly frequency distributions of total horizontal and total normal incident solar radiation for each month at Apalachicola, Florida, for the 25, 50, 75, 95, and 99 percentiles and the extreme value measured.

## E. Applications of Solar Radiation Data

The solar radiation measurements are a direct measurement of the amount of heat received on the ground surface. Therefore, using the Stefan-Boltzmann law, the actual temperature a surface reaches when exposed to the sun can be calculated.

If we consider a perfectly black surface of low mass, completely isolated from heat conduction to the surroundings, then solar radiation will cause the temperature of the surface to rise until a balance is reached, i. e., where the heat gained by the surface equals the heat loss. The temperature of the surface would then be

$$T_S = \left( \frac{I_{TS}}{\sigma} \right)^{\frac{1}{4}} \quad (4)$$

where  $T_S$  = Surface temperature

$I_{TS}$  = Solar radiation intensity received on the surface,

$\sigma$  = Stefans-Boltzman constant,

$$= 8.17 \times 10^{-11} \text{ g-cal min}^{-1} (\text{deg K})^{-4}$$

Assuming that the surface is normal to the sun at 1200 hours in January at Cape Kennedy, Florida, the extreme solar radiation intensity on the surface can be found from Table 3 as  $1.84 \text{ g-cal min}^{-1}$ . Then from equation (4)

$$\begin{aligned} T_S &= \left( \frac{1.84}{8.7 \times 10^{-11}} \right)^{\frac{1}{4}} = 387^\circ \text{K} \\ &= 114^\circ \text{C} \\ &= 237^\circ \text{F} \end{aligned}$$

Such a temperature rarely occurs in nature because the assumed conditions are difficult to duplicate, although the air inside a B-47 bomber, parked at the airfield at Yuma Test Center, Yuma, Arizona, was above  $180^\circ \text{F}$  for 3 hours, reached  $213^\circ \text{F}$  in an item of equipment inside the cockpit for two hours, and was  $250^\circ \text{F}$  in an item of equipment mounted on the antenna outside the cockpit. Air temperature on this day reached  $108^\circ \text{F}$ . In this situation, the cockpit acted with the transparent windows as a black body cavity [6].

The temperature of a surface in the sun, will be lower than the values computed for a black surface because of several other factors:

1. The emittance and absorptivity will be lower than for a black body. Equation (4) can be modified to take care of this:

$$T_S = E \left[ \left( \frac{I_{TS}}{\sigma} \right)^{\frac{1}{4}} - T_A \right] + T_A \quad (5)$$

where

$E$  = emittance of the surface. For simplicity it is assumed to be equal in value to the absorptivity for the same wavelength of incoming light.

$T_A$  = Air temperature. For conditions of extreme solar radiation values, the maximum temperature for the period should be used; i. e., for January at Cape Kennedy, the value of  $T_A$  would be 87°F or 303.7°K [7].

2. Because of wind and thermal gradients near the surface, convection will increase the amount of heat transfer, resulting in a lower resultant temperature. Wind is the big factor in this, and equation (5) can be modified to take care of wind as follows:

$$T_S = \frac{E W_c}{100} \left[ \left( \frac{I_{TS}}{\sigma} \right)^{\frac{1}{4}} - T_A \right] + T_A, \quad (6)$$

where

$W_c$  = correction for wind speed in percent from Figure 3.

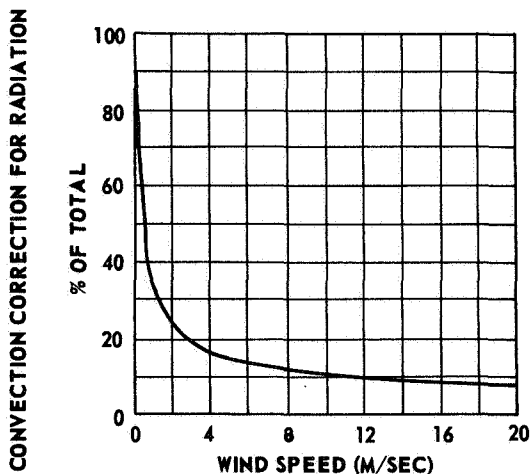


FIGURE 3. CONVECTION (WIND SPEED) CORRECTION FOR RADIATION ON A SURFACE

3. Conduction of heat through the material and through supports will carry some of the heat away from the surface. Conduction of heat to the surrounding air will be small enough to ignore except through convection discussed under item 2. If one is interested in extreme values of surface heating, then all conduction can be ignored unless the material is very thick or the supports are as large as the object being studied.

4. If the surface is not normal to the sun's rays, then the value of solar radiation needs to be corrected by

$$I_{TS} = I \sin \alpha, \quad (7)$$

where

$I$  = solar radiation normal to surface

and

$\alpha$  = angle of surface to sun's rays.

The angle  $\alpha$  will be equal to 90 degrees on a surface normal to the sun's rays as shown in Figure 4. Using the previous example and assuming the following conditions we can compute the surface temperature for a wind condition:

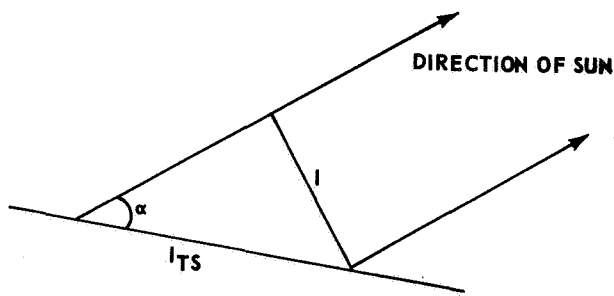


FIGURE 4. RELATIONSHIP OF A SURFACE TO A SURFACE NORMAL TO THE SUN'S RAYS

A surface with normal to the surface at 30 degrees to sun, i. e.,  $\alpha = 60$  degrees at 1200 hours in January.  $I = 1.84$  g-cal/cm<sup>2</sup>

Air temperature = 87°F = 303.71°K

Emittance of 0.60

Wind speed of 2 m/c,  $W_c = 25\%$ . Then from equation (7)

$$\begin{aligned} I_{TS} &= (1.84) (\sin 60^\circ) \\ &= (1.84) (0.86603) \\ &= 1.59 \text{ g-cal/cm}^2 \end{aligned}$$

From equation (3),

$$T_S = \frac{(0.60)(25)}{100} \left[ \left( \frac{1.59}{8.17 \times 10^{-11}} \right)^{\frac{1}{4}} - 303.7 \right] + 303.7$$

$$= 0.15 [373.7 - 303.7] + 303.7$$

$$= 0.15 [70.0] + 303.7 = 314.2^\circ \text{K}$$

$$= 41^\circ \text{C} = 106^\circ \text{F}$$

Thus, even considering the many factors which tend to reduce heating of a surface by the sun, a surface exposed to the sun may be considerably warmer than the air temperature.

### III. CONCLUDING REMARKS

This report provides information on the intensity of solar radiation at various probability levels to use in computing heat loads on objects in the sun. The methods used in the analysis of the original solar radiation data may be applied to solar radiation data at other stations to provide similar information for other areas. The computer program is available at The National Weather Records Center, ESSA, Asheville, North Carolina.

### REFERENCES

1. Daniels, Glenn E.; Scoggins, James R.; and Smith, Orvel E.: Terrestrial Environment (Climatic) Criteria Guidelines for Use in Space Vehicle Development, 1965 Revision. NASA TM X-53328, 1965.
2. Parmalee, G. V.: Irradiation of Vertical and Horizontal Surfaces by Diffuse Solar Radiation from Cloudless Skies. Heating, Piping, and Air Conditioning, vol. 26, Aug. 1954, pp. 129-136.

3. Becker, C. F.; and Boyd, J. S.: Solar Radiation Availability on Surfaces in the United States as Affected by Season, Orientation, Latitude, Altitude, and Cloudiness. J. of Solar Engineering, Science and Engineering, vol. 1, Jan. 1957, pp. 13-21.
4. Ornstein, M. P.: Solar Radiation. J. of Environmental Sciences, vol. 5, April 1962. pp. 24-27.
5. Publication H. O. No. 214, Tables of Computed Altitude and Azimuth, United States Hydrographic Office. United States Government Printing Office, 1940.
6. Cavell, W. W.; and Box, R. H.: Temperature Data on Standard and Experimental Cartridges in Pilot Ejection Devices in a B47E Aircraft Stationed at Yuma, Arizona. Memo Report No. M60-16-1, Frankford Arsenal, 1960.
7. Smith, J. W.: Distribution of Surface Meteorological Data for Cape Kennedy, Florida, NASA TM X-53118, 1964. NASA-Marshall Space Flight Center, Huntsville, Alabama

### BIBLIOGRAPHY

- Johnson, Frances S.: The Solar Constant. J. of Meteorology, vol. XI, No. 6, Dec. 1954, pp. 431-439.
- Nicolet, M.: Sur La Determination du Flux Energetique du Rayonnement Extraterrestre du Soleil. Archiv fur Meteorologie, Geophysik und Bioklimatologie, Series B, vol. 3, 1951, pp. 209-219.

TABLE I. EXTREME VALUES OF SOLAR RADIATION FOR SANTA MARIA, CALIFORNIA

Time of Day (Local Standard Time)	Total Horizontal Solar Radiation (g-cal cm <sup>-2</sup> min <sup>-1</sup> )		Diffuse Radiation Associated with Total Horizontal Solar Radiation Extremes (g-cal cm <sup>-2</sup> min <sup>-1</sup> )		Total Normal Incident Solar Radiation (g-cal cm <sup>-2</sup> min <sup>-1</sup> )		Total 45° Surface Solar Radiation (g-cal cm <sup>-2</sup> min <sup>-1</sup> )	
	Extreme	95 Percentile	Extreme	95 Percentile	Extreme	95 Percentile	Extreme	95 Percentile
JUNE								
0500	0	0	0	0	0	0	0	0
0600	0.16	0.11	0.02	0.04	1.14	0.78	0.04	0
0700	0.46	0.40	0.05	0.08	1.34	1.08	0.19	0.16
0800	0.82	0.76	0.06	0.09	1.54	1.38	0.34	0.31
0900	1.16	1.11	0.04	0.08	1.74	1.62	0.84	0.77
1000	1.45	1.42	0	0.03	1.79	1.71	0.19	1.12
1100	1.64	1.56	0	0.10	1.79	1.69	1.39	1.31
1200	1.69	1.63	0	0.08	1.74	1.68	1.49	1.38
1300	1.69	1.64	0	0.07	1.74	1.68	1.49	1.40
1400	1.59	1.54	0.06	0.12	1.74	1.68	1.34	1.29
1500	1.45	1.39	0	0.06	1.79	1.70	1.14	1.09
1600	1.21	1.19	0	0.02	1.79	1.71	0.89	0.78
1700	0.87	0.83	0.03	0.05	1.69	1.60	0.34	0.18
1800	0.46	0.42	0.05	0.08	1.39	1.23	0.19	0.13
1900	0.14	0.12	0.02	0.04	1.19	0.93	0.04	0
2000	0	0	0	0	0	0	0	0
DECEMBER								
0800	0	0	0	0	0	0	0	0
0900	0.35	0.32	0.04	0.05	1.59	1.39	0.99	0.85
1000	0.65	0.60	0.03	0.05	1.64	1.53	1.29	1.21
1100	0.86	0.80	0	0.04	1.84	1.64	1.64	1.49
1200	0.96	0.89	0.02	0.06	1.79	1.69	1.74	1.63
1300	0.99	0.89	0	0.06	1.84	1.70	1.79	1.64
1400	0.85	0.80	0.01	0.04	1.79	1.64	1.59	1.49
1500	0.66	0.60	0.02	0.05	1.69	1.54	1.34	1.21
1600	0.38	0.31	0.02	0.05	1.64	1.38	1.04	0.87
1700	0	0	0	0	0	0	0	0

TABLE II. EXTREME VALUES OF SOLAR RADIATION FOR APALACHICOLA, FLORIDA

Time of Day (Local Standard Time)	Total Horizontal Solar Radiation g-cal cm <sup>-2</sup> min <sup>-1</sup>		Diffuse Radiation Associated with Total Horizontal Solar Radiation Extremes g-cal cm <sup>-2</sup> min <sup>-1</sup>		Total Normal Incident Solar Radiation g-cal cm <sup>-2</sup> min <sup>-1</sup>		Total 45° Surface Solar Radiation g-cal cm <sup>-2</sup> min <sup>-1</sup>	
	Extreme	95 Percentile	Extreme	95 Percentile	Extreme	95 Percentile	Extreme	95 Percentile
JUNE								
0500	0	0	0	0	0	0	0	0
0600	0.12	0.07	0	0	1.09	1.00	0	0
0700	0.42	0.36	0.05	0.07	1.29	1.04	0.19	0.16
0800	0.82	0.71	0.04	0.10	1.59	1.30	0.34	0.27
0900	1.23	1.02	0	0.10	1.59	1.48	0.49	0.41
1000	1.35	1.30	0.02	0.06	1.59	1.54	0.99	0.95
1100	1.52	1.45	0.03	0.09	1.59	1.54	1.19	1.14
1200	1.58	1.53	0.10	0.16	1.64	1.55	1.29	1.24
1300	1.58	1.50	0.10	0.20	1.64	1.53	1.29	1.24
1400	1.50	1.44	0.05	0.12	1.59	1.52	1.19	1.09
1500	1.35	1.30	0.02	0.06	1.59	1.52	1.04	0.95
1600	1.10	1.01	0.05	0.12	1.54	1.44	0.54	0.44
1700	0.77	0.72	0.05	0.09	1.49	1.33	0.34	0.30
1800	0.48	0.40	0.03	0.06	1.44	1.14	0.19	0.18
1900	0.11	0.08	0	0	1.14	1.00	0.14	0.03
2000	0	0	0	0	0	0	0	0
DECEMBER								
0700	0	0	0	0	0	0	0	0
0800	0.16	0.10	0	0	1.34	1.12	0.64	0.50
0900	0.46	0.42	0.04	0.06	1.44	1.36	0.94	0.89
1000	0.79	0.71	0.01	0.07	1.69	1.60	1.39	1.29
1100	0.95	0.92	0.02	0.04	1.79	1.68	1.64	1.56
1200	1.09	1.02	0	0.03	1.79	1.70	1.74	1.66
1300	1.05	1.02	0	0.03	1.79	1.78	1.74	1.66
1400	0.94	0.89	0.02	0.05	1.74	1.67	1.59	1.63
1500	0.79	0.70	0	0.03	1.74	1.57	1.39	1.27
1600	0.46	0.41	0.04	0.06	1.54	1.40	0.99	0.91
1700	0.16	0.10	0	0	1.34	1.12	0.64	0.50
1800	0	0	0	0	0	0	0	0

TABLE III. SOLAR RADIATION - APALACHICOLA, FLORIDA

Time of Day	JANUARY											
	Total Horizontal Solar Radiation (g-cal cm <sup>-2</sup> min <sup>-1</sup> )						Total Normal Incident Solar Radiation (g-cal cm <sup>-2</sup> min <sup>-1</sup> )					
	25%	50%	75%	95%	99%	Extreme	25%	50%	75%	95%	99%	Extreme
0600												
0700												
0800	0.04	0.10	0.14	0.17	0.24	0.25	0.09	0.32	0.97	1.25	1.46	1.64
0900	1.17	0.28	0.43	0.49	0.52	0.55	0.15	0.66	1.26	1.46	1.61	1.69
1000	0.31	0.56	0.72	0.80	0.83	0.85	0.24	1.02	1.47	1.62	1.74	1.79
1100	0.40	0.79	0.94	1.01	1.07	1.10	0.44	1.34	1.61	1.72	1.82	1.89
1200	0.47	0.91	1.03	1.11	1.16	1.18	0.53	1.40	1.64	1.73	1.81	1.84
1300	0.51	0.91	1.03	1.11	1.15	1.18	0.59	1.39	1.63	1.75	1.81	1.84
1400	0.47	0.81	0.92	0.99	1.04	1.06	0.60	1.40	1.58	1.70	1.82	1.89
1500	0.37	0.63	0.72	0.78	0.88	0.90	0.51	1.28	1.47	1.60	1.80	1.94
1600	0.21	0.35	0.46	0.49	0.52	0.53	0.32	1.01	1.28	1.44	1.53	1.69
1700	0.07	0.11	0.14	0.17	0.25	0.32	0.14	0.55	0.99	1.18	1.54	1.69
1800												
1900												
FEBRUARY												
0600												
0700												
0800	0.10	0.17	0.24	0.32	0.36	0.39	0.20	0.70	1.08	1.32	1.54	1.64
0900	0.25	0.45	0.58	0.70	0.79	0.81	0.33	0.88	1.36	1.56	1.72	1.79
1000	0.40	0.75	0.89	0.95	1.03	1.08	0.46	1.29	1.52	1.70	1.79	1.84
1100	0.56	0.97	1.09	1.21	1.30	1.31	0.66	1.46	1.62	1.76	1.85	1.89
1200	0.62	1.10	1.20	1.31	1.38	1.41	0.72	1.51	1.64	1.66	1.82	1.84
1300	0.61	1.08	1.20	1.31	1.37	1.40	0.69	1.49	1.65	1.74	1.80	1.84
1400	0.53	0.97	1.08	1.17	1.24	1.27	0.56	1.41	1.60	1.70	1.75	1.79
1500	0.46	0.75	0.87	0.96	1.01	1.03	0.54	1.22	1.52	1.65	1.70	1.74
1600	0.31	0.49	0.58	0.64	0.74	0.75	0.46	1.09	1.36	1.50	1.58	1.64
1700	0.12	0.19	0.24	0.32	0.36	0.38	0.29	0.76	1.07	1.30	1.56	1.69
1800												
1900												

NOTE: Blank spaces in tables indicate zero values of solar radiation.

TABLE III. (Continued)

Time of Day	MARCH											
	Total Horizontal Solar Radiation (g-cal cm <sup>-2</sup> min <sup>-1</sup> )						Total Normal Incident Solar Radiation (g-cal cm <sup>-2</sup> min <sup>-1</sup> )					
	25%	50%	75%	95%	99%	Extreme	25%	50%	75%	95%	99%	Extreme
0600												
0700	0.04	0.07	0.10	0.13	0.16	0.17	0.31	0.75	0.96	1.13	1.24	1.39
0800	0.16	0.32	0.41	0.48	0.51	0.53	0.18	0.80	1.18	1.32	1.44	1.49
0900	0.35	0.63	0.76	0.83	0.87	0.89	0.38	1.12	1.41	1.54	1.62	1.69
1000	0.49	0.91	1.07	1.15	1.18	1.19	0.52	1.29	1.57	1.68	1.75	1.79
1100	0.69	1.12	1.28	1.34	1.40	1.43	0.72	1.42	1.62	1.69	1.76	1.79
1200	0.75	1.24	1.38	1.44	1.48	1.56	0.82	1.44	1.63	1.70	1.76	1.79
1300	0.78	1.24	1.38	1.44	1.48	1.53	0.84	1.44	1.63	1.73	1.76	1.79
1400	0.65	1.15	1.28	1.34	1.33	1.42	0.67	1.42	1.61	1.72	1.75	1.79
1500	0.55	0.92	1.06	1.11	1.15	1.18	0.63	1.33	1.53	1.64	1.68	1.69
1600	0.34	0.62	0.76	0.80	0.82	0.87	0.37	1.14	1.39	1.52	1.59	1.64
1700	0.17	0.32	0.41	0.48	0.52	0.53	0.26	0.84	1.14	1.32	1.42	1.54
1800	0.03	0.07	0.09	0.13	0.16	0.18	0.37	0.72	0.93	1.14	1.37	1.64
1900												
APRIL												
0600												
0700	0.10	0.16	0.20	0.24	0.27	0.28	0.29	0.64	0.88	1.02	1.12	1.34
0800	0.31	0.45	0.55	0.58	0.62	0.63	0.59	0.88	1.20	1.31	1.40	1.54
0900	0.54	0.79	0.89	0.94	0.97	0.99	0.69	1.24	1.41	1.52	1.64	1.74
1000	0.81	1.08	1.18	1.24	1.28	1.32	0.95	1.38	1.52	1.62	1.72	1.74
1100	0.95	1.28	1.37	1.42	1.48	1.52	1.04	1.44	1.56	1.64	1.71	1.74
1200	1.04	1.37	1.47	1.52	1.56	1.58	1.10	1.46	1.57	1.65	1.72	1.74
1300	1.04	1.38	1.47	1.54	1.58	1.59	1.10	1.47	1.57	1.66	1.72	1.74
1400	0.97	1.28	1.37	1.42	1.50	1.55	1.04	1.45	1.56	1.64	1.76	1.84
1500	0.81	1.10	1.12	1.19	1.24	1.27	0.96	1.42	1.51	1.60	1.66	1.69
1600	0.54	0.82	0.89	0.92	0.97	0.99	0.72	1.29	1.40	1.48	1.58	1.64
1700	0.34	0.48	0.55	0.59	0.63	0.64	0.56	1.04	1.19	1.30	1.42	1.54
1800	0.10	0.16	0.20	0.24	0.28	0.29	0.36	0.67	0.87	1.06	1.27	1.59
1900												

TABLE III. (Continued)

Time of Day	MAY											
	Total Horizontal Solar Radiation (g-cal cm <sup>-2</sup> min <sup>-1</sup> )						Total Normal Incident Solar Radiation (g-cal cm <sup>-2</sup> min <sup>-1</sup> )					
	25%	50%	75%	95%	99%	Extreme	25%	50%	75%	95%	99%	Extreme
0600												
0700	0.20	0.26	0.29	0.32	0.36	0.37	0.45	0.76	0.89	1.02	1.10	1.19
0800	0.44	0.57	0.61	0.65	0.70	0.72	0.69	1.02	1.17	1.29	1.36	1.39
0900	0.74	0.87	0.94	0.99	1.02	1.05	0.99	1.24	1.36	1.45	1.52	1.59
1000	1.00	1.13	1.22	1.28	1.33	1.36	1.16	1.36	1.48	1.56	1.62	1.69
1100	1.13	1.29	1.39	1.45	1.48	1.53	1.22	1.38	1.50	1.57	1.62	1.69
1200	1.21	1.42	1.48	1.54	1.58	1.60	1.24	1.43	1.52	1.58	1.62	1.69
1300	1.25	1.41	1.48	1.52	1.58	1.60	1.26	1.44	1.51	1.57	1.62	1.69
1400	1.11	1.31	1.39	1.43	1.47	1.49	1.18	1.41	1.50	1.56	1.59	1.64
1500	0.94	1.14	1.20	1.25	1.30	1.32	1.08	1.36	1.45	1.54	1.59	1.64
1600	0.68	0.88	0.94	0.99	1.03	1.05	0.87	1.26	1.36	1.47	1.52	1.54
1700	0.42	0.57	0.62	0.67	0.71	0.74	0.65	1.06	1.18	1.30	1.40	1.49
1800	0.18	0.25	0.30	0.34	0.39	0.47	0.38	0.73	0.89	1.04	1.30	1.39
1900												
	JUNE											
0600	0.00	0.04	0.06	0.07	0.08	0.12	0.36	0.62	0.76	1.00	1.08	1.09
0700	0.19	0.28	0.31	0.36	0.40	0.42	0.32	0.74	0.88	1.04	1.22	1.29
0800	0.42	0.59	0.64	0.71	0.76	0.82	0.64	1.02	1.17	1.30	1.50	1.59
0900	0.66	0.90	0.97	1.02	1.13	1.23	0.79	1.22	1.35	1.48	1.56	1.59
1000	0.76	1.10	1.22	1.30	1.32	1.35	0.84	1.28	1.44	1.54	1.58	1.59
1100	0.98	1.28	1.39	1.45	1.48	1.52	1.02	1.36	1.47	1.54	1.58	1.59
1200	1.04	1.35	1.47	1.53	1.57	1.58	1.06	1.37	1.49	1.55	1.62	1.64
1300	0.88	1.35	1.46	1.50	1.52	1.58	0.87	1.37	1.48	1.53	1.56	1.64
1400	0.76	1.28	1.38	1.44	1.48	1.50	0.75	1.34	1.46	1.52	1.56	1.59
1500	0.63	1.08	1.21	1.30	1.32	1.35	0.63	1.24	1.42	1.52	1.56	1.59
1600	0.44	0.80	0.96	1.01	1.05	1.10	0.44	1.06	1.33	1.44	1.50	1.54
1700	0.33	0.55	0.65	0.72	0.74	0.77	0.31	0.91	1.18	1.33	1.44	1.49
1800	0.17	0.27	0.33	0.40	0.44	0.48	0.20	0.68	0.92	1.14	1.34	1.44
1900	0.00	0.05	0.07	0.08	0.10	0.11	0.31	0.63	0.83	1.00	1.12	1.14
2000	0.02	0.03	0.04	0.05	0.06	0.07	0.14	0.34	0.44	0.53	0.60	0.79

TABLE III. (Continued)

Time of Day	JULY											
	Total Horizontal Solar Radiation (g-cal cm <sup>-2</sup> min <sup>-1</sup> )						Total Normal Incident Solar Radiation (g-cal cm <sup>-2</sup> min <sup>-1</sup> )					
	25%	50%	75%	95%	99%	Extreme	25%	50%	75%	95%	99%	Extreme
0600												
0700	0.19	0.27	0.30	0.33	0.36	0.38	0.37	0.72	0.88	1.02	1.12	1.34
0800	0.44	0.59	0.63	0.67	0.73	0.80	0.68	1.06	1.15	1.24	1.42	1.64
0900	0.59	0.87	0.94	0.97	1.03	1.15	0.72	1.22	1.34	1.41	1.47	1.74
1000	0.76	1.09	1.19	1.26	1.31	1.32	0.83	1.29	1.42	1.53	1.58	1.69
1100	0.80	1.25	1.37	1.44	1.40	1.62	0.80	1.33	1.47	1.54	1.60	1.74
1200	0.79	1.32	1.44	1.53	1.58	1.63	0.80	1.33	1.47	1.54	1.57	1.69
1300	0.79	1.27	1.43	1.50	1.54	1.57	0.80	1.28	1.46	1.52	1.58	1.64
1400	0.65	1.16	1.33	1.42	1.48	1.54	0.64	1.24	1.43	1.52	1.58	1.64
1500	0.56	1.02	1.17	1.25	1.30	1.35	0.58	1.16	1.39	1.50	1.56	1.64
1600	0.44	0.73	0.91	1.00	1.04	1.10	0.44	0.96	1.30	1.44	1.51	1.59
1700	0.26	0.48	0.62	0.69	0.76	0.78	0.26	0.77	1.12	1.35	1.45	1.79
1800	0.13	0.22	0.29	0.35	0.39	0.40	0.13	0.53	0.84	1.12	1.30	1.44
1900												
AUGUST												
0600												
0700	0.12	0.18	0.23	0.29	0.32	0.40	0.24	0.64	0.83	1.03	1.29	1.54
0800	0.33	0.50	0.55	0.63	0.66	0.68	0.47	1.00	1.12	1.26	1.38	1.49
0900	0.54	0.80	0.87	0.94	1.00	1.05	0.68	1.18	1.30	1.40	1.54	1.59
1000	0.80	1.09	1.14	1.22	1.26	1.32	0.91	1.34	1.42	1.51	1.57	1.64
1100	0.85	1.26	1.33	1.39	1.48	1.55	0.90	1.38	1.47	1.55	1.61	1.79
1200	0.86	1.35	1.41	1.49	1.51	1.58	0.84	1.40	1.48	1.54	1.58	1.69
1300	0.73	1.31	1.40	1.48	1.50	1.55	0.72	1.36	1.48	1.53	1.59	1.64
1400	0.59	1.19	1.29	1.35	1.39	1.44	0.58	1.28	1.43	1.50	1.56	1.59
1500	0.49	1.01	1.12	1.17	1.22	1.26	0.50	1.20	1.39	1.56	1.51	1.54
1600	0.39	0.73	0.85	0.90	0.93	0.97	0.41	1.01	1.28	1.37	1.43	1.44
1700	0.27	0.43	0.53	0.59	0.66	0.70	0.26	0.80	1.08	1.19	1.37	1.44
1800	0.09	0.15	0.21	0.26	0.30	0.32	0.10	0.43	0.72	0.98	1.17	1.29
1900												

TABLE III. (Continued)

Time of Day	SEPTEMBER											
	Total Horizontal Solar Radiation (g-cal cm <sup>-2</sup> min <sup>-1</sup> )						Total Normal Incident Solar Radiation (g-cal cm <sup>-2</sup> min <sup>-1</sup> )					
	25%	50%	75%	95%	99%	Extreme	25%	50%	75%	95%	99%	Extreme
0600												
0700	0.05	0.08	0.12	0.16	0.21	0.22	0.29	0.67	0.88	1.14	1.41	1.69
0800	0.24	0.37	0.44	0.50	0.56	0.59	0.34	0.91	1.08	1.22	1.37	1.54
0900	0.43	0.70	0.75	0.81	0.86	0.90	0.54	1.19	1.30	1.36	1.48	1.49
1000	0.70	0.98	1.05	1.12	1.16	1.18	0.85	1.35	1.44	1.52	1.62	1.69
1100	0.77	1.17	1.25	1.30	1.36	1.38	0.83	1.41	1.48	1.56	1.61	1.69
1200	0.80	1.25	1.34	1.40	1.50	1.57	0.83	1.41	1.50	1.58	1.66	1.74
1300	0.75	1.23	1.33	1.37	1.45	1.51	0.76	1.40	1.49	1.56	1.60	1.64
1400	0.65	1.13	1.23	1.30	1.36	1.35	0.66	1.23	1.48	1.56	1.59	1.64
1500	0.53	0.92	1.02	1.10	1.18	1.23	0.55	1.19	1.42	1.49	1.60	1.64
1600	0.36	0.64	0.74	0.82	0.91	0.92	0.37	1.02	1.28	1.41	1.57	1.74
1700	0.18	0.32	0.39	0.48	0.56	0.60	0.16	0.72	0.99	1.16	1.36	1.54
1800	0.04	0.08	0.10	0.16	0.22	0.23	0.18	0.53	0.76	1.09	1.36	1.44
1900												
OCTOBER												
0600												
0700	0.04	0.05	0.06	0.07	0.08	0.11	0.44	0.66	0.80	0.99	1.02	1.04
0800	0.19	0.28	0.32	0.35	0.40	0.49	0.58	0.98	1.09	1.27	1.40	1.59
0900	0.46	0.60	0.64	0.68	0.72	0.75	0.84	1.22	1.33	1.46	1.52	1.59
1000	0.69	0.86	0.92	0.98	1.01	1.03	0.99	1.36	1.46	1.58	1.64	1.69
1100	0.94	1.07	1.13	1.19	1.24	1.28	1.25	1.47	1.55	1.65	1.71	1.79
1200	1.01	1.16	1.22	1.29	1.34	1.38	1.24	1.48	1.57	1.66	1.69	1.74
1300	1.01	1.16	1.22	1.28	1.33	1.40	1.27	1.49	1.57	1.66	1.71	1.79
1400	0.82	1.05	1.12	1.17	1.21	1.24	1.03	1.44	1.53	1.62	1.68	1.74
1500	0.66	0.84	0.91	0.96	1.00	1.05	0.94	1.35	1.44	1.56	1.60	1.64
1600	0.40	0.56	0.63	0.68	0.72	0.75	0.70	1.18	1.29	1.42	1.49	1.59
1700	0.19	0.24	0.30	0.34	0.36	0.40	0.48	0.86	1.00	1.18	1.30	1.64
1800	0.04	0.05	0.06	0.07	0.08	0.08	0.39	0.59	0.74	0.81	0.82	0.84
1900												

TABLE III. (Concluded)

Time of Day	NOVEMBER											
	Total Horizontal Solar Radiation ( $g\text{-cal cm}^{-2}\text{min}^{-1}$ )					Total Normal Incident Solar Radiation ( $g\text{-cal cm}^{-2}\text{min}^{-1}$ )						
	50%	75%	95%	99%	Extreme	25%	50%	75%	95%	99.0	Extreme	
0600												
0700	0	0	0	0	0	0.03	0	0	0	0	0	0.04
0800	0.07	0.13	0.18	0.23	0.26	0.29	0.31	0.83	1.04	1.28	1.40	1.49
0900	0.22	0.40	0.48	0.56	0.60	0.62	0.31	1.03	1.28	1.46	1.56	1.74
1000	0.39	0.69	0.76	0.84	0.88	0.90	0.51	1.30	1.46	1.62	1.68	1.74
1100	0.57	0.88	0.96	1.04	1.09	1.12	0.71	1.42	1.56	1.70	1.74	1.79
1200	0.64	0.98	1.07	1.14	1.18	1.22	0.79	1.48	1.58	1.71	1.77	1.84
1300	0.73	1.00	1.07	1.15	1.21	1.22	0.97	1.49	1.60	1.72	1.76	1.89
1400	0.64	0.91	0.97	1.03	1.08	1.10	0.97	1.48	1.58	1.65	1.74	1.79
1500	0.52	0.70	0.75	0.83	0.86	0.88	0.82	1.31	1.46	1.59	1.66	1.69
1600	0.29	0.42	0.48	0.55	0.61	0.65	0.59	1.12	1.28	1.51	1.58	1.69
1700	0.09	0.14	0.17	0.21	0.25	0.27	0.38	0.85	1.04	1.30	1.61	1.84
1800												
1900												
DECEMBER												
0600												
0700												
0800	0.04	0.08	0.10	0.13	0.14	0.16	0.40	0.74	0.92	1.18	1.30	1.32
0900	0.17	0.26	0.38	0.42	0.44	0.46	0.27	0.61	1.17	1.38	1.44	1.46
1000	0.32	0.59	0.66	0.71	0.72	0.79	0.45	1.20	1.42	1.58	1.67	1.71
1100	0.42	0.78	0.86	0.92	0.94	0.95	0.53	1.38	1.55	1.68	1.76	1.80
1200	0.47	0.90	0.96	1.02	1.05	1.09	0.57	1.44	1.59	1.70	1.76	1.80
1300	0.52	0.88	0.97	1.02	1.04	1.05	0.65	1.41	1.56	1.64	1.69	1.76
1400	0.44	0.79	0.86	0.90	0.92	0.94	0.61	1.38	1.55	1.66	1.72	1.74
1500	0.33	0.62	0.66	0.72	0.74	0.79	0.46	1.27	1.44	1.57	1.72	1.74
1600	0.19	0.33	0.39	0.43	0.44	0.46	0.36	0.96	1.21	1.40	1.50	1.54
1700	0.05	0.08	0.12	0.15	0.18	0.20	0.48	0.80	1.00	1.20	1.45	1.54
1800												
1900												

# LONGITUDINAL PERSISTENCE OF MAJOR SOLAR FLARES

By

T. E. Pratt<sup>1</sup>

## ABSTRACT

The longitudinal positions have been calculated for over four hundred major optical flares of solar cycle 19, using the 27.04-day rotation period observed by Guss to yield a sharp clustering of proton flares. A significant correlation has been obtained between the longitudinal distribution of major proton flares and that of all major flares weighted according to importance. When the data are considered separately for the first and second half of the time interval, the longitudinal distribution of weighted flare activity shows the transition from four, or more, to two centers of activity observed by Sakurai for proton flares and corona green-line emission.

## I. INTRODUCTION

Some evidence has accumulated for the existence of rotating longitudinal regions of long duration on the sun which have enhanced probabilities for the production of proton accelerating flares and other forms of solar activity. These regions are not to be confused with the individual plage areas which may remain active for several solar rotations, but, rather they are centers which might last up to a full solar cycle, outliving several plages in the process.

Trotter and Billings [1] found a longitudinal clustering of the positions of enhanced yellow corona emission which rotated with about the same 27-day period as the photospheric features, but did not possess the differential rotation property to a significant extent. Subsequently, using a uniform rotation period of 27.04 days, Guss [2] obtained a sharp clustering of proton event flares, such that a single ten-degree interval contributed seven out of ten ground level neutron enhancements and 90 percent of the particle flux with energy greater than 100 MeV. Other studies of solar proton events have employed

larger lists of events which must rely more on indirect evidence.

The longitudinal clustering of proton event flares using a 27-day rotation period has been considered by Sakurai [3]. This work demonstrated that if, instead of considering the whole of cycle 19, the first and second halves are taken separately, there is a transition from four active regions, in the first half, to two in the second half. A similar effect appears to exist in the corona data of Reference 1, although this point was not specifically made in that work. In a subsequent paper [4], Sakurai extended the work to include the longitudinal distribution of the emitted intensity of the corona green-line. Again, a 27-day period yielded a transition from four to two centers of activity over the course of the solar cycle.

## II. LONGITUDINAL DISTRIBUTION

The purpose of the present work is to examine the longitudinal distribution of major optical flares to determine whether the systematics observed in the previously cited works are unique to particle acceleration phenomena or are attributes of solar flare activity in general.

The proton event data were taken for the interval between January 1, 1955, and December 31, 1961, from the compilation of Malitson [5] because this list places much reliance upon balloon and satellite data as opposed to the more indirect measurements. Consequently, while the possibility of missing events exists, the probability of a spurious event is greatly reduced. All events used contained a significant flux of protons with energies greater than 30 MeV. Not all events in the compilation were used because of the possible association of some events with more than one flare. Some of these conflicts were resolved

1. This paper was prepared in 1968 while Professor Pratt was employed for the summer in the Aero-Astrodynamic Laboratory of the George C. Marshall Space Flight Center, Marshall Space Flight Center, Alabama. Professor Pratt is presently associated with Utica College of Syracuse University, Utica, New York, 13502.

by associating the event with whichever had accompanying type IV radiation. Other events were used if the competing flares occurred within the same plage, in which case an average position was recorded. Those events not resolvable were eliminated. The result was 54 proton events used versus at least 61 in the list reliably known to have occurred.

The solar flare data were taken from the lists of major flares compiled by Jonah, Dodson-Prince, and Hedeman [6], in which a major flare was defined as one of importance  $\geq 3$  as reported by one or more observatories, or of importance  $\geq 2+$  as reported by two or more observatories and published in the Quarterly Bulletin of the I. A. U. Also recorded was the assigned McMath-Hulbert importance for each flare.

The longitudinal coordinate system was chosen such that meridian values increased clockwise as viewed from above the north pole, with the prime meridian designated as the central meridian at 0000 U. T. on January 1, 1955. The previously mentioned 27.04-day synodic rotation period was used since this gave the sharpest clustering of proton events among the studies cited.

In the analysis, the flares were weighted according to their McMath-Hulbert importance rating to reflect the approximate amount of energy emitted in  $H\alpha$ . This was done using average areas, intensities, and durations for each importance class as given by Dodson, Hedeman, and McMath [7]. The weights ranged from 1 for an importance 1, to 20 for an importance 3+. Subsequently, the sum of the flare weights for a particular longitude interval is referred to as the "flare activity" for that interval.

The longitudinal positions (mapped in Figure 1) for the major flares with and without associated proton acceleration were calculated for the various rotations. In each ten-degree interval, the number of proton events and the flare activity ratings were totaled for the Northern and Southern Hemispheres, both separately and combined. The combined results are compared in Figure 2. The correlation coefficients were calculated for the flare activity versus the number of proton events in 36 ten-degree intervals with the following results:

Northern Hemisphere	$r = .64$
Southern Hemisphere	$r = .64$
Total	$r = .66$

Subsequently, the flare activity longitudinal distribution was partitioned according to occurrence in the first or second half of the time interval under consideration. These two separate resulting distributions are plotted in Figure 3. A transition from four or more activity centers to two is apparent, and is in agreement with the previously cited results for proton flares and corona emission.

### III. CONCLUSIONS

It is concluded that the results obtained above substantiate the generally accepted theory that persistent centers of activity apply to the proton flares and their related antecedents. These results also have supplied evidence that persistent centers of activity are related to solar activity not accompanied by significant particle acceleration. Thus the evidence indicates that most solar flare activity (whether or not accompanied by proton events) may originate in a few well defined heliographic areas. It is possible that the centers apply equally effectively to all phenomena of the chromosphere and low corona to the exclusion of the photosphere. Sakurai [4] has observed that proton flare occurrence does not correlate well with sunspot number over the solar cycle, if data for both Northern and Southern Hemispheres are lumped together.

### REFERENCES

1. Trotter, D. E., and Billings, D. E.: Longitudinal Variation of a Zone of Solar Activity. *Astrophysical Journal*, Vol. 136, 1962, p. 1140.
2. Guss, D. E.: Distribution in Heliographic Longitude of Flares Which Produce Energetic Solar Particles. *Physical Review Letters*, vol. 13, 1964, p. 363.
3. Sakurai, K.: The Persistence of Solar Flare Regions Related to the Production of Energetic Protons and the Interplanetary Magnetic Fields. *Publications of Astronautics Society of Japan*, vol. 18, 1966, p. 350.
4. Sakurai, K.: Development of Solar Flares and the Acceleration of Solar Cosmic Rays. Report on Ionospheric and Space Research in Japan, vol. 21, 1967, p. 213.
5. Malitson, H. H.: Table of Solar Proton Events. NASA TR R-169, 1963.

6. Jonah, F. C., Dodson-Prince, H., and Hedeman, E. R.: Solar Activity Catalogue. LTV Astronautics Report. 00.503, vols. 1 through 5, pp. 538, 594, 650, and 654.

7. Dodson, H. W., Hedeman, E. R., and McMath, R. R.: Photometry of Solar Flares. Astrophysical Journal Supplement. Vol. 2, 1956. p. 241.

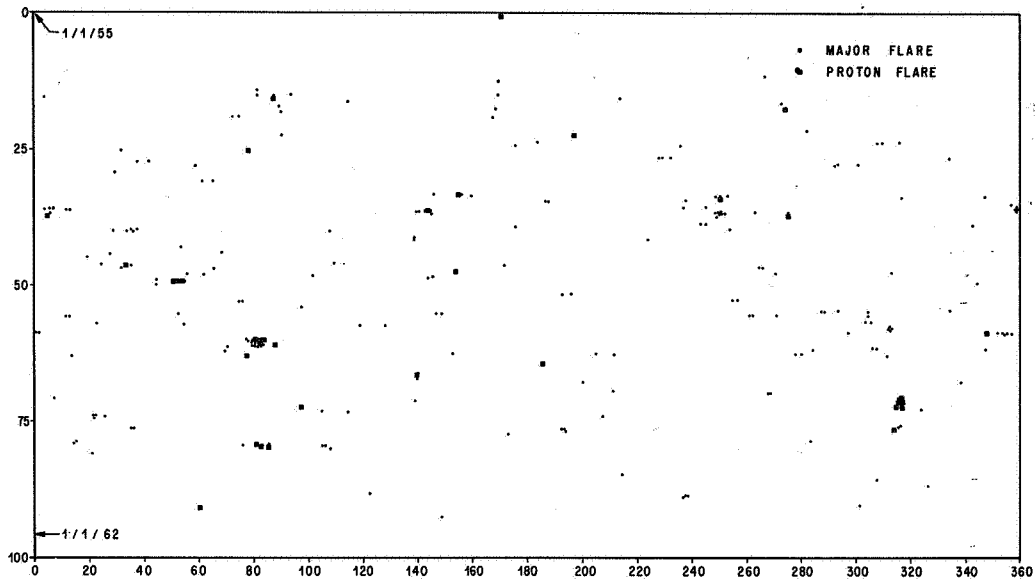


FIGURE 1A. NORTHERN HEMISPHERE MAJOR SOLAR FLARES, SOLAR ROTATION VERSUS LONGITUDE (27.04 Day Synodic Rotation Period)

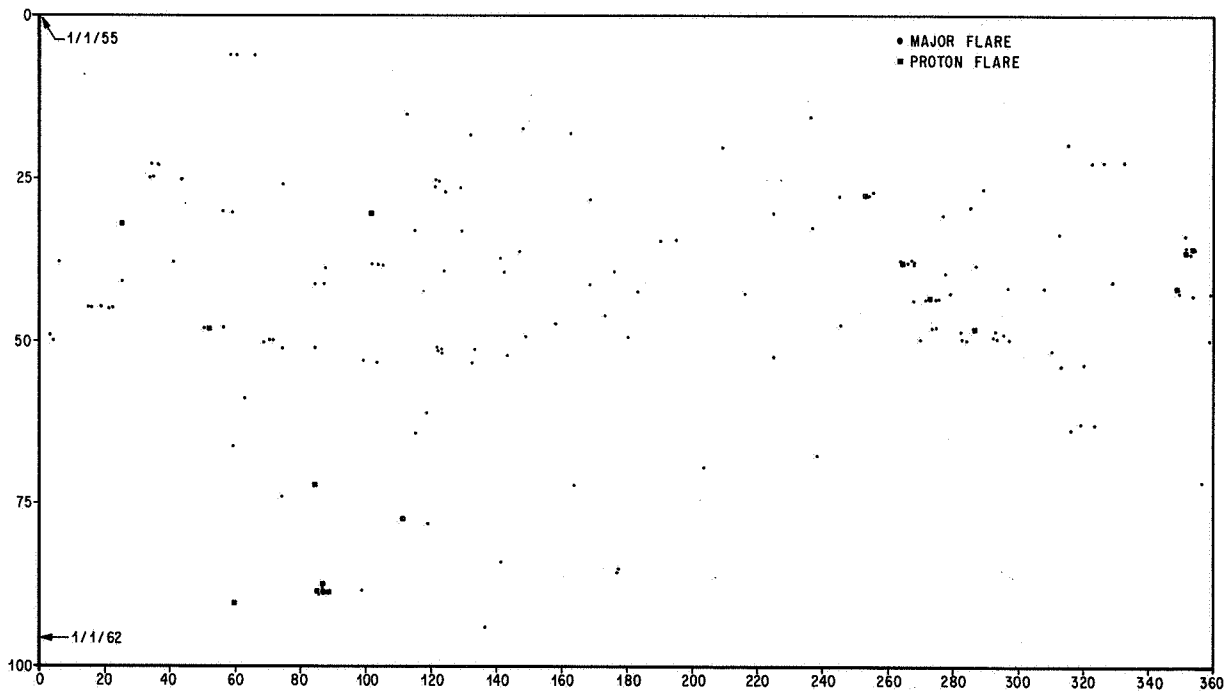
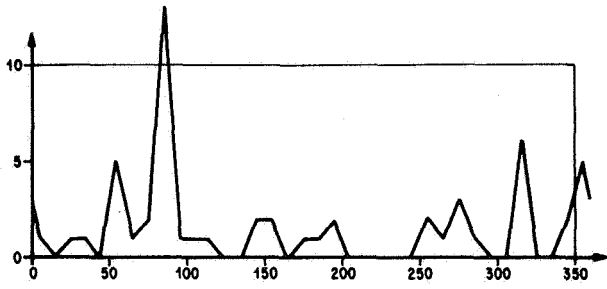
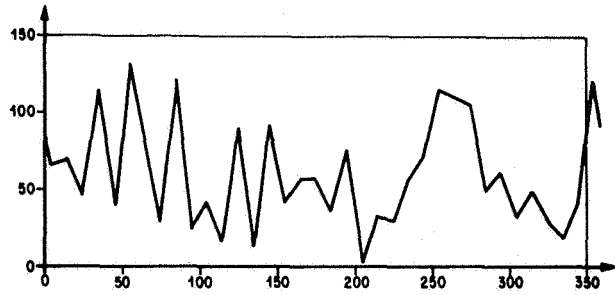


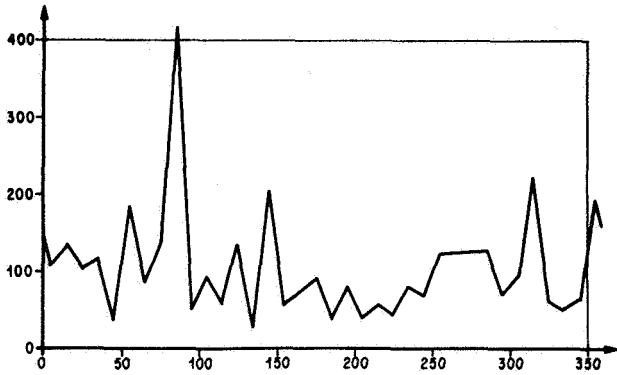
FIGURE 1B. SOUTHERN HEMISPHERE MAJOR SOLAR FLARES, SOLAR ROTATION VERSUS LONGITUDE (27.04 Day Synodic Rotation Period)



A. NO. OF PROTON EVENTS VERSUS LONGITUDE

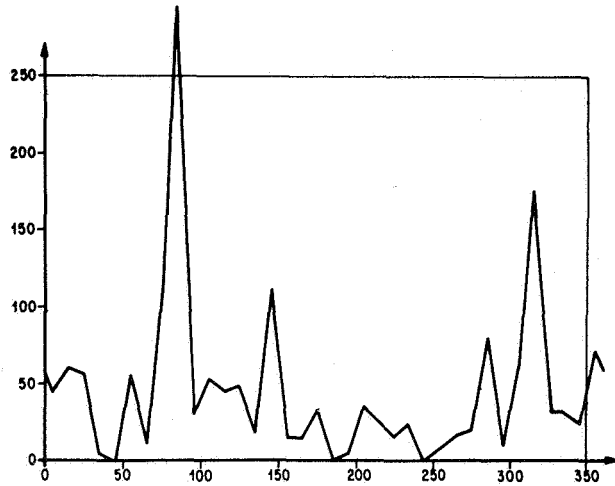


A. FLARE ACTIVITY VERSUS LONGITUDE  
(Rotation 0-50)



B. FLARE ACTIVITY VERSUS LONGITUDE

FIGURE 2. COMBINED RESULTS  
OF FLARE ACTIVITY



B. FLARE ACTIVITY VERSUS LONGITUDE  
(Rotation 50-100)

FIGURE 3. LONGITUDINAL DISTRIBUTION  
(Rotation 50-100)

# SOLAR ACTIVITY INDICES

By

H. C. Euler

## ABSTRACT

This paper considers a few solar activity related indices as the daily Zurich sunspot numbers, the observed 10.7 cm solar radiation flux as recorded near Ottawa, Canada, and a few geomagnetic indices such as daily equivalent planetary amplitude, the magnetic character, and the sum of the three-hour K indices. Also included is a discussion of the MSFC master file of digitalized solar activity data, a summary of the contour program wherein a rectangular grid is used, with each intersection a daily value of the parameter being analyzed.

## I. INTRODUCTION

Current techniques for calculating drag forces on earth satellites incorporate dynamic models of the upper atmosphere varying with time of day, season, latitude, and level of geomagnetic and solar activity. This paper considers a few indices related to solar activity such as daily relative Zurich sunspot numbers, the observed 10.7 cm solar radiation flux as recorded near Ottawa, Canada, and a few geomagnetic indices such as daily equivalent planetary amplitude,  $A_p$ ; the magnetic character,  $C$ ; and the sum of the three-hour K indices.

Sunspot numbers have been described in detail by Waldmeier [1], and geomagnetic indices have been defined by Bartels [2]. Our discussion herein is limited to a brief description of the MSFC master file of solar activity indices for use in model atmosphere programs with a description of the method of data presentation used. Comments on the indices are from the point of view of the interpretation of what they represent. The actual details of their preparation have been well established and are discussed elsewhere [1, 2].

## II. MSFC MASTER FILE OF DIGITIZED SOLAR ACTIVITY DATA

The geomagnetic indices used are those daily listings of  $A_p$ ,  $C_p$ , and the sum of the three-hour K indices over a Greenwich day prepared by the Institute for Geophysik, Gottingen, Germany, for the International Union of Geodesy and Geophysics (IUGG), Association of Geomagnetism and Aeronomy Commission Number 4.

A master file of digitized solar activity data has been compiled at MSFC in a format compatible with current MSFC atmospheric model programs.

Editing, erratum and correction programs have been established for checking the data. The program also contains some basic statistical analysis tools as subroutines, in addition to options for outputting in table, graph, or contour format with results of statistical analyses included. The master file data tapes are available for use in connection with all MSFC programs.

## III. CONTOUR PROGRAM

One of the output options is a contour chart. A rectangular grid is used with each intersection labeled with a daily value of the parameter being analyzed. Each page is a  $27 \times 27$  matrix with each row representing a Bartels solar rotation. The program interpolates between the values entered on the grid and then connects points of equal value with a straight line.

If the sun rotated as a solid surface with a period of 27 days and if the parameter being analyzed were a function of the solar rotation period, then maximum and/or minimum values of the parameter

would appear as straight vertical lines on the chart. If this line slopes from top left to lower right, then the parameter is associated with a feature that has a rotation period greater than 27 days. Interpolated values are meaningful between the columns along a row. There is no interpolated reality between the rows other than giving gradients and trends over a 27-day rotational period. The advantage of using this method of presentation is the ability to display a great deal of data on one page rather than having a long scroll, like graphs, with hidden details. It also allows us to observe trends between successive 27-day periods which might not have been seen with other methods of data presentation. Quite often solar flares occur a few days after the day where sunspot contour lines are close together.

#### IV. THE DAILY EQUIVALENT PLANETARY AMPLITUDE $A_p$

The magnetograms of twelve reference magnetic observatories are used to produce a three-hour equivalent amplitude  $a_p$ . The average of the eight three-hour equivalent planetary amplitudes during a day is the daily equivalent planetary amplitude  $A_p$ . The master file contains  $A_p$  from 1932 to present. Figure 1 shows contours of  $A_p$  from 23 July 1955 through 20 July 1957.

#### V. DAILY SUM OF PLANETARY THREE-HOUR INDEX $K_p$

The three-hour equivalent amplitude  $a_p$  is converted to a three-hour K index using a conversion table chosen by each of the twelve reference geomagnetic observatories. The eight three-hour  $K_p$  indices are then summed over a Greenwich day. The master file contains  $K_p$  from 1932 to present. Figure 2 shows contours of sum  $K_p$  from 23 July 1955 through 20 July 1957.

#### VI. MAGNETIC CHARACTER

Each geomagnetic observatory assigns a digit for the daily magnetic character,  $C$ , based upon the scale of zero for quiet geomagnetic observatory

magnetograms with the digit 1 for moderately disturbed conditions and the digit 2 for seriously disturbed conditions. The international magnetic character,  $C_i$ , is the one-decimal-place average of the twelve reference observatories magnetic character,  $C$ .  $C_i$  ranges from 0.0 through 2.0. Since 1937, a substitute for  $C_i$  based upon  $a_p$  values, called " $C_p$ ," has been used. A conversion table has been adopted to convert the upper limit of the sum of the eight  $a_p$  values to  $C_p$  [2, p. 233].  $C_i$  and  $C_p$  values are very close. The magnetic character  $C_p$  is being used to update our master solar activity data file although some of the earlier portions of the data contain the international magnetic character  $C_i$ . The master file contains  $C$  from 1932 to present. Figure 3 shows contours of  $C_p$  from 23 July 1955 through 20 July 1957.

#### VII. SOLAR 10.7 cm FLUX

The Algonquin Radio Observatory near Ottawa, Canada, has observed and recorded solar flux daily at 1700 U. T. since 1947. Although some data are missing, especially for holidays during the earlier portion of their record, Ottawa's solar flux data are widely used. In 1965 Ottawa established a small correction factor for varying atmospheric absorption during different seasons with numerical values ranging from zero in summer to 1.5 percent in winter. The MSFC master file of solar activity data uses the 1965 revision for all updating of new data. We are presently updating the older records to the 1965 revision.

MSFC master file contains daily 10.7 cm flux from 1947 to the present with interpolated values inserted for missing data. The running means of the previous 27, 54, and 81 days, as well as the monthly means and the Zurich smoothed 10.7 cm solar flux, have been computed and stored on the master file data tape. Figure 4 shows contours of Ottawa observed 10.7 cm solar flux from 23 July 1955 through 20 July 1957.

#### VIII. ZURICH RELATIVE SUNSPOT NUMBERS

Provisional Zurich sunspot numbers, dependent upon observations at the Zurich Observatory and its

stations at Locarno and Arosa, are compiled by M. Waldmeier of the Swiss Federal Observatory, Zurich, Switzerland, and distributed monthly. At the end of the year, Waldmeier compares the results of his three observatories with reports sent to him during the year from other observatories. After a few months of the new year, Zurich Observatory personnel revise some of their provisional values and issue final daily Zurich sunspot numbers for the previous year.

The master solar activity file contains final daily sunspot numbers from 1890 to the present with monthly and Zurich smoothed values also included. Figure 5 shows contours of daily Zurich sunspot numbers from 23 July 1955 through 20 July 1957.

## MATHEMATICAL ANALYSIS

The following items were computed and graphed for the indices over various time intervals: the arithmetic mean, root mean square, standard deviation (about the mean), modified standard deviation (about the mean), slope, intercept, standard error of estimate about the least squares curve fitted straight line, modified standard error of estimate about the straight line, correlation coefficients, power spectra, and Fourier coefficients. Figure 6 shows the smooth power spectra of sunspot numbers from 1 January 1890 through 8 December 1967 using 486 lags with a 6-day time interval  $\Delta t$ .

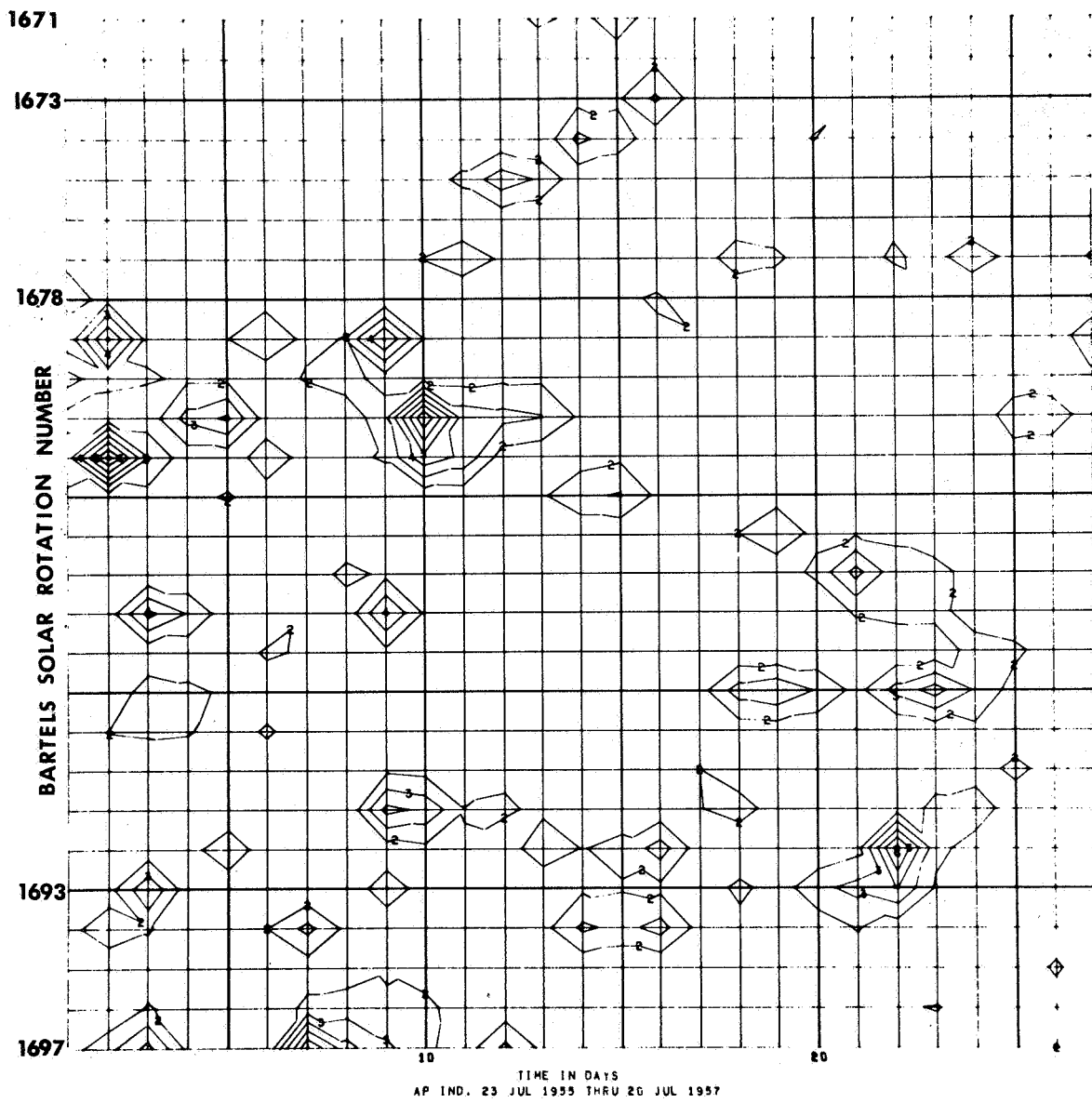
## CONCLUSIONS

Contour charts of daily solar activity indices show that the contour peaks do not have one simple constant

period between them. Some peaks may not be related to the preceding peak but rather to some other previous peak. Many sunspot contour peaks are followed after a one-day delay by a solar 10.7 cm flux peak. The  $A_p$  index may increase one, two, or three days after a solar flux peak. Large  $A_p$  values are associated with a proton event reaching the earth. Short delays are associated with high velocity and energy protons, while long delays are associated with low velocity and energy protons. Occasionally, an active region on the sun continues to be active one, two, or three rotations later, and is then quiet for a few rotations. We can distinguish some peaks near a multiple of a rotation later, although a random distribution of peaks would also place some peaks near some multiple of a rotation. The sun seldom does exactly as expected, as past experience with predictions have sadly shown; yet there is still optimism that the accuracy of solar predictions may improve.

## REFERENCES

1. Waldmeier, M.: The Sunspot-Activity in the Years 1610-1960, Zurich Schulthess and Company, Switzerland, 1961.
2. Bartels, J.: The Geomagnetic Measures for the Time-Variations of Solar Corpuscular Radiation, Described for Use in Correlation Studies in Other Geophysical Fields, IGY Annals, Vol. 4, Pergamon Press, Longon, 1957, pp. 227-236.

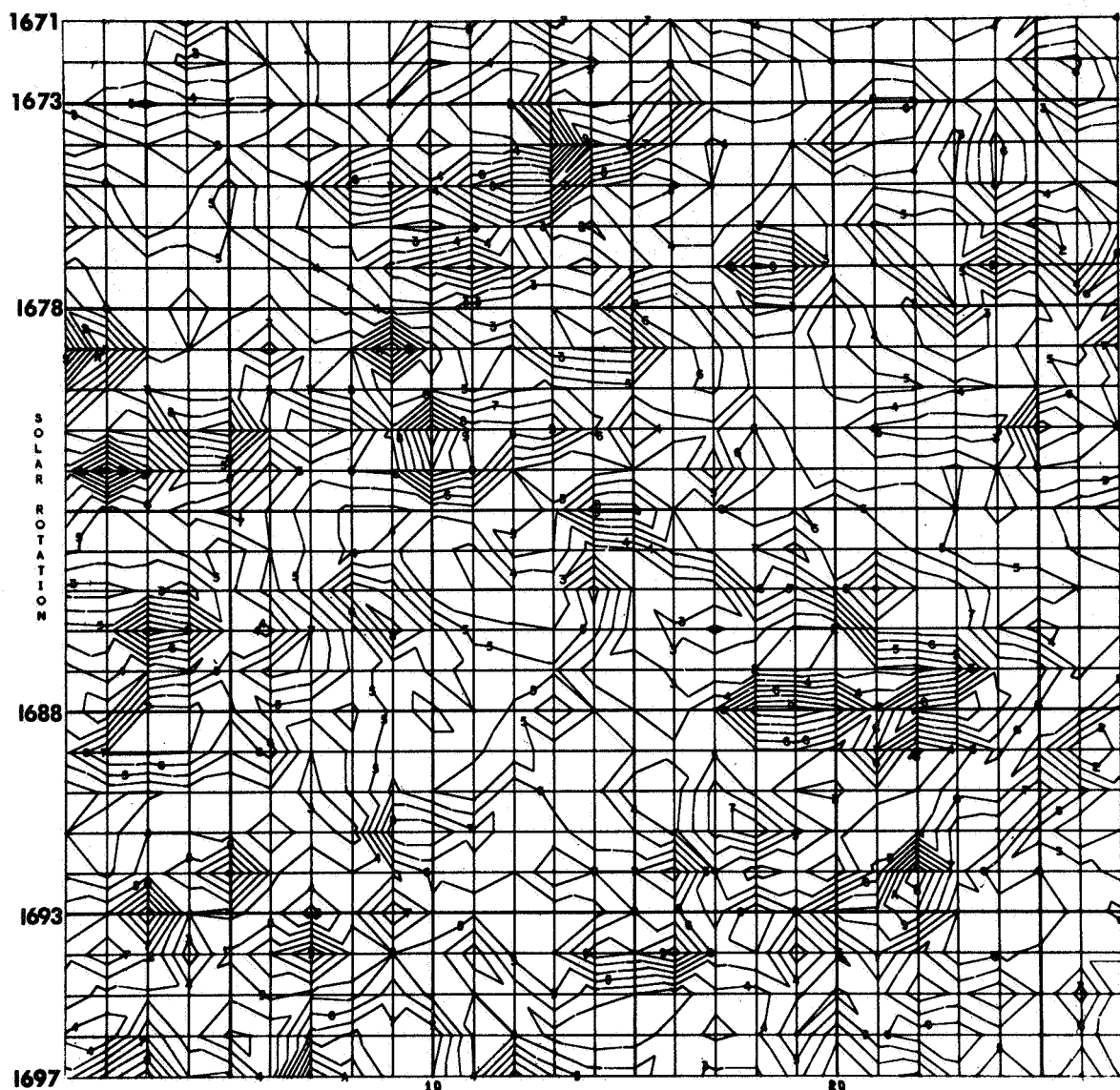


TIME IN DAYS  
 AP IND. 23 JUL 1955 THRU 20 JUL 1957

CONTOUR IDENT.

1	5.
2	25.
3	50.
4	75.
5	100.
6	125.
7	150.

FIGURE 1. CONTOURS OF  $A_p$  FROM 23 JULY 1955 THROUGH 20 JULY 1957



TIME IN DAYS  
 KP IND. 23 JUL 1955 THRU 20 JUL 1957

CONTOUR IDENT.		
1	5.	9 40.
2	5.	A 45.
3	10.	B 50.
4	15.	C 55.
5	20.	D 60.
6	25.	E 65.
7	30.	F 70.
8	35.	

FIGURE 2. CONTOURS OF SUM  $K_p$  FROM 23 JULY 1955 THROUGH 20 JULY 1957

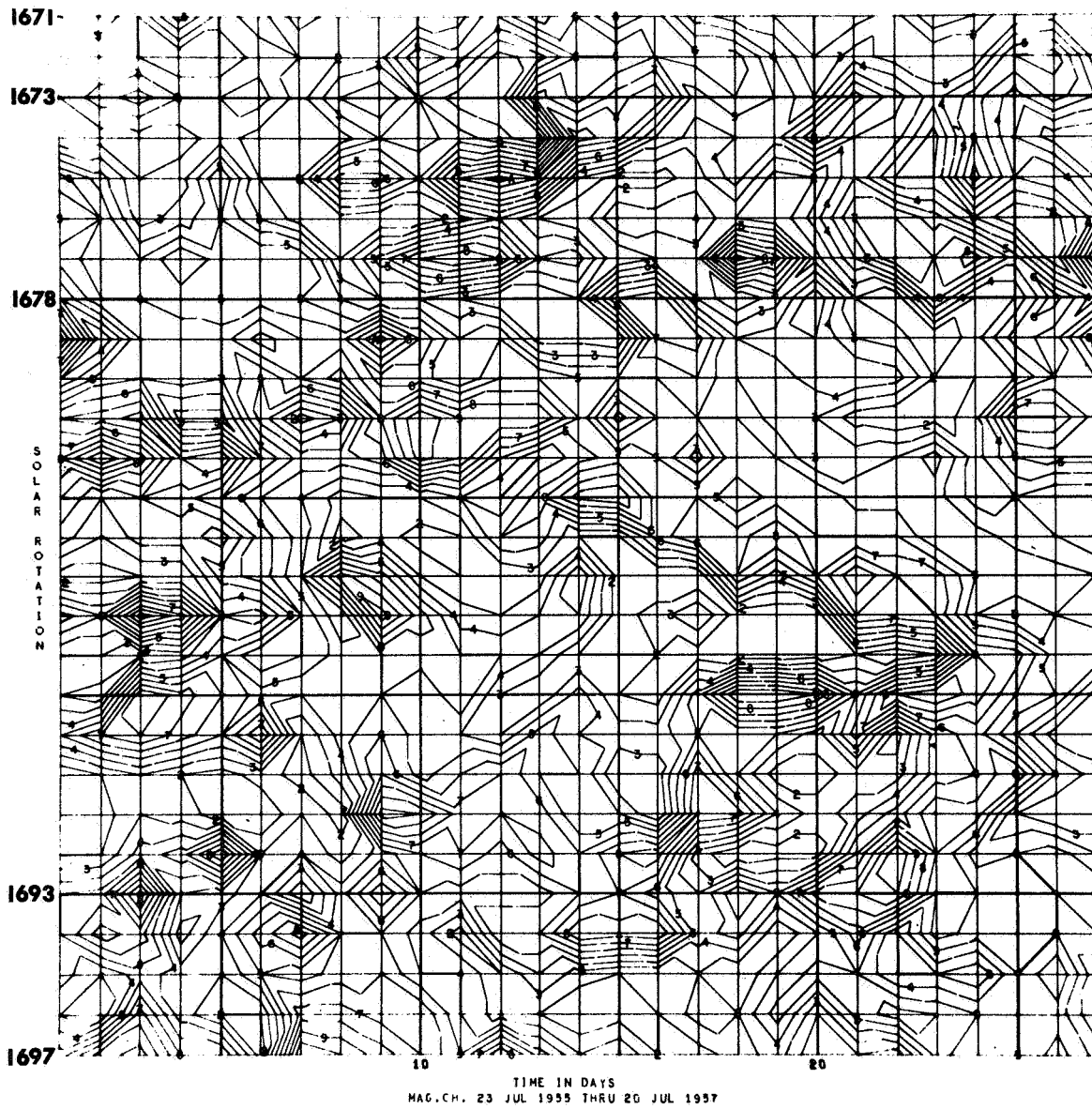


FIGURE 3. CONTOURS OF  $C_p$  FROM 23 JULY 1955 THROUGH 20 JULY 1957

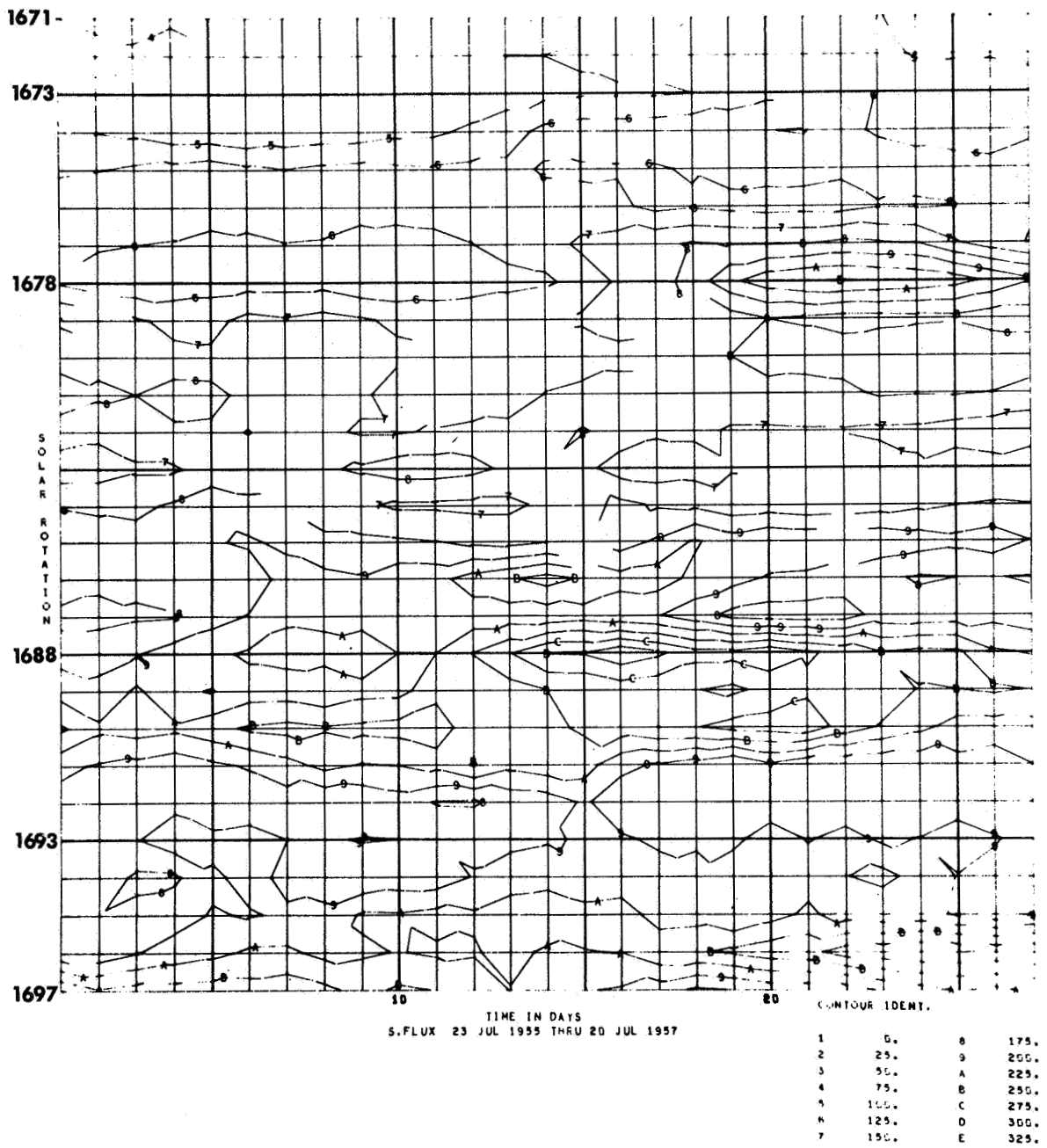


FIGURE 4. CONTOURS OF OTTAWA OBSERVED 10.7 cm SOLAR FLUX FROM 23 JULY 1955 THROUGH 20 JULY 1957

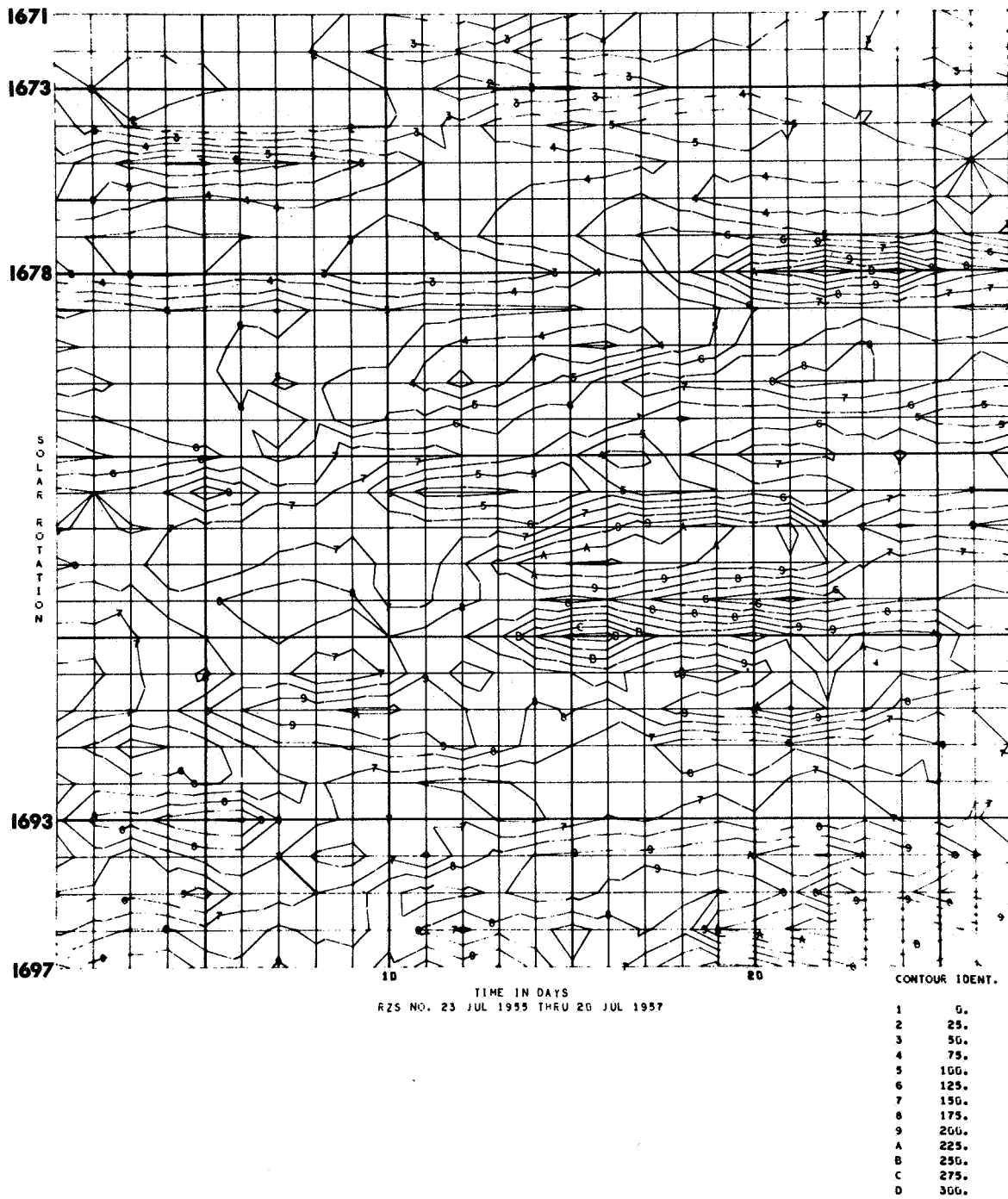


FIGURE 5. CONTOURS OF DAILY ZURICH SUNSPOT NUMBERS FROM 23 JULY 1955 THROUGH 20 JULY 1957

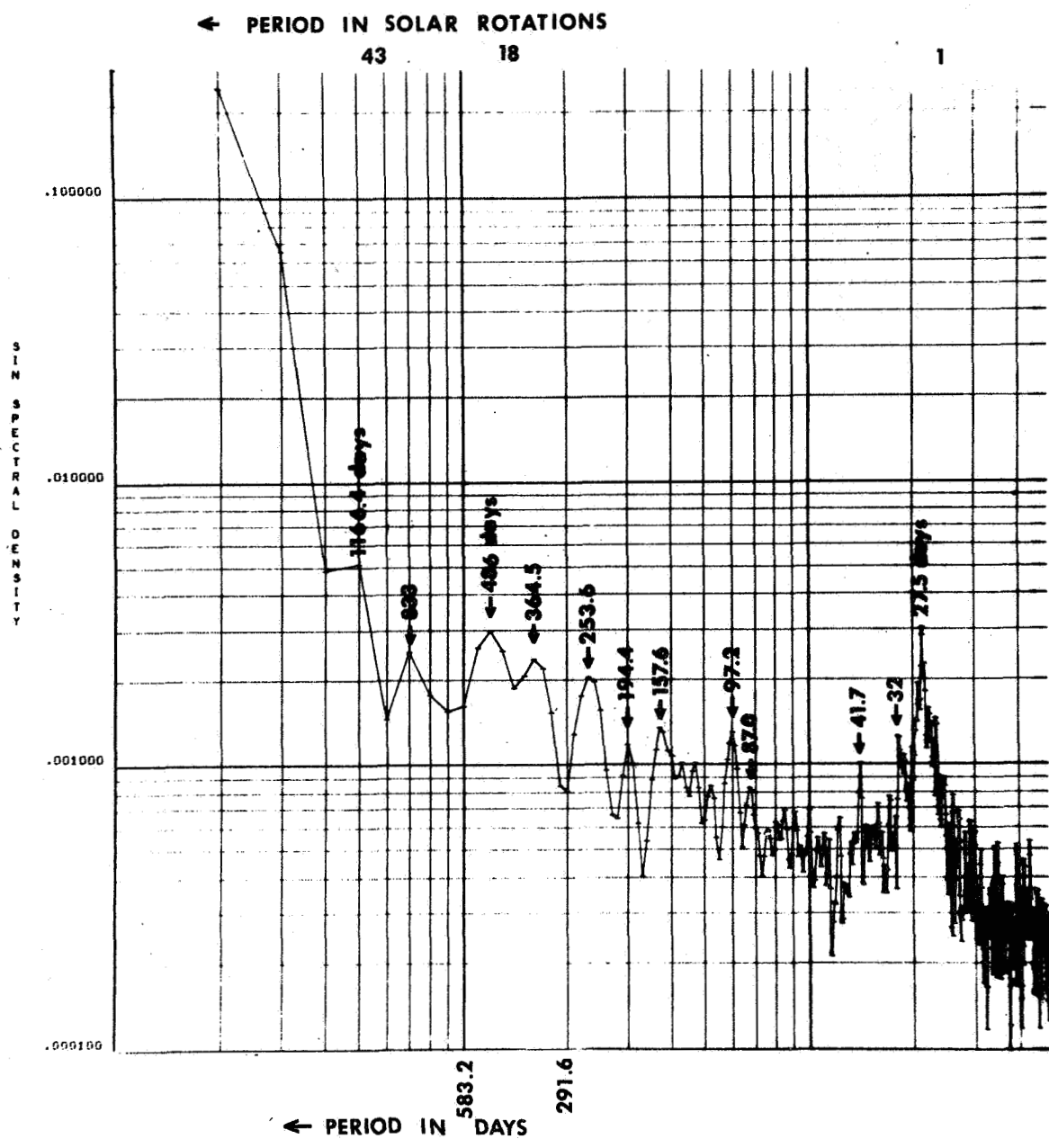


FIGURE 6. SMOOTH POWER SPECTRA OF SUNSPOT NUMBERS FROM 1 JANUARY 1890 THROUGH 8 DECEMBER 1967 USING 486 LAGS WITH A 6-DAY TIME INTERVAL  $\Delta t$

## VII. OPERATIONS ANALYSIS

# AUTOMATIC EXPERIMENT SCHEDULING AND OPTIMIZATION PROGRAM (AESOP)

By

R. F. Ball<sup>1</sup> and W. D. McFadden<sup>2</sup>

## ABSTRACT

Long duration manned space missions are planned with the primary function of providing an appropriate environment within which a large number of scientific and engineering evaluation experiments may be conducted. These missions will involve performing hundreds of experiments, each of which can be broken down into many separate tasks or events. In addition, each experiment will require the satisfying of a set of associated conditions before it can be scheduled. Consequently, it is anticipated that the magnitude of the scheduling problem will preclude the use of manual scheduling methods.

The Automatic Experiment Scheduling and Optimization Program (AESOP), a three-phase computer program that will automatically generate a set of no-conflict schedules of events for space missions, is described. A Monte-Carlo technique is used to select a schedule that is optimum to within a desired confidence interval with respect to specified parameters.

## I. INTRODUCTION

The Automatic Experiment Scheduling and Optimization Program (AESOP) [1] is a computer program that can provide a Monte-Carlo simulation of the schedule of events for space missions. The program automatically generates a prescribed number of feasible schedules, along with the values of specified parameters associated with each schedule. A time history of resource utilization is simultaneously generated with each schedule.

### A. Program Application

The program has a number of obvious uses in connection with mission planning. Among these are:

1. N feasible schedules can be made available to the analyst for comparison.
2. The dependence of given parameters on the schedule can be determined.
3. The schedule that is a statistical optimum with respect to a single parameter or a set of weighted parameters can be obtained.
4. Mission support requirements (either ground or onboard) can be determined from the time history of needed resources; this includes astronaut training requirements.
5. A vehicle-pointing requirement history can be generated to be used as an input to attitude simulation programs.
6. Mission-compatible experiment packages can be determined.

Because of the general design of AESOP, it is not inherently limited to space mission applications. In fact, it appears to be applicable (perhaps with minor modifications in some cases) to all classes of scheduling problems that satisfy the following two restrictions:

1. The set of time intervals during which each event can be performed is determinable in advance. (These time intervals are referred to as the candidate intervals of the event.)
2. The candidate intervals of any event are affected by the scheduling of a second event at most only during the scheduled duration of the second event.

The first restriction is self-explanatory. A specific example of a scheduling problem that violates the second restriction is an orbital space mission where an event to be scheduled significantly perturbs

1. Nortronics, Northrop Corporation, Huntsville, Alabama

2. Aero-Astroynamics Laboratory, George C. Marshall Space Flight Center

the orbit. In this case, the difficulty can be circumvented by prescheduling any orbit-perturbing events. The effects of the perturbations are then known, and the candidate intervals of the remaining events can be determined. Similar actions could be taken to avoid the second restriction in the general scheduling problem.

## B. Optimization Techniques

There are a number of optimization techniques which could be employed in the scheduling process. Listed below are four techniques which were considered.

1. Linear Programming
2. Dynamic Programming
3. Monte-Carlo Technique
4. Special Techniques

A number of factors contributed to the selection of the Monte-Carlo technique, one of which was the sheer complexity of the problem, making its formulation in the other formats extremely difficult. There were, however, more forceful reasons. For example, some of the parameters of interest did not seem to be linearly related to any of the controllable variables; this fact would render any linear programming result only an approximation of the optimum.

Among the special techniques examined were the so-called Traveling Salesman Algorithm, the Transportation Algorithm, and the Stockcutting Algorithm. The common shortcoming of these methods was their apparent inability to treat the multi-dimensional character of the constraint and resource requirements of the events to be scheduled. Other methods had similar shortcomings.

The Monte-Carlo technique had none of the previously mentioned disadvantages. In addition, it had the advantage of allowing the dependence of an arbitrary parameter to be determined. This may ultimately be as important as the actual optimization because it indicates which parameters are most in need of optimization. Another advantage of the Monte-Carlo method is that it is a relatively minor program modification to add the capability of optimizing on a new parameter. This contrasts with the

other optimization techniques where the optimization of a different parameter is essentially a different problem.

## C. Monte-Carlo Optimization Technique

Briefly, the Monte-Carlo technique as applied in AESOP consists of the following:

1. Randomly generating the order in which the events are to be scheduled.
2. Randomly selecting the starting time of an event from among the set of all possible starting times; i. e., from among the candidates.

Optimization information is obtained in the form of a statistical relationship between the number of schedules in the generated sample,  $N$ , and the probability,  $P_r$ , that the optimum schedule of the sample is better than a specified percentage,  $Q$ , of all possible schedules. This relationship is given by

$$P_r = 1 - p^N,$$

where  $p = Q/100$ . The value of  $p$  is sometimes called the confidence interval.

As an example of the application of this equation, suppose it is desired to know the number,  $N$ , of schedules required to have the probability be 0.95 that the best schedule in the sample  $S_1, \dots, S_N$  of  $N$  schedules is better, with respect to some specified payoff function, than 99 percent of all possible schedules. Then the preceding equation becomes

$$0.95 = 1 - \left(\frac{99}{100}\right)^N.$$

In general, the exact solution of this equation will not yield an integer value for  $N$ ; hence, the equation is solved for the smallest value of  $N$  for which the probability is at least 0.95. The value of  $N$  is found to be  $N = 296$ .

Figure 1 is a plot of  $P_r$  as a function of  $N$  for values of  $p$  of 0.90, 0.95, and 0.99. Figure 2 is a plot of  $p$  as a function of  $N$  for values of  $P_r$  of 0.90, 0.95, and 0.99.

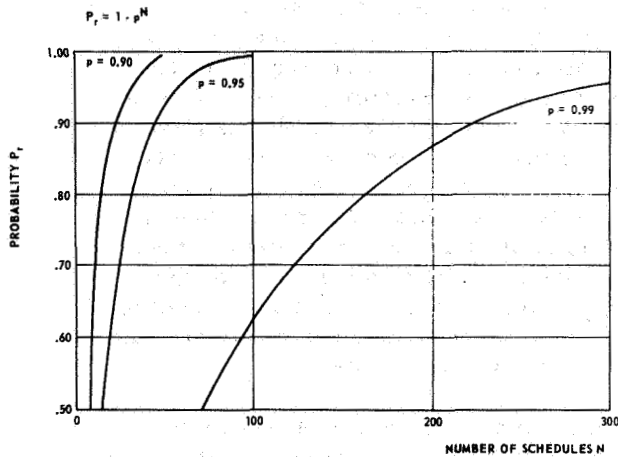


FIGURE 1. PROBABILITY AS A FUNCTION OF THE NUMBER OF SCHEDULES

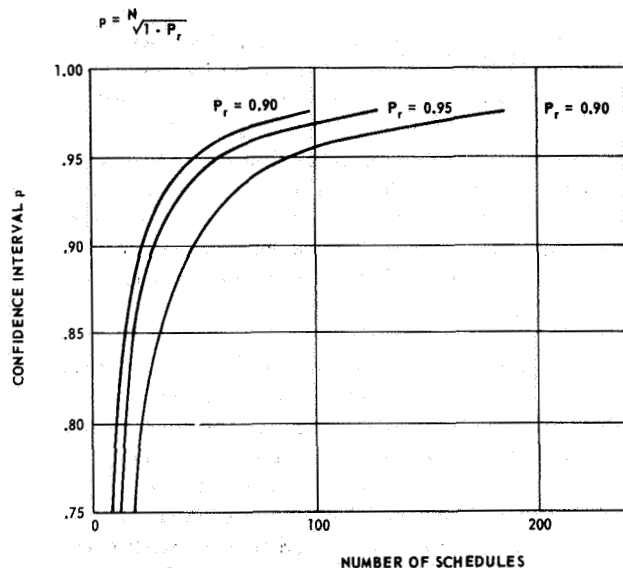


FIGURE 2. CONFIDENCE INTERVAL AS A FUNCTION OF NUMBER OF SCHEDULES

## II. PROBLEM SIMULATION

The primary consideration of the problem simulation consists of modeling the events to be scheduled and the environment in which the events must be performed. Insofar as the schedule is concerned, the essential features of the events are the constraints and the resource requirements that must be satisfied before the events can be scheduled. Hence, the events can be effectively modeled by listing their constraints and resource requirements. This dictates that the

environment in which the events are to be conducted must be modeled as some form of a time history of the satisfied constraints and available resources. The actual implementation of this time history is discussed in Subsection C.

### A. Constraints

The constraints of an event are those conditions, not involving some depletable quantity, which must be satisfied before an event can be scheduled. For example, the requirement that the vehicle be in a designated cone over a given geographical site when an event is scheduled is a constraint, but the requirement that ten watts of power be available is classified as a resource requirement, because the scheduling of the event will deplete the available quantity during the time the event is scheduled.

With one exception, the constraints associated with each event are treated as "and" conditions; i. e., all of the conditions specified by the constraint set must be satisfied before the event can be scheduled. The exception is the event that represents the transmission of stored data to a ground station. In this case, the only constraint is that the vehicle must be in a designated cone over some station that can receive the transmitted data. Because data can normally be transmitted to any of several stations, the constraints are treated as "or" constraints, so that being over any one station satisfies the constraint set. The following is a list of examples of possible constraints for space mission scheduling.

1. Subpoint of satellite in day
2. Satellite in shadow
3. Moon in view of satellite
4.  $X_1$  days  $\leq$  age of moon  $\leq X_1'$  days
5. Astronaut B available
6. Satellite is  $\epsilon_1$  degrees above Station  $K_1$
7.  $R_1 \leq$  altitude of satellite  $\leq R_1'$
8.  $\psi_1 \leq$  geocentric latitude of satellite  $\leq \psi_1'$
9.  $\nu_1 \leq$  true anomaly  $\leq \nu_1'$
10. Satellite is within  $X_1$  seconds of sunlight

11. Satellite is in view of Celestial Target  $\eta$
12. Subpoint of satellite in Region  $R_1$
13. Sun is  $X_1$  degrees above target XXX
14. Celestial Target  $\eta$  is within the angle  $\xi$  of the sun

## B. Resource Requirements

A resource requirement, as the name implies, is some amount of a depletable quantity that is required for the performance of an event. Resource requirements are further divided into temporarily depletable and permanently depletable resource requirements. Temporarily depletable resources are those resource types that are required only during the performance of an event. Examples are electrical power, supporting equipment, and astronauts. Permanently depletable resource types are those that are expended upon use, and the quantity used is not available for reuse. Examples are electrical energy, cryogenics and compressed gases.

## C. Environment Simulation

The environment in which the events for space missions are to be scheduled is obviously a function of time. Because the essential features of the events are the constraints and resource requirements, an appropriate environment simulation could be in the form of a time history of the state of the constraints and available resources. This is the form in which the environment simulation is input to AESOP.

1. CONSTRAINT HISTORY. — The constraint time history for space mission scheduling is created by an orbit prediction program known as the Cowell Geometric Constraint Generator. The constraint set format is quite general, with the actual limits being an input option to the Cowell Program.

The operation of the Cowell Program is such that the state of all constraints of interest is determined automatically by the program at the time corresponding to the start of the mission. A record is then written on an output tape specifying the time and the numbers of all constraints satisfied at this time. The program then increments the time by the value of the integration step (commonly sixteen seconds) numerically integrates the orbital param-

eters, and again examines the state of all constraints of interest. If the state of none of the constraints changes, the time is incremented again and the process is repeated. Eventually, the state of one or more constraints will change. At this point, the program writes a new record on the output tape specifying the current value of the time and the numbers of the constraints that are satisfied at this time. It is clear, then, that the constraints corresponding to the numbers written in a given tape record are satisfied during the interval of time extending from the time written in the given record until the time written in the next record.

The repetition of the preceding procedure throughout the duration of the mission results in the division of the mission into the rather naturally occurring time intervals during which the state of the constraints remains constant.

2. RESOURCE HISTORY. — Assuming that permanently depletable resources would not be replenished during a mission, each of the resource types is treated as a single quantity that must be available at the start of the mission in sufficient quantities to supply all requirements throughout the mission. If the available quantities of any of these resource types are not known, they can be left unconstrained, and the program will determine the required quantities for each schedule.

A time history of temporarily depletable resources is required as a program input if the schedule is to be constrained by available resources. An available option, however, allows any number of resource types to be left unconstrained, in which case any portions of the available resource profile that are less than zero are to be interpreted as the additional amount of the resource that is required for the given schedule.

The resource history is modeled in a manner similar to the constraint history; i. e., the mission is divided into time intervals during which the available resources are assumed to remain constant, and then the available quantity of each resource type is specified for each time interval. The resource history is input to the program as a tape, with each record containing the time corresponding to the start of a time interval and the quantity of each resource type available during the interval. The time corresponding to the end of an interval is, of course, the same as the time corresponding to the start of the next interval.

## D. Candidates

Sufficient information to generate a feasible schedule is available when the constraints and resource requirements to each event and the constraint and resource time histories are specified. The information is not in a convenient form, however, because before an event can be scheduled at any time point, the information designating requirements must be compared against the information specifying availability. This is a particular disadvantage when the Monte-Carlo technique is to be used because the same information must be examined repeatedly. Probably the most convenient form for the information is to specify the set of time intervals during which all of the constraint and resource requirements of each event are satisfied. Any intervals with durations less than the minimum time required to perform the event can be deleted. The time intervals are known as the candidate intervals of the associated event.

## E. Sequential Events

Most real events to be scheduled do not conform to the simple model of an event characterized by a constant set of constraints and resource requirements throughout their duration. A simple example might be a star-track experiment which might consist of the following activities:

1. turn on equipment
2. allow a 15-minute warm up
3. boresight the equipment
4. perform the experiment
5. turn off equipment.

The first activity would probably have no constraints, but would require an astronaut and electrical power. The second would require only electrical power (probably at a different level than the first activity). The third activity might require power and one or two astronauts. A constraint on the fourth activity could be that a given celestial object be in view. Each of these activities is inherently different, and certainly no single set of constraints and resource

requirements can characterize the complex event known as a star-track experiment.

Complex events such as the previous example can be input to AESOP as a sequence of events, each of which has constant constraint and resource requirements. The minimum and maximum time between the end of one event in a sequence and the start of the next event is an input option. Both of these values can be input as zero if the events should be scheduled in immediate succession.

## III. PROGRAM OPERATION

The essential function of AESOP is to provide a random sample of feasible schedules of events, and to calculate the values of the specified parameters associated with each schedule. The four basic required inputs are:

1. Event Constraints
2. Event Resource Requirements
3. Constraint History
4. Resource History

The information in (1) and (2) is input on cards, while that in (3) and (4) is on magnetic tape.

Because of the enormous amount of data which must be manipulated and examined to generate each feasible schedule, it has been found that a program using a straightforward approach to generating schedules will require excessive computer time. Consequently, the current version of AESOP reflects an effort to perform every essential operation in the least time. Consistent with this effort, AESOP is divided into three separate programs, known as AESOP Phase I, Phase II, and Phase III. Among the advantages gained by separating the program are:

1. A reduced amount of data that each phase needs to handle.
2. A reduced running time for each phase.
3. Greater flexibility of program operation (e.g., the program can be run with different event resource requirements without running Phase I again).

## A. Input Options

A number of input options are available that increase the versatility of the program. The discussion of this section is limited to input options of this type.

1. CONSTRAINED RESOURCES. — Any resource type (both permanently or temporarily depletable) can be either constrained to non-negative values or allowed to take on any value. If a resource type is constrained, then an event requiring that type will be scheduled only at times when the required quantity is available. Unconstrained resource types are not considered in determining the schedule time of an event. Of course, the available quantities of both constrained and unconstrained resources are depleted by the amount required by a scheduled event.

2. METHOD OF REPEATING EVENTS. — Events can be repeated according to either of two rules. One places only the restriction that different repeats of the same event cannot intersect. The second is more restrictive and allows an event to be scheduled only once in each candidate interval.

3. ASTRONAUT REQUIREMENTS. — Astronaut requirements can be input as specific astronauts, or as "any" astronaut(s). In the second case, only the required number of astronauts need be available to schedule the associated event.

4. CONFLICTING EVENTS. — The number of events that conflict directly can be input such that they will never be scheduled coincident in time. For example, an event which radiates energy in a band that another event measures might be considered to conflict directly and indicating an input that they conflict would insure that their schedule times would not overlap.

5. PRECEDENCE REQUIREMENTS. — An event can be constrained to a specified time window following the scheduled time of any other event. An example of the use of this option would be an event that must be repeated several times within an elapsed time after some equipment is boresighted.

6. PRIORITY ORDERING. — Events to be scheduled can be input in the order of priority, or the order can be allowed to be randomly generated by the program, or the order can be any combination of priority and random generation. In all cases, "order" denotes the order in which the act of scheduling the events occurs and has no relation to the time

at which the events will be scheduled to occur. This option could be used in the cases where not all events are expected to be scheduled. Priority ordering will insure that the events considered most important are scheduled first.

7. ALTERNATE SCHEDULING MODES. — Either of two scheduling modes can be selected. Using one mode, the candidate intervals of an event are updated to reflect possible conflicts or inadequate resources caused by previously scheduled events before the event is scheduled. Thus, the event can be successfully scheduled to start at any point in any of its updated candidate intervals. In the alternate mode, the starting time of the event is selected randomly from the original candidate intervals and then a check is made for possible conflicts or inadequate resources. If the resources are inadequate or if there are conflicts, another starting time is selected randomly and the conflicts and resources checked for this time. The process is repeated until either a successful schedule time is obtained or the number of unsuccessful attempts exceeds an input value. In the later case, the scheduling mode automatically reverts to the first alternative.

The advantage of the second mode is that only the portion of timeline coincident with the scheduled time of the event needs to be examined, whereas the "updating" mode requires the consideration of previously scheduled events throughout the entire timeline. The mode requiring updating of the candidate intervals can thus be expected to require longer computer times, although the reverse may be true in certain cases where the "density" of scheduled events is high throughout the mission.

## B. Phase I - Basic Operation

Phase I creates the Initial Candidate Time Line Tape by comparing the constraints of each event with the constraints satisfied in each time interval. The constraint sets for the events are read from cards while the satisfied constraints for a given time interval are read from a single record on the Constraint History tape. Each record of the Initial Candidate Time Line Tape contains the time read from the corresponding record on the Constraint History Tape plus the numbers of the events whose constraints are satisfied during the time interval. The Initial Candidate Time Line Tape is used as an input to Phase II.

The constraints for the Jth event are read from cards and ultimately stored in the array  $E(I, J)$ , where

I ranges from one through the number of constraints of the Jth event. The array E(I, J) is preloaded to all zeros. Thus, once the constraints are read in, the number of constraints of the Jth event can be determined by counting the number of successive values of I for which E(I, J) is non-zero. This number is stored in E(50, J).

A record from the Constraint History Tape is read into the array SAV(I) as the first step in creating the Initial Candidate Time Line Tape. An array, ACTIVE (J), is equivalent to SAV(J+1) to eliminate SAV(1) which denotes the starting time of the interval. Then, with K initially set to one, the constraints represented by E(L, K) for L from one to E(50, K) are compared with the satisfied constraints represented by the array ACTIVE (J). If all of the required constraints for the Kth event are found in the array ACTIVE (J) for some J, then K is stored in the output array ICVECT(NUMC), where NUMC is one greater than the number of candidates already found in the given time interval. If any constraint is not found in ACTIVE (J), K is not stored in the array ICVECT(NUMC). In either case, K is incremented by one and the process repeated until the constraints of all events have been checked. A record is then written on the Initial Candidate Time Line Tape such that the time originally stored in SAV(1) is written as the first two words of the records, and the remaining words are from a real array, PBLK(I), equated to ICVECT(I), for I from one to NUMC. Thus, a record on the Initial Candidate Time Line Tape contains the time as the first two words and the numbers of the events that are candidates during the corresponding time interval as the subsequent words.

The preceding process is continued until all records have been read from the Constraint History Tape. An exception to the process occurs for the constraints which require the vehicle to be in a specified cone over a given geographical position. If more than one constraint of this type is input for a single event, only one of the constraints need be satisfied. This feature enables the constraint set of events with multiple targets to include all of the target constraints. Without this special feature, events with multiple targets would have to be input as different events because the general requirement that all constraints be simultaneously satisfied would require that the vehicle be over all targets at once. This, of course, could not occur unless all targets were in a relatively small area.

An additional function performed by Phase I is to copy the Resource History Tape as the first file on

the same tape used to record the Initial Candidate Time Line Tape. This was necessary because the Phase II work tape requirements included all but one of the available tape drives of the computer system on which AESOP was developed. Since Phase II requires both the Resource History and the Initial Candidate Time Line as inputs, it was necessary to write both of these on the same tape. Thus, while the Resource History Tape is used functionally in Phase II, it must be physically input to Phase I.

### C. Phase II - Basic Operation

Phase II determines the final candidate intervals for use in Phase III. Phase II also determines auxiliary information used to facilitate the operation of Phase III. This information includes:

1. The total time during which an event can be scheduled.
2. The candidate intervals representing the different possible ways that astronaut requirements can be met.
3. An index, ICFI(J), denoting the particular set of ways that the astronaut requirements of the Jth event can be satisfied for each event to be scheduled.
4. A variable, MANUW(J), which denotes the maximum number of ways that the astronaut requirements of the Jth event can be met, for each event to be scheduled.

The above information is stored on a tape used as an input to Phase III, and known simply as the Phase II output tape.

The first operation of Phase II consists of reading in all necessary data cards. This is performed by subroutine INPUT. The subroutine INIT is called next to write the Resource History and Initial Candidate Time Line on separate work tapes. In the process of rewriting the Resource History, any superfluous information is eliminated, which results in a simplified Resource History (where "simplified" means that adjacent time intervals with identical values of all Resource types are merged into a single time interval). The Resource History Tape is also written on the Phase II output tape after astronaut availability information has been condensed into one word.

The next operation involves reading each record of the Initial Candidate Time Line Tape and the

Resource History Tape and comparing the constrained resource requirements of each event that is a candidate in the record with the available resources. Events for which requirements exceed availability are effectively deleted from the record. During this operation, the different ways in which astronaut requirements can be met are distinguished. These operations are performed by the subroutine RESFIL.

The Candidate Time Line Tape modified by RESFIL is then read by subroutine DELT, which determines if the total time duration corresponding to each set of successive records in which a given event is a candidate exceeds the minimum duration of the event. Events are effectively deleted from all records in any set having an insufficient duration. The durations of the different ways in which the astronaut requirement can be met are checked individually.

The Candidate Time Line Tape that is modified by subroutine DELT is such that all initial requirements of the individual events are satisfied. Except for the requirements imposed by sequences of events, any event could be successfully scheduled to start at any point in any of the time intervals for which the event is listed as a candidate (of course, once the first event had been scheduled, its effect on the candidates of unscheduled events would have to be accounted for before subsequent events were scheduled).

Subroutine CONDS is called next by Phase II to determine the candidate intervals of each event, and to modify the candidate intervals of events that are part of a sequence to reflect the conditions imposed by the sequence. The candidate intervals of the separate ways in which astronaut requirements can be met are also determined.

Finally, subroutine WRITE is called by Phase II to write auxiliary information on the Phase II output tape.

#### D. Phase III - Basic Operation

Phase III generates the actual schedules and calculates the time required to complete the schedule, the total time during which some event is scheduled, the maximum total requirement for each resource type, and the data residual associated with each schedule. The main program of Phase III is like Phase II in the respect that it is an executive routine that calls appropriate subroutines to perform specific logical operations.

The initialization subroutine, INAL, is called first to read the input data cards and the Phase II output tape. The Resource History, candidate intervals, and the candidate intervals representing the different astronaut configurations of each event are stored in random access memory.

If some of the events are not priority ordered, subroutine ORDR is called next to randomly determine the order of these events. The order in which the events will be scheduled is given by the values of the array JEXORD(I) for  $I = 1, 2, \dots, MTO$ , where MTO is a variable equal to the total number of single events and sequences to be scheduled.

An integer variable IOZ is initially set to one, and the variable KE is set to JEXORD(IOZ). KE then represents the number of either the next single event to be scheduled, or the first event of the next sequence to be scheduled, depending, of course, on whether or not KE begins a sequence. (To simplify subsequent discussion, it will be assumed that all events are part of a sequence).

If every element in the sequence beginning with event number KE has at least one candidate interval, the candidate intervals of the Ith event in the sequence are read into the arrays STI(I, J) and ESTI(I, J) for J from one to the number of candidate intervals of the Ith event.

Subroutine PRECED is then called to determine if the KEth event has a precedent requirement (it is not permissible to input precedence requirements for events in a sequence other than the first). If so, the portions of any candidate intervals of event KE that do not occur in the defined time window following a scheduled repeat of the precedent event is deleted. If all candidate intervals of KE are deleted in PRECED, IOZ is incremented by one and the process is repeated for the next sequence to be scheduled. If not all candidate intervals of KE are deleted in PRECED, IOZ is incremented by one and the process is repeated for the next sequence to be scheduled. If not all candidate intervals of event KE are deleted, then either Subroutine SCHED or UPDAT1 is called, depending on whether the scheduling mode selected on input calls for scheduling first and then checking for conflicts and resources, or updating the candidate intervals before scheduling. The particular mode is specified by the value of NUPICK. If NUPICK is greater than zero, scheduling occurs without updating. If NUPICK equals zero, updating occurs before scheduling.

With NUPICK greater than zero, the subroutine SCHED is called to generate trial schedule times for each event in the sequence. After obtaining a trial schedule time of each event in the sequence, SCHED calls RRES to read into core memory the resources available during the trial schedule time of the event. Subroutine CKRES is then called to determine if the constrained resources are adequate and to deplete the available quantities stored in core by the amount required by the event. If available constrained resources are adequate, the subroutine CKCON is called to determine if any previously scheduled event conflicts directly with the event being scheduled, and if so, whether the scheduled time of any conflicting event intersects the trial schedule time of the event being scheduled. If not, the process is repeated for the next event in the sequence. If, however, either some constrained resource is inadequate, or the trial schedule time intersects the scheduled time of a conflicting event, the trial scheduling is terminated. Then, if the number of attempts to schedule the sequence does not exceed the value of NUPICK, the entire process is repeated with new trial schedule times. If a successful schedule is obtained, the trial schedule times are changed to schedule times and subroutine RRES is called to perform some operations preliminary to writing the updated resources available during the scheduled time of each event in this sequence in the so-called New Resource Area. SCHED then returns control to the executive routine.

The sequence of operations is somewhat different when the other scheduling mode is selected. To select this mode, NUPICK is set to zero on input. Then, instead of calling SCHED, as when NUPICK is greater than zero, the executive routine calls subroutine UPDAT1 to delete any portion of the candidate intervals of the events in the sequence for which either constrained resources are inadequate, or a conflicting event is scheduled. Then, if all elements in the sequence have at least one candidate interval, subroutine SCHED is called to generate the schedule times. In this case, a successful schedule is assured, because all portions of the candidate interval which would lead to an unsuccessful schedule have been eliminated. In all other respects, the operation of SCHED is identical to the scheduling mode previously discussed.

After the schedule times of a sequence have been determined by SCHED, the executive routine calls subroutine WNEW, which writes the resources available during the schedule times of all events of the sequence in an area of memory (either core or random access memory, depending on the number of words already stored in the area) called the New

Resource Area. WNEW also updates the Resource History to reflect the new values of resources created by scheduling the sequence. If the sequence just scheduled is to be repeated, the subroutine REPFIL is called to delete the portions of the candidate intervals corresponding to the schedule times of the events. If not all candidate intervals are deleted in REPFIL, then the subroutine SEQFIL is called to eliminate the portions of any candidate intervals that do not satisfy the conditions of the sequence (if the sequence contains only one event, SEQFIL is bypassed). The entire process of scheduling the sequence is then repeated until either the required number of repeats have been scheduled, or there are no candidate intervals remaining for some event in the sequence. Then IOZ is incremented by one, and the scheduling process repeated for the next sequence to be scheduled.

When all events that can be are scheduled, three different "payoff" subroutines are called to calculate:

1. Total time to complete the schedule
2. Total time during which some event is scheduled
3. Maximum resource requirement for each resource type
4. Data residual .

If the required number of schedules have been generated, the program stops. Otherwise, the subroutine RESET is called to restore all necessary variables to their original values. Then, the program repeats the preceding operation and generates a new schedule.

## E. Program Status

The Automatic Experiment Scheduling and Optimization Program was developed for use on the UNIVAC 1108 System. The entire program has been checked out using simulated data and approximately six hours of orbital data. Final checkout is presently underway using a sample mission equivalent to fourteen days of orbit.

## REFERENCE

1. Ball, R. F.; Shannon, D. P.; and Kelley, E. H.: Automatic Experiment Scheduling and Optimization Program. TR-796-8-335, Nortronics-Huntsville, April 1968.

## VIII. STATISTICAL ANALYSIS

# NOISE ELIMINATION BY PIECEWISE CROSS CORRELATION OF PHOTOMETER OUTPUTS

By

Fritz R. Krause and Benjamin C. Hablutzel

## ABSTRACT

A piecewise cross-correlation technique has been developed to analyze the outputs of remote detection devices. The purpose of this technique is to eliminate the noise from optical background fluctuations, from transmission fluctuations, and from detectors by calculating the instantaneous product of the detector output and a reference signal. Each noise component causes positive and negative oscillations of the instantaneous product, and may thus be cancelled by an integration of the instantaneous product. The resultant product mean values will then contain the desired information on the spatial and temporal variation of emission, absorption, and scattering processes in the atmosphere.

The piecewise correlation technique differs from previous digital analyses of stationary time series by statistical and temporal variations of product mean values. The statistical variations describe the amount of still uncancelled noise. The range of these variations is calculated by determining the frequency bandwidth of the noise from the decrease of an accumulative statistical error with integration time. The temporal variations of the product mean values describe a change in the meteorological boundary conditions. They are indicated by the calculated errors which exceed the range of statistical variations that is expected for the given noise bandwidth. Furthermore, such temporal variations set a level of irreducible noise components since the uncancelled noise cannot be distinguished from the temporal variations of the meteorological boundary conditions. However, the change of these boundary conditions may very often be suppressed by suitable normalization and trend removal techniques.

The accomplishments thus far provide for automatic piecewise changes of gain factors and coordinate shifts which eliminate intolerable temporal variations of meteorological boundaries provided the signals do not exceed the dynamic range of the amplifier or the tape recorder.

Our recommendations are to continue the present studies on noise elimination in the presence of time-dependent boundary conditions. Particular emphasis should be given to the temporal variations of product mean values which are caused by changes in aerosol concentrations, optical background fluctuations, variations of wind speed and changes of wind direction. Future development of piecewise correlation techniques should be concentrated on noise elimination and interpretation of rapid-scanning remote-detection devices such that optical and meteorological phenomena might be monitored in real time.

## DEFINITION OF SYMBOLS

### 1. Independent Variables

$t$		observation time
$T$		integration time
$\Delta T$		piece length
$i$		piece number ( $t/\Delta T$ )
$m$		accumulation number ( $T/\Delta T$ )
$f$		frequency
$\tau$		time lag between photometer output and reference signal
$\tau_M = \frac{1}{6} \Delta T$		maximum time lag
$k = 1, 2, \dots N$		number of imaginary realizations

## 2. Dependent Variables

I d. c. coupled photometer output

i a. c. coupled photometer output

$x = i_A$  output from photometer A

$y = i_B$  reference signal or output from photometer B

$\sigma$  root mean square value of i

R product mean value of x and y

$\Delta R$  statistical error of product mean value

$\delta R = \frac{\Delta R}{\sigma_x \sigma_y}$  normalized statistical error of product mean value

P power inside frequency interval  $-\frac{1}{4\tau_M} \leq f \leq \frac{1}{4\tau_M}$

$\bar{s}_i = \bar{R}_i$  ordinate shift for piece i

## 3. Operators

( ) Statistic

$\bar{()}_i = \frac{1}{\Delta T} \int_{t_i - \Delta T}^{t_i} ( ) dt$  piecewise mean

$\bar{()}_m = \frac{1}{m} \sum_{i=1}^m \bar{()}_i$  accumulative mean

$\Delta \bar{()}_m^2 = \frac{1}{m-1} \sum_{i=1}^m (\bar{()}_i - \bar{()}_m)^2$  piecewise statistical error

$$\Delta \bar{()}_m^2 = \frac{1}{m} \Delta \bar{()}_m^2$$

accumulative statistical error

$$E[\bar{()}] = \frac{1}{N} \sum_{k=1}^N ( )^{(k)}$$

sample of expected value or ensemble average for one group of N realizations

$$(\sigma^{(1)})^2 = \frac{1}{N-1} \sum_{h=1}^N (\bar{()}(h) - E[\bar{()}])^2$$

sample of variance between realizations

$$\tau \bar{()}_\tau = \frac{1}{2\tau_{\max}} \int_{-\tau_{\max}}^{+\tau_{\max}} \max \bar{()}_\tau d\tau$$

average over time lags

## 4. Subscripts

i time interval (i-1)  $\Delta T \leq t \leq i\Delta T$

m accumulation over all pieces up to i=m

x from record x

y from record y

a straight time integration

w weighting with piecewise variable gains

d detrending with piecewise variable

c ordinate shifts

D combined piecewise shifts and gains

## I. INTRODUCTION

A new "piecewise" correlation technique has been developed to separate statistical variations from temporal environmental variations. The need for such a technique became apparent in crossed beam field tests [1], where the level of the environmental variations exceeded the statistical variations of the correlation curves such that the processing of additional data did not increase the statistical accuracy of the correlation curves. Piecewise modifications of meteorological records have been used successfully to isolate and to partially eliminate temporal variations of meteorological boundary conditions. The same techniques could also be applied to any other remote detection device or any other set of meteorological data.

The noise elimination is based on the integration of a lagged product between the photometer output and a reference signal. Section III gives a review of the usual noise elimination by product integration which is used for stationary time series where the boundary conditions are time-invariant [2]. The piecewise correlation was developed to extend this classical product-mean-value calculation to meteorological boundary conditions which are time dependent. In this case, the calculated product mean values will be subject to both statistical and temporal variations. In theory, temporal and statistical variations could be separated by analyzing a large group of imaginary experiments which should all have identical time dependent boundary conditions [3]. This theory is reviewed in section IV. However, it cannot be applied directly, since meteorological conditions cannot be controlled to give many realizations of the same phenomenon. The best one can hope for is that temporal variations of meteorological conditions are of such a type that suitably modified portions of one long record could be treated as independent realizations. The conditions of stationarity and the results of this approximation are discussed in section V.

Our program is new in that the variations between different piecewise estimated time averages are used to calculate accumulative statistical errors which should depend on the number of processed pieces in a universal way if the replacement of realizations with pieces is justified. Conversely, deviations from this behavior can be used to determine deviations from stationarity as discussed in section VI. Temporal variations of meteorological boundary conditions restrict the noise elimination to the level of the temporal variations, since we cannot distinguish between statistical and temporal

variations of product mean values. Fortunately, suitable normalization and trend elimination procedures are often sufficient to remove the temporal variations of boundary conditions. Piecewise variable ordinate shifts and gain factors have been proposed for trend elimination and normalization [4]. Experience thus far indicates that these piecewise modifications of photometer records were sufficient to remove temporal variations of boundary conditions and thereby increase the ability of noise elimination. The results are summarized in section VII. Conclusions and recommendations are given in section VIII.

## II. NOISE ELIMINATION BY INTEGRATION OVER PRODUCTS

The subdivision of two data records into signal and noise components and the subsequent elimination of the noise are both based on the integration of instantaneous products. This is illustrated in Figure 1 in terms of an idealized physical model that is used for the interpretation of cross-beam results [5]. Two data records,  $I_A(t)$  and  $I_B(t)$ , are obtained by monitoring the fluctuations of the radiative power which are received inside the narrow field of view of the two telescopes A and B. Each time history,  $I$ , accounts for all sources of radiative power along the entire line of sight. The temporal changes of emission, scattering, or absorption processes will cause a fluctuation,  $i$ , in the recorded time history,  $I$ , which may be calculated by subtracting the mean value,  $\bar{I}$ , that is obtained for a certain recording period  $\Delta T$ .

$$\begin{aligned} x(t, \dots) &= I_A(t) - \frac{1}{\Delta T} \int_{t_1}^{t_1 + \Delta T} I_A(t) dt \\ &= I_A(t) - \bar{I}_A(t) \end{aligned} \quad (1)$$

$$y(t, \dots) = I_B(t) - \bar{I}_B(t).$$

In our experiments, this subtraction is done automatically by using a. c. coupled amplifiers. In this case  $\Delta T$  is proportional to the time constant of the a. c. coupling element ( $\approx 100$  seconds).

Local information from the area of minimum beam separation is retrieved from the two signals  $x$  and  $y$  by determining statistically which modulations

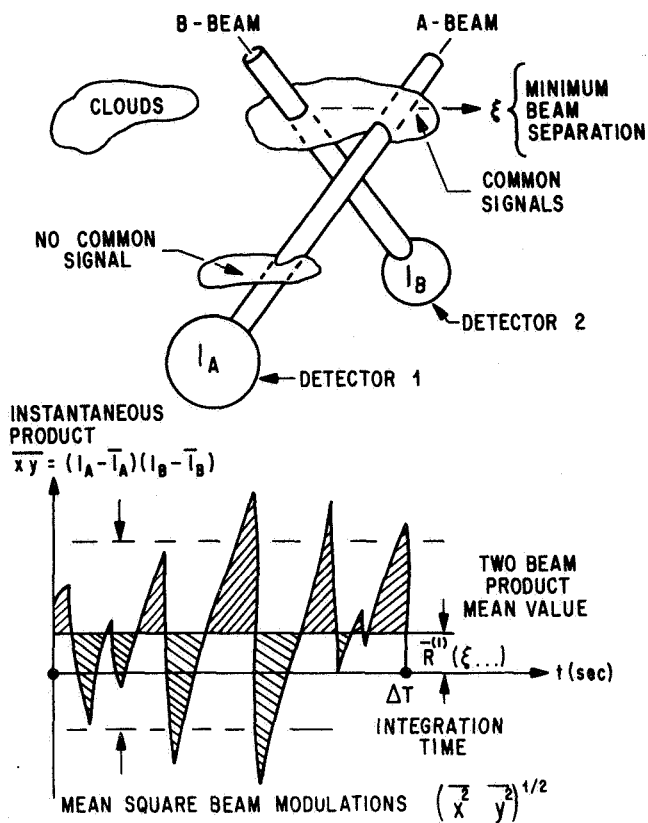


FIGURE 1. RETRIEVAL OF COMMON SIGNALS

are "common" to both beams. The concept of "common" signals developed in the analysis of communication signals and random vibrations [2] is based on "lagged product calculations." The two modulations,  $x$  and  $y$ , are analyzed for common signals by multiplying them with each other and by averaging this instantaneous product over time. This gives a "two-beam" product mean value":

$$\begin{aligned} \overline{R}^{(1)}(t_1; \Delta T; \dots) &= \overline{x(t; \dots)y(t; \dots)}^{(1)} \quad (1) \\ &= \frac{1}{\Delta T} \int_{t_1}^{t_1 + \Delta T} xy \, dt \quad (2) \end{aligned}$$

The instantaneous product oscillates between positive and negative values, and these oscillations will cancel each other, at least partially, when the product is averaged by integrating it over time, as illustrated in Figure 1. Two beams are said to have no common modulations if the two-beam product mean value vanishes. This complete cancellation will occur when the increase or decrease of radiative

power in one beam is independent of the power changes in the other beam in the sense that the change in the other beam may be positive or negative with equal likelihood. Typical examples of such independent beam modulations are the combined source and detector noise and any cloud which traverses only one beam without hitting the other beam. The partial cancellation of the oscillations of the instantaneous product is used to split a given time history  $x(t)$  into a "noise" component,  $x_N$ , and a "common" component,  $x_C$ . Both components are defined only with respect to a second reference signal  $y$ . The noise component  $x_N$  of the first record  $x$  is that component which vanishes when multiplied with the reference signal

$$\overline{x_N y}^{(1)} = 0 \quad (3)$$

Conversely, the "common" component

$$x_C = x - x_N \quad (4)$$

is that component of signal  $x$  which is responsible for the finite value of the product mean value:

$$\overline{xy}^{(1)} = \overline{(x_C + x_N)y}^{(1)} = \overline{x_C y}^{(1)} \quad (5)$$

The second signal could also be split into a common component,  $y_C$ , and a noise component,  $y_N$ , by taking the first signal,  $x$ , as the reference signal:

$$y = y_C + y_N \quad (6)$$

Substituting equation (6) into equation (5), we find that the product mean value is made up only of the common signals.

$$\overline{xy}^{(1)} = \overline{x_C y_C}^{(1)} \quad (7)$$

The integration of the instantaneous product has thus eliminated the "noise" components, and the resultant product mean value is contributed only by the signal component which is common to both data records  $x$  and  $y$ . However, the word "common" does not mean that the components  $x_C$  and  $y_C$  are identical.

It refers only to physical processes which produce similar changes in both signals that may be separated by a delay time. Of course, the more similar the signals become, the larger the magnitude of the correlation. A cloud which traverses two lines of sight

(Fig. 1) is a good example of such a physical process. Although this cloud will cause common changes in both photometer records  $x$  and  $y$ , these changes will be quite different since the two lines of sight intersect different portions of the same cloud.

### III. TEMPORAL AND STATISTICAL VARIATIONS OF PRODUCT MEAN VALUES

The value of a product mean value,  $\bar{R}$ , will depend in general on both the position,  $t$ , of the integration period and on the length,  $\Delta T$ , of the period. The variation with  $t$  reflects a temporal variation of the meteorological boundary conditions such as a change of wind speed and direction or a new type of fog in the area which is common to both lines of sight. The dependence on  $\Delta T$  may also reflect a temporal variation of the common signals. However, it is often more likely that the change is produced by the noise components which are not completely cancelled, since any finite integration period will have only a finite number of oscillations. Such incomplete cancellation of extraneous noises reflects a change which may be classified as statistical, since it is associated with the uncontrollable change of physical phenomena other than the common physical process, i.e., a random change in boundary conditions. Temporal and statistical variations usually occur simultaneously and are therefore very difficult to separate.

A detailed description of temporal and statistical variations of product mean values is possible in theory by treating the actual conducted experiments as one sample of a population of imaginary experiments which are all recorded for identical time-dependent boundary conditions. Assume that  $k = 1, 2, 3, \dots, N$  realizations of the atmospheric field have been observed. Statistical averages may then be established by averaging over the different realizations instead of averaging over time. This "ensemble" average will be denoted by the operator and will be called the "expected value":

$$E[(\ )] = \frac{1}{N} \sum_{k=1}^N (\ )^{(k)} . \quad (8)$$

Let  $x^{(k)}(t)$  and  $y^{(k)}(t)$  denote the photometer records of the  $k$ -th realization. The expected value of the product mean value would then be

$$\begin{aligned} E[\overline{xy}] &= \frac{1}{N} \sum_{k=1}^N \frac{1}{\Delta T} \int_{t_1}^{t_1+\Delta T} x^{(k)}(t) y^{(k)}(t) dt \\ &= \frac{1}{N} \sum_{k=1}^N \overline{x^{(k)} y^{(k)}} = \bar{R} . \end{aligned} \quad (9)$$

The temporal variations of this ensemble average can be determined since the time dependence of  $\bar{R}(t_1; \Delta T, \dots)$  is not cancelled when integrating across the ensemble.

The statistical variations of the experimentally accessible product mean value  $\bar{R}^{(1)}$  can also be established by analyzing the variations between the individual realization,  $k$ , and the expected value.

The "expected" statistical variation of  $\bar{R}^{(1)}$  is provided by a mean-square error calculation, or "variance":

$$\text{Var } \bar{R}^{(1)} = \frac{1}{N-1} \sum_{k=1}^N \left\{ (\ )^{(k)} - E[(\ )] \right\}^2 \quad (10)$$

A sample of the variance between individual mean values is thus given by

$$\begin{aligned} \text{Var } \bar{R}^{(1)} &= \frac{1}{N-1} \sum_{k=1}^N \left\{ \overline{x^{(k)} y^{(k)}} - E[\overline{xy}] \right\}^2 \\ &= \frac{1}{N-1} \sum_{k=1}^N \left( \frac{1}{\Delta T} \int_{t_1}^{t_1+\Delta T} x^{(k)}(t) y^{(k)}(t) dt - \bar{R} \right)^2 . \end{aligned} \quad (11)$$

The associated standard deviation  $(\text{Var } \bar{R}^{(1)})^{1/2}$  describes one likely variation between the individual realization  $\bar{R}^{(k)}$  and the expected value  $\bar{R}$ . Other variations will occur with other probabilities. Fortunately, the practical implications of the central limit theorem are that the probability of mean value variations ought to follow the normal distribution. Knowing such a universal distribution, we can then

calculate a certain limit,  $t_p (\text{Var } \bar{R}^{(1)})^{1/2}$ , which will not be exceeded by the individual variations  $\bar{R}^{(1)} - \bar{R}$  for the fraction  $p$  of all  $N$  realizations. These limits provide a confidence interval for the statistical variation between a single realization,

k = 1, and the expected product mean value. The 80 percent confidence interval would be

$$\begin{aligned} \bar{R}^{(1)} - t_{0.90}(N) (\text{Var } \bar{R}^{(1)})^{1/2} \leq \bar{R} \leq \bar{R}^{(1)} \\ + t_{0.90}(N) (\text{Var } \bar{R}^{(1)})^{1/2} \end{aligned} \quad (12)$$

The "percentile factors" of the normal distribution,  $t_p$ , are listed in Table I.

TABLE I. PERCENTILE FACTORS AND CONFIDENCE INTERVALS FOR STATIONARY RECORDS

Student's t Distribution			$\chi^2$ -Distribution			
m	$t_{0.90}$	$1/\sqrt{m}$	$\chi_{0.90}^2$	$\chi_{0.10}^2$	$\chi_{0.90}/m$	$\chi_{0.10}/m$
2	3.08	0.707	2.71	0.0158	0.823	0.063
3	1.89	0.578	4.61	0.211	0.716	0.153
4	1.64	0.500	6.25	0.584	0.625	0.191
5	1.53	0.447	7.78	1.06	0.558	0.206
6	1.48	0.408	9.24	1.61	0.507	0.211
7	1.44	0.378	10.6	2.20	0.465	0.212
8	1.42	0.353	12.0	2.83	0.433	0.210
9	1.40	0.333	13.4	3.49	0.407	0.208
10	1.38	0.317	14.7	4.17	0.383	0.204
12	1.35	0.288	17.3	5.58	0.347	0.201
14	1.34	0.267	19.8	7.04	0.318	0.190
16	1.33	0.250	22.3	8.55	0.295	0.183
18	1.33	0.236	24.8	10.1	0.277	0.179
20	1.32	0.222	27.2	11.7	0.261	0.174
25	1.32	0.200	33.2	15.7	0.230	0.160
30	1.31	0.183	39.1	19.8	0.028	0.150
61	1.30	0.128	74.4	46.5	0.142	0.112
m $\rightarrow\infty$	1.28	$1/\sqrt{m}$	m	m	$1/\sqrt{m}$	$1/\sqrt{m}$

Accumulative Means

$$\bar{(\bar{r})}_m - t_p \Delta \bar{(\bar{r})}_m \leq E[\bar{(\bar{r})}] \leq \bar{(\bar{r})}_m + t_p \Delta \bar{(\bar{r})}_m$$

Normalized Accumulative Error

$$\frac{\chi_{0.10}}{m\sqrt{B\Delta T}} \leq \delta \bar{R}_m \leq \frac{\chi_{0.90}}{m\sqrt{B\Delta T}}$$

Equation (12) gives the desired estimate for the expected statistical variations of individual product mean values. The associated confidence interval could be calculated if  $\text{Var } \bar{R}^{(1)}$  were accurately known. However equation (11) gives only one sample of this variance. A new group of N realizations would give a different sample of  $\text{Var } \bar{R}^{(1)}$ . The accurate description of the statistical variations should therefore consider not only the variations between individual realizations of a single group but also the variation between different groups of realizations. Let

$(\bar{\sigma}^{(1)})^2$  denote the "population variance" which is calculated by taking the arithmetic mean of all samples of  $\text{Var } \bar{R}^{(1)}$ , i.e., the mean over all groups. The relative variation between the variance estimate from a single group and the average over all groups could then be expressed by the new variable,

$$\chi^2 = \frac{N \text{Var } \bar{R}^{(1)}}{(\bar{\sigma}^{(1)})^2} \quad (13)$$

The probability distribution of this variable is given by another universal distribution function, the  $\chi^2$  distribution. Knowing this distribution, one can calculate a lower limit,  $\chi_{0.10}^2(N)$ , which will be exceeded by the  $\chi^2$  samples of all but 10 percent of the admitted groups. One can also calculate an upper limit,  $\chi_{0.90}^2(N)$ , which will exceed 90 percent of all  $\chi^2$  samples. Both limits together then give a confidence interval for the statistical variation of variance estimates between different groups of realizations. The 80 percent confidence interval would be

$$\frac{N \text{Var } \bar{R}^{(1)}}{\chi_{0.90}^2(N)} \leq (\bar{\sigma}^{(1)})^2 \leq \frac{N \text{Var } \bar{R}^{(1)}}{\chi_{0.10}^2(N)} \quad (14)$$

The percentile factors  $\chi_{0.10}^2$  and  $\chi_{0.90}^2$  are also listed in Table I. For  $N \geq 30$  they may be calculated from the equation [6]

$$\begin{aligned} \chi_p^2 &= \frac{1}{2} \left( z_p + \sqrt{2(N-1) - 1} \right)^2 \\ &= N \left( 1 - \frac{3}{2N} \right) \left( 1 + \frac{z_p}{\sqrt{2N-3}} \right)^2 \end{aligned} \quad (15)$$

In summary, we find that a single group of N realizations can provide the following samples:

1. The expected product mean value  $\bar{R}$ , equation (9).
2. One sample,  $\text{Var } \bar{R}^{(1)}$ , for the desired statistical variations between the individual product mean values from different realizations, equations (11) and (12).
3. The confidence interval for the statistical variations of variance estimates between different groups of N realizations, equation (14).

All of these samples are based on universal distribution functions which are independent of the particular physical process that produces the common signals. This universal behavior may therefore be used

to separate the universal statistical variations of product-mean values from specific temporal variations of these product-mean values. One such possibility is discussed in section VI.

#### IV. STATISTICAL ERROR CALCULATION FOR STATIONARY DATA

Unfortunately, the results of the last section cannot be applied directly to experimental data, since meteorological boundary conditions cannot be adjusted to obtain many realizations of the same meteorological conditions. The alternative then is to assume that the meteorological boundary conditions are sufficiently time invariant during one experiment such that individual pieces of a long record represent statistically independent realizations of these invariant boundary conditions. For this purpose, a long record of length  $T$  is subdivided into  $i = 1, 2, \dots, m$  pieces of length  $\Delta T = T/m$ . The time average over one of these pieces may be expressed by

$$\overline{(\ )}_i = \frac{1}{\Delta T} \int_{t=(i-1)\Delta T}^{t=i\Delta T} (\ ) dt. \quad (16)$$

Each of these piecewise estimates is then treated as if it came from a new realization. This means that the summation over realizations is replaced with a summation over pieces:

$$\begin{aligned} \overline{(\ )}_m &= \frac{1}{m} \sum_{i=1}^m \overline{(\ )}_i = \frac{1}{m\Delta T} \int_0^{m\Delta T} (\ ) dt \\ &= \frac{1}{N} \sum_{k=1}^N (\ )^{(k)} = E[(\ )] \end{aligned} \quad (17)$$

The following conditions [2] must be met to justify this replacement of realizations with pieces.

1. The time history of the statistic " $(\ )$ " is a self-stationary process.
2. The autocovariance function  $z(\tau)$  of this time history meets certain integrability conditions.
3. The individual piece length  $\Delta T$  exceeds the time lag range within which the autocovariance  $z(\tau)$  has become negligibly small.

Experimental data mostly meet the conditions (2) and (3). However, the condition (1) means that the replacement of realizations with pieces is only justified if the temporal variations of the product mean value are negligible. Such time histories are called stationary. For such stationary time series, all remaining variations are statistical. The means that the variations between piecewise averages and the statistical variations between sets of pieces should all follow the universal probability distributions given in the last section. The "fit" of these distributions may thus be used as a criterion for stationarity. One such criterion is developed in the remainder of this section.

The desired criterion for stationarity considers the variations of "accumulative" averages which were defined in equation (17). The accumulative average of product mean values is derived by substituting equation (17) into equation (9).

$$\begin{aligned} \overline{\overline{R}}_m &= \frac{1}{m} \sum_{i=1}^m \overline{(xy)}_i = \frac{1}{T} \sum_{i=1}^m \int_{(i-1)\Delta T}^{i\Delta T} x(t) y(t) dt \\ &= \frac{1}{N} \sum_{k=1}^N \overline{x^{(k)} y^{(k)}} = \overline{R}. \end{aligned} \quad (18)$$

The statistical variations of these accumulative averages are derived from the differences between pieces. A sample for the expected variance  $(\overline{\sigma}^{(1)})^2$  between any two pieces might be derived by substituting equation (17) into equation (10). This gives

$$\begin{aligned} \text{Var } \overline{R}^{(1)} &= \frac{1}{(N-1)} \sum_{k=1}^N \left[ \overline{x^{(k)} y^{(k)}} - \overline{R} \right]^2 \\ &= \frac{1}{(m-1)} \sum_{i=1}^m \left[ \overline{(xy)}_i - \overline{\overline{R}}_m \right]^2 \\ &= \frac{1}{(m-1)} \sum_{i=1}^m (\overline{R}_i - \overline{\overline{R}}_m) = \left[ \Delta \overline{R}_m^{(1)} \right]^2. \end{aligned} \quad (19)$$

The associated standard deviation,  $\Delta R_m^{(1)}$ , will be called "the piecewise error." Any new group of  $m$  pieces or  $m$  realizations would give another sample of the piecewise error. A confidence interval for the statistical variations of piecewise errors between

different groups of pieces is derived by substituting equation (19) into equation (14).

$$\frac{m(\Delta R_m^{(1)})^2}{\chi_{0.90}^2(m)} \cong (\bar{\sigma}^{(1)})^2 \cong \frac{m(\Delta \bar{R}_m^{(1)})^2}{\chi_{0.10}^2(m)} \quad (20)$$

The statistical error of the accumulative mean,  $\Delta \bar{\bar{R}}_m$ , should be much smaller than the error of a piecewise mean,  $\Delta \bar{R}_m$ , since the statistical variations between pieces will partially cancel each other during the summation. For stationary data the reduction will be equal to  $1/m$  since the cancellation accounts for  $m$  independent realizations of the same experiment. A sample of the mean square error of an accumulative mean is thus given by:

$$\begin{aligned} (\Delta(\bar{\bar{R}})_m)^2 &= \frac{1}{m} (\Delta(\bar{R})_m)^2 \\ &= \frac{1}{m(m-1)} \sum_{i=1}^m \left[ (\bar{R})_i - (\bar{R})_m \right]^2 \end{aligned} \quad (21)$$

The associated standard deviation,  $\Delta \bar{\bar{R}}_m$ , will be called "the accumulative error." Any new group of  $m$  pieces or  $m$  realizations would give a new sample of the accumulative error. A confidence interval for the statistical variations between these groups is derived by substituting equation (21) into equation (20) and by dividing with  $m$ . The result is

$$\frac{m(\Delta \bar{\bar{R}}_m)^2}{\chi_{0.90}^2(m)} \cong \frac{(\bar{\sigma}^{(1)})^2}{m} \cong \frac{m(\Delta \bar{R}_m)^2}{\chi_{0.10}^2(m)} \quad (22)$$

In most applications the accumulative error is normalized with the product of the accumulative root mean square values

$$\delta \bar{\bar{R}}_m = \frac{\Delta \bar{\bar{R}}_m}{\overline{(x^2)}_m^{1/2} \overline{(y^2)}_m^{1/2}} \quad (23)$$

The confidence interval for the normalized accumulative errors follows by dividing equation (23) with the product of the accumulative root mean square values:

$$\begin{aligned} \frac{m(\delta \bar{\bar{R}}_m)^2}{\chi_{0.90}^2(m)} &\cong \frac{(\bar{\sigma}^{(1)})^2}{\overline{(x^2)}_m^{1/2} \overline{(y^2)}_m^{1/2}} \\ &\cong \frac{m(\delta \bar{R}_m)^2}{\chi_{0.10}^2(m)} \end{aligned} \quad (24)$$

Expressing the population variance of piecewise means in terms of a "noise" bandwidth  $B$ ,

$$(\bar{\sigma}^{(1)})^2 = \frac{\overline{(x^2)}_m \overline{(y^2)}_m}{B \Delta T} \quad (25)$$

and substituting this definition into the last inequality, we find

$$\frac{m(\delta \bar{\bar{R}}_m)^2}{\chi_{0.90}^2(m)} \cong \frac{1}{BT} \cong \frac{m(\delta \bar{R}_m)^2}{\chi_{0.10}^2(m)} \quad (26)$$

However, the two factors  $m/\chi_{0.90}^2$  and  $m/\chi_{0.10}^2$  both asymptotically approach the value 1 according to equation (14). Therefore equation (25) gives the well known result that the relative statistical error of a product mean value should decrease with the inverse square root of integration time.

$$\delta \bar{\bar{R}}_m = \frac{\Delta \bar{\bar{R}}_m}{\overline{(x^2)}_m^{1/2} \overline{(y^2)}_m^{1/2}} \rightarrow \frac{1}{(BT)^{1/2}} \quad (26a)$$

Direct calculations of the accumulative statistical error  $\Delta \bar{\bar{R}}_m$  may thus be used to determine the noise bandwidth  $B$  from the asymptotic decrease of this error with the inverse square root of integration time. Furthermore, the knowledge of this bandwidth can then be used to calculate the confidence levels for the relative accumulative error. Rearranging the two inequalities of equation (25), we obtain

$$\frac{\chi_{0.10}(m)}{m \sqrt{B \Delta T}} \cong \delta \bar{\bar{R}}_m \cong \frac{\chi_{0.90}(m)}{m \sqrt{B \Delta T}} \quad (27)$$

Figure 2 illustrates such a direct calculation of the confidence interval that is expected for stationary data. This example employs product mean values from a cross-beam test in a supersonic jet. The abscissa is given by the inverse square root of integration time  $T$  or accumulation number  $m = T/\Delta T$ .

The ordinate gives the relative statistical error which was calculated from equation (21). The actual data follow a straight line through the origin very closely as predicted by equation (26a). The slope of this line gives a noise bandwidth of  $B = 22\,276$  cps. This noise bandwidth has been used to calculate the confidence intervals according to equation (27) and Table I. All directly calculated statistical errors fall into this interval. We can thus say that the probability is better than 80 percent that the entire record was stationary.

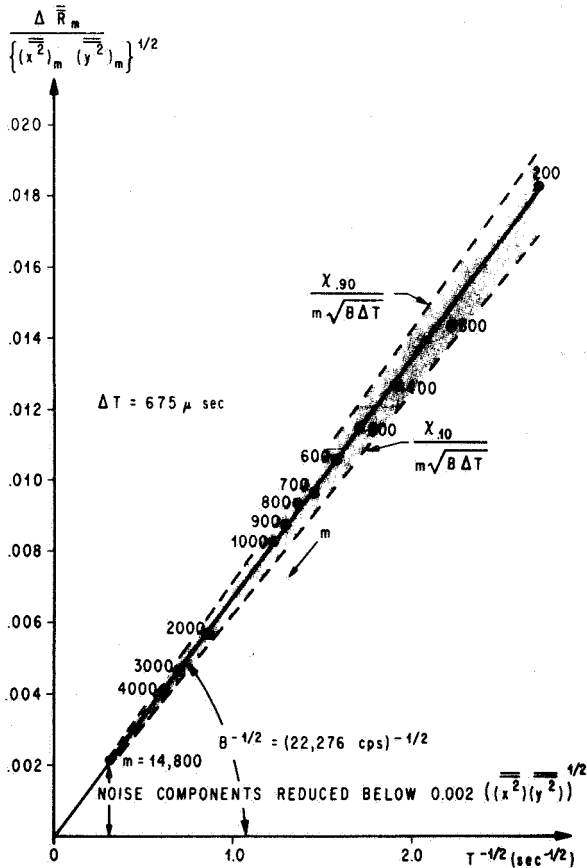


FIGURE 2. NOISE ELIMINATION FOR STATIONARY WIND TUNNEL DATA

By processing  $m = 14\,800$  pieces, it was also possible to reduce the statistical error  $\Delta_m R$  of the accumulative product mean value  $\bar{R}_m$  to 0.2 percent of the mean square value of the actually recorded

integrated signals. This demonstrates the surprising power of digital correlation techniques to retrieve very small signals out of noise. The successful development of the associated "piecewise" correlation computer program and the success of cross-beam detection of wind profiles and turbulence parameters in subsonic and supersonic jets [7] with the program provided the basis and the starting point for extending crossed-beam measurements into the atmosphere.

## V. DEVIATIONS FROM STATIONARITY AND IRREDUCIBLE NOISE

Fluctuation measurements with winds, humidity, and temperature sensors on meteorological towers indicate that the power spectra of these fluctuations may contain significant energy for frequencies down to 0.01 cps, i.e., for periods as long as 2 minutes. The length of one piece should be two to five realizations of the same meteorological conditions. We chose a piece length of  $\Delta T = 450$  seconds = 7.5 minutes for most of our work. At least 5 to 30 different realizations of a physical phenomenon are then required to establish the level or irreducible noise components and nonstationarities from the statistical variations between these pieces.

We have chosen to illustrate the noise and stationarity analysis for a marginal case where only six pieces are available. The test conditions and the photometer records  $x(t)$  and  $y(t)$  are shown in Figure 3. The piecewise means of photometer output "A",  $\bar{x}_i$  are shown in Figure 4a, together with the accumulative mean  $\bar{x}_6$  of these means. Furthermore, the statistical error of the individual piecewise mean,  $\Delta \bar{x}_6$ , is added and subtracted from each piecewise mean. The striking observation is that the mean of piece 6 makes a sudden jump so large that it exceeds the statistical errors. In case of stationary data, the different values of the piecewise means should stay within the confidence interval given by equation (12). The observed large jumps fall, however, outside such an interval; therefore, it is unlikely that these jumps are of a statistical origin. One should rather anticipate sudden changes in the meteorological boundary conditions.

The deviation from stationarity which is anticipated because of the large jump of the sixth piecewise mean is clearly indicated by the accumulative error of these means. These errors were calculated

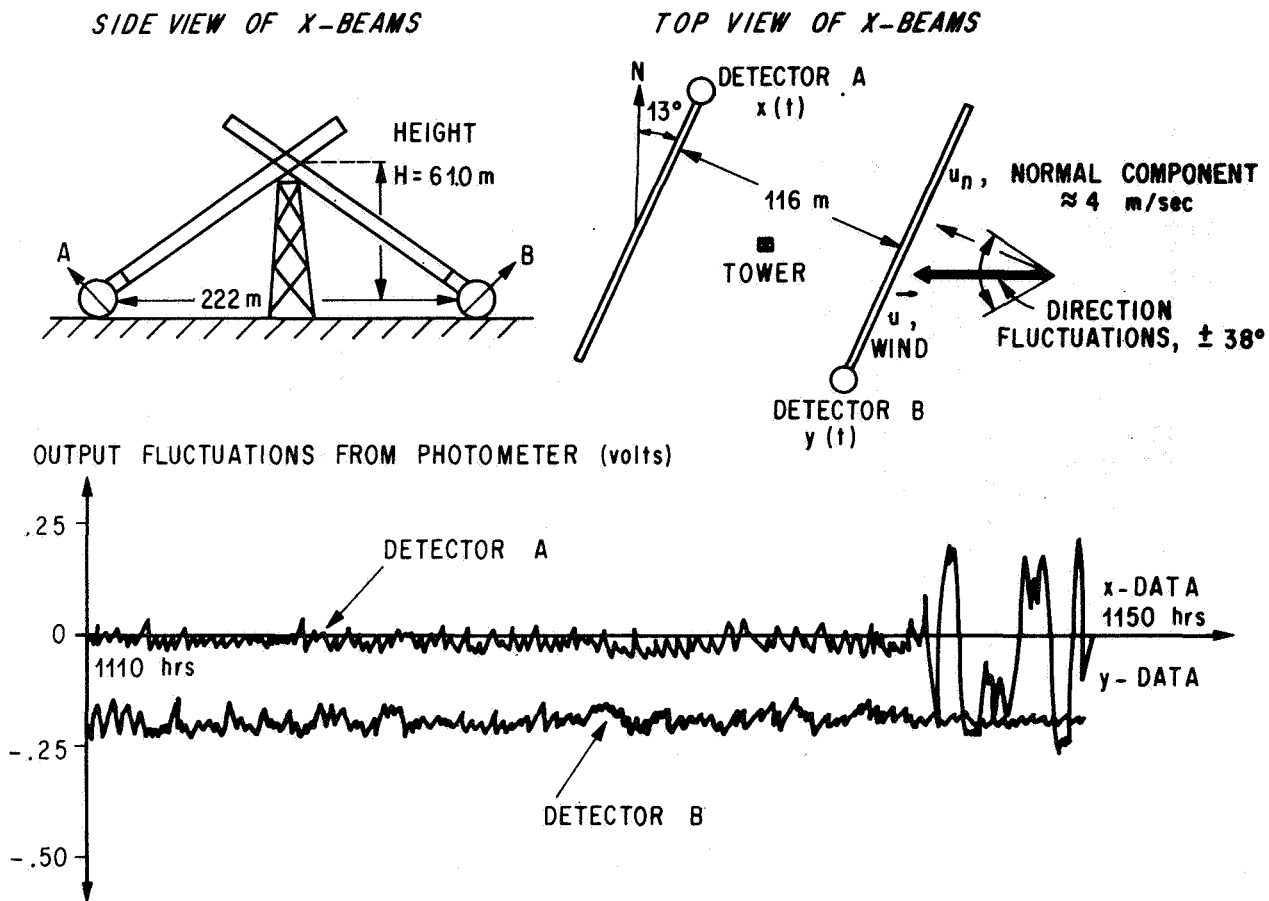


FIGURE 3. EXAMPLE OF CROSS-BEAM EXPERIMENT

according to equation (21) and plotted against  $T^{-1/2}$  as shown in Figure 4b. The expected stationary process was then defined by fitting the calculated points with a straight line through the origin. The slope of this line gives a noise bandwidth of  $B = 0.19$  cps which is then used to calculate the 80 percent confidence interval according to equation (27). However, the directly calculated errors increase suddenly between pieces 5 and 6 and exceed the confidence interval. This exceedance illustrates clearly the deviation from stationarity that was anticipated from the above visual inspection of Figure 4a.

The exceedance of the confidence interval can be used to define and analyze a deviation from stationarity in many different ways. Figure 4b illustrates the simplest of all classifications, which completely disregards the shape of the actual error curve. A period of a record is called stationary if the accumulative error falls within the 80 percent confidence interval of the expected stationary process. Conversely, a period of a record is called nonstationary if the calculated errors exceed the expected

confidence interval. The experience which was gained with this classification is summarized in Table II.

The second important aspect of the accumulative error curves is the estimate of the irreducible amount of noise. Such an analysis is based on the results of the last section which should apply within a period of stationarity. According to the discussion of equations (9) and (11), the accumulative statistical error will be contributed predominantly by the uncanceled noise components, since the meteorological boundary conditions are time invariant in a period of stationarity. The finite extent of the period of stationarity means, therefore, that an irreducible amount of noise exists which is equal to the lower limit of the accumulative statistical error inside the given period. The calculation of statistical error curve,  $\Delta \bar{R}_m(T)$ , will therefore provide a direct estimate of the irreducible noise for each period of stationarity as illustrated in Figure 4b.

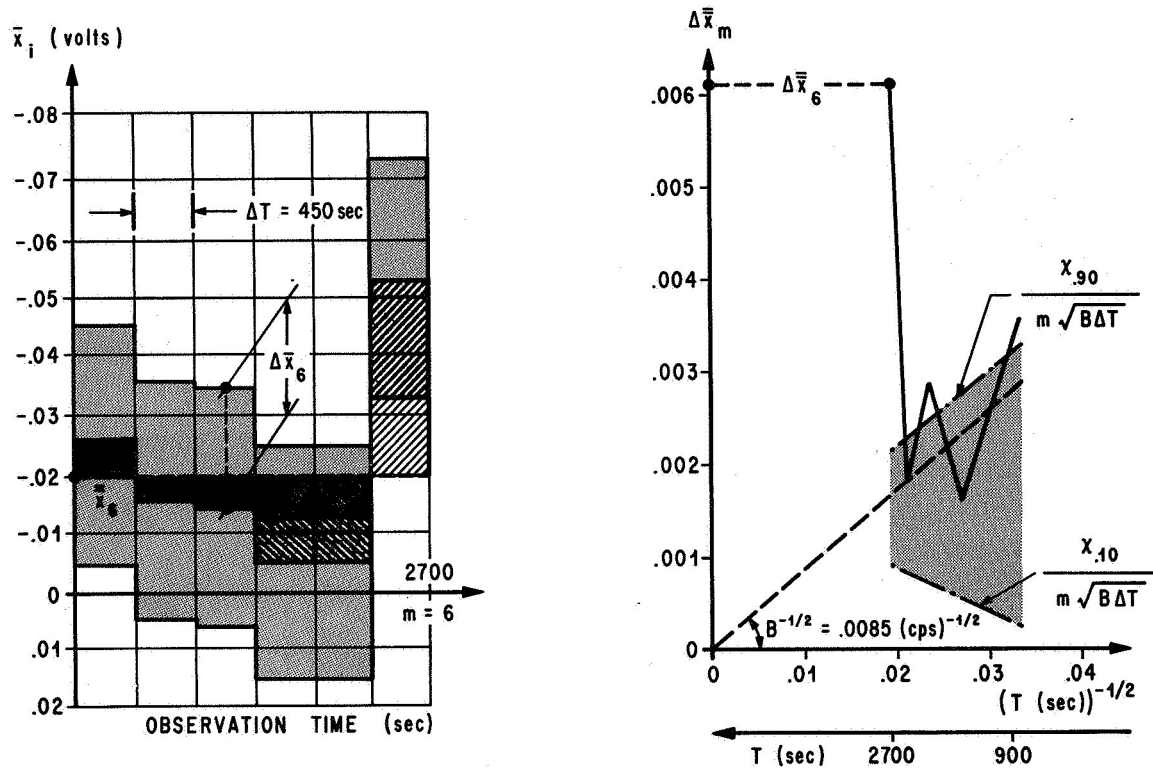


FIGURE 4. PIECEWISE MEANS AND ACCUMULATIVE STATISTICAL ERROR OF PHOTOMETER OUTPUT X

TABLE II. PRELIMINARY EXPERIENCE ON TEMPORAL PRODUCT MEAN VALUE VARIATIONS

Run	$T_{\max}$ (sec)	B (cps)	Straight Time Integration				Piecewise Gain Change			
			$T_1$ (sec)	$T_2$ (sec)	$\frac{T_1 - T_2}{T_{\max}}$ (%)	$(\delta R)_{\min}$	$T_1$ (sec)	$T_2$ (sec)	$\frac{T_1 - T_2}{T_{\max}}$ (%)	$(\delta R)_{\min}$
A	6 750	0.063	NA	NA	0	NA	0	6 750	100	0.050
B	4 050	0.044	NA	NA	0	NA	0	4 050	100	0.067
C	4 500	0.045	3600	4500	20	0.078	0	4 500	100	0.052
D	7 200	0.063	2250	7200	62	0.060	0	7 200	100	0.046
E	3 240	0.063	NA	NA	0	NA	0	3 240	100	0.065
F	4 950	0.012	0	4950	100	0.060	450	4 950	91	0.045
G	4 500	0.111	NA	NA	0	NA	0	4 500	100	0.044
H	10 350	0.250	NA	NA	0	NA	0	10 350	100	0.019
I	2 700	0.063	NA	NA	0	NA	0	2 700	100	0.040

$T_1$  = start of stationary period

$T_2$  = end of stationary period

NA = not applicable

$\frac{T_2 - T_1}{T_{\max}}$  = percentage of stationarity

## VI. PARTIAL REMOVAL OF TEMPORAL VARIATIONS BY PIECEWISE ORDINATE SHIFTS AND GAIN FACTORS

The existence of an irreducible amount of noise would be fatal to crossed-beam experiments if this irreducible noise exceeds the small levels of the common signal. However, the results of the last section imply that the "irreducible" amount is inversely proportional to the length of the period of stationarity. If one could partially remove the temporal variations of the meteorological boundary conditions, then the amount of "irreducible" noise might be further reduced by allowing a longer period of stationarity. In other words, the term "irreducible" applies only to a straight time integration as described by equation (16). Averaging procedures other than straight time integration might provide smaller "irreducible" noise levels by removing the time-dependence of boundary conditions through suitable normalization and trend elimination procedures. Jayroe and Su proposed the concept of "accumulative" means which differ from straight time integration by employing piecewise variable ordinate shifts and gain factors [4]. The applications of these shifts and gains will now be discussed for the same test run that has already been used.

A piecewise variable ordinate shift may be described as an attempt to remove large scale (i. e., low frequency) trends. Consider lagged product mean values which differ from the product mean values of equation (2) only by delaying signal  $x$  relative to signal  $y$ :

$$\bar{R}_i(\tau) = \frac{1}{\Delta T} \int_{(i-1)\Delta T}^{i\Delta T} x(t-\tau) y(t) dt . \quad (28)$$

This lagged product mean value (or temporal correlation function) is calculated for equally spaced time lags and truncated at a time lag

$$\tau_{\max} = \frac{1}{6} \Delta T .$$

Figure 5a shows such a piecewise estimated correlation function for piece 1 of our test run (Fig. 3). The ordinate of this correlation curve shall then be shifted by an amount  $P_i(0)$  which makes the area under the shifted curve vanish.

$$P_i(0) = \frac{1}{2\tau_{\max}} \int_{-\tau_{\max}}^{+\tau_{\max}} \bar{R}_i(\tau) d\tau . \quad (29)$$

This ordinate shift is equal to the cross power inside the narrow frequency band:

$$\begin{aligned} -\frac{1}{4\tau_M} &\leq f \leq \frac{1}{4\tau_M} : \\ \Delta f \cdot S(f \rightarrow 0) &= \frac{1}{2\tau_M} \cdot \lim_{f \rightarrow 0} \int_{-\infty}^{+\infty} \bar{R}_i(\tau) e^{-i2\pi f\tau} d\tau \\ &= \frac{1}{2\tau_M} \int_{-\infty}^{+\infty} \bar{R}_i(\tau) d\tau = P_i(0) . \end{aligned} \quad (30)$$

The ordinate shift  $\bar{P}_i(0)$  therefore removes all power at frequencies below  $1/4\tau_M$ , i. e., all slowly varying trends. The ordinate shift may thus be described as a piecewise trend elimination method. The application of this detrending procedure leads to the following accumulation average:

$$(\bar{R}_m)_d = \frac{1}{m} \sum_{i=1}^m [\bar{R}_i - \bar{P}_i(0)] . \quad (31)$$

Figure 5b shows the ordinate shifts,  $\bar{P}_i(0)$ , which have been calculated for the six pieces of our test run. These shifts oscillate between positive and negative values in such a way that the accumulative shift,  $\bar{P}_m(0)$ , stays very small. Apparently, the temporal variations of product mean values (Fig. 5c) may be insignificant, although the temporal variations of the mean values (Fig. 4a) are large.

Piecewise ordinate shifts are effective in removing trends. However, in many cases the temporal variations of the boundary conditions will also cause changes at higher frequencies. One change that was observed often is a piecewise jump of fluctuation amplitudes. The average fluctuation amplitude,  $\sigma$ , for a piece is given by the root mean square value,

$$\bar{\sigma}_{xi}^2 = \frac{1}{\Delta T} \int_{(i-1)\Delta T}^{i\Delta T} x^2 dt . \quad (32)$$

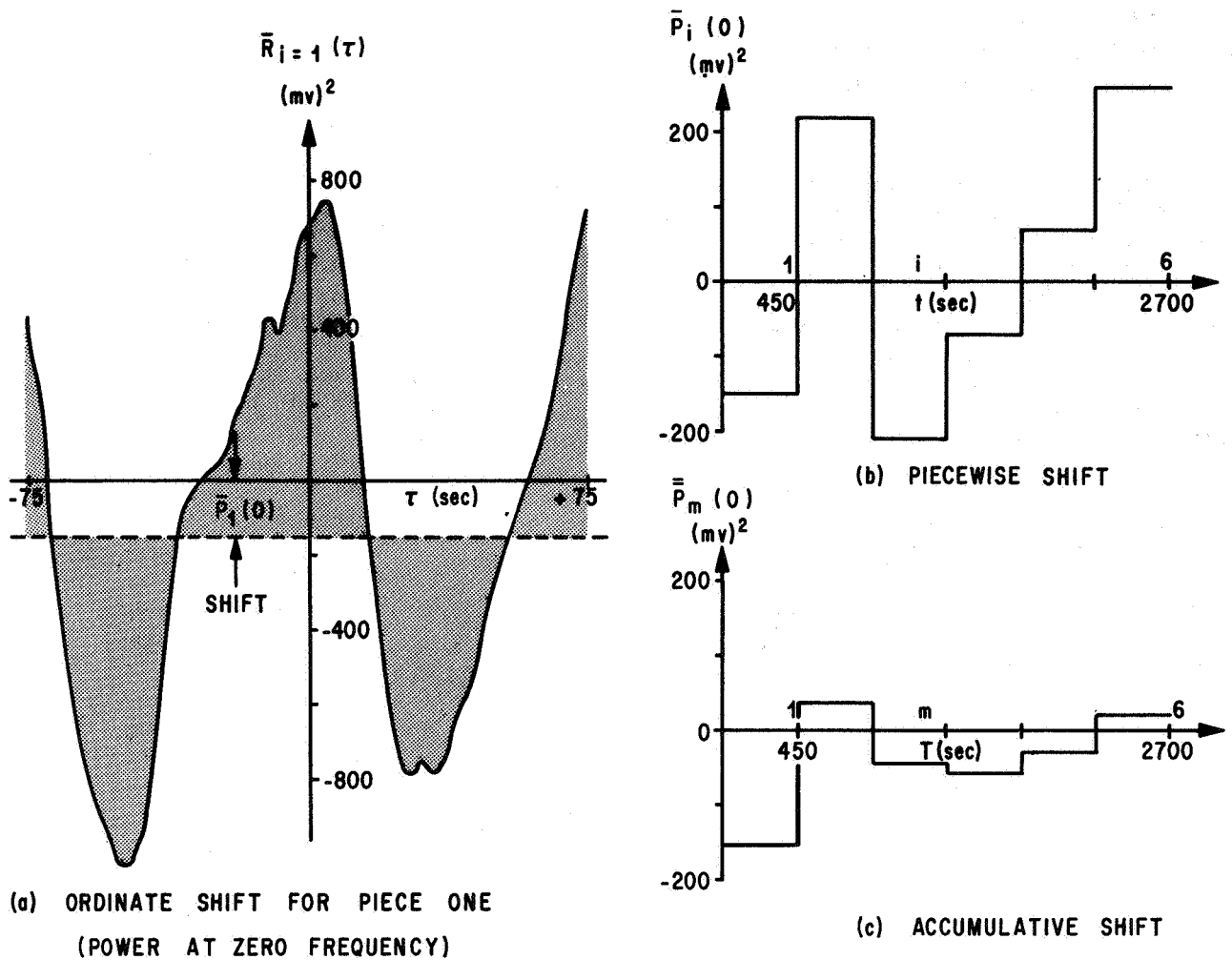


FIGURE 5. REMOVAL OF LOW FREQUENCY COMPONENTS THROUGH PIECEWISE ORDINATE SHIFTS

Temporal variations of fluctuation amplitude are then indicated by the variations of this root mean square value. Figure 6 illustrates this variation for the test run. The temporal variation of the boundary condition that was discovered (Fig. 4b) also apparently causes a large jump of the amplitude between pieces 5 and 6. However, the effect of this jump could be minimized by normalizing with the associated root mean square value. This would reduce the fluctuations of the normalized signal  $x/\bar{\sigma}_{xi}$  to the level of the previous pieces. The opposite would be true with a piece that is characterized by a sudden decrease of fluctuation levels. Temporal variations of signal amplitudes can thus be suppressed effectively by using a piecewise variable gain factor which is proportional to  $1/\sigma_i$ . Such a nondimensional

gain factor has been defined by multiplying  $1/\bar{\sigma}_i$  with the accumulative root mean square value,

$$\bar{\sigma}_m^2 = \frac{1}{m} \sum_{i=1}^m \bar{\sigma}_i^2 \quad (33)$$

The application of this gain,  $\bar{\sigma}/\bar{\sigma}_i$ , leads to a new type of accumulative average which may be denoted by

$$(\bar{R}_m)_w = \frac{\bar{\sigma}_{xm} \bar{\sigma}_{ym}}{m} \sum_{i=1}^m \frac{\bar{R}_i}{\bar{\sigma}_{xi} \bar{\sigma}_{yi}} \quad (34)$$

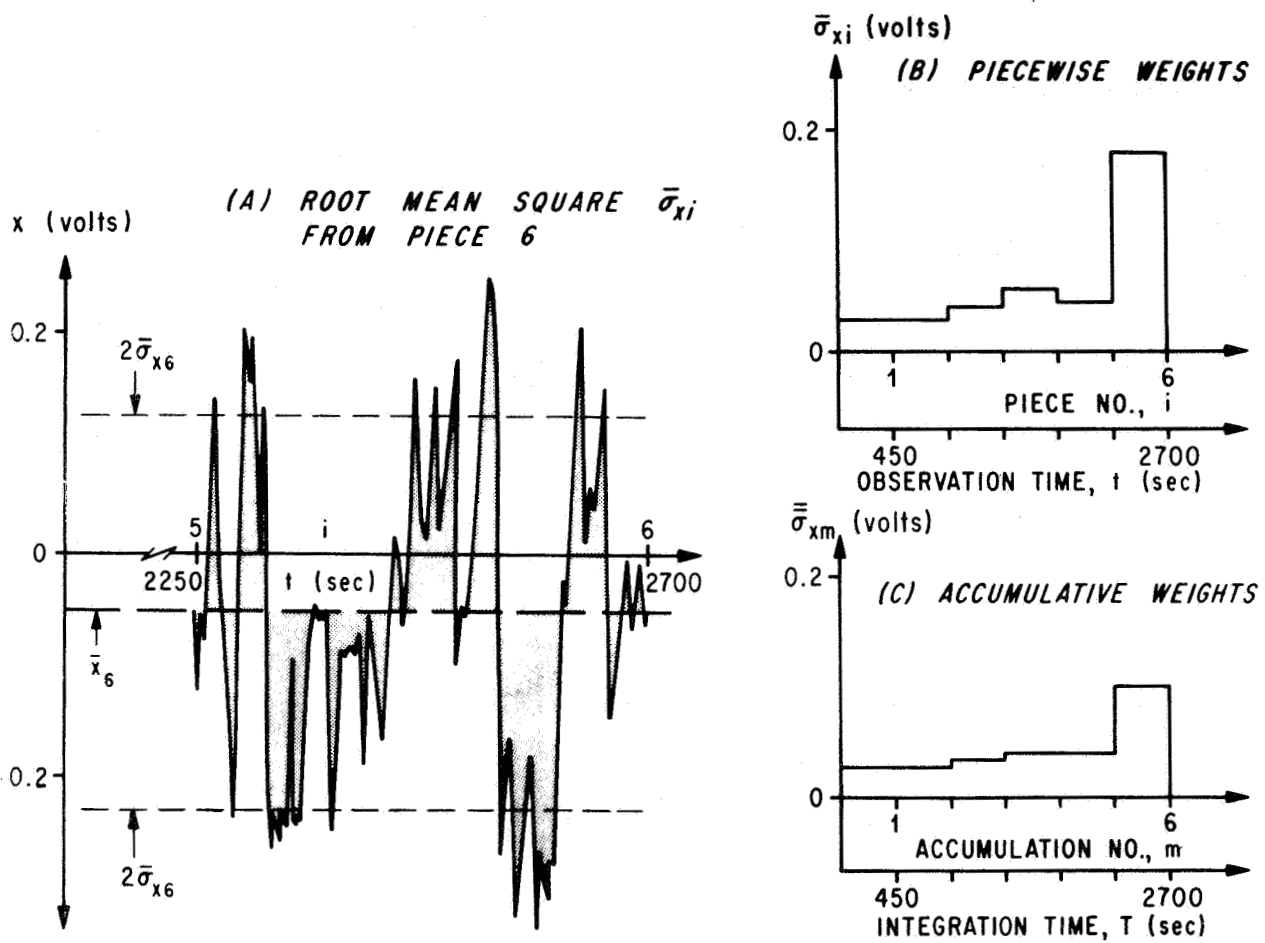


FIGURE 6. PIECEWISE GAINS

Combined weighting and detrending gives a fourth type of accumulative average:

$$(\bar{\bar{R}}_m)_c = \frac{\bar{\sigma}_{xm} \bar{\sigma}_{ym}}{m} \sum_{i=1}^m \frac{\bar{R}_i - \bar{P}_i(0)}{\bar{\sigma}_{xi} \bar{\sigma}_{yi}} \quad (35)$$

All of these different accumulation procedures may be summarized by the use of a unified accumulative average,

$$\bar{\bar{R}}(\tau; m; \dots) = \frac{\bar{\sigma}_{xm} \bar{\sigma}_{ym}}{m} \sum_{i=1}^m \frac{\bar{R}_i - \bar{s}_i}{\bar{\sigma}_x \bar{\sigma}_y} \quad (36)$$

which allows for a three choice of gain factors,  $\bar{\sigma}/\bar{\sigma}$ , and ordinate shifts,  $\bar{s}$ . The various options that have been tried to this date are characterized by the following choices:

Straight time integration: subscript a

$$\sigma_x = \bar{\sigma}_{xm}; \quad \sigma_y = \bar{\sigma}_{ym}; \quad \bar{s}_i = 0.$$

Piecewise detrending: subscript d

$$\sigma_x = \bar{\sigma}_{xm}; \quad \sigma_y = \bar{\sigma}_{ym}; \quad \bar{s}_i = P_i(0).$$

Piecewise weighting: subscript w

$$\sigma_x = \bar{\sigma}_{xi}; \quad \sigma_y = \bar{\sigma}_{yi}; \quad \bar{s}_i = 0.$$

Combined detrending and weighting: subscript c

$$\sigma_x = \bar{\sigma}_{xi}; \quad \sigma_y = \bar{\sigma}_{yi}; \quad \bar{s}_i = P_i(0).$$

The value of these choices may be judged from the behavior of the associated accumulative statistical error,

$$\begin{aligned} \delta \bar{R}(\tau; T; m)^2 &= \left( \frac{\Delta \bar{R}(\tau, T, m)}{\bar{\sigma}_x \bar{\sigma}_y} \right)^2 \\ &= \frac{1}{m(m-1)} \sum_{i=1}^m \left[ \frac{\bar{R}_i - \bar{s}_i - (\bar{R}_m - \bar{s}_m)}{\bar{\sigma}_x \bar{\sigma}_y} \right]^2 \end{aligned} \quad (36a)$$

The desired accumulation procedure should suppress the temporal variation of meteorological boundary conditions. According to section VI this suppression may be judged by fitting the tail (m large) of the error curve with a straight line. The best accumulation procedure is the one that gives the best fit. Furthermore, the slope of that line gives the noise bandwidth, B, of the piecewise modified noises and can be used to calculate the confidence interval for the entire error curve from equation (27). The whole procedure is illustrated in Figure 7 for the test run and differs from the illustration given in Figure 4 in the following aspects:

1. The statistical error refers to product mean values, not mean values.

2. The time lag dependence of the product mean value has been cancelled by integration:

$$\tau \delta \bar{R}(T, m)^2 = \frac{1}{2\tau_{\max}} \int_{-\tau_{\max}}^{+\tau_{\max}} \delta \bar{R}(\tau; T; m)^2 d\tau. \quad (37)$$

3. Four different error curves have been calculated using the different options for piecewise shifts and gains that were identified above by the subscripts a, d, w and c.

SYMBOL	ACCUMULATION METHOD
●	STRAIGHT TIME INTEGRATION $(\bar{R})_i = \bar{R}_i; \quad \sigma = (\bar{x}^2)_m^{1/2}; (\bar{y}^2)_m^{1/2}$
□	PIECEWISE GAINS $(\bar{R})_i = \bar{R}_i; \quad \sigma = (\bar{x}^2)_m^{1/2}; (\bar{y}^2)_m^{1/2}$
■	PIECEWISE SHIFTS $(\bar{R})_i = \bar{R}_i - \bar{P}_i(0); \quad \sigma = (\bar{x}^2)_m^{1/2}; (\bar{y}^2)_m^{1/2}$
▲	COMBINED PIECEWISE GAINS AND SHIFTS $(\bar{R})_i = \bar{R}_i - \bar{P}_i(0); \quad \sigma = (\bar{x}^2)_m^{1/2}; (\bar{y}^2)_m^{1/2}$

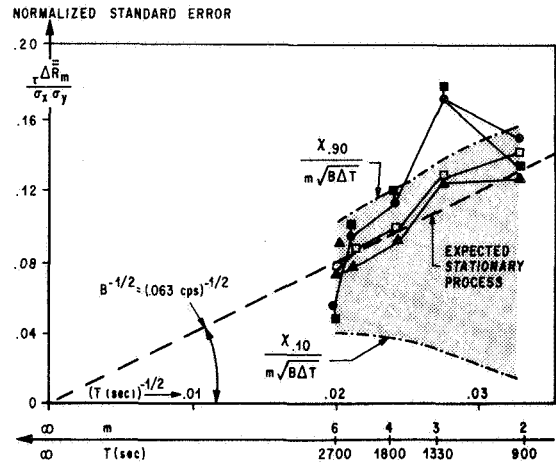


FIGURE 7. APPLICATION OF PIECEWISE SHIFTS AND GAINS TO TEST RUNS

The straight time integration curve a indicates that both the beginning and the end of the record are strongly affected by temporal variations of the boundary conditions. These variations cannot be described by low frequency trends since the piecewise detrending, curve d, is not effective to alter the shape of the error curve. Only the use of piecewise gains produces error curves (c and a) which approximate a straight line through the origin. The slope of this line gives a bandwidth  $B = 0.063$  cps which in turn is used to calculate the confidence interval  $\chi/m\sqrt{B\Delta T}$ . Both curves w and c fall into this interval; i.e., the piecewise modified photometer records are stationary with a probability exceeding 80 percent. The smallest error of these curves,  $\tau \delta \bar{R} \approx 0.075$ , gives then the irreducible amount of noise that is left after accumulating over a period of  $T = 45.00$  minutes = 2700 seconds. A further noise reduction would require a longer record.

The use of piecewise gains proved to be a very powerful tool in cases where the meteorological boundary conditions were known to be highly time invariant. One of the more dramatic changes of meteorological conditions under clear skies is the change of wind direction. Figure 8 provides an example of piecewise gain changes for moderate fluctuations of wind directions ( $\pm 22^\circ$ , run H). Without piecewise gains, we get a curve that fits the confidence interval; however, this curve does not exhibit the desired straight line fit. The use of piecewise gains improves the approximation of a stationary record significantly and also slightly improves the noise elimination. Figure 9 provides an example for extreme temporal variations of boundary conditions ( $\pm 180$  degrees, run A). The wind was blowing from all directions during the recording period. In this case, the straight time integration produces an error curve which does not resemble a stationary process at all. However, even in this extreme case, the use of piecewise gains proves sufficient to eliminate the temporal fluctuations of product mean values.

Our preliminary experience with the application of piecewise correlation methods indicates that temporal variations of product mean values occur quite frequently for observation periods between 1/2 and 2 hours. Table II gives a summary of the first 9 runs where statistical and temporal product mean value variations were separated. In six out of nine runs, the temporal variations of stationarity did not exist at all. Two of the six cases are illustrated in Figures 7 and 9.

For record lengths up to 2 hours, the use of piecewise gains and ordinate shifts has always been sufficient to remove temporal variations of product mean values provided that the amplifier or tape recorder is not driven into saturation by these temporal variations. Saturation by a large temporal variation of meteorological conditions, however, always occurred and was the dominant factor which determined the maximum record length, T. Elimination of this saturation problem should allow longer recording times and thereby contribute to a further reduction of noise below the values of  $(\delta R)_{\min}$  that are listed in Table II.

## VII. CONCLUSIONS AND RECOMMENDATIONS

The piecewise correlation technique was developed to eliminate noise in the output of remote

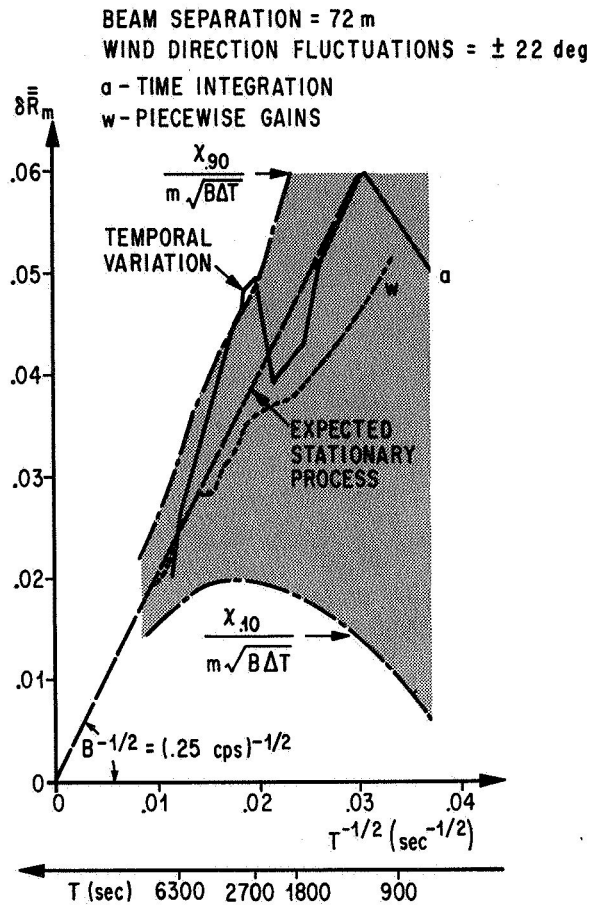


FIGURE 8. REMOVAL OF TEMPORAL PRODUCT MEAN VALUE VARIATIONS WITH PIECEWISE GAINS, RUN H

detection devices. The noise is reduced by multiplying the photometer output with a reference signal and by integrating this instantaneous product over time. This method is quite common for stationary time series where the boundary conditions of the experiment are time invariant. The piecewise correlation technique is new, in that it extends the elimination of noise to meteorological boundary conditions which are time dependent. The simple time integration of products cannot reduce the noise level below the level of temporal variations, since one cannot distinguish between statistical and temporal variations of the product mean value.

The mathematical theory of product mean value variations is based on the difference between a large group of imaginary experiments, all of

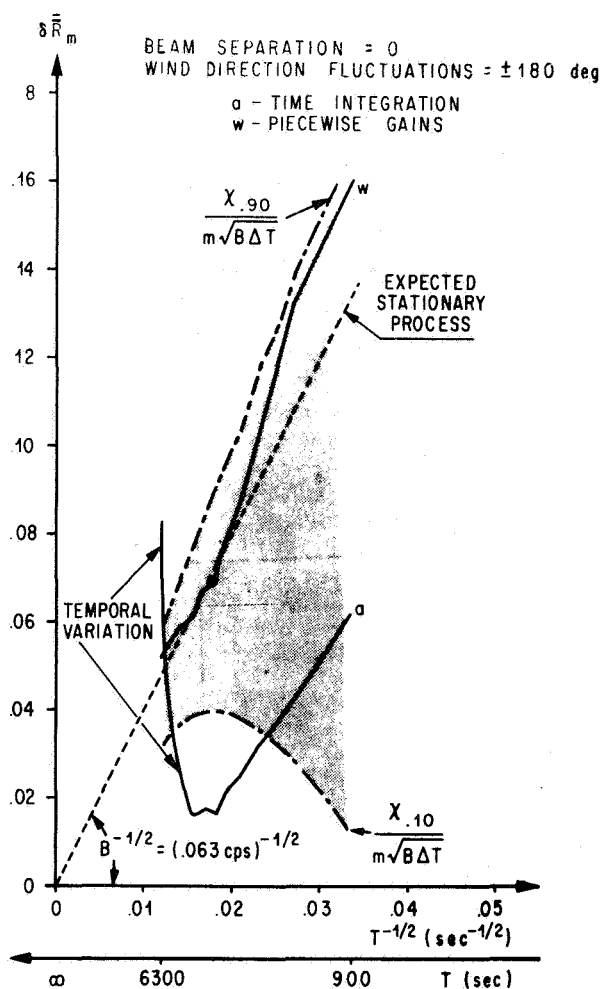


FIGURE 9. REMOVAL OF TEMPORAL PRODUCT MEAN VALUE VARIATIONS WITH PIECEWISE GAINS, RUN A

which have the same time dependent boundary conditions. This theory cannot be applied directly since meteorological conditions cannot be controlled to repeat themselves many times. However, individual pieces of a long record may often be normalized and detrended in such a way that the resultant piecewise modified data behave as if they belonged to independent realizations of the same meteorological boundary conditions. Piecewise correlation techniques are thus based on the premise that we can, in most cases, find suitable piecewise modifications of the photometer outputs and the reference signal which produce two new signals that are stationary although the experiment itself is quite nonstationary.

The effect of piecewise modifications of the photometer outputs may be judged by curve-fitting the resultant accumulative error curve with a straight line. The modifications have been successful if the accumulative error decreases linearly with the inverse square root of integration time. The slope of the straight line fit gives the frequency bandwidth of the noise components which one wishes to suppress. Knowing this bandwidth, one can also calculate a confidence interval that should contain most of the calculated statistical errors. Temporal variations of product mean values are then indicated by those errors which fall outside this confidence interval.

The experience gained with piecewise correlation techniques indicates that significant temporal variations of product mean values do occur quite frequently (50 percent of all runs). However, these temporal variations have been removed successfully by using piecewise changes of gain factors and piecewise ordinate shifts. The proposed automatic changes of gains and ordinates are thus suitable piecewise modifications. They have successfully reduced the temporal variations of product mean values below the level of the statistical variations in all cases where the temporal variations of the meteorological boundary conditions did not drive the amplifier or the tape recorder into saturation.

The piecewise correlation technique provides a new tool that can distinguish between statistical and temporal variations of product mean values. The statistical variations are due to the still uncanceled noise and the temporal fluctuations are caused by a temporal change in meteorological boundary conditions. We recommend continuing the present studies of noise elimination in the presence of time-dependent meteorological boundary conditions. Particular emphasis should be given to the temporal variations of product mean values which are caused by changes in aerosol concentrations, optical background fluctuations, variations of wind speeds and changes of wind direction.

The above recommendation is based on the technical problems that were encountered in our first cross-beam field tests. These problems and the proposed solutions may be described as follows.

Temporal variations of local scattering process were frequently observed under clear skies which are so large that both the a. c. amplifiers and tape recorders are driven into saturation. Amplifier

saturation is being reduced by installing a new coupling circuit with a stepwise variable time constant that is triggered by the incoming signal. Tape recorder saturation will be eliminated by replacing the analog recorder with an on-line digital data logging system.

Temporal variations of the optical background radiation were caused by distant clouds and haze which drift through the photometer's field of view. The associated background noise far exceeds the signal contributions from the desired target layers and may be so large that it cannot be reduced sufficiently by integration of products. In crossed-beam tests these background fluctuations have been suppressed by pointing the telescopes to the horizon beneath the cloud level. Infrared photometer systems are now being assembled which should suppress the background fluctuations by setting the monochromator bandpass to a spectral region where the optical path length terminates below the cloud level.

Temporal variations of wind speeds have often caused the dominant temporal variations of product mean values. One promising approach to eliminating noise in the presence of speed fluctuation is to replace the photometer output with its time derivative. The correlation of time derivatives is being used to retrieve the probability density of wind component fluctuations.

Large temporal variations of wind directions change the altitudes where the common signals originate. A single-beam fan arrangement is being assembled which sets a fan of six narrow fields of view by mounting a plurality of photodiodes in the focal plane of the collector optics. A new piecewise correlation program is being coded for multi-channel operation to process the output from several detectors simultaneously. The fan system will then be used to study the altitude distribution of the common signals and the restrictions on altitude resolution that are imposed by large wind direction changes.

A successful elimination of noise in the presence of time-dependent meteorological boundary conditions would provide an opportunity to extend remote detection techniques to the description of dynamic phenomena such as winds and turbulence. In particular, the theory of a rapid scanning crossed-beam system [8] indicates that wind and turbulence profiles could conceivably be monitored in real time with a single fly-by. Furthermore, a crossed-beam system mounted on an airplane or a satellite moves so rapidly that temporal variations of wind speed and wind direction

should no longer interfere with the noise elimination [9]. Our recommendation for future studies is therefore to develop piecewise correlation techniques and onboard computer systems for rapid-scanning remote-detection devices such that space and time variations of optical and meteorological phenomena might be monitored in real time in regions where balloons are not available.

We hope to continue our present field test programs to collect design information that could be used for the development of rapid-scanning remote detection devices. The long range objective of these field tests is to isolate the space-time variations of local emission, absorption and scattering processes at various altitudes and to determine the irreducible amount of noise which is imposed by the variations of the meteorological boundary conditions. The design of airplane instrument packages and of on-line computer systems should be initiated as soon as the results of the continued field tests indicate the feasibility of such a step.

## REFERENCES

1. Stephens, J. B. and Sandborn, V. A.: Remote Wind Detection with the Crossed Beam Method at Tower Heights. Presented at AIAA Conference on Aerospace Meteorology (New Orleans), May 5-9, 1968.
2. Bendat, J. S., and Piersol, A. G.: Measurement and Analysis of Random Data. John Wiley & Sons, 1966.
3. Crandall, S. H., and Mark, W. D.: Random Vibrations in Mechanical Systems. Academic Press, 1963.
4. Jayroe, R. R., and Su, M. Y.: Optimum Averaging Times of Meteorological Data with Time Dependent Means. Presented at AIAA Conference on Aerospace Meteorology (New Orleans), May 5-9, 1968.
5. Krause, F. R.: Mapping of Turbulent Fields by Crossing Optical Beams. Presented to American Physical Society, Div. of Fluid Mech. (Bethlehem, Pa.), November 1967.
6. Spiegel, M. R.: Theory and Problems of Statistics. Schaum Pub. Co., 1961.

7. Fisher, M. J. and Krause, F. R.: The Crossed Beam Correlation Method. *J. Fluid. Mech.*, Vol. 28, 1967, p. 705.
8. Krause, F. R., Hu, S. S., and Montgomery, A. J.: On Cross Beam Monitoring of Atmospheric Winds and Turbulence with Two Orbiting Telescopes. NASA TM X-53538, 1966.
9. St. John, A. D. and Blauz, W. D.: Study of Atmospheric and AAP Objectives of Cross Beam Experiments. NASA CR-61191, 1968.

## IX. PUBLICATIONS AND PRESENTATIONS

## A. Publications

### TECHNICAL NOTE D-4033

July 1967

#### ESTIMATION IN MIXED FREQUENCY DISTRIBUTIONS

By A. Clifford Cohen, Jr.

University of Georgia  
Institute of Statistics  
Athens, Georgia

L. W. Falls

George C. Marshall Space Flight Center  
Marshall Space Flight Center, Alabama 35812

#### ABSTRACT

In the analysis of atmospheric data, distributions which are asymmetrical or multimodal are often encountered. These distributions are usually composed of two or more distinct homogeneous subpopulations and are designated as "mixed" or "compound" frequency distributions.

The problem of estimating parameters in a mixed distribution is of considerably greater complexity than that of estimation in a single unimodal distribution. Not only is it necessary to estimate the parameters of each component, but the proportionality factors, which express the proportion or percentage of each component in the mixture, must also be estimated. In the case of a mixture consisting of  $K$  components each having two parameters, there are  $3K-1$  parameters to be estimated in the resultant distribution.

Karl Pearson solved such a problem as early as 1894 for a compound normal population, using the method of moments. The problem was investigated later, first by Charlier, and then in a joint effort by Charlier and Wicksell, who greatly simplified the theory.

The papers presented in this document are concerned with estimation in compound distributions and are the results of an investigation performed by the Institute of Statistics, University of Georgia, Athens, Georgia, as a part of NASA contract NAS 8-11175 with the Terrestrial Environment Branch, Aerospace Environment Division, Aero-Astroynamics Laboratory, NASA-George C. Marshall Space Flight Center, Huntsville, Alabama. Dr. A. C. Cohen, Jr., is the principal investigator and the NASA contract monitors are Mr. O. E. Smith and Mr. L. W. Falls.

The methods and procedures presented are practical and are applicable to experiments in which the data exhibit qualities that require a mixed distribution as the statistical model.

### TECHNICAL MEMORANDUM X-53634

July 14, 1967

#### AEROELASTIC LOAD GROWTH EFFECTS ON SATURN CONFIGURATIONS

By James G. Papadopoulos

George C. Marshall Space Flight Center  
Marshall Space Flight Center, Alabama 35812

#### ABSTRACT

The effects of aerodynamic loads induced by static aeroelasticity are analyzed for the Saturn configurations. This aeroelastic load growth is shown, for any given Mach number, to increase at an accelerated rate with increases in dynamic pressure. During the period of high dynamic pressure, the Saturn control requirements due to aeroelastic effects are significant. The unexplained external body moments recorded during the Saturn I Block II flights are correlated to aeroelastic load growth. Local aerodynamic bending moments are increased at a time in flight when the vehicle loadings are already large and near design limits. This aeroelastic load growth is additional to that of flexible bending mode dynamics and should be included when analyzing wind profiles for vehicle loadings.

## TECHNICAL MEMORANDUM X-53639

July 31, 1967

### A PERFORMANCE STUDY FOR THE APPLICATION OF THE SATURN V TO HIGH ENERGY EARTH ESCAPE MISSIONS

By Ronald G. Toelle

George C. Marshall Space Flight Center  
Marshall Space Flight Center, Alabama 35812

#### ABSTRACT

The results of a performance survey for the application of the product-improved Saturn V launch vehicles to various escape energies are presented. Two upper stage (S-II/S-IVB) propulsion systems (J-2 and J-2S) were investigated. Exchange ratios of payload with respect to vehicle parameters versus  $C_3$  (twice the energy per unit mass) are presented for a  $C_3$  range of 0 to  $125 \text{ km}^2/\text{sec}^2$ . The effect of booster variations and proposed vehicle improvement for different missions can be mapped into the payload through the judicious use of the exchange ratios. These data are primarily for use as a guide to payload planning for various earth escape and interplanetary missions. The results of this performance survey are presented graphically.

## TECHNICAL MEMORANDUM X-53640

July 31, 1967

### SOME PROPERTIES OF LOW ALTITUDE ATMOSPHERIC TURBULENCE AT CAPE KENNEDY, FLORIDA

By James R. Scoggins

George C. Marshall Space Flight Center  
Marshall Space Flight Center, Alabama 35812

#### ABSTRACT

Low altitude scalar wind speed data from NASA's 150-meter meteorological tower at the Kennedy Space

Center, Florida are analyzed for 6 selected cases, one during stable, and five during neutral or slightly unstable stability conditions. The analysis includes mean wind profiles, intensity of turbulence, auto- and lag-cross-correlations, integral length and time scales of turbulence, and spectra. The results are interpreted in terms of the problem of space vehicle response to ground winds.

## TECHNICAL MEMORANDUM X-53641

July 31, 1967

### AN ANALYSIS OF THE MOLECULAR KINETICS OF THE THERMOSPHERE PROBE

By James O. Ballance

George C. Marshall Space Flight Center  
Marshall Space Flight Center, Alabama 35812

#### ABSTRACT

A Monte Carlo computer analysis of the free molecular flow characteristics of the thermosphere probe used to measure gas temperature and density in the altitude range of 140 kilometers to 350 kilometers is described. The transmission probability which is required to relate the ambient density to the measured density is calculated for a simplified geometric configuration which compares well with measured signals except at high angles of attack where the simplified model of the system fails. The time response of the system seems to be adequate for the mode of measurements, and comparison with measured signals indicates that the incoming molecules made no more than 1 specular reflection if, indeed, any at all.

## TECHNICAL MEMORANDUM X-53642

July 31, 1967

### WAKE AND INTERREFLECTION EFFECTS IN THE CALCULATION OF FREE MOLECULAR FLOW DRAG COEFFICIENTS

By James O. Ballance

George C. Marshall Space Flight Center  
Marshall Space Flight Center, Alabama 35812

## ABSTRACT

A Monte Carlo technique has been applied to the problem of calculating drag coefficients in free molecule flow where one body shields a second body from the incoming flow and where multiple collisions with the bodies are allowed. First, the applicability of the Monte Carlo approach is demonstrated showing that it produces compatible results with other theories considering various parameters such as the accommodation coefficient, the mode of reflection, the angle of attack, etc. Then, a system of two coaxial circular discs are studied showing the effects of shielding of one body by another, and the effects of multiple collision. Although the interaction effects of the system always tended to decrease the drag coefficients, for practical purposes, they could be ignored. It was also shown (1) that hyperthermal flow-type calculations can be modified slightly to assume some small divergence in the flow which is dependent on the speed ratio and (2) that modifications will provide very good agreement to the wake effects observed in the Monte Carlo solution.

## TECHNICAL MEMORANDUM X-53643

July 31, 1967

### A METHOD OF SOFT TETHER STATIONKEEPING

By B. S. Perrine, Jr.

George C. Marshall Space Flight Center  
Marshall Space Flight Center, Alabama 35812

## ABSTRACT

This report considers the motion of one spacecraft in a near-circular orbit which is fastened to another with a flexible tether line. The equations of motion are obtained through a closed form solution to the approximate differential equation. A method is

devised by which pulls can be made on the tether in a repeatable sequence so that the two spacecraft will remain in the vicinity of one another when there are differential drag forces acting on them. This method is then applied to the case of a Lunar Module/Apollo Telescope Mount (LM/ATM) tethered to an S-IVB Orbital Workshop (OWS).

## TECHNICAL MEMORANDUM X-53644

August 8, 1967

### AN ALGORITHM FOR THE DETERMINATION OF THE DEFINITENESS OF A REAL SQUARE MATRIX

By Russell M. Hayes, Jr.

George C. Marshall Space Flight Center  
Marshall Space Flight Center, Alabama 35812

## ABSTRACT

An algorithm is described whereby the definiteness property of a real square matrix may be easily computed. The technique is based on well known theorems of matrix algebra which have been modified slightly to permit easy manual or machine computation.

A FORTRAN program using the algorithm was written and was run on both the IBM 1130 and the SDS 930 digital computers. The computation time for a  $7 \times 7$  matrix was approximately one second on the IBM 1130 and much less than one second on the SDS 930.

## TECHNICAL MEMORANDUM X-53650

August 28, 1967

### ON DYNAMICS OF TWO CABLE-CONNECTED SPACE STATIONS

By Frank C. Liu

George C. Marshall Space Flight Center  
Marshall Space Flight Center, Alabama 35812

## ABSTRACT

Presented is an analysis of the dynamic problems of two cable-connected space stations rotating about an axis normal to their orbital plane to provide artificial gravity. The dynamics of cable-connected stations in which the cable tension is zero (non-opening case) are not treated herein. Differential equations of vibration of the elastic cable and the angular moments of the stations are derived. These motions are coupled through the nonhomogeneous boundary conditions of the cable. This mathematical difficulty is resolved by using the concept of concentrated fictitious masses. The cable equation is solved by using Galerkin's approach for both free and forced oscillations. A general  $n$ th order determinantal frequency equation of free vibration of the system is obtained. The responses of the space stations to applied time-varying moments are presented in analytical forms.

## TECHNICAL MEMORANDUM X-53654

September 8, 1967

### SOME FLIGHT MECHANICS CONSIDERATIONS FOR THE VOYAGER MISSION

By Clyde D. Baker, James C. Blair,  
and Wilton E. Causey

George C. Marshall Space Flight Center  
Marshall Space Flight Center, Alabama 35812

## ABSTRACT

Four aspects of Aero-Astrodynamic Laboratory studies of the Voyager mission are discussed as presented in a status review to Center management. The four areas are (1) the effects of Earth-Mars-Sun geometry on launch opportunities, (2) the influence of trajectory design requirements on the Voyager mission, (3) present performance capabilities of the Saturn V Voyager vehicle, and (4) the proposed launch vehicle load relief control system.

## TECHNICAL MEMORANDUM X-53655

September 14, 1967

### A PROPOSED HYPOTHETICAL EXPLORATION MISSION IN THE FLAMSTEED CRATER REGION OF THE MOON

By Otha H. Vaughan, Jr.

George C. Marshall Space Flight Center  
Marshall Space Flight Center, Alabama 35812

## ABSTRACT

A hypothetical 14-day lunar surface mission is proposed for two astronauts to investigate the lunar terrain and larger features about a preselected landing site. Because the Surveyor I spacecraft soft-landed in the Flamsteed Crater region and demonstrated that an unmanned spacecraft can safely land in this particular area, this site will, for purposes of this paper, be considered a suitable site in which to carry out a proposed scientific exploration mission. The proposed mission will be supported by a lunar shelter (to be landed up to six months before the manned landing) which will serve both as a shelter and a communications center with the earth. A small roving vehicle will be used for manned traverses within a radius of eight kilometers about the shelter, and a flying vehicle will be used for flights up to 30 kilometers away. Scientific instrumentation will be provided for experiments in several disciplines. The geological and geophysical investigations include (1) sample collection, seismic, magnetic, and gravity surveys, and long-term tidal and quake measurements, and (2) measurements of radiation, temperature, micrometeoroid flux, etc. An engineering investigation on the Surveyor I spacecraft and its components will also be conducted.

## TECHNICAL MEMORANDUM X-53656

September 22, 1967

### STATIC AERODYNAMIC CHARACTERISTICS OF THE ABORTED APOLLO-SATURN V VEHICLE

By Robert M. Glasgow<sup>1</sup>

George C. Marshall Space Flight Center  
Marshall Space Flight Center, Alabama 35812

## ABSTRACT

This report, which supersedes TM X-53587, presents the revised static aerodynamic characteristics of the aborted Apollo-Saturn V vehicle. These data are based primarily on wind tunnel tests of scale models. Total normal and axial force characteristics with local normal force, local axial force, and local pressure distributions necessary for performance, control, and basic structural analyses of the vehicle are presented. All results are presented for various Mach numbers between 0 and 3.0 and vehicle angle-of-attack variations between 0 and 16 degrees.

---

1. Northrop Space Laboratories, Huntsville, Alabama

## TECHNICAL MEMORANDUM X-53657

September 25, 1967

### STATIC AERODYNAMIC CHARACTERISTICS OF THE APOLLO-SATURN IB VEHICLE

By Billy W. Nunley

George C. Marshall Space Flight Center  
Marshall Space Flight Center, Alabama 35812

## ABSTRACT

The revised static aerodynamic characteristics of the Apollo-Saturn IB vehicles to be used for control, performance and structural analyses are presented. These data are based primarily on wind tunnel tests of scale models. Total vehicle, vehicle components, lift-off, separation, and second stage aerodynamic characteristics are included. Total vehicle aerodynamics include static stability characteristics, axial force characteristics, load distributions, and pressure distributions. These data are presented at various angles of attack and Mach num-

bers, with the exception of pressure and axial force coefficient distributions, which are presented at zero angle of attack. Vehicle components included are command module, launch escape system, and fins.

## TECHNICAL MEMORANDUM X-53661

September 28, 1967

### LUNAR ENVIRONMENT: DESIGN CRITERIA MODELS FOR USE IN LUNAR SURFACE MOBILITY STUDIES

By Otha H. Vaughan, Jr.

George C. Marshall Space Flight Center  
Marshall Space Flight Center, Alabama 35812

## ABSTRACT

The photographic data obtained by the Ranger (VII, VIII and IX), the Surveyor I, the Orbiter I, II and III, and Russia's Luna IX and XIII space vehicles have been analyzed and interpreted in the development of lunar terrain models for use in the design of lunar roving vehicles. An attempt has been made to make the design criteria as realistic as possible with the information now available from these lunar probes. As additional information about the lunar surface is gained from additional flights of the Surveyor series, these models will be re-evaluated and revised whenever necessary.

## TECHNICAL MEMORANDUM X-53663

October 17, 1967

### WIND COMPARISON ANALYSIS OF PIBAL VERSUS ANEMOMETER

By Michael Susko

George C. Marshall Space Flight Center  
Marshall Space Flight Center, Alabama 35812

## ABSTRACT

The differences of lower atmosphere wind velocities obtained by a mast-mounted anemometer and 10-gram pilot balloons (pibals) are discussed. Wind velocity measurements were made by an anemometer mounted at the 15.24 meter level on a mast; whereas, simultaneous wind measurements were calculated from time referenced pibal photographs taken as the pibals passed the anemometer.

The absolute value of the mean difference in wind speed is  $0.53 \text{ m sec}^{-1}$  whereas the RMS value is  $0.62 \text{ m sec}^{-1}$ . The absolute value of the mean difference in wind direction is 4.9 degrees, while the RMS value is 5.6 degrees.

The data were obtained from forty experiments during 1966 and 1967 at Marshall Space Flight Center, Alabama.

### TECHNICAL MEMORANDUM X-53668

November 1, 1967

#### ENVIRONMENT OF MARS: AN INTERPRETATION OF ATMOSPHERIC AND SURFACE CHARACTERISTICS

Edited by Otha H. Vaughan, Jr., and  
D. K. Weidner

George C. Marshall Space Flight Center  
Marshall Space Flight Center, Alabama 35812

## ABSTRACT

A realistic definition of the Mars environment that is based on observational data and theoretical considerations is presented. Many atmospheric and surface models have been postulated for the much-observed planet; however, most of these models are based on specific types of earth-based observational data (thermal, spectographic, photographic, radar)

or purely theoretical considerations of both. This report has made use of these types of data, along with data from Mariner IV, to develop atmospheric and surface models which are more consistent with all presently available data. The editors believe that these models are the most realistic for use as design criteria guidelines at the present time.

This document supersedes the following Technical Memoranda:

TM X-53167, "The Martian Environment," dated November 1964.

TM X-53484, "The Atmosphere of Mars: A Derivation of Engineering Design Parameters," dated June 29, 1966.

### TECHNICAL MEMORANDUM X-53673

November 20, 1967

#### STRUCTURAL DEFORMATIONS IN THE SATURN INSTRUMENT UNIT

By Larry A. Kiefling

George C. Marshall Space Flight Center  
Marshall Space Flight Center, Alabama 35812

## ABSTRACT

During the Saturn V dynamic test, local deformations of significant amplitude were measured at the flight sensor locations in the instrument unit. These local deformations were previously thought to be negligible. The cause is identified as a radial force component at the joint of the LM adapter cone and the instrument unit cylindrical shell due to the axial resultants from the bending moment. The deformation patterns for a shell analysis of the structure are shown. The local deformation is found to be proportional to the bending moment only and the proportionality constant is determined for three instrument locations. Typical amplitudes for Saturn V modes and a selection of points from the Saturn IB dynamic test program are presented.

## TECHNICAL MEMORANDUM X-53674

November 22, 1967

### COMPARISON OF THE ATLAS/CENTAUR (SURVEYOR) AND IGM GUIDANCE CONCEPTS

By W. G. Green and W. B. Tucker

#### ABSTRACT

The current IGM guidance concept and the Atlas/Centaur (Surveyor) guidance concept are both quite capable of performing the guidance functions associated with (1) injection into near-circular earth orbits ranging outward to synchronous altitude, or highly eccentric earth orbits; (2) injection into lunar or interplanetary transfer orbits; (3) deboost into orbit about a planetary body, and (4) deboost into a landing ellipse (assuming no atmosphere) from which soft-landing procedures may be initiated. Neither concept in its current form is considered capable of performing midcourse corrections nor orbit modification maneuvers in general, unless a data link is used to supply steering parameters directly for these maneuvers.

---

This document presents the results of work performed by Lockheed's Huntsville Research & Engineering Center, while under subcontract to Northrop Space Laboratories (NSL PO 5-09287) in support of the Aero-Astrodynamics Laboratory of Marshall Space Flight Center (MSFC) Mission Support Contract NAS8-20082. This task was conducted in response to the requirement of Appendix E-1, Schedule Order No. 50.

## TECHNICAL MEMORANDUM X-53677

November 28, 1967

### SURVEY AND COMPARATIVE ANALYSIS OF CURRENT GEOPHYSICAL MODELS

By Jesco von Puttkamer

George C. Marshall Space Flight Center  
Marshall Space Flight Center, Alabama 35812

#### ABSTRACT

By using currently accepted constants of geodesy, notably several different sets of oblateness coefficients, seven models of the geometry of the earth and its gravitational field, including the currently valid NASA Standard Model, are numerically derived and compared with each other and with a newly developed geoid based on recent measurements of the secular and periodic perturbations of artificial satellite orbits.

## TECHNICAL MEMORANDUM X-53690

January 3, 1968

### AN ANALYSIS OF THE ROUGHNESS LENGTH ASSOCIATED WITH THE NASA 150-METER METEOROLOGICAL TOWER

By George H. Fichtl

George C. Marshall Space Flight Center  
Marshall Space Flight Center, Alabama 35812

#### ABSTRACT

The surface roughness length at the NASA 150-meter meteorological tower located at KSC is determined as a function of wind direction. The roughness length estimates, which were calculated with wind profile laws consistent with the Monin and Obukhov similarity hypothesis, were determined for thirty-nine wind and temperature profiles. Most of the cases were obtained during the hours of 0700 and 1600 EST, and the duration of each test ranged between one-half to one hour. The mean wind speed data were obtained at the 18- and 30-meter levels, and the mean temperature data were obtained at the 18- and 60-meter levels. For those wind directions  $\theta$  in the ranges of  $0^\circ \leq \theta < 150^\circ$ ,  $180^\circ \leq \theta < 240^\circ$ , and  $300^\circ \leq \theta < 360^\circ$  the roughness length is 0.23 m; for those wind directions in the ranges  $150^\circ \leq \theta < 180^\circ$  and  $240^\circ \leq \theta < 300^\circ$ , the roughness length has the values 0.51 m and 0.65 m, respectively.

## TECHNICAL MEMORANDUM X-53571

January 9, 1968

### FEASIBILITY STUDIES OF A SHORT DURATION HIGH REYNOLDS NUMBER TUBE WIND TUNNEL

By John W. Davis and Hal S. Gwin

George C. Marshall Space Flight Center  
Marshall Space Flight Center, Alabama 35812

#### ABSTRACT

A relatively inexpensive short duration test facility is described in which extremely high Reynolds number flows are practical in the subsonic, transonic, and supersonic speed ranges. Basically, the method described is a type of blowdown wind tunnel in which the air storage vessels have been replaced by a long tube filled with high pressure gas. Upon bursting of a diaphragm, a short duration steady flow is achieved behind the centered rarefaction fan which propagates into the supply tube. Useful testing may be accomplished during this period by expanding the gas to the desired test condition by conventional means.

Experimental results are presented indicating primarily the transient starting characteristics of a small scale pilot model facility tested. Experimentally determined test data showed close agreement with those predicted by unsteady expansion theory.

## TECHNICAL MEMORANDUM X-53693

January 11, 1968

### A COLLECTION OF PAPERS RELATED TO PLANETARY METEOROLOGY

By Don K. Weidner

George C. Marshall Space Flight Center  
Marshall Space Flight Center, Alabama 35812

## ABSTRACT

The scientific papers contained in this document represent a one-year effort of the MSFC planetary atmosphere study program. Emphasis was placed upon the Mars atmosphere because of MSFC involvement in the Voyager program, but in view of the decline in interest for planetary exploration, the emphasis is now being placed upon the upper earth atmosphere. However, since the planetary atmosphere study program was established with versatility in mind, the techniques used in generating Mars atmospheric information may also be applied to the earth's atmosphere.

The first three papers, which are concerned with atmospheric processes, provide theoretical concepts of the Mars atmospheric composition and temperature. Techniques used in computing the ground surface temperature and generating model atmospheres are described in papers 4 and 5, respectively. The next two papers provide empirical models of the Mars atmosphere and are followed by a paper on the atmosphere of Mercury. The feasibility of obtaining Martian atmospheric information from vacuum chamber simulation experiments is discussed in the last three papers.

## TECHNICAL MEMORANDUM X-53699

January 29, 1968

### NASA'S 150-METER METEOROLOGICAL TOWER LOCATED AT THE KENNEDY SPACE CENTER, FLORIDA

(Revised January 1968)

By John W. Kaufman

George C. Marshall Space Flight Center  
Marshall Space Flight Center, Alabama 35812

and Lester F. Keene

John F. Kennedy Space Center  
Kennedy Space Center, Florida

## ABSTRACT

This report describes the basic functional operations of NASA's 150-meter Meteorological Tower Facility located in the Merritt Island Launch Area at KSC, Florida. Meteorological instrumentation and data acquisition schemes for obtaining lower atmospheric profile measurements of temperature, winds, and humidity are discussed. Specific information on such matters as meteorological sensor response, electronic circuitry of the meteorological facility, and explicit details of recorder systems has purposely been omitted.

### TECHNICAL MEMORANDUM X-53709

February 21, 1968

#### ASTRODYNAMICS, GUIDANCE AND CONTROL

Review #1

George C. Marshall Space Flight Center  
Marshall Space Flight Center, Alabama 35812

## ABSTRACT

This volume is a collection of papers designed as a summarial review of the activities of the Astrodynamics and Guidance Theory Division of the Aero-Astrodynamics Laboratory. These papers present a cross section of the studies being conducted by, and under the supervision of, the three branches and one office within the division. In addition, suggested areas for future research are presented in the context of these reports.

### TECHNICAL MEMORANDUM X-53712

February 28, 1968

#### A SIMPLE EXPLANATION OF THE FUNDAMENTAL PRINCIPLE OF CROSS-BEAM REMOTE SENSING

By B. H. Funk, Jr.

George C. Marshall Space Flight Center  
Marshall Space Flight Center, Alabama 35812

## ABSTRACT

The stimulus for this paper was the apparent difficulty which many persons have in understanding the cross-beam method of remote sensing. In explaining the principles involved, simple hypothetical cases are discussed to illustrate the fundamentals upon which the system is based. To further clarify the discussion, a numerical example is discussed.

### TECHNICAL MEMORANDUM X-53714

March 1, 1968

#### ONE-DIMENSIONAL WAVE MOTION IN PRISMATIC BARS DUE TO IMPULSE LOADS WITH AND WITHOUT COULOMB DAMPING

By Donald Dean Tomlin, Jr.

George C. Marshall Space Flight Center  
Marshall Space Flight Center, Alabama 35812

## ABSTRACT

Several cases of wave motion without damping were solved to obtain background information which would aid in solving cases of wave motion with coulomb damping. The nonlinearities introduced by coulomb damping could be linearized so that they could be solved by using Laplace Transforms for the following cases: semi-infinite rod with a step stress impulse loading and a square wave stress impulse loading for  $\tau \geq \alpha/c$  and  $\tau = \alpha/2c$ ; and a finite rod with a step stress impulse loading.

### TECHNICAL MEMORANDUM X-53716

March 13, 1968

# IMPULSE BASE FLOW FACILITY TECHNICAL HANDBOOK

By Hal S. Gwin

George C. Marshall Space Flight Center  
Marshall Space Flight Center, Alabama 35812

## ABSTRACT

This handbook is intended for potential users of the George C. Marshall Space Flight Center's Impulse Base Flow Facility who are not familiar with its operation.

The facility, its purpose, and operating characteristics are described along with the instrumentation and data processing equipment. Responsibilities of the potential user are also defined.

## TECHNICAL NOTE 3815

April, 1968

# SCALAR AND COMPONENT WIND CORRELATIONS BETWEEN ALTITUDE LEVELS FOR CAPE KENNEDY, FLORIDA, AND SANTA MONICA, CALIFORNIA

By Glenn E. Daniels and Orvel E. Smith

George C. Marshall Space Flight Center  
Marshall Space Flight Center, Alabama 35812

## ABSTRACT

The analysis of large quantities of atmospheric data for use in space vehicle design studies requires the application of statistical methods. An envelope of means or any given percentile derived from a sample of winds taken at discrete altitudes is not necessarily a mean profile and may not define a physically attainable wind profile. Coefficients of correlations with means and standard deviations may be used in a statistical model to derive realistic wind profiles.

The statistics presented in this report are based on rawinsonde wind data samples for Cape Kennedy, Florida, and Santa Monica, California, which are greatly improved samples over those previously available. These samples represent an improvement in that they are from a more recent observational period with fewer missing measurements than earlier records and because the data have been carefully edited, checked, and serially completed for missing data.

## TECHNICAL MEMORANDUM X-53722

April 10, 1968

# DAMPING OF THERMOELASTIC STRUCTURES

By William Mitchell Gillis

George C. Marshall Space Flight Center  
Marshall Space Flight Center, Alabama 35812

## ABSTRACT

This report considers longitudinal waves traveling in a cylindrical rod. After a review of the classical results of wave propagation in unbounded elastic solids and in elastic cylinders, the subject of thermal modification of elastic properties is undertaken. The resultant effects upon the purely elastic wave motion consists of a change in the propagation velocity and the addition of a damping effect upon the mechanical energy of the elastic wave due to heat conduction. The thermoelastic effects upon a longitudinal elastic wave are shown to be small in terms of the propagation velocity. However, more significantly, the thermoelastic damping effect is large for very high frequency waves traveling in small diameter bars. The behavior of the thermoelastic damping coefficient is linked to a "thermoelastic bar number," developed herein. Finally, approximations are developed, based upon the value of the thermoelastic bar number, to predict the behavior of the thermoelastic damping coefficient as a function of frequency.

## TECHNICAL MEMORANDUM X-53734

April 23, 1968

## COMPARTMENT VENTING AND PIPE FLOW WITH HEAT ADDITION

By H. G. Struck and John A. Harkins

George C. Marshall Space Flight Center  
Marshall Space Flight Center, Alabama 35812

### ABSTRACT

One-dimensional quasi-steady theory is used to develop an engineering method to determine the time-dependent pressure in vented launch-vehicle compartments during the first few minutes of the ascending flight.

This method, by nature an iteration procedure, is intended to provide the structural design engineer with the reduced loads on the compartment walls resulting from the venting process. The basic program is set up for the CDC-3200 digital computer which can handle presently only up to  $N = 5$  compartments where the inner compartments must have only one connecting orifice and the last compartment can have up to  $NV = 5$  orifices venting into the atmosphere. Furthermore, the compartments have to be placed in series. Though the compartment and orifice number can be raised indefinitely, it is advisable to restrict the number to as few as possible to keep the computation time low.

The basic program has been extended to offer combinations of compartment and connecting orifices. Compartment leaks and their accompanying coefficients, as well as venting through a duct of varying cross section, have been included. The effect of heating or cooling the duct flow can also be computed.

### TECHNICAL MEMORANDUM X-53733

April 30, 1968

## A METHOD OF BENDING VIBRATION ANALYSIS FOR A VEHICLE WITH FLEXIBLY SUSPENDED COMPONENTS

By Homer Pack

George C. Marshall Space Flight Center  
Marshall Space Flight Center, Alabama 35812

### ABSTRACT

A method is developed for finding the natural modes and frequencies of a vehicle with flexibly suspended components. The vehicle is idealized as a system of one nonuniform beam and any number of flexibly suspended masses. A vibration analysis is first made of the beam, omitting the masses, by a modified Stodola method. The equations for the connected system are then derived using Lagrange's equations.

### TECHNICAL MEMORANDUM X-53735

May 3, 1968

## A DISCUSSION OF THE STABILITY REQUIREMENTS FOR A LAUNCH VEHICLE FLIGHT CONTROL SYSTEM

By Jerome R. Redus

George C. Marshall Space Flight Center  
Marshall Space Flight Center, Alabama 35812

### ABSTRACT

It is asserted in this report that what is truly desired of a launch vehicle flight control system is the ability to bound the dynamic responses of the launch vehicle to winds aloft and vehicle anomalies. Within this context, the necessity of imposing the customary stability requirements on a launch vehicle flight control system is questioned. Arguments for and against the usual stability requirements are presented. It is concluded that the question is an important one which needs resolution. Comments from interested persons are solicited.

### TECHNICAL MEMORANDUM X-53746

June 18, 1968

## SATURN AS-501 POSTFLIGHT TRAJECTORY

By Jonathan B. Haussler and Clinton L. Varnado

George C. Marshall Space Flight Center  
Marshall Space Flight Center, Alabama 35812

## ABSTRACT

This report presents the postflight trajectory for the Saturn V AS-501 test flight. The primary mission of AS-501, the first of the Saturn V series, was to demonstrate the structural integrity of the Saturn V launch vehicle and test the Command Module lunar return re-entry performance. Trajectory-dependent parameters are given in earth-fixed, space-fixed ephemeris and geographic coordinate systems. A complete time history of the powered portions of flight is presented at 1-second intervals during the S-IC phase and 5-second intervals during the remaining phases. Tables of initial conditions and various orbital parameters, for both the parking and waiting orbits, are included in a discussion of the orbital phase of flight.

## TECHNICAL MEMORANDUM X-53754

July 11, 1968

### WIND VECTOR CALCULATION USING CROSS-BEAM DATA AND DETECTOR ARRANGEMENT FOR MEASURING HORIZONTAL WINDS

By W. H. Heybey

George C. Marshall Space Flight Center  
Marshall Space Flight Center, Alabama 35812

## ABSTRACT

In atmospheric experimentation three ground-based detectors suffice for determining wind vectors that could be present in a certain space volume. While this is true in general, the geometry simplifies a great deal, when these vectors can be taken as horizontal. Since to do so will often be warranted, the pertinent method for a proper arrangement of detector positions and attitudes has been developed in detail. With a suitable layout, winds reasonably con-

stant near a selected height, if blowing into and out of a quarter of the rose, can be calculated with sufficient accuracy and confidence. The error analysis assumes that the observational time uncertainty is at most  $\pm 0.1$  sec.

To observe wind vectors in the remaining directions, or at several heights simultaneously, the use of more detectors (or of the available multiple detectors) is called for. This is subject matter for future investigation, as is the more intricate problem posed by non-horizontal winds.

## TECHNICAL MEMORANDUM X-53759

July 22, 1968

### DRAG ON FLAT PLATES OSCILLATING IN INCOMPRESSIBLE FLUIDS AT LOW REYNOLDS NUMBERS

By Harry Buchanan

George C. Marshall Space Flight Center  
Marshall Space Flight Center, Alabama 35812

## ABSTRACT

An investigation of the flow about two-dimensional plates oscillating in an incompressible fluid at low Reynolds numbers is presented. The case in which the fluid mass is stationary and the plate oscillates is compared to the case of a plate submerged in an oscillating stream using potential theory. A series of experiments is described in which force-time histories were recorded for a plate oscillating through a basin of fluid at rest. In addition, a series of dye streak photographs shows the characteristic fluid motion. A drag coefficient is defined and values are computed from the experimental data. This coefficient is shown to be a function of both Reynolds number and a dimensionless period parameter. At very low values of Reynolds number the coefficient increases sharply with decreasing Reynolds number. A discussion of the application of this data to the problem of slosh damping by baffles under low gravity conditions is presented.

## B. Presentations

### ON OKAMURA'S UNIQUENESS THEOREM

By John H. George

#### ABSTRACT

This paper presents a discussion of the uniqueness theorem of R. D. Moyer showing that it is a consequence of a uniqueness theorem of H. Okamura.

Published in American Mathematical Society Proceedings, August 1967.

### ORBITS AND TRAJECTORIES

By C. C. Dearman, Jr.

#### ABSTRACT

This presentation gives a review of current studies and future research in the areas of orbit determination and trajectory analysis.

Presented at the "Tennessee Advanced Space and Aeronautics Workshop," George Peabody College, Nashville, Tennessee, August 11-16, 1967.

### ON AIZERMAN'S CONJECTURE AND BOUNDEDNESS

By J. H. George<sup>1</sup> and W. G. Vogt<sup>2</sup>

#### ABSTRACT

For a linear system  $\dot{x} = Ax + bf(\sigma)$  with single nonlinear feedback  $\sigma = cTx$ , the Aizerman conjecture

states that if  $f(\sigma)/\sigma \in (K_1, K_2)$ , where for  $K \in (K_1, K_2)$  the matrix  $A + KbcT$  has all eigenvalues with negative real parts, then the null solution  $x = 0$  is asymptotically stable in the large. This conjecture is known to be not true. This paper raises the question as to whether or not the Aizerman conjecture implies boundedness of the solution  $x(t)$ . A simple sufficient condition for this is given.

Published in IEEE Transactions on Automatic Control, June 1967.

1. Aero-Astroynamics Laboratory, George C. Marshall Space Flight Center/NASA, Marshall Space Flight Center, Alabama.
2. University of Pittsburg, Pittsburg, Pennsylvania.

### EXPERIMENTAL DETERMINATION OF DRAG FORCES ON A DISC, CYLINDER, CONE, AND SPHERE IN A LOW DENSITY FLOW NEAR MACH FOUR

By Josh D. Johnson

#### ABSTRACT

Drag forces were measured on a disc, cylinder, cone, and sphere in the Marshall Space Flight Center Low Density Wind Tunnel. The test medium was gaseous carbon dioxide. Mach numbers ranged from 3.30 to 4.03 and Knudsen numbers varied from 0.025 to 0.937. Experimental data are compared with theoretical calculations for continuum, near free molecule, and free molecule flow. Since the experimental data were in the slip and transition flow regimes, direct comparisons with these theoretical calculations were impossible; however, the data did exhibit an increase in drag coefficient as the Knudsen number increases, which is a characteristic of flow in these regimes. Also, the results indicated a need for a more sensitive drag balance and a need for additional wind tunnel nozzle boundary layer control.

M. S. Thesis, Aerospace Engineering, 1967, University of Alabama

# DIURNAL SURVEY OF THE THERMOSPHERE (I) NEUTRAL PARTICLE RESULTS

By Dr. R. Tausch<sup>1</sup>, H. B. Nieman<sup>1</sup>,  
G. R. Carigan<sup>1</sup>, R. E. Smith<sup>2</sup> and  
J. O. Ballance<sup>2</sup>

## ABSTRACT

This paper presents the results of a series of six MUMP (Marshall University of Michigan Probe) payloads launched on 24 January 1967, at Cape Kennedy, Florida. The purpose of the payloads was to determine the neutral molecular nitrogen density and temperature and the electron density and temperature in the 130-to 325-km altitude region throughout one diurnal cycle. The payload instrumentation included an omegatron mass analyzer and an electron temperature probe with their support electronics. All payloads functioned well, and complete data acquisition was realized. The data of the neutral particle experiment are presented and compared with current atmospheric model predictions. A summary discussion of probable errors involved in the measurement technique is included.

Presented at the 1967 COSPAR Meeting, London, England, July 1967.

1. Space Sciences Laboratory, University of Michigan, July 1967.
2. Aero-Astroynamics Laboratory, George C. Marshall Space Flight Center, Marshall Space Flight Center, Alabama.

# DIURNAL SURVEY OF THE THERMOSPHERE (II) CHARGED PARTICLE RESULTS

By A. F. Nagy<sup>1</sup> and W. T. Roberts<sup>2</sup>

## ABSTRACT

This paper presents the charged particle results of the diurnal study carried out on 24 January 1967

with six rocket-borne payloads. The diurnal variation of the electron temperatures, which were measured by cylindrical Langmuir probes, are presented. The results are discussed and compared with existing theoretical predictions. Results of measurements made at the same time by Thomson scatter facilities at different geographic locations are also given for comparison.

Presented at the 1967 COSPAR Meeting, London England, July 1967.

1. Space Physics Research Laboratory, University of Michigan, Ann Arbor, Michigan.
2. Aero-Astroynamics Laboratory, George C. Marshall Space Flight Center, Marshall Space Flight Center, Alabama.

# DEVELOPMENT OF THE ITERATIVE GUIDANCE MODE WITH ITS APPLICATION TO VARIOUS VEHICLES AND MISSIONS

By Doris C. Chandler<sup>1</sup> and Isaac E. Smith<sup>2</sup>

## ABSTRACT

This paper discusses the iterative guidance mode and its application to three-dimensional upper-stage vacuum flight. It is an inertial or closed-system mode in that the only inputs required after liftoff are available from the onboard navigation system. That is, the iterative scheme computed steering commands as a function of the state of the vehicle — velocity, position, longitudinal acceleration, and gravitational acceleration — and the desired cutoff conditions. The guidance commands are updated each guidance cycle, using the updated state of the vehicle. The iterative guidance scheme is a path-adaptive guidance scheme in that it will retain its optimization properties under all expected types and magnitudes of vehicle perturbations without any loss in accuracy at cutoff. Its optimality and accuracy are demonstrated by examples of Saturn IB and Saturn V flights.

Published in *Journal of Spacecraft and Rockets*, Vol. 4, No. 7, July 1967.

1. Aero-Astroynamics Laboratory, George C. Marshall Space Flight Center, Marshall Space Flight Center, Alabama.
2. Northrop Space Laboratories, Huntsville Alabama.

## DYNAMIC PROBLEMS IN SPACE VEHICLE DESIGN

By Robert S. Ryan

### ABSTRACT

A lecture was presented on the basic dynamic problems of space vehicle design and included discussion of on-pad dynamics, lift-off dynamics, inflight wind induced dynamics, and orbit dynamics. A discussion period followed the lecture.

---

Presented to Tennessee Science Teachers and Science Awards Winner Workshop at Peabody College, Nashville, Tennessee, August 1967.

## MESOSCALE WAVE MOTIONS AS REVEALED BY IMPROVED WIND PROFILE MEASUREMENTS

By R. E. Mandel<sup>1</sup> and James R. Scoggins<sup>2</sup>

### ABSTRACT

The mesoscale structure of atmospheric winds between the surface and 20 km is analyzed using data obtained from the FPS 16 radar/Jimsphere precision wind measuring system. The accuracy and resolution of these data are far superior to those obtained from conventional rawinsonde measurements. Preliminary analysis of several series of ascents in which observations were made at 2-hr intervals over 12-hr periods reveals that significant mesoscale variations in wind speed are common, particularly in and above the region of maximum wind. The observed oscillations frequently have amplitudes exceeding  $5 \text{ m sec}^{-1}$  and have periods of from 3 to 15 hr. The vertical extent of any particular perturbation rarely exceeds 2 km.

---

Published in Journal of Applied Meteorology, Vol 6 No. 4, August 1967.

1. Lockheed Missiles and Space Company, Huntsville, Alabama.
2. Formerly with Aero-Astroynamics Laboratory, George C. Marshall Space Flight Center, Marshall Space Flight Center, Alabama, now Associate Professor, Department of Meteorology, Texas A and M University, College Station, Texas.

## RESUME OF ADVANCED CONTROL SYSTEMS FOR LAUNCH VEHICLES

By J. C. Blair and J. R. Redus

### ABSTRACT

This paper attempts to summarize the current status of investigations into the use of advanced control techniques for design of launch vehicle flight control systems. Discussed is a statistical approach to design of systems for minimum probability of failure, possible approaches to design of compensation networks achieving near optimal system performance with realizable sensors and filters, and design to achieve insensitivity of performance to parameter variations.

---

Presented at the "SAE Committee on Aerospace Vehicle Flight Control Systems" at Boston, Massachusetts, August 9-11, 1967.

## EFFECT OF WIND PENETRATION ON FLEXIBLE VEHICLES

By James G. Papadopoulos

### ABSTRACT

Present six-degrees-of-freedom wind monitor Saturn Simulation programs assume an instantaneous constant wind velocity over the entire vehicle length. Contrary to this popular but simplified assumption,

the study presented here indicates that wind penetration effects are not only desirable but necessary for any serious analysis of vehicle response to a wind profile.

Wind penetration effects are evaluated in the frequency domain by developing a solution for theoretical transfer functions. Numerical calculations are made for a Saturn SA-9 vehicle. Analytical transfer functions for angle of attack and average engine gimbal deflection are compared to a spectral analysis of actual flight test data.

---

Presented at the AIAA Guidance, Control, and Flight Dynamics Conference, Huntsville, Alabama, August 14-16, 1967.

## POWERED FLIGHT TRAJECTORY DETERMINATION TECHNIQUES AS APPLIED TO SATURN V VEHICLES

By J. B. Haussler

### ABSTRACT

The onboard telemetered guidance data and the external tracking data when combined in a composite solution can produce a smooth, continuous trajectory of sufficient accuracy for use in a detailed post-flight evaluation. In solving for guidance and tracker error model coefficients, there are several assumptions and limitations imposed by the nature of the data available and the computer facility utilized. Justification is given for using truncated error models and for the assumption that guidance error model coefficients and tracker error model coefficients can be considered uncorrelated. By using the telemetered guidance as the generating parameter and estimating the error coefficients with the Kalman recursive method, a very efficient and versatile computer program resulted. Up to 18 guidance error coefficients and up to 10 tracker error coefficients from as many as 15 different trackers can be estimated in a single solution. Although the guidance and tracker coefficients do not represent a detailed evaluation of those systems, they do furnish information which can assist in the analysis of these systems. Results on actual data from

recent Saturn vehicles verify the method as a practical tool for obtaining a post-flight trajectory.

---

Presented at the AIAA Guidance, Control and Flight Dynamics Conference, Huntsville, Alabama, August 14-16, 1967.

## ITERATIVE GUIDANCE APPLIED TO GENERALIZED MISSIONS

By Helmut J. Horn, Doris C. Chandler,  
and Volis L. Buckelew

### ABSTRACT

The iterative guidance mode (IGM) was developed to satisfy the launch vehicle requirements of the Saturn-Apollo flights. Improvements in the formulation of the guidance equations extend the application of the IGM to more general missions: (1) A more sophisticated prediction of the "effective" gravity vector which permits use of the guidance scheme for extended trajectory arcs without deterioration of the optimization characteristics; (2) development of equations which permit the use of total energy as an additional end constraint, reducing or entirely eliminating the need of precomputation and curve-fitting for a major group of missions; (3) the reduction of sensitivity to noise in the acceleration measurement, which is achieved by computing and filtering a fictitious thrust, the product of measured acceleration, and computed mass. The effectiveness of these modifications, which are presented against the background of a short derivation of the basic equations, is numerically evaluated for selected trajectories.

---

Presented at the AIAA Guidance, Control and Flight Dynamics Conference, Huntsville, Alabama, August 14-16, 1967.

## SATELLITE DECAY AND ORBITAL LIFETIME

By Robert H. Benson

## ABSTRACT

This presentation was given at the Fifth Annual Summary Lecture Series in Aerospace Science and Engineering. It points out some of the reasons why orbital decay and lifetime analyses are necessary. It also touches on some of the features of the orbital decay and lifetime prediction model in use at the Marshall Space Flight Center, with emphasis on some of the parameters which affect lifetime and decay predictions. These included atmospheric density, the satellites orbital characteristics, solar radiation pressure, drag coefficient and the effective drag area presented by the motion of the satellite in orbit. In addition, some of the results obtained in lifetime predictions and model verifications were illustrated based on 53 decayed satellites. The areas where continued research is being carried on, to improve decay and lifetime predictions, were also discussed. These include solar activity prediction and how solar activity influences atmospheric density, aerodynamic research, and the prediction of the attitude motion of passive satellites over long periods of time.

---

Presented at Fifth Annual Summer Lecture Series in Aerospace Science and Engineering on August 25, 1967, Huntsville, Alabama.

## REMOTE DETECTION OF LOCAL TEMPERATURES AND LOCAL PARTIAL PRESSURES WITH CROSSED-BEAM SPECTROSCOPY

By F. R. Krause and J. B. Stephens

### ABSTRACT

The physical interpretation of crossed-beam tests is formulated mathematically for a set of experiments, which differ only by using a different optical wave number for one of the two photometer units.

Crossed-beam methods differ from single path observations in that modulations of radiative power are used instead of mean values. These modulations come from inhomogeneous detector's narrow field of view. Two passive remote detection systems are employed to select a region from triangulation of the two beams. The beam modulations are multiplied and

averaged over time to discriminate against all beam modulations which originate outside the selected region. The measurements of the resulting two-beam product mean value is then repeated by setting one detector at different optical wave lengths to obtain a "crossed-beam spectrum." The physical interpretation of these spectra then allows us to analyze the optical and thermodynamic properties inside a region already selected by triangulation and statistical correlation methods. This general concept of crossed-beam spectroscopy is illustrated for a statistical band model of pressure-broadened lines. The analytical formulation indicates that, with the proper choice of only two wavelengths, we may obtain the mean absorption, as well as both the local mean temperature and partial pressure. In addition, these two-line measurements disentangle the space-time covariance of pressure and temperature variations and open direct experimental studies of turbulent heat and mass transfer in inhomogeneous flows.

---

Presented at the Specialist Conference on Molecular Radiation and its Application to Diagnostic Techniques, George C. Marshall Space Flight Center, Marshall Space Flight Center, Alabama, October 5-6, 1967.

## USE OF PROBABILITY IN LAUNCH VEHICLE DESIGN

By Robert S. Ryan

### ABSTRACT

A simple explanation of probability was given and its application to vehicle design for inflight winds.

---

Presented to the Huntsville High School Math Society, Huntsville, Alabama, November 1967.

## USE OF WIND SHEARS IN THE DESIGN OF AEROSPACE VEHICLES

By Robert S. Ryan<sup>1</sup>, James R. Scoggins<sup>2</sup>,  
and Alberta King<sup>3</sup>

## ABSTRACT

The relative influence of various wind-profile properties on launch vehicle design and operation is studied. Particular emphasis is placed on the influence of wind shears and turbulence on dynamic response during the boost phase of the flight. Four hundred and seven individual detailed (Jimsphere) wind profiles are the primary wind inputs for this analysis. Time response of the vehicle to each profile is computed and a statistical evaluation of the results is made. It was found that small-scale wind-shear effects should be included in structural design, especially for forward vehicle stations, and that profiles with high wind speeds and moderate wind shears create high structural loads at all stations.

---

Published in the Journal of Spacecraft and Rockets, Vol. 4, No. 11, November 1967.

- 1., 3. Aero-Astrodynamic Laboratory, George C. Marshall Space Flight Center, Marshall Space Flight Center, Alabama.
2. Formerly with Aero-Astrodynamic Laboratory, George C. Marshall Space Flight Center, Marshall Space Flight Center, Alabama, now Associate Professor, Department of Meteorology, Texas A and M University, College Station, Texas.

## MAPPING OF TURBULENT FIELDS BY CROSSING OPTICAL BEAMS

By F. R. Krause

### ABSTRACT

Crossed-beam test arrangements have been developed for optical detection systems to extend remote detection methods to dynamic phenomena. The method differs from conventional remote detection concepts by employing the modulation rather than the mean value of the optical signal. These modulations are integrated along the line of sight since they account for all inhomogeneous particle or temperature distributions which move across the optical beam. Local information on space and time correlation of

thermodynamic state variables at the region of minimum beam separation can, however, be retrieved from the integrated beam modulations as well as from light source and detector noise by digital cross-correlation methods which had been developed originally for random vibration analysis and communication theory. The crossed-beam concept is illustrated by reviewing velocity component profiles and turbulence scales which have been measured with space-fixed beams. Systematic mappings of round sub- and supersonic air jets were carried out by M. J. Fisher and exploratory wind measurements at a meteorological tower are being performed by A. J. Montgomery under a joint research program with the IIT Research Institute. The potential of crossed-beam test arrangement is illustrated by a short summary of the theory that has been developed for rapid scanning airplane or satellite born passive optical detection systems.

---

Presented at the 1967 Annual Meeting of the Division of Fluid Mechanics, American Physical Society, Washington D. C., November 1967.

## CANONICAL REALIZATIONS

By R. W. Ganderson<sup>1</sup> and W. G. Vogt<sup>2</sup>

### ABSTRACT

This paper establishes a canonical form for the general, multi-input case for the linear, constant coefficient, dynamical system

$$\dot{x} = Ax + Bu$$

$$v = Cx$$

corresponding to  $p \geq 1$  where A, B, and C are matrices of dimension  $n \times n$ ,  $n \times p$ , and  $g \times n$  and x, u, and v are n, p, and g-vectors, respectively. Further, the development leads to a new necessary and sufficient condition for the complete controllability of the system. As an immediate corollary, it follows that the minimum number of inputs necessary for the complete controllability of the system is the number of nontrivial invariant polynomials.

---

Presented at the "Asilomar Conference in Circuits and Systems," at Monterey, California, November 1-3, 1967.

1. Aero-Astroynamics Laboratory, George C. Marshall Space Flight Center, Marshall Space Flight Center, Alabama.
2. University of Pennsylvania, Philadelphia, Pennsylvania.

## ON THE EQUIVALENCE OF CERTAIN STABILITY PROPERTIES

By John H. George<sup>1</sup> and R. W. Gunderson<sup>2</sup>

### ABSTRACT

This paper analyzes the relationship between definitions of the concept of "stability" of solutions of ordinary differential equations, as given by various individual authors, in an attempt to prove the equivalence of these definitions and their identity with the Liapunov stability concept. Relations between certain properties of solutions are established while imposing successively stronger assumptions on the right-hand side of ordinary differential equations.

Published in SIAM Review, January 1968

1. Formerly with Aero-Astroynamics Laboratory, George C. Marshall Space Flight Center, Marshall Space Flight Center, Alabama, now at University of Wyoming, Laramie, Wyoming.
2. Aero-Astroynamics Laboratory, George C. Marshall Space Flight Center, Marshall Space Flight Center, Alabama.

## GUIDANCE AND CONTROL OF ROCKETS

By Clyde D. Baker

### ABSTRACT

This presentation discusses new criteria for the guidance and control of launch vehicles from a conceptual point of view. Also discussed is the iterative guidance mode used in the second and third stages

of the Saturn V to determine an optimum flight path to minimize propellant consumption.

Presented at "Electrical Engineering Colloquium," Rensselaer Polytechnic Institute, Troy, New York, March 19, 1968.

## DEVELOPMENT OF NATURAL ENVIRONMENT CRITERIA DOCUMENTS FOR AEROSPACE VEHICLE AND GROUND SUPPORT DEVELOPMENT

By Glenn E. Daniels

### ABSTRACT

The many factors that were considered at the Marshall Space Flight Center in the preparation of the natural Environment Criteria Documents for aerospace vehicle and ground support development are discussed.

It was discovered early in the Saturn program that Mil Standard 210A covered too general an area and had insufficient detail to be useful.

Statistics have been an important tool, permitting use of extreme values considerably less than the absolute extreme, thus permitting design of many items within the current state of the art. Statistics have also been of great use in design of ground support equipment to protect the vehicle before launch and to determine the probability of delay of launch for a specific design level.

Methods of presentation and type of information have been continuously reviewed. Each environment has been considered as an individual environment, but much effort has been expended in studies to find the best ways of combining environments or of including one environment as part of another. The description of an environment has been accomplished in several ways:

(1) by words describing details of the environmental effects, methods of applying the information, and description of realistic atmospheric cyclic changes that are adaptable to test cycles,

(2) by presenting tables whenever exact numerical values are needed and in some cases computer programs are available when extensive data are needed, and

(3) by providing graphs to show trends of data or where the overall picture or pattern of the data is needed. The document is such that it can be referenced as a supporting document in specifications and other documents used for interface control.

The documents are revised periodically to provide better data and to provide new data. All revisions have been carefully made such that no major changes have occurred in any previously negotiated contract to prevent any costly redesign.

Published in Proceedings of the Institute of Environmental Sciences, St. Louis, Mo., April 1968.

## WORKSHOP REACTION CONTROL SYSTEMS

By James R. Kimzey

### ABSTRACT

The seminar presentation covered the general goals of the AAP mission and the means by which they would be accomplished. The SIV-B Workshop control system and the existing digital simulation of the system were discussed in some detail.

Presented at the Army Weapons System Seminar, Rock Island Arsenal, Illinois, April 1968.

## ERRORS OF RADIOSONDE AND ROCKETSONDE TEMPERATURE SENSORS

By Glenn E. Daniels

### ABSTRACT

A method is proposed where two thermistors of different emissivities are used on the radiosonde to compute the corrected air temperature. This method could be extended to rocketsonde temperature measurements by using two bead thermistors of different sizes to determine temperature errors and aerodynamic heating errors.

Published in the Bulletin of the American Meteorological Society, Volume 49, Number 1, January 1968.

## TABLES OF THE PROBABILITY AND DENSITY FUNCTIONS FOR THE BIVARIATE EXTERNAL DISTRIBUTIONS

By E. J. Gumbel<sup>1</sup>, C. K. Mustafi<sup>1</sup>  
and Orvel E. Smith<sup>2</sup>

### ABSTRACT

Let X and Y be two random variables with probability functions

$$\Phi(x) = \exp(-e^{-X}) \text{ and } \Phi(Y) = \exp(-e^{-Y}),$$

respectively. It follows, then, from the results in References 1 and 2 that

$$(1) \quad \Phi_1(X, Y, a) = \exp[-e^{-X} - e^{-Y} + a(e^X + e^Y)^{-1}], \quad 0 \leq a \leq 1$$

and

$$(2) \quad \Phi_2(X, Y, m) = \exp[-(e^{-mX} + e^{-mY})^{1/m}], \quad m \geq 1$$

are probability functions of the random variables (X, Y), with margins  $\Phi(X)$  and  $\Phi(Y)$ . It may be verified that both  $\Phi_1(X, Y, a)$  and  $\Phi_2(X, Y, m)$  are stable bivariate extremal distributions. For  $a = 0$  in (1) and  $m = 1$  in (2), the bivariate probability functions split up into the product of two marginal probability functions. In these cases, the two variables are independent. The corresponding density functions are given by

$$\varphi_1(X, Y, a) = \{ \exp[-e^{-X} - e^{-Y} - X - Y + a(e^X + e^Y)^{-1}] \}$$

(3)

$$\{ 1 - a(e^{2X} + e^{2Y})(e^X + e^Y)^{-2} + 2ae^{2X+2Y}(e^X + e^Y)^{-3} + a^2 e^{2X+2Y}(e^X + e^Y)^{-4} \}$$

$$(4) \quad \varphi_2(X, Y, m) = \Phi_2(X, Y, m) [(e^{-mX} + e^{-mY})^{1/m} - 2 e^{-mX - mY} \{(e^{-mX} + e^{-mY})^{1/m} + m - 1\}].$$

These two distributions have been analyzed in Reference 2. It transpired that the first distribution can only be used in limited situations. The increase of association between X and Y as  $\underline{a}$  varies from 0 to 1 is even less than the increase of association between the two variables as  $\underline{m}$  increases from 1 to 2. Thus, for practical applications, we have tabulated the values of  $\Phi_1(X, Y, a)$  and  $\varphi_1(X, Y, a)$  for  $a = 1$  and  $X, Y = -2.0(.2)7.0$ . The case  $a = 0$  will be covered by the case  $m = 1$ , in which case the variables are independent.

The second distribution can be used in more general situations. We have tabulated the values of  $\Phi_2(X, Y, m)$  and  $\varphi_2(X, Y, m)$  for  $m = 1(.1)10$  and  $X, Y = -2.0(.2)7.0$ . It is shown in Reference 2 that

$$\lim_{m \rightarrow \infty} \Phi_2(X, Y, m) = \begin{cases} \Phi(X) & \text{if } x \leq Y \\ \Phi(Y) & \text{if } x > Y \end{cases}$$

Tables for  $\Phi(X)$  and the corresponding density  $\varphi(X)$  are available in Reference 3, which may be used for large values of  $m$ .

Supported by the National Science Foundation under Grant NSF GK-695 and by the U. S. Department of the Interior under Grant WP-00457 with the Federal Water Pollution Control Administration.

Published by Department of Industrial Engineering, Columbia University, New York, New York, April 1, 1968.

1. Columbia University, New York, New York.
2. Aero-Astroynamics Laboratory, George C. Marshall Space Flight Center, Marshall Space Flight Center, Alabama.

## CROSSED-BEAM MEASUREMENTS OF TURBULENCE AND SOUND SOURCE INTENSITIES IN SUPERSONIC JETS

By Fritz R. Krause<sup>1</sup> and Mike J. Fisher<sup>2</sup>

## ABSTRACT

Crossed-beam test arrangements have been developed for optical detection systems to extend remote detection methods to dynamic phenomena. The method differs from conventional remote detection contents by employing the modulation rather than the mean value of the optical signal. These modulations are integrated along the line of sight since they account for all inhomogeneous particle or temperature distributions which move across the optical beam. Local information on space and time correlation of thermodynamic state variables at the region of minimum beam separation can, however, be retrieved from the integrated beam modulations as well as from light source and detector noise by digital cross-correlation methods which had been developed originally for random vibration analysis and communication theory. The crossed-beam concept is illustrated by reviewing velocity component profiles and turbulence scales, which have been measured with space fixed beams. Systematic mappings of round sub- and supersonic air jets were carried out by M. J. Fisher. The potential of crossed-beam test arrangement is illustrated by a short summary of the theory that has been developed for the direct, one-shot estimate of local sound source intensities in supersonic free shear layers.

Presented at Lectures in Science Series, "The Boeing Company, April 23, 1968.

1. Aero-Astroynamics Laboratory, George C. Marshall Space Flight Center, Marshall Space Flight Center, Alabama.
2. IIT Research Institute, Chicago, Illinois.

## REMOTE DETECTION OF CLEAR AIR TURBULENCE AT TOWER HEIGHTS

By Fritz R. Krause and B. C. Hablutzel

## ABSTRACT

A passive optical technique for the remote detection of clear-air turbulence from fluctuations in

scattered sunlight has been developed. Remote local flow regions are selected by triangulation between the narrow field of view of two ground based telescopes.

Validity of the crossed-beam concept has been established in subsonic and supersonic jets by comparing velocity components, turbulence scales and temporal correlation functions that had been measured with cross-beam system and hot wires. Preliminary experimental results are now being presented, which were taken with an anemometer on a meteorological tower and with crossed optical beams intersecting just upstream of the anemometer.

Atmospheric experiments differ from wind tunnel experiments in the following aspects: (1) Passive optical detection is employed using locally scattered sunlight instead of man-made light sources. (2) Contrary to the wind tunnel experiments the wind velocity is variable. (3) The smallest local beam modulation that can be retrieved by digital cross correlation is set by temporal trends in the statistics of wind fluctuations and not by the maximum observation time. Cross-beam and anemometer data are compared to determine restrictions of cross-beam measurements which may be imposed by the above three aspects.

Presented at "Lectures in Science Series," The Boeing Company, April 24, 1968.

## A MATHEMATICAL PROGRAMMING APPROACH TO THE SCHEDULING OF EXPERIMENTS IN SPACE

By E. F. Fluschman<sup>1</sup>, Peter M. Treuenfels<sup>2</sup>  
and Paul R. Rebelein<sup>2</sup>

### ABSTRACT

Historically, experiment scheduling problems have been solved by trial and error methods which usually result in feasible but not optimal schedules. In order to circumvent this obvious shortcoming, a mathematical programming algorithm, employing integer linear programming, has been developed to schedule experiments in such a manner that the benefit derived from a space mission is maximized. At

the same time, the algorithm is capable of solving the experiment selection problem. This paper discusses the algorithm, the structure of the integer linear programming problem, a mathematical model that generates some of the logical constraints, and the limitations of the mathematical programming approach. Some, but not all, of the features of the algorithm have been programmed in Fortran IV and applied to a trial AAP mission consisting of one orbit. The results, which are also presented, indicate that the approach is both feasible and practical.

Presented at the Joint meeting of the 33rd National Meeting Operations Research Society of America and the 1968 American Meeting the Institute of Management Sciences on May 2, 1968, San Francisco, California. Published in the Proceedings of the meeting.

1. Aero-Astroynamics Laboratory, George C. Marshall Space Flight Center, Marshall Space Flight Center, Alabama.
2. Honeywell, Inc., Aerospace Division, Minneapolis, Minnesota 55413.

## DYNAMIC LOADS OF A LAUNCH VEHICLE DUE TO INFLIGHT WINDS

By Robert S. Ryan<sup>1</sup>, Thomas Coffin<sup>2</sup>  
and Lubert L. Fontenot<sup>2</sup>

### ABSTRACT

Analysis of the stability and dynamic load environment of a launch vehicle resulting from atmospheric disturbances is a very complex problem. To determine the dynamic load environment of the vehicle requires an adequate description of the wind field, vehicle dynamics and control system. The essentials of such a study, namely, methods of analysis, wind field specification and representative vehicle response parameters for evaluation, are of equal importance. This paper is concerned with the mathematical foundations of the vehicle model and method of analysis.

Under the assumption that we have an exact trajectory solution for the vehicle, the nonlinear system of complete perturbation equations is derived.

The vehicle trajectory equations are perturbed to obtain the small deviations of the vehicle from a reference trajectory as a system of linear differential equations with time-varying coefficients. The system is expressed in vector-matrix form and solved by an algorithm based on extended continuation. The method is shown to be efficient for numerical computation and the form of solution provides physical insight into the evolutionary character of the response process.

Application of the technique is exemplified by an evaluation of Saturn V dynamic response to a synthetic wind profile representing a 95% quasi-steady wind, 99% wind build-up rate and superimposed discrete gust.

---

Presented at the Third National Conference on Aerospace Meteorology, New Orleans, La., May 6-9, 1968.

1. Aero-Astrodynamics Laboratory, George C. Marshall Space Flight Center, Marshall Space Flight Center, Alabama.
2. Milpar Inc., Huntsville, Alabama

## THE INFLUENCING FACTORS IN SATELLITE ORBITAL DECAY AND LIFETIME ANALYSIS

By E. F. Fleischman and P. W. Revels

### ABSTRACT

The prediction of orbital lifetime confronts us with several challenging problems concerning the structure of the upper atmospheres, low density aerodynamics, and the orbital mechanics of uncontrolled bodies. In particular, the upper atmospheric density is known to vary with the level of solar activity; however, no reliable method of predicting solar activity for an extended period of time has been established.

The atmospheric density, one of the dominant parameters influencing the orbital decay of a satellite in a typical altitude Earth orbit, has been modeled by several static and time dependent atmospheric profiles. The static atmospheric models, which are

based on observed or measurement data for a specific time and altitude, do not meet the requirements for orbital lifetime analysis. This is exemplified through studies conducted on actual decayed satellites.

A study has been completed for 7 different atmospheric models to determine their applicability for use in our orbital lifetime program. In this study, the actual orbital lifetimes of 54 decayed satellites were compared to their calculated orbital lifetimes using each of the 7 different atmospheric models. The results of these comparisons were quite interesting.

From the mission analysis standpoint, a review is given of a recent parametric lifetime analysis for a proposed future mission. In this study, various orbital and atmospheric parameters and their effects on orbital lifetime are presented. It is the purpose of this paper to point out and illustrate some of the parameters affecting orbital lifetime, particularly the aerodynamic perturbations, and to what extent these perturbations influence mission planning.

---

Presented at the Third National Conference on Aerospace Meteorology at New Orleans on May 7, 1968, and published in the Proceedings of the meeting.

## REMOTE WIND DETECTION WITH THE CROSS-BEAM METHOD AT TOWER HEIGHT

By J. Briscoe Stephens, and R. R. Jayroe, Jr.

### ABSTRACT

A technique for the remote-detection of atmospheric winds from fluctuations in scattered sunlight has been developed using a ground-based cross-beam detection system. Wind component and spectrum measurements are compared, which have been taken with anemometers on a meteorological tower and with crossed optical beams intersecting upstream of the tower.

Validity of the crossed-beam concept has been established in subsonic and supersonic jets by comparing velocity components, turbulence scales and temporal correlation functions that had been measured with cross-beam system and hot wires. Experimental results are now presented which have been

obtained in the atmosphere. Atmospheric experiments differ from wind tunnel experiments in the following aspects: (1) Passive optical detection is employed using locally scattered sunlight instead of man-made light sources. (2) Contrary to the wind tunnel experiments the wind velocity is variable. (3) The smallest local beam modulation that can be retrieved by digital cross correlation is set by temporal trends in the statistics of wind fluctuations and not by the maximum observation time. Cross-beam and anemometer data are compared to determine restrictions of cross-beam measurements which may be imposed by the above three aspects.

---

Presented at the Third National Conference on Aerospace Meteorology, New Orleans, La., May 6-9, 1968, also published in the proceedings of the meeting.

## OPTIMUM AVERAGING TIMES OF METEOROLOGICAL DATA WITH TIME DEPENDENT MEANS

By R. R. Jayroe<sup>1</sup>, and M. Y. Su<sup>2</sup>

### ABSTRACT

The calculation of statistical errors has been developed to provide a more systematic description of time dependent means. In present statistical data reduction programs, mean values such as wind components, covariance functions and spectra are commonly calculated by averaging over an arbitrary time period. A time dependence of these means becomes apparent only by considering many steps, each of which is equal to the integration time.

Our present program differs by treating the averaging time as a variable. In the absence of nonlinear trends, the error of the mean should decrease monotonically with averaging time. Conversely, an increasing error indicates the presence of nonlinear trends. By monitoring the statistical error as a function of averaging time, one may detect a nonlinear time dependence of a mean from the minimum of the error curve over a period which is no longer than the averaging time.

The existence of a minimum in the statistical error curve also indicates an optimum averaging

time, and the smallest error within which time dependent means may be retrieved. The existence of such optimum averaging times is demonstrated for anemometer and hot wire outputs.

The program could be employed to determine the lower limit of correlated cyclic and narrow band components, which can be extracted out of a given set of meteorological data.

---

Presented at the Third National Conference on Aerospace Meteorology, New Orleans, La., May 6-9, 1968, also published in the proceedings of the meeting.

1. Aero-Astroynamics Laboratory, George C. Marshall Space Flight Center, Marshall Space Flight Center, Alabama.
2. Nortronics, Huntsville, Alabama 35805.

## CHARACTERISTICS OF TURBULENCE OBSERVED AT THE NASA 150-METER METEOROLOGICAL TOWER

By George H. Fichtl

### ABSTRACT

Recent observations of turbulence obtained at the NASA 150-m meteorological tower located at Kennedy Space Center, Fla., are presented. The wind data were obtained at the 18-, 30-, 60-, 90-, 120- and 150-m levels, while temperature data were obtained at the 3-, 18-, 60-, 120- and 150-m levels. Most of the tests were made during the daylight hours, and the duration time of each test ranged between 30-60 min.

A survey of the surface roughness length associated with the tower site is presented. Estimates of the roughness length were calculated with wind profile laws consistent with the Monin-Obukhov similarity hypothesis. In the case of those wind directions  $\theta$  in the ranges  $0^\circ \leq \theta < 150^\circ$ ,  $180^\circ \leq \theta < 240^\circ$ , and  $300^\circ \leq \theta < 360^\circ$ , the roughness length is 0.23 m, while for those wind directions in the ranges  $150^\circ \leq \theta < 180^\circ$  and  $240^\circ \leq \theta < 300^\circ$ , the roughness length has the values 0.51 m and 0.65 m, respectively. Longitudinal

turbulence spectra calculated from recent observations are also presented. It is shown that the non-dimensional frequency  $nz/u$ , associated with the peak of the logarithmic spectrum is proportional to  $z^{4/5}$ , where  $u$  is the wind speed at height  $z$  and  $n$  the frequency. Based upon an analysis of the logarithmic spectrum in the inertial subrange, it is implied that the local mechanical production of turbulent energy is balanced by the local viscous dissipation at the 18-m level.

---

Presented at the Third National Conference on Aerospace Meteorology, New Orleans, La., May 6-9, also published in the proceedings of the meeting.

## SCALE EFFECTS IN THE USE OF CLOUD STATISTICS FOR EARTH ORIENTED SPACE EXPERIMENTS

By P. E. Sherr<sup>1</sup>, S. C. Brown<sup>2</sup>,  
A. H. Glaser<sup>1</sup>, J. C. Barnes<sup>1</sup>  
and J. H. Willard<sup>1</sup>

### ABSTRACT

Nearly all existing cloud cover statistics are compilations from ground-based weather observations. The observed area is almost always less than 50 n mi and often less than 30 n mi in diameter. Earth-oriented experiments from space stations will utilize various sensors having a wide range of viewing angles (and hence Earth-viewed areas). A recent study using meteorological satellite data to supplement ground-observed cloud statistics has revealed that the frequency distribution of total cloud cover is a strong function of the size of the area over which it is defined.

Typical "U" shaped cloud cover distribution characteristic of many continental extratropical regions rapidly become "bell" shaped as the area over which the cover is defined increases from a 30 n mi diameter to a 150 n mi diameter. This effect results from the probable existence of clear and overcast 30 n mi areas within larger areas of scattered or broken cloud.

Unless the unit area of interest coincides in size with the field of view of the ground observer, conventional cloud statistics should not be used for experimental design nor for mission planning. Statistical techniques have been developed which permit transformation of conventional cloud cover distribution summaries to distributions valid for larger areas of definition. The results of such statistical transformations compare favorably with actual larger-scale cloud cover distributions laboriously compiled from meteorological satellite data.

---

Presented at the Third National Conference on Aerospace Meteorology, New Orleans, La., May 6-9, also published in the proceedings of the meeting.

1. Allied Research Associates, Inc., Concord, Massachusetts.
2. Aero-Astroynamics Laboratory, George C. Marshall Space Flight Center, Marshall Space Flight Center, Alabama.

## HIGH RESOLUTION BALLOON-BORNE TEMPERATURE SENSOR

By Frank E. Caplan<sup>1</sup> and Dennis W. Camp<sup>2</sup>

### ABSTRACT

To provide temperature data having a resolution consistent with the wind data obtained from Jimsphere flights, an instrument was developed which was light weight and has a fast time response. The weight of 125 gm presented design constraints since temperature compensation and antenna efficiency problems could be overcome by additional power dissipation.

The sensor and its associated ground station provide a means for obtaining high resolution temperature profiles. The balloon-borne unit has three major elements, the thermistor, a 5-mil aluminized board, a resistance-sensitive oscillator and a transmitter. The ground station combines a receiver, discriminator, digital counter, digital printer, and a tape recorder which records IRIG time and voice as well as the temperature data.

The Jimsphere temperature system was flight tested at Cape Kennedy, Fla., and Hanscom Field, Mass. With these and other flight data, results are included which show a comparison of the Jimsphere and rawinsonde data. Details on the variability of the Jimsphere temperature profile data to an altitude of approximately 18 km are discussed. Also presented are results of preliminary calculations of the Richardson Number using these temperature data in conjunction with high resolution Jimsphere wind profile data.

---

Presented at the Third National Conference on Aerospace Meteorology, New Orleans, La., May 6-9, 1968. Also published in the proceedings of the meeting.

1. GCA Corporation, Bedford, Massachusetts.
2. Aero-Astroynamics Laboratory, George C. Marshall Space Flight Center, Marshall Space Flight Center, Alabama.

## WIND TOWER INFLUENCE STUDY FOR NASA'S 150-METER METEOROLOGICAL TOWER AT KENNEDY SPACE CENTER, FLORIDA

By John W. Hathorn<sup>1</sup> and John W. Kaufman<sup>2</sup>

### ABSTRACT

The primary function of NASA's 150-m Meteorological Tower Facility, located in the vicinity of Launch Complex 39 at Kennedy Space Center, Florida, is to acquire lower atmospheric profile data that is used in research studies to develop environmental criteria for the design and launch of Saturn vehicles. In both research and launch support capacities, the wind measurements obtained from the tower must be free of the tower-induced influences. The tower is a lattice-type structure which yields minimal influence on wind measurements obtained from sensors on 12-ft booms on the northeast and southwest sides of the tower (boom heights above natural grade: 3, 18, 30, 60, 90, 120, and 150 m). To analyze tower influence on the winds, a theoretical and empirical study was performed to compare measured and referenced ("free stream") winds.

In the theoretical approach the stream function is computed about a solid triangular tower (with and without catwalks) using a numerical technique to solve Laplace's equation ( $\Delta^2\psi = 0$ ). The maximum influence,  $V/V_\infty$ , for the solid triangular tower at the boom-tip position when the wind is normal to the boom is 1.035 and for the solid triangular tower with catwalks is 1.045.

In the experimental approach ratios are computed between the measured and referenced wind speeds, and differences are computed between the measured and referenced wind directions. As expected, the maximum influence is when the flow is through the structure. An influence in wind speed of 1.02 to 1.03 occurs when the wind is normal to the booms. An influence of approximately 0.98 is measured by the windward sensors with winds parallel to the booms.

---

Presented at the Third National Conference on Aerospace Meteorology, New Orleans, La., May 6-9, 1968. Also published in the proceedings of the meeting.

1. The Boeing Company, Huntsville, Alabama.
2. Aero-Astroynamics Laboratory, George C. Marshall Space Flight Center, Marshall Space Flight Center, Alabama.

## ATMOSPHERIC STATISTICS FOR AEROSPACE VEHICLE DESIGN, MISSION PLANNING AND OPERATIONS

By Orvel E. Smith, Lee W. Falls,  
and S. Clark Brown

### ABSTRACT

The concept of exposure period probability and calculated risk is used to illustrate the application of ground wind statistics for aerospace vehicle design and operational problems. The concept is extended to include winds-aloft statistics to determine the probability of i-favorable launch opportunities in j-periods for mission planning purposes for vehicles with known or assumed winds-aloft launch constraints. The statistical methods are illustrated by two data samples.

These samples are hourly peak surface winds and eight years of serially completed winds aloft records for Cape Kennedy, Florida.

---

Presented at the Third National Conference on Aerospace Meteorology, New Orleans, La., May 6-9, 1968. Also published in the proceedings of the meeting.

## IONOSPHERE ELECTRON DENSITY AND TEMPERATURE VARIATIONS DURING A DAY IN JANUARY

By William T. Roberts

### ABSTRACT

On 24 January 1967, a series of six thermosphere probes was launched at Cape Kennedy to measure the diurnal variations in density and temperature of constituents in the upper atmosphere. In addition to the omegatron mass spectrometer which measured the molecular nitrogen, a Langmuir probe yielded data on the density and temperature of ionospheric electrons.

Along with the probe data Thompson scatter measurements of the electron and ion temperatures made on this day by the Millstone Hill Radar Facility and the Jicamarca Radar Observatory will be included and compared. Data obtained from the local swept-frequency ionosonde have also provided data on the bottomside ionospheric profile and these data will be used to study the state of the ionosphere at the particular time of each launch.

It is shown that the electron temperature peak occurs at a later time than expected, possibly due to a sudden increase in the magnetic field index during the latter part of the day. Strongly enough, the measured temperatures seem to indicate a slight decrease at about 2:00 p. m. and a later large increase at around 6:00 p. m. The Millstone Hill data tend to bear out the morning peak but, on the other hand, clearly indicate a temperature minimum during the 6:00 p. m. time period. The calculated ion temperatures from the probe data agree very well with the Jicamarca Radar ion temperature measurements, but

are much higher than the Millstone Hill ion temperatures in all cases.

---

Presented at the Third National Conference on Aerospace Meteorology, New Orleans, La., May 6-9, 1968. Also published in the proceedings of the meeting.

## WHERE ARE WE GOING IN SPACE

By R. W. Gunderson

### ABSTRACT

This presentation gives a review of past achievements, present studies, and future goals of our nation's space program as set forth by various scientific and governmental authorities.

---

Presented at the "Festival of Arts," Northern Montana College, Havre, Montana, May 12, 1968.

## NOISE ELIMINATION BY PIECEWISE CROSS CORRELATION OF PHOTOMETER OUTPUTS

By Fritz R. Krause and Benjamin C. Hablutzel

### ABSTRACT

A piecewise cross-correlation technique has been developed to analyze the outputs of remote detection devices. The purpose of this technique is to eliminate the noise from optical background fluctuations, from transmission fluctuations and from detectors by calculating the instantaneous product of the detector output and a reference signal. Each noise component causes positive and negative oscillations of the instantaneous product and may thus be cancelled by an integration of the instantaneous product. The resultant product mean values will then contain the desired information on the spatial and temporal variation of emission, absorption and scattering processes in the atmosphere.

The piecewise correlation technique differs from previous digital analyses of stationary time series by separating statistical and temporal variations of product mean values. The statistical variations describe the amount of still uncanceled noise. The range of these variations is calculated by determining the frequency band width of the noise from the decrease of an accumulative statistical error with integration time. The temporal variations of the product mean values describe a change in the meteorological boundary conditions. They are indicated by the calculated errors which exceed the range of statistical variations that is expected for the given noise band width. Furthermore, such temporal variations set a level of irreducible noise components since the uncanceled noise cannot be distinguished from the temporal variations of the meteorological boundary.

---

Presented to National Academy of Sciences Committee for Atmospheric Sciences Panel on "Remote Atmospheric Probing," Chicago, May 17, 1968.

## FREE VIBRATION OF A ROTATING BEAM-CONNECTED SPACE STATION

By James L. Milner

### ABSTRACT

The free vibration of a rotating beam-connected space station is analyzed with a mathematical model of the space station which represents the general three-dimensional motion of the various components of the system. The space station is composed of two space modules connected by a flexible beam, and the system is caused to spin in the plane of its orbit in order to produce an artificial gravity environment within the space modules.

The kinetic energy and potential energy of the space station are used to develop a Lagrangian function of the system. Hamilton's principle is used to determine a set of governing equations, and a set of boundary conditions representing a clamped-clamped attachment of the beam to each space module is applied to the ends of the beam. Within the limits of small deflection theory, the motion of the space sta-

tion is shown to be uncoupled into two separate types of motion, one in the plane of rotation and the other perpendicular to the plane of rotation.

An exact solution is obtained for the beam deflection in the plane of rotation. The application of the nonhomogeneous boundary conditions leads to a set of simultaneous equations in the frequency  $p^2$ , from which a characteristic determinant is developed. A procedure to solve for the zeros of the characteristic determinant is programmed for digital solution on the IBM 7094.

Results of the analysis for a given space station design are presented in the form of tables showing the natural frequencies of free vibration of the space station for various spin rates. The effect of the spin rate is shown to be an "apparent" increase in the stiffness of the beam. Mode shapes showing the normalized bending deflection of the beam in its six lowest modes of vibration are presented. By analysis of five special cases of negative values of  $p^2$ , the existence of two rigid body modes with nonzero values of  $p^2$  is demonstrated; and it is shown that the configuration studied has no instabilities for motion in the plane of the orbit.

---

Ph. D. dissertation, June 1968, Virginia Polytechnic Institute.

## DYNAMICAL POLYSYSTEMS AS GENERALIZATIONS OF CONTROL SYSTEMS

By Judsen A. Lovingood

### ABSTRACT

The purpose of this dissertation is to obtain results for dynamical systems that are generalizations of the classical dynamical systems of Birkhoff and that permit the qualitative study of solution behavior of systems of differential equations representing a control process.

---

Ph. D. dissertation, University of Alabama, University, Alabama, June 1968.

## NAVIGATION, GUIDANCE, AND CONTROL WITHIN THE CONTEXT OF OPTIMALITY

By E. D. Geissler and Clyde D. Baker

### ABSTRACT

This presentation discusses a few problems from the fields of navigation, guidance, and control with a special emphasis on the role of optimization theory in the formulation and solution of these problems.

---

Presented as a guest lecture during a short course on Guidance, Control, and Optimization Theory for Aerospace Vehicles University of Alabama, Huntsville, June 7, 1968.

## PREDICTION OF MARTIAN THERMAL ENVIRONMENT

By F. B. Tatona<sup>1</sup>, P. B. Deshpande<sup>1</sup>,  
F. T. Hung<sup>1</sup> and O. H. Vaughan<sup>2</sup>

### ABSTRACT

An analytical technique for predicting the thermal environment of Mars is described. The technique, in the form of a computer program, locates the subsolar point on Mars, calculates the shape factor of a specific point on the Martian surface with respect to the Sun, and then solves the governing radiation and conduction heat transfer equations to yield the Martian surface, subsurface, and atmospheric temperatures. In the analytical model Mars is treated as a smooth two-layer composite sphere. The Martian atmosphere is represented by a multi-layer stationary gas model. The technique is self-sufficient in that it can be used to predict the temperature at a specific planetographic latitude and longitude in terms of Earth time without use of astronomical tables. Predicted surface temperature-time histories are presented and compared with the observations of Sinton and Strong. Predicted atmospheric temperature-time histories and temperature-altitude profiles are also presented.

---

Presented at the AIAA 3rd Thermophysics Conference, Los Angeles, California, June 24-26, 1968.

1. Northrop-Nortronics, Huntsville, Alabama.
2. Aero-Astroynamics Laboratory, George C. Marshall Space Flight Center, Marshall Space Flight Center, Alabama.

## SUMMARIES - DISCUSSION OF RESEARCH PERFORMED IN AERO-ASTRODYNAMICS LABORATORY, MARSHALL SPACE FLIGHT CENTER

By J. R. Redus

### ABSTRACT

This paper summarizes the current status of research on space vehicle flight control systems performed within the Laboratory under OART sponsorship. Particular emphasis was on ATM control moment gyro system investigations, C-minimax control theory development and application, and statistical optimal control research performed under contract by Honeywell and Douglas.

---

Presented at the "NASA Intercenter meeting on Space Vehicle Automatic Control System Research and Technology," Jet Propulsion Laboratory, Pasadena, California, July 8-9, 1968.

## HIGH-ALTITUDE WIND MEASUREMENTS FROM ROCKET EXHAUST NOISE

By W. W. Bushman<sup>1</sup>, G. R. Carignan<sup>1</sup>,  
G. M. Kakli<sup>1</sup> and O. E. Smith<sup>2</sup>

### ABSTRACT

A new technique for measuring altitude profiles of atmospheric winds has been developed. The technique, which involves an analysis of the exhaust noise

of large rockets, has yielded wind data from the ground to altitudes as high as 85 km. The results obtained to date indicate that wind profiles are of sufficient accuracy to be meteorologically useful.

---

Published in *Journal of Geophysical Research, Space Physics*, Volume 73, Number 15, August 1968.

1. Space Sciences Laboratory, University of Michigan, Ann Arbor, Michigan, 48105.
2. Aero-Astroynamics Laboratory, George C. Marshall Space Flight Center, Marshall Space Flight Center, Alabama.

## APPLICATION OF C-MINIMAX OPTIMAL CONTROL THEORY TO FLIGHT CONTROL PROBLEMS

By J. R. Redus<sup>1</sup> and C. D. Johnson<sup>2</sup>

### ABSTRACT

In many realistic optimal control problems, the performance criteria most meaningful to the designer are the minimization of the "peak value" of some controlled variable, over some given interval of time. Unfortunately, the ordinary techniques of classical and modern optimal control theory, such as the Pontryagin Maximum Principle, will not accommodate practical performance indexes of the "minimum peak value" (minimax) type. This paper describes the application of a relatively new theory of minimax control (called C-Minimax control theory) to two important minimax problems associated with the control and guidance of launch vehicles and spacecraft. The performance of the theoretically exact minimax optimal controller is compared with the performance obtained from several (suboptimal) controllers designed by more conventional trial-and-error techniques.

---

Presented at the AIAA Guidance, Control, and Flight Dynamics Conference, Pasadena, California, August 12-14, 1968.

1. Aero-Astroynamics Laboratory, George C. Marshall Space Flight Center, NASA, Marshall Space Flight Center, Alabama.
2. University of Alabama, Huntsville, Alabama.

## LOAD-REDUCING FLIGHT CONTROL SYSTEMS FOR THE SATURN V WITH VARIOUS PAYLOADS

By J. M. Livingston, Jr. and J. R. Redus

### ABSTRACT

When a basic launch vehicle is employed for disparate missions and payloads, a wide range of structural loading will occur. If excessive wind-induced loading is encountered for a particular vehicle/payload/mission combination, modification of the flight control system may be the most attractive among the alternative solutions. The factors involved in the responsible design of a load-relief flight controller are examined in detail, and it is shown by discussion and example that there exists no best system for all situations. The utility and benefits of the design approach discussed in this paper are illustrated by the analysis of load-relief controllers for two widely different applications of the Saturn V launch vehicle, namely, the Saturn V/Apollo mission and the Saturn V/Voyager mission, now defunct.

---

Presented at the "AIAA Guidance, Control, and Flight Dynamics Conference," Pasadena, California, August 12-14, 1968.

## A METHOD OF TRAJECTORY ANALYSIS WITH MULTI-MISSION CAPABILITY AND GUIDANCE APPLICATION

By R. R. Burrows<sup>1</sup> and G. A. McDaniel<sup>2</sup>

### ABSTRACT

A new method of trajectory synthesis suitable for variable point mass, constant thrust, fixed staging time vehicles operating in a vacuum has been developed which performs a large variety of missions in a near time optimal manner. Introducing linear time-varying multipliers in place of control angles in the differential equations of motion and representing the gravitational term by a Taylor series in time allows explicit integrals for position and velocity to be obtained as functions of coefficients associated with the linear multipliers. The coefficients are varied iteratively by a form of the generalized secant method until a set is found solving the calculus-of-variations two-point boundary value problem. Numerical solutions are found rapidly enough to allow the possibility of real time on-board guidance. Computer simulation using Saturn class upper stage vehicles will illustrate the method both as a trajectory tool and as a guidance scheme.

Presented at the "AIAA Guidance, Control, and Flight Dynamics Conference," Pasadena, California, August 12-14, 1968.

1. Aero-Astroynamics Laboratory, George C. Marshall Space Flight Center, NASA, Marshall Space Flight Center, Alabama.
2. Lockheed Missiles and Space Company, Huntsville, Alabama.

## ON STABILITY OVER A FINITE INTERVAL

By R. W. Gunderson

### ABSTRACT

This paper examines the vector differential equation  $\dot{x} = f(x, t)$ , where the dot indicates the time

derivative and  $x$  and  $f$  belong to  $R^n$ . Theorems are treated regarding the stability of the system represented by the equation, for various  $t$  and continuous ranges of  $f$ .

Published in IEEE Transactions on Automatic Control, October 1967.

## A CABLE RETRIEVAL TECHNIQUE FOR AN ORBITING ASTRONOMICAL OBSERVATORY

By H. J. Horn, H. E. Worley  
and G. F. McDonough<sup>1</sup>

### ABSTRACT

Retrieval of a separate module tethered to an orbiting space station imposes challenging problems: (1) conservation of angular momentum requires that angular velocity increase as separation distance decreases and (2) cable forces during retrieval produce rotations of the bodies. The removal of an initial angular momentum of the two-body system requires propulsive means; however, the relative displacements can be removed and docking ports aligned by using multiple cables, or the equivalent, and controlling the tension in each cable. The paper analyzes an approach which removes relative angular velocities while keeping the closing velocity within acceptable docking limits.

Presented at the AIAA Guidance, Control and Flight Dynamics Conference, Pasadena, California, August 12-14, 1968.

1. Formerly affiliated with Aero-Astroynamics Laboratory, now with Apollo Applications Systems Engineering and Integration Office, George C. Marshall Space Flight Center, Marshall Space Flight Center, Alabama.